7 February 2014 | $10

Science

2013 VISUALIZATION CHALLENGE

AAAS

CONTENTS continued >>

page 596

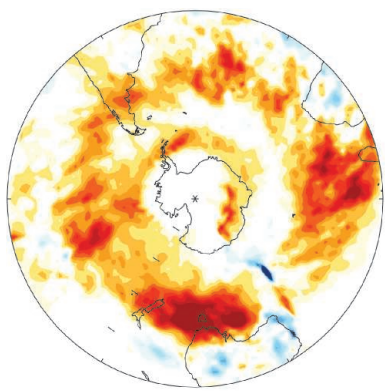

pages 588 & 641

ON THE WEB THIS WEEK

>> *Science* Podcast
This week's show features a study on tracing autism's developmental roots and a roundup of stories from our daily news site.

>> Find More Online
Check out the latest in a series of Perspectives on Challenges in Climate Science at **www.sciencemag.org/extra/climate**.

COVER

Water swirls in a vortex above two millimeter-sized coral polyps (pink and purple) in "Invisible Coral Flows," which won first place in the photography category of the 2013 *Science*/NSF International Science & Engineering Visualization Challenge. The vortex, driven by the polyps' wafting cilia, helps the coral draw in nutrients and sweep away waste products. The winning entries are featured in a special section starting on page 599 and at http://scim.ag/vischall2013.

Photo: Vicente I. Fernandez, Orr H. Shapiro, Melissa S. Garren, Assaf Vardi, Roman Stocker/Massachusetts Institute of Technology

DEPARTMENTS

RESEARCH ARTICLE

REPORTS

pages 623 & 645

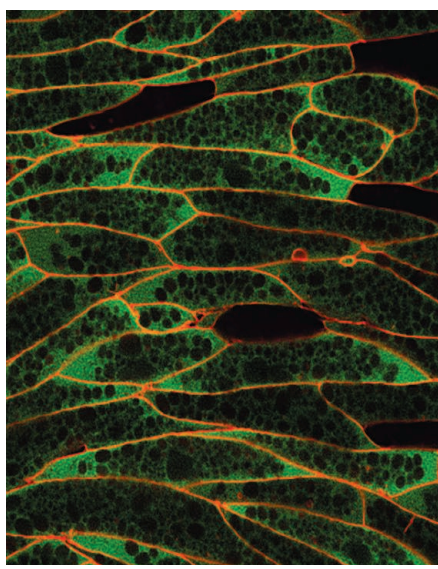

page 649

CREDIT (BOTTOM): ASAKO SHINDO/JOHN WALLINGFORD

SCIENCE (ISSN 0036-8075) is published weekly on Friday, except the last week in December, by the American Association for the Advancement of Science, 1200 New York Avenue, NW, Washington, DC 20005. Periodicals Mail postage (publication No. 484460) paid at Washington, DC, and additional mailing offices. Domestic individual membership and subscription (51 issues): $149 ($74 allocated to subscription). Domestic institutional subscription (51 issues): $990; Foreign postage extra: Mexico, Caribbean (surface mail) $55; other countries (air assist delivery) $85. First class, airmail, student, and emeritus rates on request. Canadian rates with GST available upon request, GST #1254 88122. Publications Mail Agreement Number 1069624. **Printed in the U.S.A.**

Change of address: Allow 4 weeks, giving old and new addresses and 8-digit account number. **Postmaster:** Send change of address to AAAS, P.O. Box 96178, Washington, DC 20090–6178. **Single-copy sales:** $10.00 current issue, $15.00 back issue prepaid includes surface postage; bulk rates on request. **Authorization to photocopy** material for internal or personal use under circumstances not falling within the fair use provisions of the Copyright Act is granted by AAAS to libraries and other users registered with the Copyright Clearance Center (CCC) Transactional Reporting Service, provided that $30.00 per article is paid directly to CCC, 222 Rosewood Drive, Danvers, MA 01923. The identification code for *Science* is 0036-8075. *Science* is indexed in the *Reader's Guide to Periodical Literature* and in several specialized indexes.

Observing the Upturn

When two parallel conducting wires are separated by a small insulating barrier, a current in one wire can generate a net charge displacement in the other by virtue of electron-electron interactions. Some of the models for this process predict a nonmonotonic temperature dependence of the resulting Coulomb drag voltage, with an upturn occurring at a certain low temperature T^*. **Laroche *et al.*** (p. 631, published online 23 January) observed this upturn in a pair of vertically integrated quantum wires separated by a 15-nanometer-wide barrier.

Curving Crystals

When a material with a different set of lattice parameters is grown on the surface of a crystal of a second material, the stresses at the interface can affect the growing crystal. **Meng *et al.*** (p. 634) studied the growth of colloidal crystals on top of a curved water droplet. Owing to the elastic stress caused by the bending of the crystal, strong distortions occurred in the growing crystal, but, nonetheless, large single-crystalline domains with no topological defects were formed.

Predictable Behavior

Few internally forced large-scale atmospheric circulation patterns exhibit periodic behavior, and those that do are centered in the tropics. Identifying these periodic processes is important for understanding the dynamics of weather. **Thompson and Barnes** (p. 641) report the discovery of a 20- to 30-day periodicity in the atmospheric circulation in the Southern Hemisphere. The oscillation could potentially drive large-scale climate variability throughout much of the mid-latitude Southern Hemisphere.

LEAFY Evolution

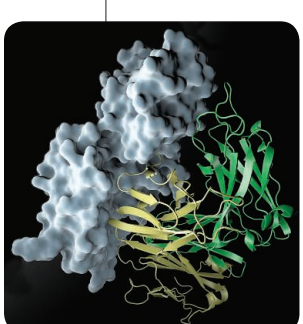

It is generally believed that redundancy across gene copies allows for the evolution of novel function in proteins. However, it is less clear how single-copy genes with crucial function may evolve. **Sayou *et al.*** (p. 645, published online 16 January; see the Perspective by **Kovach and Lamb**) examined the evolution of the essential plant transcription factor LEAFY, which is generally found as a single-copy gene. LEAFY homologs in taxa representing the major evolutionary branches of the land plants and algae exhibited three classes of LEAFY binding sites. Structural analysis identified amino acid changes in the proteins, that were responsible for contacts with specific DNA motifs and allowed the likely effects of specific amino acid changes over the evolution of land plants to be resolved.

CREDITS (TOP TO BOTTOM): ISAAC LARSEN; CHRISTINA CORBACI AND RAJESH K. GROVER

Weathering Heights

The production of soil is the result of chemical weathering of rocks and minerals. In regions where tectonic uplift brings fresh material to Earth's surface, erosion and weathering can accelerate. Using chemical tracers, **Larsen *et al.*** (p. 637, published online 16 January; see the Perspective by **Heimsath**) measured soil production rates of over 2 millimeters per year in New Zealand's Southern Alps, which are some of the fastest uplifting mountains in the world. Because chemical weathering consumes CO_2, these rapid rates may over time influence global climate.

Sculpting Actomyosin

The sculpting of embryos during development involves coordinated movement of cells in large groups. How actomyosin is controlled during such collective cell movement remains poorly understood. Working with developing *Xenopus* mesoderm, **Shindo and Wallingford** (p. 649) found that planar cell polarity proteins and septins interface with the actomyosin machinery to control collective cell movement.

Easy M

Our immune systems can produce a vastly diverse repertoire of antibody molecules that each recognize and bind to a specific foreign antigen via a hypervariable region. However, there are a few bacterial antigens—such as Protein A, Protein G, and Protein L—that instead bind to the antibody's conserved regions and can bind to a large number of different antibodies. These high-affinity broad-spectrum antibody-binding properties have been widely exploited both in the laboratory and in industry for purifying, immobilizing, and detecting antibodies. **Grover *et al.*** (p. 656) have now identified Protein M found on the surface of human mycoplasma, which displays even broader antibody-binding specificity. The crystal structure of Protein M revealed how Protein-M binding blocks the antibody's antigen binding site. This mechanism may be exploited by mycoplasma to escape the humoral immune response.

Causing Chloride Changes

Because intracellular chloride concentrations largely determine the direction and magnitude of current flow through $GABA_A$ channels, the stability of intracellular chloride concentration is important to maintain consistent synaptic inhibition. **Glykys *et al.*** (p. 670) examined the mechanisms by which chloride gradients in neurons are established, using chloride imaging with transgenically expressed clomeleon dye. Surprisingly, intracellular chloride was not primarily determined by transporters. Instead, subcellular gradients of immobile anions generated inverse chloride gradients.

The Switch That Doesn't

In mammals, a class of neurons in the brain normally switches from excitatory to inhibitory functions at birth. **Tyzio *et al.*** (p. 675; see the Perspective by **Zimmerman and Connors**) studied how these neurons function in rat and mouse models of autism. The results show that oxytocin normally accelerates the switch in function, but in these two animal models, the switch fails. The dysfunction could be replicated in normal animals using an oxytocin receptor antagonist.

Additional summaries

Stochasticity and Cell Fate

Stochastic mechanisms can diversify cell fates in nervous systems. In the *Drosophila* retina, the stochastic distribution of color-sensing photoreceptors is controlled by the random, On/Off expression of the Spineless transcriptional regulator. **Johnston and Desplan** (p. 661) found that each allele of *spineless* makes an intrinsically random expression choice controlled by an enhancer and two silencer DNA elements acting at long range. *spineless* alleles communicate between chromosomes using activating and repressing mechanisms to determine the frequency of expression and coordinate expression state. These findings suggest critical roles for intrinsically random expression decisions and interchromosomal communication in stochastic cell fate specification.

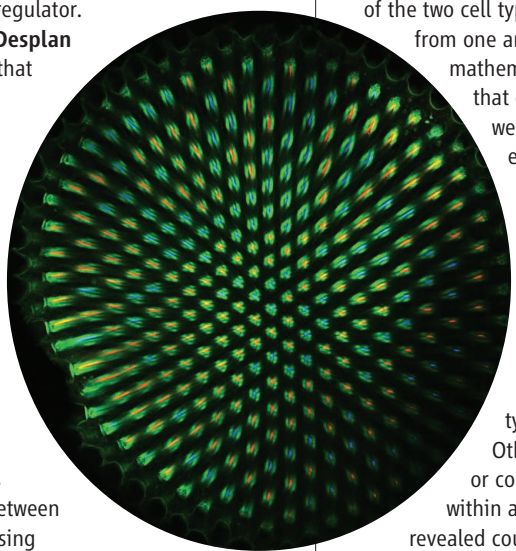

CREDIT: ROBERT J. JOHNSTON

The Message in the Medium

What is the point of autocrine signaling in which a cell produces a signal that activates receptors on its own cell surface? An internal signal seems simpler, unless there is value to allowing neighboring cells to know what other cells are up to. **Youk and Lim** (p. 628; see the Perspective by **Lee and You**) explored the broad range of signaling outcomes that can result in a system in which some yeast cells could secrete and sense a signal whereas others could only sense signals from their neighbors. The cells were engineered so that the response of the two cell types could be distinguished from one another. Experiments and mathematical modeling showed that depending on how circuits were constructed—for example, how much receptor was present, how the signal molecule was degraded, the presence of feedback, the density of the cell culture, and so on—a range of behaviors was possible: Some conditions favored activation of one type of cell over another. Others altered the timing or consistency of the response within a population. The principles revealed could also be used in other biological contexts or in the design of synthetic biological cell systems with desired regulatory properties.

Interacting and Topological

Topological insulators (TIs), which have a bandgap and a robust conducting surface state protected by time-reversal symmetry, are typically materials with weak electron-electron interaction and are well-described by band theory. A major experimental goal has been to observe such symmetry-protected topological (SPT) phases in interacting systems. **Wang *et al.*** (p. 629) used a theoretical approach to classify SPT phases of interacting fermions in three dimensions and found six other phases in addition to the noninteracting ones. The results lay the groundwork for future microscopic models and inform the experimental search for such materials.

Viral ESCRT

The ESCRT (Endosomal Sorting Complex Required for Transport) protein complex plays a role in budding into multivesicular bodies, cytokinesis, and HIV budding, but the details of how the ESCRTs facilitate viral budding are unclear. Now, using high-resolution light and electron microscopical imaging techniques, **Van Engelenburg *et al.*** (p. 653, published online 16 January) dissect the role for ESCRT proteins in HIV budding. The findings suggest that the ESCRT machinery required for the scission of HIV particles from infected cells is located within the core of the virus particle and not, as might have been expected based on previous work, on the cellular side of the membrane scission event involved in viral budding.

From Channel to Sensor

The coupling between voltage-activated calcium channels and calcium sensors of exocytosis on synaptic vesicles is a key factor that determines the timing and efficiency of transmitter release. It is still largely unclear how tight this coupling is at mature synapses in the central nervous system. **Vyleta and Jonas** (p. 665) found that mossy fiber boutons contain high concentrations of endogenous calcium buffers that normally limit the amount of calcium that reaches the calcium sensor responsible for neurotransmitter release. As a consequence, the calcium signal available to trigger release is small for the initial action potential. However, after high-frequency stimulation, the endogenous calcium buffer binds calcium and is less able to buffer calcium entry, which allows more calcium to reach the calcium sensor, increasing neurotransmitter release and synaptic facilitation.

Phillip A. Sharp is Institute Professor at the Massachusetts Institute of Technology and President of AAAS.

Alan I. Leshner is Chief Executive Officer of AAAS and Executive Publisher of *Science*.

Meeting Global Challenges

EVERY MAJOR CHALLENGE OF MODERN LIFE, SUCH AS ENSURING ENERGY, HEALTH, WATER, OR FOOD security in a sustainable world with a predicted nine billion inhabitants, has complex science and technology (S&T) components and is global in character, even though its expression often involves national idiosyncrasies. Searching for solutions requires that the scientific community operate in fundamentally new ways. How to deal with these complex global issues is a major focus of this year's annual meeting of the American Association for the Advancement of Science (AAAS), whose theme is *Meeting Global Challenges: Discovery and Innovation.*

Developing effective solutions requires converging approaches, such as the integration of knowledge from the life, physical, social, and economic sciences and engineering. Moreover, the search for solutions needs to draw upon the talents and innovative ideas of scientists, engineers, and societal leaders worldwide to overcome traditional and nationalistic paradigms that have so far been inadequate to meeting these challenges. Unfortunately, neither S&T funders nor performing institutions are well organized, nor are members of the S&T community well trained for working in these ways. That will have to change.

Education and training programs must be developed in what has come to be called "convergence science": the integration of life, physical, and engineering sciences, so that S&T practitioners have a knowledge and experience base to participate in the kinds of integrated scientific efforts that are needed. More opportunities are also needed for scientists to collaborate in international settings and participate in global science projects during their training years, so that international collaboration becomes a more natural part of the scientific culture.

Research-performing and training institutions, such as universities and research institutes, have critical roles to play. Not only is it essential that they develop appropriate training programs and help stimulate multidisciplinary international collaborations, but they also need to reconsider some traditional incentive structures. Performing institutions should encourage and reward scientists and engineers for their work in large multidisciplinary, multinational teams. Institutions should also help provide the resources necessary to nurture these types of collaborations.

Fortunately, there is increasing recognition among some science funders of the need for enhanced mechanisms for funding science in a global, multinational fashion. The Heads of International Research Organizations, an aggregation of health research funders from around the world, meets regularly, with the goal of increasing consistency in policies across countries and facilitating global cooperation to tackle major health issues. The Global Research Council has brought together the heads of 70 basic science funding agencies from diverse countries and is working toward harmonizing policies on topics such as research integrity, peer review, and access to data and publications. AAAS has convened a variety of groups to work on bringing greater coherence and consistency to policies and practices across countries, primarily at the regional level, such as in East Africa and the Asia-Pacific region.

But harmonizing science policies across countries and their funding agencies and taking advantage of collaborative opportunities will not be sufficient. The work products from these multinational, multidisciplinary teams must be rapidly translated into practical solutions. To facilitate that translation, scientists and engineers must engage with business, cultural, and political leaders. Further, the adoption of national policies that address global challenges is dependent on support by an informed citizenry and public debate stimulated by discussions with policy-makers around the world. The international multidisciplinary AAAS Annual Meeting provides forums for such discussions and should produce an array of practical strategies and solutions to bring the full power of science to bear on world challenges.

– Phillip A. Sharp and Alan I. Leshner

10.1126/science.1250725

Published by AAAS

EDITED BY SACHA VIGNIERI AND JAKE YESTON

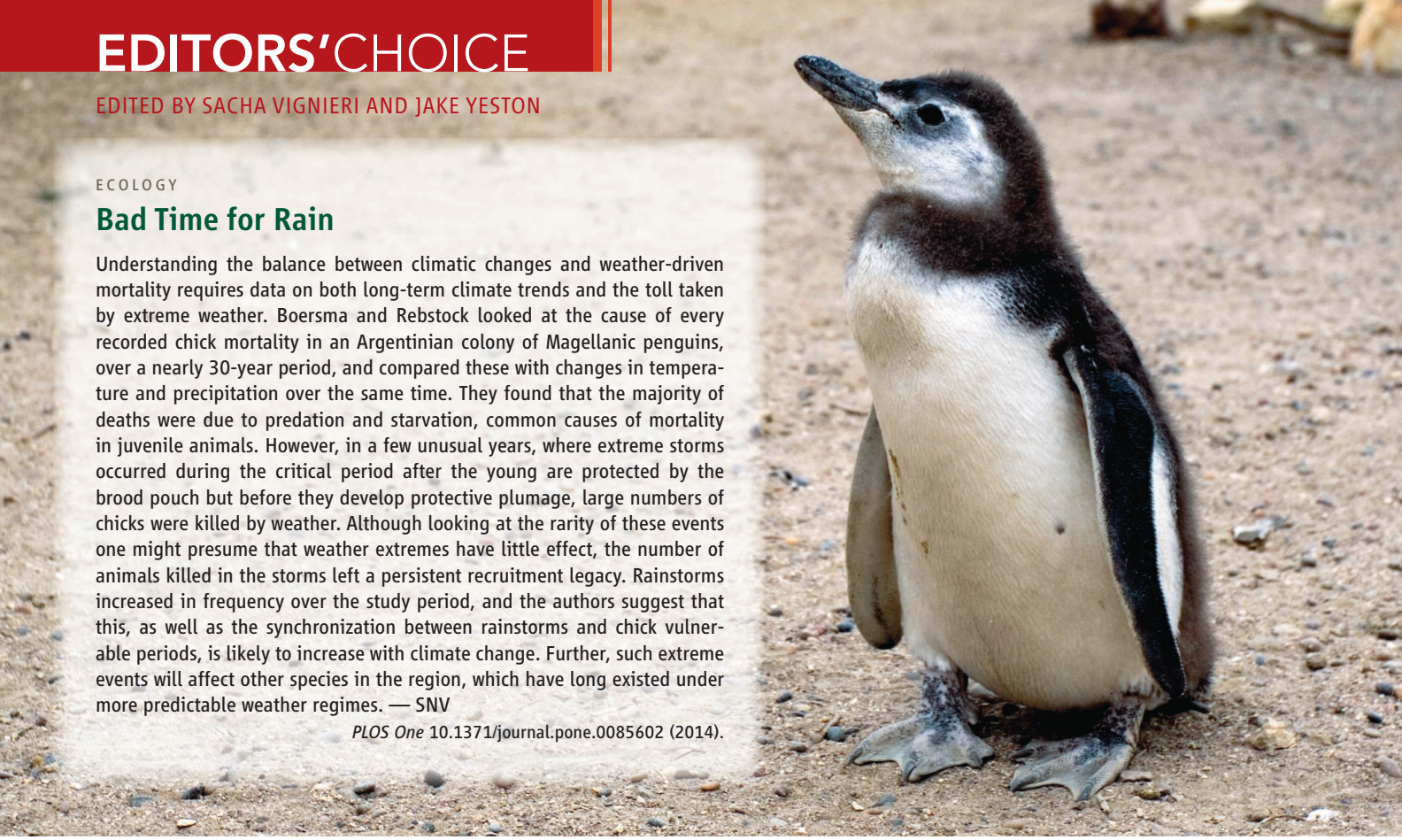

ECOLOGY

Bad Time for Rain

Understanding the balance between climatic changes and weather-driven mortality requires data on both long-term climate trends and the toll taken by extreme weather. Boersma and Rebstock looked at the cause of every recorded chick mortality in an Argentinian colony of Magellanic penguins, over a nearly 30-year period, and compared these with changes in temperature and precipitation over the same time. They found that the majority of deaths were due to predation and starvation, common causes of mortality in juvenile animals. However, in a few unusual years, where extreme storms occurred during the critical period after the young are protected by the brood pouch but before they develop protective plumage, large numbers of chicks were killed by weather. Although looking at the rarity of these events one might presume that weather extremes have little effect, the number of animals killed in the storms left a persistent recruitment legacy. Rainstorms increased in frequency over the study period, and the authors suggest that this, as well as the synchronization between rainstorms and chick vulnerable periods, is likely to increase with climate change. Further, such extreme events will affect other species in the region, which have long existed under more predictable weather regimes. — SNV

PLOS One 10.1371/journal.pone.0085602 (2014).

GENETICS

The Cost of Protection

African Americans have a three to five times greater risk of developing end-stage kidney disease and twice the risk of dying from heart disease than do individuals of European descent. In addition to socioeconomic factors, genetic factors probably contribute to these differences. Clinical geneticists have focused on two allelic variants of *APOL1* (the gene encoding apolipoprotein L1) called G1 and G2. These alleles confer protection against African sleeping sickness, which may explain why they are common in populations of African descent but rare or absent in other populations.

Two research groups independently examined the effect of the *APOL1* genotype on disease burden in African Americans. Studying chronic kidney disease, Parsa *et al*. found that patients with two copies of G1 or G2 were twice as likely to progress to end-stage disease as those with no or one copy. Ito *et al*. arrived at a similar conclusion in a study of heart disease: Individuals with two copies of G1 or G2 were twice as likely to experience a major adverse cardiovascular event as those with one or no copy. In certain settings, *APOL1* genotyping may help guide treatment decisions. — PAK

N. Engl. J. Med. **369**, 2183 (2013); *Circ. Res*. 10.1161/CIRCRESAHA.114.302347 (2013).

PLANETARY SCIENCE

Shock-Buffering Asteroid

The stereotype of an asteroid as a rigid monolith has been dispelled numerous times when spacecraft have allowed closer inspection: Many of these minor planets look more like fluffy piles of rubble. The second Chinese lunar probe, Chang'E-2, explored the asteroid Toutatis (4179) in a December 2012 flyby, and Zhu *et al.* report evidence that the body has endured repeated impact shocks that were attenuated by compression of its porous regolith. One 800-m crater seen near the south pole of Toutatis (~4.5 km long) implies an impactor of sufficient energy to have shattered a solid asteroid. However, if this collection of material is already fractured, it is more resilient to dramatic impact. The impact energy flows through the body as seismic shaking that resettles the surface and erases smaller craters, which are indeed deficient in number as compared to expectations. Further support for seismic resurfacing may lie in boulders observed on the "neck" of Toutatis, where such larger fragments experiencing shaking would eventually rattle to the surface. The authors believe that these also imply that the bi-lobed body is the result of a low-velocity sticking collision that initially damaged the impact surface and then slowly excavated the boulders. — MMM

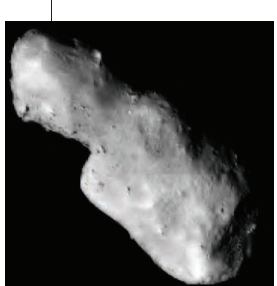

Geophys. Res. Lett. 10.1002/2013GL058914 (2013).

MOLECULAR BIOLOGY

Glassy Cytoplasm

Bacteria lack motor proteins such as myosins, kinesins, and dyneins, and molecular transport and cytoskeletal mixing are thought to rely on diffusion. Using single-molecule tracking, Parry *et al.* found that the mobility of protein filaments, large granules, and plasmids was higher in metabolically active cells. They developed a probe, based on a GFP-labeled self-assembling reovirus protein, in which size could be tuned by protein expression. Metabolically dependent motility of the probe was dependent on size, with particles of about 30 nm and higher showing significantly higher mean square displacements in metabolically active cells. The motion of large particles was characteristic of movement in a glass-forming liquid approaching the glass transition. The distribution of displacements was non-Gaussian, the system non-ergodic, and the cytoplasm displayed dynamic heterogeneity with regions of both high and low particle motility. Metabolic activity fluidized the cytoplasm so that large particles could escape a caged environment. As a result, a higher fraction of

Published by AAAS

particles showed large displacements in active cells. These properties of the bacterial cytoplasm need to be taken into account in understanding bacterial physiology, particularly transitions between dormancy and growth. — VV

Cell 10.1016/j.cell.2013.11.028 (2014).

MOLECULAR BIOLOGY

Protecting Mitochondria

The power plant of the cell, the mitochondrion, can be a hostile environment in which proteins or the whole organelle can become damaged. To prevent further disruption of the cell, whole damaged mitochondria can be engulfed and degraded by autophagosomes, and the failure of this process may cause neurodegeneration. The *Parkin* and *PINK1* genes—mutations of which are linked to neurodegenerative Parkinson's disease—function in this process. McLelland *et al.* describe a less dramatic protection mechanism in which proteins damaged by overproduction of reactive oxygen species in the mitochondria are carted in membrane vesicles to lysosomes. Like the wholesale remodeling of mitochondria themselves, this vesicle-mediated quality-control mechanism required the PINK1 and Parkin proteins. The authors propose that the protective actions of Parkin and PINK1 may play out in two stages: a more rapid one in which damaged proteins can be selectively removed in vesicles, and, in cases where damage is advanced, the recycling of the full organelles by mitophagy. — LBR

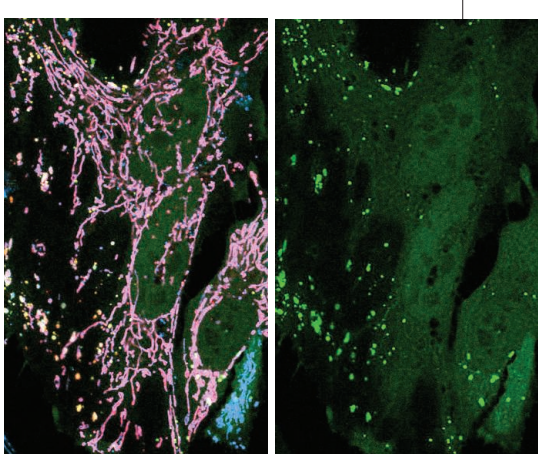

CREDIT: G. MCLELLAND *ET AL.*, *THE EMBO JOURNAL* (20 JANUARY 2014) © 2014 WILEY-VCH VERLAG GMBH & CO. KGAA. REPRODUCED WITH PERMISSION.

EMBO J. 10.1002/embj.201385902 (2014).

CHEMISTRY

Needle from a Haystack

A current challenge in nanoscale science is the selective assembly of large quantities of particles into ordered arrays. Abécassis *et al.* consider the case of colloidal semiconducting nanoplatelets, which can be considered a two-dimensional analog of anisotropic nanorods. Solutions of a single population of particles coated with oleic acid were dispersed in hexane, and exposure to a few drops of ethanol, acting as an antisolvent, led to the formation of superparticles up to 20 μm in length. These initially showed a sausage-chain structure where sections 10 to 20 units wide were joined together with defect areas much narrower in size, but these defects disappeared on aging. The authors further examined the superparticles by depositing them on a substrate, causing the plane of the platelets to lie perpendicular to the surface. In testing the optical properties, they found that the superparticles emit strongly polarized light in a direction perpendicular to the long axis. — MSL

Nano Lett. 10.1021/nl4039746 (2014).

EDUCATION

Time Well Spent?

As science, technology, engineering, and mathematics (STEM) instruction begins to shift to a more active approach, how do we best collect and analyze data on how teachers and students spend their classroom time? Smith *et al.* have developed the Classroom Observation Protocol for Undergraduate STEM, or COPUS, as a standardized protocol for collecting data on STEM teaching practices. Development spanned 2 years and involved dozens of iterations and testing scenarios designed and executed by science education specialists. COPUS works by documenting classroom behavior at 2-min intervals during a class session through the use of 25 codes in two categories: "what the students are doing" and "what the instructor is doing." The benefit of this system is that observers recording the behaviors are not required to make judgments about teaching quality, and analysis of classroom activities can be summarized for the teacher in the form of a pie chart. Moreover, minimal training is needed in order for COPUS to be used effectively. The protocol should enable faculty members to characterize the general state of teaching and learning in their departments, provide feedback to colleagues interested in assessing how their time with students is being spent, and, perhaps most importantly, identify areas where faculty professional development is needed. — MM

CBE Life Sci. Educ. **12**, 618 (2013).

Published by AAAS

AROUND THE WORLD

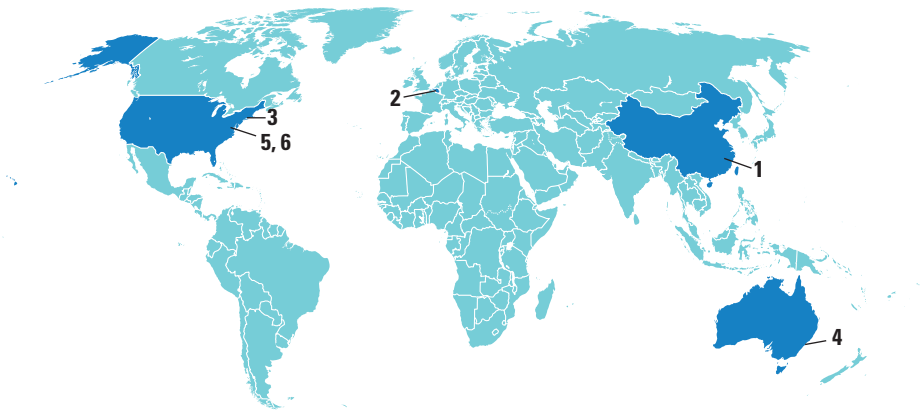

Jiangxi province, China **1**

Threat of H10N8 Surfaces

China's gallery of bird flu rogues continues to grow—and the latest addition is making experts shudder. So far only two human cases of H10N8 have been reported, but health officials warn that the strain has pandemic potential.

The virus was first isolated in December in southeastern Jiangxi province from a 73-year-old woman who succumbed to the virus. In a 5 February report in *The Lancet*, Chinese researchers note that the novel strain binds to avianlike receptors in human lungs—a feature thought to make H5N1 bird flu so deadly—and has a mutation that could make it highly infectious in people. A second H10N8 case in Jiangxi last week "is of great concern," says team member Mingbin Liu of the Nanchang Center for Disease Control and Prevention, in that it means "the H10N8 virus has continued to circulate and may cause more human infections."

The unsettling development comes as infections from another new strain, H7N9, are piling up in China.

Brussels **2**

Researchers Lobby For Data Access

Proposed E.U. laws protecting data privacy threaten essential health research, a coalition of more than 40 European science organizations wrote in a 29 January statement. Led by the U.K. Wellcome Trust, the organizations have launched a lobbying effort that urges E.U. lawmakers to reject proposed rules limiting researchers' access to patient data.

The proposal would, in many cases, flatly prohibit the use of personal data in research without specific patient consent. An earlier version allowed some access to data without specific consent if the project received approval from an ethics committee and strict confidentiality safeguards were in place. But amendments introduced in October narrowed the exceptions for researchers. If those stand, the groups argue, they would make valuable epidemiology and public health research impossible. The European Parliament is expected to vote on the measure in the spring, and it must also receive approval from the Council of Ministers.

New Haven, Connecticut **3**

Drug Company Joins With Yale to Share Data

In an unusual partnership, Johnson & Johnson will work with Yale University to make raw data from its clinical trials available to researchers. The company will share its data with the Yale University Open Data Access Project (YODA), which will in turn "review requests from investigators and physicians seeking access to anonymized clinical trials data," the company wrote in a press release last week. YODA's team will then decide which researchers can access the information for their own studies.

The company's pharmaceutical products include pills for acid reflux, schizophrenia, pain, and birth control, among many others. The data to be shared with YODA go well beyond study design and results, and include de-identified information on every volunteer. YODA is led by Harlan Krumholz, a cardiologist who has long pressed for more data access in clinical research. **http://scim.ag/JJshares**

Dump site. Dredge spoils may threaten sensitive coral reefs off Abbot Point (*above*).

Sydney, Australia **4**

Reef Sludge-Dumping Approved

The Australian agency that manages the Great Barrier Reef last week paved the way for development of one of the world's largest coal ports off the Queensland coast by approving the dumping of up to 3 million cubic meters of dredge spoils inside the UNESCO World Heritage Site. Scientists predict the project will harm the sensitive ecosystem by smothering corals and seagrasses and exposing marine mammals and other organisms to toxic substances.

After federal Environment Minister Greg Hunt signed off on the venture last month, critics had hoped the agency would take a dimmer view. Roughly 240 Australian scientists have signed a letter of protest, which points to environmental damage from the 2010 to 2011 dredging south of Gladstone Harbor. In a 31 January press statement, Bruce Elliot, the Marine Park Authority's biodiversity manager, said that the authority acknowledges the concerns of scientists and would support an alternative option should North Queensland Bulk Ports Corp. propose one. **http://scim.ag/_sludge** >>

AAAS 2014:
Science's news team will be reporting from this year's AAAS Meeting in Chicago. For breaking news, live chats, and a new video series—"What Is the Coolest Science Fact You Know?"—check out our daily coverage at **http://scim.ag/AAAS14**

Published by AAAS

>>AROUND THE WORLD

Washington, D.C. **5**

Farm Bill Boosts Research, Creates Foundation for USDA

Food and agricultural research advocates are celebrating the passage of the long-delayed "Farm Bill," which will provide $600 million for science over 5 years and kick-start a new fundraising campaign for research. The controversial $956 billion bill, which the U.S. Senate approved this week, sets national agricultural policy while providing nutritional benefits to the poor and subsidies to farmers.

The bill makes several changes: Research on so-called specialty crops, including fruits, nuts, and vegetables, will receive $80 million annually over 5 years—a 74% increase—while a biofuels program previously worth $23.6 million a year has been reduced to a total of $12 million. It also creates a nonprofit Foundation for Food and Agriculture Research as a new way to raise funds for science. The foundation is modeled on similar charities that benefit the National Institutes of Health and the Centers for Disease Control and Prevention. It will get up to $200 million in federal funds, to be matched by outside grants. **http://scim.ag/farmbill14**

Bethesda, Maryland **6**

NIH, 10 Drug Companies Partner to Study Diseases

The National Institutes of Health (NIH) this week unveiled what it called an unprecedented partnership with 10 drug companies aimed at finding new treatments for Alzheimer's, diabetes, rheumatoid arthritis, and lupus. NIH and the companies, including giants such as Eli Lilly and Sanofi, will each provide about half of the $230 million in total funding over 5 years to the Accelerating Medicines Partnership. Patient groups and the Foundation for the NIH will also participate. They will build on recent discoveries of genes that predispose to disease by pinning down which proteins involved are most promising as drug targets. "[T]his challenge is beyond the scope of any one of us and it's time to work together," said NIH Director Francis Collins in a statement.

A set of pilot projects will openly share data with the research community. One will build a Web portal for genetic and clinical data on patients with type 2 diabetes. Another will analyze tissue samples for insight into the biology behind arthritis and lupus. **http://scim.ag/AccelMed**

Meager Migration

Scientists in Mexico City last week described the dwindling of a natural wonder: Monarch butterfly colonies now cover just 0.67 hectares of Mexican forest—the smallest swath of land since data collection began in 1993 and a 44% drop from last year's previous record low. The paltry figure highlights the uncertain fate of the monarch's 4000-kilometer migration between their U.S. and Canada breeding grounds and their winter home in Mexico.

Experts lay much of the blame on the decline of milkweed plants in the U.S. Midwest. Mexico must "energetically demand" that the U.S. reform its agricultural policy with an eye toward preserving milkweed, says Omar Vidal, director general of WWF Mexico, which administers the winter colony count. Meanwhile, midwesterners attempting to help the monarchs often plant the wrong milkweed variety, the tropical *Asclepias curassavica*, which doesn't die back in winter and may eliminate the monarchs' need to migrate. http://scim.ag/_monarch

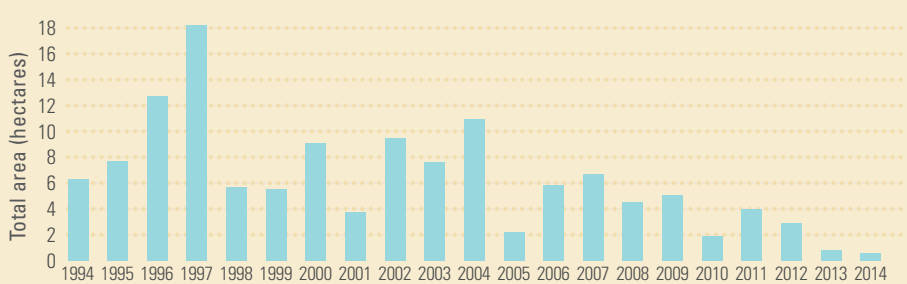

NEWSMAKERS

Japan Prize Honors Research On Hardware and Histones


Suematsu

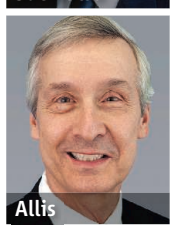
Allis

The 2014 Japan Prizes, announced last week, recognize advances in semiconductors and epigenetics. The electronics, information, and communication prize went to **Yasuharu Suematsu**, an honorary professor at the Tokyo Institute of Technology, for conceiving and developing the semiconductor lasers at the heart of the optical fiber networks that now carry voice and data communications around the globe. "The internet would not have been possible without this technology," said computer scientist Hideo Miyahara, chair of the communication prize selection committee.

David Allis, of Rockefeller University in New York City, will receive the life science prize for showing how histones, proteins that form a core around which DNA winds in cells, contribute to the regulation of gene expression. Each laureate will receive a certificate, a commemorative gold medal, and approximately $481,000 at a ceremony in Tokyo in April. The Japan Prize categories change each year within broadly defined fields of science and technology. **http://scim.ag/Japan14**

BY THE NUMBERS

20 million + Global cancer cases predicted to occur in 2025, up from an estimated 14.1 million in 2012, largely due to adoption of an industrialized country lifestyle, according to a World Health Organization report.

$6.1 billion Result of Columbia University's 2006 to 2013 capital campaign, which set a new record for Ivy League fundraising.

CREDITS (TOP TO BOTTOM): THE JAPAN PRIZE FOUNDATION (2); RICHARD ELLIS/ALAMY; (CHART SOURCE) ADAPTED FROM WWF

Published by AAAS

Random Sample

The Nose Behind the Data

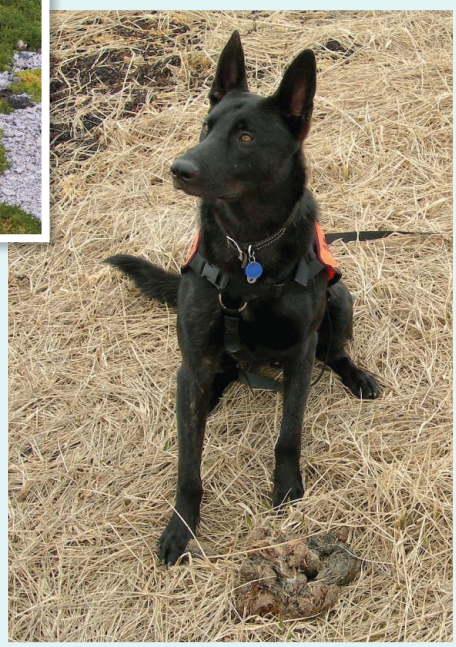

Linda Gormezano got a lot of media attention last month with her finding that polar bears are shifting their diets, but one member of her research team wasn't talking to the press: her scat-finding dog, Quinoa. Responding to the command *Búscalo*!—Spanish for "find it"—the male Dutch shepherd has sniffed out more than 1500 piles of polar bear scat from the southern reaches of the Hudson Bay. Gormezano, now a postdoctoral fellow at the American Museum of Natural History in New York City, analyzed the droppings to discover that the bears are now eating more snow geese and have added caribou and goose eggs to their diets.

Quinoa was just 6 months old when his collaboration with Gormezano began. She wanted a noninvasive way to study foraging behavior of large mammals and knew that others had trained dogs to find grizzly bear scat, floating killer whale poop, and even particular endangered plants. Quinoa's breed made him an ideal choice: agile, an astute sniffer, and more interested in playing than in food. Gormezano got polar bear and other animal poop from local zoos to teach Quinoa the difference. When he finds the right stuff, he sits and waits for her to come play tug of war or ball as his reward. Polar bears nearby don't seem to faze him, Gormezano says, although the noise from the rifle she uses to scare them off gets him riled up. Now off-duty for the season, Quinoa spends a lot of time sleeping and, she says, "he's enjoying the snow."

Teamwork. Jenkins with the personal robot PR2.

Three Q's

Last week, **Chad Jenkins**, a Brown University robotics scientist who votes as an independent, gave a TED-style pep talk to Republican members of the U.S. House of Representatives at their 3-day retreat. He described how Henry Evans, a mute quadriplegic in northern California, connects with the world using a personal robot and a quadrotor drone steered with head movements that Jenkins programmed.

Q: How did the lawmakers react?
C.J.: Most of their questions were about how Henry lives his life and if that was really him on the monitor. It was great to see their interest in the technology.

Q: Is there anything else you wanted to get across?
C.J.: Henry is an amazing story of someone whose life has been turned around through investments in basic research. I don't think you have to say it. You just hope they connect the dots.

Q: Was there a political aspect to your talk?
C.J.: My political radar isn't sharp enough. But I suspect there will be some follow-up. I'd love to spread the word about this technology.

CREDITS (TOP TO BOTTOM): © AMNH/R. ROCKWELL (2); MIKE COHEA/BROWN UNIVERSITY; LISA THOMPSON/ISLAND CONSERVATION SOCIETY; SEYCHELLES (2)

FINDINGS

Beaked Whale Species Resurrected

The beaked whale *Mesoplodon hotaula* has regained its full taxonomic status, thanks to a gift of dried whale meat. *M. hotaula* was first described by a marine biologist in Sri Lanka in 1963, then eliminated as a species 2 years later when researchers decided it was identical to another beaked whale, *M. ginkgodens*. But in 2003, islanders on an atoll in the Gilbert Islands in the Indo-Pacific gave a marine biologist whale meat left over from a recent festival. Genetic analysis of that sample—as well as other meat, teeth, and bones from other islands—revealed a distinct species: the forgotten *M. hotaula*, the research team reports this week in *Marine Mammal Science*. Counting *M. hotaula*, there are now 15 known species in the *Mesoplodon* genus (to which most beaked whales belong), making it by far the most species-rich genus of cetaceans. Yet, less is known about these deep-sea–dwelling and deep-diving creatures with odd, prominent snouts than any other whale genus. Scientists have yet to see a living *M. hotaula* at sea.

Distinct. A beaked whale of the species *M. hotaula*, stranded on the Seychelles, and a skull (*right*).

Published by AAAS

Pulling out. Paolo Boffetta says he doesn't want to have a "mud fight" over his corporate funding.

EPIDEMIOLOGY

Top Choice for French Post Drops Out in Industry Flap

France's premier epidemiology institute thought it had a strong candidate to become its new director. Paolo Boffetta, an Italian epidemiologist, spent 18 years at the International Agency for Research on Cancer (IARC), an authoritative World Health Organization body in Lyon, France. An author on more than 900 papers, Boffetta is now director of the Institute for Translational Epidemiology at Mount Sinai Hospital in New York City. He had already helped develop a 5-year plan for the French institute, the Center for Research in Epidemiology and Population Health (CESP) in Villejuif, which was submitted for an external review. But Boffetta also has ties to industry that some of his colleagues view as routine—but others regard as disqualifying him from the job.

Now, Boffetta's move from New York to the Paris suburbs, planned for 2015, is off. In stories in the French newspaper *Le Monde* in December and January, colleagues voiced concerns that Boffetta downplayed cancer risks from several substances while receiving money from industries that would benefit from such conclusions. CESP is run jointly by the French biomedical research agency INSERM and Université Paris-Sud. Jacques Bittoun, the president of that university, says that three out of 13 CESP team leaders had planned to leave if Boffetta got the job. A French association of asbestos victims had also protested the impending appointment.

Boffetta does not deny that industry funds some of his research; refusing that income stream would be "short-sighted," he says. But he initially defended his candidacy. "To suggest that I make up my conclusions depending on the funding sources does not only profoundly insult my scientific integrity, but it goes against empirical evidence," he wrote in a 15 January note to CESP staff that *Science* has seen. Catherine Hill, a cancer epidemiologist at Institut Gustave Roussy in Villejuif who worked with Boffetta on a 2007 IARC assessment of cancer causes in France, praises Boffetta's "seriousness" and rejects the idea that money could cloud his judgment.

But on 28 January, Boffetta wrote INSERM and the university that he was withdrawing his candidacy. "The job was more political than I expected," Boffetta says. "I'm happy to engage in discussion on the scientific aspects of my work, but not in a mud fight."

The controversy reflects wider disagreements among epidemiologists on how to deal with potential conflicts of interest, says Neil Pearce, an epidemiologist at the London School of Hygiene & Tropical Medicine and past-president of the International Epidemiological Association. "It seems that at least in France, if not in Europe, it's not enough to declare conflicts of interests to be fully credible on subjects as serious as the health effects of potentially toxic products," Bittoun says. "In fact, it is preferable not to have any at all."

Boffetta's work on diesel was one of the flashpoints. In June 2012, IARC officially classified diesel exhaust as carcinogenic based on a 700-page review of the literature. That same month, Boffetta published a paper online in *Critical Reviews in Toxicology* concluding that the available studies had methodological weaknesses and that as a result, "the weight of evidence is considered inadequate to confirm the diesel-lung cancer hypothesis."

As he acknowledged in the paper, Boffetta's study was supported by the Mining Awareness Resource Group (MARG), a group of mining companies and engine manufacturers. MARG had tried to stop the publication of two diesel studies in court for years, a battle it eventually lost. Boffetta says he didn't know about MARG's tactics at the

DUELING VIEWS ON DIESEL

"These epidemiological studies support a causal association between exposure to diesel-engine exhaust and lung cancer."

IARC MONOGRAPH WORKING GROUP IN *THE LANCET ONCOLOGY*

"In sum, the weight of evidence is considered inadequate to confirm the diesel-lung cancer hypothesis."

PAOLO BOFFETTA AND CO-AUTHORS IN *CRITICAL REVIEWS IN TOXICOLOGY*

CREDIT: MOUNT SINAI HEALTH SYSTEM

Published by AAAS

time he submitted his paper. He calls them "profoundly wrong," adding that he has since stopped working with the group. But he says the funding in no way changed his views.

In other papers, Boffetta contested the carcinogenicity of substances such as dioxin and beryllium, while acknowledging funding from companies that expose their workers to them. Paolo Vineis, an environmental epidemiologist at Imperial College London, says there is a "pattern" of corporate influence in Boffetta's recent output. "When someone supports the point of view of industry against the opinion of scientists working on the IARC monographs, it's difficult to conceive that this person is really independent," Vineis says.

Pearce doesn't think most epidemiologists change their views because of industry funding, but sees another danger: Industry support can give undue visibility to small scientific minorities, something that he says happens in the global warming debate as well. "Scientists say what they really believe […] but industry chooses scientists whose views are predictable because they have […] criticized similar studies in the past, and people get an unbalanced picture of what the consensus is among scientists," he says.

In Boffetta's case, some epidemiologists are also upset by a 2008 paper that they say undermined their field's credibility. In the article, Boffetta and five others highlighted the problem of false positives in epidemiology; as an example, they mentioned a 1993 study suggesting that pesticide residues had caused a breast cancer cluster in New York City, a widely publicized finding that caused a health scare but fell apart in subsequent, bigger studies. The authors called on fellow epidemiologists for more "modesty" and "humility" when interpreting results.

"I think Paolo is completely right to highlight this issue," Hill says. But Vineis, who co-authored a rebuttal piece the following year, says the paper was one-sided and echoed industry's arguments to dismiss epidemiology as a weak discipline. "Indeed, my arguments can be used this way," Boffetta concedes, "but it's better if epidemiologists discuss it. My intention was to make the discipline stronger and less vulnerable to attacks."

–TANIA RABESANDRATANA

METEOROLOGY

Heat Wave Forecasts Debut in Scorching Australia

MELBOURNE, AUSTRALIA—Once again an inferno of a summer is bearing down on Australia, where heat waves claim more lives than storms, wildfires, tropical cyclones, and floods combined. Predicting the severity of heat waves, like one last month that saw temperatures top 50°C in some parts of the country, has largely eluded meteorologists, because their toll depends not just on high temperatures but also on how unusual they are. But the Australian Bureau of Meteorology (BOM) thinks it has hit upon a winning formula for converting forecasts of heat into a measure of its likely impact on communities.

Heat waves are notoriously difficult to define. Blistering temperatures for one city can be tolerable or even pleasant in another. "Wherever you live, you've got a climate that you're adapted to," says BOM meteorologist John Nairn, who led the development of Australia's pilot system.

Several other countries and individual cities have implemented warning systems to cope with the rising tide of extreme heat events that climate change is bringing. Generally, these systems monitor forecast temperatures and compare them with locally defined thresholds. Australia's system stands out for the high resolution of its 5-day forecasts—heat waves are mapped on a 5-square-kilometer grid nationwide—and its ability to predict heat wave severity.

To account for regional temperature variations, BOM's system defines a heat wave as a period of at least three straight days with forecasted daily average temperatures all falling in the hottest 5% of days for that region from 1971 to 2000. The system also employs a heat stress index that measures each 3-day period against the previous 30 days. If a heat wave is unseasonable in timing or is preceded by a relatively mild period, the likely impact will be greater, Nairn says. Heat waves occurring earlier in summer also tend to be more lethal, studies have found.

Nairn and his team set thresholds for severe and extreme heat waves by plotting on a graph all events from 1958 to 2011 according to the metric they had developed. "There was a transition point between relatively abundant low intensity heat waves and relatively infrequent high intensity heat waves," he says. For the handful of chart-topping heat waves, "you're really in a zone of trouble."

The pilot system's indices did a good job of rating the severity of historical heat waves, he says. "The major heat waves just fell out beautifully." A 2009 heat wave that contributed to 374 deaths in the southeastern Australian state of Victoria, as well as heat waves in Paris in 2003, Moscow in 2010, and Chicago in 1995, all rated as extreme. Last month's heat wave also ranked as an extreme event in southeastern Australia; authorities say it was responsible for 174 extra deaths in Victoria.

How health agencies respond will determine how useful the forecasts are, says Geoffrey Morgan, an environmental epidemiologist at the University of Sydney. "It isn't so much about defining what the best threshold is," he says. "It's more about how you communicate … the effects of heat."

Mathilde Pascal, an epidemiologist at the French Institute for Public Health Surveillance in Paris, agrees. While France's decade-old heat wave warning system helped avert an estimated 4000 deaths during a 2006 heat wave, she says, some 2000 extra deaths were still tallied. Saving more lives in future heat spells will require more robust public health outreach to ensure that people—especially the elderly—take precautions such as drinking enough water and avoiding prolonged exposure to the sun, she says.

The heat is on. An Australian bush fire.

CREDIT: ROGERROSENTRETER/ISTOCKPHOTO.COM

BOM's pilot heat wave forecast will run until the end of the next month. If it passes muster and receives funding, the bureau plans to roll it out as an official service in the next austral summer.

–DYANI LEWIS

Dyani Lewis is a writer in Melbourne, Australia.

Sailors, beware! The notoriously fierce weather below Cape Horn turns out to be part of a regular pattern.

METEOROLOGY

Southern Hemisphere Storms Pulsate To a 25-Day Beat, New Papers Show

Roaring Forties, Furious Fifties, Shrieking Sixties—the sailors' terms for the stormy latitudes of the Southern Ocean suggest that the winds and waves there are relentless. In fact, their fury ebbs and surges. This week on page 641 of *Science*, researchers report that the storm belt in the Southern Hemisphere throbs powerfully with a 20- to 30-day beat, the manifestation of a pulsating flow of heat from the tropics to high latitudes.

The discovery caps a lengthy search for mid-latitude oscillations in the atmosphere, which meteorologists have long theorized. It also offers a new tool for understanding the workings of the southern atmosphere as well as a glimmer of hope for better long-range forecasting there. "There will be a tremendous amount of interest in this paper," says meteorologist Dennis Hartmann of the University of Washington, Seattle. The ups and downs of Southern Hemisphere weather "will be a hot topic," he says.

Atmospheric oscillations are common in the tropics, where scientists have identified an alphabet soup of roughly rhythmic changes in the atmosphere and sometimes in the ocean: the MJO; the QBO; and ENSO, or El Niño. Around 1950, meteorologists predicted that another oscillation—a so-called index cycle—should be at work in the mid-latitude atmosphere of the Northern Hemisphere, influencing the weather for much of the world's population. The idea was based on the way the atmosphere moves heat from tropical latitudes, where solar heating is greatest, to polar latitudes. The theorists proposed that feedbacks in the system would cause mid-latitude storminess to vary more or less rhythmically over several weeks.

No one has ever found any such variability in the Northern Hemisphere, but meteorologists David Thompson of Colorado State University (CSU), Fort Collins, and Jonathan Woodworth, now at DEIF Inc. in Loveland, Colorado, gave it a try in the south. In the 1950s, weather observations in the Southern Hemisphere were too spotty to consider looking for the index cycle there, but since about 1980, satellites have filled in the observational holes.

As they report in a paper in press in the *Journal of the Atmospheric Sciences*, Thompson and Woodworth succeeded in finding a 20- to 30-day oscillation in storminess around the Southern Hemisphere over the past 30 years. Technically, the storminess cycle is called the baroclinic annular mode, or BAM, pronounced the way it looks. As Thompson and Elizabeth Barnes of CSU go on to show in the *Science* paper, the BAM shows up in changes in the storms' kinetic energy, the amount of heat they transport, and the amount of precipitation they release. "The whole thing is pulsating with remarkable regularity," Thompson says of the southern mid-latitude atmosphere that stretches across a wide swath from far southern South America, South Africa, and Australia to the shores of Antarctica. In the north, the corresponding latitude band would span the contiguous United States and most of Canada.

Spatial Signatures of the BAM

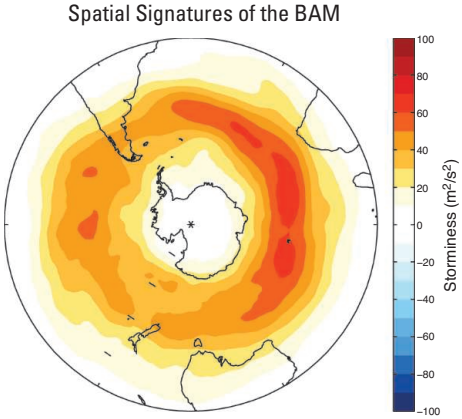

Wild waves. Storminess in the Southern Ocean follows a 20- to 30-day cycle, new analyses reveal.

Thompson and Barnes also show what makes the BAM tick. When they ran four different computer models, all of them—from a simple two-equation program to a sophisticated atmospheric simulation—produced a BAM. The key ingredient was a two-way feedback between the uneven heating of the hemisphere, with heat tending to build up at lower latitudes, and a time lag for storms to grow in response to that heat buildup and relieve it by moving heat toward the pole. As long as it takes storms a few days to grow and start moving substantial amounts of heat, the researchers found, the hemisphere's storminess will throb. The results suggest that any other Earth-like planet that rotates and gets disproportionate heat near its equator ought to have a BAM in its atmosphere, Thompson says.

On reading the *Science* paper, meteorologist Steven Feldstein of Pennsylvania State University, University Park, wondered, "Why didn't I look at this?" He finds both the detection of the oscillation and the suggested mechanism for generating it persuasive. "It's a great first step," he says. "It has potential implications for other processes and even for forecasting. It will be interesting to see where it leads."

Back to the Northern Hemisphere might be one place the work could lead, but so far no luck. Thompson and Barnes have looked at a far higher quality observational record in the north than was available in the 1950s or even the 1980s, but they still find no sign of an oscillation. Possibly, the temperature contrasts in the north between the expansive colder continents and warmer oceans are too strong for a northern BAM. But Thompson and Barnes may not be the only ones continuing the search.

–RICHARD A. KERR

Going smokeless. Richard Carmona, an anti-tobacco former U.S. surgeon general who ran unsuccesfully for the Senate, now promotes electronic cigarettes.

NEWSMAKER INTERVIEW: RICHARD CARMONA

A Former Surgeon General Lends His Support to E-Cigarettes

Richard Carmona, who crusaded against tobacco as U.S. surgeon general during the second Bush presidency, put himself at the center of a public health debate when he joined the board of e-cigarette maker NJOY, based in Scottsdale, Arizona, last March. These battery-powered devices look like cigarettes but don't use tobacco. Instead, they release a nicotine vapor that can satisfy an addict's cravings without producing tobacco-derived poisons. Unregulated by the Food and Drug Administration (FDA), e-cigarettes are gaining in popularity; sales of all brands now top $1.7 billion in the United States. While some experts see no evidence of a major new health risk and a potential for doing some good, others fear that e-cigarettes will undermine a hard-fought public health campaign to bring smoking under control.

Fifty years ago, the U.S. Office of the Surgeon General issued its seminal report indicting cigarette smoking as a cause of cancer. At the time, more than 40% of adults and those of high school age in the United States were smokers. Since then, the number has dropped to about 20% of that population. Whether e-cigarettes will help some smokers quit or provide a gateway for new tobacco users is the main unanswered question.

Described by colleagues as affable and quick-witted, Carmona was responsible for the surgeon general's 2006 report on secondhand smoke and helped push for indoor smoking bans in restaurants and bars. In an interview with *Science*, Carmona insisted that he and NJOY share a mission to make tobacco obsolete, and that e-cigarettes could help reduce harm from smoking. The interview has been edited for clarity and brevity.

–CHARLES SCHMIDT

Q: As a doctor and former surgeon general, why did you join the board of an electronic cigarette manufacturer?

R.C.: At first, I immediately rejected their offer. But with some due diligence I came to see that they were willing to do the necessary science and that we could be allies in the antitobacco movement. That said, I offered to join only under certain conditions: that they request FDA regulation—which is in the public's best interests—that they conduct and publish their own research in peer-reviewed journals, even if the findings hurt the bottom line; that they don't use my name or refer to the surgeon general in their advertising campaigns; and that they don't market to kids. So far, they've delivered on all those promises.

Q: E-cigarettes are touted as a way to stop tobacco smoking. But would you advocate that people who do that successfully then also try to wean themselves off e-cigarettes?

R.C.: Yes, but the urgency isn't as great because people who use them aren't inhaling large amounts of carcinogens and cardiovascular disease–causing agents.

Q: How can you be sure they're safe?

R.C.: As research priorities, we're asking about cons from long-term nicotine use, and we're examining the different components in side-stream vapor to make sure they're not unsafe. So far we don't see any problems. And we're also looking into long-term efficacy: How many people who use e-cigarettes quit and for how long? We just have to craft the right questions and then report back to the public.

Q: Won't e-cigarettes just lead to more people getting hooked on nicotine?

R.C.: That same question came up decades ago when nicotine gum, patches, and sprays came on the market. People said they would create new nicotine addicts and that never happened. But e-cigarettes are a different kind of nicotine delivery device, so they raise unanswered questions that we're looking into.

Q: On what basis do you think e-cigarettes can help people quit smoking?

R.C.: There is evidence that gums, patches, and sprays work, but they don't work well enough. And early evidence suggests that because e-cigarettes reinforce the physical movement of smoking, they can enhance tobacco cessation, but we don't have all the information yet. We have to continue doing the research and publishing data to demonstrate that they're helpful.

Q: What about children? Some of these e-cigarettes are candy flavored.

R.C.: As a company, we've made a commitment that these products should not be sold to kids under any circumstances. Children don't factor into NJOY's marketing, but if a customer says they like a particular flavor, then I have no problem with that—adults enjoy these flavors, too.

Q: How would you respond to critics who say you shouldn't be doing this?

R.C.: Making tobacco obsolete is part of NJOY's value … and it's consistent with my efforts to move people away from cigarettes with combustible toxins that lead to cancer and cardiovascular diseases. I accept that my colleagues have concerns and that the antitobacco world is divided on this. You've got two camps here: an abstinence-only camp that thinks anything related to tobacco should be outlawed, and those of us who say abstinence has failed, and that we have to take advantage of every opportunity with a reasonable prospect for harm reduction.

CREDITS (TOP TO BOTTOM): ROSS D. FRANKLIN/AP PHOTO; COURTESY OF NJOY

PARTICLE PHYSICS

China Builds Mammoth Detector To Probe Mysteries of Neutrino Mass

BEIJING—It isn't easy to weigh a ghost. After neutrinos were hypothesized in 1930, it took physicists 67 years to prove that these elusive particles—which zip through our bodies by the trillions each second—have mass at all. Now, a Chinese-led team is planning a mammoth neutrino detector, meant to capture enough neutrinos from nearby nuclear reactors to determine which of the three known types, or flavors, of neutrinos are heavier or lighter. That mass hierarchy could be key to explaining how neutrinos get their mass, and measuring it would be a coup for China's particle physicists.

Last month, scientists gathered in Jiangmen, in China's southern Guangdong province, to review plans for the Jiangmen Underground Neutrino Observatory (JUNO). Groundbreaking is slated for later this year on the $300 million facility, which China aims to complete by 2019. The facility, which backers say will be twice as sensitive as existing detectors, should not only pin down key properties of neutrinos themselves but not only lead to breakthroughs in neutrino physics, but revolutionize the field of geology and astrophysics." A successful project would also mark another triumph for China's neutrino research, 2 years after the Daya Bay Reactor Neutrino Experiment in Guangdong nailed a key parameter describing how different types of neutrinos morph into one another (*Science*, 16 March 2012, p. 1287).

In 1998, physicists working with the subterranean particle detector Super-Kamiokande in Japan showed that neutrinos of one flavor, muon neutrinos generated by cosmic rays in the atmosphere, can change flavor as they zip through Earth. In 2001, researchers at the Sudbury Neutrino Observatory in Canada proved that electron

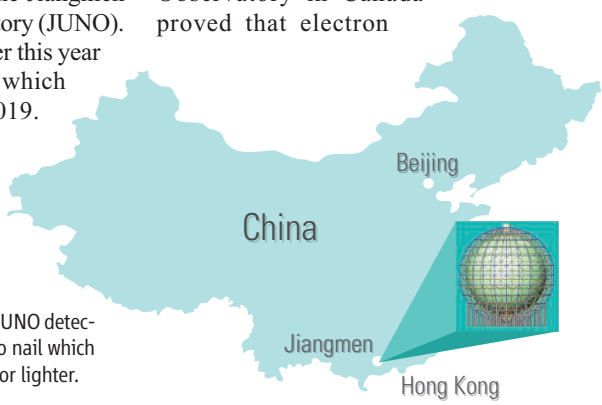

Heavy hitter. China hopes its planned JUNO detector, 38 meters across, will be the first to nail which of the three neutrino flavors is heavier or lighter.

The Race to Establish the Neutrino Mass Hierarchy

Project	Location	Source of neutrinos	Projected startup	Resolving power (in multiples of experimental uncertainty σ)
NoVA and T2K	USA and Japan	Accelerator	Running	1–3 σ
INO	India	Atmospheric	2017	2.2–2.8 σ
JUNO	China	Reactor	2019	3.2–4.4 σ
PINGU	South Pole	Atmospheric	2019	4.2–6.9 σ
LBNE	USA	Accelerator	2023	3–7 σ

also detect telltale neutrinos from nuclear reactions in the sun, Earth, and supernovas.

Other planned facilities aim to reveal the mass hierarchy (see table), but China could be the first to arrive at an ironclad result. If China can pull it off, says William McDonough, a geologist at the University of Maryland, College Park, JUNO "will neutrinos from the sun do the same. Such neutrino "oscillations" prove that neutrinos have mass: Without it, the particles would move at light speed and—according to relativity—time would stand still for them, making change impossible.

Knowing a neutrino has mass isn't the same as knowing what it weighs. In the simplest model, neutrino oscillations depend on just six parameters—the three mass differences among the neutrinos and three abstract "mixing angles." Physicists have measured all six—including the last mixing angle, which was measured by Daya Bay. They know that two of the neutrinos are close in mass and one is further off. But they don't know whether there are two lighter neutrinos and one heavier one—the so-called normal hierarchy—or an inverse hierarchy of two heavier ones and one light one.

How the masses shake out "is fundamental for a whole series of questions," says Wang Yifang, director of the Institute of High Energy Physics (IHEP) here, including whether neutrinos, like other particles, get mass from tangling with Higgs bosons or from a more exotic mechanism. The answer depends on whether the neutrino is, oddly, its own antiparticle. Physicists may be able to tell that by searching for a weird new type of radioactive decay. But, if it even exists, that decay would occur at an observable rate only if neutrinos follow an inverse hierarchy.

To explore this frontier, an international team led by Wang will build a detector 700 meters beneath a granite hill near Jiangmen, equidistant from two nuclear power plant complexes. A sphere about 38 meters in diameter will contain 20,000 tons of a material known as a liquid scintillator. About 60 times a day, one of the sextillion or so electron neutrinos spraying from the reactors every second should bump into an atomic nucleus, sparking a flash of scintillation light that the detector can measure and analyze. In the 53 kilometers that the neutrinos will traverse from reactor to detector, about 70% will change flavor, says Cao Jun, a particle physicist at IHEP. By studying the energy spectrum of the neutrinos, physicists should be able to tease out the mass hierarchy. "But it's not going to be easy because the amount of energy to be measured is minuscule," Cao says. He estimates the measurement will require 6 years of data-taking.

The key to JUNO's success will be its energy resolution. The largest liquid scintillation detector to date—KamLAND in Japan, which has 1000 tons of detector fluid—can only make out energy differences of greater than 6%. JUNO needs to double the resolution to 3%—no mean feat, especially as the larger volume of scintillator itself absorbs more light.

If it works, JUNO should also make finer measurements of the known mixing angles and mass differences. "This is particularly important for the search for a possible fourth form of neutrinos," says Lothar Oberauer

CREDIT: (INSET) IHEP; (SOURCE) M. BLENNOW *ET AL.* ARXIV 1311.1822 (2013)

Published by AAAS

of the Technical University of Munich in Germany. If the sum of all oscillations doesn't add up to 100%, then the data would point to a fourth flavor (*Science*, 21 October 2011, p. 304)—a possibility that could topple the standard model of particle physics and help explain a host of astronomical puzzles.

Another mission for JUNO is to observe geoneutrinos emitted during radioactive decay in Earth's deep interior, which generates heat that helps drive plate tectonics and power our planet's magnetic field. Detecting geoneutrinos "is the only way to get a glimpse of Earth's internal heat budget and distribution," McDonough says. The three facilities now detecting geoneutrinos, including the revamped Sudbury detector, record about 45 a year in total. JUNO should spot about 500 a year, enough to test various models of Earth's composition and heat flow, McDonough says. And that would score China another triumph in neutrino physics.

–JANE QIU

Jane Qiu is a writer in Beijing.

MARINE ECOLOGY

As Lionfish Invade, Divers Defend Threatened Ecosystems

NASSAU—The red lionfish, with its striking stripes and huge outrigger fins, wasn't hard to spot. Nor to spear: It simply studied me, utterly fearless until I killed it. Within a half-hour, my group of divers had caught four of the gorgeous fish along a coral reef here; they made excellent eating that night.

For ecosystems in the southwestern Atlantic Ocean, however, the lionfish is a curse. Marine scientists say that the voracious predator, a Pacific native believed to have been released into the Atlantic by aquarium lovers in the mid-1980s, is spreading rapidly and wiping out native fish, especially on vulnerable Caribbean coral reefs. "They'll eat just about anything they can swallow and almost nothing eats them," says ecologist Stephanie Green of Oregon State University, Corvallis.

In the Bahamas, where *Pterois volitans* was first spotted in 1985, "they're everywhere," says Pericles Maillis, a Bahamian conservationist who has led local efforts to battle the invader. "It's a doomsday scenario."

Late last year, however, Maillis and other lionfish opponents got some good news. Using ecological models to plan a surgical 18-month offensive, divers killed enough lionfish for native fish populations to rebound at 24 coral reefs near the Bahamian island of Eleuthera, researchers reported online on 2 December in *Ecological Applications*. Removing 75% to 95% of lionfish at the sites allowed prey populations to increase by 50% to 70%—with up to one-third less effort than it would have taken to totally exterminate the invaders. The study shows that "we don't have to catch every lionfish" to allow native species to recover, says Green, the lead author, although the culling must be repeated regularly.

Such targeted tactics could help beat back an invasion that has spread to some 3.3 million square kilometers of the Atlantic, ranging from Rhode Island to the Panama Canal, according to Pam Schofield of the U.S. Geological Survey in Gainesville, Florida. Population densities are often many times greater than in the lionfish's native Pacific range, but the fish's phenomenal success is a mystery. Mark Hixon of the University of Hawaii, Manoa, guesses that a predator that keeps Pacific populations in check by eating baby lionfish is "absent in the Atlantic … but we have no idea what it is."

Gotcha. A diver bags a lionfish in the British West Indies as part of an effort to protect native fish from the invader, which has spread rapidly since it was first spotted off Florida in 1985 (map).

CREDITS (TOP TO BOTTOM): U.S. GEOLOGICAL SURVEY; OREGON STATE UNIVERSITY

Lionfish invaders can snap up one-half of resident fish within just a year after arriving on a reef, recent research shows. So far, they have taken their most visible toll on small reef fish. But researchers say they also eliminate the young of large predators such as snappers and groupers, an absence that might not be noticed for years.

Recent studies have found clues as to why the invader is so lethal. For example, some common Pacific reef fish inexplicably don't recognize lionfish as a threat, although they dart for cover when other predators appear, an Australian research team reported in *PLOS ONE* this past October. That's a worrying sign that Caribbean fish aren't likely to learn to avoid lionfish either. "That scares me even more," says lionfish specialist Isabelle Côté of Simon Fraser University, Burnaby, in Canada.

To reduce lionfish numbers, policymakers in the Bahamas and elsewhere have tried to promote commercial fishing of the tasty species. You need to "eat it to beat it," says Frederick Arnett II of the Bahamas' Department of Marine Resources. One problem facing any fishery, however, is that handling lionfish requires special care: Their venomous spines can make the slightest puncture extremely painful. And their unusual appearance can make consumers skittish.

Still, in Florida, the commercial catch quintupled from 1.1 tons in 2011 to 6.1 tons in 2012, according the U.S. National Marine Fisheries Service. "But we don't know yet if it's putting a dent in the population," says Lad Akins, founder of the Reef Environmental Education Foundation in Key Largo, Florida.

In the recent Eleuthera island study, researchers examined the effectiveness of a more targeted approach by killing virtually all lionfish on one set of reefs, fewer at two other sets, and none in a fourth control group. The surprises were how fast the lionfish decimated the local fish in the control, and that the native species quickly rebounded on other reefs even when 25% of the lionfish remained. That suggests focused lionfish culls aimed at protecting juvenile fish could be useful. "If we can get divers to take the lionfish out of the shallow reefs and the mangroves where the juveniles are," Green says, "we may be able to keep some reefs relatively intact."

–CHRISTOPHER PALA

The Mountaintop Witness

Margaret Palmer started out just studying streams. She's ended up in court, passionately defending them from coal mining

ONCE AGAIN, MARGARET PALMER WAS squaring off against a lawyer for a coal company. "I don't mean to pick a fight with you," the attorney said as he cross-examined the academic ecologist, lobbing questions designed to fluster Palmer and raise doubts about her credibility. But even when he suggested her conclusions were shaped by ideology, not data, she remained composed. "Well," she said, "I'll be happy to answer any questions you have about the method."

The stakes were high in the encounter, which unfolded before a federal judge in a West Virginia courtroom last December. Three environmental groups had sued a pair of coal companies, claiming that pollution from their "mountaintop removal" strip mines was harming nearby streams. A victory by the green groups could set a legal precedent, sparking new lawsuits against the controversial mining method.

To bolster their case, the groups had recruited Palmer, a stream ecologist at the University of Maryland, College Park, to join the legal fray as an expert witness. Her help was considered a huge asset: As a result of research publications, legal testimony, and policy work, the 58-year-old scientist has become perhaps the highest profile scientific opponent of companies involved in mountaintop removal. She's briefed top government regulators and Congress, helping promote stricter oversight. She's even put in a memorable appearance on *The Colbert Report*, a popular television show.

It's a public role that many scientists would find deeply uncomfortable—and that Palmer herself once would have shunned. Earlier in her career, the tenacious but self-effacing basic researcher kept a low profile, even refusing to return calls from journalists. She dreaded the prospect of this profile, says her husband, Michael Nussman. The attention is "embarrassing for an introvert."

Over the past decade, however, Palmer has undergone a transformation, emerging as an influential voice on complex and contentious environmental issues—and inspiring other researchers to follow. In the early 2000s, she tackled the booming business of restoring rivers, raising troubling questions about its effectiveness. Later, after a heart-wrenching airplane ride, Palmer turned her attention to the headwater streams buried by mountaintop mines in the eastern United States. That experience is now helping her shape a new $27.5 million research center, funded by the National Science Foundation (NSF), designed to engage scientists in policymaking.

Palmer "wants her science to be relevant," says Margaret Janes, a retired policy analyst with the nonprofit Appalachian Mountain Advocates, who first recruited Palmer as an expert witness for court battles. And that's led to a willingness to risk some private, and public, discomfort. Her courtroom interactions with industry lawyers, for instance, are becoming "more and more hostile," Palmer says. "It's increasingly personal."

An awakening

Palmer had her feet wet from an early age. Born on an Air Force base in Florida, she was raised in Greenville, South Carolina, playing in nearby Appalachian creeks and scamper-

CREDIT: MELISSA L. ANDREYCHEK/SESYNC

Published by AAAS

Probing. Basic stream research, such as analyzing carbon and nitrogen dynamics in creeks (this one in Maryland), is still on Palmer's agenda.

ing after crayfish. "I grew up in a working-class setting," she says. "I wasn't going to be a housewife." The youngest of four sisters, Palmer was the only person in her family to go into science. A college course in invertebrate ecology got her hooked, and Palmer went on to earn a Ph.D. in coastal oceanography from the University of South Carolina, studying benthic invertebrates in estuaries.

Her first academic job, however, took Palmer far from the ocean. Arriving at Wabash College in 1983, Palmer found herself in Crawfordsville, Indiana, a small town about an hour northwest of Indianapolis. She quickly adapted her research to look at freshwater streams. And teaching at the all-male college, she says, led to a political awakening as she began to read up on feminism.

In 1987, Palmer moved to College Park, Maryland, after her husband became a congressional staffer. (He now heads the American Sportfishing Association.) In addition to biology, she taught feminist theory and the philosophy of science. "It changed my perspective on why we do the kind of science we do," she says. "On some level, it influenced my interest in doing science that has policy implications."

While she and Nussman raised two sons, Palmer studied the role of patchy habitats within streams. She discovered that natural fragmentation—such as the scattered clumps of decomposing leaves on the riverbed—boosts populations of copepods and larval flies. In another study, she found turbulence from water flowing over rough streambeds enhances restoration of ecological processes.

During the 1990s, those seemingly abstruse findings became relevant to a policy debate. Ecological restoration was becoming a big business, as government regulators required developers to compensate for damage to streams and wetlands by creating or restoring similar ecosystems elsewhere. But contractors were following crude blueprints, and Palmer's research made her skeptical that restored streams could match the intricate functions of natural ones. She kick-started a review through the National Center for Ecological Analysis and Synthesis in Santa Barbara, California, which ultimately assembled a database of 37,000 stream restoration projects. In an influential study, her team concluded that more than $1 billion per year had been spent on such projects since 1990 with scant follow-up to measure effectiveness (*Science*, 29 April 2005, p. 636). The scrutiny spurred many restoration funders to require more monitoring, although critics say that it still often ignores important ecological factors.

The restoration study was just one marker of Palmer's increasing engagement in policy. The Ecological Society of America tapped her to help craft a manifesto for "pragmatic ecological science" that could help address pressing environmental problems (*Science*, 28 May 2004, p. 1251). And not long after, she was asked to head the $15 million Chesapeake Biological Laboratory, about 100 km southeast of Washington, D.C. It wasn't easy sailing. Palmer had to lay off support staff and raze an unsafe lab, but she won a $1.7 million grant from NSF to replace an aging research pier.

> **"The fact that she's willing to testify and stick her neck out is remarkable."**
>
> PATRICK PARENTEAU, VERMONT LAW SCHOOL

Where many scientists struggle to juggle research and family, Palmer faced a three-way balancing act as an emerging public figure. One coping mechanism was a weekly dinner with two other female faculty members, a psychologist and a chemist, in College Park. Calling themselves "The No Club," they discussed invitations and obligations and recommended which ones should be declined, to manage their workloads. "You will be asked to be on more committees than you can be on," Palmer says, especially women and minorities. "You have to figure out which ones really matter."

Moving mountains

Palmer had a hard time saying no to the fight against mountaintop mining. The technique had begun in earnest in the early 1990s as companies chased thin seams of lower sulfur coal. The beds are too far underground for traditional strip mining, but not thick or deep enough for tunneling. The solution, essentially, is to blow up the top of a mountain. Bulldozers then shove the rocky debris into adjacent valleys, exposing the coal, but burying tiny headwater streams. (To date, mountaintop removal has filled in more than 2000 kilometers of streams throughout Appalachia.)

As the practice spread, it attracted controversy. Coal companies say they take pains to restore the original topography and create new rocky channels to replace buried streams, as regulations require. But community activists and environmentalists argue that the industry and government officials downplay the damage done by mining and overstate their ability to repair it.

Palmer entered the debate in 2003, after Appalachian Mountain Advocates called. The Lewisburg, West Virginia–based group wanted her to review coal companies' plans to create replacement streams, which the companies submitted with their permit applications for new mines. To show Palmer the issue firsthand, a nonprofit group called SouthWings flew her over existing mines. Palmer and her husband had built a weekend cabin in West Virginia years earlier, overlooking the Cacapon River, so she expected to see pockets of mining.

CREDIT: COMEDY CENTRAL

Leaning forward. In a 2010 appearance on *The Colbert Report*, Palmer pointedly described the problems with mining coal by removing mountaintops.

Published by AAAS

But peering out the window of the Cessna, she felt overwhelmed by the extent of wasteland. "My God," she thought. "I've got to do something."

When Palmer pored over the available data, a clear picture emerged. Aquatic habitat was damaged even far downstream from valley fills. No scientific evidence indicated that the rebuilt waterways could effectively replace small headwater streams. The government regulators who approved such mitigation, she says, tend to focus on rebuilding lost miles of streams, but not their ecological functions. When a bill to ban valley fill was introduced into the U.S. Senate in 2009, Palmer told the committee bluntly: "[T]he streams that are buried when rocks and dirt are dumped … into the valleys below are gone forever."

Some courts began to agree. In 2007, for instance, a federal judge blocked permits for several major mines, based in part on Palmer's analysis. Although a higher court ultimately struck down the heart of that decision, the attention helped build the case for tighter regulation. After Barack Obama became president in 2009, for example, senior environmental administrators asked her to brief them on the science of mining impacts. Soon, the Environmental Protection Agency (EPA) announced that they would take a closer look at requests for 79 mining permits in four states.

In 2010, the publication of an analysis led by Palmer reinforced the argument that mountaintop stream mitigation could not restore what was lost (*Science*, 8 January 2010, p. 148). The report, which included new data on streams from West Virginia, made headlines, stoked by a press conference at the National Press Club in Washington. "It gave EPA the national spotlight, the scientific validation for taking the steps it did, even with withering political opposition," says Donald Boesch, head of the University of Maryland Center for Environmental Science in Cambridge. "It had enormous impact." The resulting regulatory crackdown, which included tightening the requirements for permits, persuaded some mining companies to abandon mountaintop removal.

Scarred. Mountaintop mines, such as this one in West Virginia, end up filling stream valleys with tons of debris, creating wedges of rubble (*center*). The waste leaches sulfate and other ions that harm aquatic life.

CREDIT: DEBBIE HILL/UPI/NEWSCOM

Others have elected to fight the regulations and the research behind them. Hal Quinn, president of the National Mining Association, has said that EPA's approach "is based on bad science." For example, the industry has argued that using populations of mayflies as a gauge of stream health is inappropriate, because they say these insects are ultrasensitive to water quality. "As if it mattered, more bugs are killed overwhelmingly by car windshields than on mine sites," claims a glossy flyer produced by Walker Machinery Co., which sells and services mining equipment in 33 counties.

Getting personal

Such rancor lies just under the surface in the staid, oak-paneled courtrooms where Palmer has been asked to testify. Looking for ammunition to discredit the researcher, industry attorneys have used state sunshine laws to request copies of Palmer's university e-mails over many years. Last summer, a free-market think tank demanded EPA turn over copies of her communications with agency scientists.

Once in court, opponents have tried hard to persuade judges to throw out her testimony as that of biased activist. "[S]he has adopted an uncompromising opinion about surface mining that leaves no room for objective scientific analysis," lawyers for the Highland Mining Co. of Logan, West Virginia, argued unsuccessfully in an April 2012 case. Palmer's "fundamental opposition to all surface mines in central Appalachia … renders her opinion both untrustworthy and unhelpful to the Court."

Such attacks highlight just how seriously companies take Palmer's stature, says Patrick McGinley, a law professor at West Virginia University in Morgantown. "The desire to exclude her testimony shows the fear that the industry has that her science will persuade decision-makers."

The jousting can get prickly and personal. Palmer has spent countless hours traveling to mines to evaluate streams, reading voluminous files, preparing reports, and sitting in court, paid a consulting fee of $175 an hour and also helping pro bono. During Palmer's December testimony, Shane Harvey, the defense attorney for Elk Run Coal Co., focused on the fact that she had to find time to work on mining issues while on vacation:

Harvey: "I mean I think you told me during your deposition that you were on vacation with your sisters at the beach and

Published by AAAS

A Tale of Two Streams

Natural. Appalachian headwater streams, such as this one in West Virginia, feature diverse communities and streamside vegetation, which purify water and cycle nutrients. Complex bedrock and hydrology help dampen floods.

Artificial. Streams constructed on crushed fill, such as this one at a mountaintop mine in Kentucky, typically have fewer species, greater temperature variation, more selenium and other pollution, and flash floods.

you had to write your report down there. Do you remember that?"

Palmer: "I had to finish the report there; that's correct."

Harvey: "You had to finish it there. Okay."

Palmer: "It had been started a good while before."

At another point, Harvey tried to pin Palmer down on the industry's rosy interpretation of some key data. But she was skeptical, saying it appeared the company had cherry-picked their numbers. "I would be very surprised if when we looked at all the data if that was a consistent pattern," she said. "And that's why I said many times I'd have to go through and look at all the data, which clearly you have access to and I haven't seen."

Joe Lovett, director of Appalachian Mountain Advocates, one of the groups that have employed Palmer as a consultant, says she is unflappable. "I don't think anyone has ever tripped her up." Despite her cool demeanor, however, Palmer has found some of the confrontations unnerving. "Their implication was that I'd done a poor job of preparing and didn't know the science," she says of the coal company attorneys. Palmer herself felt she should have done better. The moments of self-doubt may arise from a self-critical personality. "She tends to think she hasn't made a difference," Nussman says.

Yet her new confidence is unmistakable, underscored by her response when *The Colbert Report* called in 2010, asking for an interview. The show has nearly 1 million viewers, and host Stephen Colbert is infamous for his withering questions. It would be uncomfortable territory for any academic. Yet Palmer agreed, seeing an opportunity to speak directly to the public.

"My God, I've got to do something," Palmer thought as she flew over a raw landscape of coal mines and obliterated streams.

Before she headed into the floodlights, she wondered "What have I gotten myself into?" But that night, Palmer hit her stride. "She was funny. She was relaxed. Colbert got in her face, and she got right back into his," recalls ecologist David Allan of the University of Michigan, Ann Arbor.

Still, any researcher faces some inherent risks when stepping into the role of an advocate. "The more you become a public figure, the less you are perceived as a science-only kind of scientist," says Patrick Parenteau, a professor of environmental law at Vermont Law School in South Royalton. Despite competing demands, Palmer has maintained her basic ecological research, which she feels helps maintain her credibility. "She's keeping her boots muddy," says her former postdoc Emily Bernhardt of Duke University in Durham, North Carolina.

A new experiment

Palmer spends much of her time now in a new office building in Annapolis that houses the NSF-funded National Socio-Environmental Synthesis Center (SESYNC), which she directs. ("Terrible acronym," Palmer told an attorney during a deposition. "All the good acronyms were gone.")

Palmer led the proposal for the center, which is dedicated to injecting science into policy. Better grounded policy, she hopes, could ultimately minimize the kind of courtroom battles and social conflict that she has experienced with mountaintop mining.

Palmer sees SESYNC as "a giant experiment" in collaboration. It brings together researchers from a broad diversity of disciplines, including economics and political science, to analyze existing data sets that could help solve environmental problems. (Coincidentally, it also shares space with Merrill Lynch, so investment bankers in double-breasted suits walk the halls with fleece-clad ecologists and sociologists.) Recent projects have created a global database of where city dwellers get their water, and examined how psychological methods could be applied to sustainable development.

The center hasn't delved into mountaintop removal issues, but Palmer continues her work. She recently finished drafting a manuscript that evaluates monitoring reports for 434 stream mitigation projects in coal country, which she got through a Freedom of Information Act request. Most show that the streams are suffering from ecological damage, and that the replacements provide poor habitat. "My fears I had when I flew over these mines are turning out to be correct," she says.

Without a doubt, she will again be making the long drive to an Appalachian courtroom to testify about those results. "The fact that she's willing to testify and stick her neck out is remarkable," Parenteau says. "God help us if no scientists would do that."

–ERIK STOKSTAD

Published by AAAS

CREDIT: ERIC PALMA

Peering Into Peer Review

Why don't proposals given better scores by the National Institutes of Health lead to more important research outcomes?

Michael Lauer's job at the National Institutes of Health (NIH) is to fund the best cardiology research and to disseminate the results rapidly to other scientists, physicians, and the public. But NIH's peer-review system, which relies on an army of unpaid volunteer scientists to prioritize grant proposals, may be making it harder to achieve that goal. Two recent studies by Lauer, who heads the Division of Cardiovascular Sciences at NIH's National Heart, Lung, and Blood Institute (NHLBI) in Bethesda, Maryland, raise some disturbing questions about a system used to distribute billions of dollars of federal funds each year.

Lauer recently analyzed the citation record of papers generated by nearly 1500 grants awarded by NHLBI to individual investigators between 2001 and 2008. He was shocked by the results, which appeared online last month in *Circulation Research*: The funded projects with the poorest priority scores from reviewers garnered just as many citations and publications as those with the best scores. That was the case even though low-scoring researchers had been given less money than their top-rated peers.

"Peer review should be able to tell us what research projects will have the biggest impacts," Lauer contends. "In fact, we explicitly tell scientists it's one of the main criteria for review. But what we found is quite remarkable. Peer review is not predicting outcomes at all. And that's quite disconcerting."

Two months earlier, Lauer and his NHLBI colleagues had published a study of 224 NHLBI-funded clinical trials that produced a similar bottom line, using a different marker of importance: how quickly the studies were published. Lauer believes that the two papers strongly suggest that reviewers did not do very well in separating the wheat from the chaff on $2 billion worth of NHLBI research.

Lauer says he's presented his work to NIH Director Francis Collins and other senior officials and that "not one of them pointed out any flaws or thought we had come up with some sort of erroneous finding." But that doesn't mean they agree with his conclusion.

Richard Nakamura, who oversees NIH's peer-review apparatus as head of the Center for Scientific Review (CSR), is skeptical of the use of after-the-fact yardsticks such as citations and time to publication to gauge impact. "CSR's focus is much more on what good scientists think will have high impact as opposed to what bibliometric measures might suggest will have high impact," he says.

Several social scientists who have thought about ways to measure the impact of peer review hail Lauer's willingness to put the current system under a microscope. Such studies could help NIH and other U.S. research agencies do a better job of allocating scarce resources, says economist Adam Jaffe, who directs Motu Economic and Public Policy Research, an institute in Wellington.

"You might learn that the money from the award itself makes a big difference, but that the ranking of specific proposals was close to random," says Jaffe, who moved to New Zealand last spring after nearly 2 decades as a professor and dean at Brandeis University in Waltham, Massachusetts. "That would mean it's important for NIH to continue funding

Published by AAAS

research, for example, but that maybe the resources used in the selection process aren't being spent effectively."

Lauer emphasizes that his studies do not mean NIH is funding bad research. Nor is he proposing radical changes in the current system, as some have (see sidebar, p. 598). But he hopes the results prod NIH to question some time-honored assumptions about peer review and focus more on ensuring that its awards are yielding the biggest payoff. "The analogy is to a doctor with a bunch of sick patients," he says. "How do I maximize their health?"

Faith in the system

Ask a scientist about peer review, and many will immediately cite Winston Churchill's famous description of democracy—"the worst form of government except all those other forms that have been tried." The comparison acknowledges the system's many flaws, including its innate conservatism and its inability to make fine distinctions, while providing a defense against attacks from both colleagues and those outside the scientific community. "CSR lives and dies by the belief that our reviews are fair, and that our only bias is around good science," Nakamura says. "And any evidence that suggests otherwise is very troubling."

That's not to say that Nakamura and his colleagues think the current system can't be improved. Last year, Collins asked a group of senior administrators to examine ways of "optimizing peer review" at NIH. In particular, the task force is looking at whether NIH needs to do more to identify and support proposals from emerging fields and, at the same time, learn how to pull the plug on once-hot areas where scientific interest has cooled. "Does the current structure perpetuate fields beyond their prime?" asks Lawrence Tabak, NIH principal deputy director and chair of the task force.

The 170 or so study sections that CSR manages are the essential element of the NIH peer-review system for external grants. Each consists of 12 to 22 outside scientists who meet three times a year to review an average of 70 applications. (Individual institutes also convene review panels of their own.) Panel members give each proposal a numerical score, and the proposal receives an impact score that is the average of individual votes. For many applications, that score is converted into a percentile ranking.

It's a massive system that requires heavy buy-in from the research community. Last year, for example, more than 24,000 scientists reviewed roughly 75,000 applications at some 2500 panel meetings. CSR's budget to manage the entire operation was $110 million.

NIH officials say that peer review is just one building block in constructing a well-balanced portfolio of grants. But they acknowledge that NIH program managers are much more likely than their counterparts at other federal agencies to worry about the consequences of funding a grant "out of order." The assumption is that study sections know best and that a panel's judgment should be overruled only for compelling reasons.

Still, Nakamura is always looking for fresh ways to assess the performance of study sections. At the December meeting of the CSR advisory council, for example, he and Tabak described one recent attempt that examined citation rates of publications generated from research funded by each panel. Those panels with rates higher than the norm—represented by the impact factor of the leading journal in that field—were labeled "hot," while panels with low scores were labeled "cold."

"If it's true that hotter science is that which beats the journals' impact factors, then you could distribute more money to the hot committees than the cold committees," Nakamura explains. "But that's only if you believe that. Major corporations have tried to predict what type of science will yield strong results—and we're all still waiting for IBM to create a machine that can do research with the highest payoff," he adds with tongue in cheek.

"I still believe that scientists ultimately beat metrics or machines. But there are serious challenges to that position. And the question is how to do the research that will show one approach is better than another."

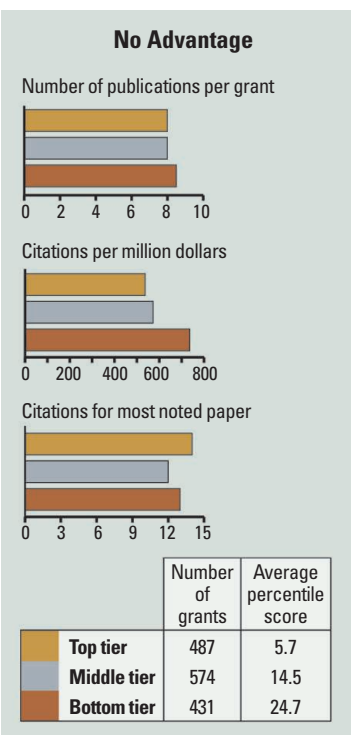

	Number of grants	Average percentile score
Top tier	487	5.7
Middle tier	574	14.5
Bottom tier	431	24.7

Equal impacts. The publication record from proposals with the best scores was no better than for those scoring in the middle and lowest tiers among heart research funded by NIH.

Bolder fixes wanted

Jaffe says he tried for more than a decade to interest top officials at both NIH and the National Science Foundation (NSF) in conducting the same type of quantitative analysis of peer review across the entire agency that Lauer has done within his program. But he was thwarted. "It's amazing to me how scientists who believe in the scientific method don't believe it should be applied to study what they do," Jaffe says. "It's just so intuitively obvious to them that [the current system of peer review] is the best way to do things."

Lauer set out to study peer review within his institute on his own, without funding from CSR. His first inkling that NIH peer review might be falling short came from reading a January 2012 study in *BMJ*. It reported that fewer than half of the researchers funded by NHLBI to test ways of preventing and treating heart disease had published their results within 30 months of the end of the trial, and that one-third of the trials never saw the light of day. A disbelieving Lauer expanded the *BMJ* sample and did his own analysis to be sure. "But they were right," he says. A long lag time might be expected for negative results, but Lauer found the record was no better for studies that came up positive.

He wondered whether the sluggish publication record was a sign of a deeper problem: Maybe the institute was failing to fund studies that journals viewed as urgent and important. And that led him to question whether the peer-review system was doing its job.

So Lauer examined whether funded proposals that were ranked higher during peer review ended up having their data published faster. They didn't. "[T]here was no significant association between the peer-review priority scores received before the trial was funded and the time to publication," he and his NHLBI colleagues wrote last fall in *The New England Journal of Medicine*.

Lauer believes that his findings reflect a bias among reviewers at NHLBI against so-called pragmatic studies, which aim to inform patient care directly by studying a procedure or drug in a typical clinical setting such as an urban hospital. "The message from a pragmatic trial is that you either will or will not do something," he says. "But fewer than 20% of our trials focus on that."

The majority of NIH clinical trials are

SOURCE: ADAPTED FROM DANTHI *ET AL.*, *CIRCULATION RESEARCH* (ADVANCED ONLINE EDITION) 2014

Making Every Scientist a Research Funder

When it comes to using peer review to distribute research dollars, Johan Bollen favors radical simplicity.

Over the years, many scientists have suggested that the current system could be improved by changing the composition of the review panels, tweaking the interactions among reviewers, or revising how the proposals are scored. But Bollen, a computer scientist at Indiana University, Bloomington, would simply award all eligible researchers a block grant—and then require them to give some of it away to colleagues they judge most deserving.

That radical step, described in a paper Bollen and four Indiana colleagues recently posted on *EMBO Reports*, retains peer review's core concept of tapping into the views of the most knowledgeable researchers. But it would eliminate the huge investment in time and money required to submit proposals and assemble panels to judge them.

Bollen's process would be almost instantaneous: In a version of expert-directed crowdsourcing, scientists would fill out a form once a year listing their favored researchers, and a predetermined portion of their annual grant money—a total of, say, 50%—would then be transferred to their choices.

"So many scientists spend so much time on peer review, and there's a high level of frustration," Bollen explains. "We already know who the best people are. And if you're doing good work, then you deserve to receive support."

Others are skeptical. "I've known Johan for a long time and have the highest regard for his ability as an out-of-the-box thinker," says Stephen Griffin, a retired National Science Foundation (NSF) program manager who's now a visiting professor of information sciences at the University of Pittsburgh in Pennsylvania. "But there are a number of issues he doesn't address."

Those sticking points include the likely mismatch between what researchers need and what their colleagues give them; the absence of any replacement for the overhead payments in today's grants, which support infrastructure at host institutions; and the dearth of public accountability for the billions of dollars that would flow from public coffers to individuals. "Scientists aren't really equipped to be a funding agency," Griffin notes.

Bollen acknowledges that the process would need safeguards to ensure that scientists don't reward their friends or punish their enemies. But his analysis suggests that the U.S. research landscape would not look all that different if his radical proposal were adopted.

Drawing upon citation data in 37 million papers over 20 years, the Indiana researchers conducted a simulation premised on the idea that scientists would reallocate their federal dollars according to how often they cited their peers. The simulation, he says, yielded a funding pattern "similar in shape to the actual distribution" at NSF and the National Institutes of Health for the past decade—at a fraction of the overhead required by the current system.

–JDM

instead aimed at testing the underlying biological mechanism of a disease or a treatment. That approach requires researchers to examine a strictly defined set of participants in a specialized clinical environment. Study sections view such an approach as more compelling, Lauer says. "When I go on the road to preach pragmatic trials," he says, "I can predict that someone will stand up and say, 'That's all well and good. But if we submit a proposal for a pragmatic trial, it will get killed in review.' "

Lauer is already at work on changing that perception. The heart division has invited researchers to submit proposals for pragmatic trials that address what he calls "important clinical questions." He's also altered the review process in two significant ways: All the proposals will go to a single panel that will only judge pragmatic trials, and its members will consist of "people who know a lot about pragmatic trials and think they are valuable."

Lauer says his second study, which looked at NIH's bread-and-butter R01 grants, highlights another problem. It divided R01 grants awarded by NHLBI into three pools based on their percentile ranking—better than 10th percentile, 10th to 20th, and 20th to 42nd. His sample went back to 2001, when NIH had the resources to fund some of the proposals in that third tier. These days, proposals in that third category have virtually no chance of being funded, so the fact that the research drew as many citations as top-ranked projects suggests that peer reviewers are ruling out a large share of potentially significant research.

The problems of peer review, Lauer says, are those that afflict any system that relies on the judgments of experts. One eye-opener for Lauer was a 2006 book by Philip Tetlock, a psychologist at the University of Pennsylvania, titled *Expert Political Judgment: How Good Is It? How Can We Know?* The book describes how experts do little better than chance in predicting political events and also vastly overrate their prognosticating abilities. Its lessons apply to peer review as well, Tetlock says "There is high-impact research that has been rejected, and low-impact research that has been funded."

Tetlock is not surprised that NIH hasn't rushed to embrace the kind of self-examination Lauer has done. "Most institutions are not enthusiastic about an objective appraisal of their track records," he says. They are also worried that the results could be used against them. "If the hit rate is not too high and the false positives are high," he says, "people may jump to the conclusion that you guys are a bunch of idiots. In fact, the agency could be doing as good a job as possible, given the unpredictability of the task."

Lauer and Jaffe say NIH should be bolder in designing experiments to improve peer review without abandoning it. In particular, they would like NIH to rigorously test critical components of the system. Possibilities include using a second set of reviewers as a control, or asking reviewers to score proposals on several specific criteria and then tallying up those subscores rather than asking for one overall rating, as is done now.

No system has a 100% hit rate on high-impact programs and never funds a low-impact program, Tetlock notes. "That would be God," he says. But he believes there is plenty of room for improvement. "By using the best science we have on how to elicit and aggregate judgments, maybe we can get our hit rate up and our false positives down," Tetlock says. "And that would be a better world."

–JEFFREY MERVIS

Dead Heat

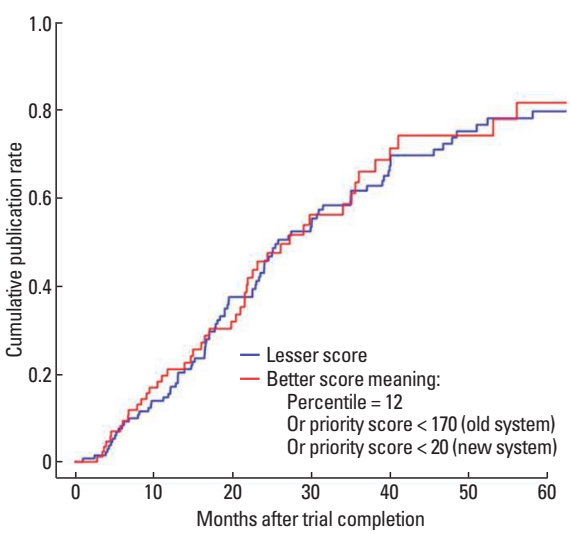

Slow off the mark. The time to publication for NHLBI clinical trials isn't linked to what review panels thought about the research.

CREDIT: ADAPTED BY M. LAUER FROM D. GORDON *ET AL.*, *NEJM* **369** (14 NOVEMBER 2013)

Published by AAAS

2013

VISUALIZATION CHALLENGE

HTTP://SCIM.AG/VISCHALL2013

FOR THE PAST 11 YEARS, *SCIENCE* AND THE U.S. NATIONAL SCIENCE Foundation (NSF) have joined forces to celebrate the old axiom: A picture is worth a thousand words. The International Science & Engineering Visualization Challenge honors the long tradition of using illustration to communicate the complexities of science, engineering, and technology to students and the public.

We asked contestants to provide visualizations that illustrate powerful scientific concepts, offering prizes in the traditional categories of illustration, posters & graphics, and photography, as well as in newer ones: games & apps and video. We were delighted by this year's responses: 227 submissions from 12 countries, including entries from 17 U.S. states and Canadian territories. The best of the submissions are both beautiful and captivating, able to excite popular interest in subjects normally treated with academic rigor.

This year's top entries feature Earth and planets sitting at the focus of multiple streams of energy driven by the sun, a game that allows thousands of users to collaborate in mapping neurons, wearable energy storage to power future electronic clothing, and other compelling science and technology. These and more winners are featured on the following pages and at http://scim.ag/VisChall2013 and www.nsf.gov/news/scivis.

Tarri Joyner of NSF organized this year's challenge. Garvin Grullón of *Science*'s Art Department designed this special section, and Mark Peplow, a science journalist in Cambridge, U.K., wrote the text.

Judith Gan
Head, Office of Legislative & Public Affairs
National Science Foundation

Tim Appenzeller
News Editor, *Science*

JUDGES

Alisa Zapp Machalek
National Institute of General Medical Sciences, Bethesda, Maryland

Lori Kozlowski
Forbes magazine, Los Angeles, California

Thomas Wagner
NASA, Washington, D.C.

Corinne Sandone
Johns Hopkins University School of Medicine, Baltimore, Maryland

Tierney Thys
National Geographic Explorer, Carmel, California

Science

NSF

Honorable Mention

Security Blanket

Lorrie Faith Cranor, Carnegie Mellon University, Pittsburgh, Pennsylvania

How much protection do your Internet passwords provide? Some 32 million passwords stolen from the games website RockYou were published on the World Wide Web in 2009, and they reveal our penchant for choosing passwords that may offer no security at all.

Last year, Lorrie Faith Cranor, avid quilter and director of the CyLab Usable Privacy and Security Laboratory at Carnegie Mellon University, created *Security Blanket*, which displays a multicolored "word cloud" of the 1000 most common passwords in the RockYou release. The passwords were sized according to their frequency and colored according to their theme.

The most common—"123456"—was chosen by three times as many people as the next most popular password and is so large that it forms a faint backdrop across the whole quilt. But beyond the other obvious passwords (such as—duh—"password"), Cranor shows that our selections often converge on the same words. "Chocolate" is the most popular food-related password; "monkey" tops the animals category; and, reassuringly, words relating to love or tenderness far outweigh profanities.

Cranor has also made a password dress for herself, which she wore to the opening of an exhibition of her quilts. "A couple of friends have suggested turning the quilt design into a line of baby linens for the children of geeky parents," she adds.

Published by AAAS

Cortex in Metallic Pastels

Greg Dunn and Brian Edwards, Greg Dunn Design, Philadelphia, Pennsylvania; Marty Saggese, Society for Neuroscience, Washington, D.C.; Tracy Bale, University of Pennsylvania, Philadelphia; Rick Huganir, Johns Hopkins University, Baltimore, Maryland

FIRST PLACE ILLUSTRATION

With a Ph.D. in neuroscience and a love of Asian art, it may have been inevitable that Greg Dunn would combine them to create sparse, striking illustrations of the brain. "It was a perfect synthesis of my interests," Dunn says.

Cortex in Metallic Pastels represents a stylized section of the cerebral cortex, in which axons, dendrites, and other features create a scene reminiscent of a copse of silver birch at twilight. An accurate depiction of a slice of cerebral cortex would be a confusing mess, Dunn says, so he thins out the forest of cells, revealing the delicate branching structure of each neuron.

Dunn blows pigments across the canvas to create the neurons and highlights some of them in gold leaf and palladium, a technique he is keen to develop further.

"My eventual goal is to start an art-science lab," he says. It would bring students of art and science together to develop new artistic techniques. He is already using lithography to give each neuron in his paintings a different angle of reflectance. "As you walk around, different neurons appear and disappear, so you can pack it with information," he says.

The painting was commissioned for the Johns Hopkins University School of Medicine's Brain Science Institute, but, Dunn says, "I want to be able to communicate with a wide swath of people." He hopes that lay viewers will see how the branching structures of neurons mirror so many other natural structures, from river deltas to the roots of a tree. "I want to help people to appreciate the beauty of the brain."

"It is just gorgeous," says judge Alisa Zapp Machalek. "The fact that science can be in an art museum is something we want to encourage."

Prints of Greg Dunn's art, including this winning painting, are available at www.gregadunn.com.

People's Choice

Human Hand Controlling Bacterial Biofilms

Lydia-Marié Joubert, Cell Sciences Imaging Facility, Stanford University, California

In our war against bacteria, the microbes are winning. That somber message is writ large in this image of a human hand covered with *Pseudomonas* bacteria.

"Antimicrobial resistance is a hot topic, especially since it has become clear that our efforts to eradicate microorganisms have made them more resilient," says Lydia-Marié Joubert, an electron microscopy specialist at Stanford University who created the image. While attending a conference at Gregynog Hall in Wales, Joubert photographed a 1.5-meter-high human hand that reaches out of the soil in the hall's gardens, sculpted by British artist Francis Hewlett. Then she overlaid micrographs of cultured biofilms, which had been stained with molecular probes to indicate the health of the cells. Those colored green are resistant to antimicrobial treatment—only a rare few are red, indicating that they have been vanquished.

"We try to control microbes," Joubert says, "but the unseen world remains victorious."

Published by AAAS

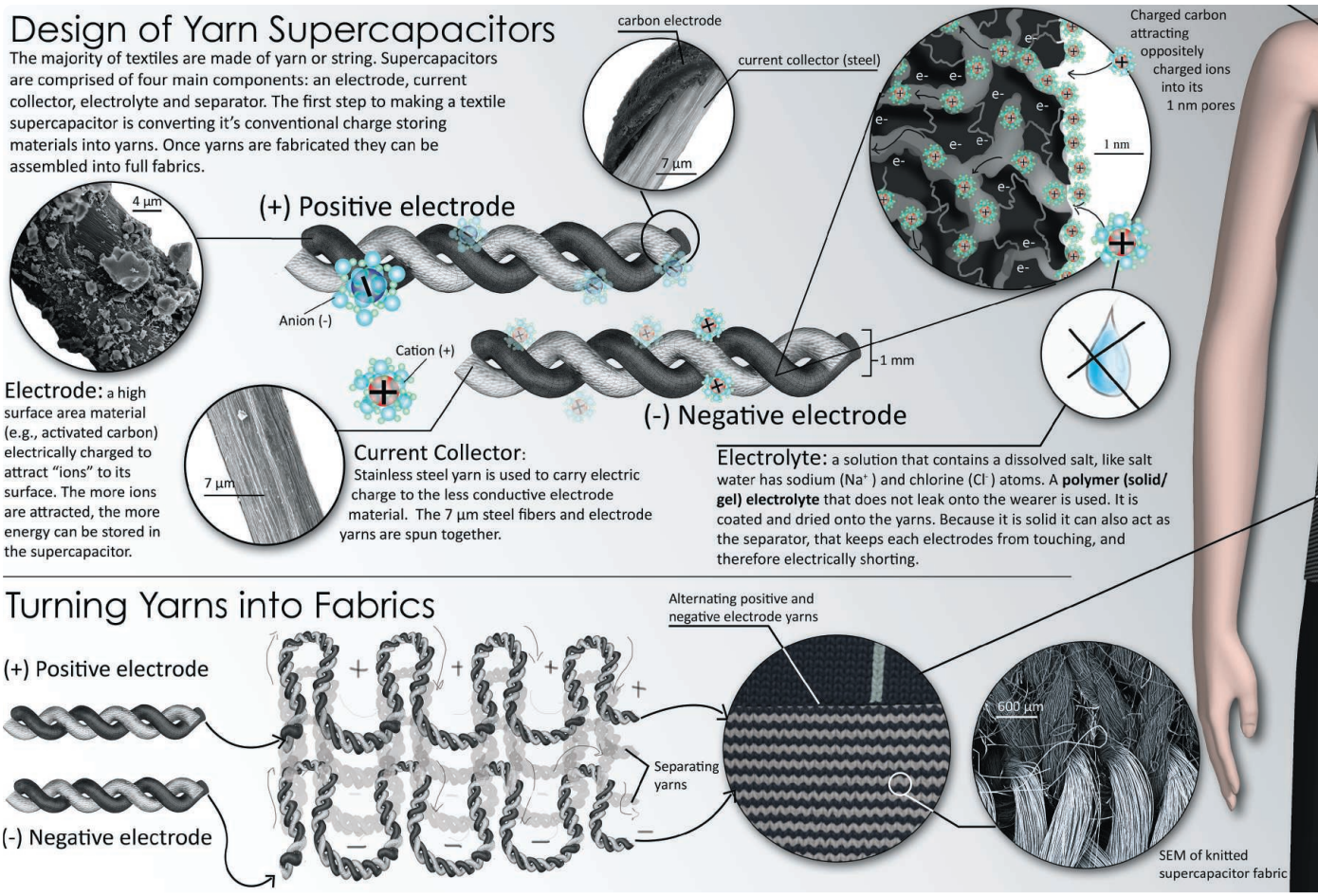

Honorable Mention

The Life Cycle of a Bubble Cluster: Insight from Mathematics, Algorithms, and Supercomputers

Robert I. Saye and James A. Sethian, Lawrence Berkeley National Laboratory and the University of California, Berkeley

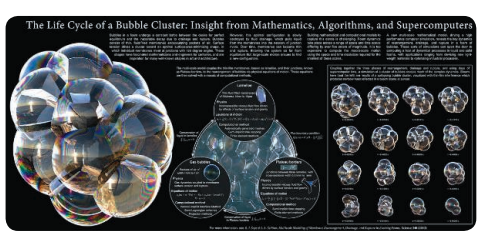

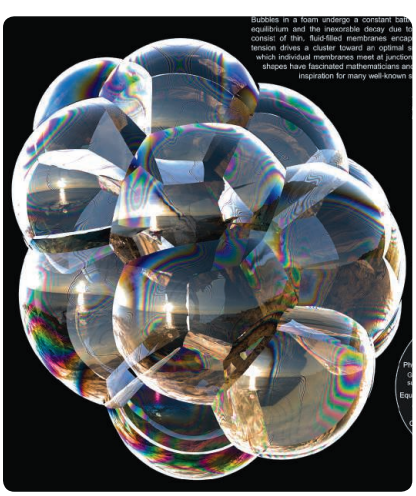

"Isn't that just a photograph of soap bubbles?" Robert Saye and James Sethian hear that all the time when people see their poster. "Naturally we are eager to point out that it is in fact a visualization of a physics computational model," says Saye, who recently completed his Ph.D. with Sethian at the Lawrence Berkeley National Laboratory and the University of California, Berkeley.

Predicting how bubbles in a foam rearrange and rupture is a tough modeling problem, because it involves intricately coupled processes that operate at very different scales. The soap films are only micrometers thick, while the gas pockets themselves might be centimeters across. Meanwhile, individual films rupture in milliseconds; bubbles rearrange in a fraction of a second; and liquid inside the film drains over tens of seconds or longer.

Running a simulation at the smallest scales to predict the macroscopic effects would eat up vast amounts of computer power. "Instead, we found a way to separate distinct time and space scales, and allow these to communicate so that the most important physics affecting foam dynamics are captured," Saye says. The model, published last year (*Science*, 10 May 2013, p. 720), could be useful in devising lightweight materials or optimizing industrial processes, he and Sethian suggest.

Watch a video of the foam simulation at www.youtube.com/watch?v=ciciWBz8m_Y.

Published by AAAS

Wearable Power

Kristy Jost, Babak Anasori, Majid Beidaghi, Genevieve Dion, and Yury Gogotsi, Drexel University, Philadelphia, Pennsylvania

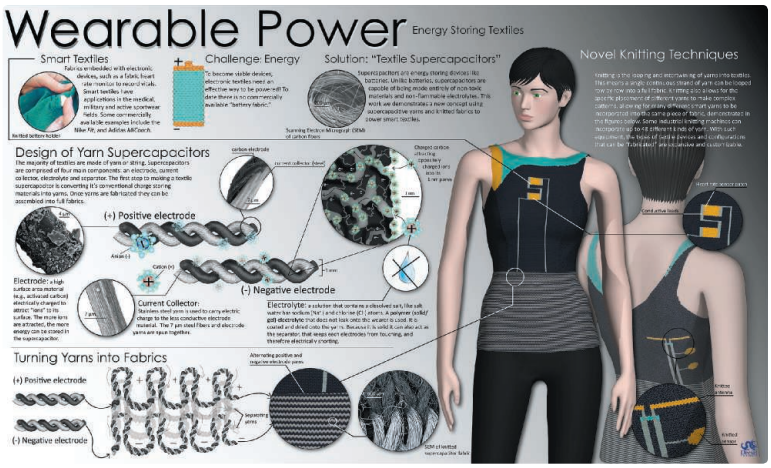

"When I try to explain that I make fabric batteries to people, they kinda give me this look like their brain has just exploded," says materials scientist Kristy Jost, who is studying for her Ph.D. at Drexel University. "Having a visual is really helpful."

"Smart textiles" offer the opportunity to create functional clothes—a vest that can measure your heart rate, for example. But flexible sensors are still powered by hard, uncomfortable batteries. "Why not make the whole system out of textiles?" Jost asks. Her research aims to create fabrics from carbon and steel yarns that are coated with electrolytes so that the resulting garment is also a wearable capacitor, able to store energy.

FIRST PLACE & PEOPLE'S CHOICE
POSTERS & GRAPHICS

Jost spends much of her time in Drexel's knitting research laboratory—yes, you read that right—which boasts state-of the-art equipment donated by Shima Seiki, a Japanese company that makes computerized 3D knitting systems. The machines can knit an entire seamless garment in 20 minutes, and Jost has become adept at using the design software that drives them—although she admits sheepishly that she has not yet learned to knit by hand.

She used her design expertise in the winning poster, which shows how the yarns intertwine to create a complete item of clothing and includes scanning electron microscope images and nanoscale diagrams to illustrate how the smart textile works at different scales. "It has an incredible amount of technical material," judge Thomas Wagner says. "It's a phenomenal piece of education."

Jost was delighted by the judges' award, but was particularly pleased that she was also the People's Choice in this category. "When you also get the People's Choice award," she says, "you know you've really communicated the science well."

Honorable Mention

Effects of Cold-stunning on Sea Turtles

Katelyn McDonald and Timothy Phelps, Johns Hopkins University, Baltimore, Maryland; Jennifer Dittmar, the National Aquarium, Baltimore, Maryland

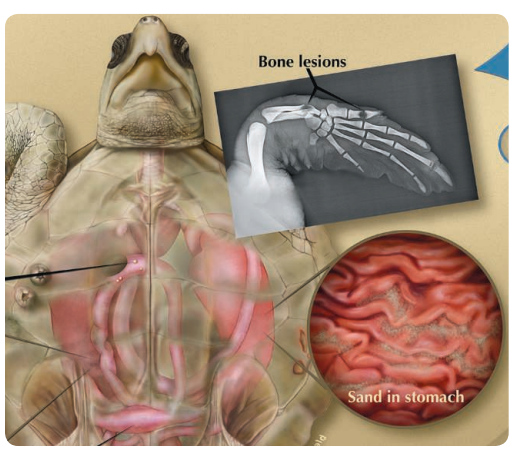

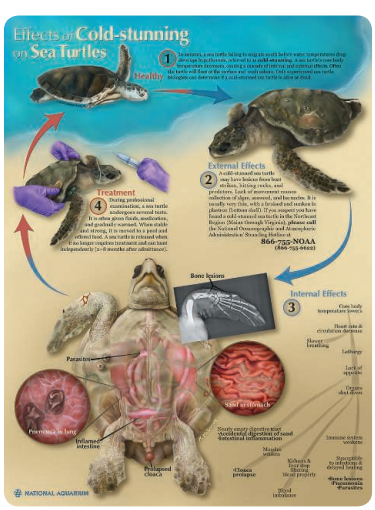

By the time October's chill winds begin to blow across the mid-Atlantic and northeastern United States, sea turtles near the coast are beginning to head south in search of warmer waters. But an unlucky few are overtaken by plummeting water temperatures and develop hypothermia. The turtle can lose consciousness and suffer shell damage and infections in a process called cold-stunning.

Katelyn McDonald, a master's student in biological and medical illustration at Johns Hopkins University, created the poster to explain cold-stunning to the general public, who may find afflicted turtles on the beach. "I am fascinated by sea turtles because of their majestic beauty, and how little is known about them, since they spend so little time on land," McDonald says.

The poster describes the physiological changes that lead to cold-stunning in a series of beautiful anatomical illustrations that were all based on medical images, but were drawn and assembled using computer design software. It also shows how to identify a cold-stunned turtle and provides the number of a turtle stranding hotline. McDonald says her goal is that the public "would learn more about the health of sea turtles, and hopefully be aware of the appearance of cold-stunned sea turtles and then call the hotline to seek help."

Published by AAAS

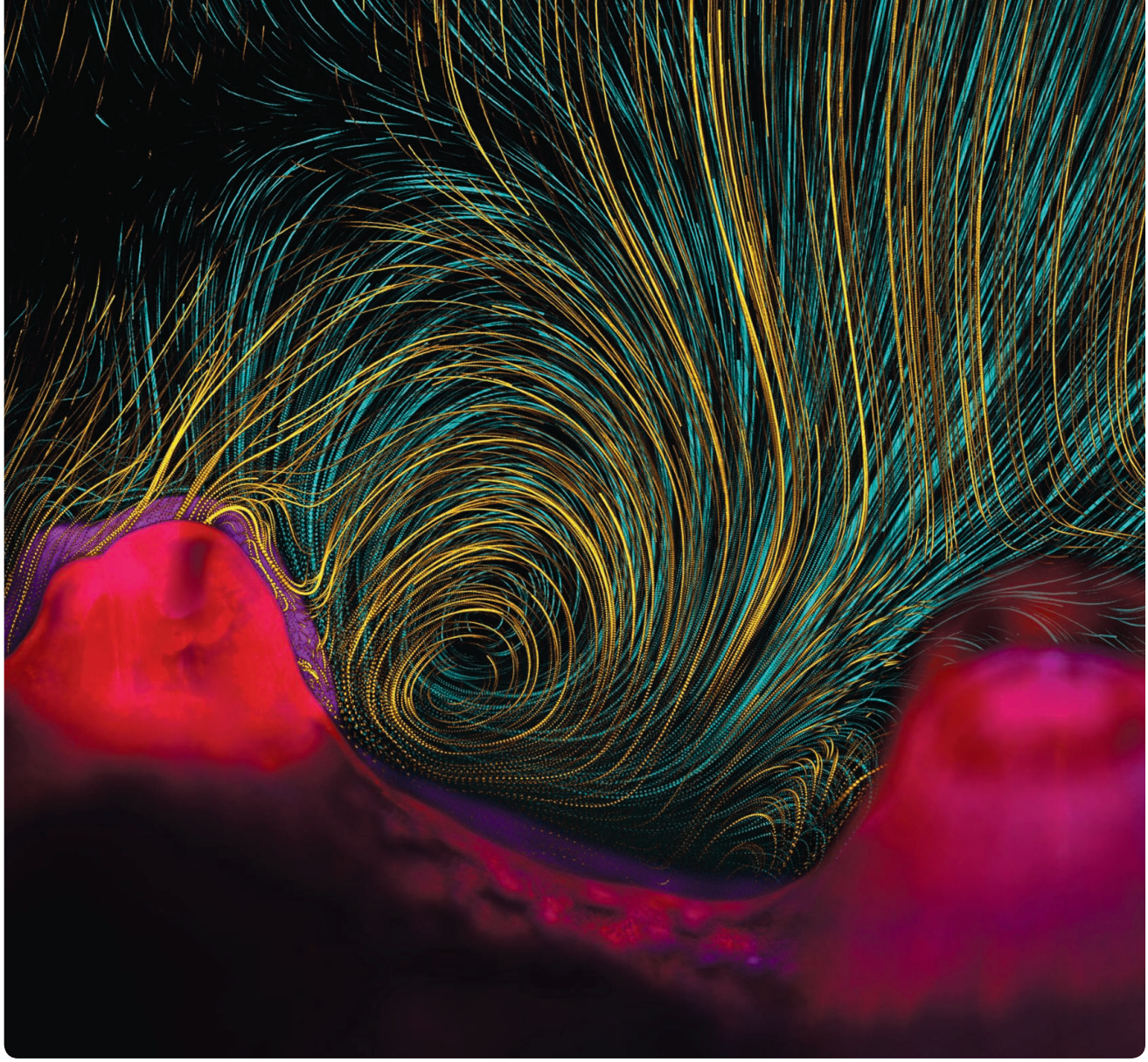

Invisible Coral Flows

Vicente I. Fernandez, Orr H. Shapiro, Melissa S. Garren, Assaf Vardi, and Roman Stocker, Massachusetts Institute of Technology, Cambridge

FIRST PLACE PHOTOGRAPHY

The swirling patterns moving around these coral polyps may look like fireworks streaking across a long-exposure photograph—but they are the result of a cunning technique that uses false colors to help compress time and movement into a single picture.

The image shows two *Pocillopora damicornis* polyps roughly 3 millimeters apart, colored pink. To reveal how the corals' wafting cilia beat the water into a vortex, the team tracked particles in the water by video and super-imposed successive frames to highlight the flow (gold). About 90 minutes later, the coral polyps have changed position (shown in purple), altering the water flow (cyan), "but the vortex stayed roughly the same," says Massachusetts Institute of Technology environmental engineer Vicente Fernandez, part of the research team that produced the image. The spacing between points in the vortex tracks even reveals the speed of the particles, he adds: "Up close you can see the steps of individual particles, see where the flow is strongest." Fernandez says that the team drew inspiration from the palette used by Andy Warhol in his *Flowers* prints, which feature vivid, strongly contrasting colors.

The vortex helps draw nutrients toward the coral and sweep away waste products, says Fernandez's colleague Orr Shapiro, an ecologist at the Weizmann Institute of Science in Rehovot, Israel. "Everywhere I look at corals now I find these vortical swirls," he adds.

"This was a unanimous winner," says judge Alisa Zapp Machalek. "It's a striking image—but it also represents an aspect of nature that, to our knowledge, had never been captured before."

Published by AAAS

Honorable Mention

Stellate leaf hairs on *Deutzia scabra*

Steve Lowry Photography, Portstewart, Northern Ireland, U.K.

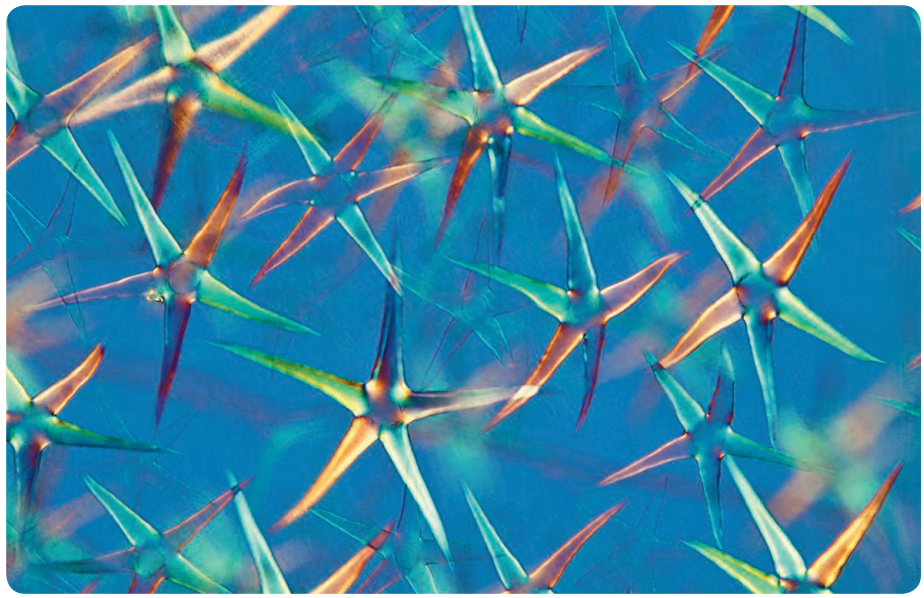

These exuberant starbursts shoot from the leaves of *Deutzia scabra*, a deciduous shrub sometimes known as "Pride of Rochester." Its leaves are covered with tiny hairs tipped by stars a quarter-millimeter across, giving it a fuzzy texture that Japanese woodworkers sometimes use for fine polishing.

Microscopist Steve Lowry created the image's vibrant hues using polarized light microscopy and emphasized the blue color by filtering the light through a crystal of selenite (calcium sulfate). He has been interested in this 19th century technique since 2007, when he produced an exhibition of images from Victorian microscope slides.

Lowry says that the image shows how this microscopy technique, whose use has waned in recent years, can still be a valuable tool in plant taxonomy. By revealing variations in the stars' density, size, and shape, for example, it can help distinguish the more than 20 different species of *Deutzia*. But it also offers aesthetic insight, he says, introducing people "to the hidden beauty of plants not visible to the human eye."

People's Choice

Polymer Micro-structure Self-assembly

Anna Pyayt and Howard Kaplan, University of South Florida, Tampa

Is this an alien microbe, glowing with unearthly vitality? Or perhaps an aerial shot of Manhattan Island after a catastrophic flood? In fact, it shows the microstructure of a 2-millimeter-long fragment of self-assembled polymers, which University of South Florida materials scientist Anna Pyayt is using to build miniature "lab-on-a-chip" devices for biomedical diagnostic applications.

Processing combinations of polymers at various temperatures or humidities creates completely different textures, she explains, which can help to control the movement and proliferation of cells inside the devices. The digitally enhanced micrographs are even more revealing after Howard Kaplan at the university's Advanced Visualization Center turns them into 3D images. "We have been using a huge 20-megapixel 3D-visualization wall to study little details and nuances of topographies that we produce in our experiments," Pyayt says. With the help of a 3D printer, they have even turned the images into tactile objects the size of a candy bar.

"To see this complex, rich structure with so many little details was amazing," Pyayt says. "The first word that we usually hear is 'Wow.' "

Published by AAAS

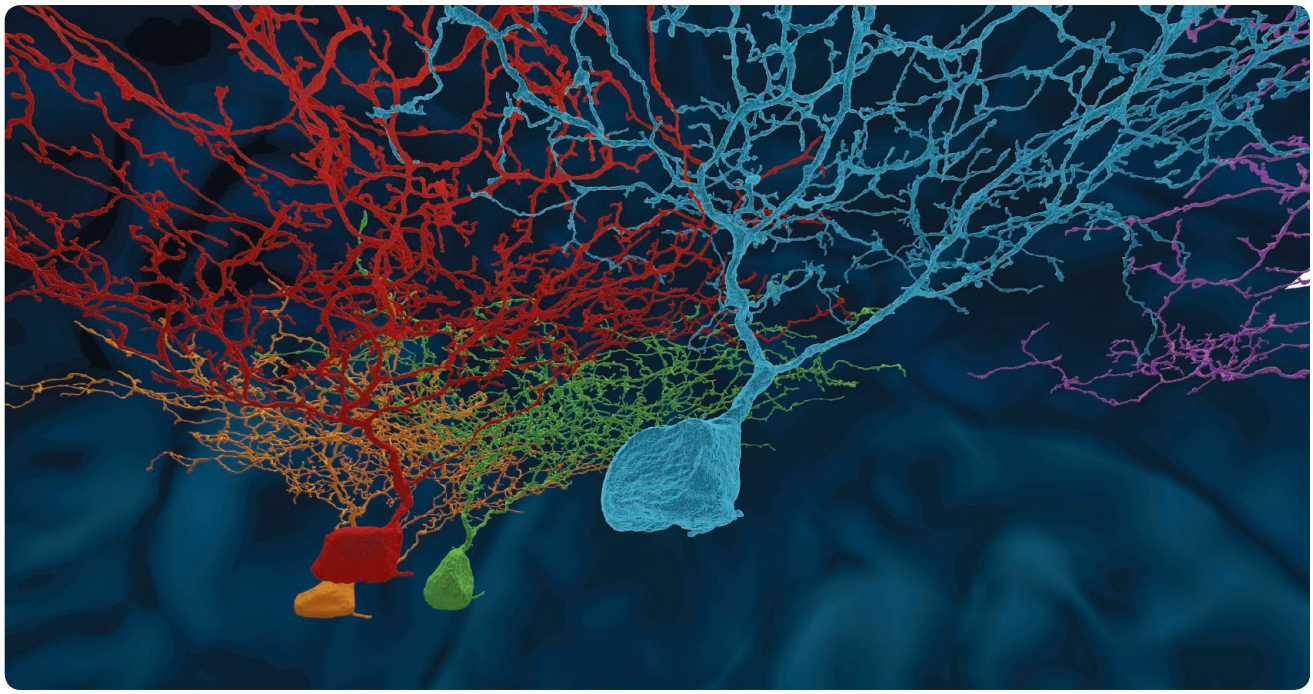

EyeWire

Mark Richardson, William Silversmith, Matthew Balkam, Jinseop Kim, Amy Robinson, Alex Norton and H. Sebastian Seung, EyeWire, Massachusetts Institute of Technology, Cambridge

Swamped by a deluge of data, some labs are using the power of crowds to make sense of their results. These citizen science projects ask nonspecialists to analyze real research data, often by looking for patterns that computers are unable to spot. Some of the most successful efforts turn the task into games, fostering a sense of competition that can keep players hooked.

EyeWire is one of the fastest growing citizen science projects ever created. After going live in December 2012, "we got to 100,000 players on our first birthday," says Amy Robinson, the project's creative director. "It solves a big technical bottleneck in neuroscience—reconstructing neuron circuits."

Run from the lab of Massachusetts Institute of Technology neuroscientist H. Sebastian Seung, the game presents players with micrographs that show the neurons in a mouse's retina. The goal is to distinguish the twists and turns of a particular neuron in 3D, in order to build up a complete map of the complex connections involved in vision.

It's proved difficult to develop artificial intelligence software that can do the job, whereas the army of human volunteers can use subtle contextual clues, such as jagged edges or discontinuities, to delineate each neuron. Seung's team is using the EyeWire maps to help them understand how the eye detects motion, and their first paper using the game's results is now under review.

One of the game's biggest strengths is the close collaboration between the EyeWire team and their recruits—everyone is consulted before new features are introduced, for example. "I'm constantly amazed by the community we've built," Robinson says. EyeWire is proof that games have become a powerful force in science communication, says judge Lori Kozlowski: "You're able to reach the public in a way that allows them to become much more comfortable with the science."

Visit the website at eyewire.org.

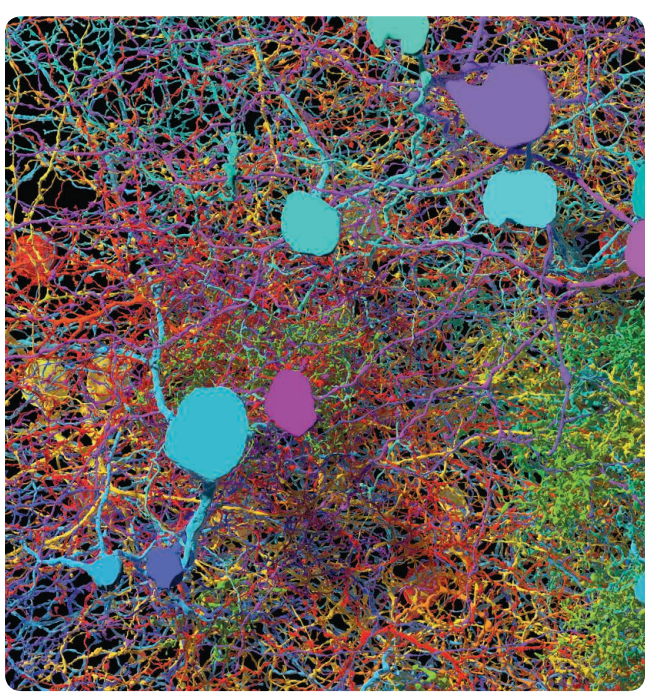

Published by AAAS

Honorable Mention

EarthViewer

Mark Nielsen and Satoshi Amagai, Howard Hughes Medical Institute, Chevy Chase, Maryland; Michael Clark, EarthBuzz Software Pte Ltd., Singapore; Blake Porch; Dennis Liu, Howard Hughes Medical Institute, Chevy Chase, Maryland

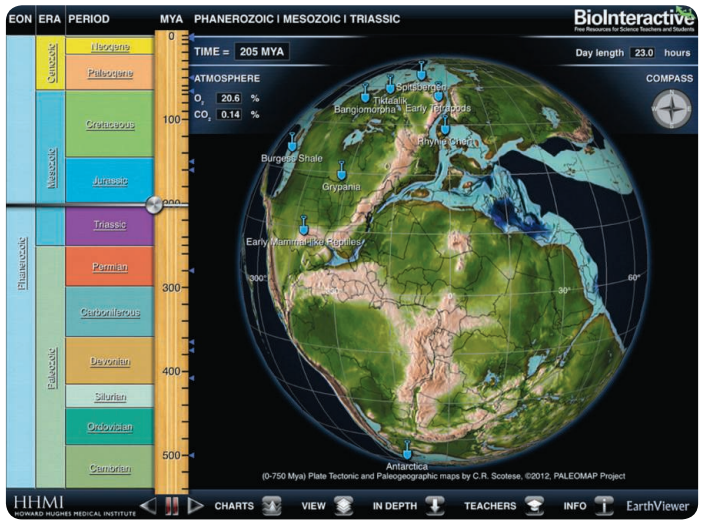

EarthViewer is an iPad app that puts our planet's deep history at your fingertips. You can scroll through billions of years in a few seconds, watching how continents shift and how changes in solar luminosity, atmospheric composition, and climate interact. A simple swipe across the screen rotates this virtual Earth, letting you explore at will. The app also comes with profiles of the creatures that inhabited the ancient Earth and allows you to zoom in on where their fossils were found.

Developed by the Educational Resources Group at the Howard Hughes Medical Institute, it is intended primarily as a teaching tool in high school. But it is pretty addictive for inquisitive adults, too—even those who have always had trouble telling the Paleocene from the Pliocene.

Visit the website at www.hhmi.org/biointeractive/earthviewer.

Honorable Mention

Deep-sea Extreme Environment Pilot (DEEP)

Daniel Rohrlick, Eric Simms, Cheryl Peach, and Debi Kilb, Scripps Institution of Oceanography, San Diego, California; Charina Cain, Birch Aquarium at the Scripps Institution of Oceanography, San Diego, California

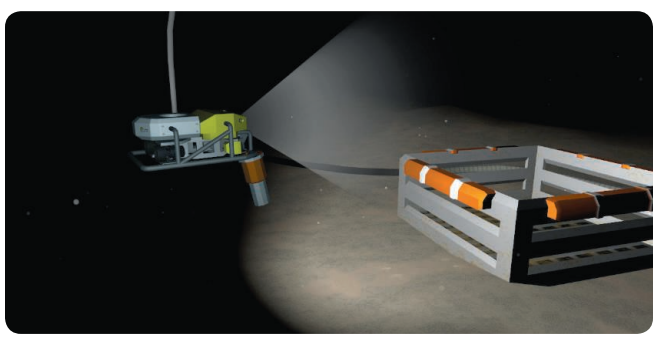

This educational game enables budding deep-sea explorers to guide a remotely operated vehicle (ROV) as it studies a virtual hydrothermal vent. Giant tubeworms sway gently as an eel swishes past; a nosy octopus even comes over for a look. As the ROV moves through its 3D environment, the pilot can take temperature readings, snap pictures, and grab samples with the craft's robot arm to complete a series of research missions.

Educators at the Scripps Institution of Oceanography developed the interactive game to inspire middle school pupils. It offers the same freedom afforded by commercial "open world" games, allowing users to explore at their own pace. Its appeal is not limited to schoolchildren, notes Daniel Rohrlick, one of the developers: "Even ROV pilots enjoy the game."

Visit the website at siogames.ucsd.edu/deep.html.

People's Choice

Meta!Blast: The Leaf

Eve Syrkin Wurtele, William Schneller, Paul Klippel, Greg Hanes, Andrew Navratil, and Diane Bassham, Iowa State University, Ames

"Most people don't expect a whole ecosystem right on the leaf surface," says Eve Syrkin Wurtele, a plant biologist at Iowa State University. Meta!Blast: The Leaf, the game that Wurtele and her team created, lets high school students pilot a miniature bioship across this strange landscape, which features nematodes and a lumbering tardigrade. They can dive into individual cells and zoom around a chloroplast, activating photosynthesis with their ship's search lamp. Pilots can also scan each organelle they encounter to bring up more information about it from the ship's BioLog—a neat way to put plant biology at the heart of an interactive gaming environment.

This is a second recognition for Meta!Blast, which won an Honorable Mention in the 2011 visualization challenge for a version limited to the inside of a plant cell.

Visit the website at www.metablast.org/scivis2013.

Published by AAAS

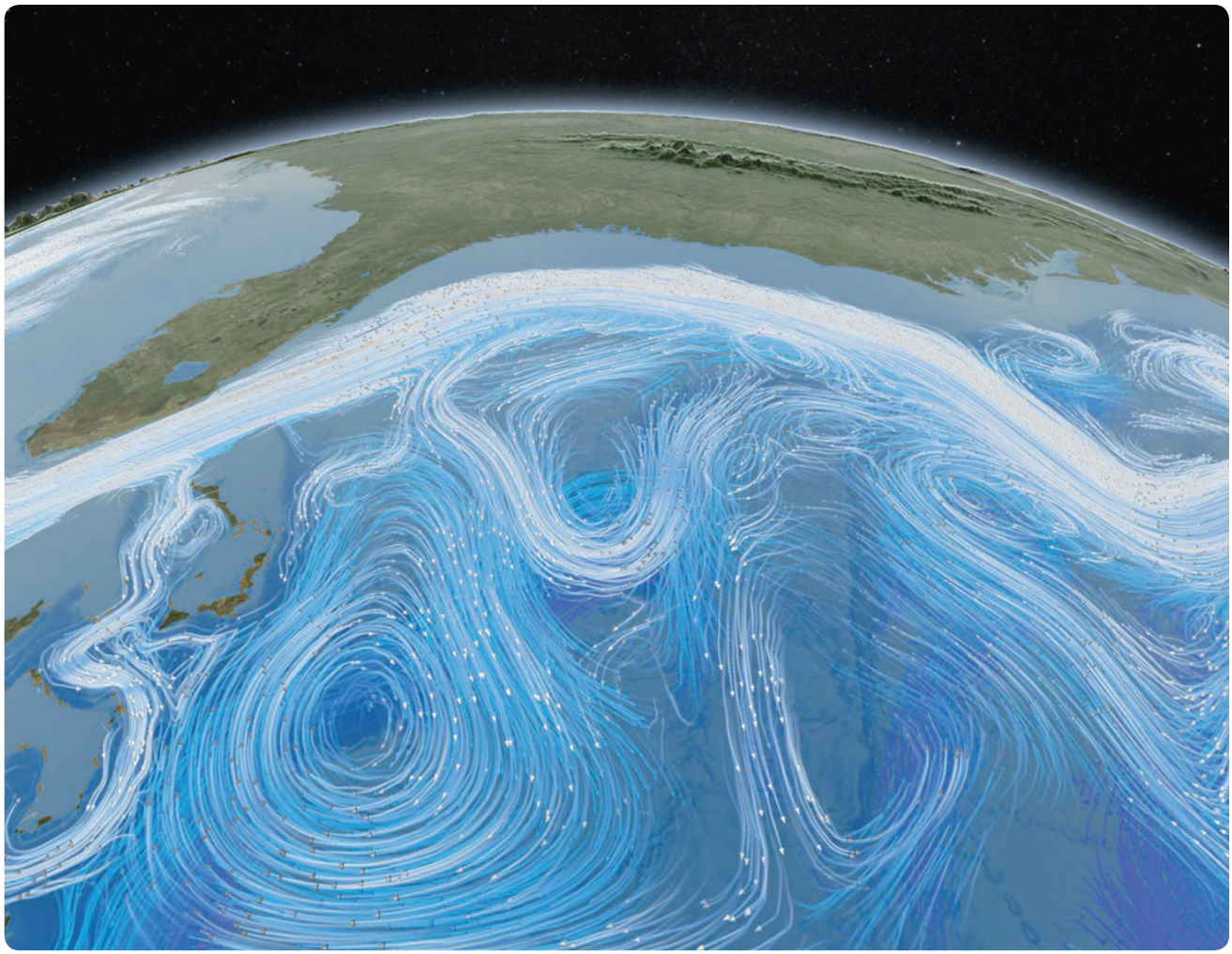

Coronal Mass Ejection and Ocean/Wind Circulation

Greg Shirah, Horace Mitchell, and Tom Bridgman, NASA Goddard Space Flight Center Scientific Visualization Studio, Greenbelt, Maryland

FIRST PLACE VIDEO

Like a million-strong armada, solar particles hurtle toward Earth—and we are flying with them. The planet's magnetic field forms a safe cocoon against the invaders, but the sun's warmth permeates our atmosphere, and we can see how it drives wind patterns in immense loops and whorls. Our flight ends with a plunge into the ocean, exploring the majestic structure of the Gulf Stream, which our guide tells us "carries enough heat energy to power the industrial world a hundred times over." It truly is an immersive experience.

The video segment is just part of a longer film called *Dynamic Earth: Exploring Earth's Climate Engine* that has played to audiences in planetaria around the world. "It's one of the top visualizations we've ever done," says Horace Mitchell, who leads NASA's Scientific Visualization Studio.

The film took about a year and a half to produce, using real satellite data and six computational models to create a vision that is both beautiful and scientifically accurate. Its long, swooping scenes reveal how different parts of the climate system interact at very different scales. "I was impressed by how the video was able to connect phenomena starting at the sun down to planet Earth," says judge Alisa Zapp Machalek.

Mitchell uses the same production software as commercial studios such as Pixar. But unlike animators, who see only what they plan and create, his team is often surprised by what their virtual creations reveal: "After we put the data in, we say 'Wow, we didn't know it was going to look like that.' "

Watch the video at www.youtube.com/watch?v=ujBi9Ba8hqs.

Honorable Mention

StemCellShorts

Ben Paylor, Michael Long, Jim Till, Janet Rossant, Mick Bhatia, David Murawsky, and James Wallace, Stem Cell Network, Ottawa

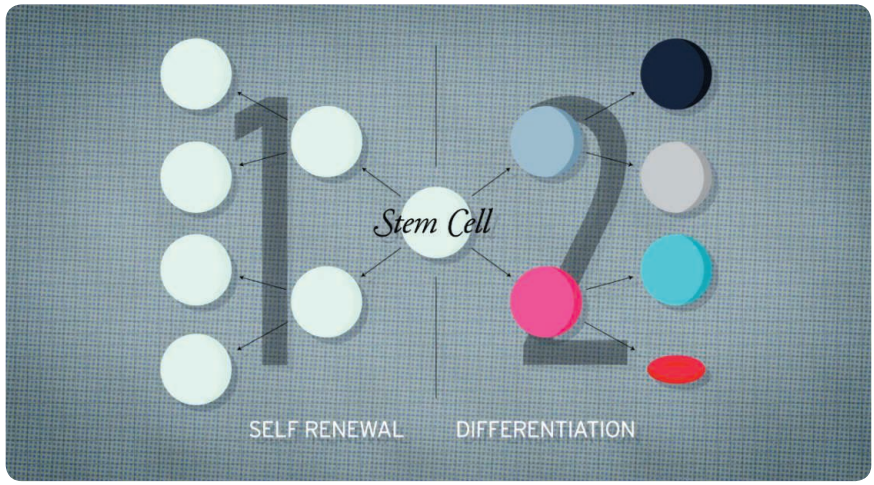

"In an animated medium, almost anything is explainable within 60 seconds," says Ben Paylor, a Ph.D. candidate at the University of British Columbia, Vancouver, in Canada. Witness these three 1-minute videos, created by Paylor and Michael Long, a postdoctoral fellow at the University of Toronto, to introduce a lay audience to stem cells in their embryonic and induced pluripotent forms.

Paylor and Long co-founded InfoShots, an animation studio based in Vancouver, to turn complicated science into compact, digestible films. After winning a grant from the Stem Cell Network, which funds applied stem cell research across Canada, they recruited eminent scientists to help script and voice these slick animations. "It was pretty amazing to hear Jim Till explain the experiments that he and Ernest McCulloch performed in the 1960s, which led to the discovery of stem cells," Long says.

Paylor and Long are now expanding the series to cover adult and cancer stem cells, as well as ethical issues surrounding stem cell research, in the hope that it will help foster informed public dialogue about the implications and future of the work.

Watch the video at youtu.be/_hbgeQzmU9U.

Honorable Mention

Immunology of the Gut Mucosa

Doug Huff and Elizabeth Anderson, Arkitek Studios, Seattle, Washington; Zoltan Fehervari, *Nature Immunology*, London; Simon Fenwick, *Nature Reviews*, London

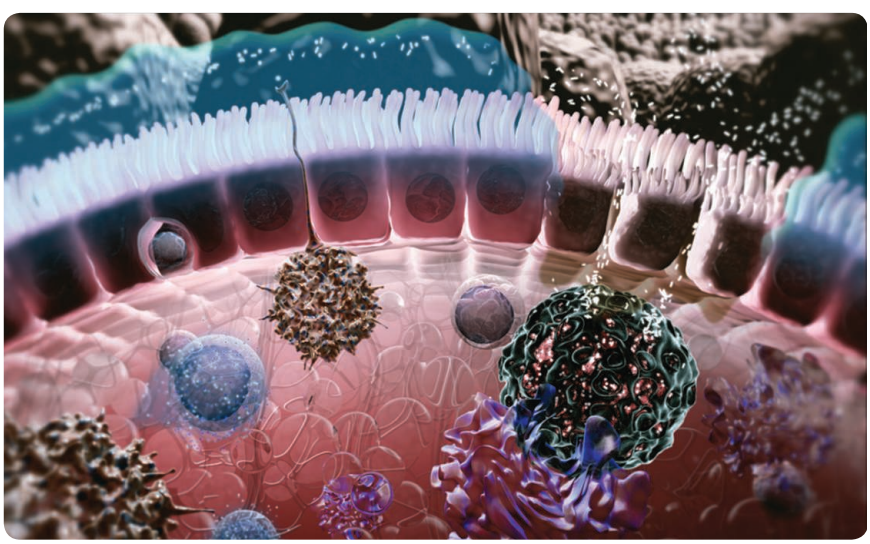

If James Cameron's long-delayed remake of the '60s sci-fi classic *Fantastic Voyage* ever hits the big screen, it might look something like this. After hurtling down a virtual throat, the 7-minute animation takes us on a tour around the gut—home to the body's largest population of immune cells—where a few hardy pathogens are beginning to cause trouble.

The film guides us deftly through the complex cast of characters that unite to battle the bacteria: T cells, macrophages, neutrophils, and more. Some of these iridescent warriors fizz with messenger molecules, while others pulse with deadly energy before exploding to destroy the bacteria. The video also shows how disorder in the ranks of immune soldiers can lead to problems such as inflammatory bowel disease.

"We've had a wonderful response, particularly from people suffering from complications of the gut who've expressed satisfaction at finally having a window on what's going on inside them," says Beth Anderson, CEO of medical visualization company Arkitek Studios, which created the video.

Watch the video at www.youtube.com/watch?v=gnZEge78_78.

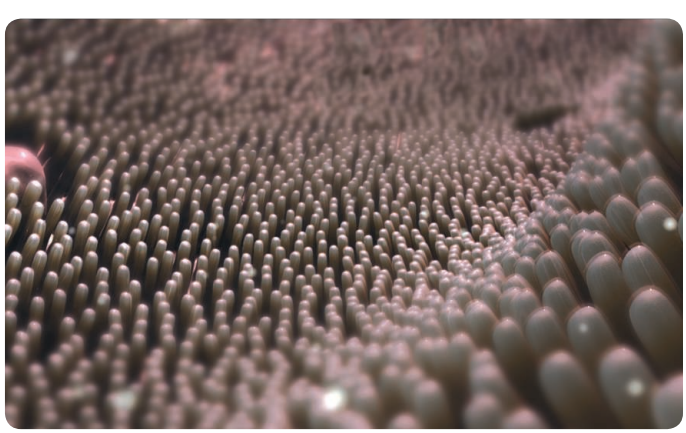

Published by AAAS

Honorable Mention

Visualizing Leaf Cells from Within

Geoffrey J. Harlow, Shuo Li, Albert C. Cruz, Jisheng Chen, and Zhenbiao Yang, University of California, Riverside

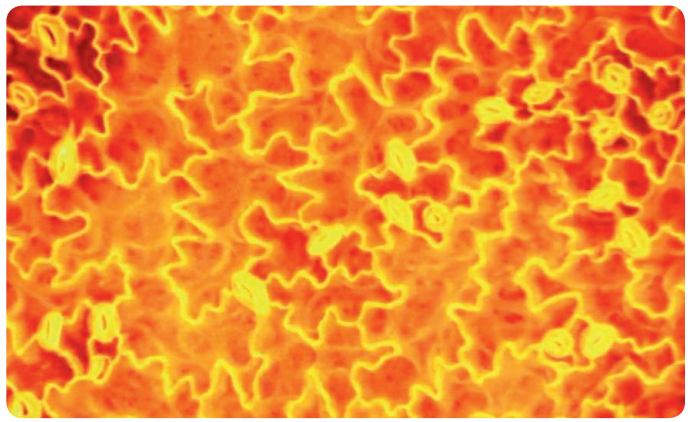

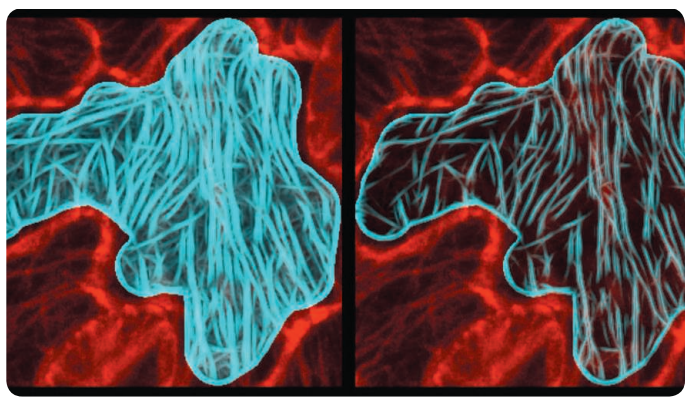

Leaves come in a dazzling variety of shapes and sizes, and Geoffrey Harlow wants to know why. As a Ph.D. candidate at the University of California, Riverside, Harlow is studying the genetic factors that influence the architecture of pavement cells, which form a strong interlocking layer across a leaf's surface and help determine its overall shape.

Looking at endless microscopy images to work out how a particular genetic mutation affected the pavement cells of the workhorse lab plant *Arabidopsis thaliana* was subjective, and time-consuming. So Harlow worked with electrical engineer Albert Cruz to develop an automated system to identify the shapes of the pavement cells and the orientation of their internal skeleton of microtubules. "I was extremely shocked at how quickly the software could speed up analysis," Harlow says. The system is more than 900 times faster than a human poring over each image, he estimates.

Harlow used free editing software to create this explanatory video about his research. The 3-minute presentation offers enough detail to satisfy fellow plant biologists, while being accessible enough for anyone to glean the import of his work. "Even my 89-year-old grandma now has a basic understanding of the pavement cell system," Harlow says.

Watch the video at youtu.be/tlc02tFoZ40.

People's Choice

Spherical Nucleic Acids

Quintin Anderson, The Seagull Company, Midland, Texas; Chad Mirkin and Sarah Petrosko, Northwestern University, Evanston, Illinois

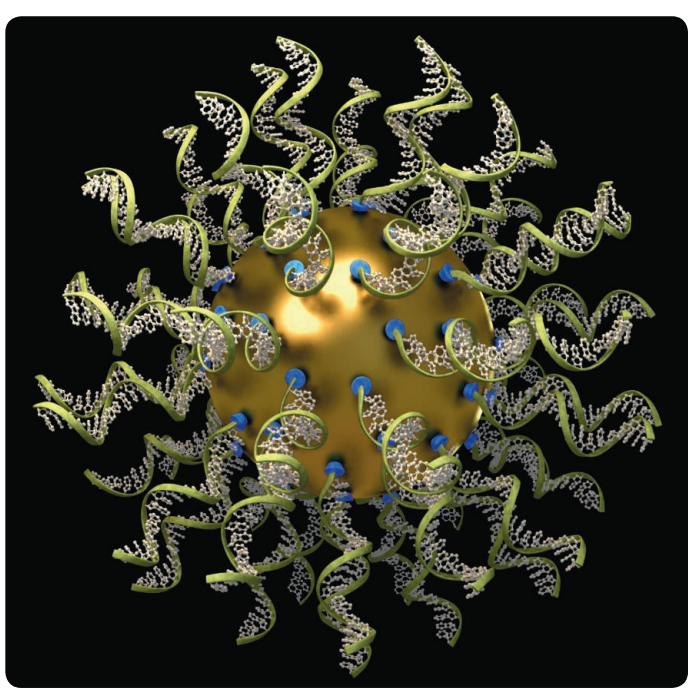

The floating golden sphere, bristling with corkscrew strands of RNA, drifts majestically toward the jostling lipid bilayer that surrounds a cell. Slowly, gently, it squeezes through the layer until it is inside the cell.

Breezing across cell membranes is just one talent of these spherical nucleic acids (SNAs) developed by nanotechnology pioneer Chad Mirkin at Northwestern University. Once inside a cell, they can fend off attacks from enzymes, which makes them hot prospects as vehicles for delivering gene therapy treatments. SNAs also bind strongly to complementary strands of genetic material, an ability being used in a commercial medical diagnostics system called Verigene.

Mirkin commissioned Quintin Anderson, creative director at scientific animation firm The Seagull Company, to create a video explaining his research to colleagues and funders. The toughest part, Anderson says, was creating the lipid bilayer. "There are hundreds of thousands of lipids in those scenes and it required a complicated mathematical algorithm to create the random movements."

Watch the video at www.youtube.com/watch?v=YxRQ1-MI24g.

Published by AAAS

Weathering and soil production
617

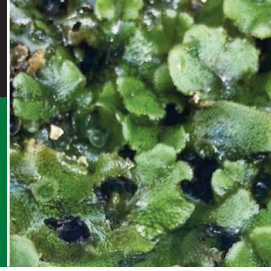

How LFY binding specificities evolve
623

LETTERS | BOOKS | POLICY FORUM | EDUCATION FORUM | PERSPECTIVES

LETTERS

edited by Jennifer Sills

Airline Policies: Sickening Results?

THE IMPACT OF MODERN AIR TRAVEL ON MAGNIFYING the spread of communicable diseases to epidemic levels has been well recognized ["Coming to an airport near you," A. R. McLean, Perspectives, 13 December 2013, p. 1330; "The hidden geometry of complex, network-driven contagion phenomena," D. Brockmann and D. Helbing, Research Article, 13 December 2013, p. 1337; (*1*–*3*)]. Although some infections may be in their incubation phase and not obvious at time of travel, many are identifiable before the affected individual boards the plane.

Presumably, responsible individuals with a communicable disease (such as influenza) would cancel public "appearances," so as to avoid contributing to the spread of the disease they had contracted. However, these individuals face economic damage as a result, because airlines refuse to refund or fully credit such responsible behavior. By doing so, the airlines seem to be discouraging infected individuals from altering their travel plans.

By refusing to provide refunds to people with communicable diseases, are airlines responsible in part for the spread of influenza and other diseases? While the question of liability may be complex, the current policies clearly have public health implications.

BRUCE ROTHSCHILD

Department of Medicine, Northeast Ohio Medical University, Rootstown, OH 44272, USA. E-mail: bmr@ku.edu

References

1. V. Colizza, A. Barrat, M. Barthélemy, A. Vespignani, *Proc. Natl. Acad. Sci. U.S.A.* **103**, 2015 (2006).
2. T. D. Hollingsworth, N. M. Ferguson, R. M. Anderson, *Emerg. Infect. Dis*. **13**, 1288 (2007).
3. B. S. Cooper, R. J. Pitman, W. J. Edmunds, *PLOS Med*. **3**, e212 (2006).

China's Ivory Market: The Elephant in the Room

LEVELS OF ILLEGAL IVORY HUNTING REACHED a peak in 2012, and in 2013 elephants were massacred at an unprecedented rate (*1*). One of the largest buyers hiding behind the massacre is China, and the Chinese market is the most important factor leading to the explosion of the illegal ivory trade.

In 2007, despite the great pressure of world opinion, the Chinese ivory industry persuaded the Convention on International Trade in Endangered Species of Wild Fauna and Flora (CITES) to grant it permission to purchase certain quotas of ivory, justifying the need by claiming to support "the traditional heritage of ivory sculpture" (*2*). However, instead of slowing the decrease in the elephant population, the CITES decision, with its goal to keep "equilibrium between protection and utilization," has become a permanent umbrella for the illegal ivory trade, and ivory gained illegally can be laundered easily on the so-called "legal market" by smuggling it into China (*3*). In China, many or most legal enterprises dealing in ivory processing and sales are involved in illegal ivory trade, and there is a bulky ivory consumer market behind this black market chaos. Due to the influence of traditional ideology and the widespread love of flaunting wealth, the abnormal consumption of ivory products in China remains obstinately common.

Recently, the Chinese government confiscated and destroyed 6 tons of ivory in an attempt to address this issue ("By the numbers," News of the Week, 10 January, p. 124). This inspiring step in the right direction sends a clear message that the government has zero tolerance for illegal ivory trade. To move forward, the relevant Chinese government departments should strictly track the legality of ivory resources and ivory products, amend as quickly as possible the supervision loopholes that exist in the illegal ivory trade under the shield of "legal ivory," and control the abnormal consumption of ivory and ivory products. These actions may be crucial to rescuing African elephants.

SHIYANG HUANG AND QIANG WENG*

College of Biological Sciences and Biotechnology, Beijing Forestry University, Beijing, 100083, China.

*Corresponding author. E-mail: qiangweng@bjfu.edu.cn

References

1. D. Cressey, *Nature* **503**, 452 (2013).
2. "The destination of ivories: The black markets in China boosted the illegal ivory trades internationally," *Southern Weekly* (9 December 2011); www.infzm.com/content/65944 [in Chinese].
3. "China became the premier destination for the ivory smuggling: The ivories were easily laundered when they entered China,"*A Xinhua Net* (13 November 2013); http://news.xinhuanet.com/legal/2013-11/13/c_125695404.htm [in Chinese].

Maritime Biosecurity Adrift

INTERNATIONAL SHIPPING HAS LONG BEEN recognized to pose a substantial environmental threat through the inadvertent transport of invasive alien species in ballast water (water collected and released to stabilize vessels at sea and maintain safe operating conditions throughout a voyage) (*1*, *2*). After more than a decade of deliberation, the International Maritime Organization (IMO) adopted the Ballast Water Management Convention (BWMC) in 2004, whose goal is to legally require nations to prevent, minimize, and ultimately eliminate the transfer of harmful aquatic organisms and pathogens through the management of ballast water and sediments (*3*).

Since adoption, the IMO has facilitated the implementation of this ambitious legal instrument by developing clearer regulatory guidelines, collaborative agreements for regional seas, and cost-effective treatment technologies (*4*). Yet, 10 years later, the BWMC is still not in force because the proportion of the world's merchant shipping tonnage registered to the 38 signatories to date (31%) remains below the 35% threshold required for ratification. Not surprisingly, current nonsignatories include several small nations that together register over 25% of the world's shipping tonnage under "flags of convenience"—i.e., the ships fly the flag of a sovereign state different from that of the ship's owners, often to benefit from cheaper labor or fees. However, in the same category are three-quarters of European Union member states, representing more than 10% of the world's shipping tonnage. Given that the EU has been evaluating options for its own invasive species strategy for several years (*5*, *6*), its ambivalence toward relevant international conventions is somewhat contradictory.

Yet, even if the BWMC is ratified in the next couple of years, the shipping industry has successfully argued for an amendment that ballast water management systems need not be installed until a ship's first renewal survey. This could potentially delay implementation by up to 5 years after ratification. There is therefore a real risk that full implementation of the BWMC will not be achieved by the 2020 Aichi Biodiversity Targets deadline that requires Parties to the Convention on Biological Diversity to manage pathways through which invasive species are introduced and established (*7*).

Since 2004, the failure to adequately manage ballast water discharges has resulted in numerous invasive alien species being recorded in coastal waters worldwide for the first time, and their impacts on marine biodiversity remain poorly understood. Further delays can only exacerbate these potential threats and will represent an enduring legacy of poor environmental governance.

PHILIP E. HULME

The Bio-Protection Research Centre, Lincoln University, P.O. Box 84, Canterbury, New Zealand. E-mail: philip.hulme@lincoln.ac.nz

References

1. J. T. Cariton, J. B. Geller, *Science* **261**, 78 (1993).
2. G. M. Ruiz *et al.*, *Nature* **408**, 49 (2000).
3. IMO, Ballast Water Management Convention (International Maritime Organization, London, 2005).
4. WWF, *Silent invasion—The spread of marine invasive species via ships' ballast water* (WWF International Gland, Switzerland, 2009).
5. P. E. Hulme, P. Pyšek, W. Nentwig, M. Vilá, *Science* **324**, 40 (2009).
6. C. Carboneras, P. Walton, M. Vilá, *Science* **342**, 930 (2013).
7. CBD, Decision X/2, The Strategic Plan for Biodiversity 2011–2020 and the Aichi Biodiversity Targets, Nagoya, Japan, 18 to 29 October 2010.

Science for Sale: Inflated Collaboration Claims

THE NEWS FOCUS STORY "CHINA'S PUBLICATION bazaar" (M. Hvistendahl, 29 November 2013, p. 1035) implies that the *Chinese Medical Journal* and some agencies are collaborating to publish paid content. In fact, the *Chinese Medical Journal* is a victim. Because the *Chinese Medical Journal* and other medical journals published by the Chinese Medical Association have good reputations in China, many Chinese authors want to publish papers in them. Meanwhile, some agencies claim that they collaborate with these journals to try to make money by cheating authors. *Science*'s evidence is largely based on reporters' inquiries posing as authors or scientists; it is possible that these agencies provided the reporters with false information in an effort to make money. If those reporters had also contacted each of the agencies and identified themselves as journalists, they may have obtained more objective information.

With its 126-year history, the *Chinese Medical Journal* enjoys an excellent reputation in China. Now the journal is a member of the International Committee of Medical Journal Editors (ICMJE), the members of which include the *New England Journal of Medicine* and *The Lancet*. The *Chinese Medical Journal* has a strict peer-review policy for each paper to be published. That is one of the reasons the journal recently identified and rejected a spoof paper within 20 days after receiving the submission (*1*). Such a journal would not cooperate with an agency to sell papers.

MOUYUE WANG

Chinese Medical Journal, Chinese Medical Association, Beijing 100710, China. E-mail: cmawmy@cma.org.cn

Reference

1. J. Bohannon, *Science* **342**, 60 (2013).

Response

OUR TEAM OF REPORTERS CONTACTED 27 agencies that advertise as helping scientists publish papers in SCI journals. Communicating with agents by phone or the messaging service QQ, we posed as scientists or graduate students in these initial inquiries because we believed that this was the only way for us to gain accurate information about the companies' activities. I later contacted or attempted to contact every agency and journal mentioned in the article, identifying myself as a journalist, to solicit their reactions to our findings.

Our interest in the *Chinese Medical Journal* came after representatives for eight of the agencies we contacted independently offered the detail that they can guarantee publication in the journal's pages. No other journal was mentioned as a collaborator more than twice.

It is certainly true that representatives for agencies that engage in academic fraud may not always tell the truth—a fact acknowledged in the article. But our suspicions were further raised by an advertisement for a ninth, allegedly corrupt agency that appeared on the *Chinese Medical Journal*'s Web site until I reached Mr. Wang by phone at his office in Beijing. Soon after I spoke with Mr. Wang, I called that agency, Sciedit, and identified myself as a reporter. While Sciedit's purported owner denied any cooperation with the *Chinese Medical Journal*, until recently, Sciedit asserted on its Web site that the journal had designated it as an official "service supplier." In this case, both parties signaled their cooperation in a public space—their Web sites—until we began our investigation. We published our report in the hope that *Science*'s readers could draw their own conclusions.

MARA HVISTENDAHL

Contributing Editor, *Science* News

CORRECTIONS AND CLARIFICATIONS

Reports: "Relaxation mechanism of the hydrated electron" by M. H. Elkins *et al.* (20 December 2013, p. 1496). Revised Figs. 1 and 2 provided by the authors during proofs incorrectly replaced the Greek character ν with a lowercase v in several places. The figures have been corrected in the HTML and PDF versions online.

Reports: "Pacific Ocean heat content during the past 10,000 years" by Y. Rosenthal *et al.* (1 November 2013, p. 617). Figure 4B has been revised in the HTML and PDF versions online to reflect minor changes in the data used (see supplementary table S3) to construct it. The supplementary materials have been updated, and an Excel file has been added online.

Letters to the Editor

Letters (~300 words) discuss material published in *Science* in the past 3 months or matters of general interest. Letters are not acknowledged upon receipt. Whether published in full or in part, Letters are subject to editing for clarity and space. Letters submitted, published, or posted elsewhere, in print or online, will be disqualified. To submit a Letter, go to www.submit2science.org.

Published by AAAS

BIOINFORMATICS

Making Sense from Sequences

Michael Fortun

No one ever spoke of "phys-informatics" when computers entered physics after World War II, Hallam Stevens notes toward the end of *Life Out of Sequence*, yet "bioinformatics" quickly came to slip naturally from tongues and keyboards to designate the seemingly novel domain created when computers later colonized biology. How bioinformatics emerged as a distinct domain of biological knowledge and practice and how it may eventually disappear, coming to be completely incorporated into its host, are the subjects of this sharp and lucid work of history and anthropology of science.

This hybridity is as essential to the book as it is to the author and his methodology. *Life Out of Sequence* presents the development of bioinformatics as, indeed, out of sequence—what Michel Foucault would have called a "history of the present," or what we could also call a Faulknerized history of science, where the past not only isn't dead but isn't even past. The book is not organized chronologically but according to enduring practices in the life sciences: the six chapters consider "building computers," "making knowledge," "organizing space," "following data," "ordering objects," and "seeing genomes." As historian, Stevens (Nanyang Technological University, Singapore) shows how each ongoing activity is what it is because of legacy technologies, concepts, or habits of mind and hand that remain active in an ever-emergent bioinformatics, like modules of DNA conserved by evolution that give form and force to later organisms. As anthropologist, he grounds these accounts in deep fieldwork at the Broad Institute, the European Bioinformatics Institute, and other key centers of bioinformatics. (That fieldwork was further enriched by Stevens's earlier training in computer science, pushing the "participant" role in participant observation about as far as it could go.)

He weaves all of this together in a narrative and analysis of bioinformatics as thick as one could hope for. Yet his clear and refined prose should extend the book's readership beyond its disciplinary audiences in the social studies of science, to welcome scientists into this reading of their field's past and present. One finds no academic fights picked here, no lengthy excursions into arcane points of theory, and no mooting of one analytic approach against another. Instead, Stevens provides a highly readable telling of how bioinformatics took shape, how it works within technological and conceptual limits that change over time, and how individual, and mostly unsung, scientists made it happen.

Life Out of Sequence
A Data-Driven History of Bioinformatics

by Hallam Stevens
University of Chicago Press, Chicago, 2013. 302 pp. $90, £63. ISBN 9780226080178. Paper, $30, £21. ISBN 9780226080208.

Stevens delivers the "data-driven" history promised by the subtitle, unpacking the central role played by data in each chapter's activity. He well understands that data can never be raw if they are to be at all informative or productive. They have to be carefully crafted, thoughtfully structured, painstakingly finished, and collectively organized—and in such scientific work those unsung scientists really sing. We meet Walter Goad and the T-10 team at Los Alamos Scientific Laboratories, whose pioneering work on GenBank implanted the algorithms and pattern-recognition approaches of particle physics into the early storage and analysis of DNA sequence information. The "organizing space" chapter (a shining example of laboratory ethnography) presents the Broad Institute's Julia Chang, Matthew Vokoun, and Scott Rosenberg, who managed and improved various parts of the data "pipeline" guided by precepts from the Japanese automobile industry. And there is James Ostell, whose originary, early-1980s software programs for managing and analyzing sequence data were unappreciated by his Harvard Ph.D. committee but highly valued for their user-friendliness by an ever-growing number of colleagues. In 1988, Ostell became the first chief of information engineering at the newly formed National Center for Biotechnology Information. Stevens follows him through his long career there, where he created ASN.1 (Abstract Syntax Notation 1) and the "data model" that would undergird the "loose federation" of heterogeneous biological databases that became Entrez and its descendant programs, which link sequence data from DNA to protein sequence information, to the biomedical literature, and to an expanding network of databases.

Here is where fine-grained historical and ethnographic understandings of sciences show their most valued aspects. Greater scientific appreciation of true biological complexity—hardly foreseen in the heady days of the decoding–the "book of life" Human Genome Project—is a product of more than brilliant minds quaffing the holy grail of a revelatory complete sequence. Our improved understanding of the complexity of living systems is as much a product of the hidden work and constructive force of these data structures and protocols. To think that genomics and bioinformatics is just a way to listen in on "what your DNA is telling you," Stevens tells us in a closing epilogue that brings out the social relevance of this history, is a misleading oversimplification. "What your DNA is telling you" depends not only on "the data" and not only on data from thousands of

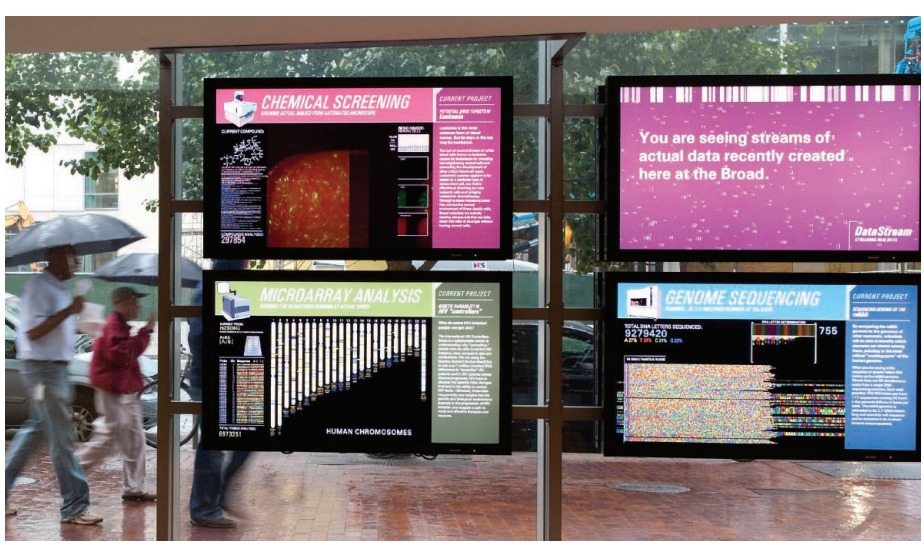

CREDIT: LEN RUBENSTEIN/BROAD INSTITUTE

Displaying data. These panels at the Broad Institute stream data from current research.

The reviewer is at the Department of Science and Technology Studies, Rensselaer Polytechnic Institute, Troy, NY 12180, USA. E-mail: fortum@rpi.edu

Published by AAAS

other genomes, collated and decoded. DNA sequence "tells" not through decoding but through reading, and those readings and tellings can only be made to "make sense" by using the pattern-making tools of bioinformatics. Those patterns and relationships, in turn, "depend on the structures into which the data are fitted: the ontologies, the databases, the file structures, and the visual representations into which they are poured." Although Stevens characterizes these structures with the term "rigidity," plasticity might be a better term for the resistant yet pliable forms that our data-work impresses upon biological information—and which allow biological information in turn to impress upon our conceptualizations and understandings of life. An effective and enjoyable remolding of oversimplified "data-to-truth" histories of science, *Life Out of Sequence* draws out the reciprocal impressions made by data systems and living systems on each other—and on the sense scientists make of life.

10.1126/science.1247757

DATA VISUALIZATION

Enabling Visual Discovery

Ben Shneiderman

Howard Wainer's insight-filled *Medical Illuminations* continues his agenda of promoting statistical thinking and visualization, here with a focus on healthcare. His sensitivities are well aligned with the huge upswing in interest in these topics, but once again he leads the way with fresh ideas, compelling examples, wise generalizations, and clever phrases.

The book comprises a baker's dozen of bite-sized chapters. Although easily digestible, these provide ample intellectual nutrition, which can be enriched by reading the informative notes. Early on, Wainer (a statistician at the National Board of Medical Examiners) cautions readers that "[f]acts without context are often likely to yield only misunderstanding of causal mechanisms." This powerful message would make a valuable pop-up for the start of every statistics and visualization program. It would remind users that automated statistical analyses need graphical displays of distributions to enable them to detect errors, unusual distributions, outliers, anomalies, and missing data. Statistics and visualization programs would also be improved if they provided easily accessible and linked visual contexts to show potentially influencing factors and to allow comparisons with related datasets.

Medical Illuminations
Using Evidence, Visualizations and Statistical Thinking to Improve Healthcare

by Howard Wainer
Oxford University Press, Oxford, 2014. 191 pp. $35, £19.99.
ISBN 9780199668793.

Wainer's advocacy of visualization continues with his study of a collection of medical journals to point out their reliance on tabular presentations rather than effective graphical displays. He uses a dot plot to show that these journals overwhelmingly use numeric tables rather than simple bar or line charts. Wainer argues for the use of more information-rich visualizations that more clearly show vital patterns, delivering the knockout punch with a taunting century-old quote: "Getting information from a table is like extracting sunbeams from a cucumber" (*1*). Less-combative sections constructively show how proper sorting, spatial layouts, and color highlighting can dramatically improve poor tables to reveal important messages and surprising relationships.

The most potent chapter, offering happy discoveries on almost every page, celebrates the 2008 centenary of the birth of graphics designer Will Burtin, who Wainer honors as "a pioneer of scientific visualization." Burtin's 1951 circular chart of the impact of three antibiotics on 18 bacteria (*2*) seems revealing and attractive enough, but in addition, each of the successive displays provides insights, charms, and context that demonstrate the creative possibilities in showing even small datasets. Wainer closes the chapter with the reminder: "a display that serves us best is one that *forces* us to see what we were not expecting. Indeed, data graphs are the most powerful tools we have for doing this." In the ensuing chapters, Wainer touches on cancer, public health reporting, diabetes, hip fractures, mammograms, prostate cancer testing, infection rates, and much more. Other topics that he discusses include strategies for extrapolating from data and a provocative challenge to the quality of some Chinese medical research. Wainer also addresses larger issues such as his desire to slow innovation and promote consistency in graphics. (He is, however, troubled by the slow adoption of demonstrated medical advances such as checklists for infection prevention.)

Although the various examples of graphics included in the book convey important lessons, I regret that Wainer doesn't disclose more about his own processes of developing visualizations. It would help readers to know what to look for in the tools they use. He makes clear that it is now so much easier for more people to generate high-quality graphics and then try many variations, so I wish he would critique commonly available tools. In addition, while I agree that static presentations in documents and slide presentations remain important, much current excitement centers on the interactive processes of exploration and discovery. Public policy groups, government agencies, and leading media websites now provide compelling datasets and web-based interactive tools for specialists and the general public. Thus, I hope that Wainer's next book takes up aspects such as rich control panels with sliders and selectors, coordinated windows to support highlighting across charts, integration of statistics with visualization, and animated presentations.

Still, *Medical Illuminations* offers ample substance along with sufficient piquant comments to ensure that readers reflect on every sentence. I fell for the closing story (revealed in the Afterword as an April Fool's prank) about state legislatures passing astonishing counterscientific laws. But I laughed aloud at the truth and appreciated the reminder of the importance of being a skeptical reader and seeking evidence for every alleged fact or scientific claim. Wainer's inspirational set of commentaries on medical applications for statistics and visualization delivers meaningful lessons for beginners and experts. I highly recommend it.

References and Notes

1. A. B. Farquhar, H. Farquhar, *Economic and Industrial Delusions: A Discussion of the Case for Protectionism* (Putnam's, New York, 1891).
2. Burtin created the diagram for the Fall 1951 issue of Upjohn's publication for physicians, *Scope* (where he served as the art director). See (*3*).
3. http://mbostock.github.io/protovis/ex/antibiotics-burtin.html.

10.1126/science.1249670

The reviewer is at the Department of Computer Science, University of Maryland, College Park, MD 20742, USA. E-mail: ben@cs.umd.edu

SOCIAL SCIENCE

Scientific Diversity Interventions

Fair treatment of other scientists is an essential aspect of scientific integrity, warranting diversity interventions.

Corinne A. Moss-Racusin,[1]* Johanneke van der Toorn,[2] John F. Dovidio,[3] Victoria L. Brescoll,[3] Mark J. Graham,[3] Jo Handelsman[3]

Although the representation of women and racial or ethnic minorities within the scientific community has increased in recent decades, the overall pace of diversification remains relatively slow (*1*). A number of factors may be involved (*2*), but one possible explanation for this limited progress is that gender and racial or ethnic biases persist throughout academia (*1*, *3*).

In response, we propose a scientific approach to the design, assessment, and broad implementation of diversity interventions. We review evidence of positive and negative outcomes of existing interventions relevant to academic scientists. We then offer an evidence-based framework identifying elements of successful interventions (see the table). Finally, we discuss research needed to define success more rigorously and policy changes to encourage widespread adoption of successful programs.

Evidence suggests that academic scientists express "implicit" biases (*4*), which reflect widespread cultural stereotypes emphasizing white men's scientific competence (*1*, *3*). For example, both male and female science faculty members presented with the identical application for a laboratory position provided significantly higher evaluations and starting salaries when the application was attributed to a male versus female student (*1*). Black principal investigators were less likely to receive U.S. National Institutes of Health research funding than white colleagues (*3*).

In contrast to conscious and deliberate "explicit" biases, implicit biases are automatically activated and frequently operate outside of conscious awareness (*4*). Although likely unintentional, implicit biases undermine skilled female and minority scientists, prevent full access to talent, and distort the meritocratic nature of academic science (*1*, *3*).

Interventions, Impacts, and Backlash

To address these issues, the science community should adopt diversity interventions that reduce both implicit and explicit biases and require empirical evidence that such interventions are effective. Once identified, these interventions should be incorporated into existing training offered to scientists, such as courses in responsible conduct of research (RCR). These courses are already required for researchers who receive funding from U.S. federal granting agencies. Although U.S. guidelines for RCR course content contain critical topics, they do not include diversity issues generally or bias specifically (*5*). Because fair treatment of other scientists is an essential aspect of scientific integrity, RCR courses provide untapped opportunities to engage scientists in reflection on the adverse effects of bias.

Campuses should not simply transfer elements of staff diversity training programs into RCR courses, because most existing interventions are not evidence-based (*6*–*9*). Similarly, interventions shown to improve intergroup relations (e.g., cooperative intergroup contact) with other target groups (*6*–*8*) should not be adopted without tailoring to address issues specific to enhancing diversity in science. Many diversity programs rely primarily on lecturing as the method of instruction (*6*), overlooking the vast literature demonstrating that active learning techniques (i.e., those that dynamically engage participants in exercises, activities, and discussions) produce superior learning outcomes (*10*) and increase the effectiveness of diversity interventions (*8*). Interventions often induce ironic negative effects (such as reactance or backlash) by implying that participants are at fault for current diversity challenges (*9*, *11*). Although some interventions have been in place for decades, few have undergone evaluation to determine whether they produce measurable effects (*6*, *9*). A cohesive framework of the design elements and outcomes of successful interventions is needed to ensure that programs are scientifically rigorous and achieve desired objectives.

There are no randomized controlled trials (RCTs) evaluating the impact of diversity interventions on the behavior of academic scientists (*6*, *7*). A recent related RCT that tested established social psychology principles for bias reduction (e.g., stereotype replacement and counter-stereotypic imaging) generated promising results (e.g., reducing implicit bias) but used undergraduate psychology participants and measured self-reported intentions rather than actual behavior change (*7*). Although these results highlight the potential of diversity interventions to reduce bias and enhance diversity,

Components of effective scientific diversity interventions

Design Elements	Examples of Approaches
Grounded in current theory and empirical evidence (*6*–*8*)	Intervention design is guided by current evidence; Hypothesized mechanisms of change are explicitly identified (*6*–*8*)
Use active learning techniques so that participants engage with course content (*8*–*10*)	Participants engage with content through writing and speaking; Strategies such as problem-solving, group discussion, and quizzes are employed (*10*)
Avoid assigning blame or responsibility to participants for current diversity issues (*9*–*11*)	Facilitators employ language indicating that we all share responsibility for diversity; Presentation and analysis of the evidence that men and women express similar implicit bias toward women [e.g., (*1*, *18*)]
Include a plan for ongoing rigorous evaluation of the intervention's efficacy with different groups (*6*–*8*)	Interventions involve collecting longitudinal self-reported data on attitudes and intentions to change behavior; If these generate promising results, RCTs with behavioral measures will be conducted (*6*–*8*)
Measurable Outcomes	**Examples of measurements**
Increase participants' awareness of research on diversity issues (i.e., bias literacy) (*15*)	Pre/post surveys of content knowledge, short writing assignments, group problem-solving of case studies (*10*, *15*)
Decrease participants' explicit and implicit biases (*4*)	Test with standard methods (i.e., validated explicit attitude scales, implicit reaction-time measures) (*4*, *7*, *13*)
Increase participants' propensity to take action on diversity issues (*18*)	Self-reports of participants' own behaviors, as well as behavioral observations from departmental colleagues, students, and trained raters (*6*, *8*, *14*, *15*, *18*,)

[1]Skidmore College, Saratoga Springs, NY 12866, USA. [2]Leiden University, 233 AK Leiden, Netherlands. [3]Yale University, New Haven, CT 06520, USA. *Corresponding author. E-mail: cmossrac@skidmore.edu

Published by AAAS

RCTs that have behavioral measures and academic scientist participants are required to validate interventions.

However, self-report and correlational studies can provide the evidence needed to warrant the more compelling (as well as costly and technically challenging) RCTs that must follow. Indeed, there is promising evidence that several interventions raise participants' awareness of diversity issues and reduce explicit and implicit biases (*4*, *6*–*8*, *12*–*17*), which suggests that large-scale RCTs of these programs are warranted. For example, the Workshop Activity for Gender Equity Simulation program enables participants to experience cumulative effects of subtle disadvantages and increases their awareness of gender-equity issues within academia (*12*).

An intervention involving a semester-long course on diversity lowered college students' scores on a computerized test of implicit racial bias more than an unrelated control course (*13*). Another program generated improvements in participants' diversity-related attitudes (e.g., increased awareness of advantages experienced by certain social groups) and actual behaviors (e.g., being inclusive; engaging in empathic listening; and actively addressing difficult, emotionally charged issues). Many of these changes persisted 4 months after the intervention and were also observed by participants' colleagues (*14*).

A recent study demonstrated that faculty and administrators from science departments who attended a theoretically grounded Bias Literacy Workshop reported significant increases in "bias literacy" (critical knowledge of bias and diversity issues) and demonstrated improved diversity-promoting behaviors (such as engaging in fair hiring practices) after the workshop (*15*). Although not RCTs, these findings suggest that certain diversity interventions can positively influence the attitudes and behavior of academics.

Other kinds of diversity interventions may paradoxically worsen bias and fail to improve diversity. Programs appear to be particularly counterproductive when they place pressure or blame on attendees, rather than presenting diversity as a shared community challenge and opportunity (*9*, *11*). A common approach urges participants to recognize their own personal culpability in perpetuating discrimination and to take corrective action by complying with societal egalitarian norms (*9*). This approach leads to backlash when its central message is perceived as accusatory, which diminishes participants' internal motivations to be nonprejudiced and induces higher levels of bias (*11*). Unintended outcomes highlight the importance of testing interventions before widespread implementation and underscore the need for an evidence-based framework of intervention elements and outcomes.

Framework for Design and Outcomes

We offer such a framework, based on available evidence on prejudice reduction strategies (*4*, *6*–*8*, *12*–*17*) and the vast literature establishing effective teaching practices (*8*, *10*, *16*). Specifically, interventions should incorporate four design elements and target at least three outcomes (see the table). An informal survey of current diversity interventions at research universities revealed that few incorporate all four, and many incorporate none of these elements.

As mixed results for existing interventions and occasional findings of backlash suggest, the first two outcomes (increased awareness and reduced bias) are necessary but not sufficient. Interventions must also enhance participants' action readiness and leave them motivated and equipped with tools to engage with diversity issues rather than paralyzed into avoiding them (*18*). Preliminary evaluation results of one program [which meets design elements (i) to (iv) and has been implemented with more than 700 science faculty members (*16*)] suggest that interventions can generate positive changes in action readiness and highlight the potential importance of this variable (*17*). Because readiness is strongly linked to behavior (*18*), these results may have encouraging implications for diversity-related outcomes.

On the basis of promising initial evidence that diversity interventions can be effective for academic audiences, we call for further research providing a scientific basis for diversity interventions. Interventions that meet the design elements in the table should now be rigorously assessed by RCTs comparing the efficacy of different interventions, elucidating the mechanisms underpinning effective interventions, and driving implementation of the most effective ones. Research aimed at identifying why successful diversity interventions work will be particularly important for designing new programs tailored to specific audiences, outcomes, and institutional contexts (*6, 8*). Research is also necessary to reevaluate intervention efficacy as biases change. For example, although explicit bias has decreased over time, implicit bias remains prevalent (*4*, *13*). Thus, interventions must also change to address evolving expressions of bias.

The U.S. federal funding agencies should add diversity issues (including implicit biases) to their mandated RCR course content guidelines (*5*) and make empirically validated diversity interventions available for widespread use. Worldwide national funding agencies and international bodies (e.g., the European Research Council) should consider similar policies. Active learning methods should be included, which may require redesign or reconsideration of currently accepted online trainings.

Without a scientific approach to diversity interventions, we are likely perpetuating the existing system, which fails to uphold meritocratic values by allowing persistent biases to influence evaluation, advancement, and mentoring of scientists. We may also inadvertently continue to fund ineffective interventions that—at best—superficially address diversity goals without producing measurable results, or—at worst—intensify biases. Applying our framework's straightforward criteria (drawn from theory and successful interventions) would bring diversity interventions in line with accepted scientific standards. A scientific approach to interventions aimed at reducing biases will increase meritocracy, diversity, and excellence throughout academic science.

References and Notes

1. C. A. Moss-Racusin *et al*. *Proc. Natl. Acad. Sci. U.S.A.* **109**, 16474 (2012).
2. S. J. Ceci, W. M. Williams, *Proc. Natl. Acad. Sci. U.S.A.* **108**, 3157 (2011).
3. D. K. Ginther *et al*. *Science* **333**, 1015 (2011).
4. C. K. Lai, K. M. Hoffman, B. A. Nosek, *Soc. Person. Psychol. Compass* **7**, 315 (2013).
5. N. H. Steneck, R. E. Bulger, *Acad. Med.* **82**, 829 (2007).
6. E. L. Paluck, D. P. Green, *Annu. Rev. Psychol.* **60**, 339 (2009).
7. P. G. Devine *et al*. *J. Exp. Soc. Psychol.* **48**, 1267 (2012).
8. C. W. Stephan, W. G. Stephan, *Improving Intergroup Relations* (Sage, Thousand Oaks, CA, 2001).
9. F. Dobbin, A. Kalev, in *Oxford Handbook of Diversity and Work*, Q. M. Roberson, Ed. (Oxford Univ. Press, New York, 2013), pp. 253–281.
10. J. Handelsman, S. Miller, C. Pfund, *Scientific Teaching* (Freeman, New York, 2007).
11. L. Legault *et al*. *Psychol. Sci.* **22**, 1472 (2011).
12. S. A. Shields, M. H. Zawadzki, R. N. Johnson, *J. Div. Higher Ed.* **4**, 120 (2011).
13. L. A. Rudman *et al*. *J. Pers. Soc. Psychol.* **81**, 856 (2001).
14. J. Prime, H. Foust-Cummings, E. R. Salib, C. A. Moss-Racusin, *Calling All White Men: Can Training Help Create Inclusive Workplaces?* (Catalyst, New York, 2012).
15. M. Carnes *et al*. *J. Divers. High. Educ.* **5**, 63 (2012).
16. C. Pfund *et al*. *Science* **324**, 470 (2009).
17. C. A. Moss-Racusin *et al*., Supplementary materials (Center for Scientific Teaching, Yale Univ., New Haven, CT, 2013); http://cst.yale.edu/sites/default/files/efficacymanuscript_1.pdf.
18. L. A. Rudman *et al*. in *Advances in Experimental Social Psychology*, P. G. Devine, E. A. Plant, Eds. (Elsevier, New York, 2012), pp. 167–227.

Acknowledgments: We thank J. Frederick, R. Lue, S. Miller, C. Pfund, J. Stith, and J. Young. This work was supported by a Howard Hughes Medical Institute Professors Program grant and NIH grant 1R13GM090574-01 to J.H., and Sloan grant 213-3-05 to J.H. and C.A.M.-R.

10.1126/science.1245936

GEOCHEMISTRY

Limits of Soil Production?

Steep mountain regions can weather faster and produce soil more quickly than previously thought.

Arjun M. Heimsath

Rocky mountain ranges may appear static but are constantly in motion. Tectonic forces push the mountains up, while physical and chemical processes break rocks down to sediment that is transported to river plains and ultimately to the sea. This cycle is thought to regulate global climate over million-year time scales (*1*) while also responding to climate forcing itself (*2*). It remains unclear whether mountain uplift drives climate change, or whether climatic cooling drives uplift by causing faster erosion (*3*). On page 637 of this issue, Larsen *et al*. (*4*) provide data that help to quantify these controls on mountain building, reporting faster sediment production rates and higher chemical weathering rates than previously measured. Their results also provide key insights into soil sustainability over shorter time scales (*5*).

Mountain building can only drive global climate trajectories if weathering of silicate rocks removes enough CO_2 from the atmosphere over geologic time scales to lower atmospheric concentrations of this critical greenhouse gas. Proponents for mountain controls on climate point to extensive bedrock exposure, ready for weathering, in young mountain ranges and to the temporal correlation between periods of active mountain building and global cooling. However, it remains unclear whether mountainous regions are big enough and weather fast enough to account for the CO_2 drawdown needed to change climate (*6*) and whether the few measured weathering rates can be extrapolated across mountain ranges. It is also unknown whether there are limits to the rate of soil production, which helps to govern the presence of soil.

Soil can only persist at a given location if erosion is not removing it faster than it is being produced. On steep slopes there are typically extensive areas of bare rock, as well as areas where soil cover allows forests, tundra, and other forms of life to exist (see the figure). These steep slopes are thought, therefore, to exist at the threshold of soil production and provide the opportunity to examine the complex response of a hillslope to a wide range of erosion rates (*7*). If there is an upper limit to soil production rates (*8*), it is unclear how soil cover can be present in regions thought to be eroding well beyond the purported upper soil production limit.

PHOTO CREDIT: ROMAN A. DIBIASE/CALIFORNIA INSTITUTE OF TECHNOLOGY

Competing processes. The steep slopes of Mount Lukens rise abruptly from the suburban sprawl of Los Angeles, California. Landslides and debris flows remove sediment produced from the weathered rock, while active tectonic forces push the mountains higher. The extent of rock outcrop is shown in red on the overlain shaded relief map (*12*). Larsen *et al*. report that soil-mantled landscapes in much wetter New Zealand can persist in rapidly uplifting mountain ranges because of high rates of soil production and chemical weathering.

Many challenges remain before these debates can be fully resolved. First and foremost, rates of soil production, erosion, and chemical weathering must be quantified across different landscapes. Larsen *et al*. now report exactly these data from the western Southern Alps of New Zealand. They also document pervasive soil and vegetation cover on slopes that erode faster than 1 mm per year. Their findings are based on concentrations of rare isotopes (^{10}Be) produced in the very grains of silicate minerals that react with CO_2 during chemical weathering. This isotope is produced by cosmic-ray bombardment of Earth's surface and is widely used to determine average erosion rates and point-specific soil production rates. Larsen *et al*. also measure concentrations of a nonreactive element (Zr) in the same samples to quantify the degree of chemical depletion in the weathered rocks producing the sediments. They use these depletion fractions in concert with the erosion and soil production rates to infer chemical weathering rates.

These data are not easy to come by. Larsen and colleagues traversed some of Earth's most rugged topography to collect their samples. The data reveal an exponential decline of soil production with increasing soil thickness, defining a higher soil production function, at higher erosion rates, than previously predicted. The data thus support the view that feedback between erosion and soil production enables rapidly eroding landscapes to retain a cloak of soil (*7*). Larsen *et al*. also show that chemical weathering rates are higher than a previously suggested kinetically controlled limit (*9*), providing key evidence for the important role that mountains play in controlling climate.

Resolving the couplings between silicate weathering and global climate requires similar data from both mountains and lowlands. Sample collection is the first challenge. The logistics are demanding even in locations not ravaged by war or severely affected by human development. Extracting and measuring ^{10}Be concentrations is expensive, involves specialized laboratoriess, and is time-consuming. ^{10}Be concentrations yield rates averaged over hundreds to hundreds of thousands of years, making it difficult to use the method to quantify rates that change over time. Calculated chemical weathering rates depend on the assumption that Zr concentrations are homogenous in unweathered rock and that

School of Earth and Space Exploration, Arizona State University, Tempe, AZ 85287, USA. E-mail: arjun.heimsath@asu.edu

Published by AAAS

the Zr is immobile in solution. Given these challenges, field-based data such as those reported by Larsen *et al*. are indispensable and provide crucial tests for models (*10*).

Obtaining similar data for agricultural soils presents challenges not faced by studies such as that of Larsen *et al*., yet this is where the greatest societal concerns lie (*11*). As food demand increases, so too will the need to conserve Earth's soil resources. The extent of soil conservation measures will depend on which side of the soil production–erosion balance agricultural soils fall.

References

1. M. E. Raymo, W. F. Ruddiman, *Nature* **359**, 117 (1992).
2. K. X. Whipple, *Nat. Geosci.* **2**, 97 (2009).
3. P. Molnar, P. England, *Nature* **346**, 29 (1990).
4. I. J. Larsen *et al*., *Science* **343**, 637 (2014); 10.1126/science.1244908.
5. D. R. Montgomery, *Proc. Natl. Acad. Sci. U.S.A.* **104**, 13268 (2007).
6. J. K. Willenbring, A. T. Codilean, B. McElroy, *Geology* **41**, 343 (2013).
7. A. M. Heimsath, R. A. DiBiase, K. X. Whipple, *Nat. Geosci.* **5**, 210 (2012).
8. J. L. Dixon, F. von Blanckenburg, *C. R. Geosci.* **344**, 597 (2012).
9. K. L. Ferrier, J. W. Kirchner, *Earth Planet. Sci. Lett.* **272**, 591 (2008).
10. A. J. West, *Geology* **40**, 811 (2012).
11. D. R. Montgomery, *Dirt: The Erosion of Civilizations* (Univ. of California Press, Berkeley, CA, 2007).
12. R. A. DiBiase, A. M. Heimsath, K. X. Whipple, *Earth Surf. Process. Landf.* **37**, 855 (2012).

10.1126/science.1250173

ATMOSPHERE

Next Season's Hurricanes

Seasonal predictions of hurricane activity remain challenging, especially at a regional scale.

Gabriel A. Vecchi[1] and Gabriele Villarini[2]

Tropical cyclones (TCs) are a hazard to life and property (*1*, *2*), as was tragically apparent following Super Typhoon Haiyan's landfall in the Philippines in 2013 and Hurricane/extratropical system Sandy's landfall in the New York tri-state area in 2012. Yet TCs also provide vital water, sometimes relieving drought (*3*). Predictions of the path and intensity of individual TCs are usually sufficiently good several days in advance that action can be taken. In contrast, predictions of seasonal TC activity months in advance must still be made more regionally relevant to produce information that can be acted on, for example, to improve storm preparedness.

Challenges in CLIMATE SCIENCE
scim.ag/climatechall

Seasonal TC predictions focus on the probability of a range of outcomes integrated over broad regions, rather than the individual storms and narrower geographic foci used in 3- to 5-day weather forecasts. Whereas weather-scale TC predictions may lead to targeted actions such as evacuations, seasonal predictions are currently used to develop and price instruments to distribute risk (such as insurance). Improved skill and regional specificity of seasonal TC prediction could be useful to water resource, emergency, and energy management efforts. Furthermore, a better ability to forecast seasonal hurricanes can help build a more robust understanding of the ways in which climate controls hurricane activity, perhaps leading to increased confidence in multidecadal hurricane projections.

[1]Geophysical Fluid Dynamics Laboratory, National Oceanic and Atmospheric Administration, Princeton, NJ 08542, USA. [2]IIHR-Hydroscience and Engineering, University of Iowa, Iowa City, IA 52246, USA. E-mail: gabriel.a.vecchi@noaa.gov

Basin-Wide Success

In recent years, several approaches have been developed to predict seasonal TC activity averaged over an entire basin, such as the North Atlantic or Northwest Pacific, several months before the season in question. These approaches include statistical (*4*) and dynamical general circulation models (*5*–*7*), as well as hybrid statistical-dynamical methods (*8*–*10*). They are used in operational seasonal TC outlooks made by meteorological agencies. Evaluated over multiple years and decades, these predictions are skillful at predicting the year-to-year changes in the total number of hurricanes, when compared to forecasts based on knowing only the long-term average or activity over the years preceding a season. The predictive skill of basin-wide activity can be seen in individual years. For example, for months prior to the 2010 season, Atlantic hurricane frequency was consistently predicted to be large (see the first figure), and 2010 was indeed the second most active hurricane season since 1970.

Learning from Failure

Even though predictions are skillful in predicting year-to-year changes in TC activity over many years, they are not perfect. A glaring example is the recent 2013 Atlantic hurricane season (see the first figure), for which nature failed to follow the almost unanimous prediction that the North Atlantic should have a normal to slightly enhanced number of hurricanes (~6 to 9). Instead, it was one of the most anemic hurricane seasons ever recorded.

A season like 2013 is humbling. Yet only by understanding and learning from past failed predictions will the prediction community be able to successfully move forward. In disentangling the causes of the low hurricane activity of 2013, we must ask ourselves whether our prediction systems neglected something foreseeable, and then account for this in future predictions. But

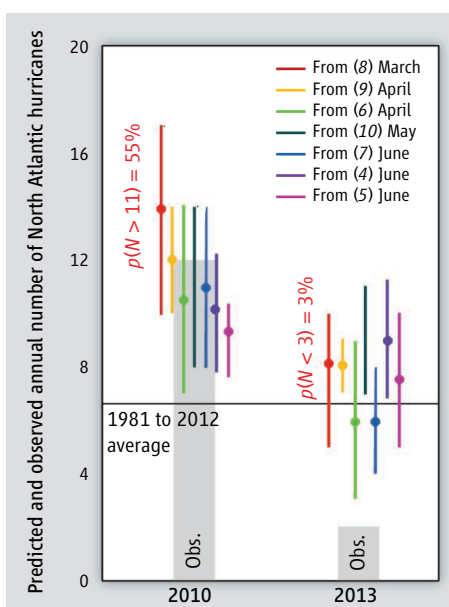

Seasonal North Atlantic hurricane prediction. The very active 2010 season was successfully predicted by a range of methodologies (*4*–*10*), but these prediction systems generally failed for the very inactive 2013 season. Central estimates are circles; vertical bars show ranges [70% range for (*8*, *10*); ±1σ for (*4*–*7*, *9*)]. The legend gives the month when each prediction was issued. For (*8*), the predicted exceedance probabilities for the observed hurricane counts are given to the left of the vertical bar. For data, see supplementary materials.

CREDIT: (LEFT) V. ALTOUNIAN/*SCIENCE*

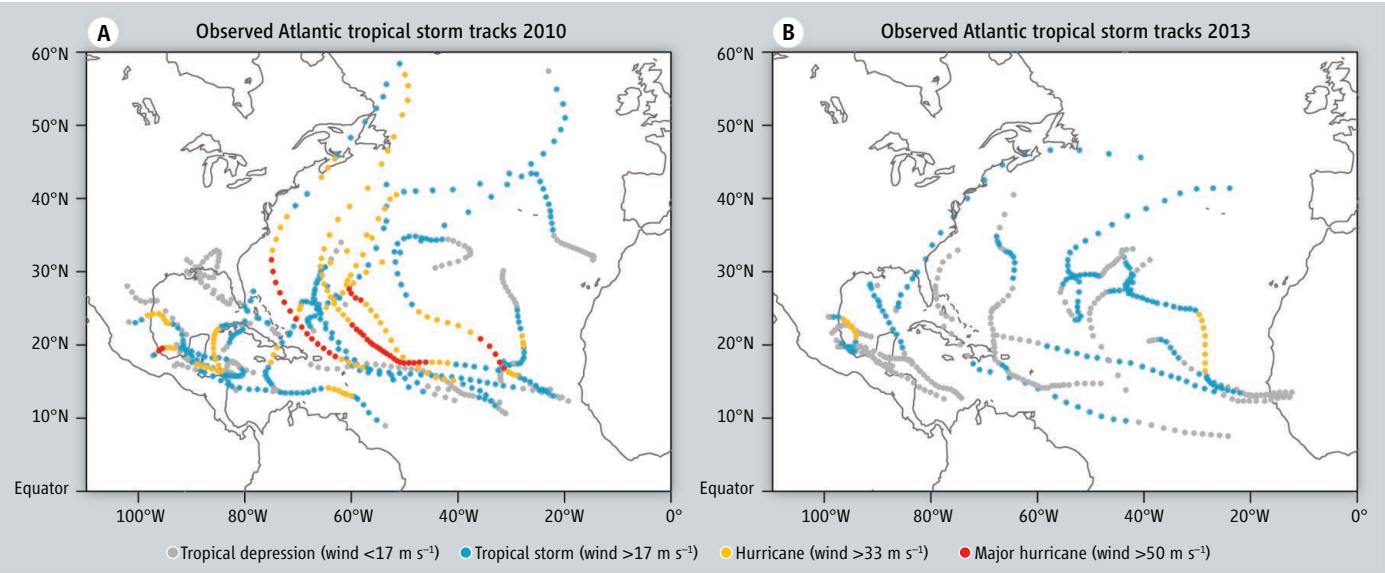

Not just how many but where. Observed TC tracks for 2010 (**A**) and 2013 (**B**). TC locations are shown at 6-hour intervals, with colors indicating their intensity. For data sources, see supplementary materials.

the predictability of the climate system has limits, and it may be that the causes of the inactivity in 2013 were inherently unpredictable. Although extreme failure is improbable in any given year, over many years its likelihood at some (unknowable) point can become substantial even in the best possible prediction system.

Toward Regional Information

Despite being a key first step, basin-wide predictions do not provide sufficient information for most applications, which require a capability to predict the likelihood of TC occurrence at a more regional scale. The 2010 Atlantic hurricane season presents a poignant example. As discussed above, this season was widely and successfully predicted to be very active at a basin scale. Yet a relatively modest number of hurricanes made landfall (although some of those landfalls did tragically result in fatalities). The dearth of landfalls was particularly pronounced in the U.S. coastline, where no hurricanes made landfall (see the second figure, panel A). An active basin-wide season does not necessarily translate into an active landfall season, nor does an inactive season in parts of the basin necessarily translate into an inactive season along the coasts. In 2013, the Atlantic was inactive both in basin-wide activity and landfalls (see the second figure, panel B).

Prediction efforts must be pushed beyond basin-wide TC activity toward the much more challenging goal of improving skill at the regional scale. These efforts will be helped by advances in understanding what controls the geographical distribution of TCs. For example, aspects of the regional distribution of TC activity may be connected to potentially predictable modes of climate variability and change (*11*, *12*). Enhanced computer power has helped to increase the spatial refinement of climate models (*5*–*7*, *13*, *14*) and improved prediction methodologies (*6*–*9*), a crucial step for delivering skillful regional predictions. Many hazards associated with landfalling TCs (such as winds, storm surge, heavy rainfall, and flooding) vary among regions, and local information is therefore essential for predicting TC impacts.

Communicating Uncertainty

The climate system is chaotic, and all climate predictions are inherently probabilistic (making a statement of the likelihood of certain events) rather than deterministic (making specific statements about the course of the future). Relative to predictions of basin-wide activity, predictions at the regional scale are more likely both to invite action and to have larger uncertainties. It is thus crucial to develop an explicit and accurate representation of the uncertainties associated with the predictions. The potential utility of predictions would be enhanced through communication between the developers of prediction methodologies and the eventual users of the prediction products. At the least, users of predictions should demand—and be capable of using—information about past prediction performance and expected uncertainty.

Improved understanding and modeling capabilities are bringing us to the threshold of more skillful, region-specific, and explicitly probabilistic predictions of seasonal TC activity. In seizing this opportunity, scientists must acknowledge the limitations of their methods. Although we have focused on seasonal hurricane predictions, the issues we raise—prediction verification, learning from failed predictions, and correctly describing and communicating uncertainty—apply to all efforts to predict climate and its impacts.

References and Notes

1. P. Peduzzi *et al.*, *Nat. Clim. Change* **2**, 289 (2012).
2. R. A. Pielke Jr., *et al.*, *Nat. Hazards Rev.* **9**, 29 (2008).
3. J. Kam, J. Sheffield, X. Yuan, E. F. Wood, *J. Clim.* **26**, 3067 (2013).
4. P. J. Klotzbach, W. M. Gray, *Geophys. Res. Lett.* **36**, L09711 (2009).
5. T. E. LaRow, L. Stefanova, D. W. Shin, S. Cocke, *Geophys. Res. Lett.* **37**, L02804 (2010).
6. J. Schemm, L. Long, paper presented at the Workshop on High Resolution Climate Modeling, Trieste, ICTP, Italy, 10 to 14 July 2009.
7. F. M. Vitart *et al.*, *Geophys. Res. Lett.* **34**, L16815 (2007).
8. G. A. Vecchi *et al.*, *Mon. Weather Rev.* **139**, 1070 (2011).
9. H. Wang *et al.*, *J. Clim.* **22**, 4481 (2009).
10. E. S. Blake, R. J. Pasch, G. D. Bell, paper presented at the 29th Conference on Hurricanes and Tropical Meteorology, organized by the American Meteorological Society, 10 May 2010, Tucson, AZ.
11. J. P. Kossin, S. J. Camargo, M. Sitkowski, *J. Clim.* **23**, 3057 (2010).
12. A. J. Colbert, B. J. Soden, *J. Clim.* **25**, 657 (2012).
13. T. Delworth *et al.*, *J. Clim.* **25**, 2755 (2012).
14. R. Bell, J. Strachan, P. L. Vidale, K. Hodges, M. Roberts, *J. Clim.* **26**, 7966 (2013).

Acknowledgments: Supported by NSF grant AGS-1262099 and by the NOAA Climate Program Office. We thank J. Baldwin, T. Delworth, A. Johansson, S. Kapnick, D. Lavers, and G. Saville for useful comments, and P. Klotzbach, T. LaRow, J. Schemm, F. Vitart, H. Wang, and NOAA's Climate Prediction Center for making prediction data available to us.

Supplementary Materials

www.sciencemag.org/content/343/6171/618/suppl/DC1
Materials and Methods
Table S1

10.1126/science.1247759

NEUROSCIENCE

Could Autism Be Treated Prenatally?

Treatment of rodent models of autism spectrum disorder with a drug that alters the function of a neurotransmitter ameliorates autistic-like behavior in offspring.

Andrew W. Zimmerman[1] and Susan L. Connors[2]

Autism spectrum disorder (ASD) has presented a conundrum: How can the behavioral signs and symptoms that define the condition arise from different etiologies and lead to so many varied phenotypes? Genetics and the environment, including prenatal and perinatal factors, long have been suspected to interact in the causation of ASD. Evidence for neuronal dysfunction and the frequent development of epilepsy strongly support increased excitatory and decreased inhibitory neuronal activity in ASD. In particular, altered functions of γ-aminobutyric acid (GABA), the main inhibitory neurotransmitter (in the mature brain), have been of interest because GABA's effects are excitatory during prenatal development but become inhibitory at birth (*1*, *2*). What has been unclear is the cellular physiology that underlies this "GABA switch." On page 675 of this issue, Tyzio *et al*. (*3*) show that a defect in this switch is associated with abnormal chloride concentration in neurons in two different animal models of ASD. Normal electrophysiology and behavior can be restored in their offspring by the prenatal administration of the compound bumetanide, which blocks a key chloride transporter. The findings raise the possibility of preventing the autistic phenotype in offspring by predelivery pharmacological treatment.

The switch in GABA activity in cortical neurons results from a shift in intracellular chloride concentration ($[Cl^-]_i$) that is controlled by two membrane proteins, NKCC1 and KCC2 (a chloride importer and exporter, respectively). Changes in the expression of these chloride transporters lead to a progressive increase in the inhibitory effect of GABA during early brain development. The GABA switch at birth is sensitive to the hormone oxytocin. Maternal oxytocin initiates an abrupt reduction of intracellular chloride and an increase in GABAergic neuron inhibition in the fetal brain. These effects are neuroprotective and play a role in organizing ongoing early brain development (*4*, *5*). The GABA switch is also sensitive to the drug bumetanide, an antagonist of the NKCC1 chloride importer.

Multiple genes have been described that predispose to ASD, such as the causative gene of fragile X syndrome (FRX) [called *Fragile X Mental Retardation 1* (*FMR1*)] and environmental factors such as prenatal exposure to the anticonvulsant valproic acid (VPA). Tyzio *et al*. examined two seemingly unrelated rodent models of ASD: mice lacking the *Fmr1* gene (referred to as FRX mice) and rats exposed to VPA at mid-gestation. The authors found that the GABA switch can be prevented at birth in normal rats by an oxytocin receptor antagonist, thereby producing postnatal "autistic-like" behavioral changes similar to those seen in VPA rats and FRX mice. The behavior changes have been associated with persistently elevated $[Cl^-]_i$, which drives GABA's excitatory effects as well as oscillations in electrical activity that continue into adulthood. In both FRX mice and VPA rats, the GABA switch is abolished in hippocampal neurons; treatment of cells in both animals with isoguvacine, a GABA receptor agonist, increased, rather than decreased, neuronal excitation. The GABA switch was recently found to be delayed in FRX mice, along with altered expression of the chloride transporters (*6*).

Discovery of a cellular abnormality (change in $[Cl^-]_i$) that is common to two disparate animal models of ASD implies that the GABA switch can be modified by either a genetic factor or an external factor applied as late as mid-gestation. There may be many ultimate causes for failure of the GABA switch

[1]Department of Pediatrics (Neurology), Center for Autism and Neurodevelopmental Disorders, University of Massachusetts Medical School, Worcester, MA 01655, USA. [2]Lurie Center for Autism, Massachusetts General Hospital for Children, Harvard Medical School, Lexington, MA 02421, USA. E-mail: andrew.zimmerman@umassmemorial.org; slconnors@mgh.harvard.edu

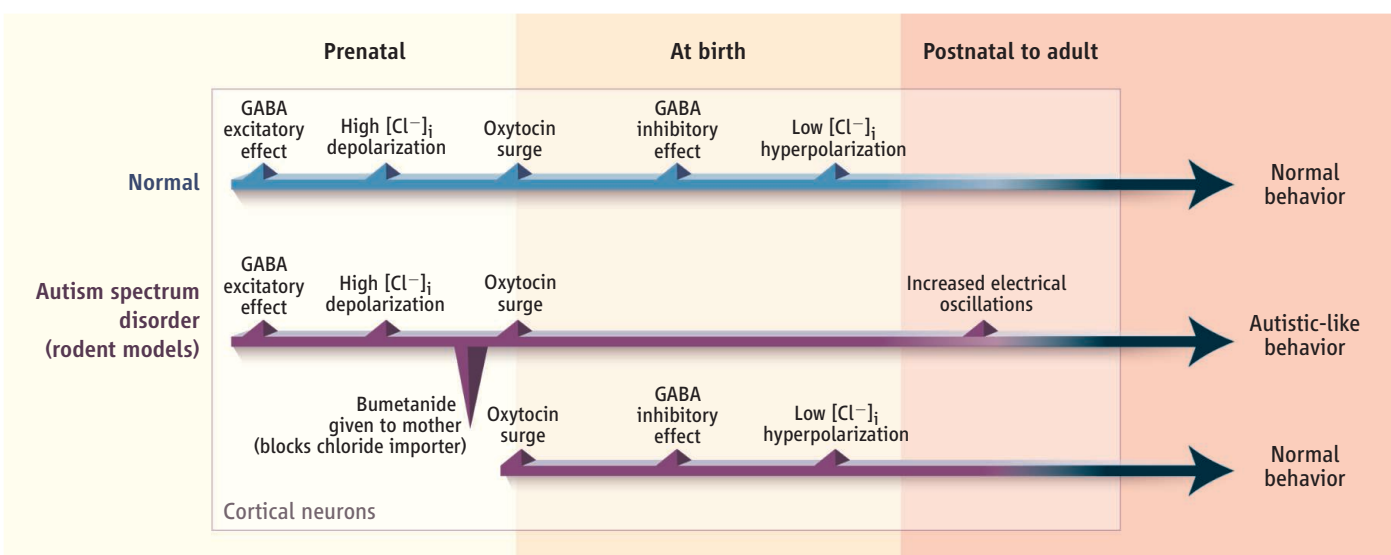

CREDIT: V. ALTOUNIAN/*SCIENCE*

Treat and switch. The switch from excitatory to inhibitory GABAergic signaling in rodent cortical neurons is mediated by oxytocin during the transition from prenatal to postnatal life. In rodent models of ASD (the FRX mouse and VPA rat), the normal shift from high to low intracellular chloride concentration does not take place but can be restored to normal in both cases by prenatal maternal oral administration of bumetanide.

Published by AAAS

at birth and during postnatal brain development. The second half of gestation in humans is a period of rapid development of the cortical GABAergic system that continues into infancy (*7*). During this time, this GABAergic network may be vulnerable to insults at many levels, in addition to genetic susceptibility and epigenetic regulation (*8*). Obstetrical complications, prematurity, and perinatal injuries have been nonspecifically associated with ASD and intellectual disability (*9*), and all might act through one or more parts of the mechanism that shifts $[Cl^-]_i$, along with the critical effects of oxytocin and its receptor. Abnormalities of GABA signaling have also been associated with neonatal seizures (*10*) and the genetic risk for schizophrenia (*11*).

The use of exogenous oxytocin for the initiation or augmentation of labor in humans has been the focus of much speculation as a possible cause of ASD. For example, oxytocin has been associated with increased odds of ASD, especially in male children (*12*). However, it is possible that pregnancy conditions that lead to the administration of oxytocin may predetermine abnormal development of GABA-associated physiology. It is also possible that improved obstetric and neonatal care allow survival of infants with preexisting brain damage (*13*). Endogenous maternal oxytocin is essential for the switch from excitatory to inhibitory GABA activity in the fetal brain during delivery, but it is not known whether additional exogenous oxytocin during delivery (in animals or humans) may ameliorate abnormally shifting $[Cl^-]_i$. Unfortunately, it is not possible to measure intracellular $[Cl^-]_i$ directly in humans. There is strong evidence, however, for abnormal amounts of GABA, GABA receptors, and enzymes that synthesize GABA (GAD65 and 67) in ASD (*2*). The chloride transporters can also be measured in cerebrospinal fluid, and a reduced KCC2/NKCC1 ratio has been reported in Rett syndrome, a neurodegenerative developmental disorder (*14*).

Successful treatment of both the FRX and VPA rodent models of ASD by maternal oral administration of bumetanide 1 day before delivery is the most promising finding of Tyzio *et al*. (see the figure). The authors show that abnormal electrophysiological and behavioral characteristics can be restored by correcting $[Cl^-]_i$. Treatment with bumetanide has already been shown to ameliorate autistic symptoms in a clinical trial of 3- to 11-year-old children with ASD, which suggests that abnormal $[Cl^-]_i$ may be a persistent and a treatable feature of ASD beyond infancy (*15*). Given the increased emphasis on early detection of ASD and discovery of its biomarkers, the possibility for perinatal treatment with an agent such as bumetanide is an enticing possibility for the prevention or early treatment of the disorder. However, this would require an accurate way to determine whom to treat because symptoms of ASD often do not appear until the second year of life. With this new insight into a convergent pathogenic mechanism downstream from different etiologies, we may now begin to understand the variability, as well as sameness, among people with ASD and related disorders.

References

1. G. J. Blatt, S. H. Fatemi, *Anat. Rec.* **294**, 1646 (2011).
2. S. Coghlan *et al*., *Neurosci. Biobehav. Rev.* **36**, 2044 (2012).
3. R. Tyzio *et al*., *Science* **343**, 675 (2014).
4. R. Tyzio *et al*., *Science* **314**, 1788 (2006).
5. Y. Ben-Ari, I. Khalilov, K. T. Kahle, E. Cherubini, *Neuroscientist* **18**, 467 (2012).
6. Q. He, T. Nomura, J. Xu, A. Contractor, *J. Neurosci.* **34**, 446 (2014).
7. G. Xu *et al*., *J. Neuropathol. Exp. Neurol.* **70**, 841 (2011).
8. B. M. Flashner, M. E. Russo, J. E. Boileau, D. W. Leong, G. I. Gallicano, *Neuromol. Med.* **15**, 339 (2013).
9. A. T. Langridge *et al*., *PLOS ONE* **8**, e50963 (2013).
10. V. I. Dzhala *et al*., *J. Neurosci.* **30**, 11745 (2010).
11. T. M. Hyde *et al*., *J. Neurosci.* **31**, 11088 (2011).
12. S. G. Gregory *et al*., *J. Am. Med. Assoc. Pediatr.* **167**, 959 (2013).
13. V. Guinchat *et al*., *Acta Obstet. Gynecol. Scand.* **91**, 287 (2012).
14. S. T. Duarte *et al*., *PLOS ONE* **8**, e68851 (2013).
15. E. Lemonnier *et al*., *Transl. Psychiatry* **2**, e202 (2012).

10.1126/science.1250214

CHEMISTRY

Envisioning the Bioconversion of Methane to Liquid Fuels

Robert J. Conrado and Ramon Gonzalez

Advances in enzymatic pathways and bioreactor design could allow microorganisms to transform methane into chemicals and fuels.

Efforts to use natural gas in transportation, either directly or by conversion to a liquid fuel, have been spurred by recent increases in available supply and a growing price spread between natural gas and petroleum, especially in the United States (*1*). Conversion of natural gas-to-liquids (GTL) can take advantage of existing engine and delivery infrastructure, but GTL approaches operate on scales similar to that of petroleum refineries and suffer from low energy and carbon efficiencies, as well as high capital cost (*2*). Small-scale methane sources that are often flared or vented and that add greenhouse gas emissions also need an economical route for recovery. Biological methane conversion has the potential to directly activate methane at ambient temperatures and pressures on a scale similar to that of sugar fermentation (*3*) and could circumvent partial oxidation routes used industrially that dominate costs and reduce efficiency. Further process simplification is possible by one-step conversion, producing a single-molecule product and reducing the need for heat integration.

Advanced Research Projects Agency–Energy (ARPA-E), U.S. Department of Energy, 1000 Independence Avenue, SW, Washington, DC 20585, USA. E-mail: ramon.gonzalez@doe.gov

Despite these opportunities, aerobic methanotrophs represent the only available route for methane bioconversion, activating methane to methanol via methane monooxygenase (MMO) (*4*, *5*) and subsequently converting methanol to formaldehyde en route to fuel production. However, aerobic methane bioconversion has two primary challenges: low energy and carbon efficiencies and low-productivity cultures. To access small-scale and time-varying resources, process intensification leading to an order-of-magnitude increase in volumetric productivities is needed and will require technical breakthroughs in three areas—high-efficiency methane activation routes, alternative pathways for conversion of an activated intermediate to a liquid fuel, and high-productivity bioreactors.

High-Efficiency Methane Activation

Direct application of the MMO pathway to activate the strong C–H bonds in methane would face several challenges. One is that MMO requires a reduced electron carrier to activate the dimetal active site, and no energy is captured in the subsequent oxidation of methane to methanol. Thus, the production of a reduced energy carrier

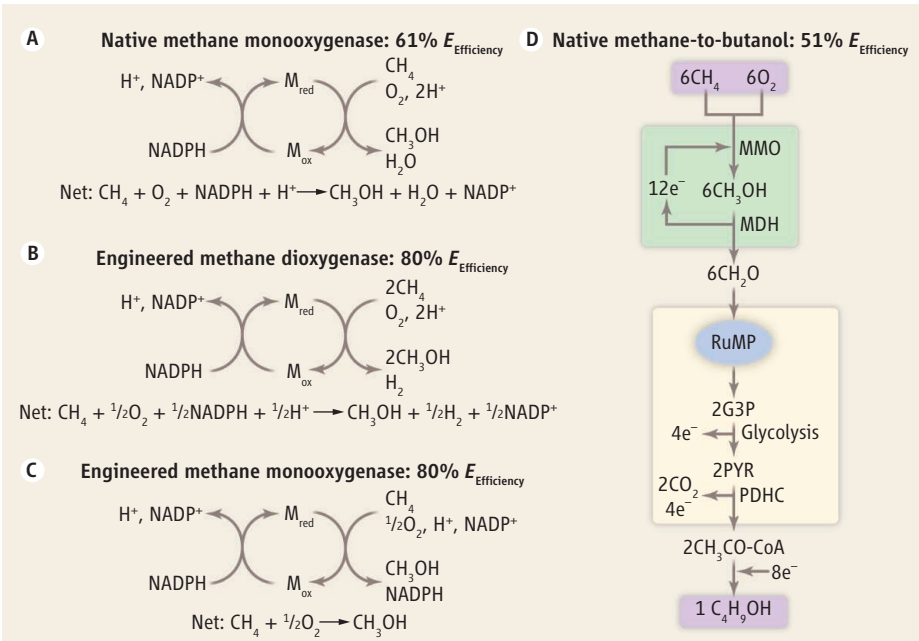

Routes for methane activation and bioconversion pathways. Existing (**A**) and envisioned (**B** and **C**) methane activation routes, along with corresponding net stoichiometries and energy efficiencies ($E_{Efficiency}$). M_{red} and M_{ox} correspond to generic reduced and oxidized metal centers at the enzyme active site (i.e., Fe/Cu in MMO). **(D)** Extension of methane activation through native MMO (A) would convert methanol to formaldehyde through methanol dehydrogenase (MDH). Subsequent C–C bond formation occurs through the RuMP cycle, and resulting glyceraldehyde-3-P (G3P) is converted to pyruvate (PYR) via glycolysis. The pyruvate dehydrogenase complex (PDHC) decarboxylates pyruvate to acetyl-CoA (CH_3CO-CoA), which is used to synthesize *n*-butanol. This design results in a 51% energy efficiency (based on LHV of methane and *n*-butanol) and 67% carbon yield ($6CH_4 + 6O_2 \rightarrow C_4H_9OH + 2CO_2 + 7H_2O$). Colored boxes represent methane activation (green), conversion (yellow), and substrates and products (purple). The blue circle represents a carbon cycle. The energy-efficiency calculations in this figure were simplified by substituting H_2 for NADPH (energetically equivalent and each carries $2e^-$) (*12*).

such as NADPH (reduced form of nicotinamide adenine dinucleotide phosphate) during oxidation of methanol to formaldehyde by methanol dehydrogenase (MDH) offsets the consumption of NADPH during methane activation. In sum, the conversion of methane to methanol results in a loss of nearly 40% of the energy in the starting methane molecule, based on corresponding lower heating values (LHVs) (see the figure, panel A).

Two efficient activation strategies capture energy from methane to methanol oxidation or activate multiple methane molecules at the same active site. Engineering a dioxygenase-like enzyme to activate methane, as is used on cyclic hydrocarbons (*6*), would reduce the energy input by half because two methane molecules could be activated for the same energy input (see the figure, panel B). Harnessing the energy released by this highly exothermic reaction could lead to an engineered MMO that requires no net energy input (see the figure, panel C). A similarly efficient route could be driven by anaerobic activation through a recently characterized enzyme, methyl–coenzyme M reductase (MCR) (*7*), which produces H_2 as a byproduct from the first activation step. Even though consumption of H_2 may be required to ensure that this coupled reaction is exergonic, this reaction sequence would still enable capture of the +6 oxidation state of an activated methyl group. Other promising possibilities to activate methane efficiently include less-characterized enzymes such as methylsuccinate synthase, methane dehydrogenase, and methane carboxylase (*8*).

Engineering C–C Bond Formation and Fuel Synthesis Pathways

The low efficiency of aerobic methane activation to methanol via native MMO would result in the release of a third of the carbon in CH_4 as CO_2 during conversion to liquid fuels like *n*-butanol (see the figure, panel D). Currently, methanotrophs can elongate formaldehyde to pyruvate either through the ribulose monophosphate (RuMP) cycle, which uses formaldehyde directly, or through the Calvin-Benson-Bassham (CBB) CO_2-fixation cycle from fully oxidized formaldehyde. In sum, low product yield and high metabolic energy losses limit energy efficiency to 51% and result in a high requirement for heat transfer, compressor work, and gas-liquid mass transfer. The low productivity of methane fermentation with methanotrophs (and low activity of MMO expression in heterologous hosts such as *Escherichia coli*) is also a burden on capital expenditure. Taking advantage of more efficient methane activation routes discussed in the previous section will require engineered C–C bond formation. For example, for *n*-butanol synthesis, the 12 electrons generated in conversion of methanol to formaldehyde are not needed to activate methane if efficient activation is achieved (see the figure). Applying this energy to additional carbon fixation and product formation could enable a 50% increase in energy efficiency with no CO_2 release (a net reaction of $6CH_4 + 3O_2 \rightarrow 1.5C_4H_9OH + 4.5H_2O$ and 77% energy efficiency). Integration of the energy-efficient RuMP cycle and CO_2-fixation would allow recapture of the CO_2 generated during pyruvate decarboxylation to acetyl–coenzyme A (acetyl-CoA) (see the figure, panel D). Engineered CO_2-fixation pathways could leverage recent work in heterologous engineering of efficient natural and synthetic carbon cycles in novel hosts (*9*), and subsequent conversion of acetyl-CoA to fuels and chemicals (*10*).

Development of decarboxylation-independent pathways could increase efficiency by limiting CO_2 production and capture, which are catalytically slow reactions and allow CO_2 escape. A recently engineered nonoxidative glycolysis (NOG) pathway, for example, when in combination with the RuMP cycle produces acetyl-CoA without going through a pyruvate intermediate (*11*).

High-Productivity Bioreactors

Despite having lower reactor productivity by a factor of 25 to 100, deployed corn-ethanol facilities achieve productivities per land area similar to those of Fischer-Tropsch facilities, 6 metric tons of product per hectare per hour, because bioprocesses proceed with fewer processing steps (*12*). Nevertheless, the low solubility of methane in aqueous-phase systems and the slow kinetics of methane-metabolizing enzymes present additional challenges compared with sugar fermentation. Synergy between metabolic engineering and process design could have multiple benefits, including high-turnover enzymes and high catalyst loading (*13*), accumulating tailored biofuel products that could both increase methane solubility and simplify process separations, and reducing metabolic and process heat losses (includ-

Published by AAAS

ing heat removal from pump and compressor stages) to accommodate this highly exothermic process over a narrow temperature range for operation.

References and Notes

1. U.S. Energy Information Administration, Annual Energy Outlook 2012 with Projections to 2035 (EIA Publication 0383, 2012); www.eia.gov/forecasts/aeo/pdf/0383(2012).pdf.
2. D. A. Wood, C. Nwaoha, B. F. Towler, *J. Nat. Gas Sci. Eng* **9**, 196 (2012).
3. W. G. Hettinga *et al*., *Energy Policy* **37**, 190 (2009).
4. R. Balasubramanian *et al*., *Nature* **465**, 115 (2010).
5. M. Merkx *et al*., *Angew. Chem. Int. Ed. Engl.* **40**, 2782 (2001).
6. C. Bagnéris, R. Cammack, J. R. Mason, *Appl. Environ. Microbiol.* **71**, 1570 (2005).
7. S. Shima *et al*., *Nature* **481**, 98 (2012).
8. A. V. Callaghan, *Front. Microbiol.* **4**, 89 (2013).
9. A. Bar-Even, E. Noor, N. E. Lewis, R. Milo, *Proc. Natl. Acad. Sci. U.S.A.* **107**, 8889 (2010).
10. C. Dellomonaco, J. M. Clomburg, E. N. Miller, R. Gonzalez, *Nature* **476**, 355 (2011).
11. I. W. Bogorad *et al*., *Nature* **502**, 693 (2013).
12. Details of areal productivity and of the reactions in the figure are available at *Science* Online.
13. D. Riesenberg, R. Guthke, *Appl. Microbiol. Biotechnol.* **51**, 422 (1999).

Supplementary Materials

www.sciencemag.org/content/343/6171/621/suppl/DC1
Supplementary Text

10.1126/science.1246929

EVOLUTION

There Can Be Only One

How can a single-copy transcription factor evolve new DNA binding specificities without loss of function?

Jeffery D. Kovach and Rebecca S. Lamb

Gene duplications are a key source of genetic novelty during evolution. This is especially true of transcription factors in land plants (*1*). Duplication of a transcription factor followed by the acquisition of changes can lead to establishment of a new regulatory network. The presence of duplicate copies allows mutations to accumulate in one copy without affecting the regulation of the downstream targets. However, some transcription factors are not members of large families but are present as single-copy or low-copy genes despite having essential roles in growth and development. How do such factors evolve new DNA binding specificities without negative effects that would be selected against? On page 645 of this issue, Sayou *et al*. (*2*) show how one such transcription factor, LEAFY (LFY), evolved novel binding affinities.

LFY was originally identified in the model flowering plant species *Arabidopsis thaliana*; *lfy* mutants fail to make flowers and are therefore sterile (*3*). The LFY transcription factor family has a highly conserved DNA binding domain with structural similarity to helix-turn-helix domains (*4*). LFY binds to a DNA as a dimer. In all plants where its function has been investigated, it is essential, either for reproduction or for cell division. *LFY* genes are present as a single-copy gene in most plants, with the exception of gymnosperms (*5*). LFY orthologs from most groups of plants can function when expressed in *Arabidopsis*; however, a *LFY* ortholog from the moss *Physcomitrella patens* cannot function because it is unable to bind to the *Arabidopsis* LFY target promoters (*5*).

Department of Molecular Genetics, Ohio State University, Columbus, OH 43210, USA. E-mail: lamb.129@osu.edu

The LFY family has previously been postulated to be specific to land plants. However, Sayou *et al*. show that orthologs exist in streptophyte algae, extending the evolutionary history of this gene family and further supporting the relationship between this group of algae and land plants. They also identify orthologs from two groups of basal land plants, the hornworts and liverworts, helping fill in gaps in the LFY phylogeny. All these proteins share considerable sequence identity in their DNA binding regions.

The authors show that three distinct DNA sequences are bound by the LFY proteins: type I (majority of land plants), type II (mosses), and type III (algae and hornworts). Type III sites lack a three-base-pair spacer shown to be important for dimer stabilization in AtLFY (*5*), suggesting that the dimer structure might be different at type III sites. Crystal structures of the three types of LFY proteins bound to DNA show that the differences in affinity can be attributed to just three residues within the conserved DNA binding domain. Thus, orthologous transcription factors encoded by single transcription can evolve distinct binding preferences through changes within conserved regions. Such changes are known to occur after gene duplication events (*6*).

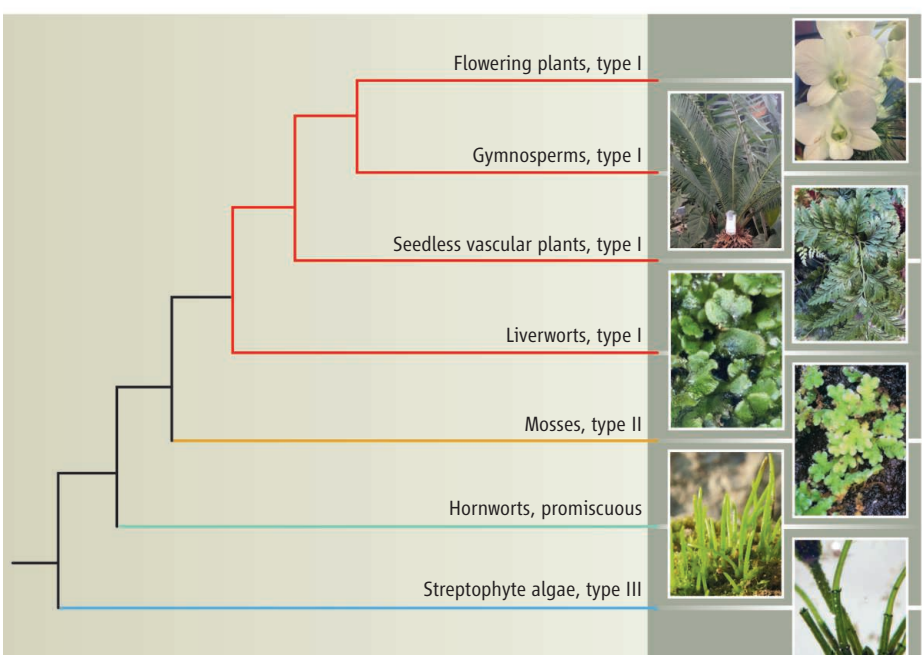

The value of promiscuity. Sayou *et al*. show that the DNA binding specificity of the LFY transcription factor evolved through a promiscuous intermediate. In the simplified phylogeny of land plants and streptophyte algae shown here (*6*, *7*), the binding specificities are color-coded. Images are representative species from each group of organisms.

PHOTO CREDITS: REBECCA S. LAMB

How did these different binding affinities evolve in the apparent absence of a duplicate gene copy that would mask the loss of function caused by a change in DNA binding selectivity? Sayou *et al*. show that a LFY protein from hornworts, a group thought to have branched off from the rest of the land plants early in their evolution (*7*, *8*), is promiscuous in its binding activity: It binds preferentially to type III DNA sequences but can also bind to both type II and type I sequences.

Based on these observations, the authors propose a model by which a single-copy transcription factor can evolve novel binding sequences without losing function. In this model, the DNA binding site selectivity did not change abruptly during evolution of the LFY family. Rather, an intermediate that can bind multiple sites arose. This intermediate could still regulate its original target genes but could also regulate new target genes. This process would avoid potential deleterious effects arising from loss of LFY-regulated gene activity. In the lineage leading to the mosses, the type II binding specificity became fixed, whereas in the lineage leading to liverworts, seedless vascular plants, gymnosperms, and flowering plants, type I binding specificity became fixed.

Left unanswered is how the DNA binding sites bound by the LFY protein evolved and how this reflects the function of LFY in various organisms. In the moss *Physcomitrella*, *LFY* controls cell division (*9*). In contrast, LFY's main role in flowering plants is regulation of reproduction. The functions of *LFY* genes in other plants and streptophyte algae are unknown. It is also unclear whether core LFY target genes are shared between organisms with different LFY DNA binding specificities. The changes in DNA binding specificity may have led to a shift in gene targets and thus in LFY function; alternatively, binding sites may have evolved along with changes in the DNA binding domain.

It remains to be shown whether other transcription factors also evolve through promiscuous intermediates. Another open question is what drives *LFY* to be a single-copy gene in most plant genomes; most transcription factors are preferentially retained after duplication, whereas genes with an essential housekeeping function are more often reduced to a single copy (*10*). The potential for disruption of multiprotein complexes by the presence of mutated duplicate proteins might lie behind this reduction. This process has been shown to influence the evolution of other transcription factors (*11*). In addition, the contribution to DNA site selection and dimer stabilization of another conserved region found in LFY proteins should be explored. This domain mediates dimerization independently of DNA binding and contributes to stable DNA binding in AtLFY (*12*), but its function in other plants is unknown. It may be important for the stabilization of LFY dimers on type III sites. Clearly, much remains to be learned about the evolution of this important transcription factor.

References

1. S. H. Shiu, M. C. Shih, W. H. Li, *Plant Physiol.* **139**, 18 (2005).
2. C. Sayou *et al*., *Science* **343**, 645 (2014); 10.1126/science.1248229.
3. E. A. Schultz, G. W. Haughn, *Plant Cell* **3**, 771 (1991).
4. C. Hamès *et al*., *EMBO J.* **27**, 2628 (2008).
5. A. Maizel *et al*., *Science* **308**, 260 (2005).
6. I. R. Gonçalves *et al*., *Genetics* **196**, 149 (2014).
7. D. L. Nickrent, C. L. Parkinson, J. D. Palmer, R. J. Duff, *Mol. Biol. Evol.* **17**, 1885 (2000).
8. O. Malek, K. Lättig, R. Hiesel, A. Brennicke, V. Knoop, *EMBO J.* **15**, 1403 (1996).
9. T. Tanahashi, N. Sumikawa, M. Kato, M. Hasebe, *Development* **132**, 1727 (2005).
10. R. De Smet *et al*., *Proc. Natl. Acad. Sci. U.S.A.* **110**, 2898 (2013).
11. C. R. Baker, V. Hanson-Smith, A. D. Johnson, *Science* **342**, 104 (2013).
12. N. S. Siriwardana, R. S. Lamb, *Plant J.* **71**, 736 (2012).

10.1126/science.1250348

CELL BIOLOGY

Cells Listen to Their Inner Voice

Anna Jisu Lee and Lingchong You

A signaling circuit that controls the release and detection of the same signaling molecule can trigger diverse behaviors in a cell population.

Picture yourself on top of a mountain shouting out aloud—alone. You will hear only your own voice and its echoes. Now, picture yourself in a crowded stadium cheering for your team. You will hear the collective voice of all those cheering around you. Scaled down a million times, this phenomenon can occur in a population of cells. On page 628 of this issue, Youk and Lim demonstrate (*1*) two distinct modes of communication in yeast cells: self-communication, in which a cell primarily senses the signal produced by itself, and neighbor communication, in which a cell senses the signal collectively produced by all cells nearby. These properties have important implications for understanding cell dynamics in different biological contexts and across species, and for exploring design principles of biological networks.

Chemical-mediated communication is critical for controlling the physiological function of diverse organisms, from bacteria to mammalian cells. Particularly, this notion has transformed the way we perceive microbes. Rather than being truly "single-celled," microbes often engage in extensive communication to carry out functions essential for their survival (*2*), including biofilm development, production of virulence factors, and antibiotic resistance. Likewise, mammalian cells also communicate to regulate functions (*3*) that include homeostasis, growth, and cell-fate decisions. These diverse functions in bacteria and mammalian cells, although seemingly unassociated, share a common core module comprising the production, secretion, and detection of diffusible signals (*4*), or a "secrete-and-sense" module according to Youk and Lim.

The crucial role of chemical-mediated communication in social behaviors is reflected in terms like "quorum sensing" and "sociomicrobiology" (*5*, *6*). In synthetic biology, this mechanism has been extensively used to program dynamics involving one or multiple cell populations (*7*–*9*). When discussing such communication, it is often implied that each cell in a population senses the signal collectively produced by all cells in the vicinity. However, this implicit assumption is not always valid (*10*). For example, an isolated bacterium can also trigger a quorum-sensing response due to physical confinement—such as that of a mammalian cell or a small droplet of a cell culture (*4*, *11*). In this case, the bacterium is "listening" only to itself.

Youk and Lim demonstrate that even in the presence of other signal-producing cells, a cell may still realize self-sensing. The fundamental principle underlying this self-sensing is

Department of Biomedical Engineering, Duke University, CIEMAS 2355, 101 Science Drive, Durham, NC 27708, USA. E-mail: you@duke.edu

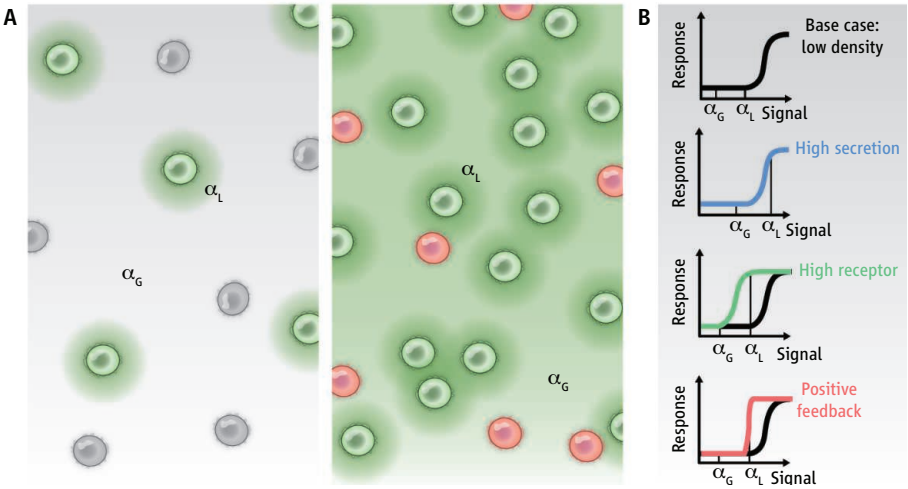

Tunable communication. (**A**) At a low cell density (left), each cell forms a cloud of local signal concentration (α_L). The global signal concentration (α_G) is lower than α_L because α_G increases at a slower rate. "Secrete-and-sense" cells (green) are self-activated; their activation by neighboring cells (gray) is limited. At a high cell density (right), more cells contribute to α_G, leading to activation in "sense-only" cells (red). (**B**) In the base case, α_G is lower than α_L and both are lower than the activation threshold to trigger a cellular response. Faster signal secretion increases both α_G and α_L such that α_L can trigger a response, leading to self-communication. Higher receptor abundance can reduce the activation threshold, leading to differential responses triggered by α_L and α_G. However, further increase in secretion and receptor abundance could diminish this difference and reduce self-communication. Positive feedback can make the response steeper and the activation threshold lower, facilitating self-activation. This can result in bimodal switching behavior at a low cell density.

the incomplete mixing of the culture medium around individual cells. At any moment, there is always a "cloud" of liquid surrounding a cell that is not well mixed, defining a local environment. The dimension of this cloud is characterized by the Kolmogorov mixing length scale (*12*) (see the figure). At a low cell density, cells are much farther apart than the mixing length scale, and the local signal concentration (α_L) is much greater than the global signal concentration (α_G). As a result, each cell primarily senses the signal produced by itself. At a high cell density, however, more cells contribute to the global pool of the signal, and α_G becomes comparable to α_L in magnitude, enabling communication between neighboring cells.

Youk and Lim tested this idea by engineering yeast cells to secrete-and-sense the α-factor, the mating pheromone of yeast. These cells were designed to produce a green fluorescent protein in response to the pheromone signal. To distinguish self- and neighbor communication, the authors engineered a "sense-only" strain for comparison that does not produce the signal but can respond to it by expressing a red fluorescent protein. By quantifying the responses of the two strains, Youk and Lim demonstrate varying degrees of self- and neighbor communication. The balance between the two modes can be readily tuned by controlling the amount of signal receptors expressed by cells, modulating the signal degradation rate, and introducing feedback control. In particular, at a low cell density, higher receptor abundance, faster signal secretion, or positive feedback control can promote self-communication. The common consequence of these strategies is an increased difference between the response to a local signal concentration and that to a global signal concentration. Conversely, faster degradation of the signal leads to diminished self-communication.

An appealing property of chemical-mediated communication is its potential to coordinate gene expression among a population of cells. At a low cell density, however, accumulation of signaling molecules around individual cells reduces the effective strength of neighbor communication, thus limiting the ability of the latter to reduce cell-cell variability. This variability becomes amplified by positive feedback. Indeed, Youk and Lim observed that their positive-feedback circuit led to distinctive bimodal switching behavior at a low cell density. By contrast, a high cell density enhanced neighbor communication, which in turn led to coherent activation by the same positive-feedback circuit.

Why do these modes of communication matter? The tunability of cell communication enables programming of tremendously versatile functions, as demonstrated by Youk and Lim. Similar dynamics may occur in the natural setting, resulting from signaling networks built around the same core secrete-and-sense regulatory motif. In this regard, the study of Youk and Lim represents an example of building synthetic gene circuits to enable quantitative exploration of design principles of biological networks (*13*, *14*). In a natural system, the function of a secrete-and-sense motif can be masked by complex interactions with other cellular components, making it difficult to analyze the design features of the motif. To this end, the circuits engineered by Youk and Lim provide a unified framework to examine the quantitative and qualitative properties of chemical-mediated communication.

The study by Youk and Lim highlights the underappreciated role of the transport property of molecules in defining the nature of biological interactions. Past studies have shown that the length scale of diffusible signals can constrain the outcomes of inter- or intrapopulation communication (*11*, *15*). Youk and Lim show that a fundamental constraint arising from liquid mixing enables cells to switch between social and asocial modes of interactions, using the same signaling molecule. This raises a cautionary note against equating the presence of a secrete-and-sense module to social interaction (*10*, *16*). Whether the module controls asocial or social interactions depends on kinetic rate constants associated with the module and the cell density. This property has profound implications for understanding the evolutionary dynamics of bacterial cooperation, where apparently cooperative traits are often regulated by such secrete-and-sense modules.

References

1. I. H. Youk, W. A. Lim, *Science* **343**, 1242782 (2014); 10.1126/science.1242782.
2. J. A. Shapiro, *Annu. Rev. Microbiol.* **52**, 81 (1998).
3. W. G. Junger, *Nat. Rev. Immunol.* **11**, 201 (2011).
4. A. Pai, L. You, *Mol. Syst. Biol.* **5**, 286 (2009).
5. C. M. Waters, B. L. Bassler, *Annu. Rev. Cell Dev. Biol.* **21**, 319 (2005).
6. M. R. Parsek, E. P. Greenberg, *Trends Microbiol.* **13**, 27 (2005).
7. F. K. Balagaddé *et al.*, *Mol. Syst. Biol.* **4**, 187 (2008).
8. T. Danino, O. Mondragón-Palomino, L. Tsimring, J. Hasty, *Nature* **463**, 326 (2010).
9. W. Weber, M. Daoud-El Baba, M. Fussenegger, *Proc. Natl. Acad. Sci. U.S.A.* **104**, 10435 (2007).
10. R. J. Redfield, *Trends Microbiol.* **10**, 365 (2002).
11. E. C. Carnes *et al.*, *Nat. Chem. Biol.* **6**, 41 (2010).
12. L. D. Landau, E. M. Lifshitz, *Course of Theoretical Physics*, vol. 6, *Fluid Mechanics* (Butterworth-Heinemann, Oxford, UK, 1987).
13. S. Mukherji, A. van Oudenaarden, *Nat. Rev. Genet.* **10**, 859 (2009).
14. J. B. Xavier, *Mol. Syst. Biol.* **7**, 483 (2011).
15. H. Song, S. Payne, M. Gray, L. You, *Nat. Chem. Biol.* **5**, 929 (2009).
16. S. A. West, K. Winzer, A. Gardner, S. P. Diggle, *Trends Microbiol.* **20**, 586 (2012).

10.1126/science.1250244

RETROSPECTIVE

Janet Rowley (1925–2013)

The landmark studies of a brilliant but modest geneticist connected chromosomal translocations with cancer causation.

Mel Greaves

Janet Rowley, geneticist and lifelong member of the University of Chicago, died on 17 December 2013, aged 88. She was regarded with huge admiration, respect, and affection by her peers and by two generations of younger scientists, many of whom benefited from her mentorship. Her impact on cancer genetics has been extraordinary and is all the more impressive because of her light touch, brilliance, and modesty. She often described her research achievements as "just observational" or due to serendipity of being in the right place at the right time. There is an element of truth in this, but it belies her outstanding creative intellect.

Born Janet Davison in New York City in 1925, she was a high flier entering the University of Chicago–affiliated Hutchins College at age 15. She would later earn her M.D. from the University of Chicago in 1948 and marry her classmate, Donald Rowley. But success took time. In these days of fast-paced cancer genomics and big science, it is both salutary and refreshing to recall that the breakthrough moment for Janet came at age 47, when she had been working part time for 20 years and was at home with her four children, scrutinizing cut-out snippets of chromosomes from leukemic cells. The idea that chromosome abnormalities might be causally important in cancer goes back to the German biologist Theodor Boveri 100 years ago, but for decades the prevailing view was that these changes were nonspecific, chaotic, and probably a consequence of instability rather than the cause of cancer. That changed when, in 1960, Peter Nowell and David Hungerford described a chromosomal abnormality in chronic myeloid leukemia (CML). Curiously, this had minimal impact at the time despite its rapid confirmation by a team in Edinburgh who designated the term "Philadelphia chromosome," and Nowell and Hungerford's prescient conclusion that chromosome change was likely causative in CML. It was technology and a very perceptive eye that made the difference.

In 1970, Janet took a (second) sabbatical at Oxford University, where she learned the new banding methods for chromosome karyotyping. These provided a hitherto unattainable level of resolution of chromosome structure. Scrutinizing chromosome images from a patient with acute myeloid leukemia, she identified a chromosome translocation—the t(8;21), later recognized as generating the RUNX1-ETO fusion. *The New England Journal of Medicine* declined her paper describing this landmark finding, but the relatively obscure journal, *Annales de Génétique*, published it in 1973. At the same time, Janet discovered that the Philadelphia chromosome in CML was a consequence of a translocation between chromosomes 9 and 22. Through her persistence, the paper describing this finding was eventually published in *Nature*. Janet had the insight to immediately appreciate the profound biological importance of these studies—if different subtypes of leukemia had consistent, specific chromosomal abnormalities, then these were likely to be causal, providing landmarks for the genes involved in driving the disease.

At first, these discoveries were greeted with some skepticism or, as Janet said, "with amused tolerance," but her gentle persuasion and rock-solid replicated data held sway. She maintained that it was the 1977 discovery of a third consistent translocation—the t(15;17) in acute promyelocytic leukemia—that proved decisive in her own mind. The rest is history. And for the Philadelphia chromosome translocation, later identified as generating the *BCR-ABL1* fusion gene with activated ABL1 kinase, the history has been spectacular, culminating in the development and successful application in the clinic of small-molecule kinase inhibitors that have transformed the treatment and survival prospects for patients with CML. Janet subsequently identified many other chromosomal changes and consistent chromosome translocations in subtypes of leukemia. Initially appearing to be a feature of blood cell cancers, translocations were later discovered in many other cancers, including sarcomas and prostate and lung cancers. Translocations are dramatic genomic events and evoked colorful imagery and metaphors, which Janet was adept at using in her papers and lectures: "dangerous liaisons," "finding order out of chaos," and "Rosetta Stone for understanding cancer" all come to mind.

Janet received more than 60 prestigious awards and prizes, including the Albert Lasker Award, the National Medal of Science, the Franklin Medal, the Japan Prize, and the Presidential Medal of Freedom, the highest civilian honor in the United States. In 1988, I shared with Janet the King Faisal International Prize for Medicine. We, and our respective families, enjoyed a somewhat surreal but wonderful time in Riyadh hobnobbing with Saudi princes. Only one major prize eluded her, and why she did not get the call from Stockholm remains a mystery to me and, I would guess, many others.

With so much achievement and recognition and in her eighties, Janet could have been forgiven for slowing down and easing into retirement. But, always with an eye to the new, Janet would have none of it. She continued to cycle to the lab from her Hyde Park home and threw herself into studying microRNAs and epigenetics of cancer with gusto.

Academic colleagues visiting Chicago over many years would be treated to breakfast at the Rowley household. This usually included a compulsory tour of the small but exotic garden, which was a source of joy for Janet. I last spent time with Janet in Chicago in June of last year. Although her illness and its treatment were taking some physical toll on her, Janet's enthusiasm for science was undiminished; she remained alert, insightful, and gracious, as ever. She exemplified the qualities needed to enjoy science, and life, to the full—insatiable curiosity, collegiality, the courage to take calculated risks, persistence, attention to detail, and most of all, passion toward work. Janet Rowley led a wonderfully balanced and fulfilled life, and she leaves us a magnificent legacy.

10.1126/science.1251005

PHOTO CREDIT: UNIVERSITY OF CHICAGO

The Institute of Cancer Research, London SM2 5NG, UK. E-mail: mel.greaves@icr.ac.uk

Secreting and Sensing the Same Molecule Allows Cells to Achieve Versatile Social Behaviors

Hyun Youk and Wendell A. Lim*

READ THE FULL ARTICLE ONLINE
http://dx.doi.org/10.1126/science.1242782

Cite this article as H. Youk, W. A. Lim, *Science* **343**, 1242782 (2014).
DOI: 10.1126/science.1242782

Introduction: Cells that simultaneously secrete and sense the same signaling molecule are ubiquitous. Bacteria sense a quorum by secreting and sensing an autoinducer; T cells induce a monoclonal immune response by secreting and sensing a cytokine; and epithelial cells can become cancerous through misregulated secreting and sensing of a growth factor. Many of these cells use the same core signaling-circuit motif to realize a diverse repertoire of biological functions. The full range of functions that the "secrete-and-sense" circuit motif can achieve, and the design principles underlying its functional flexibility, remain poorly understood.

Methods: We constructed a synthetic secrete-and-sense circuit motif in budding yeast that enabled the yeast to secrete and sense the mating pheromone. We systematically altered key parameters of the circuit—secretion rate, receptor abundance, positive feedback linking sensing with secretion, and signal degradation—to reveal how they enabled various cellular behaviors. Through single-cell measurements, we assessed the degree to which a secrete-and-sense cell responded to its own secreted signal (self-communication) versus the signal secreted by its neighbors (neighbor communication) to achieve diverse cellular behaviors.

Results: We show that the core secrete-and-sense circuit motif can precisely tune the cell's "sociability"—the cell's degree of self- versus neighbor communication—using one molecule and receptor pair. At the extremes, the circuit enables purely social behaviors (e.g., quorum sensing) in which cells mainly use neighbor communication, or purely asocial behaviors (e.g., epidermal growth factor signaling in epithelial cells) in which cells mainly use self-communication, commonly referred to as "autocrine signaling." Crucially, we uncover rich behaviors that rely on simultaneous self- and neighbor communication, including some that have been observed in nature but whose mechanistic origins have been unclear. For example, positive feedback that links sensing with secretion can yield a bistable behavior in which all cells in the population act as an ensemble to be either quiescent or maximally activated. Incorporation of an active signal degradation enables bimodal activation, in which the different proportions of the population bifurcate into distinct activation states, with the ratio of the two states determined by simultaneous self- and neighbor communication. This behavior explains how isogenic cells can differentiate into distinct states with defined ratios.

Discussion: We integrate simple models, single-cell measurements, and a bottom-up synthetic biology approach to reveal a range of population-level behaviors that arise from the core secrete-and-sense circuit motif. We determine how the intracellular circuit elements result in distinct classes of self- and neighbor communication, and in turn leads to various population-level behaviors. Our work reveals "phase diagrams" that summarize the relationship between the circuit architecture and different phases of population-level behaviors for the secrete-and-sense circuit. Our first-principles approach may be generalized to reveal relationships between the structures of other fundamental cell-signaling circuits and the multicellular behaviors that they enable.

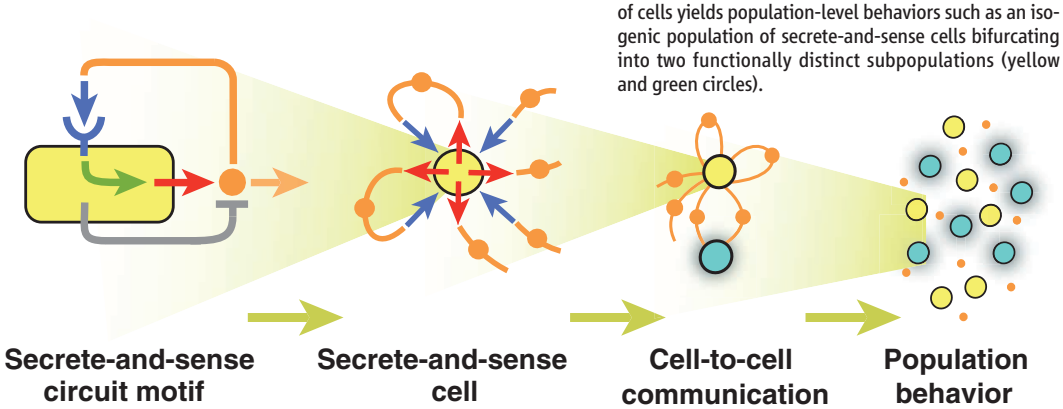

From circuits to multicellular behaviors: a bottom-up synthesis of hierarchy. The secrete-and-sense circuit controls how each cell (yellow circle) communicates through a signaling molecule (orange circle), which in turn controls the cell-to-cell communication. The collection of cell-to-cell communication in all pairs of cells yields population-level behaviors such as an isogenic population of secrete-and-sense cells bifurcating into two functionally distinct subpopulations (yellow and green circles).

FIGURES AND TABLES IN THE FULL ARTICLE

SUPPLEMENTARY MATERIALS

The list of author affiliations is available in the full article online.
*Corresponding author. E-mail: lim@cmp.ucsf.edu

Secreting and Sensing the Same Molecule Allows Cells to Achieve Versatile Social Behaviors

Hyun Youk[1,2] and Wendell A. Lim[1,2,3]*

Cells that secrete and sense the same signaling molecule are ubiquitous. To uncover the functional capabilities of the core "secrete-and-sense" circuit motif shared by these cells, we engineered yeast to secrete and sense the mating pheromone. Perturbing each circuit element revealed parameters that control the degree to which the cell communicated with itself versus with its neighbors. This tunable interplay of self-communication and neighbor communication enables cells to span a diverse repertoire of cellular behaviors. These include a cell being asocial by responding only to itself and social through quorum sensing, and an isogenic population of cells splitting into social and asocial subpopulations. A mathematical model explained these behaviors. The versatility of the secrete-and-sense circuit motif may explain its recurrence across species.

A central goal of systems biology is to understand how various cells use the common small repertoire of circuit elements to communicate with each other to achieve diverse functions (*1*–*19*). Of particular interest is the class of circuits that are found in cells that simultaneously secrete and sense the same extracellular molecule (Fig. 1A) because it is ubiquitous across species. Examples of such cells include (Fig. 1B) bacteria that secrete and sense the autoinducers for quorum sensing (*20*–*37*), human pancreatic β cells that secrete and sense insulin (*38*, *39*), vulva precursor cells in *Caenorhabditis elegans* that secrete and sense the diffusible Delta (*40*–*44*), and human T cells that secrete and sense the cytokine interleukin-2 (IL-2) to regulate their growth (*45*–*49*). In some cases, a cell that secretes and senses the same molecule communicates with itself ("self-communication") but not with its neighboring cells, whereas in other cases such a cell communicates with its neighboring cells ("neighbor communication") but not with itself. Moreover, in some cases, the secrete-and-sense cell communicates both with itself and with its neighbors (Fig. 1C). The advantages of using secrete-and-sense circuits have been unclear in many situations. For example, if a cell's primary purpose is self-communication, then it is unclear why the cell secretes a molecule instead of relying entirely on intracellular signaling. To address these questions, we experimentally explored the full functional capabilities of the secrete-and-sense circuits that arise from the interaction between self-communication and neighbor communication. We sought common design principles that tie together the seemingly disparate examples of secrete-and-sense circuits. We used the budding yeast's mating pathway as a model system in which we could systematically modify the secrete-and-sense circuits to determine what features affect the degree of self-communication versus neighbor communication. We demonstrate that varying the key parameters of the secrete-and-sense circuits allows cells to achieve diverse classes of behaviors, thus suggesting that secrete-and-sense circuits' functional flexibility may explain its recurrence throughout nature.

[1]Department of Cellular and Molecular Pharmacology, University of California, San Francisco, San Francisco, CA 94158, USA. [2]Center for Systems and Synthetic Biology, University of California, San Francisco, San Francisco, CA 94158, USA. [3]Howard Hughes Medical Institute, University of California, San Francisco, San Francisco, CA 94158, USA.

*Corresponding author. E-mail: lim@cmp.ucsf.edu

Results

Basic Secrete-and-Sense Circuit in Yeast

Our model "secrete-and-sense system" is the haploid budding yeast that has been engineered to secrete and sense the mating pheromone α-factor (*50*–*60*) (Fig. 1D). The cell senses the α-factor through its membrane receptor Ste2 and responds by expressing the green fluorescent protein (GFP) through the α-factor–responsive promoter *pFUS1* (Fig. 1D and fig. S1) (*51*). The cell increases GFP expression as the concentration of the exogenous α-factor increases. We used a *far1*Δ strain that did not arrest its cell cycle or mate upon stimulation by α-factor.

Disentangling Effects of Self-Communication and Neighbor Communication

To establish whether the cell's response to sensing the molecule that it secreted (self-communication) could be distinguished from its response to the same molecule that had been secreted by its neighboring cells (neighbor communication), we designed an experiment in which we cultured our secrete-and-sense strain with another strain, called the "sense-only" strain, which senses but does not secrete α-factor (Fig. 2A). The sense-only strain could only respond to the α-factor secreted by the secrete-and-sense strain. On the other hand, a secrete-and-sense cell could potentially respond to both the α-factor that it secreted (self-communication) and the α-factor secreted by the other secrete-and-sense cells in the same batch liquid culture environment (neighbor communication). Thus, we reasoned that if we detected any difference between the reporter GFP level of the secrete-and-sense strain (referred as cell A throughout Fig. 2) and that of the sense-only strain (referred as cell B throughout Fig. 2), then we could ascribe such effects to self-communication.

Construction of Library of Secrete-and-Sense Strains

We constructed a set of secrete-and-sense strains (Fig. 2B) and a set of sense-only strains (strain list in table S1). In each secrete-and-sense strain, doxycycline-inducible promoter *pTET07* expressed the *MFα1* gene that encodes α-factor (*MATa*; *bar1*Δ *far1*Δ) (Fig. 2B and fig. S2). Doxycycline, a small molecule that readily diffused into the cell to control gene expression through the promoter *pTET07*, was used to tune the secretion rate of the α-factor. Increasing concentration of doxycycline caused an increasing expression of the genes under the control of *pTET07*. The GFP expression was controlled by the promoter *pFUS1* that is induced by the α-factor (fig. S1) (*51*). We constructed various secrete-and-sense strains by varying the promoter that expressed Ste2. For each secrete-and-sense strain, we constructed an analogous sense-only strain that lacked the *MFα1* gene. Each sense-only strain also constitutively expressed the fluorescent protein mCherry, which the secrete-and-sense strains lacked. This allowed us to use a flow cytometer to distinguish the sense-only strains from the secrete-and-sense strains when they were cultured together.

Experimental Demonstration of Self-Communication

We cultured our basic secrete-and-sense strain with its partner basic sense-only strain. Both of these "basic" strains had the same endogenous promoter *pSTE2* controlling expression of the Ste2 receptor (fig. S3). We grew these strains together at equal initial cell densities in 5 ml of liquid medium in which we maintained a constant concentration of doxycycline. We used a flow cytometer to measure each strain's mean single-cell GFP fluorescence during the time course. We cultured these strains at various total cell densities [optical densities (ODs)] and doxycycline concentrations (figs. S4 to S7). When both the initial total cell density and the doxycycline concentration were low (for example, OD = 0.001, [doxycycline] = 6 μg/ml; Fig. 2C, left panel), the mean GFP fluorescence of the basic secrete-and-sense strain (cell A in Fig. 2C, left panel) swiftly increased then plateaued, whereas the mean GFP fluorescence of the basic sense-only strain (cell B in Fig. 2C, left panel) stayed at a basal value throughout the time course. This shows that each basic secrete-and-sense cell sensed and responded to the α-factor

that it secreted, whereas the amount of α-factor shared between cells (including between any two basic secrete-and-sense cells) was too low to activate the mating pathway. Thus, each basic secrete-and-sense cell self-communicated in this regime of low cell density and secretion rate. In cultures with the same initial total cell density but with a higher doxycycline concentration (OD = 0.001, [doxycycline] = 30 μg/ml; Fig. 2C, right panel), the basic secrete-and-sense strain's GFP fluorescence again swiftly increased to a higher plateau than it did in the culture with the lower production of α-factor (that is, compare cell A in both panels of Fig. 2C). GFP fluorescence of the basic sense-only strain also increased over time, albeit more slowly than that of the basic secrete-and-sense strain. Thus, increasing the secretion rate increased the degree of neighbor communication (including between different secrete-and-sense cells). The discrepancy between the amounts of GFP fluorescence of the two strains indicates that each basic secrete-and-sense cell, in addition to communicating with its neighbors, also self-communicates by sensing and responding to the higher concentration of its own secreted α-factor. If there were no self-communication, both strains would have the same GFP fluorescence.

We examined cultures of the two basic strains at a 100-fold higher total cell density (OD = 0.1; Fig. 2D). In the high cell density coculture with a low doxycycline concentration ([doxycycline] = 6 μg/ml; Fig. 2D, left panel), the basic sense-only strain's GFP fluorescence increased faster and to higher values than it did in the coculture with the same doxycycline concentration but with the lower cell density (that is, compared to cell B in Fig. 2C, left panel). Thus, the greater cell density caused the degree of neighbor communication to increase. The change in cell density did not affect the basic secrete-and-sense strain's self-communication because the cell density does not affect its secretion rate of α-factor per cell, which is the main determinant of the degree of self-communication for the basic secrete-and-sense strain. In cultures with a high total cell density and a high secretion rate (OD = 0.1, [doxycycline] = 30 μg/ml; Fig. 2D, right panel), there was virtually no difference in GFP fluorescence between the two strains. Hence, in these cultures, neighbor communication was dominant.

Together, our coculture experiments (Fig. 2, C and D) emphasize that self-communication and neighbor communication, despite both using the same signaling molecule, do not always lead to the same behavior over time in a cell that secretes and senses the same molecule. In general, the dynamics of the cell's response to a signal depends not just on the type of the signaling molecule being sensed but also on how the concentration of that molecule changes over time, and distinct dynamics of the same signaling pathway over time can lead to distinct cell fates (*17*). We developed a mathematical model that showed that the secrete-and-sense cell's response to self-communication and neighbor communication yields distinct dynamical responses because of the fact that the two modes of communication involve different time scales (*61*). Our model also explains the main features of our culture experiments and quantifies the degree of self-communication and neighbor communication (*61*).

High Receptor Expression and Secretion Rate Enhance Self-Communication

We examined how varying the amount of the α-factor receptor Ste2 affected the degrees of self-communication and of neighbor communication. To do so, we repeated above experiments with strains that varied in the amount of Ste2 expressed (Fig. 2B, strains in table S1). In each pair, the secrete-and-sense and the sense-only strains used the same constitutive promoter to express Ste2 (figs. S8 and S9). We cultured each pair of strains as low cell density cultures (OD = 0.001; Fig. 2E), as high cell density cultures (OD = 0.1; Fig. 2F), and in a wide range of doxycycline concentrations. We used a flow cytometer to measure the mean single-cell GFP fluorescence of each strain after culturing each pair of strains for 5 hours in doxycycline together. By subtracting the mean single-cell GFP fluorescence of the sense-only strain (cell B) from that of the secrete-and-sense strain (cell A), for each of the seven pairs of strains in 11 different concentrations of doxycycline, we obtained "heat maps" for low cell density (OD = 0.001 for both strains; Fig. 2E) and high cell density (OD = 0.1 for both strains; Fig. 2F) cultures. The color of each pixel in the heat maps (of 7 × 11 pixels) represents the difference in the mean single-cell GFP fluorescence of the two strains for each culture condition.

The heat map for low cell density (Fig. 2E) showed combinations of receptor abundance and secretion rate that enabled the secrete-and-sense cells to self-communicate, and those that did not allow for self-communication. Specifically, in the region of the heat map defined by high secretion rates ([doxycycline] > 0.6 μg/ml) and high receptor expression values (top right quadrant in Fig. 2E), secrete-and-sense cells had higher GFP fluorescence than their counterpart sense-only cells

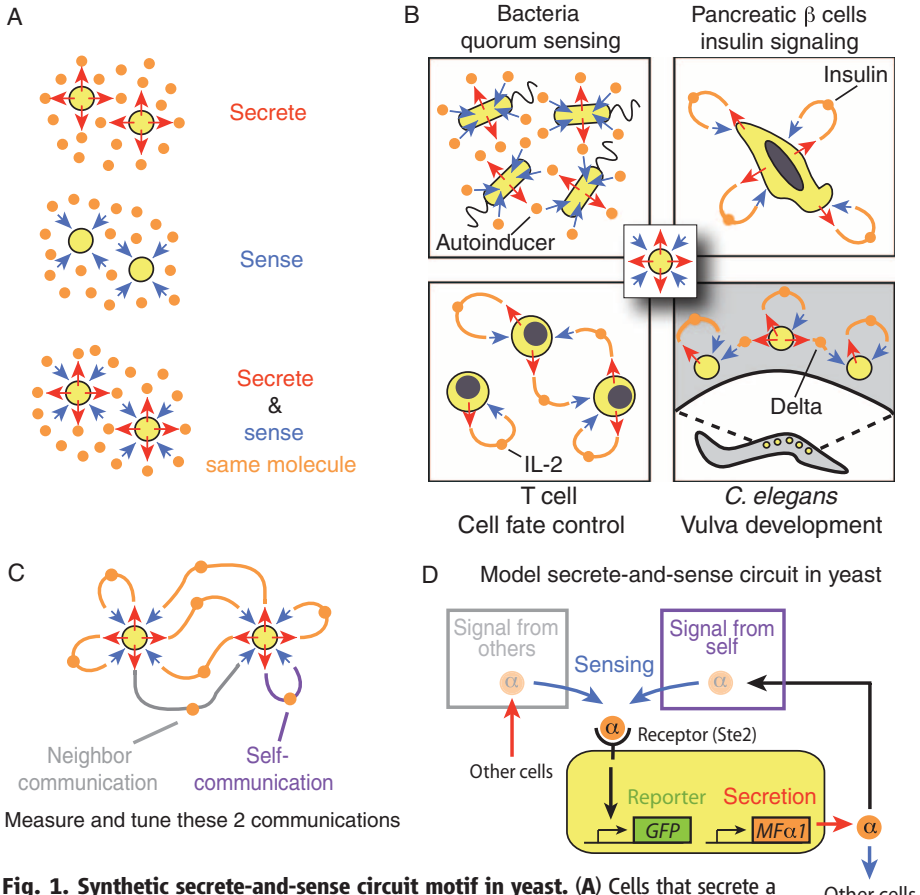

Fig. 1. Synthetic secrete-and-sense circuit motif in yeast. (**A**) Cells that secrete a signaling molecule without sensing (top), cells that sense a molecule without secreting (middle), and cells that secrete and sense the same signaling molecule (bottom). (**B**) Examples of "secrete-and-sense" cells in nature: bacteria secrete and sense an autoinducer for sensing a quorum, human pancreatic β cells secrete and sense insulin, human T cells secrete and sense the cytokine IL-2 to control their proliferation, and the vulva precursor cells in *C. elegans* secrete and sense the diffusible Delta for specifying their cell fates. (**C**) Schematic of self-communication and neighbor communication between two identical secrete-and-sense cells. (**D**) Schematic of synthetic secrete-and-sense system: haploid budding yeast (yellow box) engineered to secrete and sense α-factor (orange circle). GFP fluorescence is a readout of the concentration of α-factor sensed by the cell.

whose GFP fluorescence remained near basal values (*61*). This indicates that a secrete-and-sense cell with a high secretion rate and a high receptor expression is an "asocial" cell that self-communicates by efficiently capturing its own α-factor because of its highly abundant receptors. The secrete-and-sense cells with high secretion rates ([doxycycline] > 0.6 μg/ml) and lower range of receptor expression values (lower right quadrant of the heat map in Fig. 2E) had nearly the same GFP fluorescence values as their counterpart sense-only cells. This indicates that a secrete-and-sense cell with a low receptor expression and high secretion rate is a "social" cell that is unable to self-communicate because its receptor abundance is too low to capture its own α-factor for activating its mating pathway, but is ideal for communicating with its neighbors because of its high secretion rate (*61*). The secrete-and-sense cells with low secretion rate ([doxycycline] < 0.6 μg/ml; the left half of heat map in Fig. 2E), including those with high receptor abundances, had nearly the same GFP fluorescence as their counterpart sense-only cells. This indicates that these secrete-and-sense cells cannot self-communicate because they do not secrete enough α-factor, leading to negligible self-communication and neighbor communication in low cell density. The heat map for high cell density (Fig. 2F) showed that secrete-and-sense cells and sense-only cells had nearly identical GFP fluorescence at all secretion rate and receptor expression values once they had grown together for a sufficiently long time. This indicates that increasing the density of secrete-and-sense cells increases the neighbor communication because of the increased total population-level secretion of α-factor.

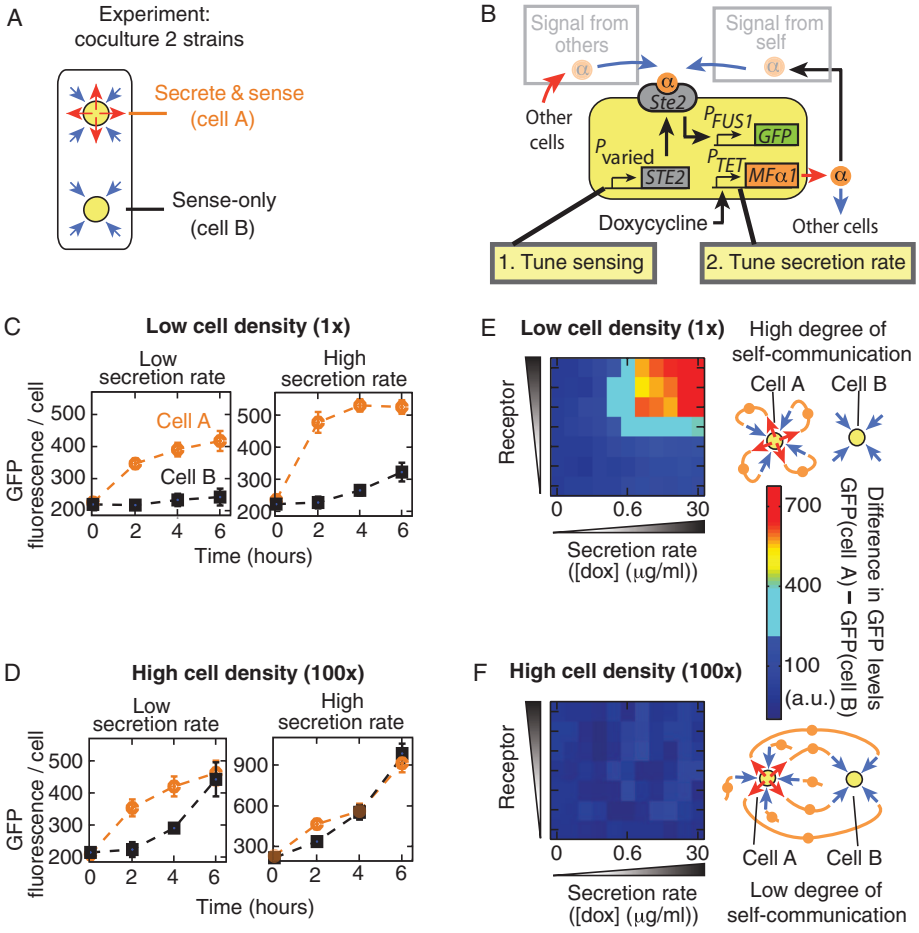

Fig. 2. Varying receptor abundance and secretion rate to tune degrees of self-communication and neighbor communication. (**A**) Secrete-and-sense strain ("cell A") and sense-only strain ("cell B") were cultured together for all experiments in this figure. (**B**) Each secrete-and-sense strain used a different promoter P_{varied} to express *STE2*, but all used the *pTET07* to express *MFα1*. For each secrete-and-sense strain, a matching sense-only strain with the same Ste2 abundance was constructed. (**C** and **D**) Equal densities of "basic secrete-and-sense strain" and "basic sense-only strain" were cultured together for two representative doxycycline concentrations {[doxycycline] = 6 μg/ml ("low secretion rate") and 30 μg/ml ("high secretion rate")} and at two total cell densities [(C) low (OD = 0.001) and (D) high (OD = 0.1)]. Each strain's single-cell GFP fluorescence at various time points is shown. Error bars, SEM (n = 3). (**E** and **F**) Each secrete-and-sense strain (cell A) was cultured with its partner sense-only strain (cell B) (that is, Ste2 expressed by the same promoter in both strains). Seven such pairs of strains were cultured for 5 hours in 11 different concentrations of doxycycline (dox) (table S1 and fig. S8), yielding heat maps with 7 × 11 pixels for (E) low (OD = 0.001) and (F) high (OD = 0.1) cell densities. Each pixel represents the difference between the GFP fluorescence of cell A and of cell B at the end of the time course (subtracting GFP fluorescence of cell B from that of cell A, averaged from three independent experiments).

Positive Feedback on Self-Communication and Neighbor Communication Enables Binary Cell Fates

We next examined how the secrete-and-sense cell's degree of sociability could be further modulated by two regulatory mechanisms that are ubiquitous in naturally occurring secrete-and-sense circuits: positive feedback link (detection of the molecule leads to increased secretion of the molecule) (*62*–*64*) and active degradation of the signaling molecule (for example, secretion of a protease) (*20*).

We first investigated the influence of self-communication and neighbor communication on the positive feedback link. To the basic secrete-and-sense circuit (used in Fig. 2, B and C), we added a positive feedback link (highlighted in blue, Fig. 3A) in which production of α-factor was induced by the mating pathway by linking the *rtTA* expression by the promoter *pFUS1* and having the promoter *pTET07* expressing *MFα1*. We engineered this synthetic positive feedback link so that its strength could be tuned by increasing the doxycycline concentration (fig. S10). We cultured this positive feedback–equipped secrete-and-sense strain by itself in a wide range of doxycycline concentrations and at various cell densities. For each condition, we used a flow cytometer to obtain the histograms of mean single-cell GFP fluorescence at various time points (Fig. 3, B and C, and figs. S11 and S12). When the cell density was low (OD = 0.001) and the positive feedback was weak (for example, [doxycycline] = 3 μg/ml), this strain's GFP fluorescence remained at basal values throughout the time course (Fig. 3B, left column). This corresponds to an "OFF state" in which the cell secretes the α-factor at a low basal rate (indicated by its low basal GFP fluorescence). When positive feedback was strong in cultures of low cell density (for example, [doxycycline] = 40 μg/ml; Fig. 3B, right column), cells, which were initially in the OFF state, increased their signal response over time (corresponding to increasing its signal secretion rate) and, after 8 hours, reached a maximally allowed response—the "ON state"—in which cells secreted α-factor at the maximal possible rate (Fig. 3B, right column, and fig. S11). Thus, positive feedback enabled the initially quiescent secrete-and-sense cell to be "activated" to become maximally secreting cells. This behavior occurs in many natural secrete-and-sense cells with a similar positive feedback link (for example, cytokine signaling in T cells) (*47*, *48*, *62*, *63*, *65*–*68*).

At a high cell density (OD = 0.1), if the positive feedback was weak (for example, [doxycycline] = 3 μg/ml; Fig. 3C, left column), the cells activated, whereas they remained in the OFF state

in cultures of lower cell density with the same doxycycline concentration (Fig. 3B, left column) (fig. S12). This indicates that increased neighbor communication, through the population's collective amplification of the basal level secretion from each cell, probably accounts for this activation (Fig. 3C, left column).

To address whether these activation properties were primarily due to self-communication or neighbor communication, we incubated the positive feedback–equipped basic secrete-and-sense strain (Fig. 3A) with the analogous sense-only strain (characterized in fig. S10) under various doxycycline and cell density conditions (fig. S13). At low total cell density (OD = 0.001), the sense-only strain's GFP fluorescence initially remained at the basal values at the onset of the activation of the secrete-and-sense strain at all doxycycline concentrations. Thus, self-communication, through a cell's small rate of basal secretion, primarily accounts for the "self-activation" at this low cell density (fig. S13). At a high total cell density (OD = 0.1), the sense-only strain's GFP signal increased at the same time and at the same rate as the secrete-and-sense cells, indicating that neighbor communication primarily caused the activation (fig. S13). Thus, at sufficiently high density, secrete-and-sense cells with positive feedback collectively amplify each cell's basal secretion of α-factor, leading to a "neighbor activation."

To summarize, self-activation can occur without any neighbor communication, whereas neighbor activation can occur in regimes where self-communication is insufficient for self-activation of the secrete-and-sense cells with the positive feedback link. Neighbor communication strengthens the positive feedback, enabling even a very weak positive feedback secrete-and-sense circuit to behave as if it had a strong positive feedback. Self-communication, through sufficiently strong positive feedback, enables the secrete-and-sense cells with a very low secretion rate to self-activate so that they can communicate with their neighbors. The interplay between self-communication and neighbor communication creates the overall population-level behavior, in which all cells activate in near unison (Fig. 3D) (*61*). Our work shows that understanding this collective behavior of the secrete-and-sense circuit with the positive feedback link requires knowing the properties of both the intracellular circuit and the communication between the secrete-and-sense cells.

Signal Degradation with Positive Feedback Enables Bimodal Cellular Differentiation

We also examined the effects of an active signal degradation mechanism in secrete-and-sense circuits. We engineered our positive feedback–equipped basic secrete-and-sense strain to express the Bar1 protease (*50*, *52*–*54*), which degrades α-factor in the periplasmic space of the yeast cell (Fig. 4A). We constructed a set of such strains, each with a different constitutive promoter that controls the Bar1 expression (strength of promoters shown in figs. S8, S14, and S15).

A strain that had a weak constitutive expression level of Bar1 (Fig. 4, B and C, fig. S15) was incubated by itself at low (OD = 0.001) or high (OD = 0.1) cell density and in various concentrations of doxycycline. When its positive feedback was weak (for example, [doxycycline] = 6 μg/ml), the strain remained in the OFF state in the low cell density culture (Fig. 4B, left column) and was activated at high cell density (Fig. 4C, left column). Increasing expression of Bar1 decreased the rate at which activation occurred (fig. S15). When positive feedback was sufficiently strong (for example, [doxycycline] = 20 μg/ml), for the low (Fig. 4B, right column) and high (Fig. 4C, right column) cell densities, a transient mixture of OFF-state and ON-state cells was observed in the isogenic culture. In this bimodal population, consisting of isogenic cells that were all initially in the OFF state, all the cells in the OFF state were eventually activated to the ON state (fig. S15). At high cell density (OD = 0.1), the cells were activated faster (Fig. 4C, right column), consistent with our finding that increasing the degree of neighbor communication increased the rate at which the secrete-and-sense cells could be activated.

By examining the individual time courses for all our strains with Bar1 expression (fig. S14 and S15), we obtained a phase diagram that summarizes how the population-level behaviors depend on the positive feedback strength and the Bar1 abundance (Fig. 4D). From our mathematical model (*61*), we obtained an intuitive explanation of this phase diagram. When the cells express very high amounts of Bar1, no activation (self or neighbor) can occur because the high activity of Bar1 degrades the basally secreted α-factor produced by each cell. When the cell density is low, the secrete-and-sense cells rely on self-communication for their activation. If in the low cell density cultures, the secrete-and-sense cells

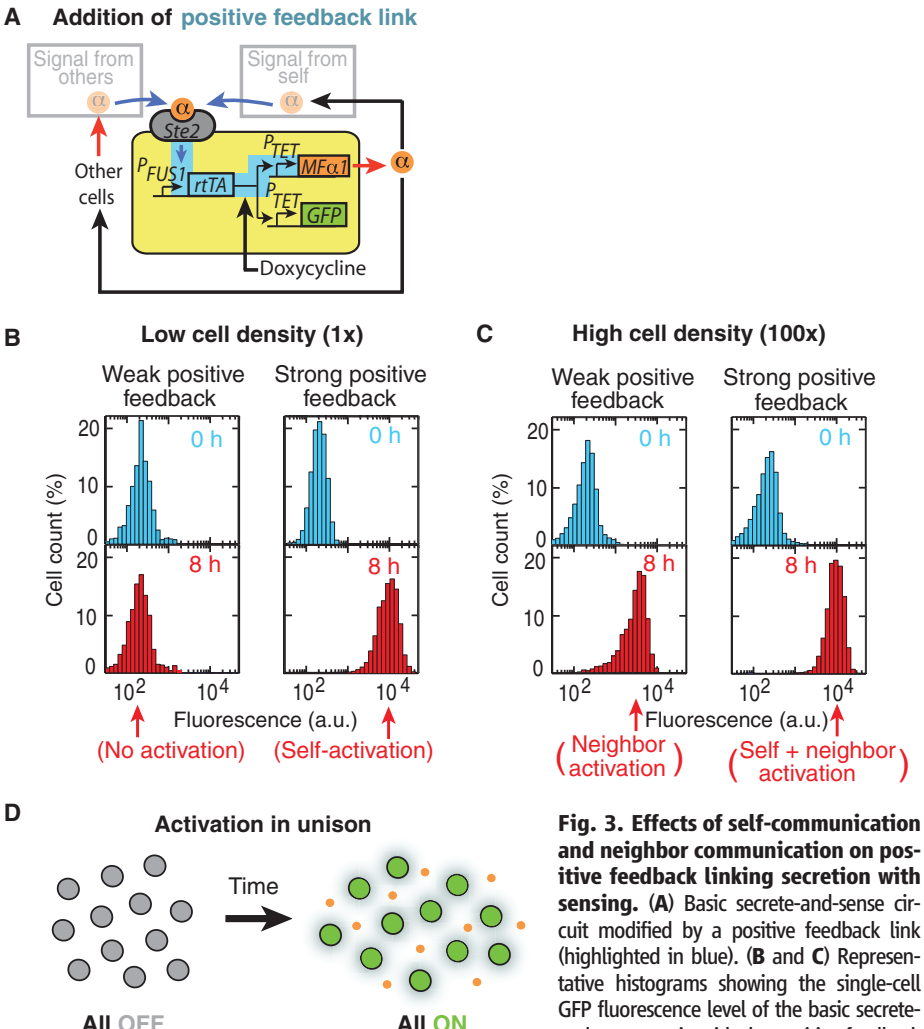

Fig. 3. Effects of self-communication and neighbor communication on positive feedback linking secretion with sensing. (**A**) Basic secrete-and-sense circuit modified by a positive feedback link (highlighted in blue). (**B** and **C**) Representative histograms showing the single-cell GFP fluorescence level of the basic secrete-and-sense strain with the positive feedback link obtained by a flow cytometer. This strain was cultured by itself at two different initial cell densities [(B) low cell density (OD = 0.001) and (C) high cell density (OD = 0.1)] and in two representative concentrations of doxycycline {[doxycycline] = 3 μg/ml (weak positive feedback) and 40 μg/ml (strong positive feedback)}. Blue histograms, beginning of the time course (0 hour); red histograms, 8 hours into the time course (full data sets in figs. S11 and S12). Under each panel, the corresponding type of activation behavior is mentioned. a.u., arbitrary units. (**D**) Main population-level behavior: activation of all cells in near unison.

express a low amount of Bar1 and use a strong positive feedback link, then they can self-activate in a digital (ON or OFF) manner, which manifests as a transient bimodal population of quiescent and maximally secreting cells (Fig. 4E). This results from cell-to-cell variability in the threshold for activation (that is, the amount of α-factor required for activation). At a sufficiently high cell density, neighbor activation dominates, and because every cell essentially senses the same concentrations of α-factors produced by collective basal secretion, the bimodal activation can disappear (as cell-to-cell variability becomes less relevant) and cells can activate together in a graded fashion (*61*). Without the positive feedback, signal degradation's role is weakening the secreted signal. However, when coupled with positive feedback, signal degradation has important effects on the population-level behaviors of secrete-and-sense circuits that reach beyond just weakening of the secreted signal. This may suggest why signal degradation mechanisms are often present in conjunction with positive feedback links in naturally occurring secrete-and-sense circuits. Bar1, coupled with positive feedback, enables a secrete-and-sense cell to delay its response to signal and a population to "hedge its bets" by responding in two distinct ways (that is, bimodal activation, Fig. 4E) by tuning the threshold for activation. Moreover, cells can suppress self-activation while only allowing neighbor activation.

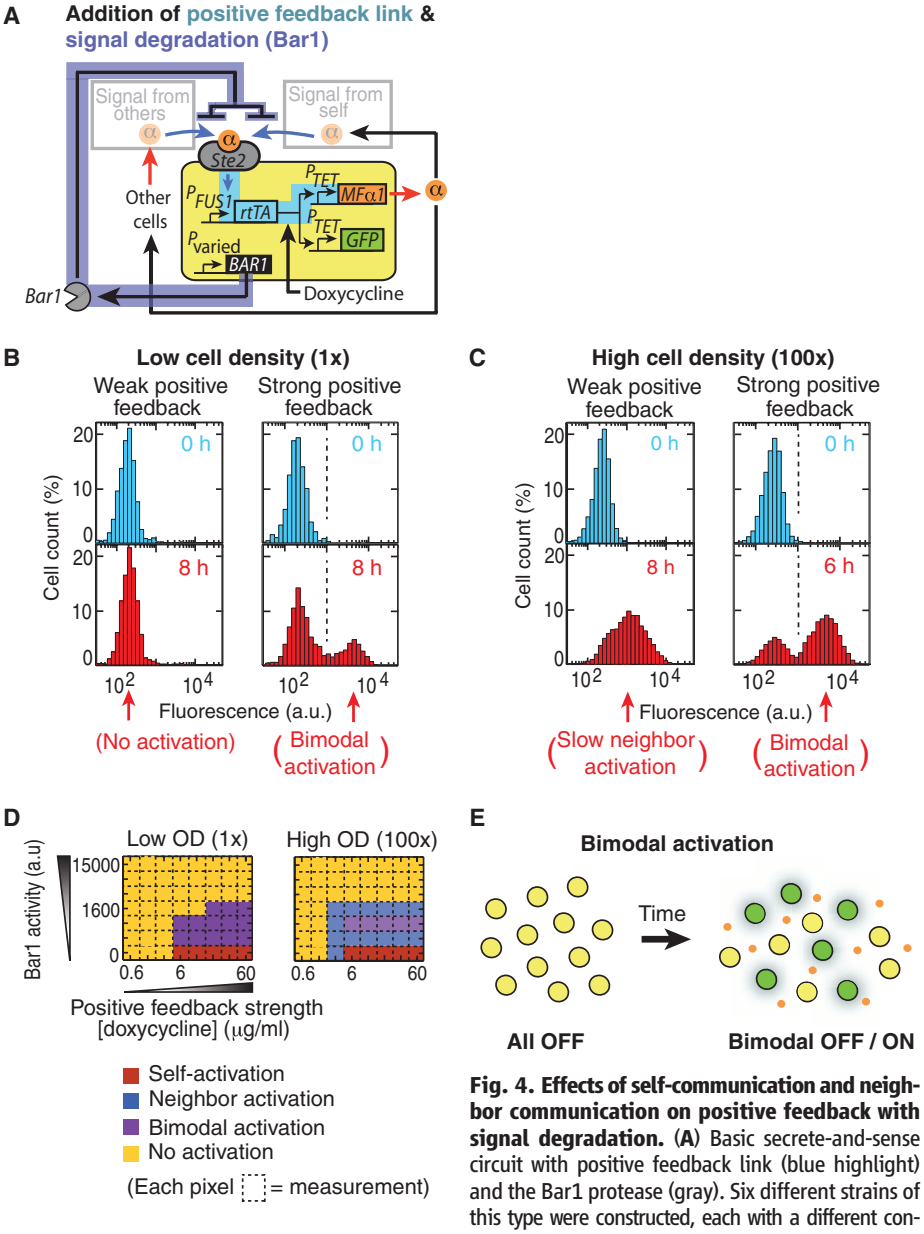

Fig. 4. Effects of self-communication and neighbor communication on positive feedback with signal degradation. (**A**) Basic secrete-and-sense circuit with positive feedback link (blue highlight) and the Bar1 protease (gray). Six different strains of this type were constructed, each with a different constitutive promoter P_{varied} controlling expression of *BAR1*. (**B** and **C**) An example strain (with *pCYC1-BAR1*) cultured by itself at two different initial cell densities [(E) low cell density (OD = 0.001) and (F) high cell density (OD = 0.1)] and in two representative doxycycline concentrations {[doxycycline] = 6 μg/ml (weak positive feedback) and 20 μg/ml (strong positive feedback)}. Representative histograms showing the single-cell GFP fluorescence levels of this strain are plotted at two different time points (blue and red histograms). Under each panel, the corresponding type of activation behavior is mentioned (figs. S14 and S15). (**D**) Phase diagrams from analyzing each time course for the seven secrete-and-sense strains, each with different amounts of Bar1 (including none, Fig. 3) and positive feedback strengths at low (OD = 0.001) and high (OD = 0.1) cell density cultures (summarizes fig. S11, S12, S14, and S15). (**E**) Main population-level behavior: bifurcation of an isogenic population into subpopulations of transiently quiescent and maximally secreting cells.

Intuitive Phenomenological Model

We developed a simple mathematical model that ties together various roles of self-communication and neighbor communication (*61*). Its central idea is that self-communication competes with neighbor communication because they both use the same molecule and receptor. A secrete-and-sense cell can build a locally high concentration of α-factor that it secreted. In low cell densities, this occurs faster than the rate at which the concentration far from the secrete-and-sense cell (the "global concentration") changes. Sensing of the locally high α-factor concentration leads to the fast increases in the secrete-and-sense cell's response (self-communication in Fig. 5A and fig. S16), whereas the slowly changing global concentration of the α-factor leads to a slow response in sense-only cells at low cell density (neighbor communication in Fig. 5A and figs. S17 to S19) (*61*). Paradoxically, self-communication in effect insulates a secrete-and-sense cell from responding to the α-factor that is secreted by the other secrete-and-sense cells. Our model quantifies and summarizes the degree of self-communication and neighbor communication in a phase diagram of these key features (Fig. 5B) (*61*). It also aids in understanding the competition between the positive feedback and the effects of the active signal degradation (figs. S20 to S23) (*61*). Our simple model thus provides an intuitive explanation of the main principles underlying the results of our experiments.

Discussion

Translating Knowledge from Synthetic to Natural Systems

By integrating simple mathematical models, measurements on single cells and whole populations, and a bottom-up synthetic biology approach, we revealed a diverse repertoire of biological functions that secrete-and-sense cells can achieve. Crucially, this integrated approach uncovered design principles that enable the circuit to tune the balance between self-communication and neighbor communication among cells—a crucial mechanism for achieving myriad cellular behaviors and an important general issue in biology. Our work provides a framework for designing synthetic secrete-and-sense circuits and better understanding of the diverse behaviors of seemingly disparate natural secrete-and-sense cells (Table 1). For example, bacterial quorum sensing—a purely social behavior (Fig. 5C)—relies on the low

secretion rate of an autoinducer and the low expression level of a low-affinity receptor to prohibit self-communication and allow only neighbor communication (*27*, *31*, *33*, *69*). Epithelial cells predominantly self-communicate through a signaling loop, commonly referred to as "autocrine signaling loop" (*38*–*49*, *70*–*74*), by expressing large amount of epidermal growth factor (EGF) receptor and secreting EGF, which the receptor recognizes, at sufficiently high rates (*73*)—a purely asocial behavior (Fig. 5C).

Self-activation (Fig. 5C) occurs in T helper (T_H) cells when they use positive feedback on the cytokine IL-2 that they secrete and sense to sharply increase their proliferation rate in a switch-like fashion. Specifically, T_H cells increase both the expression of high-affinity IL-2 receptor and secretion rate of IL-2, which enhances their self-communication through IL-2 that enables them to turn on their proliferation switch. This promotes a monoclonal expansion of cells within an initially polyclonal population of T cells, even though all cells in the population have the same underlying network for processing IL-2 signal (*45*–*48*, *62*).

Aside from known cellular behaviors, our work suggests that simultaneous self-communication and neighbor communication may be a crucial mechanism to consider for interpreting behaviors of secrete-and-sense cells that are currently poorly understood. In particular, there are numerous examples of poorly understood cytokine-mediated decisions in immunology and developmental biology. For example, recent studies have revealed that naïve T_H cells can realize a tunable hybrid of the two T_H cell states, T_H1 and T_H2, which is controlled by secreting and sensing cytokines interferon-γ and IL-4 (*75*, *76*). Self-communication and neighbor communication through these cytokines have both been implicated as the main factors that determine the distribution of the hybrid cell fates in the population, but the details are unknown. Our work suggests that the simultaneous self-communication and neighbor communication in these T cells may be understood by measuring the cell density and individual T cell's receptor expression and secretion rate through single-cell measurement techniques. In the cells of developing embryos, secreting and sensing hedgehog signaling molecules such as the Sonic hedgehog (Shh) are crucial for cell fate specification, including in the embryos of fruit flies, mice, and humans (*77*). Although it is known that these cells use combinations of autocrine

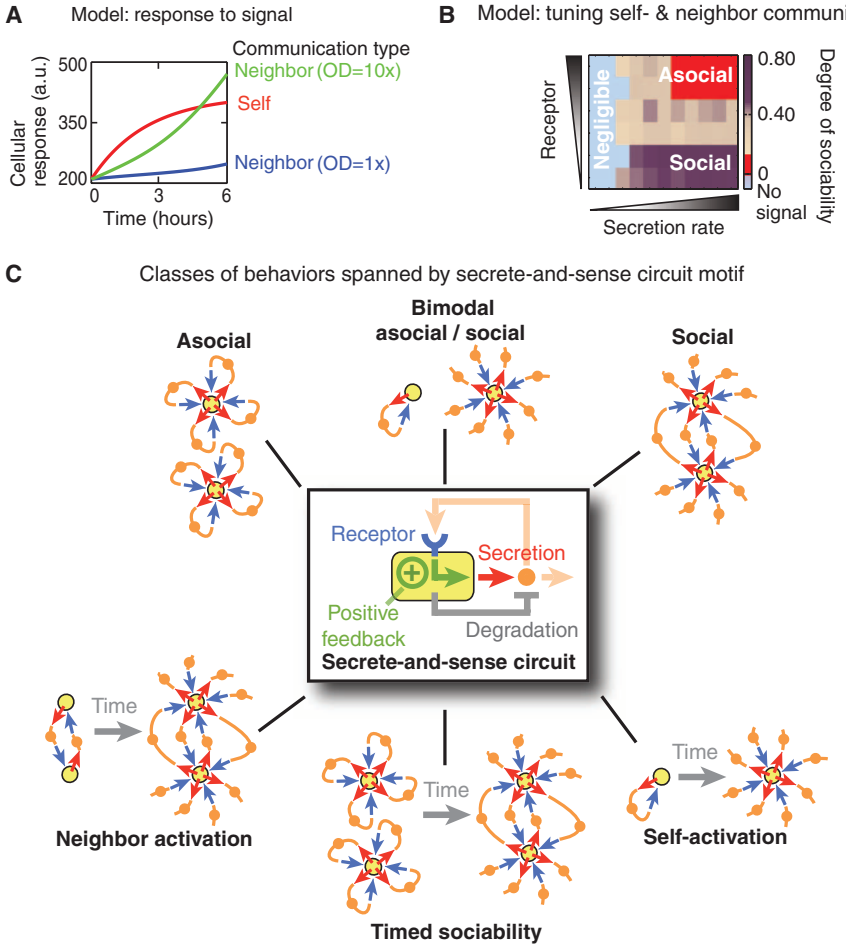

Fig. 5. A simple mathematical model provides intuition. (**A** and **B**) A phenomenological model provides qualitative insights underlying the main features of the secrete-and-sense circuit revealed by our experiments (*61*). (A) Model explains the individual cellular response of a secrete-and-sense cell that self-communicates (red curve) and of a sense-only cell at a low cell density (blue curve) and at a higher cell density (green curve). These curves are analogous to those seen in Fig. 2, C and D. (B) Model summarizes self-communication and neighbor communication in a phase diagram representing the "degree of sociability" [defined in the supplementary text (*61*)]. (**C**) Summary of the main behavioral classes spanned by the secrete-and-sense circuit motif.

Table 1. Design table for engineering secrete-and-sense cells with desired biological functions motivated by our synthetic secrete-and-sense circuit. Examples of biological functions of secrete-and-sense cells that can be understood and engineered on the basis of the design principles revealed by our synthetic circuit.

Desired biological function	Possible circuit parameters for realizing desired biological function	Mode of communication used (neighbor/self)	Class of behavior (Fig. 5C)
Quorum sensing	Low receptor abundance Weak positive feedback	Neighbor	Purely social
Monoclonal expansion of cells in a polyclonal culture due to sensing of self-secreted cytokines	High receptor abundance and high secretion rate Strong positive feedback	Self	Purely asocial Self-activation Timed activation
Creating two functionally distinct cell states	Moderate to strong positive feedback	Self and neighbor	Self-activation Neighbor activation Timed activation
Differentiating an isogenic population into two populations of functionally distinct cells that coexist with a defined ratio	Moderate positive feedback with low signal degradation Strong positive feedback with moderate signal degradation	Self and neighbor	Bimodal activation Self-activation Neighbor activation Timed activation

and paracrine signaling of hedgehog signaling molecules for proper cell fate specification, the difference in the dynamics of individual cells' response to the same signaling molecule determined by self-communication and neighbor communication has not received much attention. Insights provided by recent studies on quantitative single-cell dynamics in developing embryos indicate that the different time scales of individual cell's response, such as those that would be generated by self-communication and neighbor communication through the same molecule, are central for a reliable and timely developmental patterning that is reproducible between individuals (*78*–*83*). This is especially true in spatially organized cells—an important scenario that our work did not address. Our work suggests that in addition to identifying the signaling pathways, the approaches we use to distinguish whether a pathway is self- or neighbor-activated is crucial to understand the developmental process of animals.

In engineering secrete-and-sense cells, our work shows that it is possible to design microbes that can achieve "diffusion sensing" (*84*), a hypothetical mechanism for self-communication in bacteria akin to mammalian autocrine signaling (*70*), which was proposed but lacked a clear demonstration. Our work suggests that by increasing the receptor expression of bacteria that sense a quorum, they can be converted to diffuse sense, which may be useful in bioproduction applications. Such cells may integrate self-sensing and quorum sensing to make sophisticated and autonomous decisions about optimal switching times between growth and production phases. Indeed, some of the yeast strains engineered in our study may be useful for large-scale biofermentation, in which adding external inducer molecules is prohibitively expensive. Moreover, the ability to tune self-communication versus neighbor communication in multicellular microbial systems, such as the social amoebae *Dictyostelium discoideum* or biofilms, may provide a way to better understand the advantages of cooperative versus self-driven behaviors (*20*–*25*, *85*, *86*).

Evolution appears to favor efficient circuits and signaling elements that can accomplish many different tasks (*13*, *14*). The diverse social behaviors that are enabled by the functional flexibility of the secrete-and-sense circuits (Fig. 5C) may explain the frequent occurrence of this class of circuits in nature.

Dissecting Multicellular Behaviors Through Bottom-Up Synthetic Biology Approach

Beyond understanding secrete-and-sense circuits, our approach may be generalized to reveal how cells use fundamental cell signaling circuits to achieve complex multicellular behaviors. Synthetic cell signaling circuits, including some capable of quorum sensing, have often been used to demonstrate targeted cellular behaviors and engineering goals (for example, cellular logic gates) (*3*, *28*, *33*, *34*, *37*, *87*–*94*). Our work highlights the alternate use of synthetic circuits—for exploring their full capabilities and understanding them in a framework that unites natural and synthetic multicellular systems that share the same circuit motif (*95*–*97*). Although only a handful of canonical signaling pathways and circuit motifs are repeatedly used across species, how they produce multicellular behaviors is poorly understood at a systems level (*98*). By building synthetic signaling circuits that mimic the natural signaling circuits, one can perturb each circuit element in individual cells, measure its effects on intracellular and intercellular interactions, and then bridge these interactions to the whole population-level behavior. Doing so may help us understand how the myriad interactions from molecules to cells are coordinated to yield coherent, higher-order macroscopic multicellular behaviors (*2*).

Materials and Methods

Plasmid and Strain Construction

A list of yeast strains used in our study is in table S1, and a list of single-copy yeast-integrating plasmids is in table S2. Full details of plasmid and strain construction are available in the materials and methods. Here, we summarize the yeast and plasmid constructs and the basic construction process. All strains were derived from the haploid strain W303 (*MATa his3 trp1 leu2 ura3*). In particular, the strains CB008 and CB009 (table S1) (*51*), which were both derived from W303 and *far1*Δ, were our starting base strains for generating all other strains. The family tree of our strains and their genotypes are provided in table S1. Two main differences between CB008 and CB009 are that CB008 contains the endogenous BAR1 and lacks pFUS1-GFP, whereas CB009 is *bar1*Δ and has pFUS1-GFP integrated at the mfa2 locus. We knocked out genes in yeast using the standard polymerase chain reaction (PCR)–mediated gene deletion method, in which the undesired gene in the yeast genome is swapped with a PCR product that contains the selective marker gene in its place through a homologous recombination. The selection markers we used were as follows: *HIS3*, *URA3*, *TRP1*, *LEU2*, *KanMX* (resistance to G418, Geneticin, Life Technologies), *HphMX* (resistance to hygromycin B, Life Technologies), and *natMX* (resistance to nourseothricin, Sigma-Aldrich). Yeast transformations were performed with the standard polyethylene glycol/lithium acetate method.

Flow Cytometry

Single-cell fluorescence was measured using a Becton Dickinson LSRII (custom-designed) flow cytometer with a robotic arm for handling samples in a 96-well plate. GFP fluorescence was measured using a coherent sapphire laser with an excitation wavelength of 488 nm. For both dose response and time course experiments, unless otherwise stated, sample aliquots were treated with cycloheximide (5 μg/ml) (Sigma-Aldrich) before measuring single-cell fluorescence. In obtaining the single-cell mean fluorescence values, differences in cell sizes were accounted for through forward and side scatter distributions in the flow cytometer, thus ensuring fair comparisons of fluorescence values.

Culturing Yeast Strains

We cultured all our yeast strains in a standard synthetic medium with 2% glucose at 30°C. For inducing gene expression in yeast with doxycycline ("doxycycline hyclate, 98% purity," Sigma-Aldrich), we aliquoted previously dissolved doxycycline (in double-distilled water) directly into the growth medium to a desired final concentration. Unless otherwise stated, all our yeast strains were cultured in 5 ml of synthetic medium that was constantly mixed by a rotatory wheel at 30°C. For induction with α-factor (Zymo Research), cells were cultured with desired amounts of the α-factor in 5 ml of synthetic medium.

Main Features of Mathematical Model

Full details of our mathematical model and step-by-step derivations of all the equations listed below are available in the supplementary text. Here, we summarize basic mathematical techniques and physical intuition used in building our model. The main physics underlying our model is the notion of "mixing length scale" from fluid mechanics (*99*). It characterizes the distance over which a fluid element (coherent collection of fluid molecules) can travel before losing its collective properties and mixing with the rest of the fluid. A fluid element smoothly flows in the laminar flow region, but upon crossing the boundary between laminar and turbulent flow regimes, its collective motion is destroyed as its individual fluid molecules mix with the surrounding fluid (*99*). When a mechanical device is rotating a tube that contains a liquid medium, such as in our experiments, the device cannot transmit its energy efficiently down to an arbitrarily small length scale to break off all fluid elements. As detailed in our calculations in the supplementary text, this led to a turbulent flow in the macroscopic length scale (on the order of millimeters) but a laminar flow in the microscopic length scales (below about 500 μm, depending on the Reynolds number) in our experimental setup. Hence, a secrete-and-sense cell could create and maintain a concentration gradient of α-factor around itself in our cultures. As shown in the supplementary text, at OD = 0.1 and a high Reynolds number of 10,000, we computed the Kolmogorov mixing length scale (*99*) for our experimental setup to be about 30 μm, which was about five times larger than the average diameter of haploid yeast cells (*61*). A more realistic lower Reynolds number yielded a larger Kolmogorov mixing length. Hence, a secrete-and-sense cell could self-communicate by sensing the concentration gradient formed by the α-factor that it secreted, which could be maintained just around the cell and determined by solving the diffusion equation. Beyond a distance from the cell that is larger than the Kolmogorov mixing length, α-factor from all secrete-and-sense cells became "well mixed" together because of the turbulent flow regime. For this regime, we used a "mean field" approximation to compute the α-factor concentration. As detailed

in the supplementary text, solving the diffusion equation in three dimensions with the appropriate boundary conditions (constant secretion rate, no α-factor infinitely far away from the cell) yielded the concentration c over time t of α-factor at the surface of the secrete-and-sense cell with radius R (*100*) (also eq. S1 in the supplementary text):

$$c(R,t) = \frac{\sqrt{t}F_0}{\sqrt{\pi D}}\left\{1 - e^{\frac{-R^2}{Dt}} + \frac{R\sqrt{\pi}}{\sqrt{Dt}}erfc\left(\frac{R}{\sqrt{Dt}}\right)\right\} \quad (1)$$

where D is the diffusion coefficient of α-factor in water [D = 150 μm^2/s, estimated by using the Stokes-Einstein relation and is similar to the value used by more detailed and insightful models of the mating pathway (*53*, *54*)] and F_0 is the flux of the α-factor molecules secreted radially outward at the cell surface [molecules/(area × time)]. From Eq. 1, we used the standard first-order ordinary differential equation model for constitutive gene expression to derive the basic secrete-and-sense cell's GFP abundance G_{self} due to pure self-communication, which was described by Eq. 2 (also eq. S3 in the supplementary text):

$$G_{\text{self}}([\alpha],t) = \left(G_0 - \frac{k([\alpha])}{\sigma}\right)e^{-\sigma t} + \frac{k([\alpha])}{\sigma} \quad (2)$$

where G_0 is the basal GFP level, σ is the first-order protein degradation rate of GFP, and $k([\alpha])$ is the net production rate (transcription and translation combined) of GFP as a function of the concentration of α-factor. Specific values for these parameters were determined as detailed in the supplementary text (*61*). We used a similar approach to model neighbor communication, resulting in Eq. 3 that described the basic sense-only cell's GFP level G_{others} (also see eq. S6 in the supplementary text):

$$\frac{dG_{\text{others}}}{dt} = k(\rho(t)) - \sigma G_{\text{others}} \quad (3)$$

where $\rho(t)$ is the global concentration of the α-factor due to the collective secretion of all the secrete-and-sense cells (details in the supplementary text). By numerically solving Eq. 3, we obtained G_{others}. Equations 2 and 3 together quantified the degrees of self-communication and neighbor communication in our secrete-and-sense cells. Full details of these analyses are available in the supplementary text.

References and Notes

1. Y. Afek *et al.*, A biological solution to a fundamental distributed computing problem. *Science* **331**, 183–185 (2011). doi: 10.1126/science.1193210; pmid: 21233379
2. P. Mehta, T. Gregor, Approaching the molecular origins of collective dynamics in oscillating cell populations. *Curr. Opin. Genet. Dev.* **20**, 574–580 (2010). doi: 10.1016/j.gde.2010.09.004; pmid: 20934869
3. O. Mondragón-Palomino, T. Danino, J. Selimkhanov, L. Tsimring, J. Hasty, Entrainment of a population of synthetic genetic oscillators. *Science* **333**, 1315–1319 (2011). doi: 10.1126/science.1205369; pmid: 21885786
4. D. Sprinzak *et al.*, *Cis*-interactions between Notch and Delta generate mutually exclusive signalling states. *Nature* **465**, 86–90 (2010). doi: 10.1038/nature08959; pmid: 20418862
5. G. von Dassow, E. Meir, E. M. Munro, G. M. Odell, The segment polarity network is a robust developmental module. *Nature* **406**, 188–192 (2000). doi: 10.1038/35018085; pmid: 10910359
6. J. V. Wong, B. Li, L. You, Tension and robustness in multitasking cellular networks. *PLOS Comput. Biol.* **8**, e1002491 (2012). doi: 10.1371/journal.pcbi.1002491; pmid: 22577355
7. W. H. de Ronde, F. Tostevin, P. R. ten Wolde, Multiplexing biochemical signals. *Phys. Rev. Lett.* **107**, 048101 (2011). doi: 10.1103/PhysRevLett.107.048101; pmid: 21867046
8. R. Hermsen, B. Ursem, P. R. ten Wolde, Combinatorial gene regulation using auto-regulation. *PLOS Comput. Biol.* **6**, e1000813 (2010). doi: 10.1371/journal.pcbi.1000813; pmid: 20548950
9. J. Y. Chen, J. R. Lin, K. A. Cimprich, T. Meyer, A two-dimensional ERK-AKT signaling code for an NGF-triggered cell-fate decision. *Mol. Cell* **45**, 196–209 (2012). doi: 10.1016/j.molcel.2011.11.023; pmid: 22206868
10. T. Bollenbach, R. Kishony, Resolution of gene regulatory conflicts caused by combinations of antibiotics. *Mol. Cell* **42**, 413–425 (2011). doi: 10.1016/j.molcel.2011.04.016; pmid: 21596308
11. L. Espinar, M. Dies, T. Cagatay, G. M. Süel, J. Garcia-Ojalvo, Circuit-level input integration in bacterial gene regulation. *Proc. Natl. Acad. Sci. U.S.A.* **110**, 7091–7096 (2013). doi: 10.1073/pnas.1216091110; pmid: 23572583
12. Y. Hart, U. Alon, The utility of paradoxical components in biological circuits. *Mol. Cell* **49**, 213–221 (2013). doi: 10.1016/j.molcel.2013.01.004; pmid: 23352242
13. S. S. Shen-Orr, R. Milo, S. Mangan, U. Alon, Network motifs in the transcriptional regulation network of *Escherichia coli*. *Nat. Genet.* **31**, 64–68 (2002). doi: 10.1038/ng881; pmid: 11967538
14. R. Milo *et al.*, Network motifs: Simple building blocks of complex networks. *Science* **298**, 824–827 (2002). doi: 10.1126/science.298.5594.824; pmid: 12399590
15. J. Gao, S. V. Buldyrev, H. E. Stanley, S. Havlin, Networks formed from interdependent networks. *Nat. Phys.* **8**, 40–48 (2012). doi: 10.1038/nphys2180
16. E. H. Davidson, Emerging properties of animal gene regulatory networks. *Nature* **468**, 911–920 (2010). doi: 10.1038/nature09645; pmid: 21164479
17. J. E. Purvis, G. Lahav, Encoding and decoding cellular information through signaling dynamics. *Cell* **152**, 945–956 (2013). doi: 10.1016/j.cell.2013.02.005; pmid: 23452846
18. J. Tegner, M. K. S. Yeung, J. Hasty, J. J. Collins, Reverse engineering gene networks: Integrating genetic perturbations with dynamical modeling. *Proc. Natl. Acad. Sci. U.S.A.* **100**, 5944–5949 (2003). doi: 10.1073/pnas.0933416100; pmid: 12730377
19. J. E. Ferrell Jr. *et al.*, Simple, realistic models of complex biological processes: Positive feedback and bistability in a cell fate switch and a cell cycle oscillator. *FEBS Lett.* **583**, 3999–4005 (2009). doi: 10.1016/j.febslet.2009.10.068; pmid: 19878681
20. T. Gregor, K. Fujimoto, N. Masaki, S. Sawai, The onset of collective behavior in social amoebae. *Science* **328**, 1021–1025 (2010). doi: 10.1126/science.1183415; pmid: 20413456
21. S. De Monte, F. d'Ovidio, S. Danø, P. Graae Sørensen, Dynamical quorum sensing: Population density encoded in cellular dynamics. *Proc. Natl. Acad. Sci. U.S.A.* **104**, 18377–18381 (2007). doi: 10.1073/pnas.0706089104; pmid: 18003917
22. D. J. Schwab, A. Baetica, P. Mehta, Dynamical quorum-sensing in oscillators coupled through an external medium. *Physica D* **241**, 1782–1788 (2012). doi: 10.1016/j.physd.2012.08.005; pmid: 23087494
23. S. Sawai, P. A. Thomason, E. C. Cox, An autoregulatory circuit for long-range self-organization in *Dictyostelium* cell populations. *Nature* **433**, 323–326 (2005). doi: 10.1038/nature03228; pmid: 15662425
24. L. Li, E. C. Cox, H. Flyvbjerg, 'Dicty dynamics': Dictyostelium motility as persistent random motion. *Phys. Biol.* **8**, 046006 (2011). doi: 10.1088/1478-3975/8/4/046006; pmid: 21610290
25. T. Umeda, K. Inouye, Cell sorting by differential cell motility: A model for pattern formation in Dictyostelium. *J. Theor. Biol.* **226**, 215–224 (2004). doi: 10.1016/j.jtbi.2003.08.016; pmid: 14643191
26. W. L. Ng, B. L. Bassler, Bacterial quorum-sensing network architectures. *Annu. Rev. Genet.* **43**, 197–222 (2009). doi: 10.1146/annurev-genet-102108-134304; pmid: 19686078
27. K. C. Tu, T. Long, S. L. Svenningsen, N. S. Wingreen, B. L. Bassler, Negative feedback loops involving small regulatory RNAs precisely control the *Vibrio harveyi* quorum-sensing response. *Mol. Cell* **37**, 567–579 (2010). doi: 10.1016/j.molcel.2010.01.022; pmid: 20188674
28. L. You, R. S. Cox III, R. Weiss, F. H. Arnold, Programmed population control by cell-cell communication and regulated killing. *Nature* **428**, 868–871 (2004). doi: 10.1038/nature02491; pmid: 15064770
29. I. B. Bischofs, J. A. Hug, A. W. Liu, D. M. Wolf, A. P. Arkin, Complexity in bacterial cell–cell communication: Quorum signal integration and subpopulation signaling in the *Bacillus subtilis* phosphorelay. *Proc. Natl. Acad. Sci. U.S.A.* **106**, 6459–6464 (2009). doi: 10.1073/pnas.0810878106; pmid: 19380751
30. P. Mehta, S. Goyal, T. Long, B. L. Bassler, N. S. Wingreen, Information processing and signal integration in bacteria quorum sensing. *Mol. Syst. Biol.* **5**, 325 (2009). doi: 10.1038/msb.2009.79; pmid: 19920810
31. A. Eldar, Social conflict drives the evolutionary divergence of quorum sensing. *Proc. Natl. Acad. Sci. U.S.A.* **108**, 13635–13640 (2011). doi: 10.1073/pnas.1102923108; pmid: 21807995
32. A. Pai, Y. Tanouchi, L. You, Optimality and robustness in quorum sensing (QS)-mediated regulation of a costly public good enzyme. *Proc. Natl. Acad. Sci. U.S.A.* **109**, 19810–19815 (2012). doi: 10.1073/pnas.1211072109; pmid: 23144221
33. T. C. Williams, L. K. Nielsen, C. E. Vickers, Engineered quorum sensing using pheromone-mediated cell-to-cell communication in *Saccharomyces cerevisiae*. *ACS Synth. Biol.* **2**, 136–149 (2013). doi: 10.1021/sb300110b; pmid: 23656437
34. T. Danino, O. Mondragón-Palomino, L. Tsimring, J. Hasty, A synchronized quorum of genetic clocks. *Nature* **463**, 326–330 (2010). doi: 10.1038/nature08753; pmid: 20090747
35. S. W. Teng *et al.*, Active regulation of receptor ratios controls integration of quorum-sensing signals in *Vibrio harveyi*. *Mol. Syst. Biol.* **7**, 491 (2011). doi: 10.1038/msb.2011.30; pmid: 21613980
36. A. Chatterjee *et al.*, Antagonistic self-sensing and mate-sensing signaling controls antibiotic-resistance transfer. *Proc. Natl. Acad. Sci. U.S.A.* **110**, 7086–7090 (2013). doi: 10.1073/pnas.1212256110; pmid: 23569272
37. M. T. Chen, R. Weiss, Artificial cell-cell communication in yeast *Saccharomyces cerevisiae* using signaling elements from *Arabidopsis thaliana*. *Nat. Biotechnol.* **23**, 1551–1555 (2005). doi: 10.1038/nbt1162; pmid: 16299520
38. I. B. Leibiger, B. Leibiger, P. O. Berggren, Insulin signaling in the pancreatic β-cell. *Annu. Rev. Nutr.* **28**, 233–251 (2008). doi: 10.1146/annurev.nutr.28.061807.155530; pmid: 18481923
39. C. A. Aspinwall, J. R. T. Lakey, R. T. Kennedy, Insulin-stimulated insulin secretion in single pancreatic beta cells. *J. Biol. Chem.* **274**, 6360–6365 (1999). doi: 10.1074/jbc.274.10.6360; pmid: 10037726
40. E. Hoyos *et al.*, Quantitative variation in autocrine signaling and pathway crosstalk in the *Caenorhabditis* vulval network. *Curr. Biol.* **21**, 527–538 (2011). doi: 10.1016/j.cub.2011.02.040; pmid: 21458263
41. N. Chen, I. Greenwald, The lateral signal for LIN-12/Notch in *C. elegans* vulval development comprises redundant secreted and transmembrane DSL proteins. *Dev. Cell* **6**, 183–192 (2004). doi: 10.1016/S1534-5807(04)00021-8; pmid: 14960273
42. G. Seydoux, I. Greenwald, Cell autonomy of *lin-12* function in a cell fate decision in *C. elegans*. *Cell* **57**, 1237–1245 (1989). doi: 10.1016/0092-8674(89)90060-3; pmid: 2736627
43. P. W. Sternberg, H. R. Horvitz, The combined action of two intercellular signaling pathways specifies three cell fates during vulval induction in *C. elegans*. *Cell* **58**, 679–693 (1989). doi: 10.1016/0092-8674(89)90103-7; pmid: 2548732

44. F. Corson, E. D. Siggia, Geometry, epistasis, and developmental patterning. *Proc. Natl. Acad. Sci. U.S.A.* **109**, 5568–5575 (2012). doi: 10.1073/pnas.1201505109; pmid: 22434912
45. D. A. Cantrell, K. A. Smith, The interleukin-2 T-cell system: A new cell growth model. *Science* **224**, 312–1316 (1984). doi: 10.1126/science.6427923; pmid: 6427923
46. T. A. Waldmann, The biology of interleukin-2 and interleukin-15: Implications for cancer therapy and vaccine design. *Nat. Rev. Immunol.* **6**, 595–601 (2006). doi: 10.1038/nri1901; pmid: 16868550
47. Y. Savir, N. Waysbort, Y. E. Antebi, T. Tlusty, N. Friedman, Balancing speed and accuracy of polyclonal T cell activation: A role for extracellular feedback. *BMC Syst. Biol.* **6**, 111 (2012). doi: 10.1186/1752-0509-6-111; pmid: 22925037
48. O. Feinerman *et al.*, Single-cell quantification of IL-2 response by effector and regulatory T cells reveals critical plasticity in immune response. *Mol. Syst. Biol.* **6**, 437 (2010). doi: 10.1038/msb.2010.90; pmid: 21119631
49. E. M. Fallon, D. A. Lauffenburger, Computational model for effects of ligand/receptor binding properties on interleukin-2 trafficking dynamics and T cell proliferation response. *Biotechnol. Prog.* **16**, 905–916 (2000). doi: 10.1021/bp000097t; pmid: 11027188
50. L. Bardwell, A walk-through of the yeast mating pheromone response pathway. *Peptides* **25**, 1465–1476 (2004). doi: 10.1016/j.peptides.2003.10.022;pmid: 15374648
51. C. J. Bashor, N. C. Helman, S. Yan, W. A. Lim, Using engineered scaffold interactions to reshape MAP kinase pathway signaling dynamics. *Science* **319**, 1539–1543 (2008). doi: 10.1126/science.1151153; pmid: 18339942
52. N. Barkai, M. Rose, N. Wingreen, Protease helps yeast find mating partners. *Nature* **396**, 422–423 (1998). doi: 10.1038/24760; pmid: 9853747
53. N. Rappaport, N. Barkai, Disentangling signaling gradients generated by equivalent sources. *J. Biol. Phys.* **38**, 267–278 (2012). doi: 10.1007/s10867-011-9240-x; pmid: 23450187
54. M. Jin *et al.*, Yeast dynamically modify their environment to achieve better mating efficiency. *Sci. Signal.* **4**, ra54 (2011). doi: 10.1126/scisignal.2001763; pmid: 21868361
55. J. Gonçalves-Sá, A. Murray, Asymmetry in sexual pheromones is not required for ascomycete mating. *Curr. Biol.* **21**, 1337–1346 (2011). doi: 10.1016/j.cub.2011.06.054; pmid: 21835624
56. N. Hao *et al.*, Regulation of cell signaling dynamics by the protein kinase-scaffold Ste5. *Mol. Cell* **30**, 649–656 (2008). doi: 10.1016/j.molcel.2008.04.016; pmid: 18538663
57. N. T. Ingolia, A. W. Murray, Positive-feedback loops as a flexible biological module. *Curr. Biol.* **17**, 668–677 (2007). doi: 10.1016/j.cub.2007.03.016; pmid: 17398098
58. R. C. Yu *et al.*, Negative feedback that improves information transmission in yeast signalling. *Nature* **456**, 755–761 (2008). doi: 10.1038/nature07513; pmid: 19079053
59. H. D. Madhani, *From a to α: Yeast as a Model for Cellular Differentiation* (Cold Spring Harbor Laboratory Press, New York, 2006).
60. E. McCullagh, A. Seshan, H. El-Samad, H. D. Madhani, Coordinate control of gene expression noise and interchromosomal interactions in a MAP kinase pathway. *Nat. Cell Biol.* **12**, 954–962 (2010). doi: 10.1038/ncb2097; pmid: 20852627
61. Full details are available as supplementary materials on *Science* Online.
62. Y. Hart, Y. E. Antebi, A. E. Mayo, N. Friedman, U. Alon, Design principles of cell circuits with paradoxical components. *Proc. Natl. Acad. Sci. U.S.A.* **109**, 8346–8351 (2012). doi: 10.1073/pnas.1117475109; pmid: 22562798
63. J. E. Ferrell Jr., Feedback regulation of opposing enzymes generates robust, all-or-none bistable responses. *Curr. Biol.* **18**, R244–R245 (2008). doi: 10.1016/j.cub.2008.02.035; pmid: 18364225
64. G. Hornung, N. Barkai, Noise propagation and signaling sensitivity in biological networks: A role for positive feedback. *PLOS Comp. Biol.* **4**, e8 (2008). doi: 10.1371/journal.pcbi.0040008; pmid: 18179281
65. J. Hasty, J. Pradines, M. Dolnik, J. J. Collins, Noise-based switches and amplifiers for gene expression. *Proc. Natl. Acad. Sci. U.S.A.* **97**, 2075–2080 (2000). doi: 10.1073/pnas.040411297; pmid: 10681449
66. R. Hermsen, D. Erickson, T. Hwa, Speed, sensitivity, and bistability in auto-activating signaling circuits. *PLOS Comput. Biol.* **7**, e1002265 (2011). doi: 10.1371/journal.pcbi.1002265; pmid: 22125482
67. O. Feinerman, J. Veiga, J. R. Dorfman, R. N. Germain, G. Altan-Bonnet, Variability and robustness in T cell activation from regulated heterogeneity in protein levels. *Science* **321**, 1081–1084 (2008). doi: 10.1126/science.1158013; pmid: 18719282
68. P. Sansone *et al.*, IL-6 triggers malignant features in mammospheres from human ductal breast carcinoma and normal mammary gland. *J. Clin. Invest.* **117**, 3988–4002 (2007). doi: 10.1172/JCI32533; pmid: 18060036
69. T. Long *et al.*, Quantifying the integration of quorum-sensing signals with single-cell resolution. *PLOS Biol.* **7**, e68 (2009). doi: 10.1371/journal.pbio.1000068; pmid: 19320539
70. M. B. Sporn, G. J. Todaro, Autocrine secretion and malignant transformation of cells. *N. Engl. J. Med.* **303**, 878–880 (1980). doi: 10.1056/NEJM198010093031511; pmid: 7412807
71. M. Coppey, A. M. Berezhkovskii, S. C. Sealfon, S. Y. Shvartsman, Time and length scales of autocrine signals in three dimensions. *Biophys. J.* **93**, 1917–1922 (2007). doi: 10.1529/biophysj.107.109736; pmid: 17720734
72. S. Y. Shvartsman, H. S. Wiley, W. M. Deen, D. A. Lauffenburger, Spatial range of autocrine signaling: Modeling and computational analysis. *Biophys. J.* **81**, 1854–1867 (2001). doi: 10.1016/S0006-3495(01)75837-7; pmid: 11566760
73. A. E. DeWitt, J. Y. Dong, H. S. Wiley, D. A. Lauffenburger, Quantitative analysis of the EGF receptor autocrine system reveals cryptic regulation of cell response by ligand capture. *J. Cell Sci.* **114**, 2301–2313 (2001). pmid: 11493669
74. S. Y. Shvartsman *et al.*, Autocrine loops with positive feedback enable context-dependent cell signaling. *Am. J. Physiol. Cell Physiol.* **282**, C545–C559 (2002). doi: 10.1152/ajpcell.00260.2001; pmid: 11832340
75. Y. E. Antebi *et al.*, Mapping differentiation under mixed culture conditions reveals a tunable continuum of T cell fates. *PLOS Biol.* **11**, e1001616 (2013). doi: 10.1371/journal.pbio.1001616; pmid: 23935451
76. M. Fang, H. Xie, S. K. Dougan, H. Ploegh, A. van Oudenaarden, Stochastic cytokine expression induces mixed T helper cell states. *PLOS Biol.* **11**, e1001618 (2013). doi: 10.1371/journal.pbio.1001618; pmid: 23935453
77. L. Lum, P. A. Beachy, The Hedgehog response network: Sensors, switches, and routers. *Science* **304**, 1755–1759 (2004). doi: 10.1126/science.1098020; pmid: 15205520
78. T. Gregor, D. W. Tank, E. F. Wieschaus, W. Bialek, Probing the limits to positional information. *Cell* **130**, 153–164 (2007). doi: 10.1016/j.cell.2007.05.025; pmid: 17632062
79. F. Liu, A. H. Morrison, T. Gregor, Dynamic interpretation of maternal inputs by the Drosophila segmentation gene network. *Proc. Natl. Acad. Sci. U.S.A.* **110**, 6724–6729 (2013). doi: 10.1073/pnas.1220912110; pmid: 23580621
80. H. G. Garcia, M. Tikhonov, A. Lin, T. Gregor, Quantitative imaging of transcription in living Drosophila embryos links polymerase activity to patterning. *Curr. Biol.* **23**, 2140–2145 (2013). doi: 10.1016/j.cub.2013.08.054; pmid: 24139738
81. J. O. Dubuis, R. Samanta, T. Gregor, Accurate measurements of dynamics and reproducibility in small genetic networks. *Mol. Syst. Biol.* **9**, 639 (2013). doi: 10.1038/msb.2012.72; pmid: 23340845
82. M. Haskel-Ittah *et al.*, Self-organized shuttling: Generating sharp dorsoventral polarity in the early *Drosophila* embryo. *Cell* **150**, 1016–1028 (2012). doi: 10.1016/j.cell.2012.06.044; pmid: 22939625
83. D. Ben-Zvi, B. Z. Shilo, A. Fainsod, N. Barkai, Scaling of the BMP activation gradient in *Xenopus* embryos. *Nature* **453**, 1205–1211 (2008). doi: 10.1038/nature07059; pmid: 18580943
84. R. J. Redfield, Is quorum sensing a side effect of diffusion sensing? *Trends Microbiol.* **10**, 365–370 (2002). doi: 10.1016/S0966-842X(02)02400-9; pmid: 12160634
85. D. A. Brock, T. E. Douglas, D. C. Queller, J. E. Strassmann, Primitive agriculture in a social amoeba. *Nature* **469**, 393–396 (2011). doi: 10.1038/nature09668; pmid: 21248849
86. J. Gore, H. Youk, A. van Oudenaarden, Snowdrift game dynamics and facultative cheating in yeast. *Nature* **459**, 253–256 (2009). doi: 10.1038/nature07921; pmid: 19349960
87. S. Basu, Y. Gerchman, C. H. Collins, F. H. Arnold, R. Weiss, A synthetic multicellular system for programmed pattern formation. *Nature* **434**, 1130–1134 (2005). doi: 10.1038/nature03461; pmid: 15858574
88. J. J. Tabor *et al.*, A synthetic genetic edge detection program. *Cell* **137**, 1272–1281 (2009). doi: 10.1016/j.cell.2009.04.048; pmid: 19563759
89. F. K. Balagaddé *et al.*, A synthetic *Escherichia coli* predator–prey ecosystem. *Mol. Syst. Biol.* **4**, 187 (2008). doi: 10.1038/msb.2008.24; pmid: 18414488
90. A. Tamsir, J. J. Tabor, C. A. Voigt, Robust multicellular computing using genetically encoded NOR gates and chemical 'wires'. *Nature* **469**, 212–215 (2011). doi: 10.1038/nature09565; pmid: 21150903
91. S. Regot *et al.*, Distributed biological computation with multicellular engineered networks. *Nature* **469**, 207–211 (2011). doi: 10.1038/nature09679; pmid: 21150900
92. K. E. Galloway, E. Franco, C. D. Smolke, Dynamically reshaping signaling networks to program cell fate via genetic controllers. *Science* **341**, 1235005 (2013). doi: 10.1126/science.1235005; pmid: 23950497
93. J. Bonnet, P. Yin, M. E. Ortiz, P. Subsoontorn, D. Endy, Amplifying genetic logic gates. *Science* **340**, 599–603 (2013). doi: 10.1126/science.1232758; pmid: 23539178
94. C. Liu *et al.*, Sequential establishment of stripe patterns in an expanding cell population. *Science* **334**, 238–241 (2011). doi: 10.1126/science.1209042; pmid: 21998392
95. M. B. Elowitz, W. A. Lim, Build life to understand it. *Nature* **468**, 889–890 (2010). doi: 10.1038/468889a; pmid: 21164460
96. A. Velenich, J. Gore, Synthetic approaches to understanding biological constraints. *Curr. Opin. Chem. Biol.* **16**, 323–328 (2012). doi: 10.1016/j.cbpa.2012.05.199; pmid: 22682889
97. S. Chen, P. Harrigan, B. Heineike, J. Stewart-Ornstein, H. El-Samad, Building robust functionality in synthetic circuits using engineered feedback regulation. *Curr. Opin. Biotechnol.* **24**, 790–796 (2013). doi: 10.1016/j.copbio.2013.02.025; pmid: 23566378
98. N. Perrimon, N. Barkai, The era of systems developmental biology. *Curr. Opin. Genet. Dev.* **21**, 681–683 (2011). doi: 10.1016/j.gde.2011.10.004; pmid: 22079435
99. L. D. Landau, E. M. Lifshitz, *Course of Theoretical Physics. Volume 6: Fluid Mechanics* (Butterworth-Heinemann, Oxford, UK, 1987).
100. K. Francis, B. O. Palsson, Effective intercellular communication distances are determined by the relative time constants for cyto/chemokine secretion and diffusion. *Proc. Natl. Acad. Sci. U.S.A.* **94**, 12258–12262 (1997). doi: 10.1073/pnas.94.23.12258; pmid: 9356436

Acknowledgments: We thank A. Mitchell, S. Itzkovitz, T. Long, M. Thomson, E. Puchner, K. Roybal, L. Morsut, D. Sivak, A. Raj, and J. Gore for insightful discussions. This work was supported by NIH grants R01 GM55040, R01 GM62583, PN2 EY016546, and P50 GM081879, the NSF Synthetic Biology Engineering Research Center (SynBERC), and the Howard Hughes Medical Institute (HHMI) (to W.A.L.). H.Y. is an HHMI Fellow of the Damon Runyon Cancer Research Foundation (DRG-2089-11).

Supplementary Materials

www.sciencemag.org/content/343/6171/1242782/suppl/DC1
Materials and Methods
Supplementary Text
Figs. S1 to S23
Tables S1 to S2
References (*101*, *102*)

4 July 2013; accepted 13 December 2013
10.1126/science.1242782

Classification of Interacting Electronic Topological Insulators in Three Dimensions

Chong Wang,[1] Andrew C. Potter,[1,2] T. Senthil[1]*

A fundamental open problem in condensed-matter physics is how the dichotomy between conventional and topological band insulators is modified in the presence of strong electron interactions. We show that there are six interacting electronic topological insulators that have no noninteracting counterpart. Combined with the previously known band insulators, these produce a total of eight topologically distinct phases. Two of the six interacting topological insulators can be described as Mott insulators in which the electron spins form spin analogs of the topological band insulator. The remaining phases are obtained as combinations of these two "topological paramagnets" and the topological band insulator. We prove that these eight phases form a complete list of all possible interacting topological insulators and discuss their experimental signatures.

The last few years have seen tremendous progress (*1*–*5*) in our understanding of electronic topological insulators (TIs) modeled by band theory. However, there is currently very little understanding of the interplay between strong electron interactions and the phenomenon of topological insulation. Can interaction-dominated phases be in a topological insulating state? Are there new kinds of TIs that might exist in interacting electron systems that have no noninteracting counterpart? These questions acquire particular importance in light of the ongoing experimental search for topological phenomena in strongly correlated materials with strong spin-orbit coupling.

A fascinating minimal generalization of a TI to interacting systems is the so-called symmetry-protected topological (SPT) phases (*6*). In contrast to more exotic generalizations (*7*, *8*), SPT phases have a bulk gap and no intrinsic topological order (*6*) but nevertheless have nontrivial surface states that are robust in the presence of a global internal symmetry.

We focus here on the all-important example of time-reversal symmetric insulating phases of electrons with a conserved global charge [corresponding to a global $U(1)$ symmetry]. Noninteracting insulators with this symmetry in three dimensions (3*D*) belong in one of two distinct categories (*1*–*3*, *9*): topological and trivial band insulators (corresponding to a $\mathbb{Z}_2$ classification).

We show that with interactions, there are six additional nontrivial topological insulating states corresponding to a classification by the group $\mathbb{Z}_2^3$. This group structure means that all these interacting TIs can be obtained as combinations of three "root" states. One of the three root states is the standard topological band insulator. The other two require interactions. We show that they can be understood as Mott insulating states of the electrons where the resulting quantum spins have themselves formed an SPT phase (*10*). In (*11*), such SPT phases of quantum spins were termed "topological paramagnets" and their properties in 3D were elucidated. The three root states and their properties are briefly described in Table 1.

A classic 1D example of a topological paramagnet is the Haldane spin-1 chain, which has nontrivial end states that are protected by symmetry. Substantial progress toward classifying SPT phases in diverse dimensions (*12*–*17*) has been reported. The physical properties of various such bosonic SPT phases in both two (*18*–*21*) and in three dimensions (*11*, *22*–*26*) have also been described in some detail and provide crucial insights for the present work.

Previous progress in understanding interacting electronic SPT phases is restricted to one (*12*, *27*) and two (*19*, *28*–*31*) spatial dimensions. A formal abstract classification for some symmetries (which includes neither charge conservation nor spin-1/2 electrons) in 3D in (*32*) leaves many physical questions unanswered. Here, we use a different strategy: to first constrain the symmetries and statistics of monopole sources of external electromagnetic fields. We then incorporate these constraints into a theory of the surface and determine the resulting allowed distinct states.

We start with the effective Lagrangian L_{eff} for an external electromagnetic field, obtained by integrating out all the matter fields. For any fully gapped insulator in 3D, this takes the following form:

$$L_{\text{eff}} = L_{\text{Max}} + L_\theta \tag{1}$$

Here, L_{Max} is the usual Maxwell term and L_θ is the so-called theta term:

$$L_\theta = \frac{\theta}{4\pi^2}\mathbf{E}\cdot\mathbf{B} \tag{2}$$

where $\mathbf{E}$ and $\mathbf{B}$ are the external electric and magnetic fields respectively. L_θ describes the linear magneto-electric response; for example, an applied magnetic field induces electric polarization: $\mathbf{P} = \frac{e^2\theta}{2\pi h}\mathbf{B}$ (*2*).

Under time reversal, $\theta \to -\theta$; in a fermionic system, the physics is periodic under $\theta \to \theta + 2\pi$. Time-reversal symmetric insulators thus have $\theta = n\pi$ with n an integer. Trivial time-reversal symmetric insulators have $\theta = 0$, whereas free fermion TIs have $\theta = \pi$ (*33*). Any new interacting TI that also has $\theta = \pi$ can be combined with the usual one to produce a TI with $\theta = 0$. Thus, it suffices to restrict attention to the possibility of new TIs that have $\theta = 0$.

Consider the symmetry properties of monopole sources of the external magnetic field. At a nonzero θ, this elementary monopole carries electric charge $\frac{\theta}{2\pi}$ so that it is neutral when $\theta = 0$. Under time reversal, the monopole becomes an anti-monopole as the magnetic field is odd. Formally, if we gauge the global $U(1)$ symmetry to introduce a dynamical monopole field m, it must transform under time reversal T as

$$T^{-1} m T = e^{i\alpha} m^\dagger \tag{3}$$

$$T^{-1} m^\dagger T = e^{-i\alpha} m^\dagger \tag{4}$$

Table 1. Three "root" topological insulators. Listed are their representative symmetry-preserving surface states, and surface signatures when either time-reversal $\mathcal{T}$ or charge conservation is broken on the surface (with topological orders confined). σ_{xy} is the surface electrical Hall conductivity in units of $\frac{e^2}{h}$. κ_{xy} is the surface thermal Hall conductivity and $\kappa_0 = \frac{\pi^2}{3}\frac{k_B^2}{h}T$ (T is the temperature). N is the number of gapless Majorana cones protected by time-reversal symmetry when the surface becomes a superconductor. A combination of these measurements could uniquely determine the TI.

Topological insulator	Representative surface state	$\mathcal{T}$-breaking transport signature	$\mathcal{T}$-invariant gapless superconductor
Free fermion TI	Single Dirac cone	$\sigma_{xy} = \frac{\kappa_{xy}}{\kappa_0} = \pm 1/2$	None
Topological paramagnet I	$\mathbb{Z}_2$ spin liquid with Kramers doublet spinon (e) and vison (m) (denoted $eTmT$)	$\sigma_{xy} = \kappa_{xy} = 0$	$N = 8$ Majorana cones
Topological paramagnet II	$\mathbb{Z}_2$ spin liquid with Fermionic spinon (e) and vison (m) (denoted $e_f m_f$)	$\sigma_{xy} = 0; \frac{\kappa_{xy}}{\kappa_0} = \pm 4$	$N = 8$ Majorana cones

[1]Department of Physics, Massachusetts Institute of Technology, Cambridge, MA 02139, USA. [2]Department of Physics, University of California, Berkeley, CA 94720, USA.

*Corresponding author. E-mail: senthil@mit.edu

However (*23*) [see section 1 in (*34*)], by combining with a gauge transformation, we can set the phase $\alpha = 0$. Physically, this is because the time-reversed partner of a monopole lives in a different topological sector with opposite magnetic charge and hence is not simply a Kramers partner.

This fixes the symmetry properties of the bulk monopole. There are still, in principle, two distinct choices corresponding to the statistics of the monopole: It may be either bosonic or fermionic. We will consider them in turn below. Bosonic monopoles will be shown to allow for the topological paramagnets mentioned above and nothing else. Fermionic monopoles will be shown to not occur in electronic SPT phases.

Consider the surface of any insulator with $\theta = 0$ and a bosonic monopole. To incorporate these constraints, it is convenient to consider a superconducting surface. Then, the suitable degrees of freedom are $\frac{hc}{2e}$ vortices and (neutralized) Bogoliubov quasiparticles (*35*) (spinons), which have mutual semion interactions. In general, we can also allow for coexisting topological order, i.e., other fractionalized quasiparticles, in the surface superconductor (*36*). This gives a description of the surface that is particularly convenient for studying not just the superconducting phase but also some topologically ordered insulating phases.

Imagine tunneling a monopole from the vacuum to the system bulk. Because the monopole is trivial in both regions, the tunneling event—which leaves a $\frac{hc}{e}$ vortex on the surface—also carries no nontrivial quantum number. Hence, the surface dual effective field theory has a bosonic $\frac{hc}{e}$-vortex that carries no nontrivial quantum number. We can therefore proliferate (condense) the $\frac{hc}{e}$-vortex on the surface, which disorders the superconductor and yields an insulator with the full symmetry $U(1) \ltimes \mathcal{T}$ unbroken. However, as is well known from dual-vortex descriptions (*35*, *37*) of spin-charge separation in 2*D*, the resulting state has intrinsic topological order.

In this surface topologically ordered symmetry-preserving insulator, a quasiparticle of charge q sees the $\frac{hc}{e}$-vortex as a $2\pi q/e$ flux. Hence, the $\frac{hc}{e}$-vortex condensate confines all particles with fractional charge and quantizes the charge to $q = ne$ for all the remaining particles in the theory [section 3 in (*34*)]. However, we can always remove integer charge from a particle without changing its topological sector by binding physical electrons. Hence, the particle content of the surface topological order is $\{1, \varepsilon, ...\} \times \{1, c\}$, where only the physical electron c in the theory is charged, and all the nontrivial fractional quasiparticles in $\{1, \varepsilon, ...\}$ are neutral. Because time-reversal operation preserves the $U(1)$ charge, its action has to be closed within the neutral sector $\{1, \varepsilon, ...\}$. We can therefore describe the surface topological order as a purely charge-neutral quantum spin liquid with topological order $\{1, \varepsilon, ...\}$, supplemented by the presence of a trivial electron band insulator, $\{1, c\}$. In particular, any gauge-invariant local operator made out of the topological theory must be neutral (up to binding electrons), but in an electron system, a local neutral object has to be bosonic. Hence, the theory should be viewed as emerging purely from a neutral boson system. This implies that the bulk SPT order should also be attributed to the neutral boson (spin) sector, i.e, it should be a SPT of spins in a Mott insulating phase of the electrons (a topological paramagnet).

The SPT states of neutral bosons with time-reversal symmetry are classified (*11*, *23*, *24*) by $\mathbb{Z}_2^2$, with two fundamental root nontrivial phases. These can both be understood as Mott insulators in topological paramagnet phases. Adding to this the usual $\theta = \pi$ TI captured by band theory, we have three root states corresponding to a $\mathbb{Z}_2^3$ classification (Table 1). To establish that there are no other states, we need to still consider the other possibility left open for the bulk response: a fermionic monopole.

The possibility that the monopole may be fermionic in a system that also has fermionic charges is naïvely consistent with time-reversal symmetry. However, the putative fermionic monopole state does not admit a physical edge to vacuum and, hence, cannot occur in a purely electronic system. To illustrate the difficulty, consider a Bose-Fermi mixture, with both the boson b and the electron c carrying charge-1. Now, put the electron into a trivial band insulator and the boson into a bosonic SPT state. Then, the charge-neutral external monopole source becomes a fermion (*23*, *25*). We may attempt to get rid of the bosons in the bulk by taking their charge gap to infinity (i.e., projecting them out of the Hilbert space). However, they will inevitably make their presence felt at the boundary. Indeed, we show in section 4 of (*34*) by a direct and general argument that fermionic statistics of the monopole in an SPT phase imply the existence of physical charge-1 bosons at the boundary. This is not possible in a purely electronic system.

Having exhausted the possible SPT phases by systematically studying monopole quantum numbers, we now describe phenomena that in principle can be used to completely experimentally identify the various TIs. We consider breaking symmetry at the surface to obtain states with no intrinsic topological order. The results are summarized in Table 1. A different, conceptually powerful characterization in terms of a gapped topologically ordered surface state is decribed in section 2 of (*34*).

First, consider surface states breaking time-reversal symmetry (and having no intrinsic topological order). Of the eight insulating phases we obtained, four have electromagnetic response $\theta = \pi$ (of which one is the topological band insulator) and four have $\theta = 0$ (of which one is the trivial insulator). The θ term in the response means that such a surface state will have quantized electrical Hall conductivity $\frac{e^2}{h}\nu$ with $\nu = \frac{\theta}{2\pi} + n$, where n can be any integer signifying conventional integer quantum Hall effect on the surface. A further distinction is obtained by considering the thermal Hall conductivity κ_{xy} in this surface state. In general, in a quantum Hall state $\kappa_{xy} = \nu_Q \frac{\pi^2}{3}\frac{k_B^2}{h} T$, where k_B and T are Boltzmann's constant and the temperature, respectively. The number ν_Q is a universal property of the quantum Hall state.

Two of the $\theta = \pi$ insulators have $\nu_Q = \nu = 1/2 + n$ (including the topological band insulator), whereas the other two have $\nu_Q = \nu \pm 4$. Similarly, two of the $\theta = 0$ insulators (including the trivial one) have $\nu_Q = \nu = n$, whereas the other two have $\nu_Q = \nu \pm 4$ (*38*). Thus, a combined measurement of electrical and thermal Hall transport when T is broken at the surface can provide a very useful practical (albeit partial) characterization of these distinct TIs.

Next, we consider surface superconducting states (again without topological order) obtained by depositing an *s*-wave superconductor on top. It was noticed in (*39*) that, in such a scenario, the surfaces of the topological paramagnets I and II become identical to that of a topological superconductor [see also section 5 of (*34*) for a simpler derivation]. The corresponding free fermion superconductor has $N = 8 (\mathrm{mod}\ 16)$ gapless Majorana cones at the surface protected by time-reversal symmetry. Thus, inducing superconductivity on the surface of either topological paramagnet I or II leads to eight gapless Majorana cones that are in principle observable through photoemission measurements. Taken together with the T-breaking surface transport, we have a unique fingerprint for each of the eight TIs.

Finally, as a by-product of our considerations, we address a number of other fundamental questions about interacting TIs. For the free fermion systems, the Kramers structure is what allows a TI with $\theta = \pi$. What precise role, beyond free fermion band theory, does the Kramers structure of the electron play in enabling $\theta = \pi$? We show nonperturbatively that any gapped insulator with a $\theta = \pi$ response and no intrinsic topological order necessarily has charge carriers that are Kramers doublet fermions. We also use a similar insight to show the necessity of magnetic ordering when the exotic bulk excitations of the topological Mott insulator phase of (*7*) are confined. Finally, we show that time-reversal breaking electronic systems with global charge $U(1)$ symmetry have no interacting TI phase in three dimensions. These results are described in sections 6 and 7 of (*34*).

Our results set the stage for a number of future studies, including identification of the new TIs in microscopic models and in real materials. Strongly correlated materials with strong spin-orbit interactions are natural platforms for the various TI phases we have described. We expect that our results will inform the many ongoing searches (e.g., in rare-earth insulators or in iridium oxides) for topological phenomena in such materials.

References and Notes

1. M. Z. Hasan, C. L. Kane, *Rev. Mod. Phys.* **82**, 3045–3067 (2010).
2. X.-L. Qi, S.-C. Zhang, *Rev. Mod. Phys.* **83**, 1057–1110 (2011).
3. M. Z. Hasan, J. E. Moore, *Annu. Rev. Condens. Matter Phys.* **2**, 55–78 (2011).

4. A. Kitaev, *AIP Conf. Proc.* **1134**, 22 (2009).
5. S. Ryu, A. P. Schnyder, A. Furusaki, A. W. W. Ludwig, *New J. Phys.* **12**, 065010 (2010).
6. Phases with "intrinsic" topological order (*41*), such as fractional quantum Hall states, have exotic bulk excitations with fractional statistics and are distinct from trivial insulators even in the absence of symmetry.
7. The "topological Mott insulator" (*8*) has exotic gapless bulk excitations.
8. D. Pesin, L. Balents, *Nat. Phys.* **6**, 376–381 (2010).
9. L. Fu, C. L. Kane, E. J. Mele, *Phys. Rev. Lett.* **98**, 106803 (2007).
10. One may attempt to construct SPT phases of fermion system by first forming bosons as composites out of the fermions, which then form a bosonic SPT state. Not all boson SPTs remain distinct states in an electronic system [see section 2 of (*34*)], but those that do can all be viewed as topological paramagnets. The only other electronic root state is the original topological band insulator.
11. A. Vishwanath, T. Senthil, *Phys. Rev. X* **3**, 011016 (2013).
12. L. Fidkowski, A. Kitaev, *Phys. Rev. B* **83**, 075103 (2011).
13. A. M. Turner, F. Pollmann, E. Berg, *Phys. Rev. B* **83**, 075102 (2011).
14. X. Chen, Z.-C. Gu, X.-G. Wen, *Phys. Rev. B* **83**, 035107 (2011).
15. N. Schuch, D. Pérez-Garcia, I. Cirac, *Phys. Rev. B* **84**, 165139 (2011).
16. X. Chen, Z.-C. Gu, Z.-X. Liu, X.-G. Wen, *Science* **338**, 1604–1606 (2012).
17. X. Chen, Z.-C. Gu, Z.-X. Liu, X.-G. Wen, *Phys. Rev. B* **87**, 155114 (2013).
18. M. Levin, Z.-C. Gu, *Phys. Rev. B* **86**, 115109 (2012).
19. Y.-M. Lu, A. Vishwanath, *Phys. Rev. B* **86**, 125119 (2012).
20. T. Senthil, M. Levin, *Phys. Rev. Lett.* **110**, 046801 (2013).
21. Z.-X. Liu, X.-G. Wen, *Phys. Rev. Lett.* **110**, 067205 (2013).
22. C. Xu, T. Senthil, *Phys. Rev. B* **87**, 174412 (2013).
23. C. Wang, T. Senthil, *Phys. Rev. B* **87**, 235122 (2013).
24. F. J. Burnell, Xie Chen, L. Fidkowski, A. Vishwanath, http://arxiv.org/abs/1302.7072.
25. M. A. Metlitski, C. L. Kane, M. P. A. Fisher, *Phys. Rev. B* **88**, 035131 (2013).
26. X. Chen, Y.-M. Lu, A. Vishwanath, http://arxiv.org/abs/1303.4301.
27. E. Tang, X.-G. Wen, *Phys. Rev. Lett.* **109**, 096403 (2012).
28. S. Ryu, S.-C. Zhang, *Phys. Rev. B* **85**, 245132 (2012).
29. X.-L. Qi, *New J. Phys.* **15**, 065002 (2013).
30. H. Yao, S. Ryu, http://arxiv.org/abs/1202.5805.
31. Z.-C. Gu, M. Levin, The effect of interactions on 2D fermionic symmetry-protected topological phases with Z2 symmetry. http://arxiv.org/abs/1304.4569.
32. Z.-C. Gu, X.-G. Wen, http://arxiv.org/abs/1201.2648.
33. X.-L. Qi, T. L. Hughes, S.-C. Zhang, *Phys. Rev. B* **78**, 195424 (2008).
34. Supplementary materials are available on *Science* Online.
35. T. Senthil, M. P. A. Fisher, *Phys. Rev. B* **62**, 7850–7881 (2000).
36. Such a phase with coexistence of topological order and superconductivity was denoted SC* in (*35*).
37. L. Balents, M. P. A. Fisher, C. Nayak, *Phys. Rev. B* **60**, 1654–1667 (1999).
38. A note for experts: $\nu_0 - \nu$ is determined only up to 8, so we have $\nu_0 - \nu = 0 (\mathrm{mod}\ 8)$ for half of the insulators and $\nu_0 - \nu = 4 (\mathrm{mod} 8)$ for the other half.
39. L. Fidkowski, X. Chen, A. Vishwanath, *Phys. Rev. X* **3**, 041016 (2013).
40. M. A. Metlitski, C. L. Kane, Matthew P. A. Fisher, http://arxiv.org/abs/1306.3286.
41. X.-G. Wen, *Quantum Field Theory of Many-Body Systems: From the Origin of Sound to an Origin of Light and Electrons* (Oxford Univ. Press, Oxford, 2004).

Acknowledgments: We thank X. Chen, C.-M. Jian, and particularly A. Vishwanath for useful discussions and B. Swingle and P. A. Lee for comments on our manuscript. This work was supported by U.S. Department of Energy DESC-8739- ER46872 (T.S. and C.W.), by NSF grant DGE-0801525 (A.C.P.), and partially by the Simons Foundation by award no. 229736 (T.S.). T.S. also thanks the hospitality of Harvard University, where this work was partially done. After this work was completed, we learned of (*40*), which also pointed out the relation between Kramers fermion and $\theta = \pi$ TI.

Supplementary Materials

www.sciencemag.org/content/343/6171/629/suppl/DC1
Supplementary Text
References (*42*–*47*)

16 July 2013; accepted 7 January 2014
10.1126/science.1243326

1D-1D Coulomb Drag Signature of a Luttinger Liquid

D. Laroche,[1,2] G. Gervais,[1]* M. P. Lilly,[2] J. L. Reno[2]

One-dimensional (1D) interacting electronic systems exhibit distinct properties when compared to their counterparts in higher dimensions. We report Coulomb drag measurements between vertically integrated quantum wires separated by a barrier only 15 nanometers wide. The temperature dependence of the drag resistance is measured in the true 1D regime where both wires have less than one 1D subband occupied. As a function of temperature, an upturn in the drag resistance is observed below a temperature $T^* \sim 1.6$ kelvin. This crossover in Coulomb drag behavior is consistent with Tomonaga-Luttinger liquid models for the 1D-1D drag between quantum wires.

The exact role played by electron-electron interactions is greatly influenced by the dimensionality of the system. In three dimensions, many interacting fermionic systems are well described by Landau's Fermi liquid (FL) theory, in which "quasiparticles" are the elementary mean-field excitations of the system. In the strict one-dimensional (1D) limit, however, any perturbation in the motion of a single particle will affect all others, so mean-field (FL) theory is not applicable. A Hamiltonian with exact analytic solutions can be constructed for a 1D quantum fluid (*1*–*3*); however, the experimental realization of this so-called Tomonaga Luttinger liquid (TLL) in solid-state materials has proved to be difficult. TLL behavior may have been observed in correlated materials, such as quasi-1D organic conductors and carbon nanotubes (*4*, *5*). In clean semiconductors, where the disorder can be kept at an extremely low level, 1D-1D and 1D-2D tunneling experiments have shown strong evidence for spin-charge separation (*6*, *7*) and charge partition (*8*), as predicted by TLL models of semiconductor quantum wires. Here, we report on a 1D-1D Coulomb drag resistance that, below a crossover temperature T^*, increases with decreasing temperature. This upturn in the drag signal is consistent with predictions from Tomonaga-Luttinger theory of 1D-1D drag (*9*, *10*).

The Coulomb screening by free carriers in semiconductors is weak, and so the interaction between charges is long ranged. When two parallel conducting wires are separated by a small insulating barrier, a current in one wire generates a net charge displacement in the other so that a voltage develops by virtue of electron-electron interactions alone. The resistivity of this so-called Coulomb drag, defined as $R_D \equiv -V_{drag}/I_{drive}$, where I_{drive} is the drive current and V_{drag} is the drag voltage, follows a T^2 dependence at low temperatures in 2D systems (*11*), in accordance with FL theory.

In 1D systems, however, FL theory is expected to break down because of the increased correlations and the Peierls instability. Several theoretical studies have explored the effects of electron-electron interactions on the drag resistance of coupled 1D-1D systems in terms of momentum transfer and TLL theory, with both backscattering (*9*, *12*–*17*) and forward scattering (*10*) contributing to the drag signal. These theories predict a positive drag signal between two wires with negative charge carriers (i.e., $R_D \geq 0$), and models that include contributions from forward scattering predict an upturn in the drag at a temperature T^*. Alternatively, 1D-1D Coulomb drag can also be described in terms of rectification of energy fluctuations (*18*, *19*), where both positive and negative drag signals can occur with a monotonic temperature dependence. In all cases, the strength of the drag signal will be influenced by a variety of parameters such as the 1D electron density, the interwire separation, the number of 1D subbands, and the mismatch in the 1D electron densities.

Most experiments measuring 1D-1D Coulomb drag have been realized in a lateral geometry, where the interwire separation is large ($d \geq$ 200 nm) and where the barrier between the wires is soft (electrostatic) (*20*, *21*). To circumvent the shadowing effect of the gates and so to decrease the interwire distance, a vertical design can be implemented (Fig. 1) in which the two wires are separated by a hard barrier defined by molecular beam epitaxy (*22*). This approach results in two tunable 1D systems, each with their own source-drain contacts (*23*). We investigate the temperature dependence of the drag signal in such a system in a regime where less than one 1D subband is occupied in each wire.

Typical examples of Coulomb drag measurements as a function of gate voltage are presented in Fig. 2, A and B, alongside conductance

[1]Department of Physics, McGill University, Montreal, H3A 2T8 Canada. [2]Center for Integrated Nanotechnologies, Sandia National Laboratories, Albuquerque, NM 87185, USA.

*Corresponding author. E-mail: gervais@physics.mcgill.ca

measurements in both wires for sample 2-L and 2-C, respectively. Steps are observed in the conductance of the wires, but as the wires are nonballistic, the conductance is not exactly quantized in units of $2e^2/h$, where e is the elctronic charge and h is Planck's contant. Such plateau-like features at reduced conductance $G < 2e^2/h \times N$, with N the number of quantum-mechanical channels, have been observed previously (*24*), and it was found that well-defined 1D subbands were still formed in the wires. Three main features are observed in the 1D-1D drag (*22*): (i) peaks in the drag signal concomitant with the opening of 1D subbands, (ii) negative Coulomb drag at low density when the conductance in the drag wire is nearly depleted, and (iii) a negative Coulomb drag occurring between peaks in the drag signal (at a higher subband occupancy). We reproduced these qualitative features of the drag signal in several devices over numerous cooldowns (see, e.g., Fig. 2A); the features are consistent with

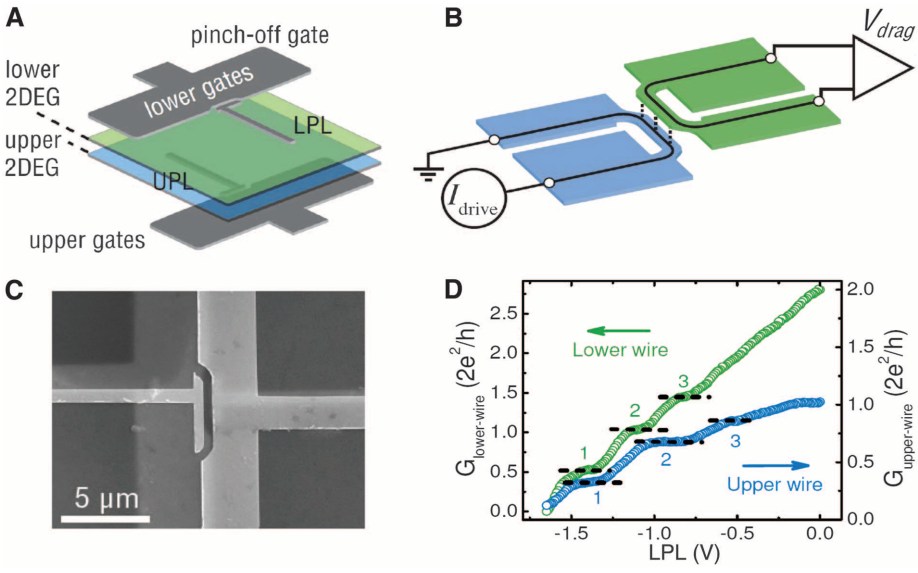

Fig. 1. Design of the vertically integrated quantum wire device. (**A**) Schematic of the active part of the double quantum wires device. The epoxy bond and stop-etch (EBASE) process causes the lower gates and two-dimensional electron gas (2DEG) to be above the upper gates and 2DEG. (**B**) In the interacting region of the device, two independent quantum wires are created, and superimposed vertically, and Coulomb drag measurements are performed. (**C**) Scanning electron micrograph of the device. The lower plunger (LPL) and pinch-off gate are visible on top of the device. The upper plunger (UPL) and pinch-off gate are also visible underneath the lower gates. After processing, the electron density in the upper (lower) layer is 1.1 (1.4) × 10^{11} cm^{-2}. (**D**) Typical conductance data of the lower quantum wire (green curve, left axis) and of the upper quantum wire (blue curve, right axis) from sample 2-C for fixed UPL = −0.23 V. Because each gate is capacitively coupled to both wires, varying the voltage in a single gate affects the conductance of both wires.

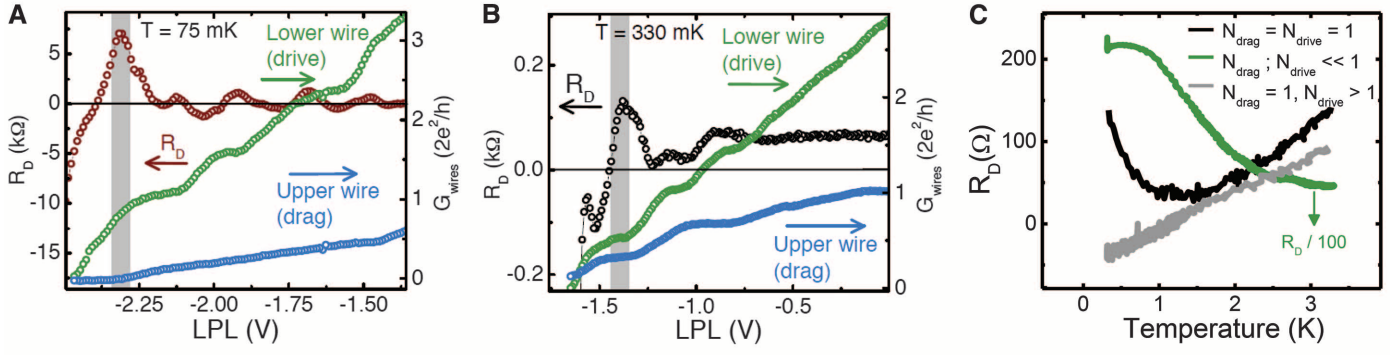

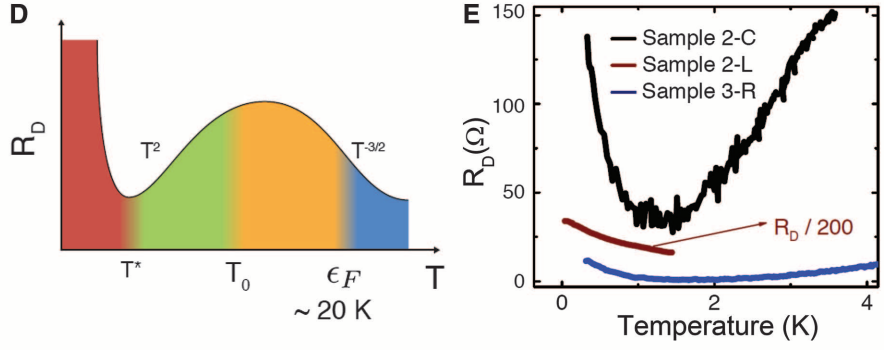

Fig. 2. Coulomb drag measurements in vertically integrated quantum wires. (**A**) Drag resistance at T = 75 mK (red curve, left axis) versus gate voltage, along with the conductance in the upper and lower quantum wires (blue and green curves, respectively; right axis) for sample 2-L for fixed UPL = −0.15 V. (**B**) Drag resistance at T = 330 mK (black curve, left axis) versus gate voltage, along with the conductance in the upper and lower quantum wires (blue and green curves, respectively; right axis) for sample 2-C for fixed UPL = −0.23 V. (**C**) Temperature dependence of the Coulomb drag signal in sample 2-C for quantum wires with a single subband occupied (black curve), less than a full subband occupied (green curve), and slightly more than a single subband occupied (gray curve). The drag signal changes drastically with the wire's subband occupancy, or 1D density. (**D**) Expected behavior of the drag resistance versus temperature based on TLL theory, including corrections from forward scattering. [Cartoon reprinted with permission from (*10*). Copyright (2003) by the American Physical Society.] Here, $T_0 = \hbar v_F d^{-1}$, d is the interwire separation, v_F is the Fermi velocity, and ε_F is the Fermi energy. (**E**) Temperature dependence of the drag signal for samples 2-L, 2-C, and 3-R. For samples 2-L and 2-C, the temperature dependence was taken with no more than one 1D subband occupancy in each wire [highlighted by a gray stripe in (**A**) and (**B**), respectively], whereas the number of 1D subbands occupied in sample 3-R is bounded by $0 < N_{drive} \leq 2$ and $0 \leq N_{drag} \leq 3$. The magnitude of the drag resistance in sample 2-L is divided by 200 for visibility; the large difference in magnitude of the drag signal between devices is likely caused by slight differences in the density mismatch of the pair of wires from sample to sample, as R_D is expected to decrease exponentially with increasing density mismatch.

standard Coulomb drag tests such as frequency and drive-current independence (*22*). The wires' subband occupancy (or 1D density) has a tremendous impact on the general behavior of the temperature dependence of the Coulomb drag signal (Fig. 2C). We now focus on the regime in which only one single 1D subband is occupied in each wire to probe electron-electron interaction in the true 1D regime.

Figure 2E shows our main result, where the temperature dependence of 1D-1D Coulomb drag is shown when only a single 1D subband is present in both wires (*25*). Notably, a transition from a high-temperature regime where 1D Coulomb drag decreases with decreasing temperature, to a low-temperature regime where the Coulomb drag diverges as $T \rightarrow 0$, is observed. This crossover occurs at a temperature in the vicinity of $T^* \simeq 1.6$ K in two samples, whereas the low-temperature behavior of the drag signal has been reproduced in three distinct samples. This upturn in the 1D-1D drag resistance is theoretically expected to occur for identical wires with relatively large interwire separation ($k_F d > 1$, where k_F is the Fermi wave vector) (*10*, *15*). In a 1D system of length L, fluctuations preclude the existence of any long-range order, and instead, the electronic system should be described to lowest order by the TTL theory (*3*) with an effective Hamiltonian $H = H_\rho + H_\sigma$ separating charge (ρ) and spin components (σ) with

$$H_i = (\hbar/2\pi)\int_0^L dz[(\partial_z\phi_i)^2 u_i/K_i + K_i u_i(\partial_z\theta_i)^2]$$

where the phases $\phi(z)_i$ and $\theta(z)_i$ are defined in terms of the second quantized electron field operator and $i = \rho, \sigma$ stands for the charge and the spin components, respectively. Its low-energy modes have dispersion $\varepsilon_i(k) = \hbar u_i k$, where u_i is the velocity of the charge or spin component and is related to the underlying many-body effective interaction parameters K_i. Assuming a system with spin-rotation symmetry for which $K_\sigma = 1$, the Luttinger charge parameter K_ρ tunes the system from attractive interactions ($K_\rho > 1$) to repulsive interactions ($K_\rho < 1$).

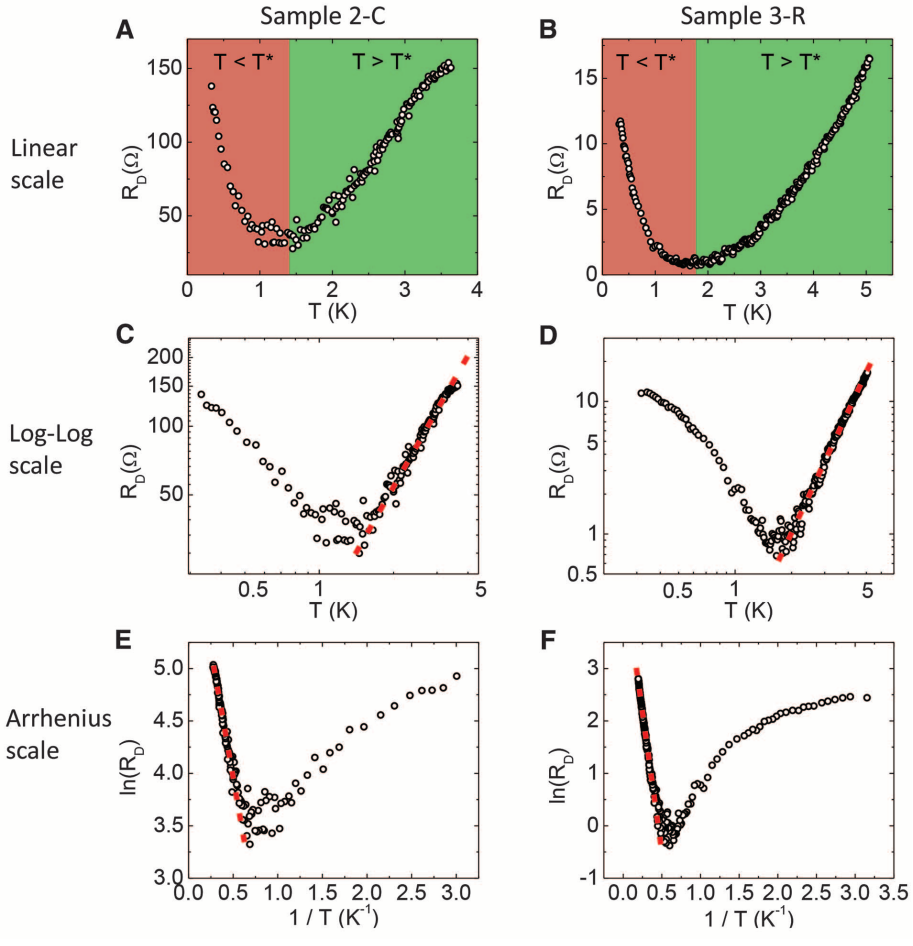

Fig. 3. Upturn in the drag resistance and TLL analysis. Drag resistance as a function of temperature for sample 2-C in a linear scale (**A**), log-log scale (**C**), and Arrhenius scale (**E**) and for sample 3-R in a linear scale (**B**), log-log scale (**D**), and Arrhenius scale (**F**). For both samples, the log-log and the Arrhenius scales appear to be linear at high temperature (red dotted line) and deviate from linearity at low temperature. The analytic form is $R_D \propto aT^\gamma$ for the log-log plot and $R_D \propto be^{-T_1/T}$ for the Arrhenius plot. For sample 2-C, the fits yield, respectively, $a = 14.5 \pm 1.3\ \Omega/K^\gamma$, $\gamma = 1.9 \pm 0.1$, and $b = 600 \pm 60\ \Omega$, $T_1 = 4.8 \pm 0.4$ *K*. For sample 3-R, the fits yield $a = 0.12 \pm 0.01\ \Omega/K^\gamma$, $\gamma = 3.0 \pm 0.1$, and $b = 120 \pm 10\ \Omega$, $T_1 = 10.7 \pm 0.4$ *K*.

Using a TLL model for identical wires (*9*) and accounting for the forward momentum-transfer corrections (*10*), an upturn temperature T^* was calculated to be $T^* \sim \varepsilon_F e^{\frac{-k_F d}{1-K_\rho^-}}$. The many-body Luttinger liquid parameter K_ρ^- here is the relative interaction parameter for antisymmetric charge displacement. It is defined as the difference between small-momentum intra- and interwire interaction parameters (*9*), yielding $K_\rho^- = 1$ for Fermi-liquid like systems. Within this model, backscattering should be the main source of the Coulomb drag signal for $T < T^*$, leading to the formation of interlocked charge density waves in the wires. At temperatures much larger than T^*, forward scattering should dominate, leading to a transition between an exponential dependence to a power-law dependence on temperature provided that $1 < k_F d \sim 2.2$ and $L > L^* \sim \hbar v_F/T^* = 0.5\,\mu$m, as is the case in our samples. Here, L^* is a critical length such that, for $L > L^*$, an exponential increase in drag resistance is expected as $T \rightarrow 0$. Using our best estimate for the electronic density in the wires from $n_{1D} = \sqrt{n_{2D}}$, and an interwire distance $d \simeq 40$ nm (corresponding to the barrier width plus half of both well widths, and the wire alignment uncertainty), we estimate $K_\rho^- \simeq 0.16 \pm 0.02$ ($K_\rho^- \simeq 0.08 \pm 0.02$) from the observed upturn temperatures in the ≃1.3 to 1.5 K (1.7 to 1.9 K) range for the wires in sample 2-C (3-R). Although it is possible for backscattering alone to create such an upturn in the temperature dependence of Coulomb drag between identical wires when $K_\rho^- > 0.5$ (*9*), our wires appear to not be in this regime and also are not exactly matched. For density-mismatched wires, backscattering alone can theoretically induce an upturn in the temperature dependence, regardless of the value of K_ρ^-, given a suitable density imbalance between the wires (*16*). Such an upturn has also been predicted to occur in the spin-incoherent regime of the Luttinger liquid where the spin exchange energy $J = \varepsilon_F e^{-2.9/\sqrt{na_B}}$ is suppressed (*15*), where $a_B = \varepsilon\hbar^2/m^* e^2$ is the Bohr radius, ε is the dielectric constant, and m^* is the electron effective mass. This regime is expected to occur for $na_B \ll 1$ and $T^* < J < T < \varepsilon_F$. In our wires, we estimate $J \sim 150$ mK $< T^*$ and $na_B \sim 0.4$, and therefore it is unlikely that our data fall into this regime.

In Fig. 3, the drag signal is shown versus temperatures for samples 2-C and 3-R on a linear, a log-log, and an Arrhenius plot. At temperatures $T > T^*$, dependence of the drag signal appears consistent with a power law given by $R_D \sim T^\gamma$, with γ given by $\gamma = 1.9 \pm 0.1$ and $\gamma = 3.0 \pm 0.1$ for sample 2-C and 3-R, respectively. This power law is expected from LL models, including corrections from forward scattering with a theoretical exponent $\gamma = 2$. We caution, however, that this model considers Coulomb drag between wires with identical 1D densities. This is unlikely to be the case in our system because the parent

electronic densities in the two 2D layers differ by ~20%, and even a slight density imbalance of less than 2.5% between the wires might have strong effect on the temperature dependence of the drag signal (*10*). Defining a measure of density imbalance $T_1 = k_F\delta(v)$, where $\delta(v)$ is the difference between the Fermi velocities in both wires, the drag resistance is expected to be suppressed as $R_D \propto \frac{T}{T_1}e^{-T_1/T}$, provided $T_1 \geq T \geq 450$ mK. In our samples, the 1D density imbalance can be as large as 12%, giving $T_1 \sim 5.4$ K. Therefore, rather than a simple power-law dependence, the drag signal should behave as a convolution between this exponential decay and a power law, offering a pathway of explanation for the discrepancy between the exponent γ in the two samples. Extracting the experimental value of T_1 from a linear fit of the Arrhenius plots in the high-temperature regime, we obtain $T_1 = 4.8 \pm 0.4\text{K}$ $(T_1 = 10.7 \pm 0.4\text{K})$ for sample 2-C (3-R). These extracted T_1 values are comparable to the calculated $T_1 = 5.4\text{K}$ value from the estimated density imbalance in our wires. Despite this apparent agreement with a TLL model for Coulomb drag, including forward-scattering corrections, we stress that we cannot entirely discriminate between scenarios involving backscattering alone because it also predicts an exponential decrease of R_D with decreasing temperature for $T > T^*$ (*16*). Finite-length effects could also modify the temperature dependence of the drag resistance. These effects are expected to be notable at low temperature and large drive bias voltage, i.e, for $u/\theta = \frac{V_{drive}}{V_L}/\frac{T}{T_L} = eV_{drive}/T \gg 1$, where V_L and T_L are determined from the plasmon frequency of the system (*26*). For our wires, we estimate $u/\theta \sim 1.2/T$, and thus finite-length effects are expected to become negligible for $T > 0.6$ K, and so unlikely to modify the drag signal in the high-temperature regime, as well as the observed upturn.

At temperatures below T^*, the drag signal is expected theoretically to diverge with decreasing T in the $T \rightarrow 0$ limit, with the exact form of the signal depending on the mismatch conditions between the wires (*16*). This increase in drag resistance is a consequence of forward scattering dying out at the lowest temperatures and of algebraic decaying correlations of a TLL. Although we unambiguously observe a drag signal increasing with decreasing temperature down to $T \simeq 75$ mK (Fig. 2E, sample 2-L), the present data do not allow us to extract the exact functional dependence upon temperature of the drag signal below T^*. We also note that mesoscopic fluctuations and finite-size effects (*26*–*28*) could contribute to a nonmonotonic temperature dependence of the drag resistance in the low-temperature regime. Future work is required to further explore the physics of 1D-1D drag in the $T \rightarrow 0$ limit.

As is well known, the conductance of a quantum wire in the ballistic regime only possesses a very weak temperature dependence. On the contrary, the 1D-1D drag signal depends heavily on temperature, as well as on subband occupancy. Our observation of an upturn in the 1D-1D Coulomb drag signal confirms, at least qualitatively, an important prediction of Luttinger liquid models of quantum wires and potentially support theories accounting for the nonlinearity in the electron dispersion. The understanding of physics of interacting 1D systems is still in its infancy, and as such, little is known regarding interacting Luttinger liquids. In the future, it may be possible to study in similarly fabricated devices interacting Luttinger liquids formed of interacting electron and holes, with different effective masses. Such devices might also be used to determine the existence of a nuclear spin helix, a recently predicted novel quantum state of matter (*29*).

References and Notes

1. S. I. Tomonaga, *Prog. Theor. Phys.* **5**, 544–569 (1950).
2. J. M. Luttinger, *J. Math. Phys.* **4**, 1154–1162 (1963).
3. F. D. M. Haldane, *Phys. Rev. Lett.* **47**, 1840–1843 (1981).
4. M. Bockrath *et al.*, *Nature* **397**, 598–601 (1999).
5. H. Ishii *et al.*, *Nature* **426**, 540–544 (2003).
6. O. M. Auslaender *et al.*, *Science* **308**, 88–92 (2005).
7. Y. Jompol *et al.*, *Science* **325**, 597–601 (2009).
8. H. Steinberg *et al.*, *Nat. Phys.* **4**, 116–119 (2008).
9. R. Klesse, A. Stern, *Phys. Rev. B* **62**, 16912–16925 (2000).
10. M. Pustilnik, E. G. Mishchenko, L. I. Glazman, A. V. Andreev, *Phys. Rev. Lett.* **91**, 126805 (2003).
11. T. J. Gramila, J. P. Eisenstein, A. H. MacDonald, L. N. Pfeiffer, K. W. West, *Phys. Rev. Lett.* **66**, 1216–1219 (1991).
12. K. Flensberg, *Phys. Rev. Lett.* **81**, 184–187 (1998).
13. Y. V. Nazarov, D. V. Averin, *Phys. Rev. Lett.* **81**, 653–656 (1998).
14. V. V. Ponomarenko, D. V. Averin, *Phys. Rev. Lett.* **85**, 4928–4931 (2000).
15. G. A. Fiete, K. LeHur, L. Balents, *Phys. Rev. B* **73**, 165104 (2006).
16. T. Fuchs, R. Klesse, A. Stern, *Phys. Rev. B* **71**, 045321 (2005).
17. A. P. Dmitriev, I. V. Gornyi, D. G. Polyakov, *Phys. Rev. B* **86**, 245402 (2012).
18. A. Levchenko, A. Kamenev, *Phys. Rev. Lett.* **101**, 216806 (2008).
19. R. Sánchez, R. López, D. Sánchez, M. Büttiker, *Phys. Rev. Lett.* **104**, 076801 (2010).
20. P. Debray *et al.*, *J. Phys. Condens. Matter* **13**, 3389–3402 (2001).
21. M. Yamamoto, M. Stopa, Y. Tokura, Y. Hirayama, S. Tarucha, *Science* **313**, 204–207 (2006).
22. D. Laroche, G. Gervais, M. P. Lilly, J. L. Reno, *Nat. Nanotechnol.* **6**, 793–797 (2011).
23. Materials and methods are available as supplementary material on *Science* Online.
24. O. M. Auslaender *et al.*, *Phys. Rev. Lett.* **84**, 1764–1767 (2000).
25. Because all devices were fabricated from the same parent heterostructure according to the same fabrication process, we assume that the 1D density of a given wire is roughly similar when tuned at a single 1D subband occupancy.
26. J. Peguiron, C. Bruder, B. Trauzettel, *Phys. Rev. Lett.* **99**, 086404 (2007).
27. N. A. Mortensen, K. Flensberg, A. P. Jauho, *Phys. Rev. Lett.* **86**, 1841–1844 (2001).
28. B. N. Narozhny, I. L. Aleiner, *Phys. Rev. Lett.* **84**, 5383–5386 (2000).
29. B. Braunecker, P. Simon, D. Loss, *Phys. Rev. B* **80**, 165119 (2009).

Acknowledgments: We acknowledge the technical assistance of D. Tibbetts and J. Hedberg and we thank I. Affleck for illuminating discussions. This work has been supported by the Division of Materials Sciences and Engineering, Office of Basic Energy Sciences, U.S. Department of Energy (DOE). This work was performed, in part, at the Center for Integrated Nanotechnologies, a U.S. DOE, Office of Basic Energy Sciences, user facility. Sandia National Laboratories is a multiprogram laboratory managed and operated by Sandia Corporation, a wholly owned subsidiary of Lockheed Martin Corporation, for the U.S. DOE's National Nuclear Security Administration under contract DE-AC04-94AL85000. We also acknowledge the financial support from the Natural Sciences and Engineering Research Council of Canada (NSERC), the Canadian Institute For Advanced Research (CIFAR), and the Fonds Québécois de la Recherche sur la Nature et les Technologies (FQRNT). All data and fabrication recipes presented in this work are available upon request to G.G.

Supplementary Materials

www.sciencemag.org/content/343/6171/631/suppl/DC1
Materials and Methods

2 August 2013; accepted 14 January 2014
Published online 23 January 2014;
10.1126/science.1244152

Elastic Instability of a Crystal Growing on a Curved Surface

Guangnan Meng,[1] Jayson Paulose,[2] David R. Nelson,[1,2] Vinothan N. Manoharan[2,1]*

Although the effects of kinetics on crystal growth are well understood, the role of substrate curvature is not yet established. We studied rigid, two-dimensional colloidal crystals growing on spherical droplets to understand how the elastic stress induced by Gaussian curvature affects the growth pathway. In contrast to crystals grown on flat surfaces or compliant crystals on droplets, these crystals formed branched, ribbon-like domains with large voids and no topological defects. We show that this morphology minimizes the curvature-induced elastic energy. Our results illustrate the effects of curvature on the ubiquitous process of crystallization, with practical implications for nanoscale disorder-order transitions on curved manifolds, including the assembly of viral capsids, phase separation on vesicles, and crystallization of tetrahedra in three dimensions.

Since Nicolaus Steno's pioneering work on crystal growth in the 17th century (*1*), it has been established that the shape of a crystal is a vestige of its growth pathway. Near equilibrium, crystals grown from the melt form compact, faceted structures that minimize interfacial area and energy (*2*, *3*); further from equilibrium, kinetic instabilities (*4*) permit the formation of crystals with much larger interfacial areas, such as dendrites and snowflakes (*5*).

Less well understood is the role of elastic stress, which can arise from the curvature—or lack thereof—of the space in which the crystal grows. For example, two-dimensional (2D) crystals of spheres on a spherical substrate are strained because of the incompatibility of the preferred triangular lattice packing with the Gaussian curvature of the sphere, which bends the lattice lines. Similarly, in Euclidean 3D space, the absence of curvature frustrates the crystallization of tetrahedra (*6*, *7*). Large, compliant crystals can alleviate this curvature-induced elastic stress by incorporating topological defects such as grain boundary scars (*8*, *9*) or pleats (*10*) in the ground state. But for rigid crystals on curved manifolds, for which topological defects such as dislocations have large core energies, the increase of elastic stress with crystal size can also affect the growth process, such that the ground states may be inaccessible. The effects of curvature on the growth pathways are potentially important for analogous processes involving the ordering of identical subunits in curved spaces, such as the assembly of viral capsids (*11*), filament bundle packing (*12*), self-assembly of molecular monolayers (*13*), functionalization of nanoparticles (*14*), and the growth of solid domains on vesicles (*15*–*17*).

We use confocal microscopy to examine the structures of rigid 2D colloidal crystals growing on the inside walls of highly curved spherical water droplets (Fig. 1A). The particles start in the interior of the droplet, but within a short time nearly all of them attach to the droplet surface through depletion attraction (*18*). Once at the interface, the particles attract one another through the same interaction. The short range of the attraction creates a wide coexistence region (fig. S1) between a low-density 2D fluid and a rigid, brittle crystal phase that, unlike the 2D crystals made from repulsive particles (*8*–*10*), cannot easily deform to cover the entire droplet. Because the high interfacial tension of the oil-water interface precludes distortion of the enclosing spherical droplets, and because the depletion attraction confines particles to the droplet interface, the crystals are forced to adopt the curvature of the droplet as they grow.

This constraint has a marked effect on the crystal structures observed at long durations: Whereas 2D crystals grown on flat surfaces are compact, crystals grown on spherical surfaces are composed of slender, single-crystal segments that wrap around the droplets (Fig. 1B). In droplets with higher surface coverage, the thin segments, which we call "ribbons," join together to form branched patterns with voids and gaps between them.

If these crystals were on flat surfaces, the voids could be filled by additional particles. But the parallel transport caused by the Gaussian curvature forces the crystalline directions to be mismatched at the void borders (Fig. 2A), making it impossible to continue the crystal without introducing topological defects. Such defects are, however, absent in our system, in contrast to curved crystals made from repulsive particles (*8*–*10*). As we show by digitally unwrapping the crystal structures (Fig. 2A), each crystal is a single grain, and the only defects are vacancies.

Morphologically, these structures resemble dendritic crystals. We quantify the morphology using two metrics: the circularity, a measure of the perimeter/area ratio, and the fractal dimension, a measure of anisotropy. In contrast to the compact crystals formed on flat surfaces, crystals grown on curved surfaces have much lower circularity (Fig. 2B and fig. S2) and fractal dimension (fig. S3).

In flat space, crystals with such large interfacial energies can only result from kinetic instabilities. Here, however, such instabilities are unlikely to be the cause of the anisotropy, as we do not observe dendritic crystals forming on flat surfaces under growth conditions that are otherwise identical to those of the curved surfaces (Figs. 1B and 2B). Kinetic instabilities occur when the diffusion of particles along the crystal-fluid interface is slow relative to the growth rate. This happens when the domain size is comparable to the Mullins-Sekerka wavelength λ_s (*19*, *20*), which is only weakly affected by curvature (*18*). We estimate λ_s to be at least 100 μm (*18*), much larger than the typical width (25 μm or less) of our curved crystals. We therefore exclude kinetic instabilities as the cause of the morphology. We can also exclude kinetic effects arising from fluid-fluid coexistence, as our system is far from the metastable fluid-fluid critical point (*18*).

The remaining possibility is an elastic instability. A continuum model shows that such an instability occurs because the crystal must compress as it grows larger, owing to the Gaussian curvature of the growth surface. Consider forcing a flat, disc-shaped crystal of diameter a onto a sphere with radius R. For domain sizes comparable to the sphere radius or smaller, the change in circumference—or, equivalently, the elastic strain—scales as $(a/R)^2$, so that the net free energy change, including the elastic energy cost, to form a circular solid domain on a curved surface is

$$\Delta G(a) = \gamma \cdot (\pi a) - \Delta f \cdot \frac{\pi a^2}{4} + \frac{\pi}{24576} Y \cdot \frac{a^6}{R^4} \qquad (1)$$

(*18*, *21*), where Y is the 2D Young's modulus, γ is the line tension, and Δf is the chemical potential

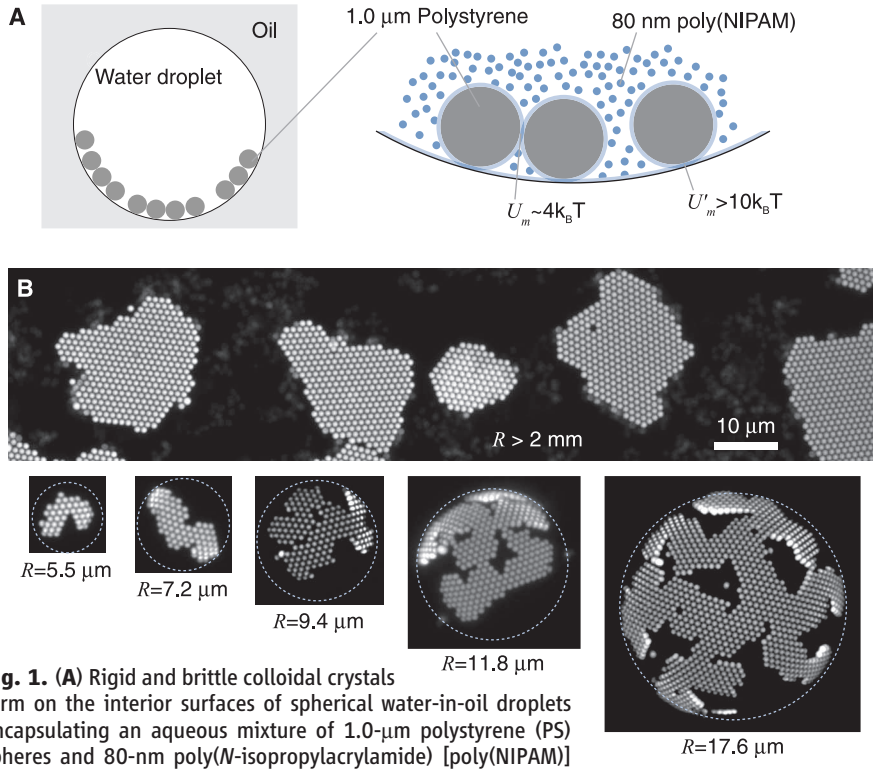

Fig. 1. (**A**) Rigid and brittle colloidal crystals form on the interior surfaces of spherical water-in-oil droplets encapsulating an aqueous mixture of 1.0-μm polystyrene (PS) spheres and 80-nm poly(*N*-isopropylacrylamide) [poly(NIPAM)] particles (*18*). The small particles induce depletion attractions (*30*, *31*) between the PS spheres with a strength of about $4k_BT$, where k_BT is the thermal energy. The depletion force also binds the particles to the interface with a strength of about $10k_BT$ (*18*). The range of attraction in both cases is about 80 nm, or about 8% of the PS sphere diameter. A surfactant barrier prevents the large spheres from breaching the interface (*18*). (**B**) Representative confocal fluorescence micrographs of crystals grown for a few hours on droplets of various curvatures. Radii of curvature R are noted below micrographs; dotted circles show the droplet surfaces, determined by fitting a spherical model to the particle positions. We use a very large droplet (R > 2 mm) to approximate a flat surface.

[1]Department of Physics, Harvard University, Cambridge, MA 02138, USA. [2]School of Engineering and Applied Sciences, Harvard University, Cambridge, MA 02138, USA.

*Corresponding author. E-mail: vnm@seas.harvard.edu

difference between the coexisting solid and fluid phases. On flat substrates ($R \to \infty$), the elastic energy vanishes, and crystallites larger than a critical nucleus size $a_c = 2\gamma/\Delta f$ can grow isotropically without limit (dashed line in Fig. 3A). But on curved substrates, the elastic energy increases with domain size a, as measured along a geodesic. Isotropic growth becomes unfavorable beyond a critical size $a^* \sim (\Delta f/Y)^{1/4}R$ (solid line in Fig. 3A). This restriction on isotropic growth is the origin of the elastic instability (*22*). The predictions of this simple model are consistent with our measurements of the maximum isotropic domain size, which scales linearly with R (fig. S4A).

Although the crystal could grow larger by incorporating topological defects (*23*, *24*), the short range of the attraction in our system makes such defects energetically costly. Geometry dictates that some interparticle distances near a five-fold or seven-fold defect are larger than the interaction range, effectively breaking the corresponding bonds. Incorporating a five-fold defect, for example, breaks five bonds. This explains the observations in Fig. 2: The stiffness of the potential favors tearing rather than stretching to accommodate stress.

Thus, if the crystal is to continue to grow, it must do so by increasing its perimeter/area ratio. It must grow anisotropically. More specifically, the crystal should transition from a disk to a ribbon, or multiple ribbons, when its size exceeds a^*. This behavior arises because the elastic energy of a ribbon scales with the fifth power of its width w but only linearly with its length l (*21*, *25*). The net free energy change of forming a ribbon-like crystalline domain is

$$\Delta G(w,l) \approx \gamma \cdot 2\,(l+w) - \Delta f \cdot lw + \frac{9}{5120} Y \cdot \frac{w^5 l}{R^4} \quad (2)$$

This energy function is shown as a landscape in Fig. 3B. By maintaining a constant width (set by the curvature in the later stages of growth), the crystallite can grow to arbitrarily large lengths, limited only by the number of particles and the area available for growth. The anisotropic growth allows the crystal to avoid the size restriction imposed by elastic energy at the modest cost of a larger interfacial energy.

To test this model, we measured the dynamics of growth in single domains (Fig. 4A and movie S1). We find that a crystal first grows isotropically until it reaches a critical size, then grows anisotropically, increasing its length while maintaining a much smaller but constant width. Examination of the final crystal shapes for several hundred droplets (Fig. 4B and fig. S4B) shows that the length of the domains can grow to several times the droplet radius, while the width is restricted to a fraction of the radius of curvature. The near-constant value of w/R seen in Fig. 4 qualitatively agrees with our model, which predicts that the elastic stress limits the width to $w \propto R$, whereas l can increase without penalty. By fitting the model to the observed domain widths, we extract an effective spring constant for the interparticle interaction that is consistent with theoretical and independent experimental estimates (*18*), again lending support to the model.

The observation of the final, branched crystal shapes is also consistent with our physical picture. A domain can extend its length along any of the three crystallographic axes. If it changes its growth axis, it will bend by ±60°, and if it grows in two directions at once, a branch forms. All of these growth patterns are roughly equivalent energetically, as long as the width of the growing section remains less than the critical width dictated by elasticity and curvature. Hence, we expect to see, and do see, changes in direction and branches in the domains. The branches can also arise from the merger of crystallites that have nucleated independently. The branched structures resulting from such mergers maintain their curvature-dependent width w in each section (see movies S2 to S4). The voids in these structures persist because the crystal directions are mismatched in adjacent sections of the crystal. In contrast, crystallites on flat substrates have no width restriction or curvature-induced mismatch and can therefore easily merge into isotropic shapes.

We conclude that anisotropic crystal growth, usually a result of a kinetic instability, can also occur by slow growth under the geometric constraint of Gaussian curvature. Our results illustrate a generic route for the growth of rigid, defect-free structures in curved spaces. This route may be

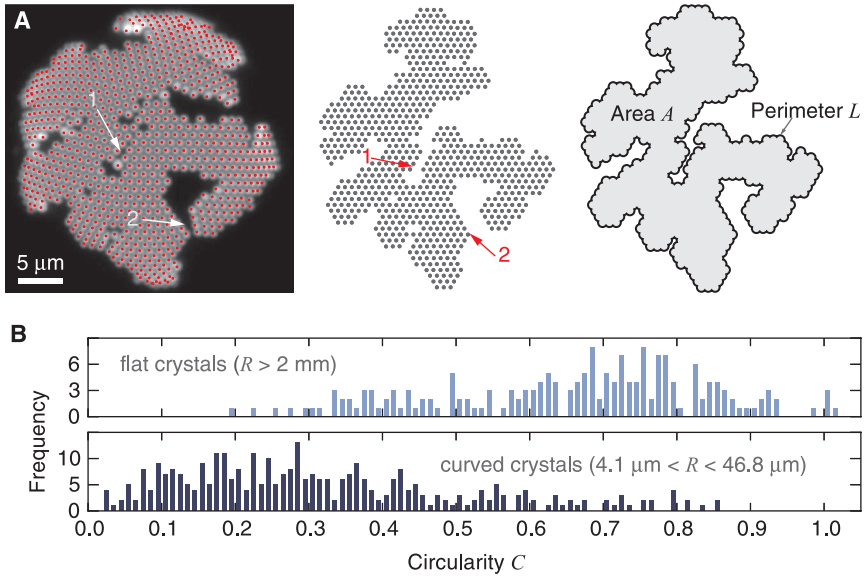

Fig. 2. (**A**) From the 3D positions of the particles (red dots), we digitally flatten the curved crystals (*18*), showing that they are single grains with no topological defects. Arrow 1 shows an apparent grain boundary that is actually a row of vacancies; arrow 2 shows a void that arises because the curvature bends the lattice vectors. (**B**) Histograms show that the values of the dimensionless circularity $C = 4\pi A/L^2$, measured using morphological image operations (*18*), are in general much lower for crystals grown on curved surfaces (dark blue, 335 domains) than for crystals grown on nearly flat surfaces (light blue, 187 domains).

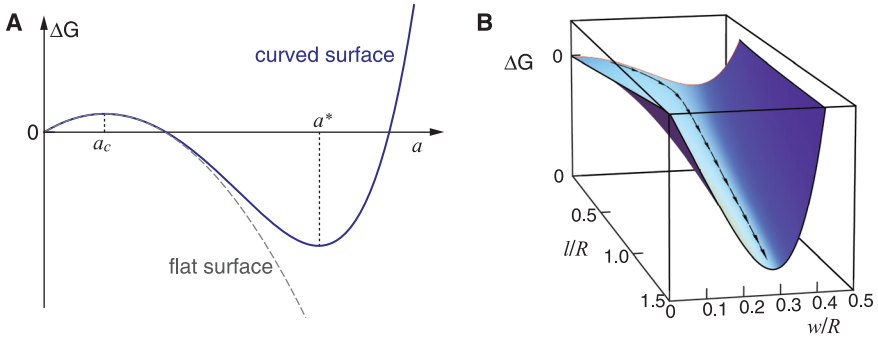

Fig. 3. A continuum model shows that the elastic stress restricts isotropic domain growth to a maximum size a^*. The crystal can escape this restriction by growing anisotropically. (**A**) Schematic free energy $\Delta G(a)$ for isotropic growth of a circular crystal of size a on a flat surface (gray dashed line) and a surface with Gaussian curvature (blue solid line). (**B**) Schematic free energy $\Delta G(w,l)$ of formation of a ribbon-shaped domain with width w and length l. The (overdamped) crystal growth follows the gradient flow (arrows) on the energy landscape.

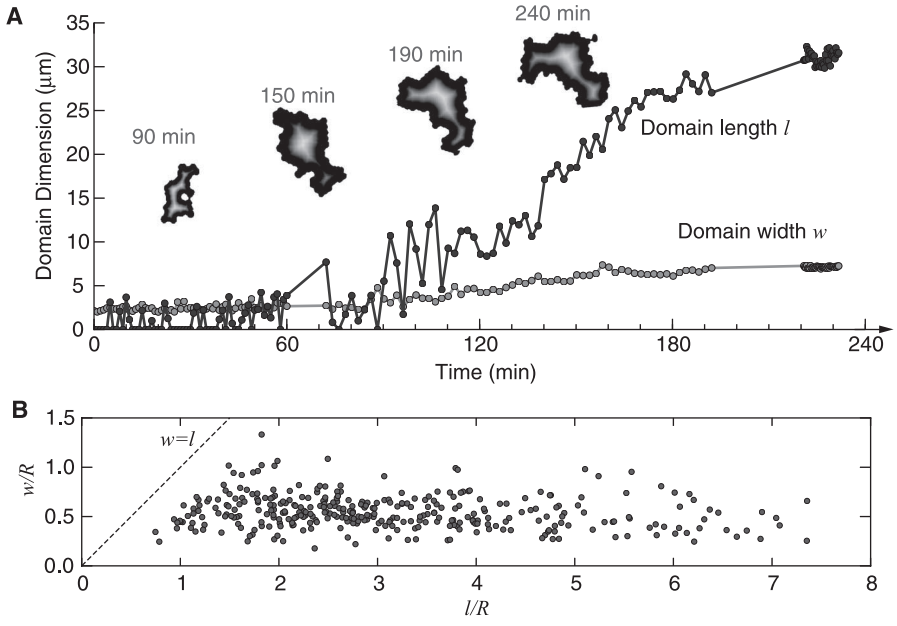

Fig. 4. (**A**) Measurements of domain length *l* (black) and width *w* (gray) as a function of time for a droplet with $R = 18$ μm (*18*). Images of domain morphologies at various times are shown at top (see also movie S1). The transition from isotropic to anisotropic growth occurs at about 100 min. (**B**) Distribution of *l* and *w*, both normalized to the radius of curvature *R*, for curved crystals. The dashed line marks the isotropic regime where $w = l$. *w*/*R* is roughly constant, in agreement with the model.

particularly relevant to nanoscale substrates, where the curvature is appreciable on molecular length scales. For example, solid domains consisting of narrow stripes radiating outward from a circular core have been observed in diverse systems, such as phases on lipid vesicles (*17*) and metal coatings on nanoparticles (*14*). Our analysis suggests that the width of the stripes and the core size should be determined by the interplay among curvature, elasticity, and bulk energy. A similar interplay may affect the assembly pathways of viral capsids. Recent in vitro experiments (*26*) show that capsids can assemble following a two-step mechanism analogous to our crystallization process: The capsid proteins first attach to a substrate (an RNA molecule) and then bind together into an ordered shell. The intermediate states of this process—long a subject of speculation (*11*)—might contain voids that, like those in our curved crystals, help the capsids avoid excess elastic stress (*27*, *28*).

Similar rules may govern other crystallization and packing problems where global geometry is incompatible with local lattice packing. For example, crystallization of tetrahedra is frustrated in flat (Euclidean) 3D space (*6*). However, logs and helices of tetrahedra are prevalent in first-order phase transitions of tetrahedra from disordered to dense quasicrystalline phases (*7*). The existence of these structures, which were first described by Bernal (*29*), may reflect a similar physical principle, in which growth along one dimension allows a crystal to escape the restrictions of geometrical frustration.

References and Notes

1. N. Steno, *The Prodromus of Nicolaus Steno's Dissertation Concerning a Solid Body Enclosed by Process of Nature Within a Solid; an English Version with an Introduction and Explanatory Notes by John Garrett Winter* (Macmillan, London, 1916).
2. I. Sunagawa, *Crystals: Growth, Morphology, & Perfection* (Cambridge Univ. Press, Cambridge, 2005).
3. A. T. Skjeltorp, *Phys. Rev. Lett.* **58**, 1444–1447 (1987).
4. J. S. Langer, *Rev. Mod. Phys.* **52**, 1–28 (1980).
5. K. G. Libbrecht, *Rep. Prog. Phys.* **68**, 855–895 (2005).
6. D. Nelson, F. Spaepen, *Solid State Phys.* **42**, 1 (1989).
7. A. Haji-Akbari *et al.*, *Nature* **462**, 773–777 (2009).
8. A. R. Bausch *et al.*, *Science* **299**, 1716–1718 (2003).
9. P. Lipowsky, M. J. Bowick, J. H. Meinke, D. R. Nelson, A. R. Bausch, *Nat. Mater.* **4**, 407–411 (2005).
10. W. T. M. Irvine, V. Vitelli, P. M. Chaikin, *Nature* **468**, 947–951 (2010).
11. W. H. Roos, R. Bruinsma, G. J. L. Wuite, *Nat. Phys.* **6**, 733–743 (2010).
12. I. R. Bruss, G. M. Grason, *Proc. Natl. Acad. Sci. U.S.A.* **109**, 10781–10786 (2012).
13. G. A. DeVries *et al.*, *Science* **315**, 358–361 (2007).
14. H. Bao, W. Peukert, R. Klupp Taylor, *Adv. Mater.* **23**, 2644–2649 (2011).
15. R. Lipowsky, *Nature* **349**, 475–481 (1991).
16. J. Korlach, P. Schwille, W. W. Webb, G. W. Feigenson, *Proc. Natl. Acad. Sci. U.S.A.* **96**, 8461–8466 (1999).
17. A. Bandekar, S. Sofou, *Langmuir* **28**, 4113–4122 (2012).
18. See supplementary materials on *Science* Online.
19. W. W. Mullins, R. F. Sekerka, *J. Appl. Phys.* **34**, 323 (1963).
20. W. W. Mullins, R. F. Sekerka, *J. Appl. Phys.* **35**, 444 (1964).
21. S. Schneider, G. Gompper, *Europhys. Lett.* **70**, 136–142 (2005).
22. A. Y. Morozov, R. F. Bruinsma, *Phys. Rev. E* **81**, 041925 (2010).
23. Y. Chushak, A. Travesset, *Europhys. Lett.* **72**, 767–773 (2005).
24. D. R. Nelson, *Defects and Geometry in Condensed Matter Physics* (Cambridge Univ. Press, Cambridge, 2002).
25. C. Majidi, R. S. Fearing, *Proc. R. Soc. London Ser. A* **464**, 1309 (2008).
26. R. F. Garmann, M. Comas-Garcia, A. Gopal, C. M. Knobler, W. M. Gelbart, *J. Mol. Biol.* 10.1016/j.jmb.2013.10.017 (2013).
27. W. S. Klug, W. H. Roos, G. J. Wuite, *Phys. Rev. Lett.* **109**, 168104 (2012).
28. A. Luque, D. Reguera, A. Morozov, J. Rudnick, R. Bruinsma, *J. Chem. Phys.* **136**, 184507 (2012).
29. J. D. Bernal, *Proc. R. Soc. London Ser. A* **280**, 299–322 (1964).
30. S. Asakura, F. Oosawa, *J. Chem. Phys.* **22**, 1255 (1954).
31. R. Roth, B. Götzelmann, S. Dietrich, *Phys. Rev. Lett.* **83**, 448–451 (1999).

Acknowledgments: We thank F. Spaepen for helpful discussions. Supported by the Harvard Materials Research Science and Engineering Center through NSF grant DMR-0820484.

Supplementary Materials

www.sciencemag.org/content/343/6171/634/suppl/DC1
Materials and Methods
Figs. S1 to S4
References (*32*–*58*)
Movies S1 to S4

19 August 2013; accepted 7 January 2014
10.1126/science.1244827

Rapid Soil Production and Weathering in the Southern Alps, New Zealand

Isaac J. Larsen,[1]*† Peter C. Almond,[2] Andre Eger,[2]‡ John O. Stone,[1] David R. Montgomery,[1] Brendon Malcolm[2]

Evaluating conflicting theories about the influence of mountains on carbon dioxide cycling and climate requires understanding weathering fluxes from tectonically uplifting landscapes. The lack of soil production and weathering rate measurements in Earth's most rapidly uplifting mountains has made it difficult to determine whether weathering rates increase or decline in response to rapid erosion. Beryllium-10 concentrations in soils from the western Southern Alps, New Zealand, demonstrate that soil is produced from bedrock more rapidly than previously recognized, at rates up to 2.5 millimeters per year. Weathering intensity data further indicate that soil chemical denudation rates increase proportionally with erosion rates. These high weathering rates support the view that mountains play a key role in global-scale chemical weathering and thus have potentially important implications for the global carbon cycle.

Plate tectonics has long been thought to influence climate through links among rock uplift, relief generation, erosion, silicate weathering, and CO_2 cycling (*1*, *2*). Determining the form of the functional relationship between hillslope erosion and weathering rates is critical for understanding how or if mountains influence global weathering budgets and climate

(*3*–*6*). Current models predict that soil weathering is supply-limited and dependent on the supply of fresh minerals when erosion rates are low, but that weathering becomes increasingly kinetically limited as erosion rates increase, due to reduced mineral residence times in the soil (*3*–*5*). However, there are few observational constraints on soil production and soil weathering rates in Earth's most rapidly uplifting mountains, and it is unclear whether chemical weathering rates continue to increase or decline as erosion rates increase beyond about 100 metric tons km^{-2} $year^{-1}$ (~0.04 mm $year^{-1}$) (*6*).

We determined soil production and catchment-scale denudation rates by measuring concentrations of in situ–produced ^{10}Be in soil and sediment, respectively, and inferred chemical denudation rates using Zr mass balance (*7*) in the western Southern Alps of New Zealand (Fig. 1). The study sites are located east of the Alpine Fault, where rock uplift, exhumation, and erosion rates reach 10 mm $year^{-1}$ (*8*–*11*) and watershed-scale weathering fluxes are extremely high (*12*). Mean annual precipitation exceeds 10 m $year^{-1}$, supporting dense temperate montane rainforest and subalpine shrub ecosystems that grow on <1-m-thick soils formed from highly fractured schist (*13*–*15*).

Soil production rates on ridgetops range from 0.1 to 2.5 mm $year^{-1}$ and decline exponentially with increasing soil thickness at two of the three sites with a sufficient number of samples ($n \geq 5$) to define a regression relationship (Fig. 2A). The form of these exponentially declining soil production functions is consistent with those determined for other landscapes (*16*). However, comparison with data compiled from sites worldwide indicates that soil production rates in the western Southern Alps reach levels more than an order of magnitude greater than measured elsewhere (Fig. 2B), demonstrating that soil production can play a far greater role in mountain denudation than previously documented.

Chemical depletion fractions increase with soil thickness (Fig. 2C) and decline with increasing soil production rates (Fig. 2D), which is consistent with declining soil residence times that models predict at high denudation rates (*3*–*5*) and measurements from the San Gabriel Mountains (*17*). However, the high P values preclude concluding that the regression slopes are significantly different from zero. Thus, weathering may be supply-limited at the very high denudation rates we observe. Regardless of whether the chemical denudation data conform to supply- or kinetically limited weathering, the chemical denudation rates inferred from the Zr and ^{10}Be data increase linearly with physical erosion rates (Fig. 2E). Comparison of our soil chemical denudation rates against a compilation of worldwide data indicates that soil chemical denudation rates in the western Southern Alps are the highest values yet determined, and the power-law scaling exponent of ~1.0 indicates that chemical denudation rates increase linearly as erosion rates increase by nearly three orders of magnitude (Fig. 3A). The relationship between soil chemical denudation and physical denudation rates observed in the western Southern Alps is consistent with data from more slowly eroding landscapes (*18*) and extends the range of soil production rates over which weathering and denudation rates increase in proportion to one another to much higher values than previously recognized. If the relationship becomes nonlinear or reverses to an inverse correlation, as predicted by several models (*3*–*5*), it does so at rates higher than we observe in the western Southern Alps. Hence, our findings do not support the view that mountains are inefficient sites for weathering because of "speed limits" to soil production and chemical denudation (*19*); values from the western Southern Alps break the proposed speed limits for both soil production and soil weathering.

^{10}Be concentrations in sediment indicate that total denudation rates for watersheds in the western Southern Alps range from 1 to 9 mm $year^{-1}$ (Fig. 1). Small catchments that drain areas within 1 to 2 km of the Alpine Fault have the lowest denudation rates of 1 to 2 mm $year^{-1}$. Larger catchments and subcatchments that drain areas farther to the east of the Alpine Fault denude at rates of 4 to 12 mm $year^{-1}$. The spatial pattern of decreasing watershed-scale denudation toward the Alpine Fault is consistent with crustal velocity fields predicted by simple shear deformation (*20*) and vertical deformation measured by global positioning systems (*21*).

The maximum soil production rate that we measured in the western Southern Alps equals or exceeds denudation rates for the more slowly eroding watersheds. However, for a given catchment, soil production rates are a fraction of the catchment-averaged denudation rates. Hillslopes below the tree line in the western Southern Alps have very little bedrock exposure, even though soil production rates are lower than catchment-averaged denudation rates. The landscape maintains a soil mantle because the return interval for landslides, which must account for the balance of catchment-averaged denudation not attributable to soil production (*10*), is long enough at any point on the landscape that soils develop between failures (*22*). The soil-mantled hillslopes and high soil production rates in the western Southern Alps indicate that, contrary to previous suggestions (*23*), hillslopes are not necessarily stripped of soil at high uplift rates. Although strong evidence for a transition from soil-mantled to bedrock hillslopes exists for the San Gabriel Mountains (*22*, *24*), mean annual precipitation in the San Gabriel Mountains is an order of magnitude lower than in the western Southern Alps. We suspect that the emergence of bare bedrock hillslopes in tectonically active landscapes is modulated in large part by climate, with soil production able to proceed at higher rates in wetter, and thus more vegetated, regions, such as our study area.

The high mean annual precipitation promotes rapid leaching (*14*) and supports high annual vegetation productivity (*25*), which we suggest, along with pervasively fractured bedrock, contribute to the high soil production rates that we observe. The primarily biotic driver of soil production is vegetation, because burrowing mammals, which contribute to soil production in other landscapes (*16*), are not endemic to New Zealand. Coarse and fine roots readily penetrate bedrock by exploiting foliation planes and fractures generated by tectonics (*15*) and erosional unloading (fig. S1). Root expansion in fractures, especially

[1]Department of Earth and Space Sciences and Quaternary Research Center, University of Washington, Seattle, WA 98195–1310, USA. [2]Department of Soil and Physical Sciences, Lincoln University, Christchurch 7647 New Zealand.

*Corresponding author. E-mail: larseni@caltech.edu
†Present address: Division of Geological and Planetary Sciences, California Institute of Technology, Pasadena, USA.
‡Present address: Institute of Earth and Environmental Science, University of Potsdam, Germany.

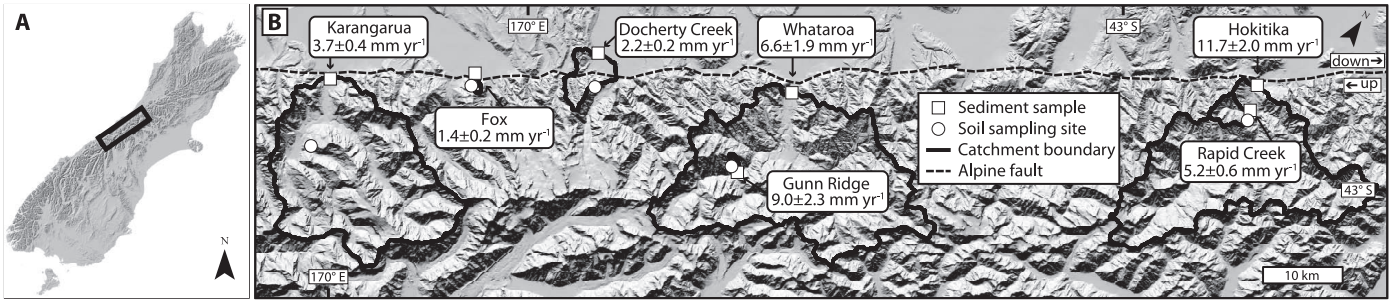

Fig. 1. Study sites. Location of the field area on New Zealand's South Island (**A**), sample locations, and watershed scale denudation rates (±1 SE) (**B**).

foliation planes within a few cm of the soil-bedrock interface, likely plays a key role in converting rock to soil, both by physically breaking rock and by enhancing chemical weathering through organic acid production and increased subsurface CO_2 concentrations.

The high soil production rates in the western Southern Alps are consistent with estimated soil residence times of only a few centuries (*14*) and rapid weathering and leaching (*26*) documented at other sites on the South Island's west coast. Soil production rates also increase with watershed-scale denudation rates, as observed in more slowly eroding landscapes (*22*). Soil production rates have not been measured in other mountains undergoing uplift rates comparable to those in the western Southern Alps. However, in the Taiwan orogen, hillslopes are soil-mantled even though landslides—which primarily mobilize soil—erode the landscape at rates >2 mm $year^{-1}$ (*27*). Similarly, hillslopes in the Tsangpo Gorge of the eastern Himalaya are soil mantled, despite erosion rates >4 mm $year^{-1}$ (*28*), suggesting that soil production rates in other landscapes are also sufficiently rapid that hillslopes are not stripped to bedrock, despite high rates of rock uplift and erosion.

Global river solute and sediment yield data (*29*) demonstrate that catchment-averaged chemical denudation rates span a similar range of values as global soil chemical denudation rates, although the power-law scaling exponent less than unity differs from the soils data (Fig. 3B). River solute data indicate that catchment-scale chemical denudation rates in the western Southern Alps are of the same magnitude as soil chemical denudation rates. However, chemical denudation accounts for <5% of catchment-scale denudation (*12*, *30*). Similarly, the mean soil chemical denudation rates that we determined are 1 to 7% of the ^{10}Be-based total denudation rates determined for each watershed, whereas mean chemical denudation is 16 to 32% of the soil production rate at each of the ridgetop sites. The differing ratio of chemical to total denudation rates observed for soils versus catchments is likely due to a high proportion of unweathered rock in the debris delivered to rivers by landslides. A more detailed geochemical budget is required to assess weathering fluxes from deep bedrock (*6*) and landslide-affected terrain (*31*), but if soil dynamics at the sites we sampled are at least broadly representative of those occurring throughout the landscape, our results suggest that soil weathering may be an important contributor to the high weathering flux in the western Southern Alps (*12*, *30*, *32*).

The high denudation rates in the western Southern Alps are consistent with global fluxes determined using river load data, which demonstrate that young, wet mountains make up only 14% of the ocean-draining land area but account for 62% of sediment, 38% of total dissolved solid, and 60% of dissolved silica delivered to Earth's oceans (*29*). Hillslopes in rapidly uplifting mountains appear to bypass the hypothesized weathering speed limit because high rates of orographic precipitation support ecosystems that physically break up rock and promote weathering and leaching, allowing rapid soil production to contribute to the high orogen-scale weathering fluxes.

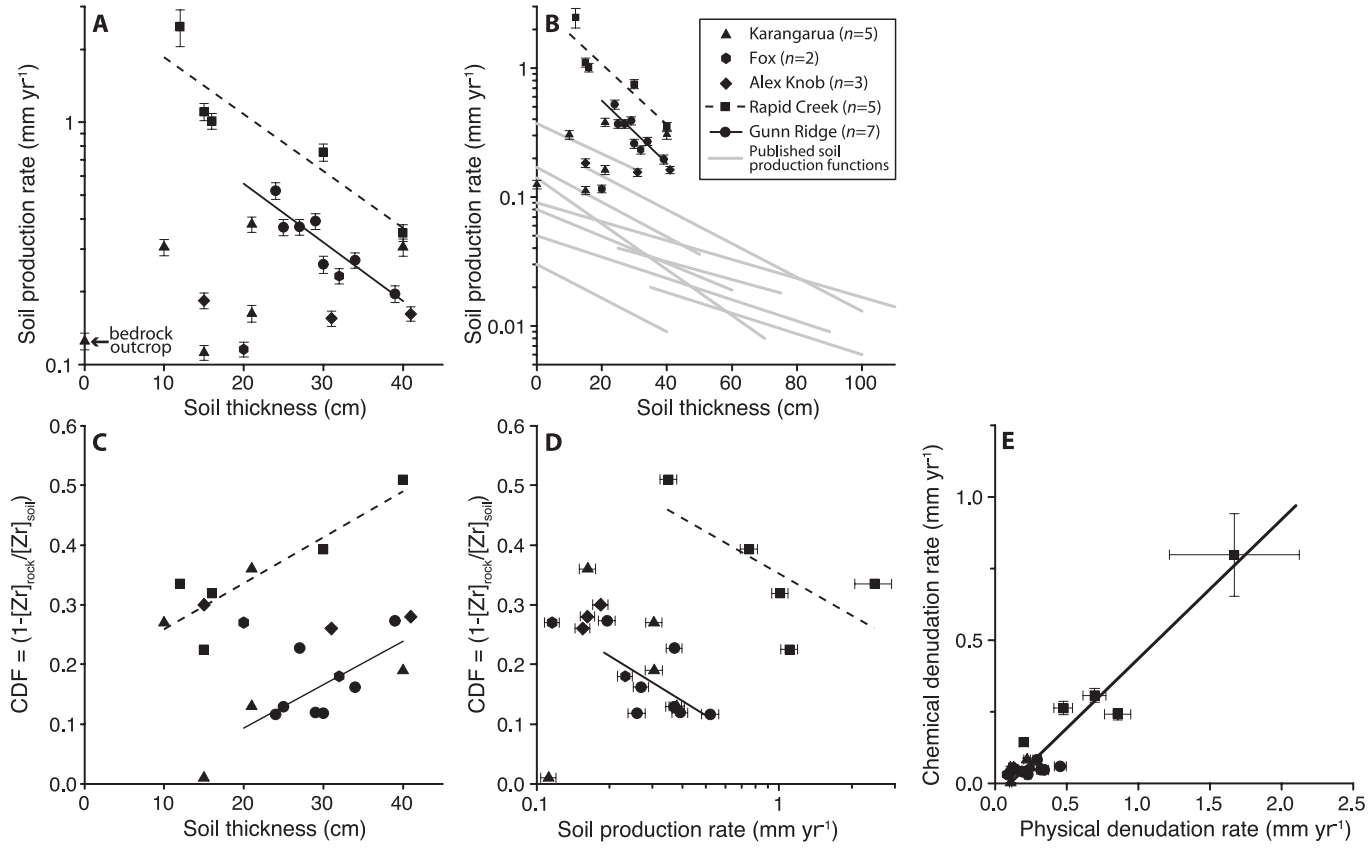

Fig. 2. Soil production rates, chemical depletion data, and chemical versus physical denudation rates. (**A**) Soil production rate versus soil thickness for the western Southern Alps. Soil production rates decline exponentially with increasing soil thickness at the Gunn Ridge and Rapid Creek sites, and the respective exponential regression fits are $y = 1.71(+0.71/-0.50)e^{-0.056(\pm0.012)x}$, $R^2 = 0.82$, $P = 0.005$ and $y = 3.18(+1.33/-0.94)e^{-0.054(\pm0.015)x}$, $R^2 = 0.83$, $P = 0.03$. (**B**) Western Southern Alps soil production rates and soil production functions plotted with a worldwide compilation of soil production functions; see supplementary materials for data sources. (**C**) Chemical depletion fraction (CDF) versus soil thickness for the western Southern Alps. CDF values increase with soil thickness as $y = 0.0073(\pm0.0040)x - 0.052(\pm0.12)$, $R^2 = 0.39$, $P = 0.13$ for Gunn Ridge and $y = 0.0077(\pm0.0023)x + 0.18(\pm0.057)$, $R^2 = 0.79$, $P = 0.04$ for Rapid Creek. (**D**) CDF versus soil production rates for the western Southern Alps. CDF values decline as soil production rates increase, as $y = -0.11(\pm0.070)\ln(x)+0.036(\pm0.081)$, $R^2 = 0.35$, $P = 0.16$ for Gunn Ridge and $y = -0.10(\pm0.062)\ln(x)+0.35(\pm0.039)$, $R^2 = 0.48$, $P = 0.20$ for Rapid Creek. (**E**) Chemical denudation rate versus physical denudation rate for the western Southern Alps. Chemical denudation rates increase linearly as physical denudation rates increase. The linear reduced major axis (RMA) regression fit shown by the line is $y = 0.49(\pm0.036)x-0.052(\pm0.017)$, $R^2 = 0.89$, $P < 0.001$. Error bars and parentheses indicate ±1 SE; P values based on t statistics.

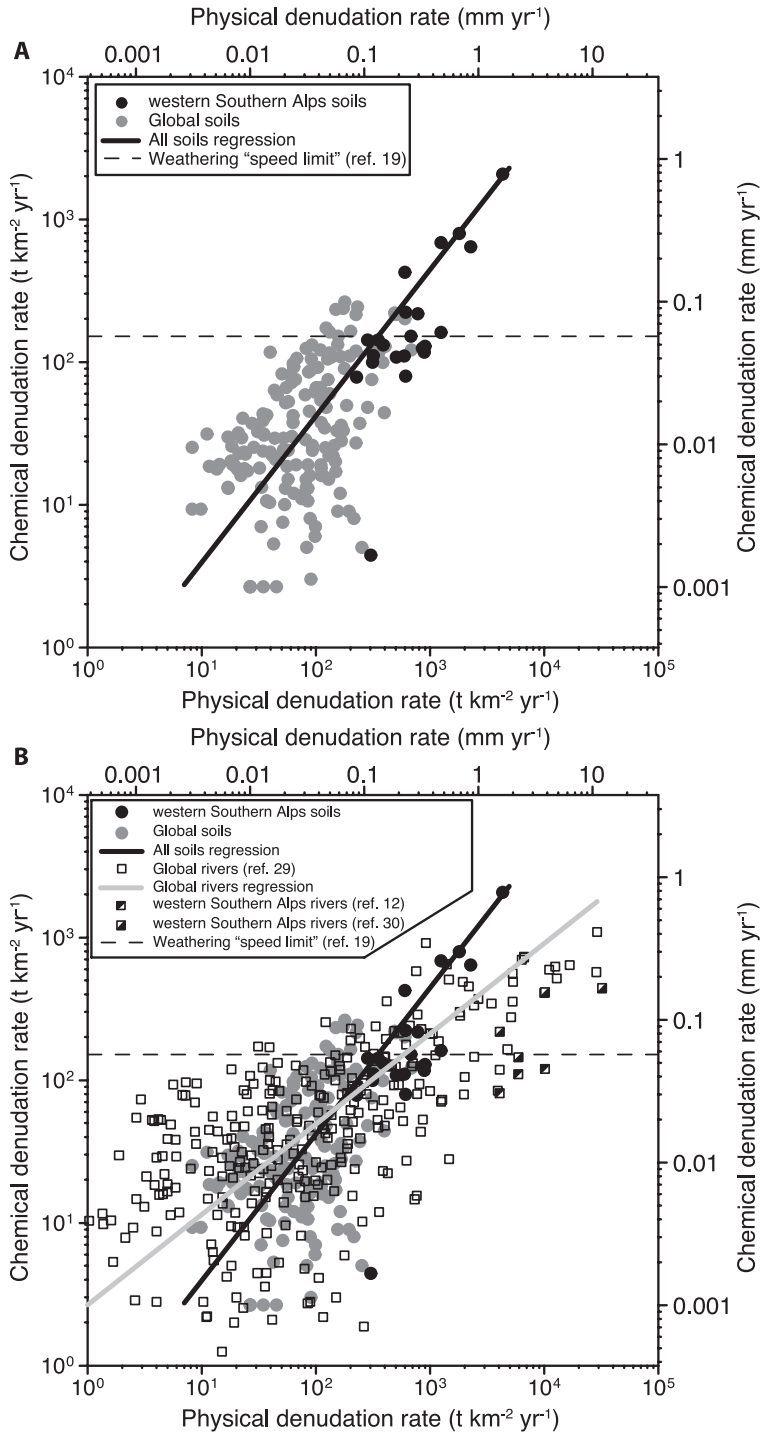

Fig. 3. Chemical versus physical denudation rate for worldwide soil and river data. (**A**) The RMA power-law fit to the soil mass flux data is $y = 0.37(+0.12/-0.09)x^{1.025(\pm 0.059)}$, $R^2 = 0.38$, $P < 0.001$, indicating that chemical denudation increases linearly as physical denudation rates increase by nearly three orders of magnitude. (**B**) The RMA power-law fit to the river mass flux data (*29*) is $y = 2.66(+0.39/-0.35)x^{0.63(\pm 0.028)}$, $R^2 = 0.41$, $P < 0.001$. The hypothesized global weathering speed limit (*19*) (horizontal dashed line) is shown for reference. Also shown are river flux–based denudation data from the western Southern Alps (*11*, *12*, *30*); note that river and soil chemical denudation rates in the western Southern Alps are of similar magnitude. The upper and right axes with length units are related to the mass flux axes by a density of 2.65 g cm^{-3} and thus are approximate and for reference only, because rock density varies among the samples. See supplementary materials for data sources.

References and Notes

1. T. C. Chamberlin, *J. Geol.* **7**, 545–584 (1899).
2. M. E. Raymo, W. F. Ruddiman, *Nature* **359**, 117–122 (1992).
3. K. L. Ferrier, J. W. Kirchner, *Earth Planet. Sci. Lett.* **272**, 591–599 (2008).
4. E. J. Gabet, S. M. Mudd, *Geology* **37**, 151–154 (2009).
5. G. E. Hilley, C. P. Chamberlain, S. Moon, S. Porder, S. D. Willett, *Earth Planet. Sci. Lett.* **293**, 191–199 (2010).
6. A. J. West, *Geology* **40**, 811–814 (2012).
7. Materials and methods are available as supplementary materials on *Science* Online.
8. R. J. Norris, A. F. Cooper, *J. Struct. Geol.* **23**, 507–520 (2001).
9. J. M. Tippett, P. J. J. Kamp, *J. Geophys. Res.* **98** (B9), 16119–16148 (1993).
10. N. Hovius, C. P. Stark, P. A. Allen, *Geology* **25**, 231–234 (1997).
11. D. M. Hicks *et al.*, *J. Hydrol. N.Z.* **50**, 81–142 (2011).
12. A. D. Jacobson, J. D. Blum, *Geology* **31**, 865–868 (2003).
13. G. A. Griffiths, M. J. McSaveney, *N. Z. J. Sci.* **26**, 197–209 (1983).
14. L. R. Basher, P. J. Tonkin, M. J. McSaveney, *Z. Geomorphol.* **69**, 117–131 (1988).
15. B. A. Clarke, D. W. Burbank, *J. Geophys. Res.* **116** (F4), F04009 (2011).
16. A. M. Heimsath, W. E. Dietrich, K. Nishiizumi, R. C. Finkel, *Nature* **388**, 358–361 (1997).
17. J. L. Dixon, A. S. Hartshorn, A. M. Heimsath, R. A. DiBiase, K. X. Whipple, *Earth Planet. Sci. Lett.* **323–324**, 40–49 (2012).
18. C. S. Riebe, J. W. Kirchner, R. C. Finkel, *Earth Planet. Sci. Lett.* **224**, 547–562 (2004).
19. J. L. Dixon, F. von Blanckenburg, *C. R. Geosci.* **344**, 597–609 (2012).
20. J. Braun, F. Herman, G. Batt, *Earth Planet. Sci. Lett.* **300**, 197–204 (2010).
21. J. Beavan *et al.*, *Geophys. Res. Lett.* **37**, L16305 (2010).
22. A. M. Heimsath, R. A. DiBiase, K. X. Whipple, *Nat. Geosci.* **5**, 210–214 (2012).
23. K. X. Whipple, E. Kirby, S. H. Brocklehurst, *Nature* **401**, 39–43 (1999).
24. R. A. DiBiase, A. M. Heimsath, K. X. Whipple, *Earth Surf. Process. Landf.* **37**, 855–865 (2012).
25. R. G. Hilton, P. Meunier, N. Hovius, P. J. Bellingham, A. Galy, *Earth Surf. Process. Landf.* **36**, 1670–1679 (2011).
26. A. Eger, P. C. Almond, L. M. Condron, *Geoderma* **163**, 185–196 (2011).
27. Z.-X. Tsai, G. J.-Y. You, H.-Y. Lee, Y.-J. Chiu, *Earth Surf. Process. Landf.* **38**, 661–674 (2013).
28. I. J. Larsen, D. R. Montgomery, *Nat. Geosci.* **5**, 468–473 (2012).
29. J. D. Milliman, K. L. Farnsworth, *River Discharge to the Coastal Ocean: A Global Synthesis* (Cambridge Univ. Press, New York, 2011).
30. W. B. Lyons, A. E. Carey, D. M. Hicks, C. A. Nezat, *J. Geophys. Res.* **110** (F1), F01008 (2005).
31. E. Gabet, *Earth Planet. Sci. Lett.* **264**, 259–265 (2007).
32. J. Moore, A. D. Jacobson, C. Holmden, D. Craw, *Chem. Geol.* **341**, 110–127 (2013).

Acknowledgments: We thank the NSF East Asia and Pacific Summer Institutes program (OISE-1015454 to I.J.L.), Royal Society of New Zealand, NASA Earth and Space Science fellowship program, Geological Society of America, and University of Washington Department of Earth and Space Sciences for support; A. Heimsath, J. Roering, F. von Blanckenburg, and N. Hovius for stimulating conversations; H. Greenberg for geographic information system support; K. Larsen for assistance collecting sediment samples; R. Sletten for assistance importing samples; A. Heimsath and A. J. West for thorough reviews; and the New Zealand Department of Conservation for granting access to study sites. Data are available in the supplementary materials. I.J.L. and P.C.A. designed and planned the field component of the study; I.J.L., A.E., and B.M. conducted the field sampling; A.E. described soils; and I.J.L. and J.O.S. separated ^{10}Be. I.J.L. wrote the manuscript, with input from all coauthors.

Supplementary Materials

www.sciencemag.org/content/343/6171/637/suppl/DC1
Materials and Methods
Supplementary Text
Figs. S1 to S7
Tables S1 to S7
References (*33–92*)

19 August 2013; accepted 30 December 2013
Published online 16 January 2014;
10.1126/science.1244908

Periodic Variability in the Large-Scale Southern Hemisphere Atmospheric Circulation

David W. J. Thompson* and Elizabeth A. Barnes

Periodic behavior in the climate system has important implications not only for weather prediction but also for understanding and interpreting the physical processes that drive climate variability. Here we demonstrate that the large-scale Southern Hemisphere atmospheric circulation exhibits marked periodicity on time scales of approximately 20 to 30 days. The periodicity is tied to the Southern Hemisphere baroclinic annular mode and emerges in hemispheric-scale averages of the eddy fluxes of heat, the eddy kinetic energy, and precipitation. Observational and theoretical analyses suggest that the oscillation results from feedbacks between the extratropical baroclinicity, the wave fluxes of heat, and radiative damping. The oscillation plays a potentially profound role in driving large-scale climate variability throughout much of the mid-latitude Southern Hemisphere.

The most robust periodic variability in the climate system is found in association with orbital forcing (*1*). The rotation of Earth on its axis drives the diurnal cycle; the axial tilt of Earth, combined with its orbit about the Sun, causes the seasonal cycle; and low-frequency variations in the eccentricity, axial tilt, and precession of Earth's orbit together produce periodic climate variability on time scales of millennia. Periodic heating from the Sun creates atmospheric thermal tides on a range of time scales.

Large-scale atmospheric variability due to internal climate dynamics is generally not periodic. The most notable exceptions are found in the tropics. The Madden-Julian oscillation is characterized by circulation and precipitation anomalies that propagate eastward in the tropical troposphere on time scales of ~40 to 70 days (*2*). The quasi-biennial oscillation is marked by alternating eastward and westward wind anomalies that propagate downward in the tropical stratosphere on time scales of ~24 to 27 months (*3*). The El Niño/Southern Oscillation phenomenon is weakly periodic, with enhanced spectral power on periods of ~2 to 7 years (*4*). In contrast, large-scale atmospheric variability in the extratropics is typically not periodic but rather is consistent with Gaussian red noise (*5*, *6*).

Recent evidence suggests an additional source of periodic variability in the climate system that has been largely overlooked in previous work. The periodicity emerges in the extratropical Southern Hemisphere and is associated with variability in the Southern Hemisphere baroclinic annular mode [BAM (*7*)]. Here we illustrate the robustness and climate implications of quasiperiodic behavior in the BAM, explore the dynamical mechanisms that give rise to it, and demonstrate the robustness of similar periodic behavior in a hierarchy of numerical models.

Department of Atmospheric Science, Colorado State University, Fort Collins, CO, USA.

*Corresponding author. E-mail: davet@atmos.colostate.edu

The Southern Hemisphere BAM is the baroclinic analog of the more widely studied southern annular mode (SAM). The two structures play very different roles in cycling energy through the Southern Hemisphere circulation. The SAM dominates the variance in the Southern Hemisphere zonal-mean kinetic energy, whereas the BAM dominates the variance in the Southern Hemisphere eddy kinetic energy (*8*). The SAM is driven by the variations in eddy fluxes of momentum (*6*), whereas the BAM is driven by variations in the eddy fluxes of heat (*7*). The SAM is marked by north-south vacillations in the extratropical jet about its climatological axis (*9*, *10*), whereas the BAM is marked by pulsing of the extratropical eddy kinetic energy throughout much of the middle to high-latitude Southern Hemisphere (*7*). Finally, the SAM is well modeled as Gaussian red noise (*9*), whereas the BAM exhibits marked periodicity on time scales of ~20 to 30 days (*7*).

The BAM is characterized by fluctuations in the lower tropospheric eddy fluxes of heat and upper tropospheric eddy kinetic energy that span much of the Southern Hemisphere (Fig. 1, A and C) (*7, 11, 12, 13*). It is thus associated with variations in both the generation and amplitude of wave activity throughout much the Southern Hemisphere (*14*). The BAM also has a distinct signature in precipitation: Periods of enhanced eddy kinetic energy (the positive polarity of the BAM) are marked by increases in precipitation throughout much of the Southern Hemisphere midlatitudes (Fig. 1E) (*15*). The linkages between the BAM and the hemispheric means of all three key physical fields are highly robust (Table 1). Consistent with the life cycle of developing baroclinic waves (*16*), the signatures of the BAM in the eddy fluxes of heat and precipitation precede the signature of the BAM in upper tropospheric eddy kinetic energy by ~1 day [see also (*7*)].

The periodicity in the BAM extends to the hemispheric-mean time series of wave amplitudes in the upper troposphere (Fig. 1B), wave generation in the lower troposphere (Fig. 1D) (*14*), and precipitation (Fig. 1F) (*17*). The spectral peaks in all three time series are based on a large number of degrees of freedom and are extremely robust (*17*). The periodicity in the large-scale Southern Hemisphere circulation is also reproducible in hemispheric-mean remotely sensed precipitation derived from the Advanced Microwave Scanning Radiometer (AMSR)-E instrument [Fig. 1F, red line (*11*)] and is thus not an artifact of the ERA-Interim reanalysis (*11*). A similar spectral peak was noted in eddy kinetic energy derived from only 1 year of relatively sparse balloon measurements taken in 1971–1972 for the Eole experiment (*18*) and in only one winter of zonal-wind measurements taken in 1979 for the Global Weather Experiment (*19*). The spectra in Fig. 1 reveal that Southern Hemisphere–mean atmospheric wave activity and precipitation exhibit robust periodicity on ~20 to 30 time scales in more than 30 years of data.

What physical process gives rise to the observed periodic behavior in Southern Hemisphere extratropical circulation? The periodicity in the hemispheric-mean fields of eddy kinetic energy and the eddy fluxes of heat indicates a negative feedback in the dynamics that drive their variability. Such a feedback is known to exist between the extratropical baroclinicity and the wave fluxes of heat. Baroclinic instability theory predicts that periods of enhanced baroclinicity lead to rapid growth in baroclinic waves and thus to periods of anomalously poleward eddy heat fluxes (*20*, *21*). Conversely, the thermodynamic energy equation dictates that anomalously poleward eddy heat fluxes lead to reductions in the baroclinicity [through the convergence and divergence of the eddy heat flux (*20*)]. The baroclinicity is known to play a key role in setting the climatological-mean structure of the wave fluxes of heat in both hemispheres (*22, 23, 24*). Two-way feedbacks between variability in the baroclinicity and the growth of baroclinic waves are observed in the Northern Hemisphere (*25*). The observational analyses shown in Fig. 2 confirm that analogous feedbacks are also observed in the Southern Hemisphere.

Figure 2 shows the eddy fluxes of heat (contours) and the baroclinicity (shading) regressed on standardized values of Southern Hemisphere–mean eddy heat fluxes as a function of lag and latitude (Fig. 2A) and lag and height (Fig. 2B). The Southern Hemisphere mean is defined as the area and density weighted average calculated over 30° to 70°S and 250 to 950 hPa. The heat flux index is multiplied by –1, so that positive values of the index denote poleward (southward) heat fluxes and vice versa. The baroclinicity is expressed in terms of the Eady growth rate, which provides a quantitative estimate of the growth rate of baroclinic eddies

$$\sigma_{BI} = 0.31 g N^{-1} T^{-1} \left| \frac{\partial T}{\partial y} \right| \qquad (1)$$

where σ_{BI} is the growth rate, g is the acceleration due to gravity, N is the Brunt-Väisälä frequency, T is temperature, and y is the meridional direction (*26*).

By construction, the regression map in Fig. 2A is dominated by large poleward heat fluxes (solid contours) that peak around lag 0. The poleward heat fluxes persist for several days (Fig. 2A) and extend throughout the Southern Hemisphere troposphere (Fig. 2B). The period immediately after the peak in the poleward eddy fluxes of heat is marked by a rapid reduction in the baroclinicity (blue shading at positive lag), as expected from the thermodynamic energy equation. The period immediately preceding the peak in the poleward eddy fluxes is marked by positive anomalies in the baroclinicity (warm colors at negative lag), which is consistent with baroclinic instability theory. The precursor in the baroclinicity at negative lag has a slightly longer time scale than the response at positive lag. In both cases, the anomalies in the baroclinicity extend throughout the depth of the troposphere and peak just above the 500-hPa level (Fig. 2B).

The observational results presented in Fig. 2 suggest that the BAM is associated with two-way feedbacks between the baroclinicity and eddy fluxes of heat. The periodicity driven by such feedbacks can be explored in a simple stochastic model based on linearized versions of Eq. 1 and the thermodynamic energy equation.

To develop the model, we first applied two simplifying assumptions to Eq. 1 to generate a prognostic equation for the anomalous eddy fluxes of heat averaged over the Southern Hemisphere baroclinic zone. We assumed that (i) the growth rate of baroclinic waves (the left-hand side of Eq. 1) is proportional to the time rate of change of the eddy flux of heat, and (ii) variations in the baroclinicity (the right-hand side of Eq. 1) are due primarily to variability in the meridional temperature gradient. The former assumption follows from the direct relationship between the vertical flux of wave activity and the eddy flux of heat (*27*). The latter assumption is supported by the fact that the changes in the Eady growth rate shown in Fig. 2 are dominated by the variations in the meridional temperature gradient (supplementary materials). Equation 1 was then linearized about the climatological mean state to yield an expression for the time rate of change of the eddy fluxes of heat as a function of the baroclinicity

$$\frac{\partial}{\partial t}\langle v^* T^* \rangle = -\alpha \langle b \rangle + \varepsilon(t) \qquad (2)$$

where v^*T^* and $b \overset{\text{def}}{=} \frac{\partial T}{\partial y}$ denote the anomalous eddy fluxes of heat and meridional temperature gradient, respectively, and the brackets denote the average over the Southern Hemisphere baroclinic zone (defined here as 40° to 55°S). The regression coefficient α corresponds to the amplitude of the feedback between the baroclinicity and the eddy fluxes of heat. The term $\varepsilon(t)$ reflects stochastic forcing of the heat fluxes by weather "noise" and prevents the model from reaching a steady state where $\langle v^* T^* \rangle = \langle b \rangle = 0$.

We then applied two simplifying assumptions to the zonal-mean thermodynamic energy equation to form a prognostic equation for the anomalous baroclinicity. In this case, we assumed that (i) the net forcing of the baroclinicity by the wave fluxes of heat is linearly proportional to the heat fluxes themselves, and (ii) the damping of the baroclinicity due to both adiabatic and diabatic processes can be modeled as Newtonian cooling. The resulting equation was subsequently linearized about the climatological mean state to yield an expression for the time rate of change of the baroclinicity as a function of the heat fluxes

$$\frac{\partial \langle b \rangle}{\partial t} = \beta \langle v^* T^* \rangle - \frac{\langle b \rangle}{\tau} \qquad (3)$$

where the regression coefficient β corresponds to the amplitude of the feedback between the eddy fluxes

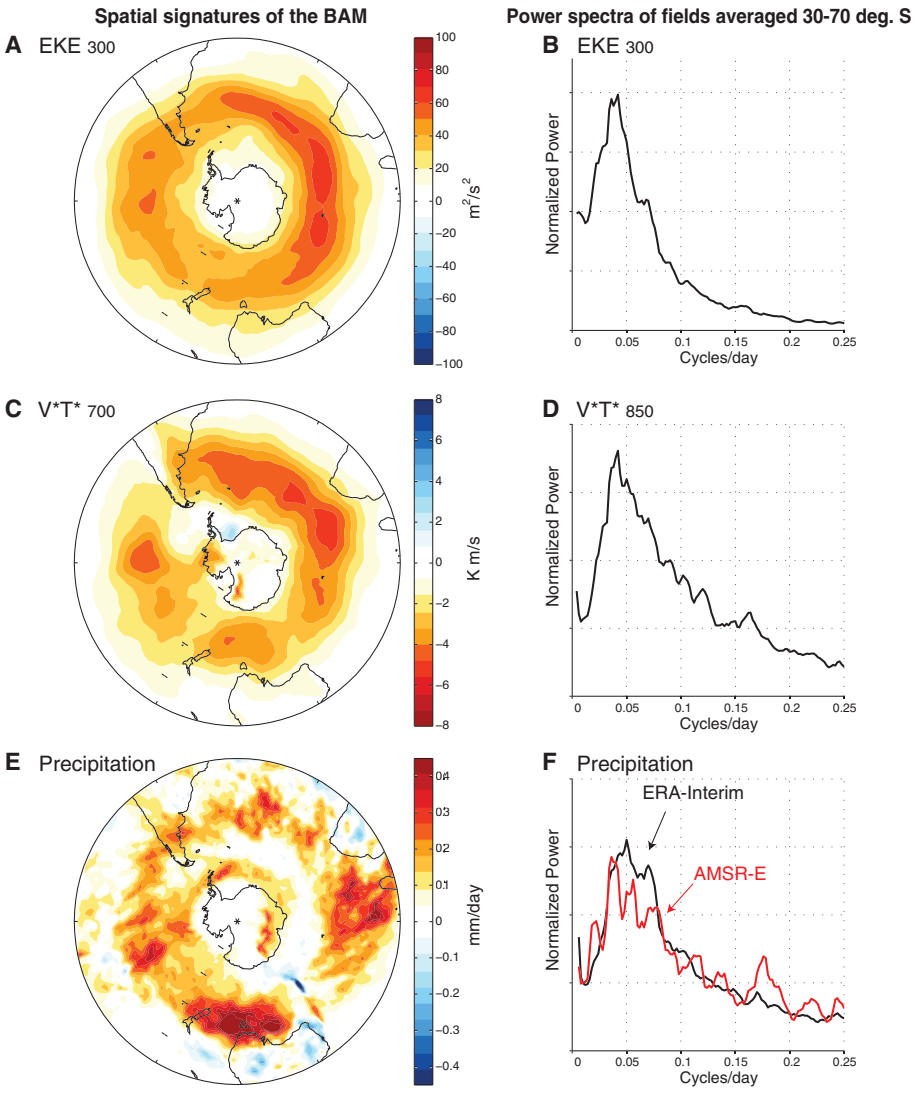

Fig. 1. (A to F) Space and time signatures of the Southern Hemisphere BAM. The left panels show the fields indicated regressed onto the BAM index time series (*12, 13, 15*). The right panels show power spectra for hemispheric averages of the fields indicated (*17*). Red values in (C) denote southward (negative) heat fluxes. The spectra in (F) show results for precipitation derived from ERA-Interim [black (*11*)] and AMSR-E [red (*11*)]. All other panels are based on the ERA-Interim model (*11*). As discussed in the text, the heat fluxes and precipitation peak 1 day before the peak in eddy-kinetic energy, and thus the regressions in (C) and (E) are lagged by –1 day with respect to the BAM index.

Table 1. Correlations between the BAM index (*12*) and hemispheric means (30° to 70°S) of the fields indicated. Correlations are based on all days of 1979–2010 (11,678 days). The BAM is defined as the leading PC of eddy-kinetic energy (*12*). As discussed in the text, the heat fluxes and precipitation peak 1 day before the peak in eddy-kinetic energy. All correlations are statistically different from zero at the 99% level, based on a one-tailed test of the *t* statistic. EKE is the eddy kinetic energy.

Field	$[v^*T^*]$ at 850 hPa	EKE at 300 hPa	Total precipitation
Correlation with BAM index	$r = -0.67$ (lag –1)	$r = +0.98$ (lag 0)	$r = -0.49$ (lag –1)

of heat and the baroclinicity. The Newtonian cooling term $\frac{\langle b \rangle}{\tau}$ reflects the damping of the baroclinicity by both diabatic processes and vertical motion. The parameter τ denotes the damping time scale.

Equations 2 and 3 were then solved numerically and analytically to generate expressions for the model eddy fluxes of heat and their periodicity. Figure 3A shows the frequency of oscillation in $\langle v^* T^* \rangle$ from the analytic solution (neglecting the stochastic term; see the supplementary materials) as a function of the feedback parameters (abscissa) and damping time scale (ordinate). Figure 3B shows the spectra of $\langle v^* T^* \rangle$ from the numerical solution with the stochastic term, using the feedbacks observed at the 500-hPa level. The solutions to the model and the calculation of the observed parameters are discussed in the supplementary materials.

The simple coupled model yields several key insights into the conditions that lead to oscillatory behavior in the Southern Hemisphere circulation.

1) As shown in the supplementary materials, the model heat fluxes oscillate at a frequency given by

$$\omega = \frac{24 \times 3600}{2\pi} Im\left\{\left(\sqrt{\frac{1}{(2\tau)^2} - \alpha\beta}\right)\right\} \text{day}^{-1} \quad (4)$$

The frequency of the oscillation in $\langle v^* T^* \rangle$ is thus a function of the product of the feedback parameters $\alpha\beta$ and the damping time scale τ (Eq. 4). The frequency of the oscillation increases as the feedback amplitudes increase and/or as the damping time scale increases.

2) The derivation of the model parameters from observations is described in the supplementary materials. The red circles in Fig. 3A indicate the frequencies predicted by the model based on the observed feedbacks and damping time scales calculated at all tropospheric levels from 950 to 300 hPa. The range of predicted oscillation frequencies is slightly lower than the observed range, depending on the level chosen to calculate the observed feedbacks. When the observed middle tropospheric feedbacks are inserted into Eq. 4, the model heat fluxes oscillate at a frequency that is strikingly similar to the observed frequency (red curve in Fig. 3B).

3) Oscillating solutions in $\langle v^* T^* \rangle$ are only possible when the damping time scale $\tau > \frac{1}{2\sqrt{\alpha\beta}}$. For the observed middle tropospheric values of α and β, the model heat fluxes only oscillate if the damping time scale is longer than ~2 days (Fig. 3A). When the damping time scale is shorter than this value, the spectrum of the model heat fluxes is red (Fig. 3B). From a physical perspective, if the damping is very large (τ is very small), the perturbations in the baroclinicity are damped before they have time to affect the eddy fluxes of heat.

The results of the simple model given in Eqs. 2 and 3 suggest that periodicity in the extratropical wave fluxes of heat (and thus the eddy kinetic energy) should arise in any numerical model that includes two-way interactions between the baroclinicity and baroclinic waves. Figure 4 shows the spectra of the hemispheric-mean eddy fluxes of heat and eddy kinetic energy from three general circulation models (GCMs) of varying complexity (*28*): (i) a fully coupled atmosphere/ocean GCM (top row); (ii) an aquaplanet GCM with no orography, simplified radiation, and a slab ocean (middle row); and (iii) a dry dynamical core with parameterized physics (bottom row). All three classes of models exhibit periodic behavior in the hemispheric-mean eddy heat fluxes and eddy kinetic energy. The similarities between the

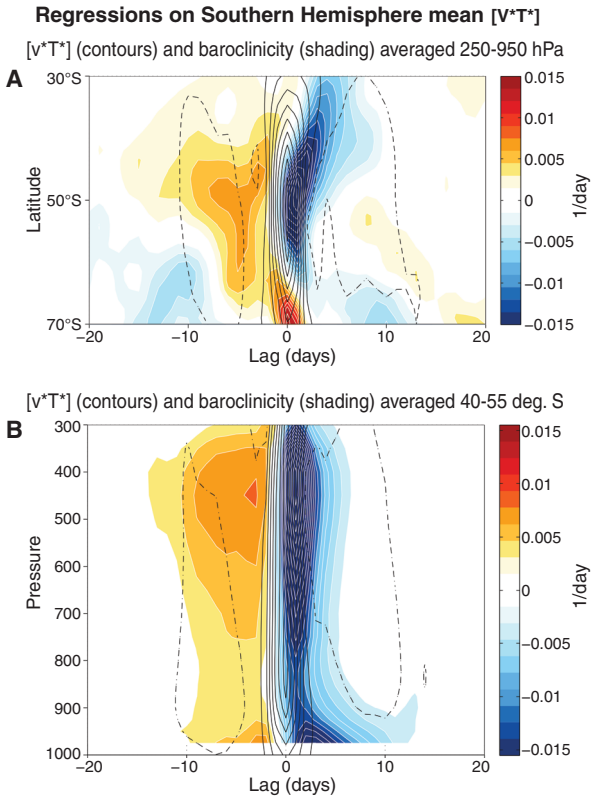

Fig. 2. Regressions on the Southern Hemisphere–mean eddy fluxes of heat. The Southern Hemisphere mean is defined as an average over 30° to 70°S and 250 to 950 hPa. The baroclinicity is quantified as the Eady growth rate (see text). The contour intervals are 0.5 K m/s (**A**) and 0.6 K m/s (**B**). The solid contours denote southward (negative) heat fluxes.

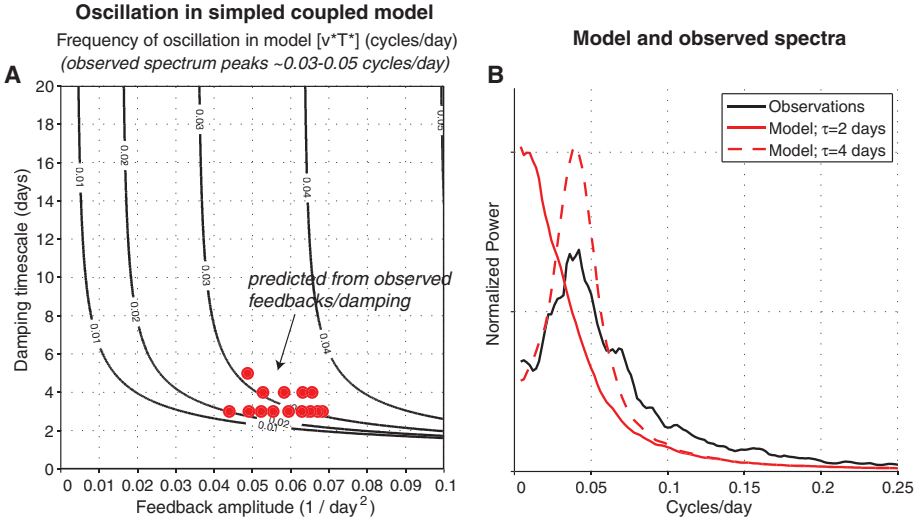

Fig. 3. Simulating periodic behavior in the heat fluxes in a simple coupled model. (A) The analytic solution of the oscillation frequency in the eddy fluxes of heat obtained from the simple model of Eqs. 2 and 3. Results are shown as a function of the product of the model feedback parameters ($\alpha \times \beta$; abscissa) and damping times cale (ordinate). Frequency units are cycles per day. Red circles indicate the range of frequencies predicted from the observed feedbacks and damping time scales at all tropospheric levels. **(B)** Power spectra derived from the simple model using the feedback parameters at 500 hPa for the damping time scales indicated. The observed spectrum is for Southern Hemisphere mean eddy kinetic energy and is reproduced from Fig. 1B. See the supplementary materials for details of the calculations.

modeled and observed spectra are most pronounced in the case of the fully coupled and aquaplanet GCMs. The dry dynamical core also exhibits broad spectral power on weekly time scales in the eddy kinetic energy and eddy fluxes of heat, but the peak in the spectrum of the eddy heat fluxes extends to higher frequencies than it does in the observations.

The observed periodicity in the Southern Hemisphere circulation is reminiscent of that proposed more than 60 years ago in association with the Northern Hemisphere "index cycle" (*29*, *30*). Research on the index cycle waned in the 1960s because of a lack of supporting observational evidence (*31*). We were likewise unable to find evidence of oscillatory behavior in the Northern Hemisphere that was similar to that shown here. The apparent lack of analogous periodicity in the large-scale Northern Hemisphere circulation may be due to the relatively narrow west-east scale of the Northern Hemisphere storm tracks. It may also be due to the relatively large climatological-mean baroclinicity found over the western North Atlantic and North Pacific basins due to the land-sea contrasts there. Both factors could limit the ability of baroclinicity anomalies associated with atmospheric variability to influence the heat fluxes: the former because anomalies in baroclinicity may be advected downstream of the storm tracks before they influence the heat fluxes; the latter because the anomalies in baroclinicity due to atmospheric variability are much smaller than those due to the Northern Hemisphere climatological-mean state.

The results shown here demonstrate that the large-scale Southern Hemisphere circulation exhibits robust periodicity in a range of key physical parameters. They reveal that the periodicity is consistent with two-way feedbacks between the baroclinicity and the eddy fluxes of heat. They also reveal that similar periodicity is evident in a hierarchy of numerical models. To what extent the periodicity in the baroclinic annular mode contributes to the variance in local weather over specific regions of the Southern Hemisphere remains to be determined. But the periodicity clearly has potentially profound implications for understanding and predicting Southern Hemisphere climate variability over broad spatial scales.

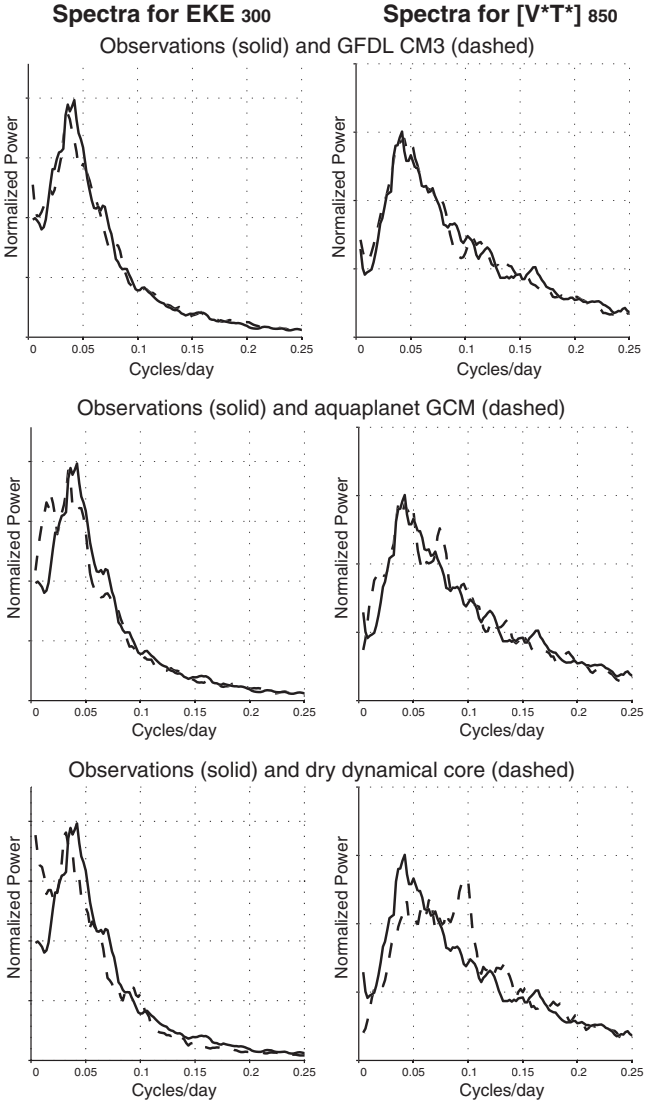

Fig. 4. Comparing observed and simulated power spectra. (Left) Spectra of eddy kinetic energy at 300 hPa averaged 30° to 70°S. **(Right)** Spectra of the eddy fluxes of heat at 850 hPa averaged 30° to 70°S. Solid lines show the observed spectra; dashed lines show spectra for the climate models indicated on the figure. Models are described in (*28*). The calculation of the spectra is described in (*17*).

References and Notes

1. D. L. Hartmann, *Global Physical Climatology* (Academic Press, San Diego, CA, 1994).
2. C. Zhang, *Rev. Geophys.* **43**, RG2003 (2005).
3. M. P. Baldwin *et al*., *Rev. Geophys.* **39**, 179–229 (2001).
4. E. M. Rasmusson, T. H. Carpenter, *Mon. Weather Rev.* **110**, 354–384 (1982).
5. S. B. Feldstein, *J. Clim.* **13**, 4430–4440 (2000).
6. D. J. Lorenz, D. L. Hartmann, *J. Atmos. Sci.* **58**, 3312–3327 (2001).
7. D. W. J. Thompson, J. D. Woodworth, *J. Atmos. Sci.*; available online at http://journals.ametsoc.org/loi/atsc (2014).
8. The SAM and southern BAM are defined as the leading empirical orthogonal functions (EOF)/principal components (PC) time series of the zonal-mean kinetic and eddy kinetic energies, respectively. If **X** is a two-dimensional data matrix that samples space and time, then the leading EOF of **X** is the spatial function that explains the largest possible fraction of the variance in **X**. The leading PC of **X** is the expansion coefficient time series associated with the leading EOF. The leading EOF is found as the eigenvector associated with the largest eigenvalue of the covariance matrix of **X**.
9. D. L. Hartmann, F. Lo, *J. Atmos. Sci.* **55**, 1303–1315 (1998).
10. D. W. J. Thompson, J. M. Wallace, *J. Clim.* **13**, 1000–1016 (2000).
11. All observational results except the red curve in Fig. 1F are based on the interim European Centre for Medium-Range Weather Forecasts (ECMWF) Re-Analysis (ERA-Interim) data from 1 January 1979 to 31 December 2010. The red curve in Fig. 1F is based on Version 7 of the Advanced Microwave Scanning Radiometer (AMSR)-E precipitation data, obtained from Remote Sensing Systems. For details of ERA-Interim, see (*32*).
12. The results in the left panel of Fig. 1 and in Table 1 are based on standardized values of the BAM index, defined here as the leading PC of zonal-mean eddy kinetic energy computed over all levels and latitudes within the domain from 1000 to 200 hPa and 20° to 70°S. The data are weighted by the area represented by each grid box and the mass represented by each vertical level in the ERA-Interim before calculating the PC time series.
13. The zonal-mean eddy fluxes of heat and eddy kinetic energy are defined as $[v^*T^*]$ and $\frac{1}{2}[v^{*2} + u^{*2}]$, respectively, where asterisks denote departures from the zonal mean and brackets denote the zonal mean. Eddy fluxes and eddy kinetic energy are calculated from 4*x* daily data before computing daily averages.
14. The eddy fluxes of heat are proportional to the vertical flux of wave activity. Thus, the vertical divergence of the eddy fluxes of heat in the lower troposphere is proportional to the generation of wave activity there.
15. The ERA-Interim precipitation is based on the 12-hour forecast of 12 Greenwich mean time total precipitation. The ERA-Interim precipitation is a model-derived quantity but is calculated using physically consistent parameterizations that link atmospheric motions to precipitation.
16. A. J. Simmons, B. J. Hoskins, *J. Atmos. Sci.* **35**, 414–432 (1978).
17. All spectra are found by (i) Calculating the spectra for subsets of the time series that are 500 days in length. A Hanning window is applied to each subset, and the overlap between adjacent subsets is 250 days. (ii) Averaging the power spectra over all subsets and then applying a three-point running mean to the resulting mean power spectra. Every 10 years of data yield ~40 degrees of freedom per spectral estimate. The spectral estimates in Fig. 1, B, D, and F (black curve) have ~120 degrees of freedom; the spectral estimates

for AMSR-E precipitation shown in Fig. 1F (red curve) have ~40 degrees of freedom.
18. P. J. Webster, J. L. Keller, *J. Atmos. Sci.* **32**, 1283–1301 (1975).
19. J. W. Kidson, *Mon. Weather Rev.* **114**, 1654–1663 (1986).
20. G. K. Vallis, *Atmospheric and Oceanic Fluid Dynamics* (Cambridge Univ. Press, Cambridge, 2006).
21. R. S. Lindzen, B. F. Farrell, *J. Atmos. Sci.* **37**, 1648–1654 (1980).
22. B. J. Hoskins, P. J. Valdes, *J. Atmos. Sci.* **47**, 1854–1864 (1990).
23. P. J. Kushner, I. M. Held, *Geophys. Res. Lett.* **25**, 4213–4216 (1998).
24. H. Nakamura, A. Shimpo, *J. Clim.* **17**, 1828–1844 (2004).
25. D. W. J. Thompson, T. Birner, *J. Atmos. Sci.* **69**, 1811–1823 (2012).
26. The baroclinicity is defined as the meridional slope of the isentropic surfaces relative to Earth's surface. It thus includes two components: the meridional gradient in temperature and the vertical gradient in temperature (i.e., the static stability).
27. D. G. Andrews, M. E. McIntyre, *J. Atmos. Sci.* **33**, 2031–2048 (1976).
28. The Geophysical Fluid Dynamics Laboratory (GFDL) CM3 is a coupled chemistry climate model. The analyses shown here are based on a simulation performed for the Coupled Model Intercomparison Project (CMIP5), phase 5. See (*33*). We analyzed one ensemble of the historical simulation over years 1970–2004. The aquaplanet simulation is identical to that used in (*34*). The model is integrated at T85 resolution for 21 years, with the first 2 years discarded for spin-up. All model parameters are set to the values from the control experiment of Frierson *et al*. (*34*). The idealized dry GCM is the GFDL spectral dry dynamical core of (*35*). The model does not include radiation or moisture and uses Newtonian relaxation to a zonally symmetric equilibrium temperature profile and Rayleigh damping of the low-level winds to simulate boundary layer friction. The model is integrated at T42 (42-wave triangular truncation) resolution for 6000 days with 2000 days for spin-up. Both the aquaplanet and the dry dynamical core do not have topography and are run under perpetual equinoctial conditions with no diurnal cycle.
29. C.-G. Rossby, H. C. Willett, *Science* **108**, 643–652 (1948).
30. J. Namias, *J. Meteorol.* **7**, 130–139 (1950).
31. J. M. Wallace, H.-H. Hsu, *Tellus* **37A**, 478–486 (1985).
32. D. P. Dee *et al*., *Q. J. R. Meteorol. Soc.* **137**, 553–597 (2011).
33. L. J. Donner *et al*., *J. Clim.* **24**, 3484–3519 (2011).
34. D. M. W. Frierson, I. M. Held, P. Zurita-Gotor, *J. Atmos. Sci.* **63**, 2548–2566 (2006).
35. I. M. Held, M. J. Suarez, *Bull. Am. Meteorol. Soc.* **75**, 1825–1830 (1994).

Acknowledgments: We thank R. Garreaud and J. M. Wallace for helpful discussion of the results, R. Barnes for insight into the analytic model, S. Wills for assistance with the AMSR-E data, and three anonymous reviewers for helpful comments on the manuscript. D.W.J.T. is supported by the NSF Climate Dynamics program.

Supplementary Materials

www.sciencemag.org/content/343/6171/641/suppl/DC1
Supplementary Text
Figs. S1 and S2
Reference

25 October 2013; accepted 7 January 2014
10.1126/science.1247660

A Promiscuous Intermediate Underlies the Evolution of LEAFY DNA Binding Specificity

Camille Sayou,[1,2,3,4]* Marie Monniaux,[1,2,3,4]* Max H. Nanao,[5,6]*† Edwige Moyroud,[1,2,3,4]*‡ Samuel F. Brockington,[7] Emmanuel Thévenon,[1,2,3,4] Hicham Chahtane,[1,2,3,4] Norman Warthmann,[8]§ Michael Melkonian,[9] Yong Zhang,[10] Gane Ka-Shu Wong,[10,11] Detlef Weigel,[8] François Parcy,[1,2,3,4,12]† Renaud Dumas[1,2,3,4]

Transcription factors (TFs) are key players in evolution. Changes affecting their function can yield novel life forms but may also have deleterious effects. Consequently, gene duplication events that release one gene copy from selective pressure are thought to be the common mechanism by which TFs acquire new activities. Here, we show that LEAFY, a major regulator of flower development and cell division in land plants, underwent changes to its DNA binding specificity, even though plant genomes generally contain a single copy of the *LEAFY* gene. We examined how these changes occurred at the structural level and identify an intermediate LEAFY form in hornworts that appears to adopt all different specificities. This promiscuous intermediate could have smoothed the evolutionary transitions, thereby allowing LEAFY to evolve new binding specificities while remaining a single-copy gene.

The rewiring of transcriptional networks is an important source of evolutionary novelty (*1*–*3*). Variation often occurs through changes in cis-regulatory elements, which are DNA sequences that contain binding sites for transcription factors (TFs) regulating nearby genes (*3*, *4*). There is less evidence for regulatory changes affecting the protein-coding sequence of TFs. Such changes are expected to be under highly stringent selection because they could impair the expression of many downstream targets. Gene duplication provides a solution to this dilemma, as additional TF gene copies may acquire new functions, provided that the aggregate copies fulfill the function of the original TF (*5*). Indeed, TF DNA binding specificity has been shown to diversify within multigene families (*6*, *7*). In some cases, however, TF coding genes remain as single-copy genes because of phenomena such as paralog interference (*8*), which can impede neofunctionalization. When essential TFs are maintained as single-copy genes, the extent to which they can evolve is not clear. To address this question, we examined the *LEAFY (LFY)* gene as an evolutionary model.

Except in gymnosperms, in which two paralogs (*LEAFY* and *NEEDLY*) are usually present (Fig. 1A), *LFY* exists mostly as a single-copy gene in land plants (*9*). *LFY* plays essential roles as a key regulator of floral identity in angiosperms, as well as in cell division in the moss *Physcomitrella patens* (*10*). *LFY* encodes a TF that binds DNA through a highly conserved dimeric DNA binding domain (DBD) (*11*). Despite this conservation, PpLFY1, a LFY homolog from the moss *P. patens*, is unable to bind the DNA sequence recognized by LFY from *Arabidopsis thaliana* (AtLFY) (*9*), suggesting that LFY DNA binding specificity might have changed during land plant evolution.

We mined the transcriptomes from algal species, whose origin predates the divergence of mosses and tracheophytes, and found *LFY* homologs in six species of streptophyte green algae (Fig. 1A and fig. S1) (see also supplementary materials and methods). Thus, *LFY* is not specific to land plants. Despite this extended ancestry, the LFY-DBD sequence, including the amino acids in direct contact with DNA, remains highly conserved (Fig. 1B and fig. S1). We used high-throughput SELEX (systematic evolution of ligands by exponential enrichment) (*12*) experiments to systematically analyze the DNA binding specificity of LFY proteins from each group of plants. After

[1]CNRS, Laboratoire de Physiologie Cellulaire et Végétale (LPCV), UMR 5168, 38054 Grenoble, France. [2]Université Grenoble Alpes, LPCV, F-38054 Grenoble, France. [3]Commissariat à l'Energie Atomique et aux Energies Alternatives, Direction des Sciences du Vivant, Institut de Recherches en Technologies et Sciences pour le Vivant, LPCV, F-38054 Grenoble, France. [4]Institut National de la Recherche Agronomique, LPCV, F-38054 Grenoble, France. [5]European Molecular Biology Laboratory (EMBL), 6 Rue Jules Horowitz, BP 181, 38042 Grenoble, France. [6]Unit of Virus Host-Cell Interactions, Université Grenoble Alpes–EMBL–CNRS, UMI 3265, 6 Rue Jules Horowitz, 38042 Grenoble Cedex 9, France. [7]Department of Plant Sciences, University of Cambridge, Downing Street, Cambridge CB2 3EA, UK. [8]Department of Molecular Biology, Max Planck Institute for Developmental Biology, 72076 Tübingen, Germany. [9]Botanisches Institut, Lehrstuhl I, Universität zu Köln, Biozentrum Köln, Zülpicher Strasse 47b, 50674 Köln, Germany. [10]Beijing Genomics Institute (BGI)–Shenzhen, Beishan Industrial Zone, Yantian District, Shenzhen 518083, China. [11]Department of Biological Sciences, Department of Medicine, University of Alberta, Edmonton, Alberta T6G 2E9, Canada. [12]Centre for Molecular Medicine and Therapeutics, Child and Family Research Institute, University of British Columbia, Vancouver, British Columbia V5Z 4H4, Canada.

*These authors contributed equally to this work.
†Corresponding author. E-mail: francois.parcy@cea.fr (F.P); mnanao@embl.fr (M.H.N.)
‡Present address: Department of Plant Sciences, University of Cambridge, Downing Street, Cambridge CB2 3EA, UK.
§Present address: Research School of Biology, The Australian National University, Acton, ACT 0200, Australia.

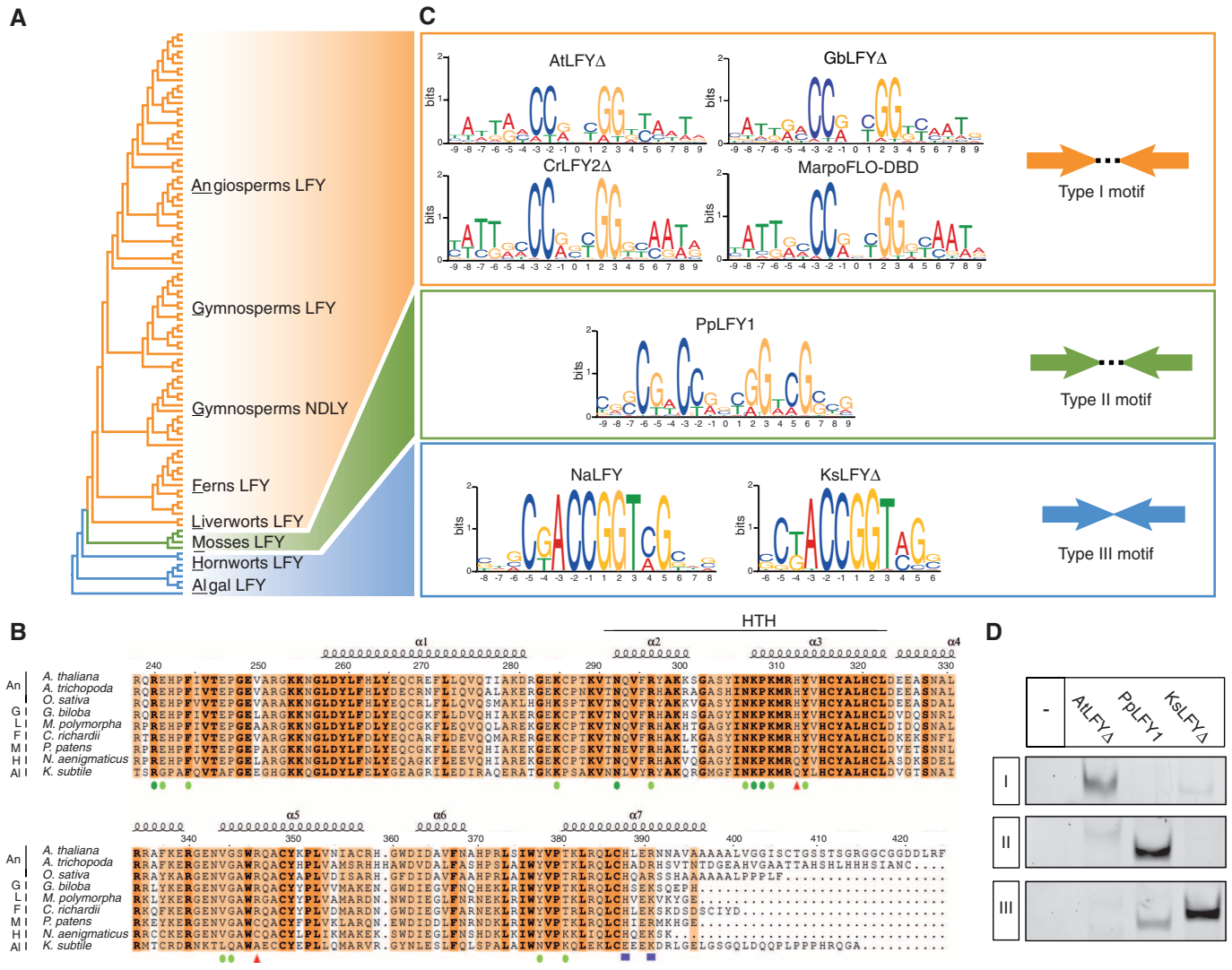

Fig. 1. Evolution of LFY DNA binding specificity. (**A**) Simplified *LEAFY* phylogeny (detailed in fig. S5). DNA binding specificities are color coded: type I, orange; type II, green; or type III, blue. (**B**) Alignment of LFY-DBDs. Amino acid numbering and secondary structure annotation (α, alpha helices; HTH, helix-turn-helix domain) are based on AtLFY from *A. thaliana*. Single-letter abbreviations for the amino acid residues are as follows: A, Ala; C, Cys; D, Asp; E, Glu; F, Phe; G, Gly; H, His; I, Ile; K, Lys; L, Leu; M, Met; N, Asn; P, Pro; Q, Gln; R, Arg; S, Ser; T, Thr; V, Val; W, Trp; and Y, Tyr. Dark green dots, DNA base contacts; light green dots, phosphate backbone contacts; red triangles, residues involved in the PpLFY1-specific DNA contacts; purple rectangles, residues involved in the interaction between DBD monomers. (**C**) SELEX motifs for AtLFYΔ, GbLFYΔ (*Ginkgo biloba*), CrLFY2Δ (*Ceratopteris richardii*), MarpoFLO-DBD (*Marchantia polymorpha*), PpLFY1 (*P. patens*), NaLFY (*N. aenigmaticus*), and KsLFYΔ (*K. subtile*) are shown. Δ denotes proteins starting at amino acid 40 (on the basis of the AtLFY sequence). Cartoons at right depict binding site organization: half-site (arrows) with or without a 3-bp spacer. (**D**) EMSA with AtLFYΔ, PpLFY1, and KsLFYΔ proteins (10 nM) and the three types (I, II, III) of DNA probes. Only the protein-DNA complexes are shown.

optimizing alignments (*13*), we found that the SELEX motifs fell into three groups (Fig. 1C and fig. S2), suggesting that LFY changed specificity at least twice.

Most LFY proteins from land plants (angiosperms, gymnosperms, ferns, and liverworts) bind the same DNA motif (type I) as AtLFY (*13*). PpLFY1, however, binds to a different motif (type II), despite possessing the same 15 DNA binding amino acids as AtLFY (Fig. 1B). These SELEX results explain why all embryophyte LFY homologs, except PpLFY1, display AtLFY-like activity when expressed in *A. thaliana* (*9*). Motifs I and II share a similar overall organization, consisting of two 8–base pair (bp) inverted half-sites separated by three nucleotides, but their peripheral positions differ. The newly identified hornwort and algal LFY proteins bind to a third motif (type III) that resembles motif II, but without the central 3-bp spacer (Fig. 1C). With AtLFY, PpLFY1, and KsLFY (from *Klebsormidium subtile*) as representative proteins of the three specificities, we confirmed that each protein displays a strong preference for one motif type (Fig. 1D, fig. S3, and table S1).

Given the broad conservation of the LFY-DBD sequence, we asked how these different specificities could be explained molecularly. We solved the crystal structure of PpLFY1-DBD bound to a motif II DNA (Fig. 2A and table S2) and compared it to the previously determined AtLFY-DBD dimer–type I DNA complex (*11*). The two ternary complexes are highly similar (root mean square deviation of protein backbone atoms of 0.6 Å). However, PpLFY1-DBD makes additional contact with DNA: Aspartic acid 312 (D312) interacts with the cytosine base (C) at position 6 of the DNA binding motif, which is the nucleotide most different between motifs I and II obtained by SELEX (Figs. 1C and 2B). In AtLFY, position 312 is occupied by a histidine residue (H312), which is pulled away from the DNA by an arginine (R345), a conformation that precludes direct H312-DNA contact. In contrast, in PpLFY1, a cysteine residue (C345) replaces R345, which does not affect the positioning of D312, thus al-

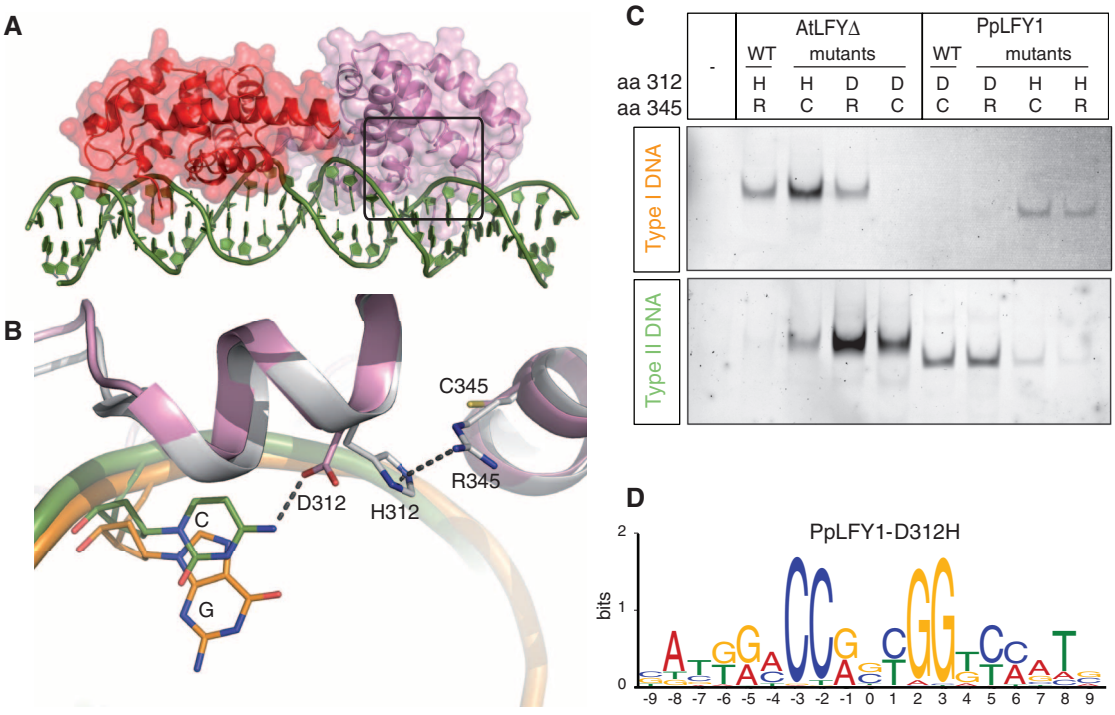

Fig. 2. Structural basis for type II specificity. (**A**) Crystal structure of PpLFY1-DBD (red and pink) bound to DNA (green). The boxed area is detailed in (B) after applying a 70° rotation. (**B**) Superimposition of AtLFY-DBD (gray)–DNA (orange) and PpLFY1-DBD (pink)–DNA (green) complexes. Specificity determinant residues and bases are represented as sticks. For amino acids: H, histidine; R, arginine; D, aspartate; C, cysteine; for DNA bases: C, cytosine; G, guanine. (**C**) Effect of specific mutations on the DNA binding specificity of AtLFYΔ and PpLFY1 in EMSA. Note that the H312-C345 combination allows binding to both motifs I and II. All proteins are at 25 nM, and only the protein-DNA complexes are shown. WT, wild type; aa, amino acid. (**D**) SELEX motif of the PpLFY1-D312H protein, bearing a strong resemblance to motif I.

lowing it to contact the cytosine base. To test the importance of positions 312 and 345, we swapped these residues between PpLFY1 and AtLFY (Fig. 2, C and D). This was sufficient to convert specificity from type I to type II and vice versa, confirming the key role of these two positions. This result is consistent with an in vivo study showing that a PpLFY1-D312H (D312H, Asp^{312}→His^{312}) mutant can bind a type I sequence and partially complement a *lfy* mutation in *A. thaliana* plants (*9*).

We next investigated binding to motif III. Motif III half-sites are similar to those of motif II (Fig. 1C), owing to the presence of a glutamine (Q) at position 312 in type III LFYs: Q is known to interact with multiple bases (*14*) (fig. S4), and the small residues present at position 345 (cysteine, alanine, or serine) allow Q312 to freely interact with position 6. Critically, motif III differs from motif II by the lack of the central 3-bp spacer (Fig. 1C). Modeling a LFY-DBD– motif III ternary complex by removing the 3-bp spacer in the type II DNA sequence (Fig. 3A) revealed that the interaction between helices α1 and α7, which stabilizes dimeric AtLFY- and PpLFY1-DBD positioning (*11*), could no longer exist for motif III.

Consistent with this observation, interacting regions of helices α1 and α7 [including the key amino acid H387 on α7 (*11*)] are highly conserved from bryophytes to angiosperms (type II and I), but are variable in algae (type III) (Fig. 1B and fig. S1). To test the importance of the α1-α7 interaction in binding to 3-bp–spaced half-sites, we mutated PpLFY1 H387 and R390 residues (which make most α1-α7 contacts). This was sufficient to shift the DNA binding preference of PpLFY1 from type II to type III (Fig. 3B). These observations suggest that LFY-DBD preferentially binds to 3-bp–spaced half-sites (motifs I and II) when the α1-α7 interaction surface is present and to motif III in the absence of this surface. Nevertheless, both the pseudosymmetry of motif III (fig. S2) and the size of LFY-DNA complexes (fig. S4) suggest that LFY binds motif III as a dimer, possibly through an alternative dimerization surface. These analyses pinpoint the molecular basis of DNA specificity changes to three amino acid sites: Positions 312 and 345 determine the half-site sequence, and position 387 determines the dimerization mode.

However, if, as shown in *P. patens* and angiosperms, LFY plays a key role throughout plant evolution, how could these changes have been tolerated? Because once arisen, they would have instantaneously modified the expression of the entire set of LFY target genes. Our *LFY* phylogeny (fig. S5) yields two insights: (i) Although we cannot completely rule out the occurrence of transient ancient duplications, all known duplication events occurred subsequent to changes in the binding specificity of the protein; therefore the *LFY* gene probably evolved new DNA binding modes independently of changes in copy number. (ii) The hornwort *LFY* lineage diverges from a phylogenetic node that lies between the type III and type I-II binding specificities. On closer examination, we realized that NaLFY from the hornwort *Nothoceros aenigmaticus* had type III specificity according to the SELEX experiment, despite having the H387 dimerization residue

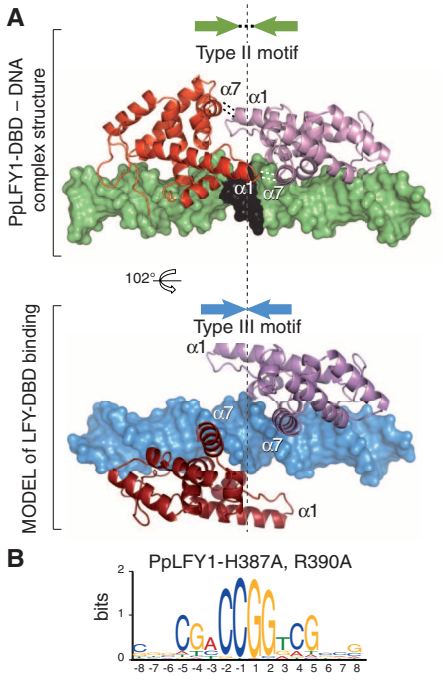

Fig. 3. Structural model for type III specificity. (**A**) (Top) PpLFY1-DBD dimer (in red and pink) bound to DNA (in green, except the black 3-bp spacer). Interactions between monomers (involving α helices α1 and α7) are shown with dashed lines. (Bottom) Modeled type III binding with DNA shown in blue. The dashed vertical line denotes the center of the pseudopalindromic DNA sequence. (**B**) SELEX motif of PpLFY1-H387A, R390A, showing a strong resemblance to motif III.

typical for type I and II specificities (Fig. 1, B and C). Using electrophoretic mobility shift assay (EMSA) experiments, we assayed NaLFY and NaLFY-DBD DNA binding and found that their dimers (fig. S6) could bind all three types of DNA motifs (Fig. 4, and figs. S3 and S7). We also established that NaLFY binding to motifs I and II was allowed by the presence of a functional α1-α7 interaction surface (Fig. 4). The SELEX experiment most likely identified only motif III because of its slightly more efficient binding to NaLFY (fig. S3 and table S1).

Our amino acid reconstruction analyses across the LFY phylogeny identify the phylogenetic location of the three specificity transitions that occurred during LFY evolution (Fig. 4 and fig. S8). Initially, the ancestral algal LFY bound motif III as a dimer (with Q312 and C345 half-site determinants). Subsequently, the evolution of the α1-α7 interaction surface generated a promiscuous LFY intermediate with two modes of DBD dimerization and a versatile glutamine residue at position 312, which bound all three types of DNA motifs. Mutations affecting positions 312 and 345 then completed the transition to type I or II specificities. Although this precise path cannot be unambiguously determined by reconstruction alone (Fig. 4 and fig. S8), the biochemical data reveal that two LFY states (Q312-C345 and H312-C345) bind to both motifs I and II (Figs. 2C and 4). Our scenario, using either of these two states as an intermediate, provides an evolutionary route through a promiscuous platform that avoids deleterious transitions. Furthermore, this scenario is equally parsimonious in the context of all alternative organismal phylogenetic hypotheses (fig. S9). Whether these transitions were accompanied by a complete change in target gene sets or whether some cis elements coevolved with DNA binding specificity (*15*) is unknown. Scanning the *P. patens* genome for PpLFY1 binding sites does not suggest any global conservation of targets but does identify several MADS-box genes potentially bound by LFY in both *Arabidopsis* and *P. patens* (table S3).

A highly conserved and essential TF evolved radical shifts in DNA binding specificity by a mechanism that does not require gene duplication. Detailed structural characterization of the different modes of DNA binding across the transition to land plants enabled us to capture LFY in a state of increased promiscuity that has persisted in *N. aenigmaticus*. This promiscuous intermediate probably facilitated the evolutionary transition between specificities, as previously shown for the evolution of metabolic enzymes or nuclear receptors (*16*–*18*). Although we have focused on the more intractable problem of evolution in single-copy TFs, it is plausible that the mechanisms we describe could also contribute to the evolution of TFs encoded by multigene families.

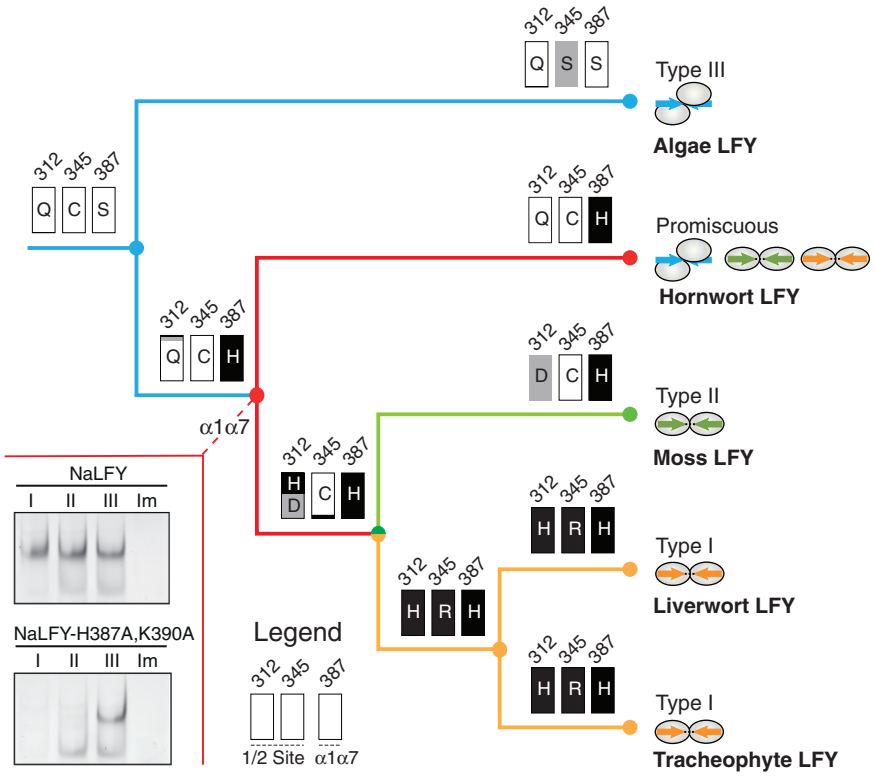

Fig. 4. Proposed evolution of LFY DNA binding specificity in green plants. The Bayesian estimation of the posterior probability of ancestral states for amino acid positions 312, 345, and 387 is depicted at the major phylogenetic nodes. Probabilities for different residues at a given position and node are indicated by the relative size of stacked boxes. The analysis shows that the ancestral LFY most likely possessed a type III specificity and that the promiscuous form arose when land plants emerged. DNA binding specificity is color-coded: type I, orange; type II, green; type III, blue; relaxed specificity, red. α1α7 refers to the α1-α7 dimerization interface. (**Inset**) NaLFY interacts with all three types of DNA binding motifs in EMSA (see also fig. S7), but not with the type I mutated probe (Im). The H387A and K390A mutations reduced the binding to type I or II motifs, but not to type III. Both proteins are at 1 μM; only the protein-DNA complexes are shown.

References and Notes

1. S. B. Carroll, *Cell* **101**, 577–580 (2000).
2. I. S. Peter, E. H. Davidson, *Cell* **144**, 970–985 (2011).
3. B. Prud'homme, N. Gompel, S. B. Carroll, *Proc. Natl. Acad. Sci. U.S.A.* **104** (suppl. 1), 8605–8612 (2007).
4. G. A. Wray, *Nat. Rev. Genet.* **8**, 206–216 (2007).
5. H. E. Hoekstra, J. A. Coyne, *Evolution* **61**, 995–1016 (2007).
6. G. Badis *et al.*, *Science* **324**, 1720–1723 (2009).
7. M. F. Berger *et al.*, *Cell* **133**, 1266–1276 (2008).
8. C. R. Baker, V. Hanson-Smith, A. D. Johnson, *Science* **342**, 104–108 (2013).
9. A. Maizel *et al.*, *Science* **308**, 260–263 (2005).
10. T. Tanahashi, N. Sumikawa, M. Kato, M. Hasebe, *Development* **132**, 1727–1736 (2005).
11. C. Hamès *et al.*, *EMBO J.* **27**, 2628–2637 (2008).
12. Y. Zhao, D. Granas, G. D. Stormo, *PLOS Comput. Biol.* **5**, e1000590 (2009).
13. E. Moyroud *et al.*, *Plant Cell* **23**, 1293–1306 (2011).
14. N. M. Luscombe, R. A. Laskowski, J. M. Thornton, *Nucleic Acids Res.* **29**, 2860–2874 (2001).
15. C. R. Baker, B. B. Tuch, A. D. Johnson, *Proc. Natl. Acad. Sci. U.S.A.* **108**, 7493–7498 (2011).
16. O. Khersonsky, C. Roodveldt, D. S. Tawfik, *Curr. Opin. Chem. Biol.* **10**, 498–508 (2006).
17. A. Aharoni *et al.*, *Nat. Genet.* **37**, 73–76 (2005).
18. G. N. Eick, J. K. Colucci, M. J. Harms, E. A. Ortlund, J. W. Thornton, *PLOS Genet.* **8**, e1003072 (2012).

Acknowledgments: We thank M. Schmid for help with sequencing; E. Masson, J. Kyozuka, M. Hasebe, C. Scutt, C. Finet, and J. C. Villarreal for sharing materials; A. Maizel and S. Rensing for discussion; and A. Maizel, R. Worsley-Hunt, A. Mathelier, M. Blazquez, O. Nilsson, C. Zubieta, and J. Chen for critical reading of the manuscript. This work was supported by funds from the Max Planck Society (D.W.), the Agence Nationale de la Recherche (grant Charmful SVSE2–2011) and Coopérations et Mobilités Internationales Rhône-Alpes (F.P.), and the FP7 P-CUBE number 227764 (R.D.). The 1000 Plants (1KP) initiative, led by G.K.-S.W., is funded by Alberta Ministry of Enterprise and Advanced Education, Alberta Innovates Technology Futures, Innovates Centre of Research Excellence, Musea Ventures, and BGI-Shenzhen. GenBank accession numbers are as follows: *AmboLFY*, KF193872; *NaLFY*, KF269532; *KsLFY*, KF269535; *CsLFY*, KF269533; *CvLFY*, KF269536; and *CyLFY*: KF269534. The Protein Data bank identification number is 4BHK for the reported crystal structure. We declare no competing financial interests.

Supplementary Materials

www.sciencemag.org/content/343/6171/645/suppl/DC1
Materials and Methods
Supplementary Text
Figs. S1 to S9
Tables S1 to S5
References (*19*–*42*)
Database S1

7 November 2013; accepted 23 December 2013
Published online 16 January 2014;
10.1126/science.1248229

PCP and Septins Compartmentalize Cortical Actomyosin to Direct Collective Cell Movement

Asako Shindo and John B. Wallingford*

Despite our understanding of actomyosin function in individual migrating cells, we know little about the mechanisms by which actomyosin drives collective cell movement in vertebrate embryos. The collective movements of convergent extension drive both global reorganization of the early embryo and local remodeling during organogenesis. We report here that planar cell polarity (PCP) proteins control convergent extension by exploiting an evolutionarily ancient function of the septin cytoskeleton. By directing septin-mediated compartmentalization of cortical actomyosin, PCP proteins coordinate the specific shortening of mesenchymal cell-cell contacts, which in turn powers cell interdigitation. These data illuminate the interface between developmental signaling systems and the fundamental machinery of cell behavior and should provide insights into the etiology of human birth defects, such as spina bifida and congenital kidney cysts.

Convergent extension (CE) is an essential morphogenetic process that shapes tissues and organs during embryonic development (*1*), and defective CE is implicated in structural birth defects ranging from spina bifida to congenital kidney cysts (*2*–*4*). The longest-standing model of CE is vertebrate gastrulation (*1*, *5*, *6*), during which mediolaterally oriented cell intercalations elongate the body axis and drive the internalization of mesoderm and endoderm within the ectoderm (fig. S1A) (*7*, *8*). Pioneering experiments in *Xenopus* frogs revealed that mediolaterally polarized protrusions on gastrula mesenchyme cells make stable attachments to neighboring cells, and these protrusions are thought to exert traction, effecting interdigitation by a cell-crawling mechanism (fig. S1B, left) (*7*, *8*). Planar cell polarity (PCP) proteins are essential for polarization and stabilization of mediolateral protrusions and thus for CE (*9*, *10*). These cell behaviors and their regulation by PCP proteins are conserved across vertebrates, including mammals (*1*, *6*, *11*).

PCP proteins also control CE in vertebrate epithelial cells, where cell movement is accomplished not by crawling, but rather by active shortening of cell-cell junctions (fig. S1B, right) (*3*, *12*). This junction-shrinking mechanism is reminiscent of that observed during CE in the *Drosophila* germband epithelium, which does not require PCP proteins (*13*–*15*). In light of these findings, we addressed two fundamental questions concerning CE in vertebrate gastrula mesenchyme cells. We asked where and how actomyosin-based contraction acts to drive cell intercalation, and we asked how PCP proteins act to spatially organize such contraction.

As an initial proxy for actomyosin-based contraction, we examined phosphorylation of myosin regulatory light chains (MRLCs) (*16*). Phosphorylated myosin II (pMyoII) was enriched along mediolaterally aligned cell-cell junctions where the anterior and posterior faces of neighboring

Howard Hughes Medical Institute and University of Texas at Austin, Austin, TX 78712, USA.

*Corresponding author. E-mail: wallingford@austin.utexas.edu

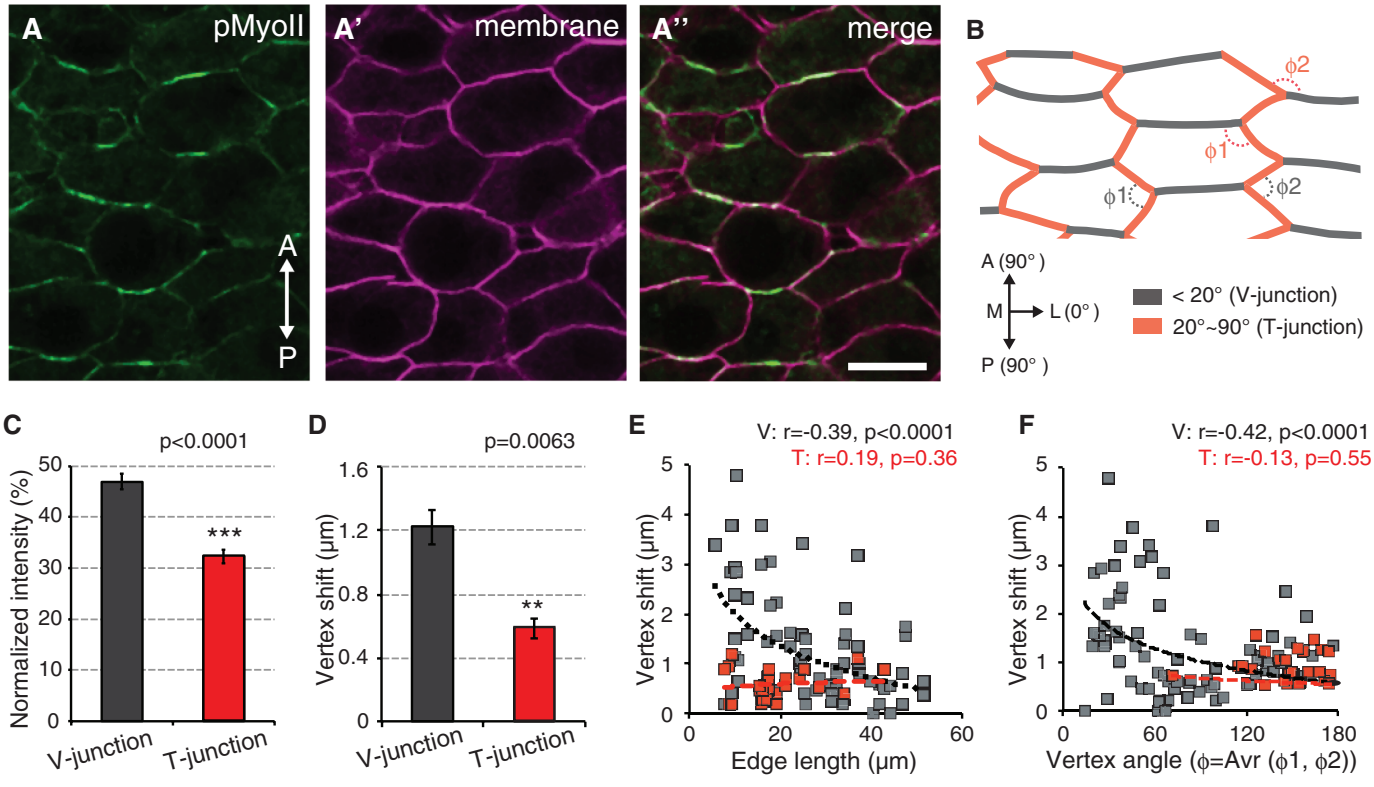

Fig. 1. Myosin-mediated cell cortex tension is planar polarized in *Xenopus* mesoderm. (**A** to **A''**) pMyoII immunostaining of notochord in vivo (scale bar indicates 20 μm). (**B**) Illustration defining t- and v-type junctions and vertex angle ϕ (gray, ϕ for v-junction; red, ϕ of t-junction). A, anterior; P, posterior; M; medial; L, lateral. (**C**) Normalized intensity of pMyoII, defined as intensity relative to the maximum (=100%) and minimum (=0%) raw intensity for each image (n = 177 for v and 221 for t; three embryos). (**D**) Average vertex position change after ablation. Error bars indicate SE. (**E** and **F**) Scatter plots showing correlation between tension and edge length (E) or vertex angle (F) (n = 84 for v and 24 for t; 54 embryos).

cells abut (Fig. 1, A to A″ and C, and fig. S2). These so-called v-junctions [nomenclature of (*17*)] displayed significant enrichment of pMyoII (Fig. 1, B and C, gray) as compared with adjoining, less-mediolaterally aligned cell edges (so-called t-junctions) (Fig. 1, B and C, red). Levels of cortical pMyoII correlated significantly with junction orientation (fig. S3A), but such correlation was not observed for the generalized cell junction marker β-catenin (fig. S3, B to D″). This enrichment of pMyoII suggests that actomyosin-based contraction along v-type junctions may drive

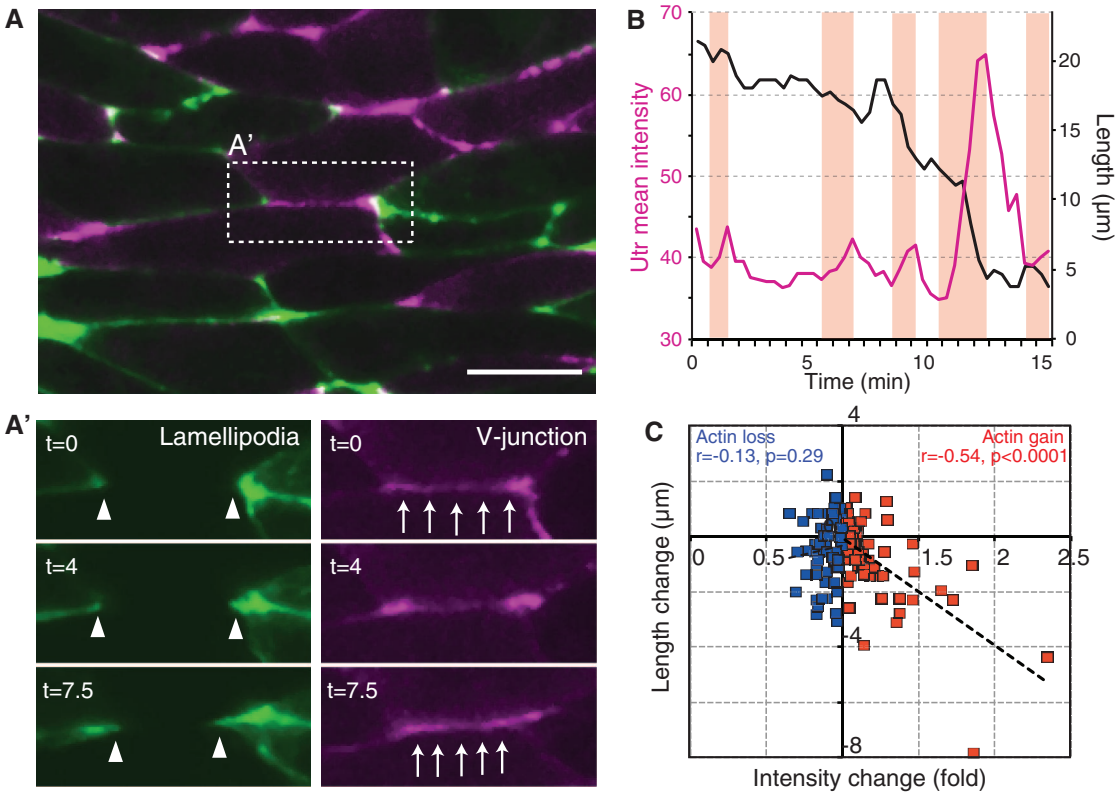

Fig. 2. Pulsed actin assembly at v-junctions during edge shortening. (**A**) Mosaic expression of two colors of the actin biosensors utrophin-FP. (**A'**) Time-lapse after the junction in box A′. Two populations of actin are visible: bipolar lamellipodia (green, arrowheads) and actin at the v-junction (magenta, arrows). (**B**) Mean intensity of utrophin (Utr, pink line) at v-junctions during edge length shortening (black line). (**C**) Edge length change is correlated with increase of utrophin intensity (red) but not with reduction in utrophin intensity (blue) (n = 133 cycles; six explants).

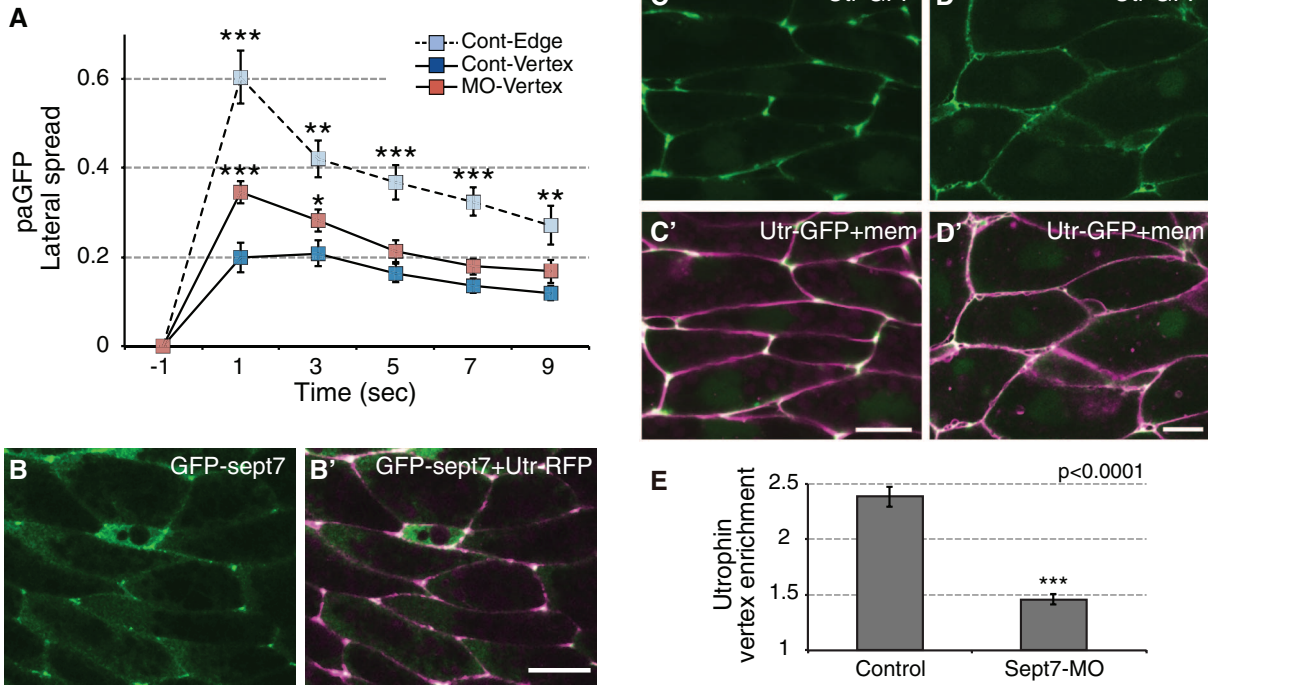

Fig. 3. Sept7 compartmentalizes cortical actin dynamics. (**A**) Quantification of the lateral spread of paGFP-Utr at a cell vertex or edge (fig. S10A) (*P < 0.05, **P < 0.001, ***P < 0.0001, n = 7 to 11 explants). (**B**) GFP-sept7 localization in explant. (**B'**) GFP-sept7 colocalizes with Utr–red fluorescent protein (RFP) at vertices. (**C** and **C'**) Utr-GFP normally localizes at vertices. (**D** and **D'**) Sept7 knockdown disrupts utrophin accumulation at the vertices. (**E**) Quantification of (C) and (D) (see also fig. S7B). Scale bar, 20 μm; error bars, SE.

mediolateral cell intercalation, and live imaging revealed the consistent association of shrinking v-junctions with cell rearrangement (fig. S4 and movies S1 and S2).

To ask directly whether enriched pMyoII at v-type junctions contributes to cell intercalation, we assessed patterns of cell cortex tension by using laser microdissection, where retraction after laser cutting indicates relative tension in the cell edge (fig. S5, A and B′) (*17*, *18*). Consistent with the pattern of pMyoII, mediolaterally aligned v-junctions displayed significantly higher cortical tension than did adjacent, less mediolaterally aligned t-junctions (Fig. 1D, fig. S5C, and movies S3 and S4). Moreover, tension in v-junctions correlated with cell edge length (Fig. 1E, gray) and changes in neighboring cell shapes, as captured by the angle ϕ (Fig. 1, B and F, gray; and fig. S6). Neither correlation was observed for t-junctions (Fig. 1, E and F, red). Together, these data suggest that accumulating tension in shrinking v-type junctions exerts a pulling force on adjacent t-junctions to drive mediolateral cell intercalation during CE in the vertebrate gastrula. A similar mechanism drives CE in *Drosophila* epithelial cells (*17*).

To further test this model, we explored actin dynamics by using live imaging of mosaic embryos expressing different colors of an actin biosensor in neighboring cells (Fig. 2A and fig. S7A). This assay illuminated the actin-rich protrusions at mediolateral cell vertices (Fig. 2A′, arrowheads) (*7*, *9*). It also revealed pulses of actin assembly along shrinking v-type junctions (Fig. 2, A′ arrows and B; fig. S7A; and movie S5). Similar pulses characterize *Drosophila* epithelial CE (*19*). Accumulation of actin significantly correlated with v-junction shrinkage (Fig. 2C).

We then took a bioinformatic approach to identify specific MRLCs that may act during CE (fig. S8, A and A′). We identified Myl9, which we found to be essential for gastrulation (fig. S8, B and C). Expression of a functional green fluorescent protein (GFP) fusion revealed pulses of Myl9 accumulation at v-junctions that correlated

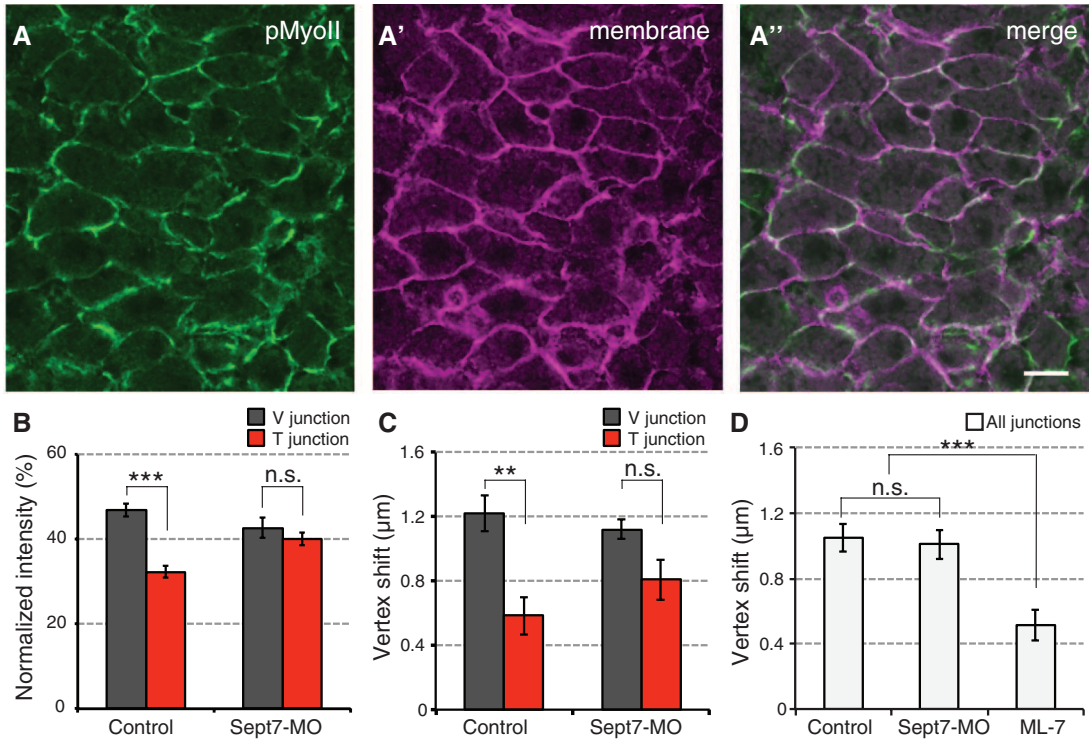

Fig. 4. Sept7 controls planar polarization of cell cortex tension. (**A** to **A″**) pMyoII immunostaining of notochord in Sept7 knockdown embryos (compare with Fig. 1A) (scale bar, 20 μm). (**B** and **C**) The normal differences in pMyoII or vertex shift after laser ablation between v- and t-junctions are lost in Sept7 morphants (Sept7-MO). For (B), $n = 74$ for v and 188 for t; three embryos. For (C), $n = 50$ for v and 28 for t; 39 explants. (**D**) Average vertex shift for all junctions is not changed after Sept7 knockdown but is significantly reduced by treatment with a myosin kinase inhibitor (for control, $n = 108$; for sept7-MO, $n = 78$; for ML-7, $n = 36$, 111 explants). n.s., not significant; error bars, SE.

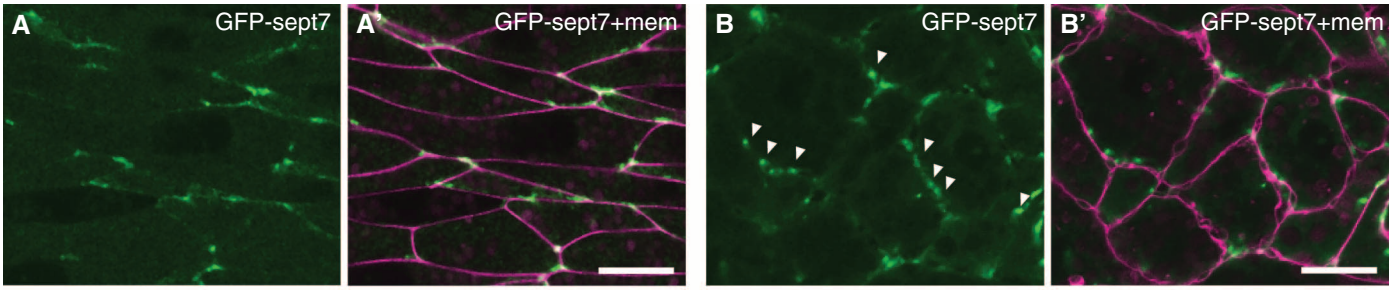

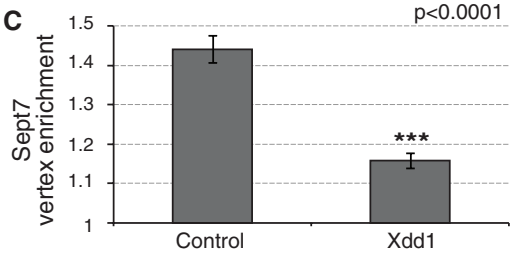

Fig. 5. PCP signaling regulates Sept7 localization. (**A** and **A′**) GFP-Sept7 localizes at vertices in control explants. (**B** and **B′**) Dominant negative dishevelled (Xdd1) promotes ectopic GFP-Sept7 localization along edges (arrowheads). (**C**) Quantification of GFP-Sept7 localization (control, $n = 67$ and six explants; Sept7-MO, $n = 50$ and six explants; scale bar, 20 μm) (see also fig. S7B).

with actin pulses at these sites (fig. S9, A to C). Neighboring t-junctions displayed neither actin nor Myl9 pulses, and Myl9 did not associate with the actin present at mediolateral cell vertices (fig. S9, C to E).

Because cell movement frequently involves spatially and functionally distinct actomyosin populations (*19*–*22*), we further interrogated actin dynamics by using a photoactivatable actin biosensor. We found that cortical actin was constrained at mediolateral vertices but spread rapidly along anteroposterior cell edges (Fig. 3A blue and fig. S10A). Thus, v-type junctions in the *Xenopus* gastrula are characterized by cortical actin flow, coordinated pulses of actin and Myl9, enriched pMyoII, and enhanced cell cortex tension. These data argue that actomyosin contraction along anteroposteriorly apposed cell edges results in their preferential shrinkage, thereby driving mediolateral cell intercalation during vertebrate gastrulation.

In this model, dynamic actomyosin must be actively partitioned to v-type cell edges. The septin cytoskeleton plays an ancient role in compartmentalizing cortical actomyosin during cytokinesis (*23*, *24*), and we previously showed that the PCP protein WDPCP (also known as Fritz) controls cell cortex dynamics and CE via septins (*25*). We therefore assessed septin localization by using a functional Sept7-GFP-fusion construct (*25*). Sept7-GFP was preferentially enriched at mediolateral cell vertices (Fig. 3, B and B′), and the intense population of actin filaments at these locations was specifically eliminated after Sept7 knockdown (Fig. 3, C to E, and fig. S7B). Moreover, the lateral spread of actin from mediolateral vertices was significantly increased after Sept7 knockdown (Fig. 3A red and figs. S10B and S7C), although knockdown did not alter actin dynamics along cell edges (fig. S10C). These data suggest that Sept7 maintains the stable actin population at mediolateral cell vertices. Sept7 knockdown also abolished the planar polarization of pMyoII, such that the normally significant difference between pMyoII levels in v-type and t-type junctions was lost in morphants (Fig. 4, A, A″, and B, and fig. S11A)

These changes in actomyosin had substantial functional consequences, because the normally significant difference in cortex tension between v- and t-type junctions was also eliminated by Sept7 knockdown (Fig. 4C). There was not, however, a global defect in actomyosin contraction, because overall cortex tension (the mean tension for all junctions) was not different between Sept7 morphants and control embryos (Fig. 4D). Most importantly, v-type junctions failed to accumulate tension and shrink after Sept7 knockdown, and convergent extension was severely inhibited (fig. S11, B to D″). Thus, both the accumulation of pMyoII and the mediolaterally directed increase in cell cortex tension along v-junctions are dependent on Sept7 function. Together with the observed effects on local actin dynamics (Fig. 3A and fig. S10B), these data suggest that Sept7 at cell vertices acts to restrict actomyosin contraction to v-type cell edges and is thereby central to their preferential shrinkage and to convergent extension.

Last, we sought to link Sept7 and actomyosin to the PCP proteins, known regulators of CE (*11*). First, we demonstrated that pharmacological manipulation of pMyoII disrupted CE and that loss of pMyoII reduced cell cortex tension (fig. S12), because these parameters had not yet been explored in this system. Then, we showed that disruption of the core PCP protein dishevelled (Dvl) in *Xenopus* gastrula mesoderm reduced overall pMyoII levels (fig. S11E), consistent with data from *Drosophila* (*26*). By contrast, Sept7 knockdown elicited a marked increase in pMyoII (fig. S11E), suggesting a model in which Sept7 at mediolateral vertices suppresses the action of PCP proteins, which, conversely, act at anteroposteriorly apposed cell faces [e.g., (*27*, *28*)]. Last, interference with Dvl function also perturbed the normal localization of Sept7 to cell vertices (Fig. 5, A to C) and disrupted the correlation between edge orientation and pMyoII intensity (fig. S13, A to D). Together, our data suggest that Dvl function is required to localize Sept7 to cell vertices, which in turn compartmentalizes cortical actomyosin and directs the shrinkage of v-type cell edges that ultimately drives cell intercalation and convergent extension (fig. S14).

We propose that substantial force for CE in *Xenopus* mesoderm is generated by contraction of mediolaterally oriented cell edges that join the anteroposterior faces of neighboring cells (fig. S14). This new model is parsimonious at many levels. First, the pattern of pMyoII-based contraction reported here is consistent with reports of core PCP protein localization at anteroposterior cell faces (*12*, *27*, *28*) and with the positive role for core PCP proteins in phosphorylating MyoII (fig. S11E) (*12*, *26*). This model is also consistent with embryological studies showing that CE in *Xenopus* requires precise anteroposterior patterning (*29*), as it does in *Drosophila* (*13*). Last, the model reconciles the long-standing archetype of vertebrate gastrulation with more recent results in *Drosophila* (*14*, *15*) and in vertebrate neuroepithelia and kidney tubules (*3*, *12*), suggesting that contraction of cell junctions via compartmentalized actomyosin is an ancient and unifying feature of CE.

Our data are also notable because spatially distinct populations of actomyosin are central to cell movement but little is known about such populations in vertebrate embryos. In *Drosophila*, CE involves a complex interplay between cortical actomyosin at v-junctions and a distinct "medial" network of actomyosin (*13*, *14*, *17*–*19*, *21*, *22*). A similar picture is emerging in vertebrates, because Dvl governs not only the polarization of cortical actomyosin deep in the cell (fig. S13) but also the oscillatory behavior of a system of actomyosin nodes and struts (*30*, *31*).

Last, the mechanistic link between core PCP proteins and septins remains unclear, but we previously discovered that WDPCP/Fritz binds to septins and controls their localization during both ciliogenesis and cell movement in *Xenopus* (*25*); a later study confirmed these results in mice (*32*). Because mutations in WDPCP/Fritz were found in human ciliopathy patients (*25*), our data here on septin function may provide new insights into the molecular links between CE, neural tube birth defects (*2*), and cystic kidney disease (*3*, *4*).

References and Notes

1. M. Tada, C. P. Heisenberg, *Development* **139**, 3897–3904 (2012).
2. J. B. Wallingford, L. A. Niswander, G. M. Shaw, R. H. Finnell, *Science* **339**, 1222002 (2013).
3. S. S. Lienkamp *et al.*, *Nat. Genet.* **44**, 1382–1387 (2012).
4. C. M. Karner *et al.*, *Nat. Genet.* **41**, 793–799 (2009).
5. W. Vogt, *Verhandl. Deutch. Zool. Gesell.* **27**, 49–51 (1922).
6. L. Solnica-Krezel, D. S. Sepich, *Annu. Rev. Cell Dev. Biol.* **28**, 687–717 (2012).
7. J. Shih, R. Keller, *Development* **116**, 901–914 (1992).
8. R. Keller *et al.*, *Philos. Trans. R. Soc. London Ser. B* **355**, 897–922 (2000).
9. J. B. Wallingford *et al.*, *Nature* **405**, 81–85 (2000).
10. J. R. Jessen *et al.*, *Nat. Cell Biol.* **4**, 610–615 (2002).
11. J. B. Wallingford, *Annu. Rev. Cell Dev. Biol.* **28**, 627–653 (2012).
12. T. Nishimura, H. Honda, M. Takeichi, *Cell* **149**, 1084–1097 (2012).
13. J. A. Zallen, E. Wieschaus, *Dev. Cell* **6**, 343–355 (2004).
14. C. Bertet, L. Sulak, T. Lecuit, *Nature* **429**, 667–671 (2004).
15. J. T. Blankenship, S. T. Backovic, J. S. Sanny, O. Weitz, J. A. Zallen, *Dev. Cell* **11**, 459–470 (2006).
16. M. Vicente-Manzanares, X. Ma, R. S. Adelstein, A. R. Horwitz, *Nat. Rev. Mol. Cell Biol.* **10**, 778–790 (2009).
17. M. Rauzi, P. Verant, T. Lecuit, P. F. Lenne, *Nat. Cell Biol.* **10**, 1401–1410 (2008).
18. R. Fernandez-Gonzalez, S. M. Simoes, J. C. Röper, S. Eaton, J. A. Zallen, *Dev. Cell* **17**, 736–743 (2009).
19. M. Rauzi, P. F. Lenne, T. Lecuit, *Nature* **468**, 1110–1114 (2010).
20. M. L. Gardel, I. C. Schneider, Y. Aratyn-Schaus, C. M. Waterman, *Annu. Rev. Cell Dev. Biol.* **26**, 315–333 (2010).
21. J. K. Sawyer *et al.*, *Mol. Biol. Cell* **22**, 2491–2508 (2011).
22. R. Fernandez-Gonzalez, J. A. Zallen, *Phys. Biol.* **8**, 045005 (2011).
23. A. S. Maddox, L. Lewellyn, A. Desai, K. Oegema, *Dev. Cell* **12**, 827–835 (2007).
24. Y. Barral, V. Mermall, M. S. Mooseker, M. Snyder, *Mol. Cell* **5**, 841–851 (2000).
25. S. K. Kim *et al.*, *Science* **329**, 1337–1340 (2010).
26. C. G. Winter *et al.*, *Cell* **105**, 81–91 (2001).
27. B. Ciruna, A. Jenny, D. Lee, M. Mlodzik, A. F. Schier, *Nature* **439**, 220–224 (2006).
28. C. Yin, M. Kiskowski, P. A. Pouille, E. Farge, L. Solnica-Krezel, *J. Cell Biol.* **180**, 221–232 (2008).
29. H. Ninomiya, R. P. Elinson, R. Winklbauer, *Nature* **430**, 364–367 (2004).
30. P. Skoglund, A. Rolo, X. Chen, B. M. Gumbiner, R. Keller, *Development* **135**, 2435–2444 (2008).
31. H. Y. Kim, L. A. Davidson, *J. Cell Sci.* **124**, 635–646 (2011).
32. C. Cui *et al.*, *PLOS Biol.* **11**, e1001720 (2013).

Acknowledgments: We thank A. Ewald, A. Wills, and M. Butler for critical reading and insightful comments on the manuscript. This work was supported by grants to J.B.W. from the NIH/National Institute of General Medical Sciences, the March of Dimes, and the Burroughs Wellcome Fund. A.S. was supported by fellowships from Uehara Memorial Foundation and Kanae Foundation for the Promotion of Medical Science. J.B.W. is an Early Career Scientist of the Howard Hughes Medical Institute.

Supplementary Materials

www.sciencemag.org/content/343/6171/649/suppl/DC1
Materials and Methods
Figs. S1 to S14
References (*33*–*35*)
Movies S1 to S5

12 July 2013; accepted 6 January 2014
10.1126/science.1243126

Distribution of ESCRT Machinery at HIV Assembly Sites Reveals Virus Scaffolding of ESCRT Subunits

Schuyler B. Van Engelenburg,[1] Gleb Shtengel,[2] Prabuddha Sengupta,[1] Kayoko Waki,[3] Michal Jarnik,[1] Sherimay D. Ablan,[3] Eric O. Freed,[3] Harald F. Hess,[2] Jennifer Lippincott-Schwartz[1]*

The human immunodeficiency virus (HIV) hijacks the endosomal sorting complexes required for transport (ESCRT) to mediate virus release from infected cells. The nanoscale organization of ESCRT machinery necessary for mediating viral abscission is unclear. Here, we applied three-dimensional superresolution microscopy and correlative electron microscopy to delineate the organization of ESCRT components at HIV assembly sites. We observed ESCRT subunits localized within the head of budding virions and released particles, with head-localized levels of CHMP2A decreasing relative to Tsg101 and CHMP4B upon virus abscission. Thus, the driving force for HIV release may derive from initial scaffolding of ESCRT subunits within the viral bud interior followed by plasma membrane association and selective remodeling of ESCRT subunits.

One of the key host factors human immunodeficiency virus (HIV) relies on to complete its infection cycle is the endosomal sorting complexes required for transport (ESCRT). By recruiting this machinery, HIV is able to mediate the final step of virus particle fission from the membrane. Otherwise, virus egress is severely inhibited (*1*–*5*). Despite great progress in demonstrating the ESCRT machinery's role in mediating HIV abscission, the nanoscale organization, and thus function, of ESCRT subcomplexes at native HIV assembly sites remains poorly defined.

ESCRT machinery participates in important cellular membrane remodeling events, such as cytokinesis and multivesicular body biogenesis (MVB), organizing into three general sets of subcomplexes. One set includes ESCRT-0, -I, and -II, which interact directly with cargo or scaffold proteins to direct assembly of downstream ESCRT complexes. Another set includes ESCRT-III subunits, which are thought to polymerize on membranes into a helical architecture to constrict and abscise membrane buds formed by early ESCRT/cargo complexes (*6*, *7*). The final set consists of the AAA+ adenosine triphosphatases (ATPases) Vps4A and Vps4B, which are thought to be necessary for HIV abscission through ESCRT-III filament remodeling and/or recycling (*7*–*9*). Together, the three sets of ESCRT subcomplexes cooperate to drive cellular membrane remodeling. Structural

[1]Cell Biology and Metabolism Program, Eunice Kennedy Shriver National Institute of Child Health and Human Development, Bethesda, MD 20892, USA. [2]Janelia Farm Research Campus, Howard Hughes Medical Institute, Ashburn, VA 20147, USA. [3]Virus-Cell Interaction Section, HIV Drug Resistance Program, Center for Cancer Research, National Cancer Institute, Frederick National Laboratory for Cancer Research, Frederick, MD 21702, USA.

*Corresponding author. E-mail: lippincj@mail.nih.gov

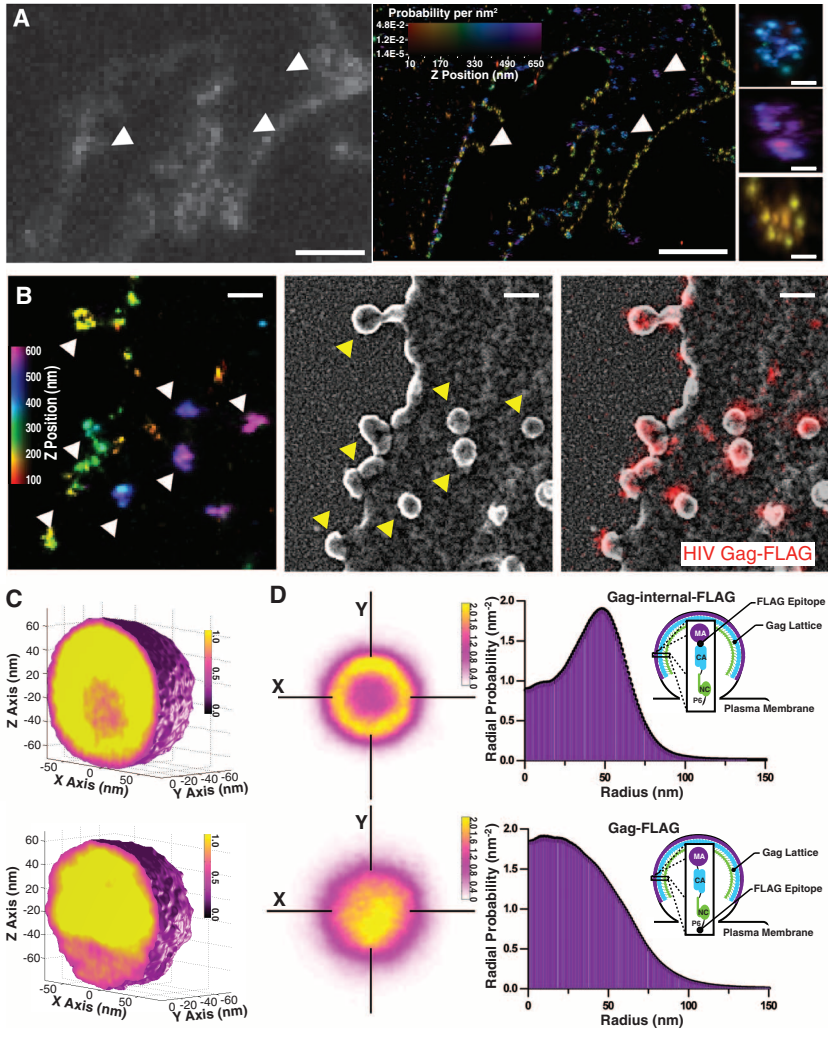

Fig. 1. Interferometric superresolution microscopy resolves the 3D organization of cell-associated HIV particles. (**A**) Diffraction-limited (left) and iPALM-based superresolution (right) images of COS7 cells expressing HIV Gag-FLAG labeled with AlexaFluor 647 (AF647)–conjugated antibody (Life Technologies, Grand Island, NY). Gag clusters from different surfaces of the membrane are clearly resolved (pseudocolored for height; white arrowheads). Scale bars, 10 μm (full image); 100 nm (right). (**B**) Correlative iPALM (left) and SEM (middle) demonstrate HIV Gag-FLAG clusters to be membrane-enveloped particles (overlay, right). Scale bars, 250 nm. (**C**) Probability density of aligned clusters from HIV Gag-internal-FLAG (top, n = 1181 clusters) and HIV Gag-FLAG (bottom, n = 1398 clusters) highlight the shell-like lattice (isosurface threshold = 0.5 localizations × nm^{-3}). (**D**) Probability slices (10 nm) display a ring-like distribution for Gag-internal-FLAG clusters (top middle) compared with the more compact Gag-FLAG clusters (bottom middle). Distance between crosshatch is 100 nm (right). Radial averages highlight the density differences owing to probe position within the HIV Gag molecule (inset model).

information obtained by means of in vitro assembly (*7*, *10*) and cellular overexpression studies (*11*) suggest a model of bud formation and abscission in which ESCRT-III filaments encircle and constrict the aperture of a membrane protrusion, acting on the base of the neck, in trans from the protrusion head. On the other hand, when directed by the midbody scaffold during cytokinesis (*12*, *13*) ESCRT-III filaments appear to polymerize from the scaffold and constrict the membrane, acting in cis with respect to the scaffolding structure. Whether ESCRT-III filaments polymerize at HIV bud sites in cis or trans to the scaffolding structure is not known because of the small dimensions of a budding HIV virion (120 to 140 nm diameter). Consequently, it remains unclear how ESCRT machinery acts to mediate viral membrane abscission and propagate HIV infection.

We used interferometric photoactivated-localization microscopy (iPALM) (*14*) to decipher the three-dimensional (3D) nanoscale organization of ESCRT components at HIV assembly sites and thereby gained insight into the mechanism for viral membrane abscission (supplementary text). ESCRT subcomplexes were selected for our analysis on the basis of their direct interaction with the structural HIV protein Gag [ESCRT-I subunit tumor susceptibility gene 101 (Tsg101)] (*15*) and their role in HIV membrane abscission (ESCRT-III and Vps4; CHMP2A, CHMP4B, and Vps4A) (*16*). The ESCRT proteins were modified with either green fluorescent protein (GFP) or photoswitchable cyan fluorescent protein 2 (PSCFP2) and stably expressed in COS7 cells. Stable cell lines expressing fluorescent ESCRT probes were validated for proper function (supplementary text).

Superresolution image analysis of HIV Gag demonstrated the ability of the iPALM method to sensitively locate and resolve subviral details of membrane-enveloped particles emanating from the plasma membrane of expressing cells (Fig. 1 and supplementary text). With the capacity to differentiate subviral protein organization within HIV bud structures, we next performed two-channel iPALM imaging of both HIV Gag and ESCRT subcomplexes. Imaging of HIV Gag and ESCRT-I (PSCFP2-Tsg101) revealed a small cytosolic pool of Tsg101 protein punctuated by clustering at Gag assembly sites (Fig. 2A and fig. S6A). PSCFP2-Tsg101 was localized within the interior of the Gag lattice of assembling particles (Fig. 2D), which is consistent with the direct interaction between the p6 domain of HIV Gag and the UEV domain of Tsg101 (*3*). PSCFP2-CHMP2A and -CHMP4B (ESCRT-III) cell lines expressing HIV Gag showed high cytosolic pools of PSCFP2 followed by membrane-localized co-clustering with Gag clusters (Fig. 2, A to D, and fig. S6B). When co-clustering was observed, the 3D distribution of ESCRT-III and Gag at assembly sites was similar and distinctly separable from the cytosolic pool of PSCFP2-CHMP2A or -CHMP4B (Fig. 2, A, B, and D). To correlate the apparent observation

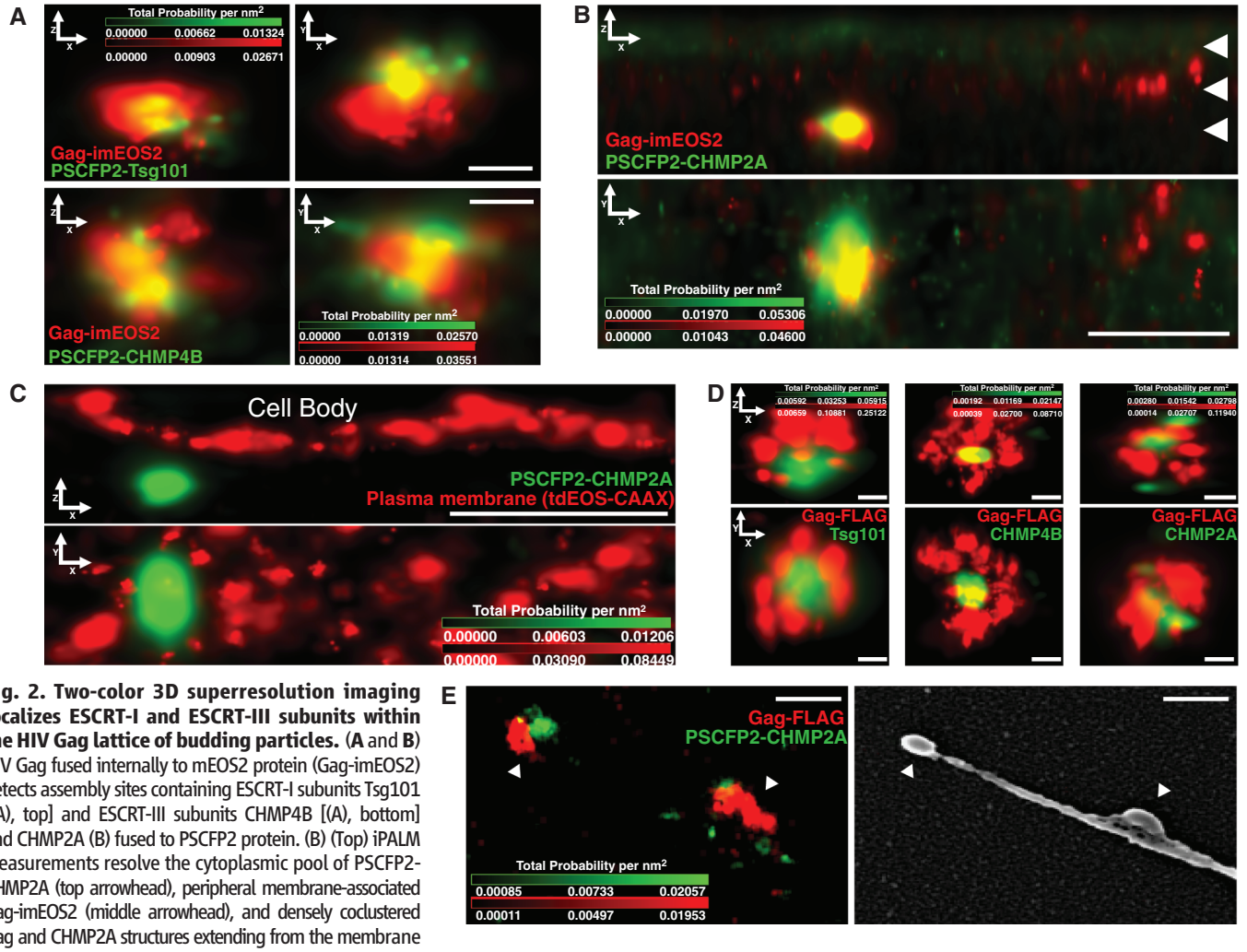

Fig. 2. Two-color 3D superresolution imaging localizes ESCRT-I and ESCRT-III subunits within the HIV Gag lattice of budding particles. (**A** and **B**) HIV Gag fused internally to mEOS2 protein (Gag-imEOS2) detects assembly sites containing ESCRT-I subunits Tsg101 [(A), top] and ESCRT-III subunits CHMP4B [(A), bottom] and CHMP2A (B) fused to PSCFP2 protein. (B) (Top) iPALM measurements resolve the cytoplasmic pool of PSCFP2-CHMP2A (top arrowhead), peripheral membrane-associated Gag-imEOS2 (middle arrowhead), and densely coclustered Gag and CHMP2A structures extending from the membrane (bottom arrowhead). Scale bars, 100 nm (A); 500 nm (B). (**C**) PSCFP2-CHMP2A coexpressed with unlabeled HIV Gag and membrane marker tdEOS-farnesyl (red) show displacement of a CHMP2A cluster (green) extending beyond the plane of the plasma membrane. Scale bar, 500 nm. (**D**) Single clusters representative of AF647-labeled Gag-FLAG and PSCFP2-ESCRT probes. Axial (top) and lateral (bottom) views show localization of PSCFP2-ESCRT probes within the HIV Gag lattice. Scale bars, 50 nm. (**E**) Correlative two-color iPALM and SEM of two virus-like particles (white arrowheads) emanating from a cell expressing Gag-FLAG (red) and PSCFP2-CHMP2A (green). The left membrane bud shows confinement of PSCFP2-CHMP2A to the head of the particle. The particle on the right is at an earlier stage of budding, apparent from the extended lateral fluorescence distribution (right arrowhead). Scale bar, 250 nm.

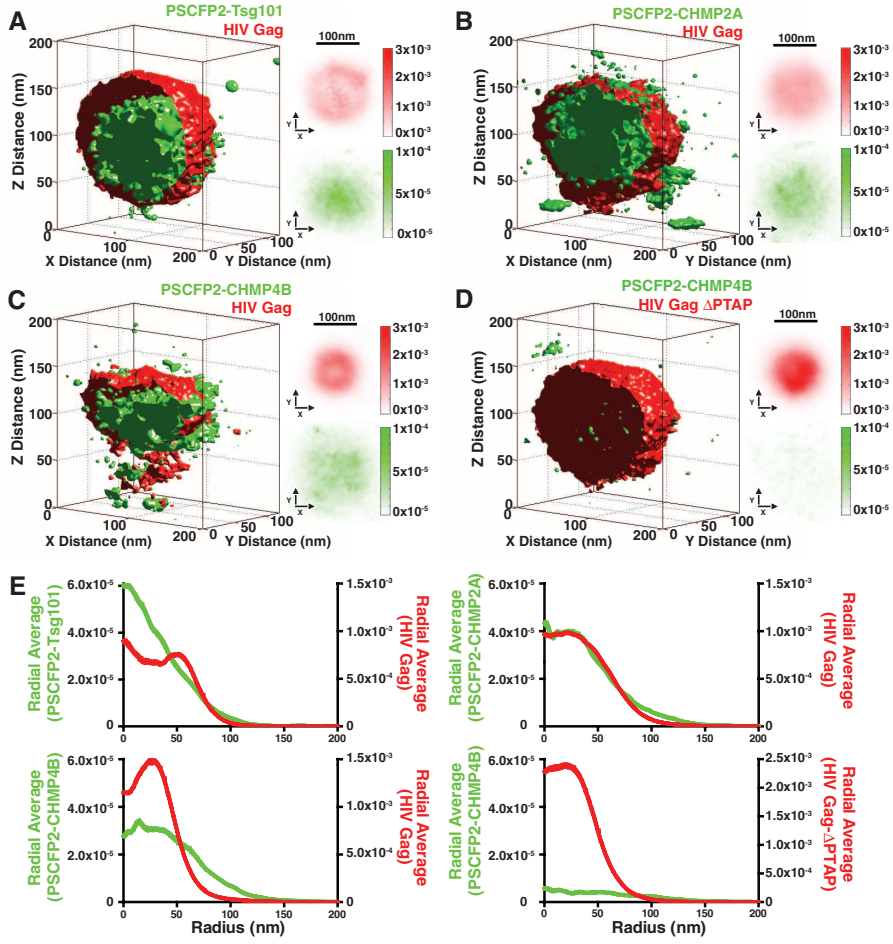

Fig. 3. Single-cluster averaging demonstrates ESCRT subunits within the interior of the HIV Gag lattice. (**A** to **D**) Cell-associated HIV Gag-FLAG clusters from PSCFP2-ESCRT–expressing cells were subjected to 3D single-cluster averaging [(A) PSCFP2-Tsg101, n = 313 clusters; (B) PSCFP2-CHMP2A, n = 460 clusters; (C) PSCFP2-CHMP4B, n = 509 clusters; and (D) PSCFP2-CHMP4B/HIV Gag ΔPTAP, n = 278 clusters]. Two-color isosurfaced probability densities show a high-probability core of PSCFP2-Tsg101 (A) and ESCRT-III subunits PSCFP2-CHMP2A/CHMP4B [(B) and (C)] (green) with respect to the HIV Gag lattice (red) (isosurface threshold, HIV Gag-FLAG = 2.5×10^{-4} nm^{-3} and PSCFP2-ESCRTs = 2.5×10^{-5} nm^{-3}). Right insets [(A) to (D)] depict 40-nm sections along the z axis [top HIV Gag (red), bottom PSCFP2-ESCRT (green)]. (D) A marked reduction in the probability density of PSCFP2-CHMP4B signal was observed upon expression of release-defective HIV Gag-FLAG ΔPTAP. (**E**) Radial average plots of sections from (A) to (D) define the highest-probability densities of ESCRT (green) subunits residing within the HIV Gag probability shell (red). Approximately 90% of PSCFP2-Tsg101 (top left), 80% of PSCFP2-CHMP2A (top right), and 61% of PSCFP2-CHMP4B (bottom right) integrated probability reside within the half-maximum Gag probability shell, whereas 10% of the integrated probability for PSCFP2-CHMP4B remains when ESCRT-I recruitment is inhibited (Gag-FLAG ΔPTAP; bottom right). Line thickness represents SEM and is <1 nm.

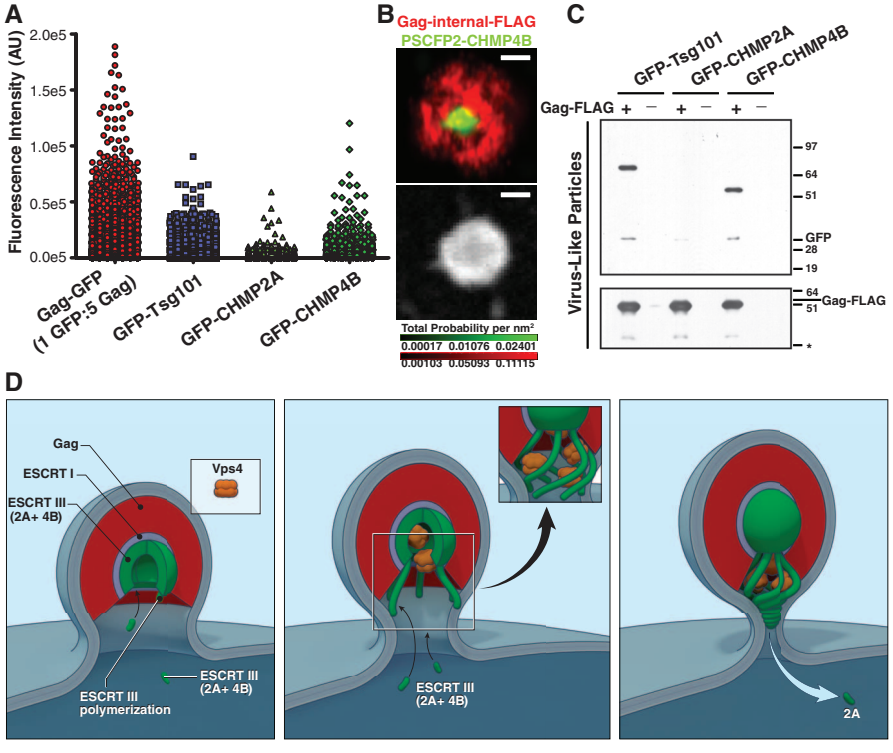

Fig. 4. Released VLPs contain ESCRT-I and ESCRT-III subunits, but reduced levels of CHMP2A relative to CHMP4B. (**A**) Quantitative fluorescence microscopy analysis of GFP-ESCRT and Gag-GFP containing single particles. The fluorescence intensity of Gag-GFP is predicted to arise from ~600 to 1000 molecules (assuming 3000 to 5000 Gag molecules per particle), suggesting that signal from GFP-ESCRT particles corresponds to hundreds of molecules per particle (data represent ≥25,000 particles from ≥2 independent samples for each probe). (**B**) Correlative two-color iPALM and scanning electron micrographs of a single released (top, red) Gag- and (top, green) CHMP4B-positive VLP. Image registration residual uncertainty of 11 nm. Scale bar, 50 nm. (**C**) Western blot analysis of purified VLP fraction from GFP-ESCRT stable cell lines. GFP-Tsg101 and GFP-CHMP4B are detected in released particles (top); however, GFP-CHMP2A levels are dramatically reduced from VLPs upon particle release (bottom; asterisk indicates proteolysis product). Reduction in the levels of GFP-CHMP2A in released particles correlates between the biochemical and fluorescence data. (**D**) Proposed virus-scaffolding model for ESCRT-mediated HIV particle release from host cells. A pre-scission pool of ESCRT-I subunit Tsg101 (gray) interacts with HIV Gag (red), leading to assembly of ESCRT-III subunits CHMP4B and CHMP2A (green). Hypothetical ESCRT-III polymerization beyond the Gag lattice and Vps4 (orange) remodeling of CHMP2A subunits leads to membrane aperture constriction and particle abscission (middle and right).

of ESCRT-III signal residing beyond the plane of the plasma membrane, we visualized the plasma membrane using a lipidated fluorescent probe. PSCFP2-CHMP2A signal was observed in discrete distributions extending away from the cytosol and beyond the membrane plane in Gag-expressing cells (Fig. 2C). Co-clusters of HIV Gag and PSCFP2-CHMP2A were confirmed with scanning electron microscopy (SEM) to be membrane-budding structures resembling virus-like particles (Fig. 2E). We further confirmed our observations of ESCRT-III localization to the HIV Gag interior using immunogold transmission electron microscopy (fig. S7).

To facilitate a robust statistical analysis of ESCRT organization at HIV assembly sites, we performed two-color single-particle averaging. The resulting probability distributions of PSCFP2-ESCRT probes and HIV Gag revealed significant signal from each ESCRT subunit within the interior of the viral lattice (Fig. 3, A to C; fig. S8; and supplementary text). Radially averaged probability density plots of HIV Gag and ESCRT probes revealed 92% of PSCFP2-Tsg101, 61% of PSCFP2-CHMP4B, 80% of PSCFP2-CHMP2A, and 78% of PSCFP2-Vps4A integrated probability residing within the estimated radius of the HIV Gag shell (Fig. 3E). This analysis highlighted a pool of PSCFP2-CHMP4B residing beyond the HIV Gag lattice (39% remaining probability), potentially indicating a signature of ESCRT-III polymer extending toward the neck of the budding structure. As a control, we observed an order of magnitude less PSCFP2-CHMP4B signal residing within the probability shell of mutant Gag particles, unable to recruit ESCRT-I ($Gag^{\Delta PTAP}$) (*1*, *2*), as compared with wild-type Gag (Fig. 3, D and E). This suggests that the Gag PTAP motif is required for localizing ESCRT-III subunits to the particle interior. These results support our single-particle observations and highlight a distinct scaffolding mechanism of ESCRT-III and Vps4A subunits within the interior of the Gag lattice.

The presence of ESCRT-III subunits within the Gag lattice suggests that a portion of this pool may become trapped within the viral particle while mediating bud neck constriction and abscission. To test this possibility, we purified virus-like particles (VLPs) from GFP-ESCRT–expressing cells and performed quantitative fluorescence microscopy (Fig. 4A). Using HIV Gag-GFP as a molecular standard, we estimated that on average hundreds of copies of GFP-ESCRT probes reside within released particles. Qualitative coincidence detection between Gag-mCherry and GFP-ESCRT proteins showed that GFP-ESCRT probes were detected in the majority of released particles (50 to 90%) (fig. S9). Correlative two-color iPALM and SEM imaging confirmed the presence of ESCRT probes within released VLPs (Fig. 4B). Western blot analysis showed that GFP-Tsg101 and GFP-CHMP4B were readily detected in purified VLP fractions (Fig. 4C). Levels of GFP-CHMP2A, but not GFP-CHMP4B or GFP-Tsg101, were reduced in released virus particles relative to membrane-associated particles (Fig. 3, A to C). This suggested that CHMP2A subunits may undergo selective remodeling upon virus abscission. This may be mediated by the ATPase activity of Vps4, given the established interaction between Vps4 and CHMP2A (*17*).

Current models have been unable to distinguish whether ESCRTs localize to the base of the neck of a virion (in trans) or to the head of the virion (in cis) in order to constrict and release the viral particle from the plasma membrane. Our results show that ESCRT-III and Vps4A probes concentrate on the interior of the HIV Gag lattice and occupy a similar volume to that of ESCRT-I. This architecture is consistent with previous cytokinesis observations that ESCRT-III subunits initiate proximal to the midbody scaffold protein CEP55 and ESCRT-I (*12*). Indeed, HIV Gag and CEP55 share features, such as dual Tsg101 and ALIX recruitment domains (*18*–*20*), as well as an apparent independence of ESCRT-II for mediating membrane abscission (*19*–*21*). Collectively, these observations suggest that structural proteins, such as HIV Gag and CEP55, act to nucleate structures composed of ESCRT-I, ESCRT-III, and Vps4 subunits (supplementary text). These subunits then serve as distinct templates (acting in cis relative to the structural scaffold) for ESCRT-III polymerization and Vps4-mediated disassembly/remodeling of CHMP2A, ultimately leading to membrane abscission (Fig. 4C). Further studies will be required to dissect the interplay between scaffolding and polymerizing/depolymerizing pools of ESCRT-III and the role this dynamism plays in mediating viral membrane constriction and abscission.

References and Notes

1. M. Huang, J. M. Orenstein, M. A. Martin, E. O. Freed, *J. Virol.* **69**, 6810–6818 (1995).
2. H. G. Göttlinger, T. Dorfman, J. G. Sodroski, W. A. Haseltine, *Proc. Natl. Acad. Sci. U.S.A.* **88**, 3195–3199 (1991).
3. J. E. Garrus *et al.*, *Cell* **107**, 55–65 (2001).
4. D. G. Demirov, A. Ono, J. M. Orenstein, E. O. Freed, *Proc. Natl. Acad. Sci. U.S.A.* **99**, 955–960 (2002).
5. J. Martin-Serrano, T. Zang, P. D. Bieniasz, *Nat. Med.* **7**, 1313–1319 (2001).
6. T. Wollert, C. Wunder, J. Lippincott-Schwartz, J. H. Hurley, *Nature* **458**, 172–177 (2009).
7. S. Lata *et al.*, *Science* **321**, 1354–1357 (2008).
8. V. Baumgärtel *et al.*, *Nat. Cell Biol.* **13**, 469–474 (2011).
9. N. Jouvenet, M. Zhadina, P. D. Bieniasz, S. M. Simon, *Nat. Cell Biol.* **13**, 394–401 (2011).
10. G. Fabrikant *et al.*, *PLOS Comput. Biol.* **5**, e1000575 (2009).
11. P. I. Hanson, R. Roth, Y. Lin, J. E. Heuser, *J. Cell Biol.* **180**, 389–402 (2008).
12. N. Elia, R. Sougrat, T. A. Spurlin, J. H. Hurley, J. Lippincott-Schwartz, *Proc. Natl. Acad. Sci. U.S.A.* **108**, 4846–4851 (2011).
13. J. Guizetti *et al.*, *Science* **331**, 1616–1620 (2011).
14. G. Shtengel *et al.*, *Proc. Natl. Acad. Sci. U.S.A.* **106**, 3125–3130 (2009).
15. Y. J. Im *et al.*, *Structure* **18**, 1536–1547 (2010).
16. E. Morita *et al.*, *Cell Host Microbe* **9**, 235–242 (2011).
17. T. Obita *et al.*, *Nature* **449**, 735–739 (2007).
18. H. H. Lee, N. Elia, R. Ghirlando, J. Lippincott-Schwartz, J. H. Hurley, *Science* **322**, 576–580 (2008).
19. J. G. Carlton, J. Martin-Serrano, *Science* **316**, 1908–1912 (2007).
20. E. Morita *et al.*, *EMBO J.* **26**, 4215–4227 (2007).
21. C. Langelier *et al.*, *J. Virol.* **80**, 9465–9480 (2006).

Acknowledgments: The authors are thankful for insight and helpful discussions from N. Elia, B. Kopek, and B. Lorenz. The authors are grateful to R. Villasmil for assistance with flow cytometry and N. Tsai for DNA sequencing. The authors also thank P. Bieniasz and M. Davidson for providing vectors.

Supplementary Materials

www.sciencemag.org/content/343/6171/653/suppl/DC1
Materials and Methods
Figs. S1 to S10
References (*22*–*33*)

29 October 2013; accepted 8 January 2014
Published online 16 January 2014;
10.1126/science.1247786

A Structurally Distinct Human Mycoplasma Protein that Generically Blocks Antigen-Antibody Union

Rajesh K. Grover,[1,2]* Xueyong Zhu,[3]* Travis Nieusma,[3] Teresa Jones,[1] Isabel Boero,[1] Amanda S. MacLeod,[4] Adam Mark,[5] Sherry Niessen,[6] Helen J. Kim,[3] Leopold Kong,[3] Nacyra Assad-Garcia,[7] Keehwan Kwon,[7] Marta Chesi,[8] Vaughn V. Smider,[1] Daniel R. Salomon,[5] Diane F. Jelinek,[9,10] Robert A. Kyle,[9,10] Richard B. Pyles,[11,12] John I. Glass,[7] Andrew B. Ward,[3] Ian A. Wilson,[3,13] Richard A. Lerner[1,2]†

We report the discovery of a broadly reactive antibody-binding protein (Protein M) from human mycoplasma. The crystal structure of the ectodomain of transmembrane Protein M differs from other known protein structures, as does its mechanism of antibody binding. Protein M binds with high affinity to all types of human and nonhuman immunoglobulin G, predominantly through attachment to the conserved portions of the variable region of the κ and λ light chains. Protein M blocks antibody-antigen union, likely because of its large C-terminal domain extending over the antibody-combining site, blocking entry to large antigens. Similar to the other immunoglobulin-binding proteins such as Protein A, Protein M as well as its orthologs in other *Mycoplasma* species could become invaluable reagents in the antibody field.

Clonal B cell proliferation, as well as lymphomas and myelomas, can result from chronic infections with organisms such as *Escherichia coli*, *Helicobacter pylori*, and Hepatitis C virus. (*1*–*6*). The main feature seems to be the approximation of two systems, each capable

of sustained replication in which the replicating microbe induces proliferation and selection of members of the replicating B cell repertoire. In this regard, we investigated mycoplasma infection because it has the features of chronicity (*7*) and, as an obligatory parasite, is largely confined to the surface of cells (*8*, *9*). In the course of our experiments, we discovered that some human mycoplasmas produce a protein that binds to immunoglobulins (Igs) with high affinity. This protein, which we refer to as Protein M, has a structure that differs from all others in the Protein Data Bank (PDB).

Because we were interested in clonal B cell proliferation in the context of chronic infections, we investigated whether monoclonal antibodies produced as a result of multiple myeloma react with mycoplasma antigens. We tested the ability of plasma from 20 multiple myeloma patients (*10*) to bind to total cellular extracts from multiple mycoplasma species, including human pathogens or commensal organisms and others that infect nonhuman vertebrates. Remarkably, these experiments showed that the antibodies in the plasma all reacted strongly with molecules present in human, but not nonhuman, pathogenic mycoplasmas (Fig. 1A and fig. S1A). The main reactivity was with a protein with an apparent molecular weight of ~50 kD in *Mycoplasma genitalium* and with several proteins with apparent molecular weights of 40 to 65 kD in *Mycoplasma penetrans* (Fig. 1A). We focused our attention on the protein from *M. genitalium* because it appeared to be more homogeneous as determined with gel electrophoresis (Fig. 1A). The Ig reactivity with the *M. genitalium* protein was similar for all patients' plasma tested (fig. S1A). To substantiate that the clonal multiple myeloma Ig is the component responsible for binding to the *M. genitalium* protein, as opposed to a highly reactive protein that copurifies with it, the Fab′ (fragment antigen-binding) of the primary monoclonal antibody in the plasma of multiple myeloma patient 13PL (13PL Fab′) was highly purified by chromatography followed by crystallization, and its reactivity was studied by using dissolved crystals as a source of the antibody (Fig. 1, B to D). The 13PL Fab′ from the dissolved crystals bound to the same antigen in mycoplasmas as antibodies isolated from whole sera (Fig. 1C). To confirm that the crystals contained an antibody, the x-ray structure was determined at 1.2 Å resolution, and only a Fab′ was present (Fig. 1D). To test whether a similar reactivity could be found in blood from nonmyeloma normal donors (fig. S1B), samples from random donors were studied. The sera from these normal donors also surprisingly reacted with the same mycoplasma proteins as did the clonal myeloma Igs, indicating that the ability of human Igs to react with this mycoplasma protein was not confined to those produced in multiple myeloma. We therefore termed the *M. genitalium* protein that reacts with Ig as Protein M.

At this point, the possibilities were that Protein M was an antigen to which most people make an antibody or was a protein that binds to Ig domains or other features that are present in most antibodies. To study these possibilities, we first isolated Protein M using an affinity column constructed from antibody 13PL. The affinity-purified Protein M was separated on SDS–polyacrylamide gel electrophoresis (SDS-PAGE) gels followed by Western blot analysis by using a different myeloma antibody to confirm the presence of the binding protein. The band on the SDS-PAGE gel corresponding to Protein M was excised, and proteomics analysis with mass spectrometry was carried out (fig. S2A). These studies showed that Protein M was *M. genitalium* protein MG281, which is an uncharacterized membrane protein (UniProtKB accession no. P47523) (fig. S2B) of 556 amino acids with a predicted transmembrane domain (residues 16 to 36) (fig. S2C). Furthermore, homologs of Protein M are present in other mycoplasma strains, such as *Mycoplasma pneumonia*, *Mycoplasma iowae*, and *Mycoplasma gallisepticum* (UniProtKB database). Antibodies did not bind to mycoplasma extracts from a Protein M–null *M. genitalium* mutant, again suggesting that Protein M might be the molecule to which antibodies bind (fig. S3A). To establish that Protein M alone is sufficient for antibody binding, a His-tagged Protein M lacking the membrane-spanning region (recombinant Protein M, residues 37 to 556) was cloned, expressed in *E. coli*, and purified by means of affinity chromatography and size-exclusion chromatography. Western blot analysis of purified Protein M showed that it reacted strongly with the monoclonal Ig from a multiple myeloma patient (fig. S3B). Protein M also bound to all isotypes of

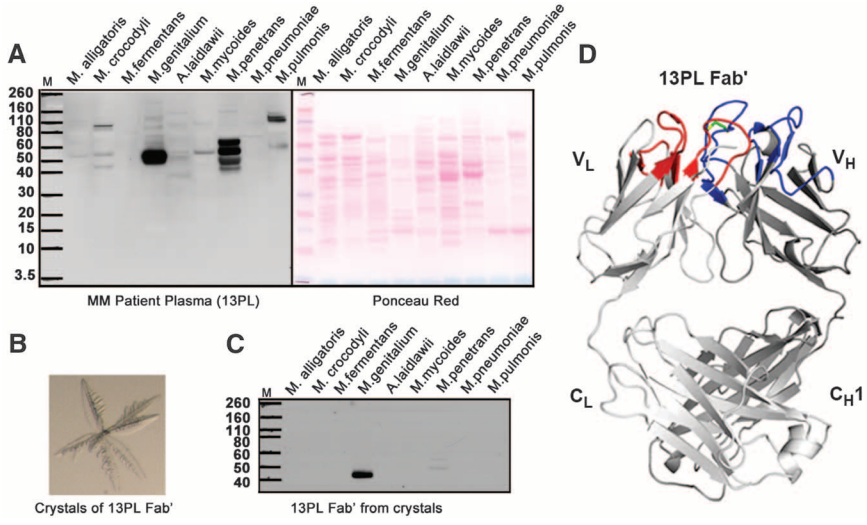

Fig. 1. Igs selectively bind to proteins in human mycoplasma. (**A**) (Left) Western blot analysis of the reactivity of plasma from multiple myeloma patient 13PL with cell extracts from *Mycoplasma alligatoris*, *Mycoplasma crocodyli*, *Mycoplasma fermentans*, *M. genitalium*, *Acholeplasma laidlawii*, *Mycoplasma mycoides*, *M. penetrans*, *Mycoplasma pneumoniae*, and *Mycoplasma pulmonis.* All mycoplasma cells were grown in appropriate media. Cells were lysed according to manufacturer's protocol by using lysis buffer from Sigma Aldrich (St. Louis, MO). Nucleic acids were degraded by means of treatment with deoxyribonuclease and ribonuclease. A protease inhibitor cocktail (Roche, Basel, Switzerland) was added to prevent proteolytic degradation. The extracts from the same number of cells were separated on SDS-PAGE gels and transferred to nitrocellulose membranes for Western blot analysis. (Right) Ponceau red-stained protein bands of the cell extracts. (**B**) Crystals of 13PL Fab′ from a multiple myeloma patient's monoclonal immunoglobulin. (**C**) Western blot analysis of the reactivity of 13PL Fab′ from the plasma of a multiple myeloma patient with the same cell extracts in (A). The 13PL Fab′ was purified by means of crystallization. The extracts were separated on SDS-PAGE gels as described in (A). (**D**) Crystal structure of 13PL Fab′ shown in ribbon diagram, with the light and heavy chains colored in light and dark gray, respectively. The loops corresponding to CDRs L1, L2, and L3 are colored red, whereas CDRs H1, H2, and H3 are colored blue. The relatively rare disulfide in human CDR3s is colored green.

[1]Department of Cell and Molecular Biology, The Scripps Research Institute, La Jolla, CA 92037, USA. [2]Department of Chemistry, The Scripps Research Institute, La Jolla, CA 92037, USA. [3]Department of Integrative Structural and Computational Biology, The Scripps Research Institute, La Jolla, CA 92037, USA. [4]Department of Immunology and Microbial Science, The Scripps Research Institute, La Jolla, CA 92037, USA. [5]Department of Molecular and Experimental Medicine, The Scripps Research Institute, La Jolla, CA 92037, USA. [6]The Center for Physiological Proteomics, The Scripps Research Institute, La Jolla, CA 92037, USA. [7]Synthetic Biology and Bioenergy Group, J. Craig Venter Research Institute, Rockville, MD 20850, USA. [8]Comprehensive Cancer Center, Mayo Clinic Arizona, Scottsdale, AZ 85259, USA. [9]Department of Internal Medicine, Division of Hematology, College of Medicine, Mayo Clinic, Rochester, MN 55905, USA. [10]Department of Immunology, College of Medicine, Mayo Clinic, Rochester, MN 55905, USA. [11]Department of Pediatrics, University of Texas Medical Branch, Galveston, TX 77555, USA. [12]Department of Microbiology and Immunology, University of Texas Medical Branch, Galveston, TX 77555, USA. [13]Skaggs Institute for Chemical Biology, The Scripps Research Institute, La Jolla, CA 92037, USA.

*These authors contributed equally to this work.
†Corresponding author. E-mail: rlerner@scripps.edu

human IgGs (fig. S4A) as well as mouse, rat, rabbit, goat, and bovine IgGs (fig. S4B). To further elucidate the minimum sequence responsible for antibody binding, the Protein M and 13PL IgG complex (mixed in a 1:1.1 molar ratio) was incubated with trypsin for 5 hours. SDS-PAGE gel analysis showed that a truncated protein remained intact after 5 hours as compared with uncomplexed Protein M, which was totally digested into smaller fragments. The trypsin-digested Protein M (Protein M TD) was found by means of mass spectroscopy to contain residues 74 to 482 (fig. S5). A His-tagged Protein M TD consisting of residues 74 to 468 (recombinant Protein M TD) was then cloned, expressed in *E. coli*, and purified by means of affinity chromatography and size-exclusion chromatography. Protein M and Protein M TD showed similar binding affinities to a panel of Igs or Fabs with binding affinity (K_d) values in the nM range (fig. S6), as determined by using Biolayer Interferometry (*11*).

Ig binding to Protein M was confined to the Fab domain of the antibody molecule, as shown with Biolayer Interferometry (fig. S6). Because a variety of antibodies with different complementarity-determining regions (CDRs) all bind to Protein M, specific interaction with the combining site of the antibody molecule appeared to be excluded. To understand the molecular basis for this interaction, crystal structures of recombinant Protein M TD in complex with two antibody Fabs PGT135 against HIV-1 gp120 with a κ light chain (K_d = 3.7 nM) (*12*) and Fab CR9114 against influenza hemagglutinin with a λ light chain (K_d = 1.9 nM) (*13*) were determined to 1.65 and 2.50 Å resolution, respectively (Fig. 2 and table S1). Although the 13PL Fab′–Protein M TD complex could not be crystallized, we were able to obtain the structure through electron microscopy, which showed a similar mode of binding (fig. S7). The Protein M structure is very different from any other known Ig-binding proteins—such as Protein G, Protein A, and Protein L—or indeed any other structures in PDB (www.pdb.org) (*14*). Protein M TD comprises a large domain (residues 78 to 440) that includes a leucine-rich repeat (LRR)–like subdomain and a smaller domain (residues 441 to 468) (Fig. 2A). Protein M TD binds predominantly to the variable light (V_L) domains of both PGT135 Fab (Fig. 2B) and CR9114 Fab (Fig. 2C) but makes some very limited interactions with the other three Fab domains. The Fab–Protein M TD interactions bury total solvent-accessible surface areas of 3590 Å^2 and 2870 Å^2 for PGT135 Fab (Fig. 2D and figs. S8A and S9A) and CR9114 Fab (Fig. 2E and figs. S8B and S9B), respectively, mainly from the V_L domains of the Fabs (*15*). The common interacting positions, which are about two-thirds occupied by hydrophilic residues in both antibodies, are located on one edge of V_L (Fig. 2F and tables S2 and S3). Ten conserved hydrogen bonds and one salt bridge are

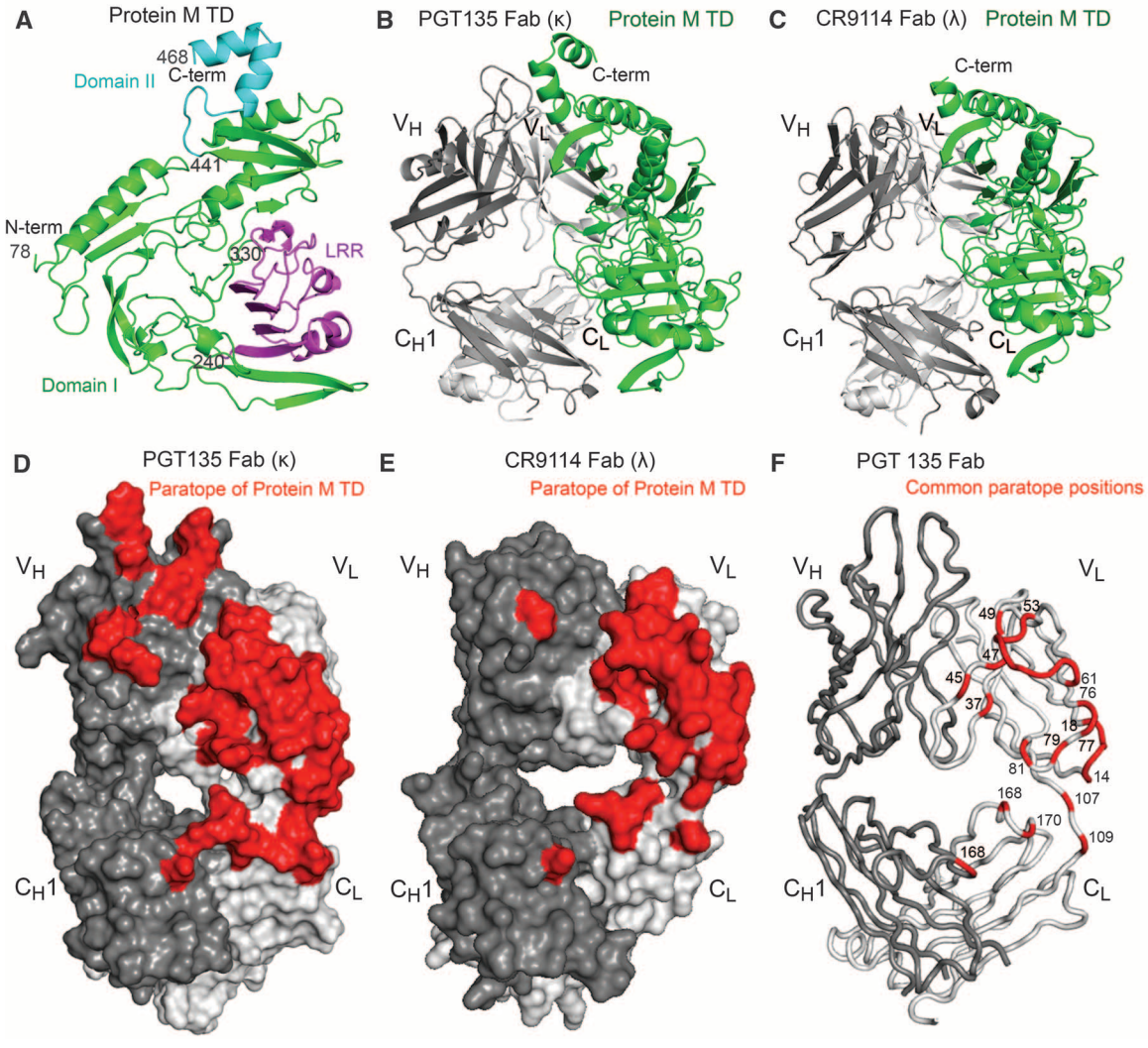

Fig. 2. Crystal structures of recombinant protein M TD in complex with PGT135 Fab and with CR9114 Fab. (**A**) Overall structure of Protein M TD from its complex with PGT135 Fab in ribbon representation. Protein M TD appears to have two main domains: a larger domain I in green (residues 78 to 440), which includes a LLR-like structure in purple (residues 240 to 330) and a smaller domain II in light blue (residues 441 to 468). (**B**) Overall structure of Protein M TD in complex with PGT135 Fab. Protein M TD is colored in green, and PGT135 Fab is colored in light gray for the light chain and dark gray for the heavy chain. Protein M TD predominantly binds V_L of PGT135 Fab but also interacts to a lesser extent with V_H, C_L, and C_H1. (**C**) Overall structure of Protein M TD in complex with CR9114 Fab. The coloring scheme is similar to that of (B). Residues 455 to 468 in domain II of Protein M TD were flexible and not modeled. Protein M TD predominantly binds V_L of CR9114 Fab. (**D**) Molecular surface representation of PGT135 Fab with the paratope of Protein M TD in red, Fab light chain in light gray, and Fab heavy chain in dark gray. (**E**) Molecular surface representation of CR9144 Fab with the paratope of Protein M TD and colored as in (D). (**F**) The common paratope residue locations (in red) of Protein M TD for PGT135 Fab and CR9114 Fab are shown on PGT135 Fab, including V_L residues 14 to 18 of FR1; 37, 45, 47, and 49 of FR2; 53 to 56 of CDR2; 57 to 61, 76, 77, 79, and 81 of FR3; residues 107 and 109 connecting V_L and C_L; as well as residues 168 and 170 of C_L and residue 168 of C_H1.

made from Protein M TD to each Fab V_L, including six hydrogen bonds to the main chain of V_L residues 15, 16, 18, 54, and 77, with the rest to the side chains of V_L Arg^{61}, Gln^{79}, and Glu^{81} (tables S2 and S3), almost all of which are highly conserved among human antibodies with both κ and λ light chains (table S4). Other residues at the common paratope positions, which make van der Waals contacts and nonconserved H-bonds or salt bridges, are less conserved except for V_L Gln^{37} and Pro^{59} (table S5) as well as the completely conserved C_L Ser^{168} and V_H1 Ser^{168}. However, some of the nonpolar interactions may be conserved even with different amino acids. The N- and C-terminal fragments (residues 37 to 74 and residues 469 to 556), which were truncated in Protein M TD as compared with Protein M, are likely disordered because the three-dimensional reconstructions of a Fab in complex with Protein M and Protein M TD by using negative-stain electron microscopy are nearly identical (figs. S10 and S11).

To determine the scope of Protein M binding to antibodies with different light-chain configurations and allotypes, the K_d of Protein M TD to 24 different light chains in a variety of formats were determined. Because the heavy chains potentially could alter the light-chain conformations, we studied the same germline light chain paired with three different heavy chains. The particular heavy chains made little difference, and the K_d varied between 1.5 and 4.8 nM for four V_H/V_L combinations (fig. S12, A to C). Similarly, when the same heavy chain was paired with four different light chains, Protein M binding ranged from 1.8 to 2.4 nM (fig. S12, D to G). We evaluated the effect of allotypic variation using five κ chain allotypes (κ1, κ2, κ3, κ4, and κ6) and three λ chain allotypes (λ2, λ5, and λ11). Allotypic variation had little effect, and the K_d for the allotypic variants ranged between 1.0 and 4.8 nM (fig. S12 and table S6). The preservation of binding affinity in the presence of allotypic variation is to be expected because the critical Protein M contacts are largely conserved among allotypes (tables S4 and S5). To determine whether antigen specificity affected Protein M, we determined K_d for Protein M TD binding to a panel of eight affinity-matured monoclonal antibodies against the same HIV-1 gp120 antigen but with different epitopes and found that K_d only varied between 0.7 and 3.8 nM (fig. S12, Q to X, and table S6).

Last, we assessed the percentage of polyclonal human Igs from the plasma of normal blood donors that was capable of binding to Protein M. After two passages through a column containing Protein M TD immobilized on Ni–nitrilotriacetic acid matrix at a flow rate of 1 ml/min, >90% of all the Igs were removed, which is in agreement with our data that showed Protein M binds to all human monoclonal antibodies that we have tested to date.

These structural studies suggested that Protein M should preclude the ability of the antibody to bind to its antigen because it displaces or distorts the CDRs and/or may use its C-terminal domain to sterically block entrance to the antibody-combining site (fig. S13). We tested the ability of recombinant Protein M and Protein M TD to block antigen-antibody union for six different antigen-antibody pairs, including two polyclonal auto-antibodies. The monoclonal antibodies used were generated against human influenza virus (*13*), HIV-1 (*16*), human Ebola (*17*), and mouse Ebola (*18*); polyclonal antibodies were purified from Goodpasture's disease patient serum (*19*) and lupus mouse serum (*20*). Blocking of the binding of serum polyclonal antibodies to antigens by Protein M is important because such sera represents a collection of antibodies rather than a single monoclonal species. Prior incubation of the antibodies with Protein M or Protein M TD (in a 1:8 molar ratio) strongly inhibited antibody binding to its cognate antigen (Fig. 3), but the order of addition is critical. Once antigen-antibody union has occurred for high-affinity antigens, Protein M does not disrupt the antibody-antigen complex (fig. S14).

This discovery, of a heretofore unknown high-affinity Ig-binding protein in human *M. genitalium*, should be considered in the context of other known Ig-binding proteins, such as Protein G, Protein A, and Protein L (*21*–*23*), which have been invaluable reagents and tools in the antibody field. The Protein M structure is very different from these other Ig-binding proteins and is also very

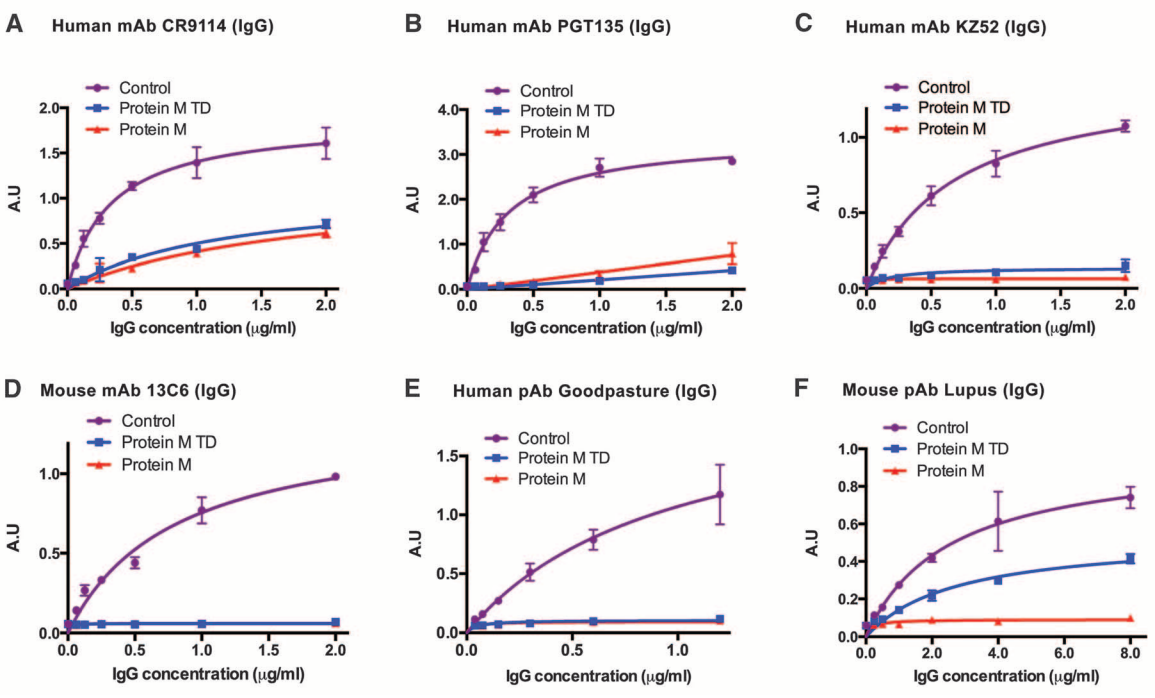

Fig. 3. Protein M blocks antigen-antibody union. (**A**) Binding of CR9114 IgG, a human broadly neutralizing antibody against influenza virus to one of its antigens, H5 hemagglutinin [influenza virus strain A/Viet Nam/1203/2004 (H5N1)] was evaluated by using enzyme-linked immunosorbent assay (ELISA) after precomplexing with recombinant Protein M (red) and Protein M TD (blue) (at a 1:8 molar ratio). Binding of the IgG to the HA in the absence of protein M was used as control (purple). The extent of binding was analyzed with a colorimetric assay. The curves were obtained with a nonlinear regression analysis in which the data were fit to a four-parameter logistic equation based on a simple binding model. Error bars represent SD of duplicate measurements. (**B**) Binding of PGT135 IgG, a human broadly neutralizing antibody against its antigen HIV-1 gp120 (JR-FL gp120 core construct) was evaluated (purple) after precomplexing PGT135 IgG with Protein M (red) and Protein M TD (blue) (at a 1:8 molar ratio). ELISA assay was performed as in (A). (**C**) Binding of KZ52 IgG, a human broadly neutralizing antibody against its Ebola antigen glycoprotein (purple), was evaluated as in (B). ELISA assay was performed as in (A). (**D**) Binding of 13C6 IgG, a mouse broadly neutralizing antibody against its Ebola glycoprotein antigen (purple) was evaluated as in (B). (**E**) Binding of antibody to COL4A3 human polyclonal serum from a patient with Goodpasture's disease to its antigen COL4A3 (purple) was evaluated as in (B). (**F**) Binding of anti-DNA polyclonal serum from a mouse with lupus to its antigen chromatin (purple) was evaluated as in (B).

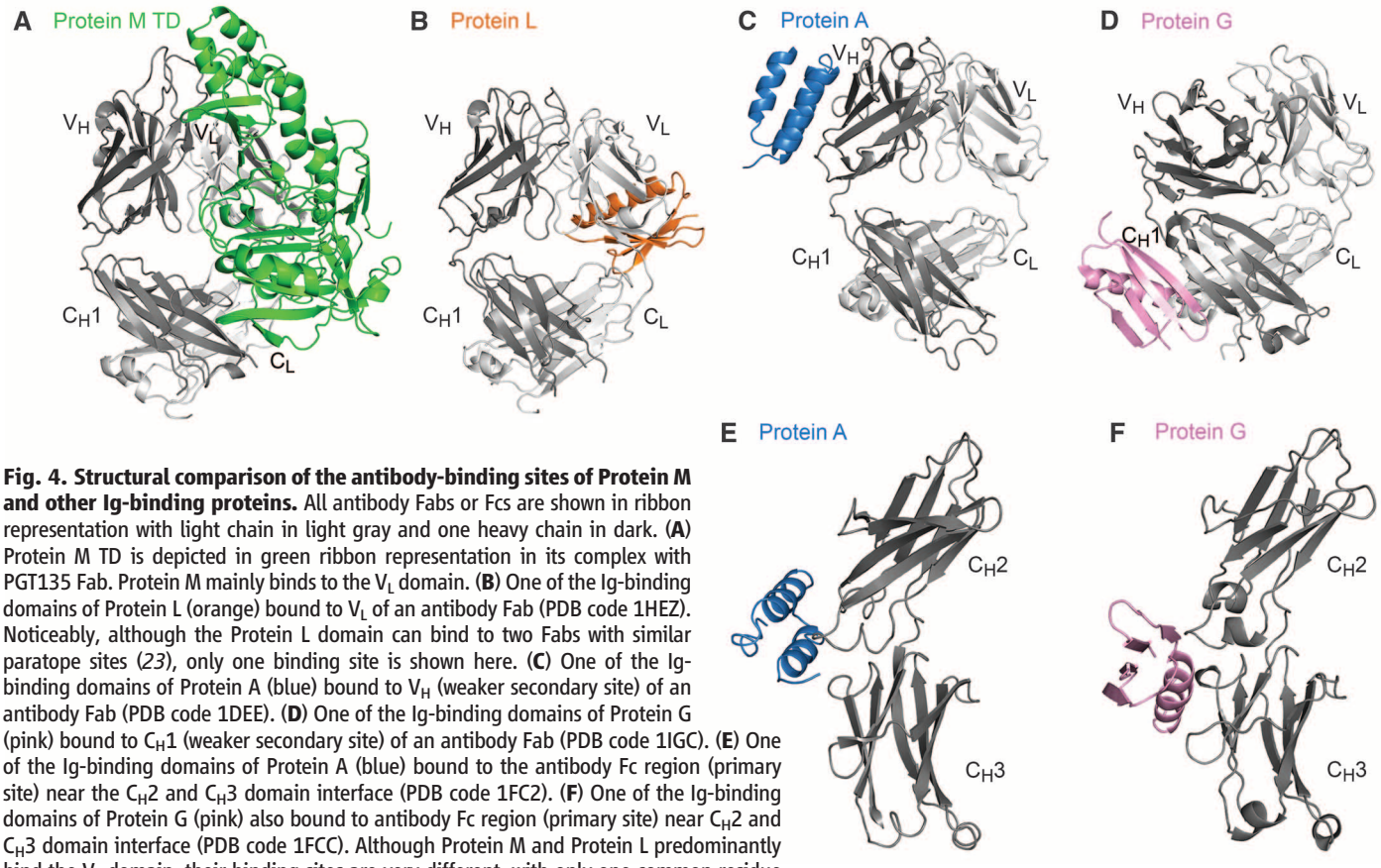

Fig. 4. Structural comparison of the antibody-binding sites of Protein M and other Ig-binding proteins. All antibody Fabs or Fcs are shown in ribbon representation with light chain in light gray and one heavy chain in dark. (**A**) Protein M TD is depicted in green ribbon representation in its complex with PGT135 Fab. Protein M mainly binds to the V_L domain. (**B**) One of the Ig-binding domains of Protein L (orange) bound to V_L of an antibody Fab (PDB code 1HEZ). Noticeably, although the Protein L domain can bind to two Fabs with similar paratope sites (*23*), only one binding site is shown here. (**C**) One of the Ig-binding domains of Protein A (blue) bound to V_H (weaker secondary site) of an antibody Fab (PDB code 1DEE). (**D**) One of the Ig-binding domains of Protein G (pink) bound to C_H1 (weaker secondary site) of an antibody Fab (PDB code 1IGC). (**E**) One of the Ig-binding domains of Protein A (blue) bound to the antibody Fc region (primary site) near the C_H2 and C_H3 domain interface (PDB code 1FC2). (**F**) One of the Ig-binding domains of Protein G (pink) also bound to antibody Fc region (primary site) near C_H2 and C_H3 domain interface (PDB code 1FCC). Although Protein M and Protein L predominantly bind the V_L domain, their binding sites are very different, with only one common residue (position 18 of V_L). These Ig-binding proteins appear to have different ranges of affinities for antibodies. Generally, for human antibodies, Protein M binds strongly to all the types; Protein G binds strongly to the antibody Fc region and weakly to the C_H1 domain; Protein A binds strongly to antibody Fc region (except to the IgG3 subtype) and weakly to V_H of V_H3 gene family; and Protein L binds strongly to V_L of κ light chains, except the VκII subgroup.

different from any other known protein structures. Unlike Protein G, Protein A, and Protein L—which all contain multiple, small, Ig-binding domains—Protein M has a large domain of 360 residues, which binds principally to antibody V_L domains, as well as a LRR-like motif (*24*) that faces away from the antibody molecule and may have an as-yet uncharacterized function. Protein M also contains a 115-residue C-terminal domain that likely protrudes over the antibody combining site. To our knowledge, compared with other known Ig-binding proteins, the Protein M TD–antibody Fab buried surface area is the largest (*25*).

Protein M binds to antibodies with either κ or λ light chains using conserved hydrogen bonds and salt bridges, from backbone atoms and conserved side chains, and some conserved van der Waals interactions as well as other nonconserved interactions. These conserved interactions provide a structural basis for the broad reactivity with Fvs, Fabs, or Igs. In contrast, the primary binding site for Protein G and Protein A is the antibody Fc domain, although secondary lower-affinity binding sites include the C_H1 domain of IgG for Protein G (*26*) or V_H of the human V_H3 gene family for Protein A (*22*). Protein L binds only to the V_L of most human κ light chains, except for the VκII subgroup (Fig. 4) (*23*). Thus, this new broad-scope, high-affinity antibody-binding protein, which binds both κ and λ chains, is likely to find a myriad of applications in immunochemistry. In addition to its general use, Protein M may be particularly important for large-scale purification of therapeutic antibodies. Last, although Protein M may be important for the host-parasite relationship, further studies are necessary to elucidate the consequences of its expression on the parasite surface.

References and Notes

1. R. K. Grover *et al.*, *Proc. Natl. Acad. Sci. U.S.A.* **109**, 6036–6041 (2012).
2. F. Bertoni, E. Zucca, *J. Clin. Invest.* **116**, 22–26 (2006).
3. R. A. Kyle, S. V. Rajkumar, *Blood* **111**, 2962–2972 (2008).
4. S. Minguet *et al.*, *Eur. J. Immunol.* **38**, 2475–2487 (2008).
5. S. Panfilio *et al.*, *Leukemia Res. Rep.* **2**, 39–40 (2013).
6. R. M. Young, L. M. Staudt, *Nat. Rev. Drug Discov.* **12**, 229–243 (2013).
7. D. Taylor-Robinson, J. S. Jensen, *Clin. Microbiol. Rev.* **24**, 498–514 (2011).
8. S. Rottem, *Physiol. Rev.* **83**, 417–432 (2003).
9. C. Citti, L. X. Nouvel, E. Baranowski, *Future Microbiol.* **5**, 1073–1085 (2010).
10. R. A. Kyle *et al.*, *Mayo Clin. Proc.* **78**, 21–33 (2003).
11. ForteBiol; a division of Pall Life Sciences. All rights reserved, 2013.
12. L. Kong *et al.*, *Nat. Struct. Mol. Biol.* **20**, 796–803 (2013).
13. C. Dreyfus *et al.*, *Science* **337**, 1343–1348 (2012).
14. A structural similarity search performed by using the Dali server (http://ekhidna.biocenter.helsinki.fi/dali_server/start) indicated that Protein M TD is not substantially similar to other structures, except for the LLR-like motif.
15. The Fab-Protein M TD interactions bury total solvent-accessible surface areas of 2490 Å^2 for PGT135 V_L domain (1280 Å^2 from Protein M TD and 1210 Å^2 from PGT135) and 2380 Å^2 for CR9114 V_L domain (1230 Å^2 from Protein M TD and 1150 Å^2 from CR9114), respectively.
16. L. M. Walker *et al.*, *Nature* **477**, 466–470 (2011).
17. J. E. Lee *et al.*, *Nature* **454**, 177–182 (2008).
18. J. A. Wilson *et al.*, *Science* **287**, 1664–1666 (2000).
19. S. Gunwar *et al.*, *J. Biol. Chem.* **266**, 15318–15324 (1991).
20. A. N. Theofilopoulos, F. J. Dixon, *Adv. Immunol.* **37**, 269–390 (1985).
21. A. M. Gronenborn *et al.*, *Science* **253**, 657–661 (1991).
22. M. Graille *et al.*, *Proc. Natl. Acad. Sci. U.S.A.* **97**, 5399–5404 (2000).
23. M. Graille *et al.*, *Structure* **9**, 679–687 (2001).
24. A. C. Doxey, B. J. McConkey, *Virulence* **4**, 453–466 (2013).
25. L. Lo Conte, C. Chothia, J. Janin, *J. Mol. Biol.* **285**, 2177–2198 (1999).
26. J. P. Derrick, D. B. Wigley, *J. Mol. Biol.* **243**, 906–918 (1994).

Acknowledgments: We thank B. Cravatt and G. Siuzdak for mass spectroscopy studies, M. Lee and C. Locke for assistance in Western blot and ELISA studies, W. Yu for protein purification, and H. Tien of the Robotics Core at the Joint Center for Structural Genomics (www.jcsg.org) for automated crystal screening. X-ray diffraction data sets were collected at the Stanford Synchrotron Radiation Lightsource beamlines 11-1 and 12-2. The b12 IgG and PGT135 IgG were kindly provided by B. Moldt in the laboratory of D. Burton, and the other anti-HIV antibody Fabs were provided by J.-P. Julien and Y. Hua. The Lupus mouse serum and mouse chromatin were kindly provided by R. Baccala. The plasmapheresis fluid from a patient with Goodpasture's disease and human recombinant COL4A3 antigen were provided by V. Pedchenko. The KZ52 IgG, 13C6 IgG, and Ebola GP were kindly provided by E. Saphire. The electron microscopy studies were supported by startup funds from The Scripps Research Institute (to A.B.W.) and conducted at the National Resource for Automated Molecular Microscopy at The Scripps Research Institute, which is supported by NIH through the National Center for Research Resources' P41 program (RR017573). We also thank NIH RO1 AI042266 (I.A.W.), NIH 5 R21 AI098057-02 (J.I.G.), NIH R01 AG020686 (M.C.), NIH U19 AI06360 (D.R.S.), and NIH K08 AR063729-01 (A.M.) for support. Coordinates and structure factors are deposited in PDB under accession codes 4NZR for Protein M TD/PGT135 Fab complex, 4NZT for Protein M TD/CR9114 Fab complex, and 4NZU for 13PL Fab'. The electron microscopy reconstructions are deposited in the Electron Microscopy Data Bank under accession codes EMD-5834 for Fab of human mAb b12 in complex with Protein M, EMD-5835 for Fab of multiple Myeloma patient human mAb 13PL in complex with Protein M TD, and EMD-5836 Fab of human mAb b12 in complex with Protein M TD. A patent covering this work (official application PCT 13/050656) entitled "Immunoglobulin-binding of human mycoplasma antigens and methods of use thereof" has been filed. This is publication 25063 from The Scripps Research Institute.

Supplementary Materials

www.sciencemag.org/content/343/6171/656/suppl/DC1
Materials and Methods
Figs. S1 to S14
Tables S1 to S6
References (*27*–*48*)

18 September 2013; accepted 18 December 2013
10.1126/science.1246135

Interchromosomal Communication Coordinates Intrinsically Stochastic Expression Between Alleles

Robert J. Johnston Jr.* and Claude Desplan†

Sensory systems use stochastic mechanisms to diversify neuronal subtypes. In the *Drosophila* eye, stochastic expression of the PAS-bHLH transcription factor Spineless (Ss) determines a random binary subtype choice in R7 photoreceptors. Here, we show that a stochastic, cell-autonomous decision to express *ss* is made intrinsically by each *ss* locus. Stochastic on or off expression of each *ss* allele is determined by combinatorial inputs from one enhancer and two silencers acting at long range. However, the two *ss* alleles also average their frequency of expression through up-regulatory and down-regulatory interallelic cross-talk. This inter- or intrachromosomal long-range regulation does not require endogenous *ss* chromosomal positioning or pairing. Therefore, although individual *ss* alleles make independent stochastic choices, interchromosomal communication coordinates expression state between alleles, ensuring that they are both expressed in the same random subset of R7s.

Developmental programs generally induce uniform or regionalized gene expression patterns to yield highly reproducible body-plan outcomes. However, stochastic mechanisms are sometimes incorporated to diversify cell types in nervous systems. Nonautonomous stochastic mechanisms using lateral inhibition strategies have been well described, whereas cell-autonomous, stochastic mechanisms involved in color opsin and olfactory receptor selection in mammals are only partially understood (*1*, *2*).

The fly eye is composed of two stochastically distributed subtypes of ommatidia (unit eyes) defined by expression of specific light-detecting Rhodopsin proteins in R7 photoreceptors (PRs). The random distribution is controlled by the stochastic expression of the Per-Arnt-Sim basic helix-loop-helix (PAS-bHLH) transcription factor Spineless (Ss). Ss expression in ~65% of randomly distributed R7s induces "yellow" (**y**R7) fate and expression of Rhodopsin4 (Rh4), whereas the absence of Ss in the remaining ~35% of R7s allows for "pale" (**p**R7) fate and Rhodopsin3 (Rh3) expression (Fig. 1, A and B). Loss of *ss* function leads to the transformation of all R7s to **p**R7 fate and Rh3 expression (fig. S1A), whereas ectopic Ss causes all R7s to acquire **y**R7 fate and express Rh4 (fig. S1B) (*1*–*5*).

Ss was observed in 65% of randomly distributed R7s throughout development (Fig. 1C and fig. S1, D to G). Ss expression in adults perfectly correlated with Rh4 expression (fig. S1C). We never observed switching of Rh expression (*6*). Therefore, Ss expression is established and stably maintained throughout the lifetime of **y**R7 cells.

We evaluated reporter lines containing fragments of the *ss* gene (*7*). Fragment 8 (*R7/R8 enhancer*) in *mini-gene1* induced *lacZ* expression in all R7s and R8s (Fig. 2, A and B), which closely resembled expression of the Salm zinc finger transcription factor (with Salr, collectively referred to as Sal) (Fig. 2C) that specifies R7 and R8 fate (*8*). Ss expression was completely lost in *sal* mutants (Fig. 2D), whereas ectopic expression of Salm in all PRs led to the activation of Ss in a random subset of outer PRs (Fig. 2E and fig. S2A) and expression of Mini-gene1 in outer PRs (fig. S2B). Thus, Sal is necessary and sufficient to activate stochastic expression of Ss in PRs. The choice to express Ss is cell autonomous because R7s and outer PRs within the same ommatidium made their decisions to express Ss independently of one another (Fig. 2E and fig. S2A).

To identify DNA silencer elements required for stochastic Ss expression, we first defined the minimal *ss* DNA sequence required for stochastic *ss* expression. We used green fluorescent protein (GFP) from transgenes or Rh4 expression as a readout of Ss expression (Ss/Rh4), because Rh4 is always a perfect indication of Ss expression in

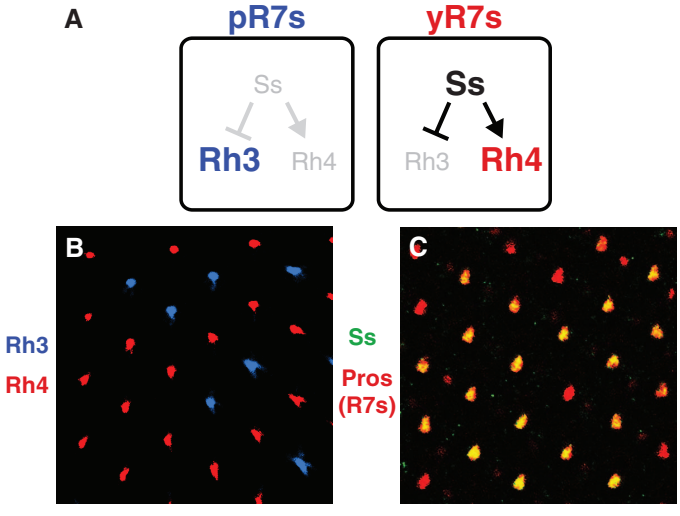

Fig. 1. The stochastic decision to express *ss* is made early and maintained. (**A**) Ss is absent from **p**R7s, allowing for Rh3 expression. Ss is expressed in **y**R7s activating Rh4 and repressing Rh3. (**B**) Stochastic distribution of Rh3- and Rh4-expressing R7s. (**C**) Ss is expressed in a random subset of R7s throughout development. Pros marks all R7s.

Department of Biology, New York University, 100 Washington Square East, New York, NY 10003, USA.

*Present address: Department of Biology, Johns Hopkins University, 3400 North Charles Street, Baltimore, MD 21218, USA.
†Corresponding author. E-mail: cd38@nyu.edu

R7s (fig. S1C) (*5*). An inversion (*9*) and *transgene1* exhibited stochastic Ss expression and therefore defined the 5′ endpoint (Fig. 2A and fig. S2C). A duplication with a breakpoint in the *ss* 3′ UTR (*10*) and *transgene2* similarly exhibited stochastic Ss expression, defining the 3′ endpoint (Fig. 2A and fig. S2D). These data determine a 55.5-kb minimal DNA sequence required for stochastic *ss* expression (Fig. 2A).

We identified two DNA elements that are critical for stochastic *ss* expression. *transgene3* and *transgene4* displayed expression in all R7s, suggesting that an intragenic silencer (*silencer2*) is required for stochastic *ss* expression (Fig. 2A and fig. S2, E and F). *transgene5* and *transgene6* also displayed expression in all R7s, suggesting that a 5′ upstream silencer (*silencer1*) is also required for stochastic *ss* expression (Fig. 2A and fig. S2, G and H). A 36-kb deficiency that removed *silencer1* (*sil1 deficiency*) and an inversion allele in which the *ss* coding region was

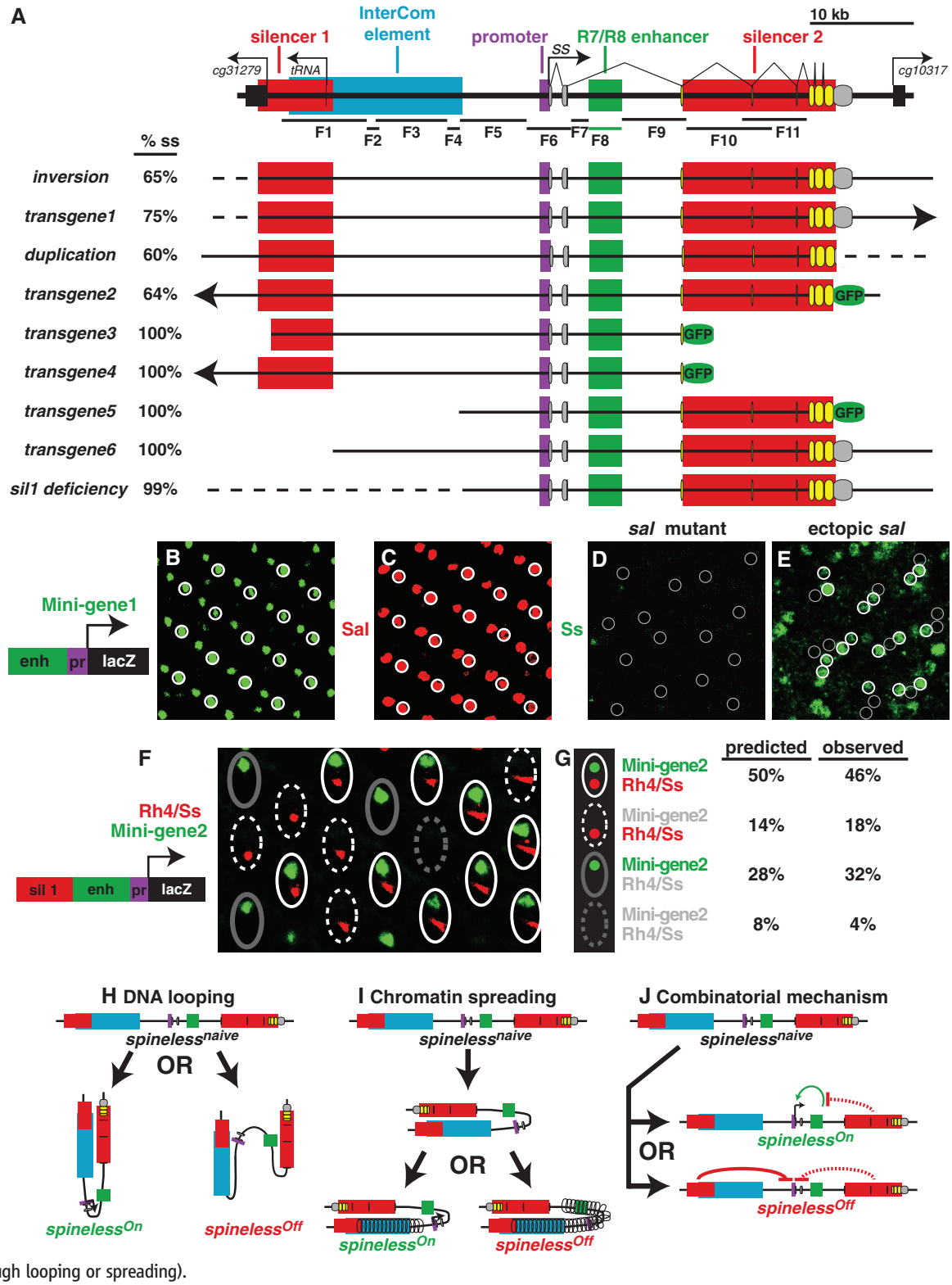

Fig. 2. The cis-regulatory logic controlling intrinsically stochastic *ss* expression. (**A**) *ss* locus schematic. F, Fragment; red boxes, *silencers*; blue box, *InterCom element*; purple box, *minimal promoter*; green box, *R7/R8 enhancer*; gray circles, untranslated exons; yellow circles, translated exons; arrows, transcriptional starts. (**B** to **E**) White circles indicate expression, and gray circles indicate no expression. (B) *Mini-gene1* is expressed in all R7s and R8s. (C) Sal is expressed in all R7s and R8s. (D) Ss expression is completely lost in *sal* mutants. (E) Ectopic Sal expression in *svp* mutants causes Ss expression in a random subset of PRs. (**F**) Mini-gene2 induces expression in a subset of R7s independently of endogenous Ss/Rh4 expression. Mini-gene2 localizes to the nucleus, whereas Rh4/Ss localizes to membranous rhabdomere structures. The four possible combinations of expression are observed: (i) white solid ovals, mini-gene2 and Ss/Rh4; (ii) white dashed ovals, Ss/Rh4 only; (iii) gray solid ovals, mini-gene2 only; and (iv) gray dotted ovals, no expression. (**G**) Four expression combinations in (F). (**H** to **J**) Models for random expression decisions. (H) The *ss* locus randomly assumes one of two (i.e., active or repressed) DNA looping configurations. (I) One silencer facilitates the nucleation of closed chromatin state spreading from the other silencer. (J) One silencer lowers expression in all R7s, whereas the other specifically provides the stochastic input (through looping or spreading).

moved 12 Mb away from *silencer1* (*ss high freq*) showed expression of Ss/Rh4 in all R7s (Fig. 2A and figs. S2I and S3, A and E), validating the requirement for *silencer1*. Therefore, stochastic Ss expression requires an enhancer and two silencer elements.

When a ~3-kb fragment of *silencer1* was placed with the *R7/R8 enh+prom* element driving reporter expression (*mini-gene2*), we observed expression in a random subset of R7s (Fig. 2F), showing that *silencer1* is sufficient to repress expression when present close to the enhancer and promoter. If the stochastic expression decision occurred intrinsically at each *ss* locus, *mini-gene2* should induce reporter expression independently of expression from the endogenous *ss* loci. We compared expression of mini-gene2 to endogenous Ss/Rh4 expression and found all four possible expression combinations (Fig. 2, F and G), suggesting that each *ss* locus makes an independent, stochastic expression decision.

transgene4, which was inserted 4.6 Mb away from the *ss* locus, drove GFP expression in all R7s (Fig. 2A). Although *transgene4* should not affect endogenous Ss expression, we observed a dramatic increase in the frequency of Ss/Rh4 expression in animals carrying *transgene4*, suggesting that *transgene4* up-regulated the frequency of Ss expression from the endogenous *ss* loci (Fig. 3C). *transgene4* up-regulated expression from *ss* loci in cis, or in trans (Fig. 3, A to D), suggesting that it contains DNA elements that are sufficient to drive regulatory interactions in the absence of chromosomal pairing. *transgene4* also up-regulated expression, although less efficiently, from the *ss* locus translocated on a different chromosome (Fig. 3, E and F), suggesting that *ss* alleles can interact at a distance but that chromosomal position plays a role in this process. These observations strongly implicate direct interactions between DNA elements in the transgene and endogenous loci but do not exclude possible indirect mechanisms such as noncoding RNAs. *transgene4* must contain a DNA element (*InterCom element*) between 25 and 8 kb upstream of the *ss* transcription start site, which is missing in *mini-gene2* (Fig. 2, F and G, and fig. S3).

We next found that one *ss* allele could up-regulate the frequency of expression from the other allele. $ss^{low\ freq1}$, an allele affecting noncoding

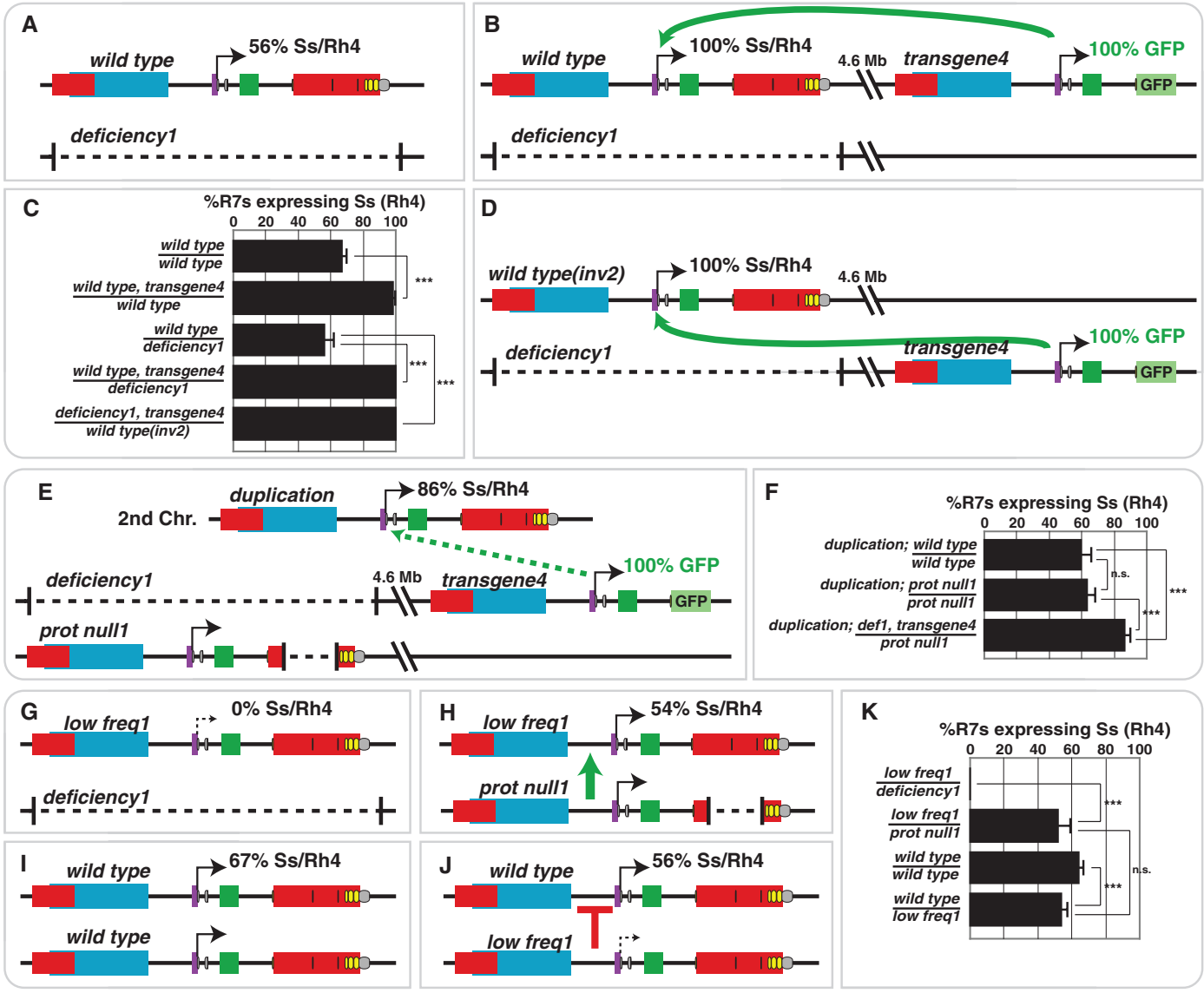

Fig. 3. *ss* regulatory regions up-regulate and down-regulate expression frequency through interchromosomal communication. (**A**) Wild-type *ss* locus over *deficiency1*. (**B**) *transgene4* up-regulates expression frequency from the endogenous *ss* gene in cis. (**C**) Quantification of (A), (B), and (D). (**D**) *transgene4* up-regulates expression frequency from the endogenous *ss* gene in trans. (**E**) *transgene4* up-regulates expression, although less efficiently, from the *ss* locus on the nonhomologous 2nd chromosome. (**F**) Quantification of (E). (**G**) Ss/Rh4 is not expressed in $ss^{low\ freq1}$ hemizygous mutants. (**H**) The normal regulatory regions of the $ss^{prot\ null1}$ allele up-regulate Ss/Rh4 expression from the $ss^{low\ freq1}$ allele. (**I**) Wild-type *ss* homozygous loci. (**J**) The regulatory regions of the $ss^{low\ freq1}$ allele down-regulate Ss/Rh4 expression from the wild-type *ss* allele. (**K**) Quantification of (G) to (J).

regions, was expressed at very low frequency when placed over $ss^{deficiency}$ alleles (Fig. 3, G and K, and fig.S4A). When $ss^{low\ freq1}$ was placed over $ss^{prot\ null1}$, a protein coding null allele with normal cis-regulatory regions, the frequency of Ss/Rh4 expression dramatically increased (Fig. 3, H and K), suggesting that the cis-regulatory elements from $ss^{prot\ null1}$ up-regulated expression frequency from $ss^{low\ freq1}$. We verified our observations with additional allelic combinations (fig. S4, A and B).

The up-regulation of expression from one allele with impaired regulatory regions but normal protein function by another allele with normal regulatory regions but impaired protein function resembles transvection, initially described by Lewis (*11*). Transvection is defined as the complementation of mutant alleles requiring position-dependent chromosomal pairing. Because the interallelic control of *ss* does not require position-dependent chromosomal pairing (Fig. 3, B, D, and E, and fig. S3B and S4, B and C) and does not appear to require regulation by known mediators of transvection (fig. S5), we conclude that this phenomenon is not a canonical case of transvection.

We also found that one *ss* allele could mediate the down-regulation of expression frequency from the other allele. The $ss^{low\ freq1}$ allele down-regulated expression frequency from the $ss^{wild\text{-}type}$ alleles, because the proportion of R7s expressing Ss/Rh4 was lower in $ss^{low\ freq1}/ss^{wild\text{-}type}$ animals compared with $ss^{wild\text{-}type}$ homozygotes (Fig. 3, I to K). Down-regulation did not require endogenous *ss* chromosomal position because it also occurred for a wild-type *ss* locus on an inversion (fig. S4C). We confirmed down-regulation with additional allelic combinations (fig. S3, A, B, and E, and fig. S4C). Thus, *ss* alleles regulate one another through long-range interchromosomal activating and repressing mechanisms to determine the frequency of *ss* expression.

If each *ss* allele makes its own expression decision, expression states will sometimes agree (both alleles on or off) and other times disagree (one allele on and the other off). We tested whether interchromosomal communication functioned to coordinate the expression state from the two *ss* alleles.

The ss^{trunc} allele has normal regulatory regions but contains a mutation that truncates the Ss protein activation domain (*5*, *10*). This truncation weakens Ss protein function such that Ss activates Rh4 normally, but fails to repress Rh3, leading to coexpression of Rh3 and Rh4 in nearly all **y**R7s and normal Rh3 expression in **p**R7s (Fig. 4B).

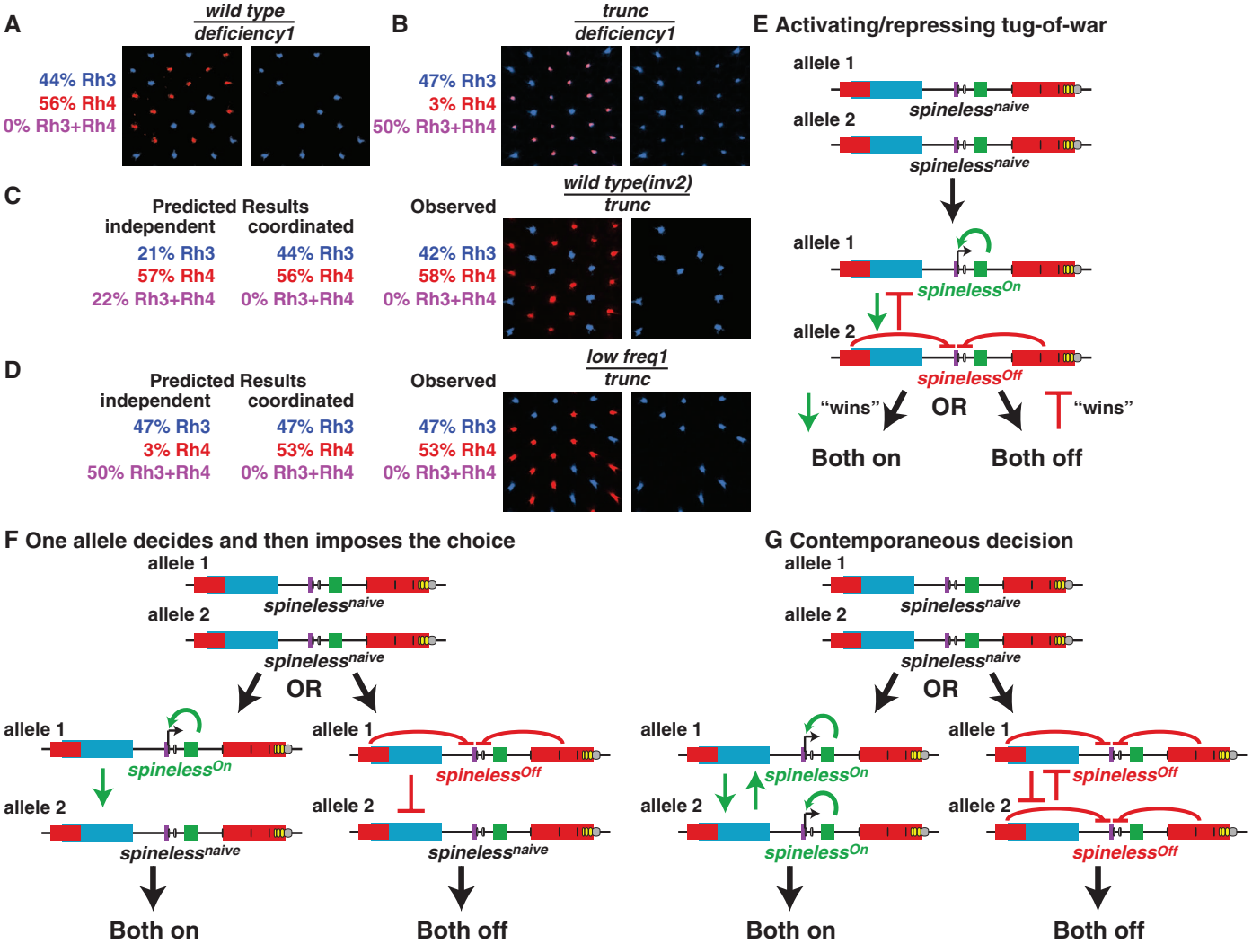

Fig. 4. Interchromosomal communication coordinates expression from *ss* alleles. (**A**) Rh3 is expressed in **p**R7s, and Rh4 is expressed in **y**R7s in wild-type hemizygous animals. (**B**) Rh3 is expressed in **p**R7s and Rh4 and Rh3 are expressed in **y**R7s in ss^{trunc} hemizygous animals. (**C**) In $ss^{wild\text{-}type(inv2)}/ss^{trunc}$ animals, Rh3 and Rh4 are always expressed exclusively. (**D**) In $ss^{low\ freq1}/ss^{trunc}$ animals, the normal regulatory regions of the ss^{trunc} allele up-regulate expression from $ss^{low\ freq1}$ into the same subset of R7s because Rh3 and Rh4 are expressed exclusively. (**E** to **G**) Models for the coordination of expression state through interchromosomal communication. (E) A temporally distinct two-step mechanism involving both alleles making independent expression decisions followed by an activating and repressing tug of war. (F) A temporally distinct two-step mechanism in which one allele makes the decision and then imposes the decision onto the other naïve allele. (G) A mechanism involving contemporaneous decisions that average the activating and repressing inputs from each allele.

We evaluated $ss^{wild\text{-}type}/ss^{trunc}$ animals to determine whether these alleles were expressed in an independent or coordinated manner. If the two *ss* alleles were expressed independently, $ss^{wild\text{-}type}/ss^{trunc}$ would produce three Rh expression outcomes: (i) Rh3 alone (neither $ss^{wild\text{-}type}$ nor ss^{trunc} are expressed); (ii) Rh4 alone ($ss^{wild\text{-}type}$ alone or both $ss^{wild\text{-}type}$ and ss^{trunc} are expressed); and (iii) Rh3 and Rh4 coexpression (ss^{trunc} alone is expressed) (fig. S6C). Alternatively, coordinated expression from the two alleles would yield two Rh expression outcomes: (i) Rh3 alone (neither $ss^{wild\text{-}type}$ nor ss^{trunc} are expressed) and (ii) Rh4 alone (both $ss^{wild\text{-}type}$ and ss^{trunc} are expressed) (fig. S6D). For these experiments, the wild-type *ss* allele was on an inverted chromosome ($ss^{wild\text{-}type(inv2)}$) to prevent pairing of homologous chromosomes. For $ss^{wild\text{-}type(inv2)}/ss^{trunc}$ flies, we observed expression of Rh4 alone and Rh3 alone, but never coexpression of Rh3 and Rh4 (Fig. 4C). The wild-type *ss* locus on a different inverted chromosome ($ss^{wild\text{-}type(inv3)}$) over ss^{trunc} displayed similar expression coordination (see the supplementary materials). Together, these data suggest that expression from the two *ss* alleles is coordinated and that endogenous *ss* position on homologous chromosomes is not critical.

We next investigated whether interchromosomal communication was able to coordinate expression from two *ss* alleles with widely different expression frequencies. $ss^{low\ freq1}$ expressed fully functional Ss protein but at a low frequency (Fig. 3G). We predicted that $ss^{low\ freq1}/ss^{trunc}$ animals should display up-regulation of Ss expression from $ss^{low\ freq1}$ due to interchromosomal communication from the normal cis-regulatory elements of ss^{trunc}. $ss^{low\ freq1}/ss^{trunc}$ flies displayed nearly perfect coordination of expression from the two alleles, with almost no coexpression of Rh3 and Rh4 (Fig. 4D), verifying that interchromosomal communication coordinates expression from the two *ss* alleles.

Because stochastic Ss expression requires an enhancer and two silencer elements, we propose three possible mechanistic models controlling the decision: (i) the *ss* locus randomly assumes one of two (i.e., active or repressed) DNA looping configurations; (ii) one silencer facilitates the nucleation of closed chromatin state spreading from the other silencer; and (iii) one silencer generally lowers expression in all R7s, whereas the other specifically provides the stochastic input (through looping or spreading) (Fig. 2, H to J).

Similarly, we envision three models for how interchromosomal communication coordinates expression: (i) a temporally distinct two-step mechanism involving both alleles making independent expression decisions followed by an activating and repressing tug of war; (ii) a temporally distinct two-step mechanism in which one allele makes the decision and then imposes the decision onto the other naïve allele; and (iii) a mechanism involving contemporaneous decisions that average the activating and repressing inputs from each allele (Fig. 4, E to G).

Interchromosomal communication is reminiscent of transvection. In contrast to transvection-like processes that allow allelic complementation between null alleles whose biological meaning is unclear, interchromosomal communication regulating *ss* appears to have dedicated biological functions to average the frequency and coordinate expression state between stochastically expressed alleles.

The color vision systems of flies and humans present an interesting case of convergent evolution. In both species, the apparent goal is the same: Use stochastic mechanisms to diversify cell fates and distribute color sensory capacities across the eye. The fly eye requires an enhancer and two silencer elements to achieve stochastic expression of *ss*, whereas the human eye uses random locus control region (LCR)–mediated activation of M (middle-wavelength sensitive) or L (long-wavelength sensitive) opsins. To avoid disagreement in allelic expression states, interchromosomal communication coordinates expression in flies, whereas X-inactivation completely turns off expression from one allele in females and there is only one copy of the locus in males, creating a mono-allelic expression decision in both cases (*1*, *2*).

Stochastic gene expression mechanisms may be a cost-effective way to diversify the repertoire of cell fates within a tissue. Although these phenomena involve stochastic processes, this randomness is very often well controlled, incorporating multiple steps, apparently to ensure robustness. Evolution has yielded many different mechanisms to determine stochastic cell fate specification in bacteria, flies, and vertebrates (*2*). As our understanding of stochastic phenomena increases, it will be interesting to see whether common, ancestral strategies become apparent or whether novel stochastic gene expression mechanisms arise in individual species.

References and Notes

1. R. J. Johnston Jr., C. Desplan, *Curr. Opin. Neurobiol.* **18**, 20–27 (2008).
2. R. J. Johnston Jr., C. Desplan, *Annu. Rev. Cell Dev. Biol.* **26**, 689–719 (2010).
3. M. F. Wernet *et al.*, *Nature* **440**, 174–180 (2006).
4. R. J. Johnston Jr., *et al.*, *Cell* **145**, 956–968 (2011).
5. S. U. Thanawala *et al.*, *Dev. Cell* **25**, 93–105 (2013).
6. D. Vasiliauskas *et al.*, *Nature* **479**, 108–112 (2011).
7. R. B. Emmons, D. Duncan, I. Duncan, *Dev. Biol.* **302**, 412–426 (2007).
8. B. Mollereau *et al.*, *Nature* **412**, 911–913 (2001).
9. L. M. Matzkin, T. J. Merritt, C. T. Zhu, W. F. Eanes, *Genetics* **170**, 1143–1152 (2005).
10. D. M. Duncan, E. A. Burgess, I. Duncan, *Genes Dev.* **12**, 1290–1303 (1998).
11. E. Lewis, *Am. Nat.* **88**, 225–239 (1954).

Acknowledgments: We are very grateful to S. Britt, I. Duncan, C. Zuker, and the Bloomington Stock Center for reagents. We thank C. Tsanis and T. Blackman for technical assistance and E. Heard, O. Hobert, J. Kassis, P. O'Farrell, V. Pirrotta, and members of the Desplan laboratory for helpful discussion concerning the project and manuscript. C.D. was supported by NIH R01 EY13010. R.J.J. Jr. was supported by a Jane Coffin Childs Memorial Fund for Medical Research postdoctoral fellowship.

Supplementary Materials

www.sciencemag.org/content/343/6171/661/suppl/DC1
Materials and Methods
Supplementary Text
Figs. S1 to S6
References (*12*–*27*)

10 July 2013; accepted 2 January 2014
10.1126/science.1243039

Loose Coupling Between Ca^{2+} Channels and Release Sensors at a Plastic Hippocampal Synapse

Nicholas P. Vyleta and Peter Jonas*

The distance between Ca^{2+} channels and release sensors determines the speed and efficacy of synaptic transmission. Tight "nanodomain" channel-sensor coupling initiates transmitter release at synapses in the mature brain, whereas loose "microdomain" coupling appears restricted to early developmental stages. To probe the coupling configuration at a plastic synapse in the mature central nervous system, we performed paired recordings between mossy fiber terminals and CA3 pyramidal neurons in rat hippocampus. Millimolar concentrations of both the fast Ca^{2+} chelator BAPTA [1,2-bis(2-aminophenoxy)ethane-*N*,*N*,*N*′,*N*′-tetraacetic acid] and the slow chelator EGTA efficiently suppressed transmitter release, indicating loose coupling between Ca^{2+} channels and release sensors. Loose coupling enabled the control of initial release probability by fast endogenous Ca^{2+} buffers and the generation of facilitation by buffer saturation. Thus, loose coupling provides the molecular framework for presynaptic plasticity.

The coupling between voltage-activated Ca^{2+} channels and Ca^{2+} sensors of exocytosis on synaptic vesicles is a key factor that determines the timing and probability of transmitter release (*1*–*3*). Work at the young calyx of Held in the auditory brainstem suggested that coupling is loose, with source-sensor distances of ~100 nm (*2*, *4*). However, recent evidence indicates that, at several excitatory and inhibitory synapses in the mature central nervous system, coupling is substantially tighter than previously thought, with source-sensor distances of only 10

to 20 nm (*5*–*9*). Tight coupling offers several functional advantages, including speed, temporal precision, and energy efficiency of synaptic transmission (*3*). Does any synapse in the mature brain make use of loose coupling, and, if so, does this have specific consequences for the functional properties of synaptic transmission? To address these questions, we focused on hippocampal mossy fiber synapses on CA3 pyramidal neurons (*10*–*14*) (Fig. 1A). These synapses express several presynaptic forms of plasticity (*15*), which may be linked to a loose coupling configuration (*16*). Furthermore, their presynaptic terminals are accessible to direct patch-clamp recording. This allowed us to quantitatively probe channel-sensor coupling by using Ca^{2+} chelators, at a level of rigor previously only achieved at the calyx of Held (*4*, *17*, *18*).

To probe the distance between Ca^{2+} channels and release sensors, we measured the effects of exogenous Ca^{2+} chelators with different binding rates (Fig. 1) (*3*, *19*). Paired recordings from mossy fiber terminals and postsynaptic CA3 pyramidal neurons were obtained by using presynaptic solutions with minimal Ca^{2+} buffer capacity (0.1 mM EGTA, control), or different concentrations of either the fast Ca^{2+} chelator 1,2-bis(2-aminophenoxy) ethane-*N*,*N*,*N*′,*N*′-tetraacetic acid (BAPTA) or the slow Ca^{2+} chelator EGTA (12, 10, and 13 pairs total, respectively; Fig. 1, B to D). Mossy fiber terminals were stimulated in the whole-cell current-clamp configuration with brief current pulses, whereas excitatory postsynaptic currents (EPSCs) were recorded in postsynaptic CA3 pyramidal neurons under voltage-clamp conditions. On average, 1 mM BAPTA and 10 mM EGTA reduced EPSC peak amplitudes to 10 ± 7% and 8 ± 2% of the control value (mean ± SEM, 4 and 10 pairs, P = 0.004 and 0.0002, respectively; Fig. 1E). Both Ca^{2+} chelators had no detectable effects on the synaptic delay (Fig. 1F; P = 0.8 and 0.1 for 1 mM BAPTA and 10 mM EGTA). However, 1 mM BAPTA and 10 mM EGTA significantly reduced the 20 to 80% rise time (to 53 and 61% of control; Fig. 1G; P = 0.0002 and 0.0001) and the decay time constant of the average EPSC (to 42 and 57% of control; Fig. 1H; P = 0.001 and 0.009).

To estimate the physical distance between Ca^{2+} channels and release sensors, we analyzed the concentration dependence of the BAPTA and EGTA effects (Fig. 2). To minimize intersynapse variability, EPSC amplitudes in the presence of chelators were normalized by the EPSC amplitudes previously measured by using noninvasive stimulation (materials and methods). BAPTA and EGTA suppressed transmitter release in a concentration-dependent manner, with half-maximal inhibitory concentrations of 0.094 ± 0.011 mM and 1.22 ± 0.46 mM, respectively (Fig. 2A) (*5*–*9*). Next, the concentration-effect data for BAPTA and EGTA were fit by a model of Ca^{2+} buffering and diffusion based on linear approximations (Fig. 2B) (*1*, *6*). The main free parameter was the coupling distance between Ca^{2+} channels and Ca^{2+} sensors, whereas several other parameters (e.g., the physicochemical properties of the buffers and the cooperativity of transmitter release) were well constrained (fig. S1). An analysis of the entire data set revealed a coupling distance of ~75 nm (distance of 73 ± 15 nm for a single-channel model; mean distance of 65 nm and cluster width of 80 nm for a multichannel model; Fig. 2, C and D). Variations in resting Ca^{2+} concentration and buffer product over a wide range gave distance values of 70 to 88 nm (Fig. 2E). Thus, the mean source-sensor distance at hippocampal mossy fiber synapses was markedly longer than at several other central synapses (*5*–*9*). However, the estimated distance was substantially shorter than the dis-

IST Austria (Institute of Science and Technology Austria), Am Campus 1, A-3400 Klosterneuburg, Austria.

*Corresponding author. E-mail: peter.jonas@ist.ac.at

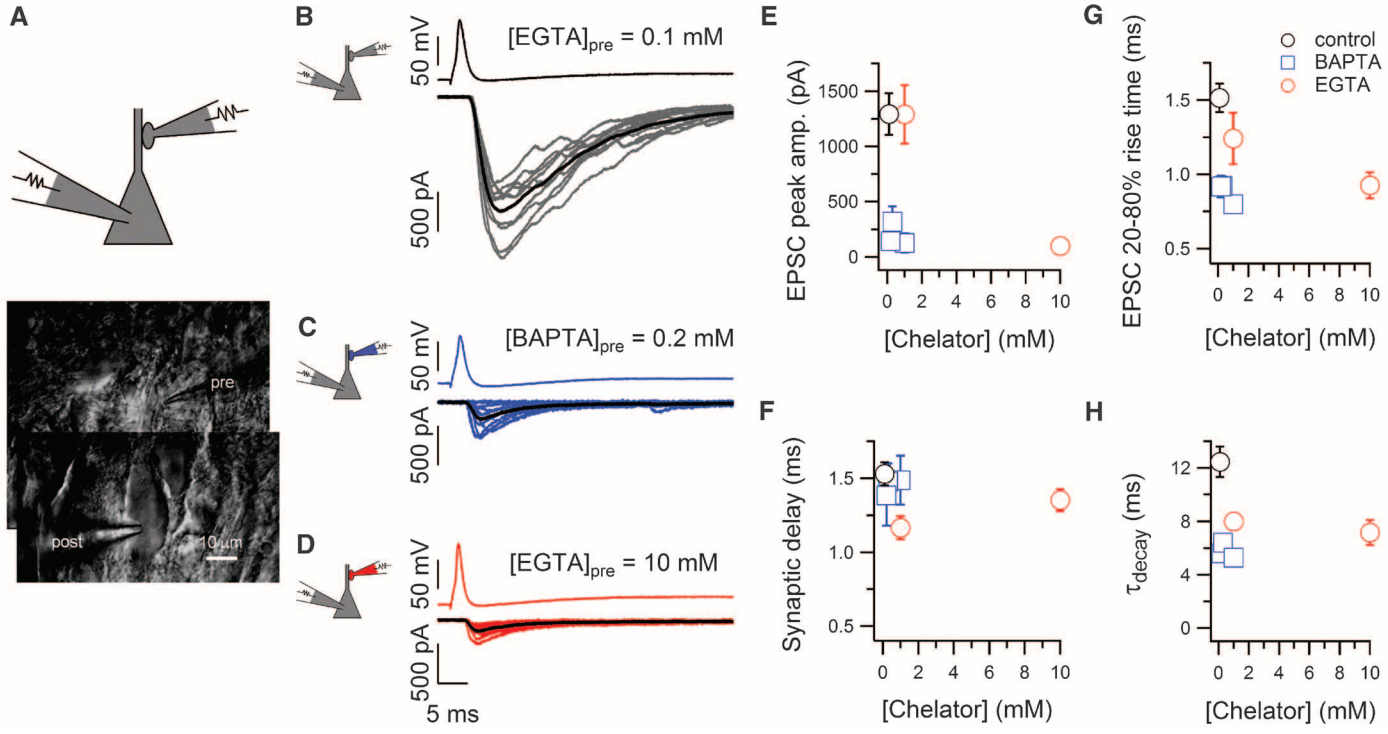

Fig. 1. Transmitter release from mossy fiber boutons is highly sensitive to the slow Ca^{2+} chelator EGTA. (**A**) (Top) Schematic showing paired whole-cell recording configuration. (Bottom) Infrared–differential interference contrast image of a paired recording between a mossy fiber bouton and a postsynaptic CA3 pyramidal neuron to which the bouton was attached at the apical dendrite. Photomontage of individual images at slightly different focal planes. Images were captured in the cell-attached mode before reaching the whole-cell configuration. (**B**) Paired whole-cell recording with 0.1 mM EGTA in the presynaptic recording pipette (control). (**C**) Paired whole-cell recording with 0.2 mM BAPTA. (**D**) Paired whole-cell recording with 10 mM EGTA. For (B) to (D), the presynaptic action potential is shown on top, and 10 consecutive EPSCs in the postsynaptic CA3 pyramidal neurons are shown superimposed (gray, blue, and red) at the bottom, overlayed with the average (black in all cases; 20-s repetition interval). (**E**) Concentration-effect relationship of EPSC peak amplitude against presynaptic BAPTA or EGTA concentration for separate paired recordings. (**F** to **H**) Mean synaptic delay (F), EPSC 20 to 80% rise time (G), and EPSC decay time constant (H) against presynaptic BAPTA or EGTA concentration. Error bars indicate SEM.

tance between neighboring release sites at mossy fiber synapses (400 to 500 nm) (*20*), suggesting that local rather than global presynaptic Ca^{2+} elevations drive transmitter release.

A hallmark property of mossy fiber synapses is the pronounced facilitation of transmitter release (*15*). However, the mechanisms of facilitation at central synapses remain controversial (*21*–*24*). We therefore examined the dynamics of transmission and tested the effects of Ca^{2+} chelators (fig. S2). Presynaptic terminals were stimulated by 50-Hz trains of brief pulses with either control or BAPTA- or EGTA-containing solutions loaded into presynaptic terminals. Mossy fiber EPSCs showed depression in control solutions (fig. S2A) but marked facilitation after loading with exogenous Ca^{2+} chelators (fig. S2, B and C). The facilitation induced by BAPTA resembled the "pseudofacilitation" in cortical pyramidal neuron–interneuron synapses, although the extent was larger than previously reported (*25*).

Why do unitary mossy fiber EPSCs under control conditions show large initial amplitude (Fig. 1B) and marked depression (fig. S2A), whereas several previous studies reported low release probability and facilitation (*11*, *15*, *26*, *27*)? To resolve this apparent contradiction, we stimulated mossy fiber boutons noninvasively in the tight-seal, bouton-attached voltage-clamp configuration with brief voltage pulses (Fig. 3, A to G; fig. S3; and table S1). Suprathreshold stimuli reliably evoked action currents, which consecutively triggered EPSCs in postsynaptic CA3 pyramidal neurons (Fig. 3, B to D). Average unitary EPSCs evoked by bouton-attached stimulation had mean synaptic delays of 1.43 ± 0.07 ms, 20 to 80% rise times of 1.33 ± 0.12 ms, and peak amplitudes of 260 ± 28 pA (27 pairs). Moreover, transmitter release from intact boutons showed a marked facilitation (Fig. 3, E and F). On average, $EPSC_2/EPSC_1$ was 3.34 ± 0.52, whereas $EPSC_3/EPSC_1$ was 3.19 ± 0.63 (21 pairs). In parallel to the onset of facilitation, the 20 to 80% rise time of average EPSCs increased gradually during train stimulation (Fig. 3G). A comparable degree of facilitation was observed for bouton-attached stimulation at near-physiological temperature (fig. S4 and table S1), consistent with properties of mossy fiber transmission in vivo (*28*). Thus, noninvasive stimulation allowed us to fully replicate the hallmark properties of mossy fiber synaptic transmission, low release probability and facilitation, at the level of unitary EPSCs (*11*, *15*, *26*, *27*).

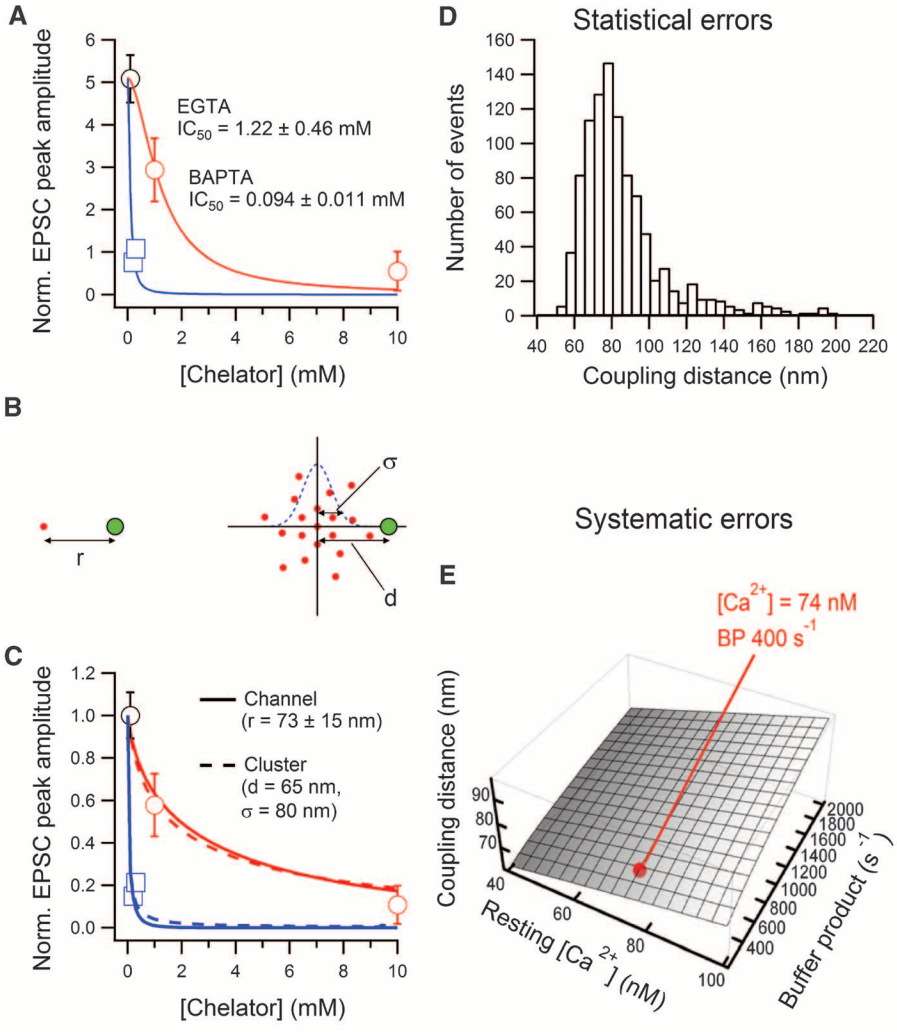

Fig. 2. Loose source-sensor coupling at mossy fiber synapses. (**A**) Concentration-effect curves for BAPTA and EGTA. EPSC peak amplitudes were normalized by the EPSC amplitude in preceding bouton-attached configuration to reduce intersynapse variability. Data points were fit with a Hill equation (Hill coefficient of 1.77, maximal amplitude of 5.08). Error bars, SEM. (**B**) Structure of the model of Ca^{2+} diffusion and buffering based on the analytical steady-state solution to the linearized reaction-diffusion equations. (Left) Single-channel model; (right) multichannel model. Red dots, Ca^{2+} channels; green dots, synaptic vesicles with Ca^{2+} sensors. (**C**) Plot of ratio of EPSC peak amplitude in the presence of chelator to that in control conditions against the concentration of BAPTA (blue squares) and EGTA (red circles). Curves represent the predictions of the models fit to the entire data set (continuous curves, single-channel model; dashed curves, multichannel model). The best fit was obtained with r = 73 nm (single-channel model) or d = 65 nm and σ = 80 nm (multichannel model). Error bars, SEM. (**D**) Statistical errors. Histogram of estimated coupling distance in 1000 bootstrap replications fit by using the single-channel model. (**E**) Systematic errors. Plot of coupling distance against resting Ca^{2+} concentration and endogenous buffer product. Red point indicates default parameter values.

Our results demonstrate that exogenous Ca^{2+} buffers markedly affect both release probability and short-term dynamics at the hippocampal mossy fiber synapse. To examine whether endogenous Ca^{2+} buffers in presynaptic terminals have similar effects, we compared transmitter release in the noninvasive recording configuration with that after washout of endogenous buffers in the same synapse (Fig. 3, H to K). Dialysis of the bouton with control pipette solution produced a marked increase in the peak amplitude of $EPSC_1$ (from 304 ± 59 to 1470 ± 242 pA; five pairs; P = 0.004; Fig. 3, I and J). Thus, endogenous Ca^{2+} buffers may control initial release probability. Furthermore, transition from bouton-attached to whole-bouton configuration with control pipette solution led to a switch from facilitation to depression (Fig. 3K). Different mechanisms may contribute to this change. First, the effects of endogenous buffers on facilitation could be indirect, mediated by changes in release probability. Alternatively, the endogenous Ca^{2+} buffers may have direct effects on facilitation. To distinguish between these possibilities, we adopted a method to correct for the overlaying effects of pool depletion (fig. S5 and materials and methods) (*17*, *29*). The extent of corrected facilitation was markedly higher in the noninvasive recording configuration than after washout of the endogenous buffers (fig. S5B). Thus, endogenous Ca^{2+} buffers have direct effects on facilitation, independently of their effects on pool depletion.

If the endogenous buffers act directly, as our results suggest, facilitation should be rescued by exogenous Ca^{2+} buffers. We perfused the presynaptic terminal with different concentrations of EGTA and BAPTA (Fig. 4, A to E). Dialysis of mossy fiber boutons with 1 mM EGTA resulted

in a pronounced increase in $EPSC_1$ amplitude (from 456 ± 32 for bouton-attached to 1292 ± 266 pA for whole-bouton stimulation; three pairs; $P = 0.11$) and reduction of paired-pulse facilitation ($EPSC_2/EPSC_1$ = 2.2 ± 0.6 versus 1.0 ± 0.4; three pairs; $P = 0.03$; fig. S6, B and C). Thus, the properties of endogenous buffers were not rescued. In contrast, dialysis of mossy fiber boutons with submillimolar concentrations of BAPTA preserved $EPSC_1$ amplitude (from 317 ± 127 pA for bouton-attached to 321 ± 138 pA for whole-bouton stimulation with 0.3 mM BAPTA; three pairs; $P = 0.97$; Fig. 4B). Moreover, BAPTA largely rescued the short-term dynamics phenotype, with facilitation followed by depression during a train of 10 stimuli (Fig. 4F). However, 0.3 mM BAPTA did not exactly mimic the onset of facilitation during repetitive stimulation. This may suggest that either the native buffers have different binding properties and concentration or that additional factors (adenosine triphosphate or guanosine triphosphate) are involved.

To further constrain both binding properties and concentration of the endogenous buffers, we compared the EPSC peak amplitude and the $EPSC_2/EPSC_1$ and $EPSC_3/EPSC_1$ ratios before (bouton-attached configuration) and after dialysis (whole-bouton configuration) over a wide range of buffer concentrations (Fig. 4, D and E). For EGTA, high concentrations of 10 mM were required to mimic the EPSC peak amplitude (Fig. 4D, red symbols). However, these concentrations failed to replicate the facilitation of transmitter release from intact boutons (Fig. 4C). In contrast, BAPTA at a concentration of 0.2 to 0.3 mM reproduced both the EPSC peak amplitude and the extent of facilitation (Fig. 4, D and E, blue symbols). These results suggest that the endogenous buffers have fast, BAPTA-like Ca^{2+}-binding properties and are present in mossy fiber terminals at submillimolar concentration (~0.2 to 0.3 mM). On the basis of washout kinetics, we were able to

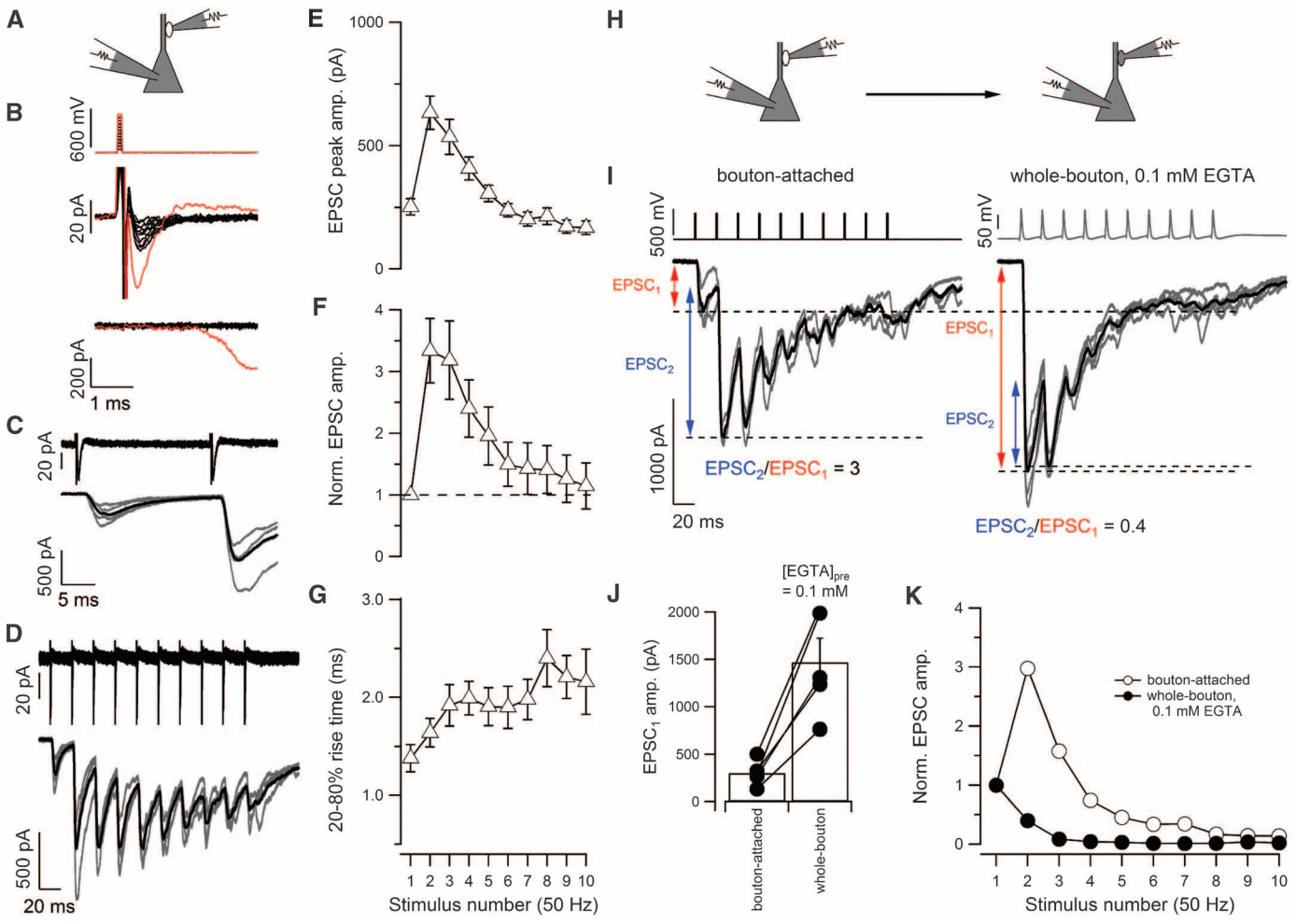

Fig. 3. Endogenous Ca^{2+} buffers control initial release probability and facilitation in mossy fiber boutons. (**A**) Schematic illustration of the tight-seal, bouton-attached voltage-clamp stimulation and recording configuration. (**B**) Unitary EPSCs evoked by presynaptic stimulation in the bouton-attached configuration. Top traces, voltage steps (50 to 600 mV, 0.1 ms) applied to the presynaptic terminal. Middle traces, currents recorded in the presynaptic terminal. Bottom traces, EPSCs in the CA3 pyramidal neuron. Red traces show successful stimulation. (**C** and **D**) Unitary EPSCs evoked by presynaptic 50-Hz bouton-attached stimulation [600 mV, 0.1 ms; same recording as in (B)]. Four consecutive sweeps are shown superimposed (gray), overlayed with the average (black). The action current is the average of four individual sweeps. (**E** to **G**) Mean EPSC amplitude (21 pairs), normalized EPSC amplitude (21 pairs), and 20 to 80% rise time (19 to 21 pairs) against stimulus number for 50-Hz bouton-attached stimulation. Data points are connected by lines for clarity; horizontal dashed line in (F) indicates unity. Error bars, SEM. (**H**) Schematic illustration of the washout experiment. (**I**) Paired recording in which the mossy fiber bouton was first stimulated in the bouton-attached voltage-clamp configuration (left) and subsequently in the whole-bouton current-clamp configuration (~1 min post break-in, right). EPSCs were recorded in the CA3 pyramidal neuron under whole-cell voltage-clamp conditions. Three and five consecutive sweeps are shown for bouton-attached and whole-bouton stimulation, respectively. (**J**) Summary of results from experiments like those shown in (I). Dialysis of the nerve terminal with control pipette solution markedly increased peak $EPSC_1$ amplitude (five pairs). Bars indicate mean ± SEM; circles represent data from individual experiments. Lines connect data points from the same experiment. (**K**) Short-term dynamics of EPSCs with bouton-attached (open circles) and subsequent whole-bouton stimulation (solid circles). Data from the same paired recording as shown in (I). Data points are connected by lines.

constrain the diffusion coefficient of the endogenous buffers to >10 $\mu m^2\ s^{-1}$ (materials and methods) (*30*).

To better understand the interrelation between loose channel-sensor coupling and the action of endogenous buffers, we developed a quantitative model of transmitter release, comprising action potential–induced Ca^{2+} inflow, buffered diffusion, and release sensor activation (Fig. 4, F to H) (*6*, *31*). When a fast Ca^{2+} buffer was included, the model adequately predicted both low initial release probability and facilitation of transmitter release (Fig. 4G). Several candidate mechanisms of facilitation have been proposed, including residual Ca^{2+} (*21*), Ca^{2+} bound to the Ca^{2+} sensor, and saturation of endogenous Ca^{2+} buffers (*23*–*25*). We tested the contribution to facilitation by resetting each individual factor to its initial value during the time interval between two subsequent action potentials (Fig. 4H). Resetting the occupancy of the Ca^{2+} sensor or the residual Ca^{2+} concentration had only minimal effects on facilitation (Fig. 4H, top right and bottom left, respectively). In contrast, resetting the occupancy of the Ca^{2+} buffer largely abolished facilitation (Fig. 4H, bottom right). Facilitation was minimal for coupling distances <25 nm but was markedly enhanced as the coupling distance was increased (Fig. 4H). Thus, loose coupling was essential for the generation of facilitation via buffer saturation. After action potential activity, the concentration of the free buffer was reduced relatively uniformly (fig. S6A), suggesting that buffer saturation was global rather than local (*32*).

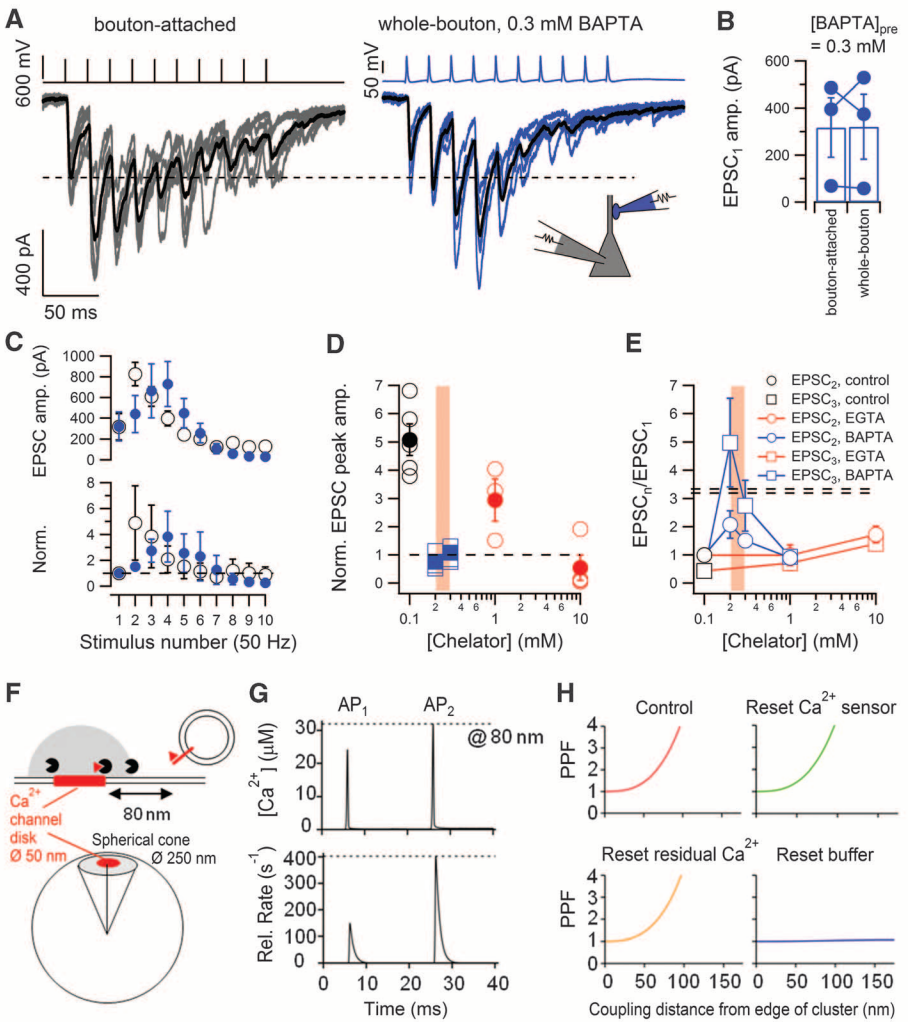

Fig. 4. A fast Ca^{2+} buffer rescues both low release probability and facilitation in experiments and transmitter release models. (**A**) EPSCs evoked by bouton-attached stimulation (left, six sweeps) and subsequent whole-bouton stimulation (right, five sweeps) with 0.3 mM BAPTA in the presynaptic recording pipette (50-Hz stimulation). Dialysis of the mossy fiber bouton with BAPTA resulted in $EPSC_1$ peak amplitude similar to that recorded with bouton-attached stimulation and synaptic facilitation followed by depression. (**B** and **C**) Summary graphs showing the effects of 0.3 mM BAPTA on $EPSC_1$ amplitude (B) and short-term dynamics (C). (**D**) Effects of different concentrations of chelators on $EPSC_1$ peak amplitude, compared to release from intact terminals (dashed line). For each experiment, $EPSC_1$ was normalized to the amplitude in preceding bouton-attached measurements. (**E**) Effects of different concentrations of chelators on facilitation compared with release from intact terminals (dashed lines indicate mean $EPSC_2/EPSC_1$ and $EPSC_3/EPSC_1$ values from data in Fig. 3F). Red shaded regions in (D) and (E) indicate the BAPTA concentration range that mimics both release probability and synaptic facilitation. (**F**) Structure of the transmitter release model. A single release site of a mossy fiber bouton was modeled as a spherical cone. Ca^{2+} channels were placed in a disc with 50-nm diameter on the surface of the sphere (red bar). The Ca^{2+} sensor was placed on the synaptic vesicle 80 nm from the border of the disk (red line). Ca^{2+} transients were calculated as the numerical solution to the set of partial differential reaction-diffusion equations. Black circles, endogenous buffer; red triangles, Ca^{2+} ions; gray hemisphere, Ca^{2+} domain. (**G**) Free internal Ca^{2+} concentration (top) and release rate (bottom) during two action potentials separated by 20-ms intervals, with the release sensor placed at 80 nm from the edge of the source. A fast endogenous Ca^{2+} buffer (0.3 mM, Ca^{2+}-binding and unbinding rates two times faster than BAPTA) was included to approximate the endogenous situation. Horizontal dashed lines indicate the maximal Ca^{2+} concentration and release rate during the second action potential. (**H**) Plot of paired-pulse facilitation ($EPSC_2/EPSC_1$) against coupling distance. Red curve, facilitation in the standard model including all facilitation mechanisms; green, reset of Ca^{2+} sensor; orange, reset of residual Ca^{2+}; blue, reset of Ca^{2+} buffer at t = 20 ms. Error bars, SEM.

Facilitation by buffer saturation was observed over a wide range of functional properties of endogenous buffers and structural properties of mossy fiber synapses (figs. S7, B and C, and S8). Simultaneous analysis of the dependence of release probability and facilitation on Ca^{2+}-binding rate (k_{on}) and buffer concentration (c_B), followed by comparison with our experimental observations in the bouton-attached configuration, further suggested that the endogenous buffers have a k_{on} > ~2 times faster than BAPTA and a c_B of ~100 to 150 μM. Among three naturally expressed Ca^{2+}-binding proteins, calbindin, calretinin, and calmodulin (*33*–*36*), none mimicked all experimentally observed release properties (figs. S7D and S9). These results are consistent with the observation that genetic elimination of calbindin has only small effects on facilitation (*22*).

The present results provide a demonstration of loose coupling between Ca^{2+} channels and release sensors at a mature cortical synapse. Our findings challenge the prevailing view that loose coupling is a purely developmental phenomenon (*5*) and instead demonstrate that coupling is regulated in a synapse-specific manner. Together with previous observations of tight coupling at fast-signaling synapses (*5*–*9*), our results suggest that loose coupling is preferentially expressed in dynamic and plastic synapses (*16*). Our results help to understand several previously elusive functional properties of hippocampal mossy fiber synapses. First, they explain the low release probability after single presynaptic action potentials (*11*, *27*) (fig. S10). This low initial release probability has been highly puzzling, given the large size of the terminals, the large number of active zones, and the huge vesicular pool (*20*, *37*, *38*).

We demonstrate that loose coupling enables access of endogenous Ca^{2+} buffers acting as "brakes" on release probability. Second, our results shed light on the mechanism of presynaptic facilitation, a hallmark property of mossy fiber synapses (*13*, *15*, *26*). Loose coupling permits facilitation via saturation of endogenous Ca^{2+} buffers (*25*) (fig. S10). Last, our results have major implications for the mechanisms of long-term potentiation (LTP) at hippocampal mossy fiber synapses. Previous studies have shown that expression of mossy fiber LTP has a presynaptic locus but is not associated with a rise in the amplitude of global presynaptic Ca^{2+} transients (*39*). These results could be explained by a change in the coupling distance, a local change in the concentration of endogenous Ca^{2+} buffers, or a combination of both. This may allow faster onset of regulation of synaptic strength than a mechanism based on changes in the number of Ca^{2+} channels (*40*).

The large size of the presynaptic terminals and the proximal location of the synapse previously led to the idea that the mossy fiber synapse acts as an efficient "teacher" synapse in the network, driving the induction of heterosynaptic plasticity in synapses between CA3 cells (*41*, *42*). However, it is also widely accepted that mossy fiber synapses operate as conditional "detonators" (*28*). A single action potential in a presynaptic granule cell is not sufficient to trigger a spike in a postsynaptic CA3 pyramidal cell but needs to act in combination with presynaptic short-term plasticity. These properties are critical for network function, making the impact of the mossy fiber synapse dependent on burst activity in granule cells (*28*, *43*). Our results reveal that loose channel-sensor coupling and the presence of fast endogenous Ca^{2+} buffers are the key properties underlying the conditional detonator function of mossy fiber synapses. The switchlike nonlinearity conveyed by this specific design may assist in the separation of storage and retrieval modes in hippocampal memory circuits (*41*).

References and Notes

1. E. Neher, *Cell Calcium* **24**, 345–357 (1998).
2. C. J. Meinrenken, J. G. G. Borst, B. Sakmann, *J. Neurosci.* **22**, 1648–1667 (2002).
3. E. Eggermann, I. Bucurenciu, S. P. Goswami, P. Jonas, *Nat. Rev. Neurosci.* **13**, 7–21 (2012).
4. J. G. G. Borst, B. Sakmann, *Nature* **383**, 431–434 (1996).
5. M. J. Fedchyshyn, L. Y. Wang, *J. Neurosci.* **25**, 4131–4140 (2005).
6. I. Bucurenciu, A. Kulik, B. Schwaller, M. Frotscher, P. Jonas, *Neuron* **57**, 536–545 (2008).
7. J. M. Christie, D. N. Chiu, C. E. Jahr, *Nat. Neurosci.* **14**, 62–68 (2011).
8. A. Scimemi, J. S. Diamond, *J. Neurosci.* **32**, 18157–18176 (2012).
9. H. Schmidt *et al.*, *Curr. Biol.* **23**, 244–249 (2013).
10. T. H. Brown, D. Johnston, *J. Neurophysiol.* **50**, 487–507 (1983).
11. P. Jonas, G. Major, B. Sakmann, *J. Physiol.* **472**, 615–663 (1993).
12. J. R. P. Geiger, P. Jonas, *Neuron* **28**, 927–939 (2000).
13. R. A. Nicoll, D. Schmitz, *Nat. Rev. Neurosci.* **6**, 863–876 (2005).
14. J. Bischofberger, D. Engel, M. Frotscher, P. Jonas, *Pflugers Arch.* **453**, 361–372 (2006).
15. P. A. Salin, M. Scanziani, R. C. Malenka, R. A. Nicoll, *Proc. Natl. Acad. Sci. U.S.A.* **93**, 13304–13309 (1996).
16. S. Nadkarni, T. M. Bartol, C. F. Stevens, T. J. Sejnowski, H. Levine, *Proc. Natl. Acad. Sci. U.S.A.* **109**, 14657–14662 (2012).
17. R. Schneggenburger, A. C. Meyer, E. Neher, *Neuron* **23**, 399–409 (1999).
18. H. von Gersdorff, J. G. G. Borst, *Nat. Rev. Neurosci.* **3**, 53–64 (2002).
19. E. M. Adler, G. J. Augustine, S. N. Duffy, M. P. Charlton, *J. Neurosci.* **11**, 1496–1507 (1991).
20. A. Rollenhagen *et al.*, *J. Neurosci.* **27**, 10434–10444 (2007).
21. B. Katz, R. Miledi, *J. Physiol.* **195**, 481–492 (1968).
22. M. Blatow, A. Caputi, N. Burnashev, H. Monyer, A. Rozov, *Neuron* **38**, 79–88 (2003).
23. F. Felmy, E. Neher, R. Schneggenburger, *Neuron* **37**, 801–811 (2003).
24. R. S. Zucker, W. G. Regehr, *Annu. Rev. Physiol.* **64**, 355–405 (2002).
25. A. Rozov, N. Burnashev, B. Sakmann, E. Neher, *J. Physiol.* **531**, 807–826 (2001).
26. K. Toth, G. Suares, J. J. Lawrence, E. Philips-Tansey, C. J. McBain, *J. Neurosci.* **20**, 8279–8289 (2000).
27. J. J. Lawrence, Z. M. Grinspan, C. J. McBain, *J. Physiol.* **554**, 175–193 (2004).
28. D. A. Henze, L. Wittner, G. Buzsáki, *Nat. Neurosci.* **5**, 790–795 (2002).
29. M. S. Thanawala, W. G. Regehr, *J. Neurosci.* **33**, 4625–4633 (2013).
30. M. Pusch, E. Neher, *Pflugers Arch.* **411**, 204–211 (1988).
31. E. Eggermann, P. Jonas, *Nat. Neurosci.* **15**, 20–22 (2012).
32. V. Matveev, R. S. Zucker, A. Sherman, *Biophys. J.* **86**, 2691–2709 (2004).
33. M. D. Brandt *et al.*, *Mol. Cell. Neurosci.* **24**, 603–613 (2003).
34. A. Müller *et al.*, *J. Neurosci.* **25**, 558–565 (2005).
35. B. Schwaller, *Cold Spring Harb. Perspect. Biol.* **2**, a004051 (2010).
36. G. C. Faas, S. Raghavachari, J. E. Lisman, I. Mody, *Nat. Neurosci.* **14**, 301–304 (2011).
37. M. E. Chicurel, K. M. Harris, *J. Comp. Neurol.* **325**, 169–182 (1992).
38. S. Hallermann, C. Pawlu, P. Jonas, M. Heckmann, *Proc. Natl. Acad. Sci. U.S.A.* **100**, 8975–8980 (2003).
39. H. Kamiya, K. Umeda, S. Ozawa, T. Manabe, *J. Neurosci.* **22**, 10524–10528 (2002).
40. J. Sheng *et al.*, *Nat. Neurosci.* **15**, 998–1006 (2012).
41. A. Treves, E. T. Rolls, *Hippocampus* **2**, 189–199 (1992).
42. K. Kobayashi, M. M. Poo, *Neuron* **41**, 445–454 (2004).
43. J. E. Lisman, *Trends Neurosci.* **20**, 38–43 (1997).

Acknowledgments: We thank E. Neher and R. Shigemoto for critically reading the manuscript, F. Marr and M. Duggan for technical assistance, A. Solymosi for manuscript editing, and the scientific service units of IST Austria for efficient help. Supported by the Fond zur Förderung der Wissenschaftlichen Forschung (P 24909-B24) and the European Union (European Research Council Advanced Grant 268548 to P.J.).

Supplementary Materials

www.sciencemag.org/content/343/6171/665/suppl/DC1
Materials and Methods
Figs. S1 to S10
Table S1
References (*44*–*59*)

16 August 2013; accepted 11 December 2013
10.1126/science.1244811

Local Impermeant Anions Establish the Neuronal Chloride Concentration

J. Glykys,[1]* V. Dzhala,[1]* K. Egawa,[1]* T Balena,[1] Y. Saponjian,[1] K. V. Kuchibhotla,[2] B. J. Bacskai,[1] K. T. Kahle,[3] T. Zeuthen,[4] K. J. Staley[1]†

Neuronal intracellular chloride concentration $[Cl^-]_i$ is an important determinant of γ-aminobutyric acid type A ($GABA_A$) receptor ($GABA_AR$)–mediated inhibition and cytoplasmic volume regulation. Equilibrative cation-chloride cotransporters (CCCs) move Cl^- across the membrane, but accumulating evidence suggests factors other than the bulk concentrations of transported ions determine $[Cl^-]_i$. Measurement of $[Cl^-]_i$ in murine brain slice preparations expressing the transgenic fluorophore Clomeleon demonstrated that cytoplasmic impermeant anions ($[A]_i$) and polyanionic extracellular matrix glycoproteins ($[A]_o$) constrain the local $[Cl^-]$. CCC inhibition had modest effects on $[Cl^-]_i$ and neuronal volume, but substantial changes were produced by alterations of the balance between $[A]_i$ and $[A]_o$. Therefore, CCCs are important elements of Cl^- homeostasis, but local impermeant anions determine the homeostatic set point for $[Cl^-]$, and hence, neuronal volume and the polarity of local $GABA_AR$ signaling.

The γ-aminobutyric acid type A ($GABA_A$) receptor ($GABA_AR$) can subserve either inhibition or excitation, because the net flux of the permeating anions HCO_3^- and Cl^- can be reversed by modest changes in the transmembrane concentration gradient of Cl^- (*1*, *2*). NKCC1 and KCC2 are the primary cation-chloride cotransporters (CCCs) in neurons (*3*). Their unique stoichiometries result in distinct $[Cl^-]_i$ equilibria: ~3 mM for KCC2 (*4*, *5*) and ~60 mM for NKCC1 (*3*). The species of cotransporter expressed in the neuron is thought to determine $[Cl^-]_i$, but there is evidence that transporter expression is not the sole determinant of $[Cl^-]_i$ and, hence, the reversal potential for GABA (E_{GABA}). First, CCCs transport water along with cations and Cl^- as nearly isotonic saline (*6*, *7*). Neurons express no known aquaporin water channels (*8*), so the CCCs have limited capacity to alter $[Cl^-]_i$ independently of neuronal volume. Second, the transporter expressed may not correlate with the measured $[Cl^-]_i$ (*9*). Third, electrophysiological and fluorometric studies demonstrate a wide distribution

[1]Department of Neurology, Massachusetts General Hospital, Harvard Medical School, Boston, MA 02115, USA. [2]Skirball Institute for Biomolecular Medicine, New York University School of Medicine, New York, NY 10016, USA. [3]Department of Neurosurgery, Massachusetts General Hospital, Harvard Medical School, Boston, MA 02115, USA. [4]Department of Cellular and Molecular Medicine, University of Copenhagen, 2200 Copenhagen, Denmark.

*These authors contributed equally to this work.
†Corresponding author. E-mail: staley.kevin@mgh.harvard.edu

of $[Cl^-]_i$ that rarely matches the equilibrium for either NKCC1 or KCC2 (*10*–*15*). Finally, subcellular differences in E_{GABA} indicate that $[Cl^-]_i$ is likely to vary within the cytoplasm of individual neurons (*16*, *17*), a condition that cannot be efficiently maintained solely by transporters because of the high rate of dissipation of local $[Cl^-]_i$ by cytoplasmic diffusion (*18*).

A solution is suggested by the fact that Cl^- is only a minor component of the intracellular anionic milieu. The neuronal membrane is impermeable to most cytoplasmic anions, including phosphate groups associated with deoxy- and ribonucleotides, and the majority of intracellular proteins whose amino and carboxyl moieties are negatively charged at physiological pH (*19*). For any value of cytoplasmic volume and osmolarity, the sum of cytoplasmic impermeant anions ($[A]_i$) and $[Cl^-]_i$ must be constant, as $[HCO_3^-]$ is fixed by pH requirements. Thus, $[Cl^-]_i$ should be constrained by $[A]_i$. However, cotransport of Cl^- and cations across a membrane that is impermeant to $[A]_i$ creates an unstable Gibbs-Donnan condition with higher intracellular than extracellular osmotic pressure (*20*). The exclusion of Na^+ from the cytoplasm by Na^+- and K^+-dependent adenosine triphosphatase (Na^+,K^+-ATPase) is thought to create a balancing Gibb-Donnan condition (*7*, *20*), but this mechanism ignores intracellular K^+ and is not supported by pharmacological inhibition of neuronal Na^+,K^+-ATPase (*21*). The sulfates on the proteoglycans of the extracellular matrix (*22*) make up a more plausible impermeant extracellular ion. Manipulation of extracellular proteoglycans alters cell volume, membrane potential, and neuronal network excitability, consistent with Donnan effects (*23*). We investigated whether $[Cl^-]_i$ is set by the local concentrations of impermeant anions on either side of the neuronal membrane.

Direct $[Cl^-]_i$ measurements were performed by using two-photon excitation microscopy imaging in acute and organotypic brain slices of mice expressing Clomeleon [ratiometric fluorophore sensitive to changes in $[Cl^-]_i$ (*18*)]. In neonatal neurons from CA1 hippocampal slices from postnatal day 8 to 9 (P8 to P9), where NKCC1 is the primary transporter expressed (*24*), there was a broad distribution of somatic $[Cl^-]_i$ of 14.7 ± 6.5 mM (median ± SD; $n = 237$ neurons; six slices) (Fig. 1, A and B). In adult CA1 hippocampal slices (P32 to P44), where KCC2 is the primary transporter (*3*), the somatic $[Cl^-]_i$ was also widely distributed 13.7 ± 8.9 mM ($n = 227$ neurons; eight slices) (Fig. 1C). Similar results were found in acute brain slices from neocortex layers IV/V and CA1 organotypic hippocampal slices (figs. S1,

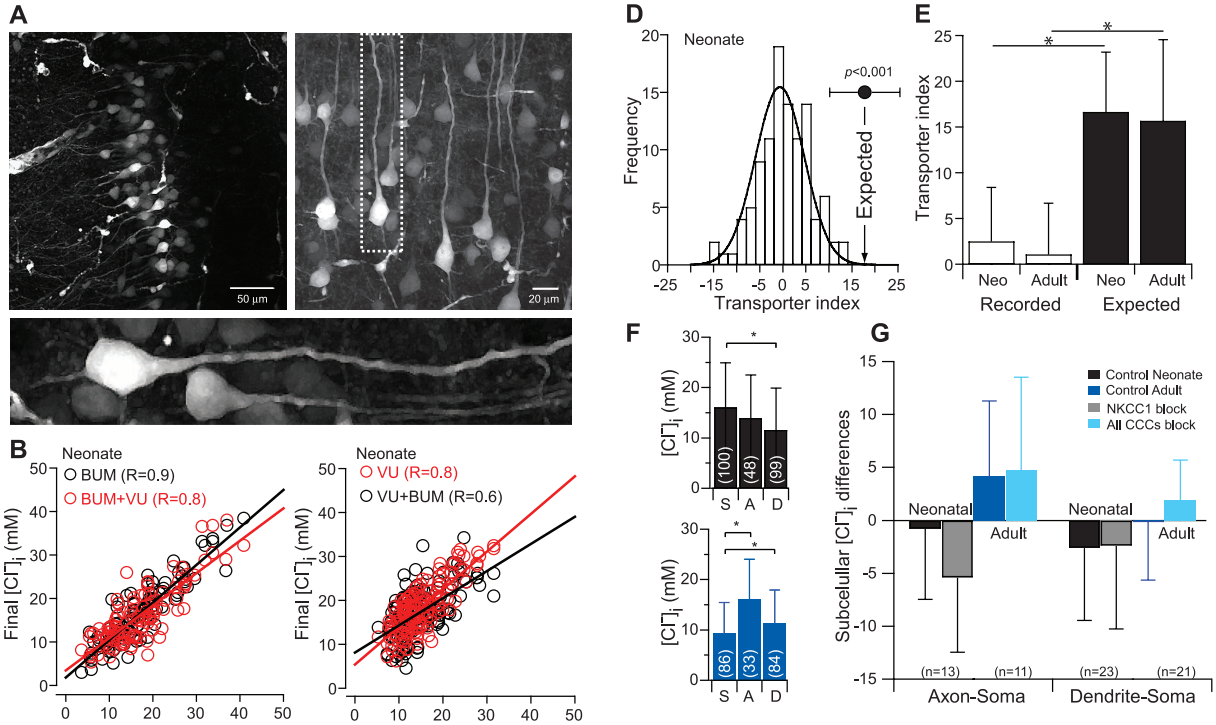

Fig. 1. $[Cl^-]_i$ is not solely determined by transport activity. (**A**) Two-photon microscopy image of Clomeleon yellow fluorescent protein (YFP) from acute hippocampal slice CA1 (left) and neocortex layer IV/V (right). (Bottom) Detailed image of neuron outlined on right above. (**B**) P8 to P9 hippocampal slice. (Left) Initial versus new steady-state $[Cl^-]_i$ after 30-min NKCC1 block followed by an additional 30-min block of KCC2. Lines, linear fit. (Right) Similar to left but KCC2 block was first, followed by KCC2 and NKCC1 blocks. (**C**) As (B) but in P32 to P44 CA1 neurons. (**D**) Transporter index histogram of all neonatal hippocampal neurons (calculated as in methods and fig. S5), 2.5 ± 5.9 ($n = 237$; median ± SD). Black circle indicates expected value for canonical cooperation of KCC2 and NKCC1. (**E**) Transporter index of all recorded neonatal CA1 neurons (2.5 ± 5.9) and adult CA1 neurons (1.07 ± 5.6; $n = 227$) and expected values (neonatal: 16.7 ± 6.5; $n = 237$; adult: 15.7 ± 8.9; $n = 227$). *$P < 0.001$, Mann-Whitney rank-sum test. (**F**) (Top) $[Cl^-]_i$ from P6 to P8 layer IV/V neocortical pyramidal cells [soma (S): 16.0 ± 8.9 mM; axon (A): 13.9 ± 8.6 mM; dendrite (D): 11.5 ± 8.3 mM; difference among all three groups, $P < 0.001$, Friedman test; *$P < 0.05$ multiple-comparison Dunn's method]. (Bottom) $[Cl^-]_i$ from P28 to P30 layer IV/V neocortical pyramidal cells [soma (S): 9.3 ± 6.1 mM; axon (A): 16.1 ± 7.9 mM; dendrite (D): 11.4 ± 6.5 mM; *$P < 0.001$]. (**G**) Subcellular gradient differences between axon-soma and dendrite-soma. Blockade of NKCC1 in neonates (10 µM bumetanide) and NKCC1 and KCC2 in adults (100 µM bumetanide) did not alter the subcellular $[Cl^-]_i$ gradients (paired neuron-process; $P > 0.05$; paired t test, error bars, SD).

A and C, and S2, A and B; and tables S1 and S2). Thus, most neurons have $[Cl^-]_i$ not congruent with the equilibrium conditions of either KCC2 or NKCC1.

If $[Cl^-]_i$ was primarily maintained by CCCs, the change in $[Cl^-]_i$ after transport block should be the opposite of the canonical direction of the primary expressed transporter: KCC2 block should increase $[Cl^-]_i$; NKCC1 block should decrease $[Cl^-]_i$. In neonatal CA1 slices (P8 to P9), blocking NKCC1 with bumetanide 10 μM did not alter $[Cl^-]_i$ (15.8 ± 7.6 to 16 ± 7.3 mM, $n = 105$ paired cells) (Fig. 1B and fig. S3A). Addition of 10 μmol of the specific KCC2 antagonist VU0240551 (*25*) induced a minimal decrease in $[Cl^-]_i$ to 15 ± 6.9 mM (Fig. 1B and fig. S3A), and $[Cl^-]_i$ did not become passively distributed across the membrane such that the reverse potential for Cl^- (E_{Cl}) ≈ resting membrane potential. After CCC block, $[Cl^-]_i$ increased in neurons with a low initial $[Cl^-]_i$ and decreased in neurons with a high initial $[Cl^-]_i$ (fig. S3A), regardless of the order of antagonist application (Fig. 1B and fig. S3B) in adult CA1 slices (P32 to P44) (Fig. 1C and fig. S3, C and D), in CA1 organotypic hippocampal slices after 6 to 11 days in vitro (DIV6 to DIV11) (fig. S2, A to C and E to G), and in acute layer IV/V neocortical pyramidal neurons (P8 to P9 and P27 to P31) (fig. S1 and tables S1 and S2). If no drug was added, $[Cl^-]_i$ was stable (fig. S4, C to E). In summary, the initial $[Cl^-]_i$ was a better predictor of the change in $[Cl^-]_i$ than was the species of blocked transporter. To quantify this, we summed the absolute values of the change in $[Cl^-]_i$ during sequential block of KCC2 and NKCC1. If NKCC1 and KCC2 are working against each other in the same neuron to create a broad distribution of $[Cl^-]_i$, this sum value should be large (fig. S5). However, this sum was nearly 0 in all neuronal populations studied (Fig. 1, D and E, and fig. S2, D and H). Therefore, the broad distribution of $[Cl^-]_i$ cannot be explained by the net effects of oppositely directed NKCC1 and KCC2 cotransport.

$[Cl^-]_i$ varies not only between neurons but also between subcellular regions (*16*), which is difficult to reconcile with the high intracellular mobility of $[Cl^-]_i$ (*18*). We measured millimolar differences in $[Cl^-]_i$ at the soma versus the proximal 40 μm of the axon and the proximal 200 μm of the apical dendrites of neonatal and adult neocortical neurons (sparse neocortical expression of Clomeleon permitted identification of individual processes and soma) (Fig. 1F). Subcellular differences in $[Cl^-]_i$ were not maintained by local CCCs because, after CCC block, $[Cl^-]_i$ gradients were unchanged ($P > 0.05$, paired t test) (Fig. 1G).

These data are not consistent with the hypothesis that $[Cl^-]_i$ is determined by the species of expressed cotransporter. Rather, the data suggest that KCC2 and NKCC1 both serve as conduits for transmembrane Cl^- flux whose direction is determined by other factor(s). We therefore tested the hypothesis that $[A]_i$ and the polyanionic extracellular matrix glycoproteins $[A]_o$ determine the local $[Cl^-]$ and, thus, E_{Cl} and the effect of $GABA_A$ receptor activation.

Prediction 1. If the sum of $[A]_i + [Cl^-]_i$ is constant, then the broad distribution of $[Cl^-]_i$, together with the large intercellular variance in the primary constituents of $[A]_i$ [cytoplasmic protein and nucleic acid concentrations (*26*)], can be used to test for the predicted reciprocal relation between $[A]_i$ and $[Cl^-]_i$. $[A]_i$ and $[Cl^-]_i$ were imaged in Clomeleon organotypic hippocampal slice cultures to facilitate the prolonged dye incubation required to estimate $[A]_i$. CA1 pyramidal neurons demonstrated a wide range of somatic $[Cl^-]_i$ of 14.8 ± 6.3 mM at DIV10 to DIV12 ($n = 305$ neurons; four slices) (Fig. 2, A to C). After Cl^- imaging, slices were incubated for 2 hours in SYTO64 10 μM, which binds to the cytoplasmic-nuclear nucleic

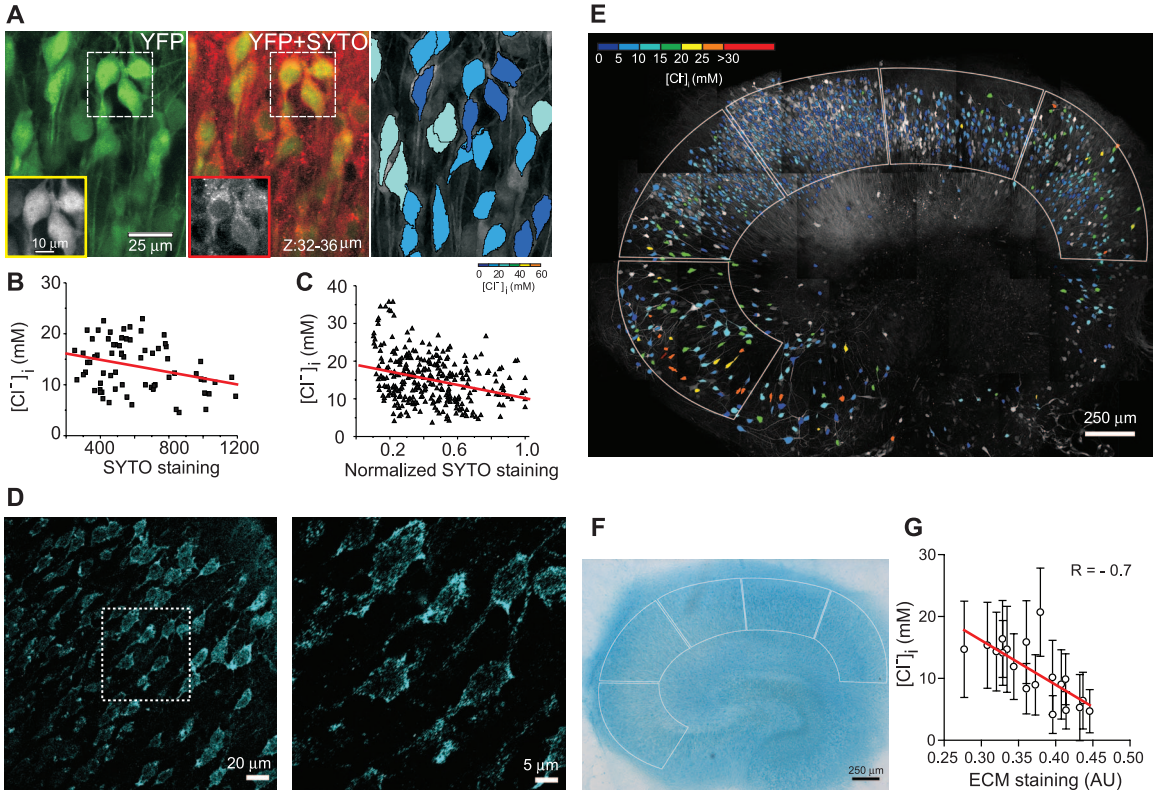

Fig. 2. Correlation of $[A]_i$ and $[A]_o$ with neuronal $[Cl^-]_i$. (**A**) (Left) Two-photon microscopy *z*-stack image of YFP (green) from CA1 pyramidal layer in an organotypic hippocampal slice from a Clomeleon-expressing mouse. (Middle) SYTO64 staining (red) of cytoplasmic and nuclear nucleic acids overlaid on the YFP image. (Boxes) YFP and SYTO64 fluorescence in individual neurons. (Right) Pseudo-colored neurons on the basis of the YFP/CFP (cyan fluorescent protein) ratio. (**B**) $[Cl^-]_i$ as a function of SYTO64 staining. $R = -0.29$, $P = 0.01$; $n = 70$ neurons; one slice. (**C**) $[Cl^-]_i$ as a function of normalized SYTO64 staining. $R = -0.3$, $P < 0.001$; $n = 305$ neurons; four slices. Line, linear fit. (**D** to **F**) Correlation between sulfated extracellular matrix and $[Cl^-]_i$. (D) Confocal images of Alcian blue staining in CA1 pyramidal layer of an organotypic hippocampal slice. Outlined area magnified on right. (E) $[Cl^-]_i$ distribution before Alcian blue staining. Outlines: Region of interest used to calculate average $[Cl^-]_i$ and Alcian blue staining intensity. (F) Alcian blue staining of slice in (E), transmitted light. (**G**) Correlation between $[Cl^-]_i$ and extracellular matrix (Alcian blue staining) obtained in each region of interest, four slices. Error bars, SD; AU, arbitrary units. Line, linear fit ($P < 0.001$).

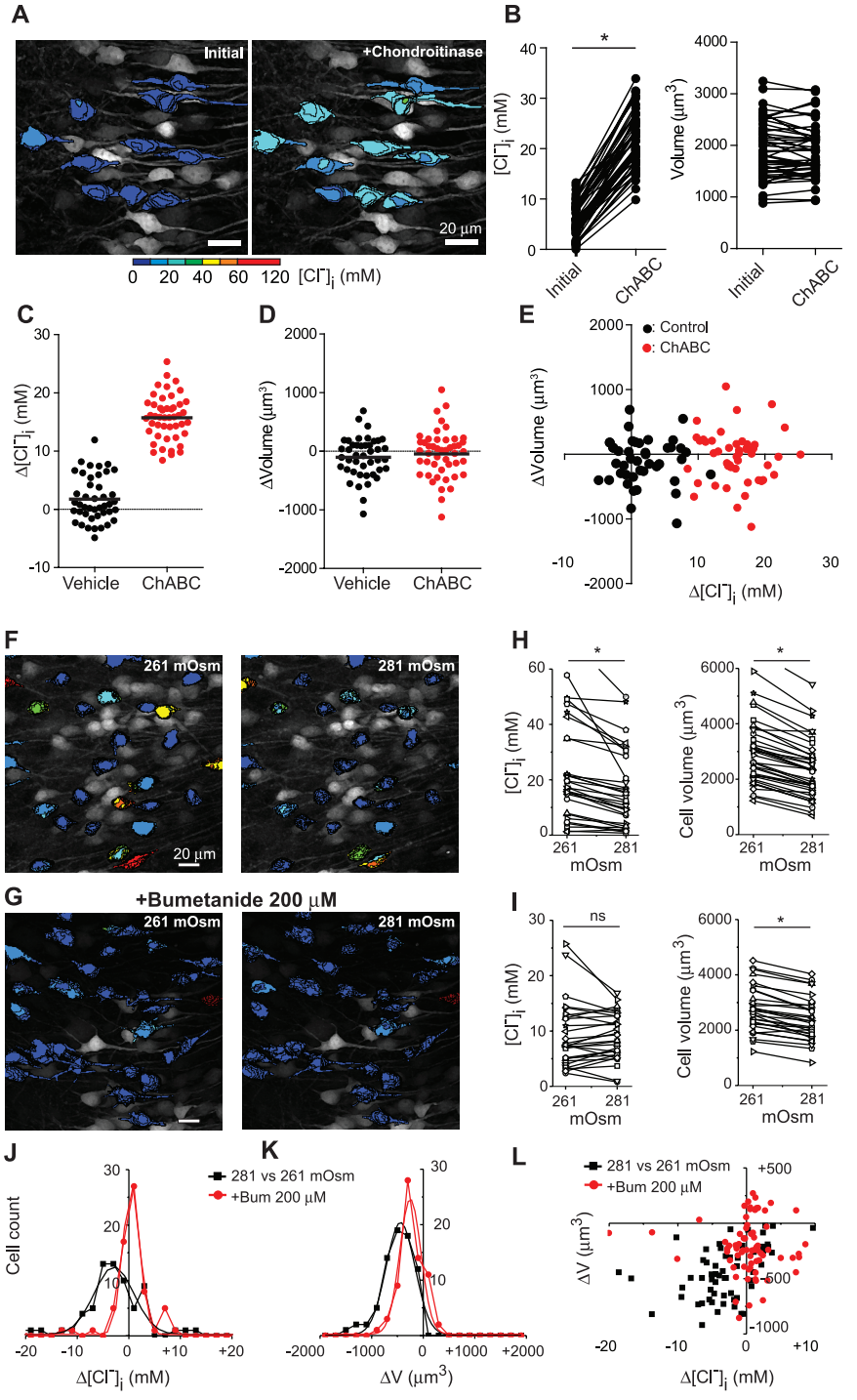

Fig. 3. $[Cl^-]_i$ is changed by disruption of the extracellular matrix and by increased extracellular osmolarity. (**A**) Pseudo-colored, two-photon microscopy z-stack image before and after incubation with chondroitinase ABC (ChABC) in an organotypic hippocampal slice. (**B**) Significant effect of ChABC on $[Cl^-]_i$, but not volume. (**C**) $[Cl^-]_i$ change by incubation with vehicle versus ChABC solution (vehicle: +0.8 ± 3.9 mM, $n = 43$; four slices; ChABC: +15.8 ± 3.8 mM, $n = 47$; four slices; $P < 0.0001$, unpaired t test). (**D**) As in (C) but plotting somatic volume (vehicle; −52 ± 174 μm³, ChABC; −23 ± 203 μm³, $P = 0.46$ unpaired t test. Change in vehicle: 1699 ± 480 to 1647 ± 464 μm³, $P = 0.08$. Change in ChABC: 1905 ± 564 to 1882 ± 516 μm³, $P = 0.51$, Wilcoxon signed rank test, same cells as (C). (**E**) Volume versus $[Cl^-]_i$ changes for each neuron in (C) and (D). *$P < 0.0001$. (**F** and **G**) Organotypic hippocampal slices expressing Clomeleon (two-photon microscopy) after increasing osmolarity with 20 mM mannitol (8% increase) and in bumetanide (G). (**H** and **I**) $[Cl^-]_i$ and neuronal volume changes in mannitol (H) and mannitol plus bumetanide (I). (**J** and **K**) $[Cl^-]_i$ and neuronal somatic volume changes induced by increased extracellular osmolarity. (**L**) Neuronal volume changes as a function of $[Cl^-]_i$ changes.

acids whose phosphate groups are a major component of $[A]_i$. SYTO64 staining intensity was negatively correlated with $[Cl^-]_i$ [correlation coefficient (R) = −0.3; $P < 0.001$] (Fig. 2, B and C). Because nucleic acids make up approximately one-third of intracellular fixed anions (*27*), the strength of the correlation between SYTO64 staining and $[Cl^-]_i$ is what would be predicted if $[A]_i$ sets $[Cl^-]_i$.

Prediction 2. If the sum of $[A]_i$ and $[Cl^-]_i$ is constant, then increasing $[A]_i$ should decrease $[Cl^-]_i$. $[A]_i$ was increased by iso-osmotic perfusion of 20 mM gluconate, pyruvate, and D-lactate, which are weak organic acids that are transported across the cytoplasmic membrane (*28*). Each perfusion reduced $[Cl^-]_i$ by 5 to 10%, consistent with a corresponding increase in $[A]_i$ due to a Nernstian distribution of the deprotonated, anionic bases at a resting membrane potential near −70 mV (fig. S6). This was unlikely a pH effect on Clomeleon fluorescence, because the pH_i effects (*29*) would alter Clomeleon fluorescence in the opposite direction from those observed (*18*). Thus, increases in $[A]_i$ are accompanied by reductions in $[Cl^-]_i$, so that the sum of $[A]_i + [Cl^-]_i$ is constant.

Prediction 3. If $[A]_o$ sets the local extracellular chloride concentration $[Cl^-]_o$, then cation-chloride cotransport should come to equilibrium at a $[Cl^-]_i$ that reflects the local $[Cl^-]_o$. Thus, $[A]_o$ should vary inversely with $[Cl^-]_i$. The polysulfated proteoglycans of the extracellular matrix create extracellular negative charge densities of 50 to 350 mEq/liter and, thus, could compose $[A]_o$ (*30*). We first verified that extracellular Na^+ does not exert a significant Donnan effect (*21*) (fig. S7). Next, $[Cl^-]_i$ was measured in organotypic Clomeleon hippocampal slices (DIV12 to DIV14). Then, slices were fixed and incubated with Alcian blue at pH 0.5 to specifically stain sulfated glycosaminoglycans (*31*). $[A]_o$ as assayed by Alcian blue staining was negatively correlated with $[Cl^-]_i$ ($R = -0.7$, $P < 0.001$) (Fig. 2, D to G, and fig. S8). These data support the possibility that polysulfated proteoglycans of the extracellular matrix make up $[A]_o$ and that, together with $[A]_i$, these macromolecular anions constrain the local $[Cl^-]$ to set the local E_{Cl}.

Prediction 4. Decreasing $[A]_o$ will increase $[Cl^-]_i$. If the sulfated carbohydrate moieties of the proteoglycans in the extracellular matrix subserve this function, then their lysis would release SO_4^- and reduce $[A]_o$. This would increase local $[Cl^-]_o$ and shift the equilibrium condition for transmembrane cation-chloride transport toward higher $[Cl^-]_i$. Accordingly, when organotypic hippocampal slices (DIV12 to DIV14) were incubated in chondroitinase ABC (ChABC) for 1 hour, neuronal $[Cl^-]_i$ increased from 5.9 ± 3.4 to 20.2 ± 5.7 mM ($n = 47$ neurons; four slices, $P < 0.0001$, Wilcoxon signed rank test) (Fig. 3, A to E). The $[Cl^-]_i$ change was significantly higher ($P < 0.0001$) than that by incubation with vehicle solution (from 9.2 ± 2.7 to 10.9 ± 4.3 mM, $n = 43$; four slices, $P = 0.02$). Somatic volume was unchanged at ~80 min (Fig. 3, B, D, and E), which likely

reflects successful compensatory volume regulation. Cell viability was not altered by incubation in ChABC (fig. S9).

Prediction 5. In a system in which $[A]_i$, $[A]_o$, and $[Cl^-]_i$ are in ionic and osmotic equilibrium, acutely altering the osmotic balance should alter $[Cl^-]_i$. Water is transported with cations and Cl^- by CCCs (*6*, *7*), and neurons lack known aquaporins (*8*). Thus, water movement contributes to the free energy of cotransport (*6*). An increase in extracellular osmolarity would favor CCC movement of water and Cl^- out of the neuron, increasing the fractional cytoplasmic concentration of $[A]_i$ and decreasing $[Cl^-]_i$. This is opposite to what would be predicted by free transmembrane water permeability: Loss of intracellular water would increase $[Cl^-]_i$ (*7*). Two-photon multiplanar micrographs of individual pyramidal cells from organotypic hippocampal slices (DIV8 to DIV12) expressing Clomeleon were reconstructed in three dimensions to measure volume and $[Cl^-]_i$ (Fig. 3, F to I). In control conditions, the somatic volume and $[Cl^-]_i$ were stable as a function of time (fig. S4). Increasing extracellular osmolarity by 8% [from 261 (the osmolarity of culture medium) to 281 mOsm] via the addition of 20 mM mannitol resulted in a rapid 21% decrease in somatic volume from 2333 ± 1192 to 1842 ± 967 μm^3 (mean ± SD, n = 73 neurons; four slices; $P < 0.001$, paired t test) and a 9% decrease in somatic $[Cl^-]_i$ from 16.6 ± 14.6 to 15.1 ± 11.1 mM ($P < 0.001$, Wilcoxon signed rank test) (Fig. 3, H, J, and L). Using the same protocol but blocking NKCC1 and KCC2 (with bumetanide 200 μM) resulted in a 9% decrease in somatic volume from 2365 ± 1005 to 2147 ± 953 μm^3 (n = 68 neurons; three slices; $P < 0.0001$, paired t test) (Fig. 3, I and K) and no change in somatic $[Cl^-]_i$ from 7.1 ± 10 to 8.3 ± 7.9 mM (P = 0.074, Wilcoxon signed rank test) (Fig. 3, I to L). The unlinking of volume and $[Cl^-]_i$ changes when CCCs were blocked is likely to represent volume regulation by other systems (*7*).

Finally, a consequence of the cotransport of water and salt by NKCC1 and KCC2 is that near-isotonic saline moves across the membrane, so that both neuronal volume and $[Cl^-]_i$ should change in parallel during cotransport. Several conditions—including hypoxic ischemic injury, trauma, and prolonged seizures—have in common the development of cytotoxic edema and increased neuronal $[Cl^-]_i$ (*15*, *32*, *33*). To test whether seizure-induced increases in neuronal volume are associated with acute increases in $[Cl^-]_i$, we performed extracellular field recording and two-photon microscopy to measure cytoplasmic volume and $[Cl^-]_i$ in organotypic hippocampal slice cultures (DIV10 to DIV12) that spontaneously develop ictal-like epileptiform discharges (*34*). Prolonged seizure activity increased both neuronal volume and $[Cl^-]_i$ (Fig. 4). Somatic volume increased by 10% from 2530 ± 1658 to 2775 ± 1741 μm^3 (mean ± SD; n = 42 neurons; four slices; P = 0.006, paired t test) and $[Cl^-]_i$ increased from 25.4 ± 7.4 to 40.8 ± 13.8 mM ($P < 0.001$, Wilcoxon signed rank test). The increase in $[Cl^-]_i$ during seizures is mediated by NKCC1 as it can be reduced by bumetanide (*15*).

These data indicate that the local $[A]_i$ and $[A]_o$ determine $[Cl^-]_i$, $[Cl^-]_o$, and, thus, E_{GABA}, and CCCs serve to maintain $[Cl^-]_i$ at this set point. Therefore, (i) the widely observed intercellular and intracellular variances in $[Cl^-]_i$ and E_{GABA} are best explained by local variation in $[A]_i$ and $[A]_o$. The species of CCC and other cellular features are likely to correlate with $[A]_i$ and $[Cl^-]_i$ [e.g., (*14*, *24*)]. (ii) The developmental reduction in $[Cl^-]_i$ would follow from the increase in neuronal $[A]_i$ during development (*35*) and experience (*36*), paralleled by increases in the proteoglycans of the extracellular matrix (*37*). (iii) The subcellular variance in $[Cl^-]_i$ arises from corresponding differences in the concentrations of relatively immobile cytoplasmic macromolecular anions (*38*). The variance in $[A]_i$ creates intracytoplasmic Gibbs-Donnan effects (*39*), such that local $[Cl^-]_i$ is at equilibrium at different local $[A]_i$. Thus, CCCs are not required to compensate for intracytoplasmic Cl^- diffusion. (iv) The influence

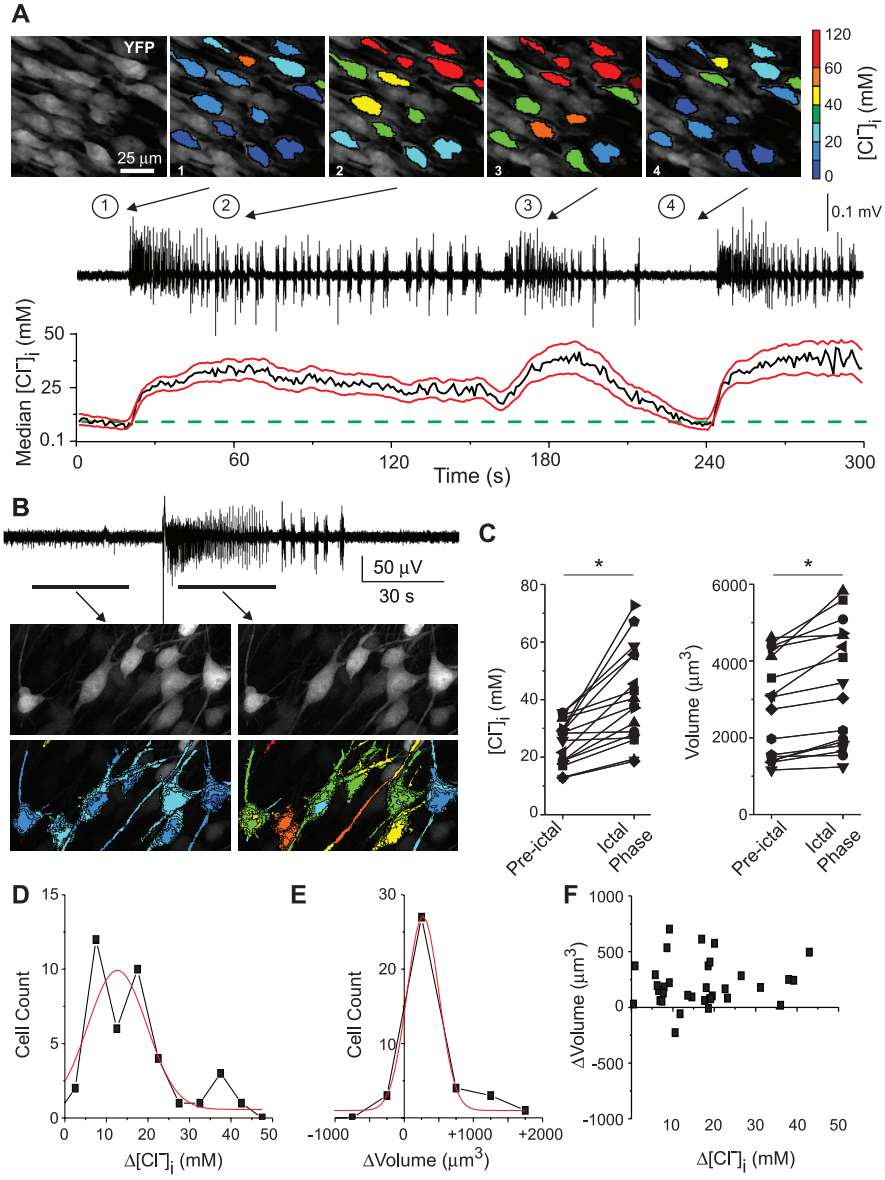

Fig. 4. $[Cl^-]_i$ and intracellular volume changes during ictal activity. (**A**) $[Cl^-]_i$ transients during spontaneous seizures in the CA1 pyramidal cell layer, organotypic hippocampal slice (DIV12). (Top) Pseudo-colored, two-photon images of CA1 neurons before and during seizures. (Middle) Extracellular field-potential recording. (Bottom) $[Cl^-]_i$ changes in a population of neurons (median, black; SD, red lines; green dotted line indicates initial $[Cl^-]_i$). (**B**) Extracellular recording of spontaneous seizure in CA1 region of organotypic hippocampal slice (DIV12). (Bottom) Two-photon microscopy z-stack image of neurons before and during spontaneous seizure. (**C**) $[Cl^-]_i$ and somatic volume changes in individual neurons during spontaneous seizure activity (*$P < 0.05$). (**D** to **F**) $[Cl^-]_i$ and somatic volume changes during recurrent seizures (n = 40 neurons; four slices).

of $[A]_o$ and $[A]_i$ on local $[Cl^-]_i$, and $[Cl^-]_o$ open possibilities for developmental and experience-dependent plasticity of E_{GABA} and $E_{glycine}$ at individual synapses, so that the variance in extracellular sulfated proteoglycans composes a potential locus of analog information storage and pathologically, a rich variety of antigens. (v) Pathological conditions that alter $[A]_o$ or $[A]_i$ will have secondary effects on both cell volume and $[Cl^-]_i$. This may explain the correlation between magnetic resonance imaging evidence of cytotoxic edema after brain injury and anticonvulsant-resistant seizures, which can occur when increased $[Cl^-]_i$ compromises $GABA_AR$-mediated inhibition (*15*, *40*). Thus, the magnitude and direction of $GABA_AR$ currents at individual synapses are among the wide variety of signaling functions subserved by intra- and extracellular macromolecular networks.

References and Notes

1. U. Misgeld, R. A. Deisz, H. U. Dodt, H. D. Lux, *Science* **232**, 1413–1415 (1986).
2. N. L. Chamberlin, R. Dingledine, *Brain Res.* **445**, 12–18 (1988).
3. F. J. Alvarez-Leefmans, E. Delpire, Eds., *Physiology and Pathology of Chloride Transporters and Channels in the Nervous System: From Molecules to Diseases* (Academic Press, San Diego, CA, 2009).
4. R. A. DeFazio, S. Keros, M. W. Quick, J. J. Hablitz, *J. Neurosci.* **20**, 8069–8076 (2000).
5. J. A. Payne, *Am. J. Physiol.* **273**, C1516–C1525 (1997).
6. T. Zeuthen, *J. Membr. Biol.* **234**, 57–73 (2010).
7. E. K. Hoffmann, I. H. Lambert, S. F. Pedersen, *Physiol. Rev.* **89**, 193–277 (2009).
8. R. D. Andrew, M. W. Labron, S. E. Boehnke, L. Carnduff, S. A. Kirov, *Cereb. Cortex* **17**, 787–802 (2007).
9. V. Balakrishnan *et al.*, *J. Neurosci.* **23**, 4134–4145 (2003).
10. J. Glykys *et al.*, *Neuron* **63**, 657–672 (2009).
11. S. Ebihara, K. Shirato, N. Harata, N. Akaike, *J. Physiol.* **484**, 77–86 (1995).
12. J. Yamada *et al.*, *J. Physiol.* **557**, 829–841 (2004).
13. R. Tyzio *et al.*, *Eur. J. Neurosci.* **27**, 2515–2528 (2008).
14. M. Martina, S. Royer, D. Paré, *J. Neurophysiol.* **86**, 2887–2895 (2001).
15. V. I. Dzhala *et al.*, *J. Neurosci.* **30**, 11745–11761 (2010).
16. J. Szabadics *et al.*, *Science* **311**, 233–235 (2006).
17. N. Doyon *et al.*, *PLOS Comput. Biol.* **7**, e1002149 (2011).
18. T. Kuner, G. J. Augustine, *Neuron* **27**, 447–459 (2000).
19. E. Gianazza, P. G. Righetti, *J. Chromatogr. A* **193**, 1–8 (1980).
20. A. Leaf, *Biochem. J.* **62**, 241–248 (1956).
21. F. J. Alvarez-Leefmans, S. M. Gamiño, L. Reuss, *J. Physiol.* **458**, 603–619 (1992).
22. C. E. Bandtlow, D. R. Zimmermann, *Physiol. Rev.* **80**, 1267–1290 (2000).
23. D. Isaev *et al.*, *J. Neurosci.* **27**, 11587–11594 (2007).
24. M. D. Plotkin, E. Y. Snyder, S. C. Hebert, E. Delpire, *J. Neurobiol.* **33**, 781–795 (1997).
25. E. Delpire *et al.*, *Proc. Natl. Acad. Sci. U.S.A.* **106**, 5383–5388 (2009).
26. A. P. Minton, *J. Biol. Chem.* **276**, 10577–10580 (2001).
27. R. J. Ellis, *Curr. Opin. Struct. Biol.* **11**, 114–119 (2001).
28. R. C. Poole, A. P. Halestrap, *Am. J. Physiol.* **264**, C761–C782 (1993).
29. E. Ruusuvuori, I. Kirilkin, N. Pandya, K. Kaila, *J. Neurosci.* **30**, 15638–15642 (2010).
30. N. O. Chahine, F. H. Chen, C. T. Hung, G. A. Ateshian, *Biophys. J.* **89**, 1543–1550 (2005).
31. T. Murakami, A. Ohtsuka, D. X. Piao, *Arch. Histol. Cytol.* **59**, 233–237 (1996).
32. B. B. Pond *et al.*, *J. Neurosci.* **26**, 1396–1406 (2006).
33. A. N. van den Pol, K. Obrietan, G. Chen, *J. Neurosci.* **16**, 4283–4292 (1996).
34. Y. Berdichevsky, V. Dzhala, M. Mail, K. J. Staley, *Neurobiol. Dis.* **45**, 774–785 (2012).
35. D. B. McClatchy, L. Liao, S. K. Park, J. D. Venable, J. R. Yates, *Genome Res.* **17**, 1378–1388 (2007).
36. J. Tanaka *et al.*, *Science* **319**, 1683–1687 (2008).
37. R. Frischknecht *et al.*, *Nat. Neurosci.* **12**, 897–904 (2009).
38. H. Song, M. Sokolov, *J. Proteome Res.* **8**, 346–351 (2009).
39. J. Ricka, T. Tanaka, *Macromolecules* **17**, 2916–2921 (1984).
40. H. C. Glass *et al.*, *J. Pediatr.* **159**, 731–735, e1 (2011).

Acknowledgments: This work was supported by National Institute of Neurological Disorders and Stroke, NIH, grant NS 40109-06 the Kennedy Endowment for Child Neurology and Mental Retardation. J.G. was supported by the American Epilepsy Society postdoctoral fellowship and NIH R25. K.E. was supported by The Japan Foundation for Pediatric Research. K.T.K. was supported by the Manton Center for Orphan Disease Research and NIH R25.

Supplementary Materials

www.sciencemag.org/content/343/6171/670/suppl/DC1
Materials and Methods
Figs. S1 to S10
Tables S1 and S2
References

2 September 2013; accepted 12 December 2013
10.1126/science.1245423

Oxytocin-Mediated GABA Inhibition During Delivery Attenuates Autism Pathogenesis in Rodent Offspring

Roman Tyzio,[1,2]* Romain Nardou,[3]* Diana C. Ferrari,[3]* Timur Tsintsadze,[1,2,3] Amene Shahrokhi,[3]† Sanaz Eftekhari,[3]† Ilgam Khalilov,[1,2] Vera Tsintsadze,[1,2] Corinne Brouchoud,[1,2] Genevieve Chazal,[1,2] Eric Lemonnier,[4] Natalia Lozovaya,[1,2] Nail Burnashev,[1,2] Yehezkel Ben-Ari[1,2,3]‡

We report that the oxytocin-mediated neuroprotective γ-aminobutyric acid (GABA) excitatory-inhibitory shift during delivery is abolished in the valproate and fragile X rodent models of autism. During delivery and subsequently, hippocampal neurons in these models have elevated intracellular chloride levels, increased excitatory GABA, enhanced glutamatergic activity, and elevated gamma oscillations. Maternal pretreatment with bumetanide restored in offspring control electrophysiological and behavioral phenotypes. Conversely, blocking oxytocin signaling in naïve mothers produced offspring having electrophysiological and behavioral autistic-like features. Our results suggest a chronic deficient chloride regulation in these rodent models of autism and stress the importance of oxytocin-mediated GABAergic inhibition during the delivery process. Our data validate the amelioration observed with bumetanide and oxytocin and point to common pathways in a drug-induced and a genetic rodent model of autism.

Autism is a developmental disorder characterized by restricted interest and communication impairment generated by genetic and environmental factors. Alterations of oxytocin signals that trigger labor and are instrumental for communication, notably, parental-infant interactions, are important in autism (*1*). Here, we characterized the cellular and network alterations that occur during the transition from fetal to postnatal life and subsequently in two animal models of autism: rats exposed in utero to valproate (VPA rats) and mice carrying the fragile X mutation (FRX mice). We focused on GABAergic inhibition, as this is deficient in human and animal models of autism, which leads to an imbalance between excitation and inhibition (*2*–*4*). In addition, during development, GABAergic currents shift from excitatory to inhibitory (*5*) because of a reduction of intracellular chloride concentration ($[Cl^-]_i$) mediated by a sequential expression of the main chloride importer (Na^+-K^+-$2Cl^-$ cotransporter, NKCC1) and the main chloride exporter KCC2 (*6*). Delivery in rodents is fundamental in this sequence, with an abrupt oxytocin-mediated reduction of $[Cl^-]_i$ levels that exerts neuroprotective (*7*) and analgesic (*8*) actions on newborns. We report that this sequence is abolished in hippocampal CA3 pyramidal neurons of VPA rats and FRX mice, and its restoration by administering bumetanide to the mother rescues the GABA developmental sequence and the autistic phenotype in rodent offspring.

In naïve rats (Fig. 1A and table S1) [see also (*7*)] and wild-type mice (Fig. 1D and table S1), the driving force of γ-aminobutyric acid type A ($GABA_A$) receptor $GABA_AR$ (DF_{GABA}) was elevated in fetal neurons on embryonic days 20 to 21 (E20 to E21) and reduced to adult values at postnatal days 15 to 30 (P15 to P30), with an abrupt reduction restricted to the delivery period (*9*). In contrast, DF_{GABA} remained elevated in

[1]Mediterranean Institute of Neurobiology (INMED), U901, INSERM, Marseille, France. [2]UMR 901, Aix-Marseille University, Marseille, France. [3]Neurochlore, Campus scientific de Luminy, 163 route de Luminy, Marseille 13273, Cedex 09, France. [4]Laboratoire de Neurosciences de Brest EA4685, Brest, France.

*These authors contributed equally to this work.
†On leave from Tehran University of Medical Sciences, Tehran, Iran.
‡Corresponding author. E-mail: yehezkel.ben-ari@inserm.fr

fetal, early postnatal stages, and P15 to P30 in VPA rats (Fig. 1A and table S1) and FRX mice (Fig. 1D and table S1). Acute applications of the specific NKCC1 chloride importer antagonist bumetanide (10 μM) or oxytocin (1 μM) significantly decreased $[Cl^-]_i$ and DF_{GABA} at P0 in neurons recorded in VPA rats and FRX mice (Fig. 1, B, C, E, and F; and table S2). Therefore, the GABA developmental sequence is abolished in two animal models of autism, with GABA exerting depolarizing actions in a bumetanide and oxytocin-sensitive manner.

The chloride exporter KCC2 is down-regulated after various insults leading to elevated $[Cl^-]_i$, hyperactivity, and more KCC2 down-regulation (*10*–*12*). KCC2 was down-regulated in the hippocampi of juvenile VPA rats and FRX mice (fig. S1, A to C, and table S3). In addition, as in epileptic neurons (*10*), there was a shift of KCC2 labeling from the membrane to the cytoplasm in neurons of VPA rats (fig. S1, D and E, and table S4). Thereby, chloride export is reduced in two animal models of autism, which supports the observed alterations of the polarity of GABA actions.

We next evaluated whether the depolarizing actions of GABA were associated with neuronal excitation. In naïve animals, the specific $GABA_AR$ agonist isoguvacine (10 μM) inhibited or did not affect spike frequency in cell-attached recordings at P0 (Fig. 1, G to J, and table S5) and P15 (fig. S2,

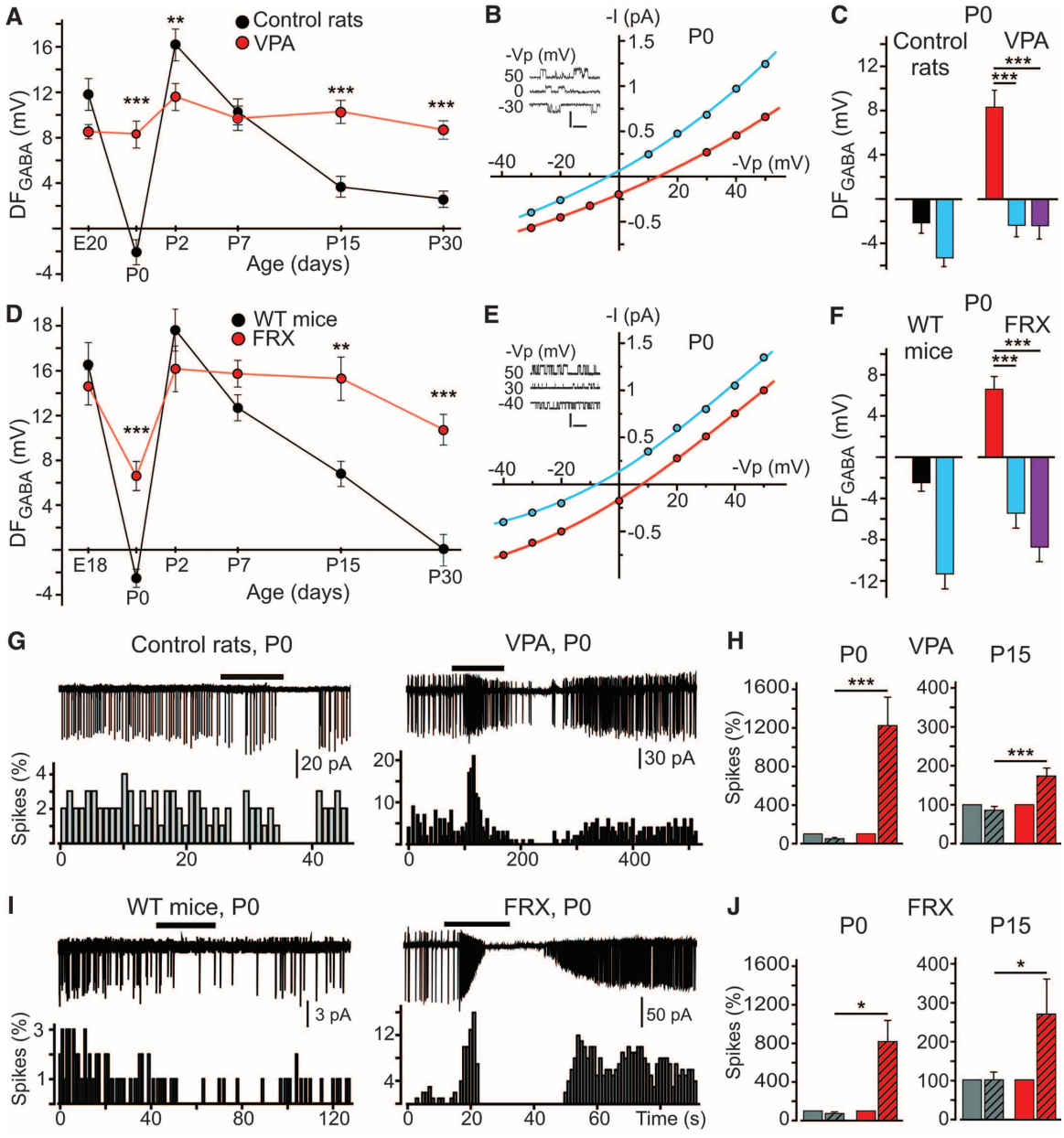

Fig. 1. Developmental excitatory-inhibitory GABA sequence is abolished in hippocampal CA3 pyramidal neurons in VPA rats and FRX mice. (**A**) Age-dependence of DF_{GABA} in control and VPA rats. (**B**) Current-voltage (*I-V*) relations of $GABA_AR$ single-channel currents at P0 in VPA rats in artificial cerebrospinal fluid (red) or bumetanide (10 μM, blue). (Inset) Single-channel openings at different holding potentials (scale bars mean 1 pA and 200 ms). (**C**) Bumetanide and oxytocin shifted DF_{GABA} from depolarizing to hyperpolarizing at P0 (control rats, black; VPA, red; bumetanide application, blue; and oxytocin application, purple). (**D** to **F**) The same as in (A) to (C) for wild-type mice (WT, black) and FRX mice (red). (**G** to **J**) Excitatory action of the $GABA_AR$ agonist isoguvacine (10 μM, black bars) on spontaneous spiking recorded in cell-attached configuration in VPA and FRX. (G) Control and VPA rats and (I) wild-type and FRX mice at P0 with and without isoguvacine. Time-course of spike frequency changes is shown under each trace. (H) Average values of normalized to control spike frequency for P0 and P15 control (gray) and VPA (red) rats and effect of isoguvacine application (hatched bars). (J) The same as in (H) but for P0 and P15 mice wild-type (gray) and FRX (red). Data are presented as means ± SEM. **P* < 0.05; ***P* < 0.01; ****P* < 0.001.

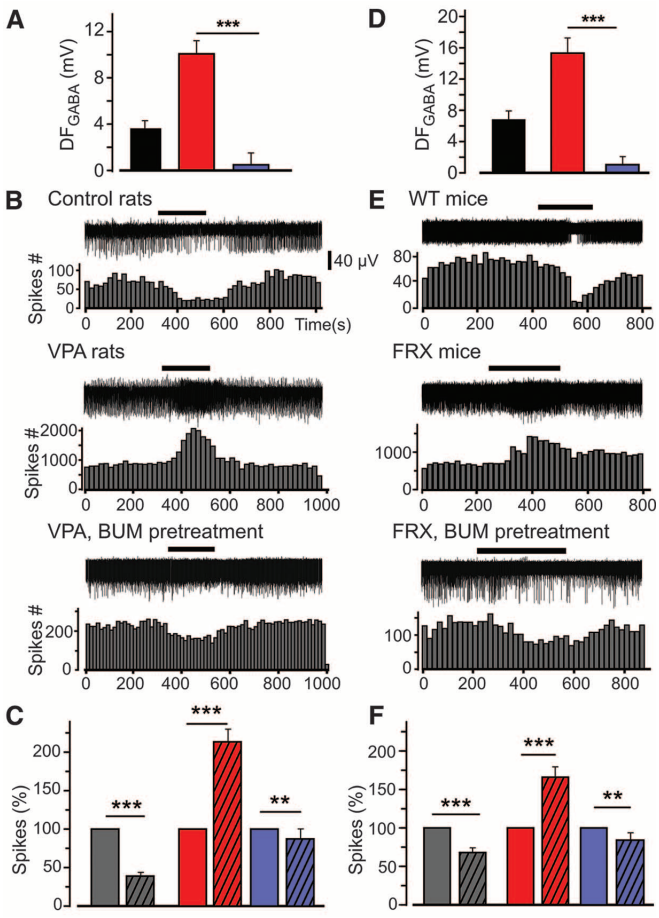

Fig. 2. Maternal pretreatment with bumetanide before delivery switches the action of GABA from excitatory to inhibitory in offspring in VPA and FRX rodents at P15. (**A**) Average values of DF_{GABA} measured in hippocampal CA3 pyramidal neurons at P15 in control (black), VPA (red), and VPA rats pretreated with bumetanide (blue). Note that pretreatment with bumetanide shifts DF_{GABA} from depolarizing to almost isoelectric level. (**B**) Effects of isoguvacine (10 µM; black bars) in rats: Representative traces of spontaneous extracellular field potentials recorded in hippocampal slices at P15 in control, VPA, and VPA rats pretreated with bumetanide (BUM). Corresponding time courses of spike frequency changes are shown under each trace. (**C**) Average histograms of normalized spike frequency in rats. Isoguvacine (hatched bars) decreased the spikes frequency in control rats (to 38.9 ± 5.1%; gray); increased it in VPA rats (to 213.5 ± 16.3%; red); and decreased it in VPA rats pretreated with bumetanide (to 82.8 ± 10.7%; blue). (**D**) The same as in (A) for mice. Wild-type mice (WT, black), FRX mice (red), and FRX mice pretreated with bumetanide (blue). (**E**) The same as in (B) for FRX mice. (**F**) The same as in (C) for FRX mice. Wild-type mice (decreased to 67.9 ± 6.1%; gray); FRX mice (increased to 165.8 ± 13.5%; red); FRX mice pretreated with bumetanide (decreased to 80.8 ± 8.2%; blue). Data are presented as means ± SEM. $^{**}P < 0.01$; $^{***}P < 0.001$.

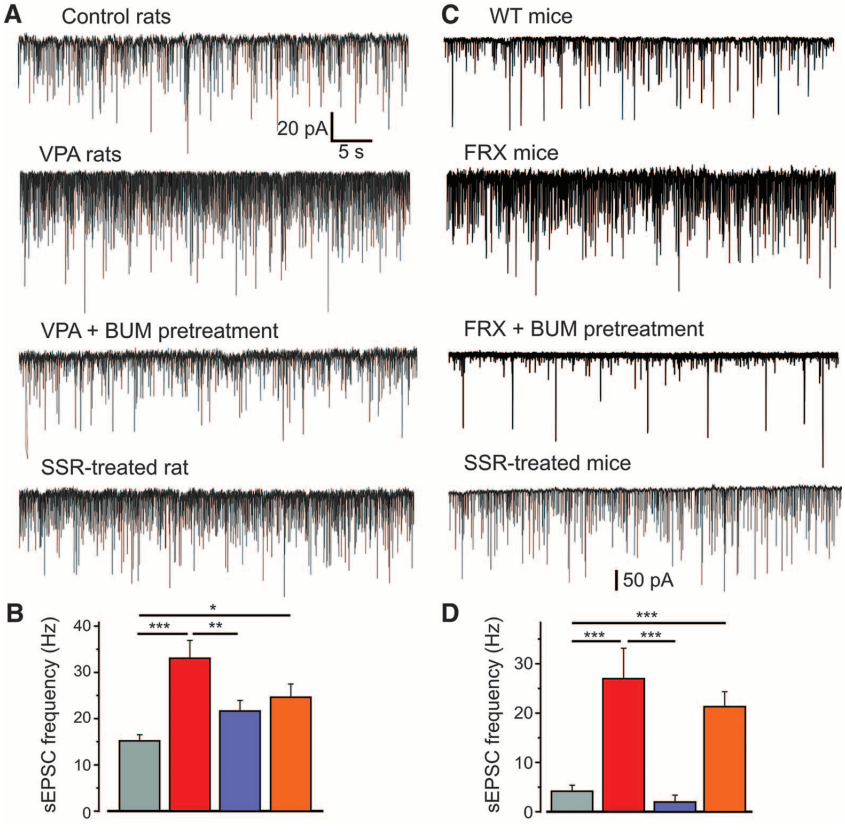

Fig. 3. Spontaneous activity is increased in VPA and FRX rodents at P15 and restored to control values by maternal pretreatment with bumetanide. Whole-cell voltage clamp recordings of sEPSCs at −70 mV from individual hippocampal CA3 pyramidal neurons in acute brain slices from P15 VPA rats or FRX mice and respective control and bumetanide or SSR126768A pretreated animals. (**A** and **C**) Representative traces of sEPSCs recorded from rats (A) and mice (C). Note that maternal pretreatment of animals with bumetanide decreases sEPSCs frequency in both models, whereas treatment with SSR126768A increases spontaneous activity of neuronal networks in rats and mice. (**B**) Average values of sEPSCs frequencies in rats: Control rats (gray) and VPA rats (red), VPA rats with maternal pretreatment with bumetanide (blue) and SSR126768A-treated rats (orange). (**D**) The same as (B) for mice. Wild-type mice (gray), FRX mice (red), FRX mice with maternal pretreatment with bumetanide (blue), and SSR126768A-treated mice (orange). One-way analysis of variance (ANOVA) Fisher's least significant difference as a post hoc test. Data are presented as means ± SEM. $^{*}P < 0.05$; $^{**}P < 0.01$; $^{***}P < 0.001$.

A and C, and table S5) and in field-potential recordings at P15 (Fig. 2, B and E, and table S11). In contrast, isoguvacine increased spike frequency in neurons of VPA rats and FRX mice in cell-attached recordings at P0 (Fig. 1, G to J) and P15 (fig. S2, B and D, and Fig. 1, H and J) and in field-potential recordings at P15 (Fig. 2, B, C, E, and F). Hence, GABA excites newborn and juvenile neurons recorded in VPA rats and FRX mice.

We next determined whether excitatory GABA is associated with enhanced network activity. In hippocampal slices of VPA rats and FRX mice, there was bursting activity at P0 and a fourfold increase of the frequency of glutamatergic spontaneous excitatory postsynaptic currents (sEPSCs) at P0 (fig. S3, A to C and F to H; and tables S6 to S8) and P15 (fig. S3, D, E, I, and J; and table S9). Application of bumetanide restored control glutamatergic sEPSC frequency at P0 (fig. S3, B and G, and table S7) and P15 (fig. S3, E and J, and table S9). Therefore, developing networks of VPA rats and FRX mice are hyperactive with bumetanide-sensitive enhanced glutamatergic activity likely due to GABAergic excitation impinging on principal cells.

We then tested the hypothesis that restoring low $[Cl^-]_i$ and inhibitory GABA actions during delivery rescues naïve electrophysiological features in juvenile offspring. We treated pregnant VPA rats and FRX mice females orally 1 day before delivery with bumetanide (2 to 2.5 mg/kg in drinking water) and recorded neuronal activity in offspring at P15. Bumetanide pretreatment restored control DF_{GABA} values (Fig. 2, A and D, and table S10), suppressed the excitatory actions of isoguvacine (Fig. 2, B, C, E, and F; fig. S4; and tables S11 and S12), and significantly reduced ongoing activity and frequency of glutamatergic sEPSCs (Fig. 3 and table S9). Thus, elevated $[Cl^-]_i$ and excitatory GABA actions at birth produce long-term effects in juvenile VPA rats and FRX mice that can be restored by maternal pretreatment with bumetanide.

As the perinatal excitatory-to-inhibitory shift of GABA is mediated by oxytocin receptors (*7*), we tested the effect of a selective oxytocin receptor antagonist SSR126768A in naïve rodents. Pretreatment of naïve mothers one day before delivery with SSR126768A in drinking water produced in juvenile rats elevated DF_{GABA} (fig. S5A and table S13), excitatory GABA actions (fig. S5B and table S14), and exacerbated glutamatergic activity (Fig. 3 and table S9). Therefore, blocking oxytocin signals during delivery in naïve animals produces actions similar to those observed in the VPA rats and FRX mice and stresses the importance of the oxytocin-GABA link.

We then used behavioral tests to determine whether treatment of mothers with bumetanide shortly before delivery prevents autistic-like behaviors in offspring. The isolation-induced ultrasonic vocalizations that pups emit when separated from their mothers (*9*, *13*) were reduced in P4 VPA rats with fewer calls and shorter total call durations than age-matched control rats. In addition, FRX mice (P8) had a higher probability of emitting downward and chevron calls than age-matched wild-type mice (Fig. 4A and table S16). Maternal pretreatment with bumetanide rescued this

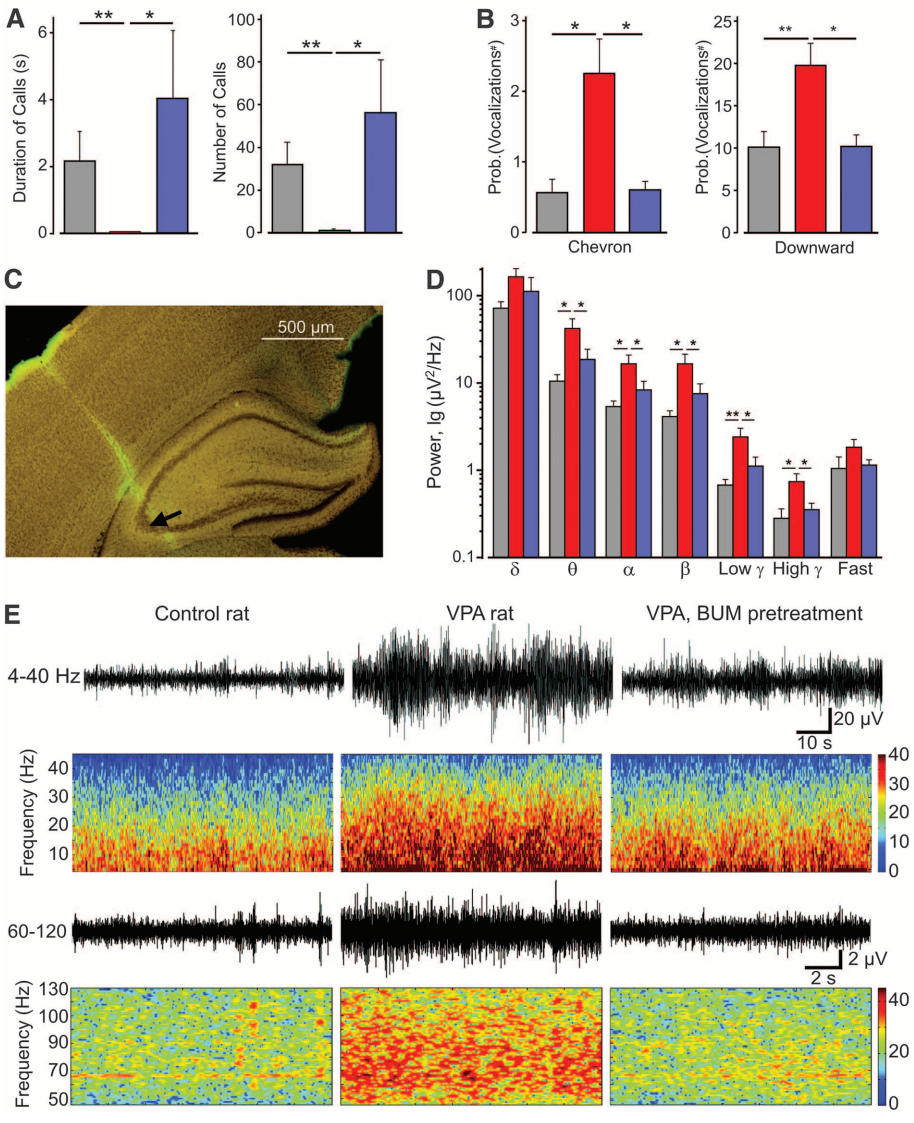

Fig. 4. Maternal pretreatment with bumetanide restores aberrant behavior and brain oscillations of animal models of autism. Isolation-induced ultrasonic vocalizations in (**A**) P4 control (gray); VPA (red, small bar in the middle); and VPA rats with maternal bumetanide pretreatment (blue); and (**B**) in P8 wild-type (gray), FRX (red), and FRX mice with maternal bumetanide pretreatment (blue). (**C** to **E**) EEG recordings in vivo were made in the CA3 area of hippocampus of head-restrained control, VPA, and VPA rats with maternal bumetanide pretreatment at the ages P13 to P15. (C) A coronal section showing the location of the DiI-labeled recording electrode (arrow). (D) Integral power of δ (0.5 to 4 Hz), θ (4 to 7 Hz), α (7 to 12 Hz), β (12 to 25 Hz), low γ (25 to 60 Hz), high γ (60 to 120 Hz) band components of EEG revealed by Fourier transform analysis. Control (gray) vs. VPA (red): for θ, α, β, and high γ, $*P < 0.05$, for low γ, $**P < 0.01$; VPA (red) versus VPA with bumetanide maternal pretreatment (blue) for θ, α, β, and high and low γ $*P < 0.05$. (E) Representative traces of CA3 pyramidal layer EEG recordings from control, VPA, and VPA rats with bumetanide maternal pretreatment after band-pass filtering at frequency ranges indicated on the left of the traces. Corresponding time-frequency representations are shown under each trace. One-way ANOVA Fisher's least significant difference post hoc test. Data are presented as means ± S.E.M.

behavioral alteration in VPA rats (Fig. 4A and table S16) and FRX mice (Fig. 4B and table S16). Furthermore, offspring of naïve mothers pretreated with SSR126768A to block oxytocin signals had an increased probability of emitting downward calls (P8, mice) and a longer latency to reach home bedding than age-matched control pups in the nest-seeking test (P9 rats) (fig. S5C and table S15). Therefore, bumetanide restores naïve behavior in VPA rats and FRX mice, and blocking oxytocin signaling produces behavioral alterations and autistic–like features.

Finally, as alterations of gamma oscillations have been observed in patients with autism (*14*), we tested whether similar changes occur in vivo in VPA rats. With intracranial electroencephalographic (EEG) recordings in the hippocampal CA3 region, hyperactivity was observed in VPA (P15) but not in age-matched naïve rats. These included enhanced network oscillation power in a broad spectrum of frequencies, including gamma but excluding fast ripples and very low (δ) frequencies. Maternal pretreatment with bumetanide restored physiological values in offspring (Fig. 4, C to E, and table S17). Therefore, the polarity of GABA actions during delivery exerts long-term effects on brain oscillations in VPA rats.

During parturition, the human fetus is subjected to an important stress associated with a high surge of catecholamine levels. This adapts neonates to extrauterine life by promoting lung maturation and increased cardiovascular performance and blood flow to the brain (*15*). However, in rodents, elevated catecholamine levels produce KCC2 down-regulation, elevated $[Cl^-]_i$ levels, excitatory GABA, and neuronal hyperactivity (*16*, *17*) that are prevented during delivery by oxytocin (*7*). Similar deleterious alterations are observed in epilepsies and other pathologic conditions (*10*–*12*, *18*). It is noteworthy that complicated deliveries have elevated catecholamines in umbilical cord blood and have been associated with an increased prevalence of autism (*15*–*20*). Whether GABA exerts excitatory actions in humans with autism is not known. However, in keeping with this hypothesis, agents that act through GABA (benzodiazepines and phenobarbital) produce paradoxical effects in patients with autism (*21*) and experimental epilepsy in rodents (*10*). Note also that rodent KCC2 activity is altered by autism-linked genetic mutations. Oxytocin improves information processing by exciting GABAergic interneurons and inhibiting their target pyramidal neurons (*22*). An excitatory shift of this link will enhance glutamatergic drive in neurons and thereby affect information-processing in the developing brain.

To conclude, our observations suggest that in addition to triggering labor and inducing trust, empathy, and parental-infant relationships in humans (*23*), oxytocin signals might exert a protective action during delivery, preventing deleterious effects of enhanced activity. Further investigations are needed to better understand the links among pregnancy complications, cesarean sections, and autism (*16*, *17*). In conclusion, our results validate the clinical actions of bumetanide (*24*) and oxytocin (*25*) and emphasize the importance of investigating how and when developmental sequences are disrupted in animal models of autism in order to develop novel therapeutic avenues (*26*).

References and Notes

1. R. L. H. Pobbe *et al.*, *Horm. Behav.* **61**, 436–444 (2012).
2. J. L. R. Rubenstein, M. M. Merzenich, *Genes Brain Behav.* **2**, 255–267 (2003).
3. N. Gogolla *et al.*, *J. Neurodev. Disord.* **1**, 172–181 (2009).
4. G. J. Blatt, S. H. Fatemi, *Anat. Rec. (Hoboken)* **294**, 1646–1652 (2011).
5. Y. Ben-Ari, J. L. Gaiarsa, R. Tyzio, R. Khazipov, *Physiol. Rev.* **87**, 1215–1284 (2007).
6. C. Rivera *et al.*, *Nature* **397**, 251–255 (1999).
7. R. Tyzio *et al.*, *Science* **314**, 1788–1792 (2006).
8. M. Mazzuca *et al.*, *Front. Cell. Neurosci.* **5**, 3 (2011).
9. Materials and methods are available as supplementary materials on *Science* Online.
10. R. Nardou *et al.*, *Brain* **134**, 987–1002 (2011).
11. M. Puskarjov, F. Ahmad, K. Kaila, P. Blaesse, *J. Neurosci.* **32**, 11356–11364 (2012).
12. H. Fiumelli, M. A. Woodin, *Curr. Opin. Neurobiol.* **17**, 81–86 (2007).
13. R. Delorme *et al.*, *Nat. Med.* **19**, 685–694 (2013).
14. L. Cornew, T. P. L. Roberts, L. Blaskey, J. C. Edgar, *J. Autism Dev. Disord.* **42**, 1884–1894 (2012).
15. H. Lagercrantz, P. Bistoletti, *Pediatr. Res.* **11**, 889–893 (1977).
16. W. Inoue *et al.*, *Nat. Neurosci.* **16**, 605–612 (2013).
17. J. S. Kim *et al.*, *J. Neurosci.* **31**, 13312–13322 (2011).
18. P. Boulenguez *et al.*, *Nat. Med.* **16**, 302–307 (2010).
19. K. Lyall, D. L. Pauls, D. Spiegelman, A. Ascherio, S. L. Santangelo, *Autism Res.* **5**, 21–30 (2012).
20. E. J. Glasson *et al.*, *Arch. Gen. Psychiatry* **61**, 618–627 (2004).
21. F. Marrosu, G. Marrosu, M. G. Rachel, G. Biggio, *Funct. Neurol.* **2**, 355–361 (1987).
22. S. F. Owen *et al.*, *Nature* **500**, 458–462 (2013).
23. T. R. Insel, *Neuron* **65**, 768–779 (2010).
24. E. Lemonnier *et al.*, *Transl. Psychiatr.* **2**, e202 (2012).
25. E. Anagnostou *et al.*, *Mol. Autism* **3**, 16 (2012).
26. Y. Ben-Ari, *Trends Neurosci.* **31**, 626–636 (2008).

Acknowledgments: We thank at INMED C. Rivera and C. Pellegrino for their assistance on the Western blot and for the panKCC2 antibody, R. Martinez for his technical help with the ultrasonic setup, and M. L. Scattoni and M. Wohr for their assistance with the vocalization experiments and analysis. This study was supported by INSERM (funds to INMED), Neurochlore, France's Agence Nationale de la Recherche (ANR-12-RPIB-0001-01), and the Simons Foundation (SFARI award #230267 to Y. B-A.). We also thank Sanofi-Syntelabo for the gift of SSR126768A. On 13 January 2011, Neurochlore filed a patent entitled "Compounds for the treatment of autism" (U.S. patent number 13/522372, worldwide PCT/EP2011/050394); Y. B-A. and E.L. are identified as inventors of this patent. Y. B-A. and E.L. are founders and shareholders of Neurochlore, a company focused on the treatment of developmental disorders. R.N. and D.C.F. own shares in Neurochlore.

Supplementary Materials

www.sciencemag.org/content/343/6171/675/suppl/DC1
Materials and Methods
Figs. S1 to S5
Tables S1 to S17
References (*27*–*30*)

14 October 2013; accepted 10 December 2013
10.1126/science.1247190

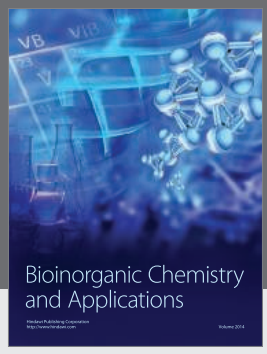

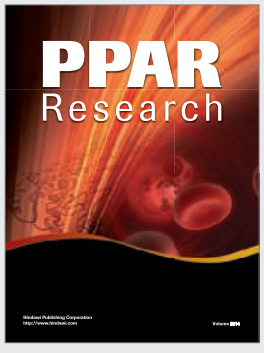

Hindawi

Submit your manuscripts at
http://www.hindawi.com

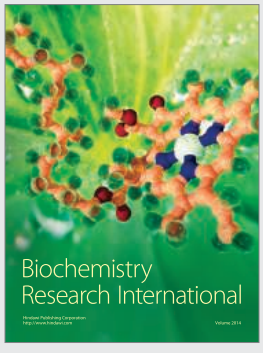

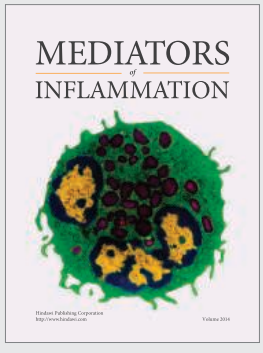

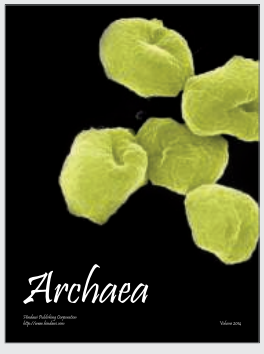

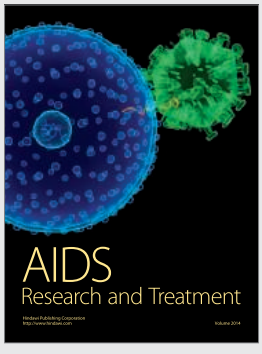

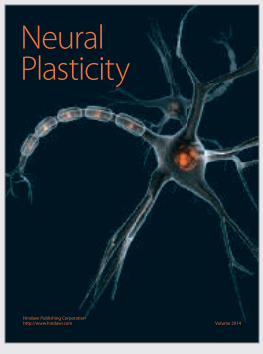

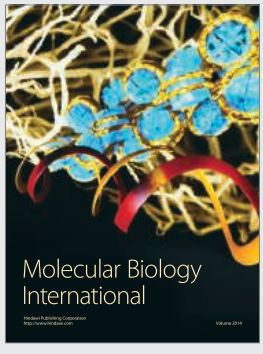

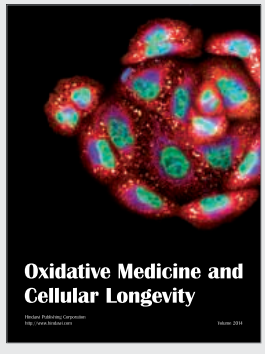

Defining the Future of the Public Research University

UC San Diego

#5 for total R&D expenditures among U.S. universities

UC San Diego's iconic Geisel Library, a meeting place for faculty and students, and home to the Dr. Seuss Collection

Breakthroughs to Better Our World

From its inception, the University of California, San Diego has attracted leading scholars with an entrepreneurial spirit and a penchant for risk-taking. The freedom to cross boundaries and to create new disciplines fuels breakthrough research with global impact. Our visionaries are looking for the next discoveries that will benefit people around the world in all walks of life.

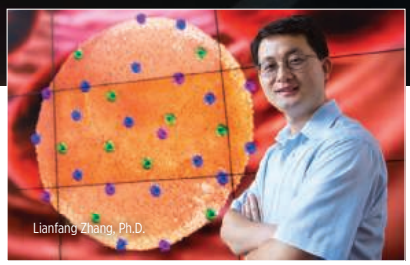

Lianfang Zhang, Ph.D.

Stealthily Delivering Drugs

Targeted drugs that treat specific tissues are often attacked by the body's immune system. **Lianfang Zhang**'s research group approaches the problem from an engineering perspective and bypasses the biology. They fool the immune system by using natural red blood cell membranes to camouflage nanosponges that deliver drugs and soak up toxins.

David Victor, Ph.D.

Examining Climate Policy

Global warming is one of today's greatest challenges and international policies to cut emissions are overdue. **David Victor**'s book *Global Warming Gridlock* explains why the world hasn't made much diplomatic progress and explores new, effective strategies. His research has produced a roadmap to a lower carbon future through bottom-up initiatives at the regional, national and global level.

Karen Christman, Ph.D.

Mending Damaged Hearts

There is no established treatment for repairing the damage to cardiac tissue caused by the 785,000 new heart attack cases each year—yet. **Karen Christman**'s lab has developed a new injectable hydrogel that encourages cells to repopulate areas of damaged tissue, and to preserve heart function by forming a scaffold to repair tissue and increase muscle.

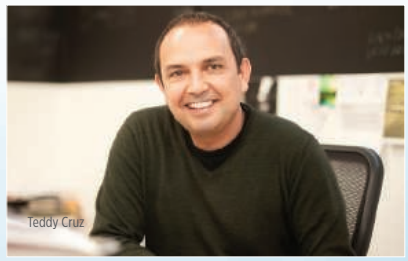

Teddy Cruz

Rethinking Space

Teddy Cruz is reimagining the way we think about architecture and urban design. Renowned for his research on the Tijuana-San Diego border, Cruz creates a humane vision that breaks down cultural barriers, while exploring the social complexity and richness of public and private space.

#1 for positive impact on the nation
-Washington Monthly

UC San Diego
Learn more at ucsd.edu.

NEW ENGLAND BioLabs® Inc.

Clone with Confidence.

Whether you are performing your first cloning experiment, or constructing multi-fragment gene assemblies, NEB® has the solution for you. Our high quality reagents are available for every workflow, and include specialized enzymes, competent cells, and novel solutions – such as Gibson Assembly®. When you are looking to clone with confidence, think of NEB.

Explore the wise choice at **CloneWithNEB.com.**

Visit CloneWithNEB.com to view online tutorials describing various cloning workflows.

WE'RE BRINGING A NEW PERSPECTIVE TO

cancer metabolism research

FIRST WE MADE IT POSSIBLE – NOW WE'VE MADE IT EASY.

XF technology provides the easiest and most comprehensive assessment of cancer cell metabolism, measuring glucose and glutamine metabolism, and fatty acid oxidation of cancer cells in a microplate, in real-time!

— David Ferrick, PhD,
CSO, Seahorse Bioscience

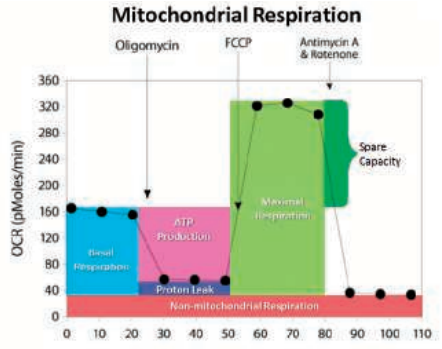

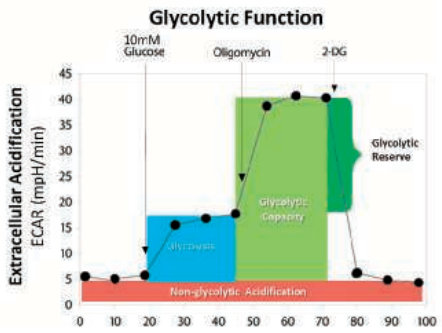

The Seahorse XF^e Extracellular Flux Analyzer

Measurements of cellular glycolysis are essential to understanding cancer, immune response, stem cell differentiation, aging, and cardiovascular and neurodegenerative diseases. The XF^e Analyzer and XF Glycolysis Stress Test Kit make it easy to measure the three key parameters of cellular glycolysis in a microplate: glycolysis, glycolytic capacity, and glycolytic reserve, revealing critical information not evident in mitochondrial respiration measurements alone.

See what's possible.

Scan this QR code to view videos and see what the XF Analyzer can achieve.
Visit www.seahorsebio.com/science for more information!

Seahorse *Bioscience*

Accurate, Fast, Cell Cycle Studies

Made easy using the BD Accuri™ C6 Personal Flow Cytometer.

Arguably, as easy as Cell Cycle is going to get.

The BD Accuri C6 is making it even easier to apply the power of flow cytometry to your research with free software templates and ready-to-go reagent kits that simplify the assessment of cell cycle and DNA status studies involving propidium iodide, 7-amino actinomycin D, and bromodeoxyuridine. You get more insight and easier workflow, whether you're a flow expert or have never used flow cytometry before.

These templates feature predefined workspace that speeds setup and analysis. Applying the power of flow cytometry, the BD Accuri C6 uses less samples and delivers greater accuracy.

Several kits are available including BD Cycletest™ Plus DNA Kit that uses PI and other active agents to obtain precise ploidy and cell cycle measurements using isolated cell nuclei and BD Pharmingen™ BrdU Kits that use 7-AAD and BrdU to provide high resolution cell cycle measurements.

Find out more about how the BD Accuri C6 puts the power of 4-color cell analysis within reach by being easy to use, simple to set up and maintain, transportable, and affordable.

bdbiosciences.com/go/templates

BD

Helping all people live healthy lives

BD Biosciences
2350 Qume Drive
San Jose, CA 95131
bdbiosciences.com

Leveraging Committee Assignments for Advancement

Serving on faculty committees can be enriching, exciting experiences that enable you to increase your knowledge of your institution and field, develop new partnerships and expand your network, and sharpen critical skills. Service also shines a spotlight on a professor's abilities, and can open the door to opportunities to pursue administrative jobs, apply for awards, and contribute to interdisciplinary research projects. But with a seemingly dizzying array of committees on which early career faculty can serve, how do you decide which to pursue, and when? Experts agree that the key is to seek opportunities that can add value to your institution and align with your interests and career aspirations.

See the full story on page 685.

Upcoming Features

Postdocs: Broadening Your Skills—February 28

Cancer Research Careers—March 28

Biotech and Pharma—June 13

Science Signaling

The Leading Journal for Cell Signaling

Publishing key findings of broad relevance in the multidisciplinary field of cell signaling

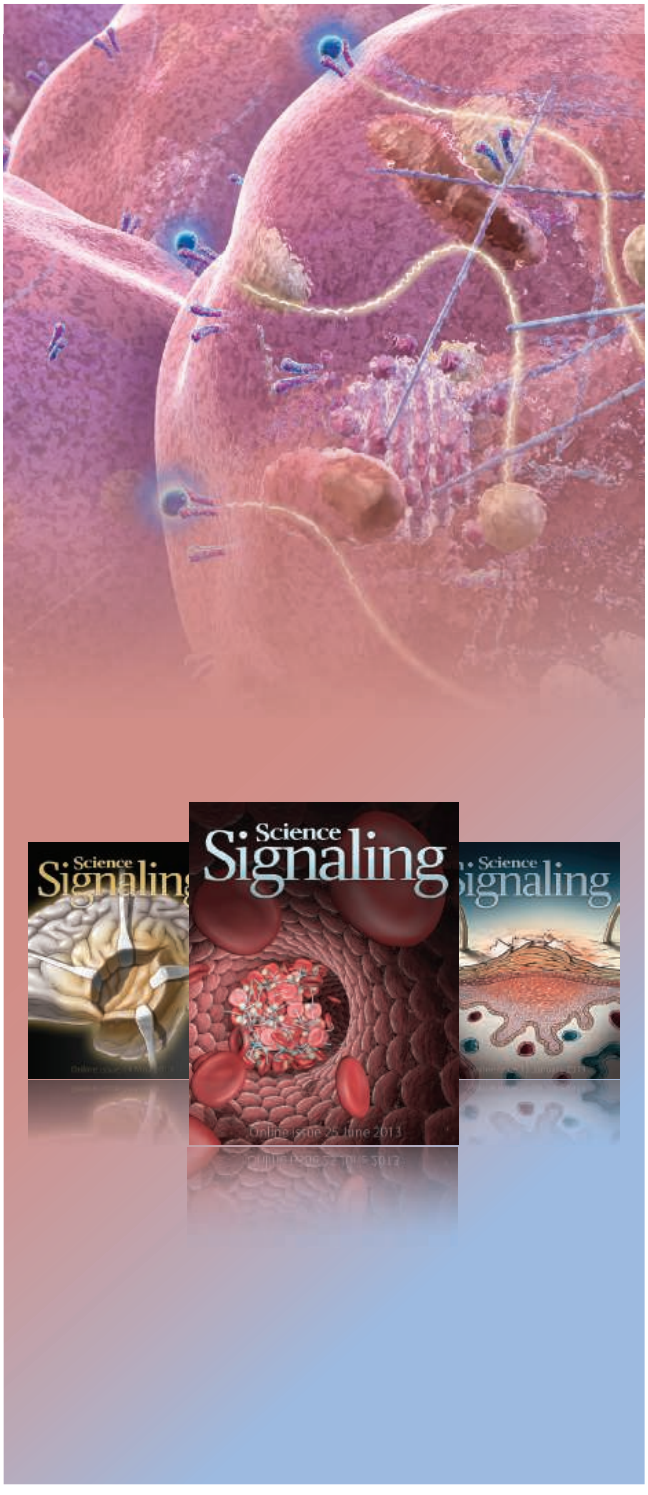

Submit your research

ScienceSignaling.org

Recommend to your library

ScienceOnline.org/recommend

Join the ranks of high-profile papers published in *Science Signaling*:

Cancer Biology
Vemurafenib Potently Induces Endoplasmic Reticulum Stress–Mediated Apoptosis in BRAFV600E Melanoma Cells
D. Beck *et al.* (F. Meier), *Sci. Signal.* **6**, ra7 (2013)

Neuroscience
Requirement for Nuclear Calcium Signaling in *Drosophila* Long-Term Memory
J.-M. Weislogel *et al.* (H. Bading), *Sci. Signal.* **6**, ra33 (2013)

Cell and Molecular Biology
A Nontranscriptional Role for HIF-1α as a Direct Inhibitor of DNA Replication
M. E. Hubbi *et al.* (G. L. Semenza), *Sci. Signal.* **6**, ra10 (2013)

Immunology
Monovalent and Multivalent Ligation of the B Cell Receptor Exhibit Differential Dependence upon Syk and Src Family Kinases
S. Mukherjee *et al.* (A. Weiss), *Sci. Signal.* **6**, ra1 (2013)

Computational and Systems Biology
Cross-Species Protein Interactome Mapping Reveals Species-Specific Wiring of Stress Response Pathways
J. Das *et al.* (H. Yu), *Sci. Signal.* **6**, ra38 (2013)

Science Signaling
AAAS

sciencesignalingeditors@aaas.org

SUPER AIR CONDENSER

Following the extraordinary response to the launch of the Findenser super air condenser, which has generated interest from around the globe, Radleys is now extending the Findenser family by introducing the Findenser Mini. Findenser Mini is shorter and ideal for use with smaller flasks up to 250 mL in size. Findenser requires no running water to operate and its unique design, effectiveness in 95% of common chemistry applications, and ability to eliminate laboratory flooding (associated with traditional water condensers) has sparked a lot of interest. Findenser and Findenser Mini have a range of popular joint sizes and can now be used with flasks from 10 mL to up to 2 L in size.

Radleys

For info: +44-(0)-1799-513320 | www.radleys.com

AUTOMATED PIPETTING PLATFORM

The new next generation, liquid handling platform, Vantage, offers contact-free pipetting over a wide volume range of 100 nL to 1 mL. The Vantage is space-efficient, affordable, and can be remotely monitored by mobile devices. Its expandable design makes it a powerful instrument for labs with simple or complex application needs. The system features Hamilton's new NanoPulse technology, which provides wide volume ranges from a single channel, and a new linear motor that increases pipetting speed while decreasing noise, heat, and vibration. New camera technology enhances traceability by verifying all labware on the system and detecting nonbarcoded labware. Labs can upgrade their Vantage system at any time with a Logistics Cabinet. The upgrade kit offers an innovative tip and plate shuttling mechanism from below the pipetting deck and customizable smart waste containers. A telescopic vertical track gripper is available to transport samples from below- or off-deck third-party devices.

Hamilton Company

For info: 800-648-5950 | www.hamiltonrobotics.com

BIOLOGICAL TISSUE STORAGE

CryoELITE Tissue Vials were designed for the safe, secure, and effective cryopreservation of biological tissue specimens. Different from cells and biofluids, tissue biospecimens have particular requirements for cryogenic storage. Offering researchers a uniform vial able to maintain sample integrity while maximizing storage capacity, and organization, the CryoELITE Tissue Vials feature a wide-mouth opening, 5 mL capacity and high-integrity closure. The CryoELITE Tissue Vial offers researchers who work with biological tissue sections ease of use, convenience, and security. CryoELITE Tissue Vials are manufactured from low binding, cryogenic-grade virgin polypropylene that meets USP Class VI classification. Lot tested and certified to be free of pyrogens, RNase/DNase, and endotoxins, the vials have a sample capacity of 5 mL and a storage temperature range of -156°C to 121°C. The externally threaded cap provides a seal that exceeds DOT and IATA classifications for diagnostic specimens and their transport and is capable of maintaining a secure closure during freeze/thaw procedures.

Wheaton

For info: 800-225-1437 | www.wheaton.com

WHOLE-GENOME GENOTYPING ARRAYS

An advanced high throughput screening (HTS) array format significantly increases the number of samples that can be processed on the Infinium BeadChip family of genotyping arrays. Illumina's Infinium assay leverages proven chemistries on a new 24-sample HTS BeadChip that supports up to 750,000 markers per sample and increases scanning capacity by up to three-fold. Illumina's HumanOmniExpress BeadChip will be the first standard array available on the 24-sample HTS BeadChip, part of a portfolio of whole-genome genotyping arrays with new affordable pricing. This powerful array contains approximately 700,000 markers including the latest updates from the 1,000 Genomes Project strategically selected to capture the greatest amount of common single-nucleotide polymorphism variation and drive the discovery of novel associations with traits and disease. It can also include up to 50,000 custom markers, making it ideal for those interested in large genotyping studies such as core labs, genome centers, and biobanks.

Illumina

For info: 800-809-4566 | www.illumina.com/infiniumHTS

ULTRAFLAT GLASS BOTTOM PLATES

The new generation of Krystal glass bottom plates are precision manufactured using a proprietary process resulting in excellent light transmission and an ultraflat optical plane (+/-15 µm) making them perfect for imaging growing cells. The complete range of 24-, 96-, and 384-well Krystal glass bottom microplates is available sterilized for tissue culture to optimize cell growth or nonsterile for assay development. Deep-black plates for fluorescent studies are available, together with brilliant-white plates which increase sensitivity for luminescence and absorbance work. The high optical clarity base of each plate in the range offers the advantage of easy positioning and crisp images when used with confocal microscopes. Constructed to a standard SBS/ANSI microplate format—Krystal glass bottom plates are fully compatible with automated liquid handling and robotic devices. All plates are supplied lidded. The glass bottomed plates can also be used for light-emitting assays measured through the glass plate base.

Porvair Sciences

For info: +44-(0)-1372-824290 | www.porvair-sciences.com

Electronically submit your new product description or product literature information! Go to **www.sciencemag.org/products/newproducts.dtl** for more information.

Newly offered instrumentation, apparatus, and laboratory materials of interest to researchers in all disciplines in academic, industrial, and governmental organizations are featured in this space. Emphasis is given to purpose, chief characteristics, and availability of products and materials. Endorsement by *Science* or AAAS of any products or materials mentioned is not implied. Additional information may be obtained from the manufacturer or supplier.

For your career in science, there's only one **Science**

A career plan customized *for* you, *by* you.

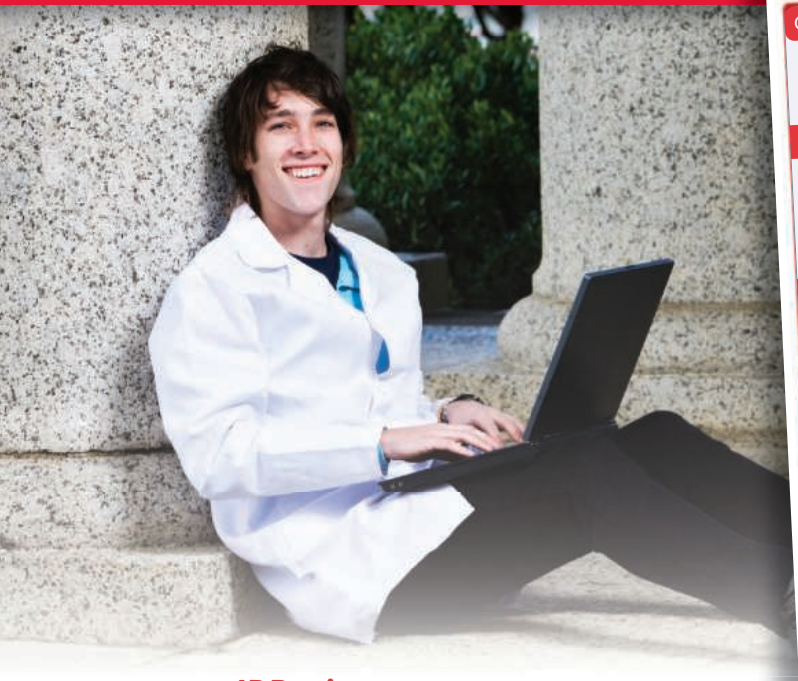

myIDP.sciencecareers.org

Recommended by leading professional societies and endorsed by the National Institutes of Health, an individual development plan will help you prepare for a successful and satisfying scientific career.

my IDP Science Careers

In collaboration with FASEB, UCSF, and the Medical College of Wisconsin and with support from the Burroughs Wellcome Fund, AAAS and *Science* Careers present the first and only online app that helps scientists prepare their very own individual development plan.

Visit the website and start planning today!
myIDP.sciencecareers.org

In partnership with:

advancing the life sciences 1912-2012 FASEB Federation of American Societies for Experimental Biology

UCSF University of California San Francisco

Medical College of Wisconsin

Burroughs Wellcome Fund

Promega

CellTox™ Green

More Biology, Less Work

CellTox™ Green enables real-time mechanistic toxicity monitoring with a simple Add & Read protocol. Multiplexing with CellTiter-Glo® allows investigators to monitor temporal changes of membrane-modulated cytotoxicity in parallel with the key cell viability biomarker, ATP.

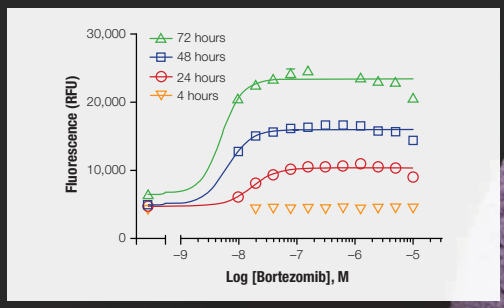

Easily monitor temporal changes in a key cytotoxicity biomarker for IC_{50} determinations.

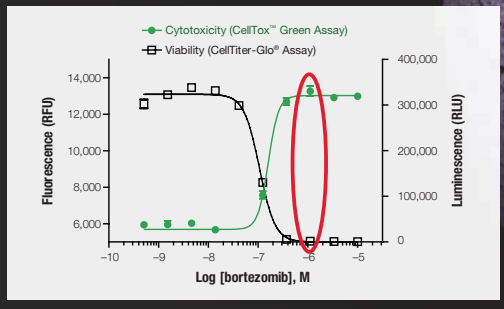

Get more informative data from same-well multiplexing of cytotoxicity and viability assays.

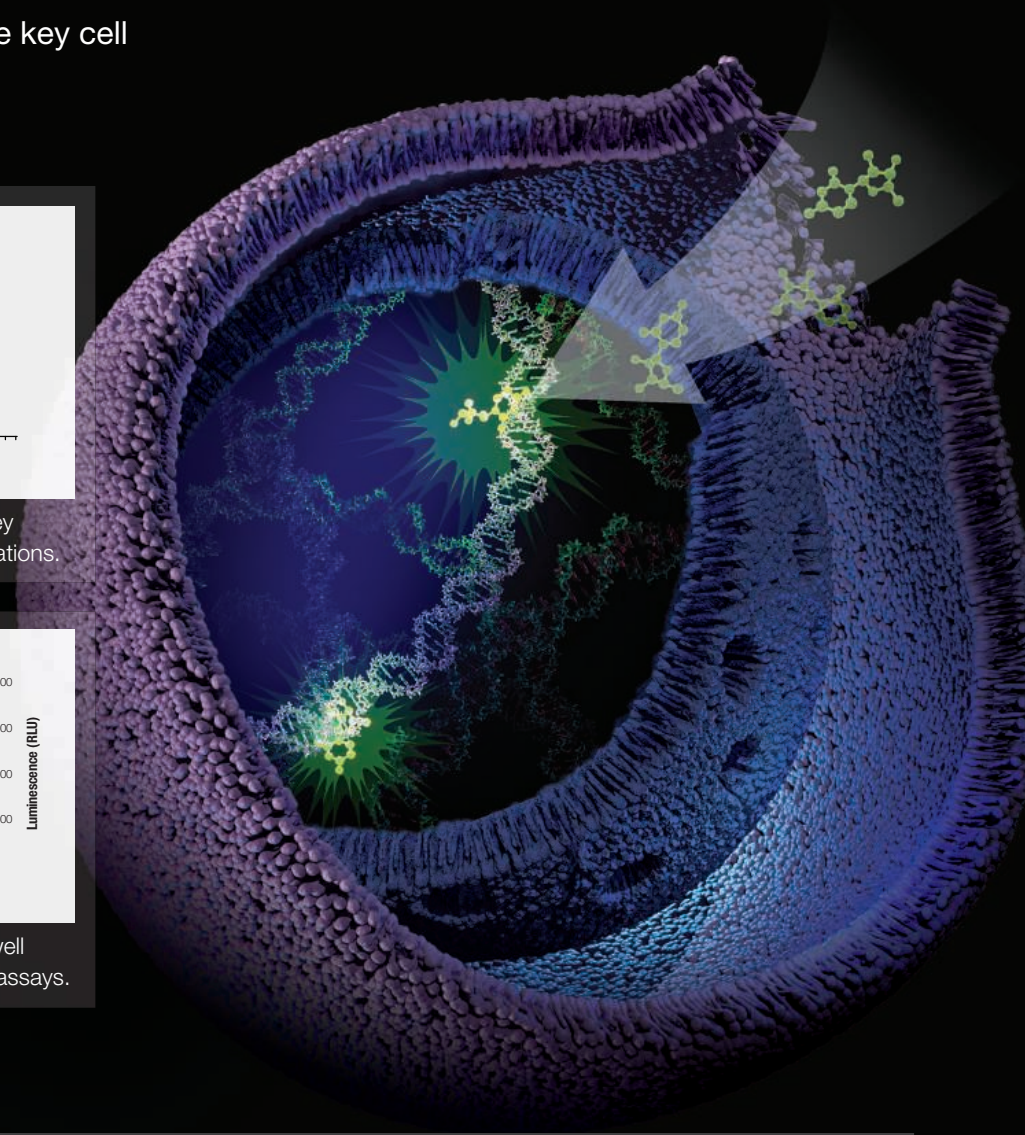

To see how easy better biology can be, request a free sample at:
www.promega.com/newcelltox

Science Careers Advertising

For full advertising details, go to ScienceCareers.org and click For Employers, or call one of our representatives.

Tracy Holmes
Worldwide Associate Director
Science Careers
Phone: +44 (0) 1223 326525

THE AMERICAS
E-mail: advertise@sciencecareers.org
Fax: 202-289-6742

Tina Burks
Phone: 202-326-6577

Marci Gallun
Phone: 202-326-6582

Online Job Posting Questions
Phone: 202-312-6375

EUROPE / INDIA / AUSTRALIA / NEW ZEALAND / REST OF WORLD
E-mail: ads@science-int.co.uk
Fax: +44 (0) 1223 326532

Axel Gesatzki
Phone: +44 (0)1223 326529

Sarah Lelarge
Phone: +44 (0) 1223 326527

Kelly Grace
Phone: +44 (0) 1223 326528

JAPAN
Yuri Kobayashi
Phone: +81-(0)90-9110-1719
E-mail: ykobayas@aaas.org

CHINA / KOREA / SINGAPORE / TAIWAN / THAILAND
Ruolei Wu
Phone: +86-1367-1015-294
E-mail: rwu@aaas.org

Science Careers
From the journal *Science* AAAS

ScienceCareers.org

School of Engineering & Applied Science
THE GEORGE WASHINGTON UNIVERSITY

ASSISTANT PROFESSOR (TENURE TRACK), DEPARTMENT OF BIOMEDICAL ENGINEERING, THE GEORGE WASHINGTON UNIVERSITY, WASHINGTON, D.C.

The George Washington University invites applications for a tenure-track assistant-professor position in the Department of Biomedical Engineering, to begin in fall semester 2014. This is an exciting opportunity for an outstanding person to join and contribute to the development of a new BME department. All areas of BME specialization will be considered. The Department will open formally in fall 2014 after moving the longstanding ABET-accredited B.S. program, and the M.S. and Ph.D. BME programs, from the Department of Electrical and Computer Engineering. The University is constructing a new 500,000 square-foot Science and Engineering Hall, adjacent to the University Hospital and Schools of Medicine and of Public Health, which will house state-of-the-art clean rooms, imaging facilities, and BME research and instructional laboratories. The School of Engineering and Applied Science will move into the building in spring 2015. The George Washington University is located in the nation's capital, with close access to many federal funding agencies and government research laboratories.

Responsibilities: The successful candidate will be expected to be an enthusiastic and effective teacher of undergraduate and graduate courses in Biomedical Engineering and, equally, to establish a strong program of high-quality externally-funded research. BME faculty members actively contribute to an environment that values diversity and nurtures collaboration, creativity, and innovation. The new professor will have opportunities to actively support the Department's efforts to attract new multidisciplinary partners across the University, and to advance and extend existing relationships with nearby government laboratories.

Basic Qualifications: Applicants must have an earned doctorate in Biomedical Engineering, Bioengineering, or a related field, outstanding academic credentials, clear evidence of potential for developing a strong externally-funded research program (as evidenced in part by peer-reviewed publications), and the ability to teach effectively at both the graduate and undergraduate levels. ABD applicants will be considered, but must complete all the requirements for the Ph.D. by expected start date.

Application Procedure: To apply, complete the online faculty application at http://www.gwu.jobs/postings/19294 and upload a cover letter, a detailed CV or resume, a concise statement of teaching and research interests, and full contact information for five professional references. Please also indicate your primary area(s) of expertise and interest, and desired professorial rank. Only complete applications will be considered. Review of applications will begin on February 17, 2014 and will continue until the position is filled.

EEO/AA Policy: The George Washington University is an Equal Opportunity and Affirmative Action Employer. Applications from women and under-represented minority groups are strongly encouraged.

School of Engineering & Applied Science
THE GEORGE WASHINGTON UNIVERSITY

FOUNDING CHAIR AND TENURED FULL PROFESSOR, DEPARTMENT OF BIOMEDICAL ENGINEERING, THE GEORGE WASHINGTON UNIVERSITY, WASHINGTON, D.C.

The George Washington University invites applications for a tenured full-professor position as Chair of the Department of Biomedical Engineering, to begin in fall semester 2014. This is an exciting opportunity for an outstanding person to develop and lead a new BME department. The Department will open formally in fall 2014 after moving the longstanding ABET-accredited B.S. program, and the M.S. and Ph.D. BME programs, from the Department of Electrical and Computer Engineering. The University is constructing a new 500,000 square-foot Science and Engineering Hall, adjacent to the University Hospital and the Schools of Medicine and of Public Health, which will house state-of-the-art clean rooms, imaging facilities, and BME research and instructional laboratories. The School of Engineering and Applied Science will move into the building in spring 2015. The George Washington University is located in the nation's capital, with close access to many federal funding agencies and government research laboratories.

Responsibilities: The successful candidate will be expected to demonstrate an intense commitment to excellence in teaching and research and to the success of our students. Equally, the new Chair will vigorously catalyze and develop further the Department's collaborations with the Schools of Medicine and of Public Health, and the GWU Hospital, attract new partners across the University, and advance and extend the existing relationships with nearby government laboratories. The new Chair will be an enthusiastic proponent of creativity, innovation, and outreach, and be an effective advocate and spokesperson for the Department, both within and beyond the University.

Basic Qualifications: Applicants must have an earned doctorate in Biomedical Engineering, Bioengineering, or a related field; outstanding research and academic achievements that make the candidate suitable for appointment as a full professor; a demonstrated capability as a visionary leader, with a strong research portfolio that evidences multi-disciplinary expertise, which can complement and expand existing departmental strengths; and the proven ability to teach effectively at both the graduate and undergraduate levels. Applicants must have evidence of substantial management ability and experience in a multi-faceted academic environment that includes success in mentoring of students and faculty, proposal writing, and grant management.

Application Procedure: To apply, complete the online faculty application at **http://www.gwu.jobs/postings/19290** and upload a cover letter, a detailed CV or resume, a concise statement of teaching and research interests, and full contact information for five professional references. Please also indicate your primary area(s) of expertise and interest, and desired professorial rank. Only complete applications will be considered. Review of applications will begin on **February 17, 2014** and will continue until the position is filled.

EEO/AA Policy: The George Washington University is an Equal Opportunity and Affirmative Action Employer. Applications from women and under-represented minority groups are strongly encouraged.

Leveraging Committee Assignments for Advancement

Serving on faculty committees can be enriching, exciting experiences that enable you to increase your knowledge of your institution and field, develop new partnerships and expand your network, and sharpen critical skills. Service also shines a spotlight on a professor's abilities, and can open the door to opportunities to pursue administrative jobs, apply for awards, and contribute to interdisciplinary research projects. But with a seemingly dizzying array of committees on which early career faculty can serve, how do you decide which to pursue, and when? Experts agree that the key is to seek opportunities that can add value to your institution and align with your interests and career aspirations.

By Alaina G. Levine

Stuart Sidle

Stuart Sidle says that committee experiences have enriched his academic career. From serving on faculty searches, the associate provost for strategic initiatives at the University of New Haven in Connecticut learned to improve both his own evaluation of potential employees and his ability to prepare for job interviews. When he sat on a curriculum committee, he learned about the course approval process which helped him lead his department when he was chair. He recommends faculty incorporate committee assignments into their career advancement plans.

And he's not alone in this opinion. "Committee work is crucial to your growth as a faculty member," says **Jeanne Hossenlopp,** vice provost for research and dean of the graduate school at Marquette University in Milwaukee, Wisconsin. Conversely, "committee work is crucial to the life of a university." **Thomas Near,** an associate professor of ecology and evolutionary biology at Yale University, agrees. "Faculty have to be savvy with our time but also generous of our time" as it relates to participating in committees, he says, because committee work "makes you a better member of the university community and improves the community itself as well."

Those serving on committees see excellent return on their investment. **Michael Palladino,** dean of the School of Science at Monmouth University in West Long Branch, New Jersey, says serving on a broad range of committees—including those that focused on curricula, governance, hiring, and fundraising—has helped him as a dean. As an untenured faculty member, he found himself "thrust" into a leadership position when serving as the vice chair of the Faculty Council when the chair went on medical leave. "It had a much bigger impact than I thought," he says. Colleagues and administrators began noticing that he was "not afraid to make decisions and was not only motivated by tenure," which ultimately helped him solidify tenure after all. "I realized that service work that advances the university helps both me and the university," he explains.

But even if you are not in a leadership role, contributing to a committee is "an effective way of contextualizing what you're doing and broadening your viewpoint," says **David Pyle,** a professor of earth sciences at the University of Oxford. "It allows you to become more engaged with the institution as a whole."

Indeed, committee assignments give you "an appreciation of how complex the work of a university is," says Hossenlopp. An institution's behind-the-scenes elements, such as hiring, fundraising, funding, and even instrumentation and laboratory support, aren't always apparent from your time in grad school or as a postdoc, explains **Jennifer Swann,** a professor of biological sciences at Lehigh University in Bethlehem, Pennsylvania. Yet they are essential aspects that keep the institution running smoothly that faculty should not only be aware of, but also contribute to in order to chart their own path to success.

Gaining Insight and Abilities

Depending on the committee, faculty can become familiar with different areas of their university as well as gain the opportunity to hone varied skill sets. Curriculum committees, for example, "help us to better train our students," says Hossenlopp. Institutional policy and promotion and tenure committees enable you to grasp university politics, says Swann. And graduate recruitment or faculty search committees are an effective way to develop talent in articulating your value to new audiences, she adds.

Not surprisingly, most committee assignments enhance mem- continued>

"Committee work is crucial to your growth as a faculty member."
—Jeanne Hossenlopp

Jeanne Hossenlopp

Upcoming Features

Postdocs: Broadening Your Skills —February 28
Cancer Research Careers—March 28
Biotech and Pharma—June 13

CREDITS: (FROM LEFT) LEHIGH UNIVERSITY; ©ISTOCKPHOTO.COM/MONKEYBUSINESSIMAGES; MARQUETTE UNIVERSITY

"I am very careful only to serve on committees that I care deeply about or on which there is a skill I can learn."
—Kristin Douglas

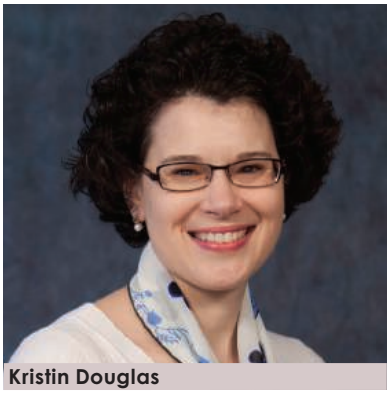
Kristin Douglas


Michael Blackburn


Jennifer Swann

bers' communication skills. Your speaking, writing, and negotiating skills are challenged as you prepare reports and presentations, says Palladino. You learn strategies for conflict resolution. And as a committee chair, you also develop expertise in delivering "bad news" and constructive criticism, says **Kristin Douglas,** a biologist and associate dean at Augustana College in Rock Island, Illinois. Your improved communication skills enable you to become a more effective advocate, for yourself, your department, and your university, adds Palladino: "You're able to talk about your institution in a more informed way."

With improved communication and amplified visibility comes the chance to expand one's network. The prospect of collaborating across interdisciplinary fields can be realized, as Pyle himself experienced. And your service can put you in contact with people with whom you might not otherwise have connections, such as trustees of the university and other institutional constituents. By serving on and later chairing his institution's diversity committee, **Prosanta Chakrabarty,** an assistant professor of biology at Louisiana State University in Baton Rouge, Louisiana, interacted more directly with his upper administration and contributed to a search for a new dean. His participation on this team directly led to an invitation to address a group of university donors, he says.

Choosing a Committee

So how do you decide which assignments to pursue, and at what point in your career? "Picking committees can be tough water to navigate when you're new" to a university, admits **Eric Bubar,** an assistant professor of physics who joined Marymount University in Arlington, Virginia in 2011.

Early in your career "you are so focused on teaching and establishing your research that you might not see the value of serving on committees," says Palladino, "but that's where skilled faculty mentors and deans comes in handy to provide advice about appropriate committee service." The department chair can also counsel you about which committees are strategically important for helping you gain tenure, which might take up too much time, and how to say no to invitations, says Hossenlopp.

Many universities have formal mentorship programs for early career faculty to assist them in their service decisions. Douglas, for example, learned that at "different points in my career that 'serving' meant different things," she explains. In her early career, she was encouraged to select committees that focus on education and curriculum development, which helped her become a better teacher. "As I got closer to tenure, my mentors advised me to join highly visible committees," because it is important for people to see you on "big power" committees, such as governance boards.

Strive to serve on committees whose interests are united with your own. "It is essential that faculty chosen to serve on particular committees have the background, skills sets, and/or desire to make valuable contributions. Aligning faculty interests with the right committee is key," says Palladino.

But don't be afraid to serve on a committee that is outside your realm of expertise, as it can be invaluable, advises Pyle. When he volunteered for a finance and fundraising committee, he was "exposed to a completely new set of problems," he says.

Highly Visible Committees

Since every university has its own culture, it is critical for a faculty member to know which committees to pursue during certain times in their career, especially in advance of receiving tenure. "Avoid Faculty Senate in your early career," says **Michael Blackburn,** who serves as co-dean of the University of Texas Graduate School of Biomedical Sciences at Houston. "You become embroiled in untenable issues."

However, "my gut instinct is that if you can have one of these highly visible positions and navigate it in a way that is sensitive to other people's opinions and viewpoints while still being able to communicate your viewpoint, that ultimately builds respect for you," says Douglas. She notes that her participation in her institution's governance committee ultimately allowed others to see her leadership talents, which helped her land the position of associate dean.

No matter what committee you are on, people are watching you, and generally, "you do a disservice when you don't speak up," says Swann. Not only do you not help the committee itself, she adds, but "if you don't say anything before tenure, no one's going to listen to you after tenure.…People put you on the committee because they want your voice."

Know When to Say No

"My mentor told me you could say yes to every offer or just yes to the ones you care about," says Douglas. "I am very careful only to serve on committees that I care deeply about or on which there is a skill I can learn." Recognize you can (almost) always decline a committee offer. "If the president asks, you can't say no," she adds with a laugh.

Some professors are courted more than others to serve on committees, which necessitates saying no more often. Case in point: female and underrepresented minority professors, who frequently are asked to serve on more committees than their white, male counterparts. Pyle sees it firsthand at Oxford: "females may end up being pressed to be on far more committees than men," he admits.

Although she herself has not experienced it, Douglas notes that "it does happen on campus, related to multicultural continued>

CREDITS: (CLOCKWISE FROM TOP) AUGUSTANA COLLEGE; LEHIGH UNIVERSITY; UT HEALTH

Karolinska Institutet

Integrated Cardio Metabolic Center

AstraZeneca

Karolinska Institutet (KI) and AstraZeneca (AZ) invite highly motivated, world-class, biomedical researchers to submit an expression of interest to carry out a fully funded, 5-year research program at the newly established KI/AZ Integrated Cardio Metabolic Centre (ICMC) in Stockholm, Sweden.

The ICMC represents a unique opportunity for academic scientists to collaborate with and work side-by-side with scientists from the pharmaceutical industry to advancing the understanding of cardiovascular and metabolic disease, and to discover and develop the next generation of medicines in this area. Apart from hosting leading scientific activities, this pioneering centre also offers an exciting prospect for researchers to shape the design of an innovative, new collaboration model between academia and industry.

Focusing on preclinical and early clinical studies, we are aiming to recruit researchers, with an open, creative and collaborative mindset, who can develop world-leading, independent research within three main strategic areas: Cardiac Regeneration, Islet Health (Diabetes) and Diabetic Nephropathy.

What's in it for you?

- Unique opportunity to work in an open academia-industry collaboration environment where your ideas, innovations and research can help shape future research collaboration models, as well as deliver true benefit to patients and society.
- Close collaboration with, access to and support from KI, AZ Mölndal, MedImmune and other world-class partners committed to advancing the understanding of cardiovascular and metabolic disease.
- Full research grants for up to five years, including salary funding, consumables and use of world-class facilities and analytical platforms.
- Research results and findings are intended to be freely publishable.

Read more at www.ki.se/icmc

Multiple Faculty Hires in Metabolomics

Now accepting applications, nominations and confidential inquiries

The University of Florida announces six new tenured or tenure-track faculty positions in metabolomics as part of a university-wide recruitment initiative to expand existing strengths in metabolomics and complementary areas such as big data, genomics and personalized medicine. We are seeking accomplished scientists with an established record of federal funding and expertise in analytical technology development, bioinformatics, and/or metabolomics applications in biomedicine or agriculture. All hires through this recruitment will be associated with UF's Southeast Center for Integrated Metabolomics, a member of the NIH Common Fund consortium of six regional metabolomics centers. Six UF colleges are participating in this recruitment: Medicine, Liberal Arts & Sciences, Agricultural & Life Sciences, Dentistry, Pharmacy, Public Health & Health Professions.

UF | UNIVERSITY of FLORIDA

Read the full announcement at **secim.ufl.edu**

To apply or request more information, contact:
metabolomics_faculty_hire@secim.ufl.edu

The University of Florida is an equal opportunity institution.

FEATURED PARTICIPANTS

Augustana College
www.augustana.edu

Lehigh University
www.lehigh.edu

Louisiana State University
www.lsu.edu

Marquette University
www.marquette.edu

Marymount University
www.marymount.edu

Monmouth University
www.monmouth.edu

The University of Texas Health Science Center at Houston
www.uth.edu

University of Illinois Springfield
www.uis.edu

University of New Haven
www.newhaven.edu

University of Oxford
www.ox.ac.uk

Yale University
www.yale.edu

Michael Palladino

"One aspect of service that I always emphasize to new faculty is service to the profession."

—Michael Palladino

representation, because there aren't as many faculty who represent that viewpoint, so there are certain people who get asked to serve more often."

The increase in diverse sources of inspiration can inject new life and creativity into a committee. But for many women and minorities on a campus, they can often feel like they are being exploited.

Swann advises to "beware the token position. To appear fair and balanced, many committees will recruit women and underrepresented minorities. But it may just be for show. Their opinions are not sought or heard, and they are often saddled with more than their share of the work. Talk to your chair or diversity officer if you are in this position."

Committees Outside Your Institution

"One aspect of service that I always emphasize to new faculty is service to the profession," says Palladino. "Serving as a panelist at a workshop or on a professional society committee (even if this starts at a regional chapter or organization) are all good opportunities." Service to journals and granting agencies as a reviewer are also essential to advancement, he adds.

Participating in your professional association's newsletter committee is a good way to launch external engagement, as Hossenlopp discovered. Early in her career, she served as the newsletter editor for the Division of Laser Science of the American Physical Society. It automatically positioned her to interact with prominent members of her field and opened her to networking channels she might not have had access to for years. "Build your professional network early, especially outside your department," she advises.

As you craft your professional advancement plan, get to know the service culture of your university and department and how (and if) committee work influences promotion decisions. This will aid you in deciding when to participate in committees that are associated with professional societies. In the Department of Biological Sciences at Louisiana State University, "they don't ask new assistant professors to serve on committees," says Chakrabarty; internal committee invitations are offered only after a faculty member has been on staff for at least three years. But even then, internal service is not as important as your external service. "I was advised not to do much university committee work because it doesn't count much toward tenure," he notes. But he did volunteer to edit a journal and run workshops at conferences, which increased his knowledge of his field, augmented his network, and magnified his reputation in the minds of other leaders in the discipline.

At Yale University, some committees have charters that necessitate untenured faculty to participate in them, says Near. But in general, the institution specifically does not consider internal service when making tenure decisions. "It's more about your reputation in the international field," he says, which means that early career faculty are encouraged to pursue assignments with professional societies that bolster their investigations and elevate their research profile. His involvement in the Society for the Study of Evolution and American Society of Ichthyologists and Herpetologists, in which he organized symposia at national meetings, helped him immensely. "It has provided tangible benefits to my research program and has kept me knowledgeable about advances in the field," he concludes. "It helps the discipline and it helps you serving as a professional in the discipline."

If your university allows it and better yet, favors it, consider participating in external committees sooner rather than later. "You are seen as a leader," says Swann. "Not enough pre-tenure faculty do this, and it can only help you."

Advancing Your Profession, Institution, and Career

For early career professors eager to serve your institution and profession through committee participation, don't make the mistake of pursuing too much too soon. "It's good to step back and realize you don't have to achieve all of your goals in 2–3 years," says Pyle. There are other people who can be tapped for assignments if you are overtaxed yourself, and there is always time after tenure to pursue stimulating committee projects that you don't have time for presently.

In fact, post-tenure committee contributions should be woven into your career strategy. "Once you get through tenure, you're supposed to broaden your horizons and be more invested in the way the university is conducting its business," says Swann. Moreover, this is the time when you can become even more engaged in your professional society and seek vital leadership roles.

"Working on a committee can be very rewarding and you can do a lot of good things for the university, which can really help your reputation," says **Malcolm McCallum,** a visiting assistant professor in the department of environmental studies at the University of Illinois at Springfield. "Just make your moves judiciously and carefully to minimize the negatives and maximize the positives."

Alaina G. Levine is a freelance science writer based in Tucson, Arizona.

DOI: 10.1126/science.opms.r1400140

CREDIT: JIM REME, MONMOUTH UNIVERSITY

Department of Biotechnology
Ministry of Science & Technology
Government of India

RAMALINGASWAMI RE- ENTRY FELLOWSHIP

Applications are solicited from Indian nationals working in overseas research institutions for the "**Ramalingaswami Re-entry Fellowship**", a re-entry scheme of the Department of Biotechnology (DBT), Ministry of Science & Technology, Government of India.

Aim of the Fellowship

The scheme is conceptualized with the aim of attracting highly skilled researchers (Indian nationals) working overseas in various cutting edge disciplines of biotechnology (agriculture, health sciences, bio-engineering, energy, environment, bioinformatics and other related areas), by providing them an attractive avenue to pursue their R&D in Indian institutions.

Who is eligible to apply ?

The applicant should possess a Ph.D., M.D., M. Tech, M.VSc. or equivalent degree with an outstanding track record as reflected in publications and other recognitions and with at least three years of post-doctoral research experience in overseas research laboratories.

Candidates (Indian nationals) working overseas are eligible to apply. ***Those who have already returned to India within one year of the closing date of this advertisement are also eligible.***

Researcher's upto 55 years of age as determined on closing date of application are eligible to apply.

Incentives of being a Ramalingaswami Fellow

1. This is a senior fellowship programme, and awardees are to be considered synonymous to the faculty/scientists at the level of Scientist-D. They are entitled to take up teaching/research assignments and supervising Doctoral/MS students.

2. The scheme provides a consolidated monthly remuneration of Rs. 75,000/-p.m. (Rs. 85,000/- p.m w.e.f. 1st April ,2014). In addition, a House Rent Allowance of Rs. 7,500/- p.m. is given to fellows. In case host institute provides accommodation to the fellow, no house rent allowance is admissible.

3. Fellows will receive a research/contingency grant of Rs. 10.00 lakhs for the 1st year, Rs. 7.50 lakhs for the 2nd year and Rs. 5.00 lakhs for the subsequent 3 yrs. for purchase of consumables, minor equipment, international and domestic travel, engaging manpower and other contingent expenditure to be incurred for the implementation of research proposal.

4. DBT encourages host institutions to provide medical benefits, transport allowance, leave travel allowance and other benefits as per their prevailing norms as applicable to their employees of the rank equivalent to Scientist D out of their own resources/ funds.

5. Fellows retain an option for drawing either the fellowship or salary if they are appointed at a suitable permanent scientific position. Fellows opting for salary can continue to avail the research /contingency grant with prior approval of DBT.

6. Ramalingaswami Re-entry Fellows could take up fellowship at any of the scientific institutes/ universities in the country. However, application should be duly forwarded by the competent authority of the host Institute.Fellows/Awardee can change his/her host institute only once during the tenure of the fellowship.

7. Awardees are eligible to apply for research grants to any of the funding agencies towards accomplishment of research proposal. However, the Co-PI has to be a permanent employee of the host institution.

Tenure of fellowship

Fellows can draw fellowship for a term of five years. Fellowship is further extendable for another term on a fresh appraisal of performance of the fellow.Those who are able to secure permanent positions will not be considered for 2nd term.

How to apply

Applications may be sent as per Proforma downloadable from DBT website (**www.dbtindia.nic.in**) and duly forwarded by the competent authority *to* ***Dr. Meenakshi Munshi , Director, Department of Biotechnology, Block-2, 7th Floor, CGO Complex, Lodhi Road, New Delhi -110 003, Email :- rls fellowship.dbt@nic.in*** latest by :- **25th March , 2014**

UF UNIVERSITY of FLORIDA College of Dentistry

Multiple Faculty Positions in Mucosal Immunology/Microbiome-Host Interactions, Assistant/Associate/ Full Professor

The University of Florida is seeking applicants for multiple positions in mucosal immunology and microbiome: host interactions for a multidisciplinary program aimed at preeminence in the field. These recruits will interact closely with more than 17 funded scientists and physicians already working in this area at the University. Investigation of the interaction between the mucosal innate immune system and the local microbiome is especially attractive. The successful applicant may study any mucosal surface, from the oral cavity and nasopharynx through the gastrointestinal tract, or the lung and pancreas; applying innovative approaches and/or unique technologies. Innate, B or T cell immunobiology and metagenomic approaches to microbiome interactions are areas of emphasis, and the role of chronic inflammation of intestinal disorders and mucosa in oncogenesis would also fit well. The ideal candidate would be investigating an area that complements and enhances the basic and clinical expertise of the host colleges: Dentistry, Medicine, and Veterinary Medicine. The position is a full-time 1.0 FTE, tenure-accruing position with a primary academic appointment in Dentistry, Medicine or Veterinary Medicine; with preference given to scientists conducting currently-funded research or imminently fundable science. The primary duties include establishing a successful laboratory research program with sustained peer-reviewed funding, research mentoring of pre- and post-doctoral fellows and other trainees, and a modest level of teaching to undergraduate or graduate students. Applicants must have a terminal doctoral degree (e.g. PhD, MD, DMD/DDS, DVM) and have completed a postdoctoral fellowship training program. Highly competitive salary and laboratory start-up will be provided commensurate with experience.

Send electronic copies of a Curriculum Vitae and letter of interest to: Chair of the Search Committee at the following email address: **DN-Office-of-Research@ad.ufl.edu**.

The University of Florida is an Equal Opportunity Institution dedicated to building a culturally diverse and inclusive faculty and staff. The selection process will be conducted in accord with the provisions of Florida's "Government in the Sunshine" and Public Records Laws. Search committee meetings and interviews will be open to the public, and all applications, resumes, and other documents related to the search will be available for public inspection.

WE MAKE LIVES BETTER UT HEALTH SCIENCE CENTER SAN ANTONIO

The Robert A. WELCH Distinguished Chair in Chemistry Department of BIOCHEMISTRY

We are seeking outstanding candidates at the Professor or senior Associate Professor level who employ biochemical and biophysical approaches to the study of molecular structures and biochemical mechanisms. Areas of interest include, but are not restricted to, cancer, neuroscience, aging, metabolic disorders and drug discovery. In addition to the Welch Chair endowment and its associated newly renovated space, significant resources from the Institution, UT System (UT STARS) and State agencies such as the Cancer Prevention and Research Institute of Texas (CPRIT) are available to outstanding candidates.

The selected candidate will be expected to play a leadership role, including involvement in the hiring of several junior faculty within the department in the coming years. Currently, the Department has 19 primary faculty covering a broad range of research interests (**http://www.biochem.uthscsa.edu/**). There is a significant structural biology focus, which is supported by uniquely integrated core facilities in X-ray crystallography, NMR spectroscopy, Mass Spectrometry, AUC, SPR, ITC, and a new Center for Innovative Drug Discovery (CIDD), including High Content/ High Throughput Screening and Medicinal Chemistry, established in collaboration with the University of Texas at San Antonio.

UTHSCSA is located northwest of downtown San Antonio in the South Texas Medical Center, gateway to the scenic Texas Hill Country, with its many recreational opportunities. UTHSCSA consists of five schools: Medical, Graduate, Dental, Nursing and Health Professions. San Antonio is the 7th largest city in the U.S. with a beautiful, historical downtown area featuring the Riverwalk with its diverse entertainment, and fine restaurants.

Please submit a Curriculum Vitae, description of research interests, list of four referees and a cover letter to **Dr. Bruce J. Nicholson, Chair of Biochemistry, MSC 7760, UTHSCSA, 7703 Floyd Curl Dr., San Antonio, TX 78229-3900**, or by E-mail to **Esther James** at **jamese@uthscsa.edu**.

The University of Texas Health Science Center at San Antonio is an Equal Employment Opportunity/Affirmative Action Employer. All faculty appointments are designated as security-sensitive positions.

MEDICAL PHARMACOLOGY AND PHYSIOLOGY FACULTY POSITION
University of Missouri
Department of Medical Pharmacology and Physiology

The Department of Medical Pharmacology and Physiology, University of Missouri invites applications for a tenure-track position **(Assistant to Full Professor)**. The successful candidate must have a Ph.D., MD, or MD/PhD degree in physiology, pharmacology, or related fields and significant extramural funding. Preference will be giving to candidates who utilize cellular and molecular approaches and are able to apply basic findings to impact human health in an effective "discovery-to-care continuum", who will contribute to a culture of innovation, and who provide expertise that contributes to expansion of School of Medicine-wide programmatic initiatives for research with regard to the effect of inflammation, diabetes, cancer, aging, gut microbiome or gender on the cardiovascular system. Candidates with expertise in the role of the brain microcirculation and inflammation in the pathogenesis of neurodegenerative disorders such as Alzheimer's disease are also desirable. It is expected that the candidate will contribute to undergraduate, graduate and medical student educational initiatives and will direct a highly productive and collaborative research program that is maintained by continued significant extramural funding.

Please send a cover letter that includes a narrative description of research and educational interests and highlights current research funding. Also include a curriculum vitae with names and contact information for three individuals who will provide letters of reference to: **MPPsearch@health.missouri.edu** (electronic submission preferred) or by mail to: **Chair – MPP Search Committee, Department of Medical Pharmacology and Physiology, MA415 Medical Sciences, University of Missouri-Columbia School of Medicine, One Hospital Drive, Columbia, MO 65212**. Active review of application will begin immediately and the search will continue until the position is filled.

Equal Employment Opportunity. The University of Missouri is an Equal Access, Equal Opportunity, Affirmative Action Employer that is fully committed to achieving a diverse faculty and staff. For more information, call the Associate Vice Chancellor of Human Resource Services/Affirmative Action officer at 573-882-4256. To request ADA accommodations, please call Human Resource Services at 573-882-7976. TTY users, please call through Relay Missouri, 1-800-RELAY (735-2966) or en Español at 1-800-520-7309.

ENDOWED PROFESSOR OF ORTHOPAEDICS & REHABILITATION

The Division of Musculoskeletal Sciences, Department of Orthopaedics and Rehabilitation at The Pennsylvania State University College of Medicine is seeking applications for the James Bobb Endowed Professor of Orthopaedics & Rehabilitation. This tenure track or tenured appointment will be at the Associate Professor or Professor level and in the area of musculoskeletal sciences or engineering. This position includes a highly competitive salary and significant start-up funding. The successful candidate should have a Ph.D. in a biological science or engineering field relevant to musculoskeletal science, an appointment at the Associate Professor level or higher at their current institution, a strong record of research accomplishment, scientific leadership in musculoskeletal research, extramural research funding, and high quality publications. This is a unique opportunity to join a well-established, highly interactive research group consisting of engineers, material, clinical and basic scientists focusing on musculoskeletal research.

Send curriculum vitae and the names of at least three references to:

Bobb Search Committee
Department of Orthopaedics
and Rehabilitation
The Pennsylvania State University
College of Medicine
500 University Drive, H089
Hershey, PA, I7033
e-mail: adas1@hmc.psu.edu

Employment will require successful completion of background check(s) in accordance with University policies.

Penn State is committed to affirmative action, equal opportunity and the diversity of its workforce.

University of Massachusetts Medical School
UMASS

Tenure-track Faculty Position
Department of Neurobiology

The Department of Neurobiology at the University of Massachusetts Medical School, established in 2001, has assembled a group of outstanding faculty with a focus on the genetic and molecular mechanisms of brain function. This group is unique in that it crosses many boundaries in the use of genetic model systems to study fundamental and interrelated areas in neuroscience including synapse development, function and plasticity, neural circuit development, maintenance and function, sensory transduction, glial cell biology and complex behaviors. The Department of Neurobiology serves as the administrative home for the interdepartmental Graduate Program in Neuroscience, with over 50 faculty members. The laboratories for the Department are housed on one floor of a state-of-the-art, 340,000 sq ft research building. **We now solicit applications for a tenure-track position at all levels.** We seek individuals of outstanding potential or demonstrated excellence in study of the nervous system. Specific areas of emphasis include, but are not limited to, cellular and molecular neuroscience, sensory processing, developmental neuroscience, brain physiology, and behavior. The positions are highly competitive with regard to start-up funds, laboratory space, and salary. Rank will be commensurate with ability and experience.

Applicants should upload a cover letter, CV, research statement and publication list to: **https://academicjobsonline.org/ajo/jobs/3809**. To expedite the review process, applicants should also invite three individuals who are familiar with their work and potential for success to upload their recommendation letters. Please refer any questions regarding the search to: **Dr. Patrick Emery, Chair of Faculty Search Committee, Associate Professor of Neurobiology, University of Massachusetts Medical School, 364 Plantation Street, Worcester, MA 01605-2324; patrick.emery@umassmed.edu**. Visit Neurobiology at: **http://www.umassmed.edu/neurobiology/**.

As an Equal Opportunity and Affirmative Action Employer. UMMS recognizes the power of a diverse community and encourages applications from individuals with varied experiences, perspective and backgrounds.

LONDON'S GLOBAL UNIVERSITY
UCL

UCL DEPARTMENT OF SCIENCE, TECHNOLOGY, ENGINEERING AND PUBLIC POLICY (UCL STEaPP)
Applied in focus
Global in reach

Now recruiting for entry in September 2014

MPA IN ENGINEERING AND PUBLIC POLICY
MPA IN SCIENCE AND PUBLIC POLICY

- One year professional Master's in Public Administration
- Study public policy in the heart of a global capital
- Courses from world-leading academics and practitioners
- Structured projects engaging real-world policy communities from around the world
- Develop the skills to mobilise policy, science and engineering knowledge and expertise to address our societies' most pressing challenges
- Graduate with an understanding of current issues and developments in science, technology and engineering that are shaping our modern world

INAUGURAL YEAR SCHOLARSHIPS AVAILABLE
Next deadline 28 February, monthly rolling admission rounds thereafter
www.ucl.ac.uk/steapp/masters steapp.admissions@ucl.ac.uk

Nanjing Agricultural University
Faculty Recruitment Notice

Nanjing Agricultural University(NAU) welcomes top talent in research and academics for full-time positions.

NAU is a national key university under the direct administration of the Ministry of Education of the People's Republic of China. NAU is a *Project 211* institution and one of the Innovation Platforms for Outstanding Disciplines under the *985 Excellence Initiative Project* launched by China's Ministry of Education.

● Eligible applicants:

Tenured professors at overseas universities or young scholars with PhDs from overseas universities.

Candidates should be involved in one or more of the following research areas: crop science, agriculture resource utilization and environment sciences, plant protection, veterinary medicine, horticulture, biology, agricultural and applied economics, land resource management, food science, history of science and civilization, ecology, animal husbandry, agrostology, public administration, industrial economics, business administration, finance, agricultural and bioinformatics, marine biology, and modern agriculture equipment engineering.

● Employee benefits:

1.Initial research funding ranging from RMB 500,000 to 10,000,000 will be provided, depending on discipline and applicants' status. Laboratory and office will be arranged.
2.NAU also provides housing and a relocation allowance.
3.Special support will be provided to each leading researchers, including a full-time administrative secretary, assistance in assembling a research team, and priority in recommendations for research funding and government talent schemes.

Tel: (86) 25-84399039 Ms. Chen Zhiying
E-mail: rcb@njau.edu.cn
Website: http://www.njau.edu.cn

首都师范大学
CAPITAL NORMAL UNIVERSITY

Faculty Positions Available at Capital Normal University

Capital Normal University invites applications for full-time positions in research and academics.

Established in 1954, Capital Normal University (CNU) is a comprehensive university offering majors in arts and humanities, sciences, technology, business management, laws, education, foreign languages, and art. CNU is a key university under the administration of Beijing Municipal Government, and a Project 211 institution.

For more detailed information, please visit the website http://www.cnu.edu.cn /pages/info_details.jsp?seq=20433&boardid=71002&classcode=71002

Eligible applicants:

Young scholars with PhDs or postdoctoral research experiences with a specific area of expertise and outstanding research achievements. The applicant must be physically healthy, and demonstrate good teamwork skills.

Professors are required to be under 45 years of age, exceptions can be made for holders of high-level academic titles; PhDs are expected to be under 35 years of age, and post-docs under 40.

Employee benefits:

CNU provides different levels of competitive salaries and start-up research funding. Housing and relocation allowances will be provided for the professors. Post-docs or PhDs from overseas universities with vice senior academic titles who have made significant academic achievements can apply for temporary housing.

To apply:

Please submit the following items to the related colleges or departments, and forward it to the Personnel Department of CNU : Curriculum Vitae; proposed work plan for 3 years; a list of papers and publications in the last 5 years; a list of awards won; a list of research projects participated or led by the applicants; and reference letters from experts in the applicant's field of study.

Please also sent paper copies of the application package to:

Personnel Department, Capital Normal University, 105 Xisanhuanbeilu, Haidian District, Beijing 100048, P.R. China
Contact: Zhou Quan, Chen Wenxin
Email: cnursc2013@163.com
Tel: 86-10-68902824
Fax: 86-10-68902240

Faculty Positions Available in Southwest University, Chongqing, China

Southwest University is a national key university of the "211" project directly under the Ministry of Education. It is located in Chongqing, the youngest municipality of China. The university hosts approximately 50,000 students, covering undergraduate, postgraduate and other programs. **For more detailed information, please visit the website: http://www.swu.edu.cn/#**

Applications for full-time professors, associate professors and distinguished scientists are welcome. Competitive salaries and start-up funds will be provided to successful candidates, in line with the national Recruitment Program of Young Experts.

The Recruitment Program of Young Experts (i.e. the Plan for Recruiting 1,000 Professorship for Young Talents): The candidates are required to be under the age of 40 and have obtained a PhD degree in a world-renowned university with at least 3 years of research experience abroad, or have obtained a PhD degree in Mainland China with at least 5 years of research and teaching experience abroad. Special offers will be granted to those who have excellent research achievements during their doctoral study.

Further information is available at http:// renshi.swu.edu.cn/rcgzbgs/ The Talents Recruitment Office, Southwest University,Beibei, Chongqing 400715, P. R. China. 0086-23-68254265.

Please kindly send applications or nominations in the form of an application letter enclosing a current CV to rencai@swu.edu.cn.

Faculty Position- Industrial Sustainability

Yale School of Forestry & Environmental Studies

Yale F&ES announces a tenured or tenure-track position for an innovative scholar working in industrial ecology, or closely allied field, with a substantial track record of research focused on sustainable resource management at multiple scales. Research should be grounded in an interdisciplinary approach that bridges the social and biophysical sciences. Areas could include environmental life cycles relating to materials, services, facilities, infrastructure, and technologies, using methods and tools such as material and energy flow analysis, lifecycle assessment, systems modeling, urban metabolism, foot-printing, input-output analysis, or complex systems theory. Interests in environmental product and technology assessment, as well as supply chain management and dematerialization, would also be advantageous.

The successful candidate is expected to build upon and enhance the School's reputation in industrial ecology through an excellent research program and active engagement with industry, government, and NGO communities. Established by pioneers in the field, the Center for Industrial Ecology at F&ES houses the Journal of Industrial Ecology and the Secretariat for the International Society for Industrial Ecology.

Applicants should have a doctoral degree in a related field, and will be expected to teach and mentor PhD, Masters and undergraduate students, as well as to develop an internationally-recognized research program that involves graduate students, including through fieldwork.

Please submit materials by Saturday, March 15, 2014 for full consideration -- **https://academicjobsonline.org/ajo/jobs/3743**. Salary and rank will be commensurate with experience. Inquiries to **fesdeansoffice@yale.edu**.

Yale University is an affirmative action/equal opportunity employer; applications from women and minorities are encouraged.

http://environment.yale.edu

FACULTY POSITIONS IN Physiology & Pharmacology

The Department of Physiology & Pharmacology at Des Moines University invites applicants for open-rank, tenure-track faculty positions. Candidates with expertise and/or preparation in cardiovascular physiology will be of particular interest.

We are committed to advancing our research enterprise and fostering an environment conducive to scholarly success through the cultivation of distinctive faculty and student researchers who discover and disseminate new knowledge. The expectation is for faculty to participate in scholarly activity including grant application, publications, research, as well as teaching to graduate and medical school students.

Candidates should demonstrate the potential to develop an innovative and extramurally funded research program and have a Ph.D. or equivalent plus a minimum of two years postdoctoral experience. Compensation and lab start-up costs are funded by the University and are not dependent on grant funding.

Please submit a letter of application, a CV, a concise statement of teaching interests and educational philosophy, a well-defined research plan including specific aims and objectives and three references at ***www.dmu.edu/employment***. Review of applications will begin immediately and continue until a successful candidate(s) is identified and hired.

DES MOINES UNIVERSITY

Des Moines University is an equal opportunity/affirmative action employer. The University seeks excellence through diversity among its administrators, faculty, employees and students. The University prohibits discrimination on the basis of race, color, national origin, creed, religion, age, disability, sex, gender identity, sexual orientation, veteran status, genetic information or any other legally protected status. Applications by members of all underrepresented groups are encouraged.

THE UNIVERSITY of TENNESSEE HEALTH SCIENCE CENTER

The University of Tennessee College of Pharmacy Medicinal Chemistry Faculty Position

The Department of Pharmaceutical Sciences in the College of Pharmacy at the University of Tennessee Health Science Center in Memphis, TN, is seeking applications for a twelve-month full-time, tenure-track faculty position at the full, associate, or assistant professor level that is state supported. The successful candidate is expected to devote a major effort to research. The applicant should have core expertise in medicinal chemistry, or related discipline such as structural biology focused on drug discovery and development. Candidates with a well-funded program in cancer, diabetes, antibiotics, drug delivery, nano-medicine, nano-technology, bio-imaging, or lipid research are highly encouraged to apply. The successful candidate is expected to have a Ph.D. or equivalent degree, the ability to acquire sustained external, investigator-initiated funding, including National Institutes of Health principal investigator funding, a commitment to excellence in teaching, and excellent oral and written communication skills.

Applications will be processed until the position is filled. Please submit curriculum vitae, summary of research interests, and contact information of three references to: **John Buolamwini, Ph.D. Professor and Vice Chair, Chair of Faculty Search Committee, Department of Pharmaceutical Sciences, 847 Monroe Ave, Suite 327, Memphis, TN 38163**, or by email at **jbuolamw@uthsc.edu**.

The University of Tennessee Health Science Center is located in Memphis, TN, an economically vibrant center, with a metropolitan population of more than 1.3 million, reflecting the richness along the bluffs of the mighty Mississippi River. The College of Pharmacy is located in a new, 187,000 square-foot building on the Health Science Center complex.

The University of Tennessee Health Science Center is an Equal Opportunity/Affirmative Action Employer.

J. Craig Venter® INSTITUTE

OPEN FACULTY POSITIONS

La Jolla, CA and Rockville, MD

For more than two decades our scientists have been at the forefront of the genomic revolution. Now, we want you to join us in our quest!

JCVI is seeking qualified applicants for positions at all levels particularly in the following research focus areas:

- **Environmental and ecological genomics**
- **Host/microbe interactions, including microbiome research**
- **Synthetic biology**
- **Bioinformatics and computational biology**
- **Virology and vaccine development**

Successful candidates will conduct innovative, independent research, collaborate with our interdisciplinary, highly collegial group of scientists within JCVI, and complement existing strengths within the Institute. Candidates must have a Ph.D. or M.D., a minimum of three years of Post-Doctoral research training, and be able to demonstrate the ability to establish and maintain a vigorous independent, externally funded research program. The level of appointment will be commensurate with experience.

JCVI offers an excellent working environment and a competitive benefits package. Interested applicants should apply directly in our career center at **www.jcvi.org**.

Equal Opportunity Employer

Faculty Positions
Department of Pharmacology
The University of Michigan

The Department of Pharmacology is seeking applications for two tenured/tenure-track positions at the **ASSOCIATE** or **PROFESSOR** level. We are seeking outstanding individuals with research experience and interests that augment current department initiatives in *Drug Metabolism, Pharmacogenetics, Clinical Pharmacology, Signal Transduction, Neuropharmacology/Behavioral Pharmacology, or Cardiovascular Pharmacology*. Qualifications include a Ph.D. in Pharmacology or a related discipline and/or M.D. degree, a strong record of nationally competitive external funding, a sustained record of excellent research productivity, and an outstanding national reputation in their field of interest. Applicants will be expected to maintain extramural funding, participate in the teaching of both medical and graduate school courses, and to support and mentor graduate students and postdoctoral fellows. An attractive startup package including excellent laboratories and generous startup funds will be available. Salary will be commensurate with experience.

The successful candidates will join a dynamic, diverse, and collaborative department in a Top 10 Medical School in a university setting with superb opportunities for continuing career development. The quality of life in Ann Arbor is outstanding. The combination of a large, major research university and a small, safe, family-oriented community make Ann Arbor an ideal environment. Ann Arbor offers an outstanding combination of sports, recreation, and cultural events.

Applicants should send their curriculum vitae, a three-page summary of their research program and future research plans, and information related to past and current teaching experience as a single PDF file to **effergie@umich.edu**. Three letters of recommendation should also be sent electronically. Address all correspondence to:

Dr. Peggy Gnegy, Chair
Pharmacology Search Committee
Department of Pharmacology
The University of Michigan Medical School
1150 West Medical Center Dr.
Ann Arbor, MI 48109-5632

Review of applications will begin on **February 24, 2014**, and will continue until both positions are filled.

The University of Michigan is an Affirmative Action/Equal Opportunity Employer. Applications from qualified women, minorities and/or disabled individuals are encouraged.

The Department of Chemistry at Marshall University seeks to fill a position in the Fall 2014 semester at the associate level. The desired discipline is in biochemistry with a focus on synthetic biology and/or protein engineering to lead a major initiative in that area. Candidates must have a PhD in biochemistry or a closely related field, and must have current NSF support for their research. The appointee must have a strong commitment to excellence in both teaching and research, and be willing to mentor junior faculty toward successful applications for external funding. For more information about our Department, please visit **www.marshall.edu/chemistry**.

The Department expects the candidate to maintain an original, high quality research program that engages undergraduate and Master's students from inception to dissemination. We seek candidates enthusiastic about incorporating research into their teaching. The Department also seeks candidates who will contribute to the University's general education curriculum, with its emphasis on a common First-Year Seminar and core curriculum courses that enhance students' critical thinking and the College's support of interdisciplinary programs of study.

Applicants must send a current curriculum vitae, statements of research plans and teaching philosophy electronically to **recruiting@marshall.edu** as a **single PDF file**. Three letters of reference should also be provided to this address separately. **All applications and supporting material must include your name and the search number (12899) in the subject line of the email.** Candidates who are invited to campus for interviews must have official *undergraduate and graduate transcripts* sent by their degree-granting institutions prior to the interview date. Review of applications will begin on **March 17, 2014** and continue until the position is filled. Marshall University is the recipient of the U.S. Labor Department's EVE Award for its Affirmative Action Employment Opportunity Programs. Additional information about Marshall University and Huntington, WV may be found at **http://www.marshall.edu/mu-advance/candidates.asp**.

Faculty Positions
Infectious Diseases Research

The Public Health Research Institute (PHRI) of Rutgers New Jersey Medical School located in Newark, New Jersey, is recruiting a new faculty member at the middle or senior levels to join a growing group of 23 laboratories. PHRI (www.phri.org) is a leading infectious diseases research center that emphasizes basic and translational sciences. Candidates must have training and experience of the highest quality and a funded research program addressing critical questions in cell biology, immunology and molecular biology that offer novel insights into pathogenicity, as well as innovative approaches for new vaccines, therapeutics and diagnostics. Preference will be given to programs focused on major viral and bacterial pathogens. We will only consider candidates who have current, long-term NIH grant support or equivalent funding from other sources. The PHRI Center is housed in a state-of-the-art research facility that has extensive core services, including a nationally-designated BL3 laboratory and animal facilities, X-ray facility for structural studies and an applied genomics center. The PHRI Center offers a robust and highly collegial research environment, generous start-up funds, and a comprehensive benefits package. Candidates should submit a curriculum vitae, a statement of research interests and accomplishments and a list of at least three references to: **Dr. Issar Smith, Public Health Research Institute, Rutgers New Jersey Medical School, 225 Warren Street, Newark, NJ 07103; Phone: (973) 854-3260; Fax: (973) 854-3101; E-mail: smithis@njms.rutgers.edu.**

Please note that effective July 1, 2013, as a result of the New Jersey Medical and Health Sciences Restructuring Act, several units from the former University of Medicine and Dentistry of New Jersey (UMDNJ) are now part of Rutgers Biomedical and Health Sciences (RBHS). For the purposes of payroll and benefits administration, the above position is a legacy UMDNJ position at Rutgers, and is eligible for benefits associated with legacy UMDNJ positions.

Rutgers, the State University of New Jersey, is an Equal Opportunity / Affirmative Action employer, and is compliant with the Americans with Disabilities Act (ADA). For more information, please visit http://jobs.rutgers.edu/TheRUCommitment.htm

RUTGERS
New Jersey Medical School

THE UNIVERSITY OF HONG KONG
香 港 大 學

Tenure-Track Associate Professor/ Assistant Professor in Ecosystem Function (Ref.: 201400024)

Applications are invited for tenure-track appointment as Associate Professor/Assistant Professor in Ecosystem Function in the School of Biological Sciences, from as soon as possible. The position will initially be made on a three-year term basis, with the possibility of renewal and with consideration for tenure during the second three-year contract. For exceptionally outstanding candidate, the appointment can be made with tenure.

Current strategic research areas of the School include: Food Safety and Food for Health, Endocrinology, Ecology, and Plant Evolution and Adaptation. Further information about the School can be obtained at http://www.biosch.hku.hk/.

Applicants should have expertise in ecosystem function and services. Preference will be given to those with an interest in marine ecosystems. The appointee is expected to teach courses related to ecology and environmental sciences, and concurrently serve as a Resident Scientist in the Swire Institute of Marine Science of the University.

A globally competitive remuneration package commensurate with qualifications and experience will be offered. At current rates, salaries tax does not exceed 15% of gross income. The appointment will attract a contract-end gratuity and University contribution to a retirement benefits scheme, totalling up to 15% of basic salary, as well as annual leave, and medical benefits. Housing benefits will be provided as applicable.

For enquiries about the existing research activities and the specific job requirements, please write to Professor S.S. Wu, Director of the School of Biological Sciences (e-mail: rudolfwu@hku.hk). Interested applicants should submit a completed application form, together with a full C.V., a research plan, and a statement on teaching philosophy to scsbs@hku.hk. Please indicate clearly the reference number and *which* level they wish to be considered for in the subject of the e-mail. Application forms (341/1111) can be obtained at http://www.hku.hk/apptunit/form-ext.doc. Further particulars can be obtained at http://jobs.hku.hk/. **Closes March 31, 2014**.

The University thanks applicants for their interest, but advises that only shortlisted applicants will be notified of the application result.

The University is an equal opportunity employer and is committed to a No-Smoking Policy

Research Positions

Careers Applied Science, Technology, and Engineering Research

Idaho National Laboratory INL

INL's Energy and Environment Science and Technology Directorate is seeking outstanding , highly creative and motivated early to mid-level career professionals to join our multi-disciplinary research teams. The Directorate is INL's principal multi-mission organization focused on research to advance clean energy systems, advanced transportation, advanced process technology and related sciences.

Multiple positions are available in the following areas:
• Bioenergy research including biomass characterization, conversion, preprocessing and molecular biology. • Analytical chemistry specializing in laser spectroscopy and mass spectrometry. • Materials science and physics with focus on performance in harsh environments, nondestructive evaluation, and radiation based imaging. • Membrane science with a focus on dense film separation and filtration. • Geology and Hydrology with a focus on hydraulic fracturing and geothermal evaluation. • Scientific visualization research in a CAVE environment with a focus on immerse visualization, virtual reality, graphics programming, and large format display technologies.

The Idaho National Laboratory is a science-based, applied engineering national laboratory dedicated to supporting the U.S. Department of Energy's mission in nuclear energy research, science, and national defense. With 3,800 scientists, researchers and support staff, the laboratory works with national and international governments, universities and industry partners to discover new science, develop technologies that underpin the nation's nuclear and renewable energy, national security and environmental missions. The Laboratory is a multi-program national laboratory. It currently performs a range of research and development activities associated with energy and national security. The laboratory currently has more than 150,000 sq. ft. of modern research facilities with a significant amount of wet laboratory space that are supported by a vast array of state-of-the-art research instrumentation. Idaho Falls is conveniently situated near many national treasures such as Yellowstone National Park, Teton National Park, Jackson, WY, etc. For more information about the area, please visit **www.visitidahofalls.com** and **www.visitidaho.org**. Interested parties should visit our website at **www.inl.gov**.

INL is an Equal Opportunity Employer M/F/D/V

NIMS ICYS

Research Position at ICYS, NIMS, Japan

The International Center for Young Scientists (ICYS) of the National Institute for Materials Science (NIMS) is now seeking a few researchers. Successful applicants are expected to pursue innovative research on broad aspects of materials science using most advanced facilities in NIMS (**http://www.nims.go.jp/eng/index.html**).

In the ICYS, we offer a special environment that enables young scientists to work independently based on their own idea and initiatives. All management and scientific discussions will be conducted in English. An annual salary between 5.03 and 5.35 million yen (level of 2013) will be offered depending on qualification and experience. The basic contract term is two years and may be renewed to one additional year depending on the person's performance. A research grant of 2 million yen per year will be supplied to the ICYS researcher.

All applicants must have obtained a PhD degree within the last ten years. Applicants should submit an application form, which can be downloaded from our web site, together with a resume (CV) and a list of publications. A research proposal on an interdisciplinary or integrated area related to the materials science should also be submitted. The application letter should reach the following address via e-mail or air mail by **March 31, 2014**. Visit our website for more details (**http://www.nims.go.jp/icys/**).

ICYS Administrative Office, National Institute for Materials Science Sengen 1-2-1, Tsukuba, Ibaraki 305-0047, Japan
e-mail: **icys-recruit@nims.go.jp**

IPP International Postdoctoral Programme
cnic

Opportunities for POSTDOCTORAL RESEARCHERS in Biomedical Research at the Spanish National Centre for Cardiovascular Research CNIC, Madrid - Spain

The CNIC is dedicated to excellence in cardiovascular research and to translating new knowledge into real improvements in clinical practice.

The scientific project of the centre has been structured in three areas:
- Cardiovascular Development and Repair Department (CDR)
- Vascular Biology and Inflammation Department (VBI)
- Epidemiology, Atherothrombosis and Imaging Department (EAI)

To be eligible, candidates must:
- Hold a PhD degree that must have been awarded no more tan five years ago (exceptions will be made for documented career brakes and candidates with children)
- Have, at least, one publication as first author in an international peer reviewed journal
- Candidates must not have resided or carried out their main activity in Spain for more than twelve months in the last three years

The CNIC can offer you:
- A 3-year contract
- An internationally competitive salary
- State of the art infrastructure and latest generation of technological equipment
- Scientific-technical support and complementary training

Deadline for submission of proposals: 4 April 2014

CNIC is an inclusive, equal opportunity employer, irrespective of nationality, ethnic origin, gender, marital or parental status, sexual orientation, creed, disability, age or political belief. Confidentiality is guaranteed throughout the selection process and all current regulations relating to the protection of personal data will be strictly adhered to.

For further information and applications, please, visit www.cnic.es

cnic MARIE CURIE ACTIONS

CALIFORNIA'S STEM CELL AGENCY

CIRM

California Institute for Regenerative Medicine

PRESIDENT, CIRM

The **California Institute for Regenerative Medicine (CIRM)** is seeking applications and nominations for the position of President.

California's stem cell agency, the California Institute for Regenerative Medicine (CIRM) was established in early 2005 following the passage of Proposition 71, the California Stem Cell Research and Cures Initiative. The statewide ballot measure, which provided $3 billion in funding for stem cell research at California universities and research institutions, was approved by California voters on November 2, 2004, and called for the establishment of a new state agency to make grants and provide loans for stem cell research, research facilities, and other vital research opportunities. As a result, CIRM has become one of the most influential agencies in the universe of stem cell research, but also an important example of how science can be promoted and supported in novel partnerships more broadly.

After just 9 years, CIRM has put California at the forefront of stem cell research. Scientists, facilities, and a broad range of projects have grown steadily, creating a body of work that encompasses fundamental discovery and translation to pre-clinical testing, and more recently, clinical trials. With the remaining resources of the state's commitment, it is CIRM's intention to focus its funding decisions increasingly on a host of projects with particular clinical promise, bringing the most promising therapies to patients as quickly as possible.

The President of CIRM is the chief executive officer and appointed by the Governing Board. In addition to being an exceptional leader, the next President must be a highly respected executive, have a strong scientific background and business acumen, exhibit sensitivity to a unique culture, and have the ability to manage a complex agency with a novel organizational model. The President will play a major role in connecting groundbreaking scientists with their colleagues, the investor community, biotechnology and pharmaceutical companies, and other potential collaborators, all with the specific purpose of demonstrating the value of stem cell discoveries in benefiting human beings.

Candidates will have an M.D., a Ph.D., or both, equivalent industry experience or a similar body of knowledge developed in professional roles.

Korn Ferry is assisting CIRM with this important search. Please forward, as soon as possible, your CV/resume, including a letter of interest, or nominations of appropriate candidates to: **Warren E. Ross, M.D., c/o Betsy Messina (betsy.messina@kornferry.com), Korn Ferry, 1835 Market Street, Suite 2000, Philadelphia, PA 19103.**

The California Institute for Regenerative Medicine is an Equal Employment Opportunity Employer and committed to a diverse workforce.

KORN FERRY

CARNEGIE INSTITUTION FOR SCIENCE

DIRECTOR
DEPARTMENT OF EMBRYOLOGY

The Carnegie Institution for Science seeks a Director for its Department of Embryology. The Director will lead a faculty working on developmental biology in a variety of model organisms and will be expected to carry out an active research program of her or his own. A full description of the Department is available at **http://emb.carnegiescience.edu**. Applicants should have a substantial and excellent record of original research in developmental biology.

The Institution was founded and endowed in 1902 by Andrew Carnegie who envisioned an independent institution for discovery. Currently, there are six research departments: Embryology in Baltimore, Terrestrial Magnetism and the Geophysical Lab (both in Washington, DC), Astronomy (in Pasadena, California and Las Campanas, Chile), Plant Biology and Global Ecology (both in Stanford, California). A significant portion of the budget is provided from endowment funds supplemented by federal and private grants. The institution is governed by an independent board of trustees.

Please send a brief statement of research interests along with a web site address, CV and bibliography (last five years) to **http://jobs.carnegiescience.edu/emb-director** no later than **March 15, 2014**.

The Carnegie Institution is an Equal Opportunity Employer and encourages applications from women, minorities, and those with disabilities.

Appointment of Vice-Presidents (Research and Technology)
National University of Singapore

The Office of the Deputy President (Research & Technology) (ODPRT) at the National University of Singapore (NUS) (Website: **http://www.nus.edu.sg/dpr/**) is responsible for the development of research and technology across the university, in all disciplinary and cross-disciplinary areas. Direct reports to the Deputy President (Research & Technology) (DPRT) include Director (Research Administration), Director (Humanities & Social Sciences Research), Director (Comparative Medicine), NUS Institutional Review Board (IRB), NUS Institutional Care & Use Committee (IACUC), NUS Graduate School for Integrative Sciences & Engineering, 5 integrative research clusters, and 27 University-level Research Institutes and Centres. ODPRT is also responsible for serving as a liaison with various granting bodies (government, NGOs, industry etc) and for the maintenance of Research Integrity at NUS.

NUS is recruiting one or more additional Vice-Presidents (Research & Technology) to assist the DPRT in managing the above portfolio. Duties will include developing several vibrant innovation clusters across faculties that forge strong links between NUS and industries within and outside Singapore, and leading and coordinating NUS's efforts in competing for major research grants within and outside Singapore.

Candidates should be internationally-recognized leaders in their respective academic fields and be expected to qualify for a Professorship in appropriate Schools/Faculties at NUS. In addition, ideal candidates should have successful track records in research management, including securing major research grants and working extensively with industries. Although we will consider outstanding candidates in all research areas, we are particularly interested to recruit in the Biological/Biomedical/Bioengineering and Physical Science/Engineering/Information Technology areas.

Applications (with a full CV) and informal/confidential enquiries can be sent to the Chair of the Search Committee, Professor Ho Teck Hua (E-mail: **dprhoth@nus.edu.sg**).

Application review will continue until the positions are filled.

Division of Research and Economic Development
Position of Director
Office of Sponsored Research and Programs

Division of Research and Economic Development invites applications for the position of Director, Office of Sponsored Research and Programs (OSRP), which reports to the Vice Chancellor for Research and Economic Development. The OSRP proactively facilitates the pre-award process and oversees certain aspects of post-award grants management. Pre-award activities include providing technical assistance to faculty and staff to ensure continuity in the submission of proposals for grants and contracts to potential funding agencies. Post-award activities include providing regulatory oversight and complete, accurate, and timely financial information pertaining to contract and grant transactions to the University, funding agencies and other external stakeholders.

Master's degree required with a minimum of ten (10) years of experience working with sponsored programs/grants/contracts at a university and/or state and federal levels.

The Division anticipates filling the Position of Director, Office of Sponsored Research and Programs by July 1, 2014; however, review of applications will commence immediately and continue until the position is filled. Applications and/or Nominations may be submitted to: **Ms. Carol J. Hicks, Executive Assistant, Division of Research & Economic Development, Hubbard-Totton Building, Suite 309, North Carolina Central University, 1801 Fayetteville Street, Durham, NC 27707**; or via email **cburne17@nccu.edu**.

The Pulmonary and Critical Care Medicine Division of the Department of Medicine at the University of Maryland School of Medicine is expanding our programs, and has two new exciting opportunities available:

Asthma Research – Seeking a physician scientist at the Associate or full Professor level to join the University of Maryland Asthma Research Program. The selected candidate will direct and grow existing programs, as well as participate in inpatient and outpatient clinical activities. Successful applicants must be BC/BE in pulmonary and critical care medicine and have ongoing NIH-sponsored basic or translational research programs focused on asthma. **Position number 3-309-694**.

Physician Scientist – This position is for an established Pulmonary Critical Care Physician Scientist with an extramurally funded research program focused on asthma, COPD, lung injury or lung fibrosis. The applicant will be expected to relocate his/her funded research program to the University of Maryland and expand the program, mentor students and postdoctoral fellows, and participate in inpatient and outpatient clinical activities at the University of Maryland Medical Center. **Position number 3-309-746**.

This position offers a generous compensation package and an environment supportive of professional development. Interested candidates should submit cover letter, CV and a brief statement summarizing clinical and research interests to **Rhonda Reed (rreed1@medicine.umaryland.edu)** Candidates can learn more about the division from our website **www.umm.edu/pulmonary/index.html**.

The University of Maryland, Baltimore is an Equal Opportunity, Affirmative Action Employer. Minorities, women, veterans and individuals with disabilities are encouraged to apply.

Please reference appropriate position number in your cover letter.

SIMONS FOUNDATION

Director, Math & Science Public Education and Outreach

The Simons Foundation is seeking a part-time Director to oversee its emerging public E&O program in math and science. The E&O Director will report to the President of the Simons Foundation.

The Director will lead a new expanded program initiative, which entails conceptualizing the vision, mission and strategic goals of the foundation's efforts to enhance the public's understanding and appreciation of science and mathematics. The Director should be a distinguished scholar with excellent management skills and convening ability. As a representative of the Simons Foundation, the Director must be an eloquent advocate for greater public understanding and support of science and mathematics. Working with a scientific advisory board, the Director will develop an overarching strategic plan for E&O programs that will position the foundation to accomplish its education and outreach mission. This will include an assessment of the national and New York landscapes of science communications in terms of content, audience and needs; an evaluation of the foundation's present niche within this sphere; the identification of measurable objectives for the foundation and metrics for appraising progress. The Director will oversee the development of a strategic grants portfolio and will identify measures of success. In addition, s/he will represent the foundation among relevant stakeholders including philanthropic partnerships and collaborations. S/he will also oversee Simons Foundation's programmatic activities in this area, including public events and multi-media outreach projects. The Director will oversee *Quanta Magazine*, an independent online publication whose mission is to enhance public understanding of research developments in mathematics and the physical and life sciences.

ESSENTIAL FUNCTIONS/RESPONSIBILITIES:
- Oversight and administration of grants with a programmatic mission to enhance the public's understanding of science.
- Creation and management of a SimonsFoundation.org landing page to feature articles solicited from scientists by the Simons Foundation for publication.
- Oversight and interaction with *Quanta Magazine*, consistent with our agreement of journalistic independence. This includes solicitation of comments from research scientists regarding *Quanta Magazine* articles in order to provide independent feedback to the foundation's management on the site's performance.
- Development of additional in-house or out-sourced media productions that will guarantee the highest quality scientific outreach materials.

MINIMUM QUALIFICATIONS:
- Education: Ph.D. in relevant field of science or mathematics is required.

Experience:
- Demonstrated accomplishments in basic research in a field of mathematics, the physical sciences, or the life sciences
- Significant leadership experience and the capacity to provide a vision of excellence for a growing program or start-up initiative
- Experience communicating and impressing the power and wonder of science or mathematics to diverse audiences
- Excellent track record of strong fiscal management and programming financial resources for achieving meaningful and measurable impact.

Related Skills & Other Requirements:
- Demonstrated experience and success in strategic planning
- Ability to inspire and forge strong collaborative partnerships
- Excellent written and verbal communication skills, including experience with print and online publications
- Grant administration knowledge
- Established ability to manage programs and events

Interested candidates should send their resume and cover letter to: jobs@simonsfoundation.org.

POSITIONS OPEN

ILLINOIS
UNIVERSITY OF ILLINOIS AT URBANA-CHAMPAIGN

POSTDOCTORAL POSITIONS in Enzymology, Microbiology, and Metabolomics

Postdoctoral positions are available for enzymologists, microbiologists, and mass spectrometrists for enzyme and pathway discovery as part of the Enzyme Function Initiative (EFI). The EFI is a Glue Grant from NIGMS/NIH (U54GM093342) with the goal of developing sequence/structure-based strategies for facilitating assignment of in vitro enzymatic and in vivo metabolic functions of unknown enzymes discovered in genome projects, a crucial limitation in genomic biology. This is being accomplished by integrating bioinformatics, structural biology, and computation with enzymology, genetics, and metabolomics. Due to the collaborative and multidisciplinary environment, the EFI provides an opportunity to receive training in several areas. For example, those with a primary interest in microbial genetics can receive training in bioinformatics and/or in metabolomics. More information about the EFI can be found at **website: http://enzymefunction.org** and to apply or request details, please contact **Dr. Katie Whalen** (**e-mail: efi-jobs@enzymefunction.org**).

POSITIONS OPEN

ASSISTANT PROFESSOR
Center for Experimental Therapeutics and Reperfusion Injury
Brigham and Women's Hospital/
Harvard Medical School, Boston, MA

This Center invites applications for a tenure-track Assistant Professor position beginning August 2014. A Ph.D. and/or M.D. will join the Center's research mission. The successful candidate will have demonstrated research programs in lipid mediators in inflammation-resolution. Continued research activities and mentoring are integral to this position. Qualified individuals with postdoctoral training should submit a cover letter and curriculum vitae online at **website: https://research.bwhanesthesia.org/research-groups/cetri/serhan-lab/position.** The names of three references and application should be addressed to **Dr. Simon Gelman,** Search Committee Chair, no later than April 20.

Successful candidates will maintain an independent research program in resolution mechanisms in inflammation and tissue injury.

Harvard Medical School is an Equal Opportunity/Affirmative Action Employer.

POSITIONS OPEN